Macromolecules
PERSPECTIVE

Macromolecules **2011**, *44*, 1–11 **1**
DOI: 10.1021/ma101247c

Block Copolymers for Fuel Cells

Yossef A. Elabd*,† and Michael A. Hickner*,‡

†*Department of Chemical and Biological Engineering, Drexel University, Philadelphia, Pennsylvania 19104, United States, and* ‡*Department of Materials Science and Engineering, Pennsylvania State University, University Park, Pennsylvania 16802, United States*

Received June 4, 2010; Revised Manuscript Received November 7, 2010

ABSTRACT: Ion-containing block copolymers hold promise as next-generation proton exchange membranes in hydrogen and methanol fuel cells. These materials' self-assembled ordered nanostructures facilitate proton transport over a wide range of conditions, a requirement for robust fuel cell performance. In this perspective, we will present an overview of the morphology and transport properties of ion-containing block copolymers that have been studied to gain insight into the fundamental behavior of these materials and, in some cases, are targeted toward applications in fuel cells and other electrochemical devices. We will discuss the challenges associated with predicting and obtaining well-ordered morphologies in block copolymers with high ion content, particularly those with chemistries that can withstand the chemical and mechanical stresses of the fuel cell, such as aromatic backbone block copolymers. New opportunities for ion-containing block copolymers in alkaline membrane fuel cells will also be reviewed.

Introduction

Proton exchange membrane (PEM) fuel cells generate electrical energy directly from a chemical fuel and have attracted considerable interest as alternative power sources for large market applications, such as transportation (hydrogen fuel cells) and portable electronics (methanol fuel cells). The advantages of fuel cells are their high efficiency and power/energy density, low-temperature operation, rapid start-up time, and potential to operate with fuels from renewable sources at a lower environmental cost compared to fossil fuels. The PEM, generally composed of a polymer with covalently tethered ionic groups, is the central component of the fuel cell serving as the electrolyte, conducting protons from the anode to the cathode, where facile transport of protons (conductivity) is directly related to fuel cell power output (Figure 1). However, PEMs currently used in fuel cells exhibit poor transport properties at desired fuel cell operating conditions, such as low proton conductivity at high temperatures (> 80 °C) and low humidities (< 50% RH) in hydrogen fuel cells and high fuel crossover rates at high fuel concentrations in methanol fuel cells.

Typically, the ion-containing polymers used in fuel cells consist of florinated or aromatic backbones with sulfonic acid pendant groups (i.e., sulfonated polymers) that require water solvation for effective proton transport and therefore adequate fuel cell performance. Recently, researchers have made significant advances toward understanding proton and small molecule transport in ion-containing polymer membranes,[1,2] and early experiments revealed that transport properties were in part dependent on polymer morphology or ionic nanostructure.[3,4] Numerous models have been proposed for the structure of sulfonated polymers used in fuel cells.[5−13] Although there are diverse observations and data regarding the detailed morphology of sulfonated polymers, there is a consensus that phase segregation between the ionic groups and polymer backbone occurs to create a nanoscaled morphology of ionic (hydrophilic) and nonionic (hydrophobic) domains. In general, findings show that protons and hydrophilic molecules (e.g., water, methanol, other polar organics) transport through this interconnected solvated ionic network and the transport properties can be highly dependent on the ionic morphology.[14−18]

Over the past decade, many efforts to synthesize new polymers for PEM fuel cells have been reported.[19−23] In all of these sulfonated polymer examples, the ionic nanostructures in terms of their size and connectivity were, in general, poorly controlled. In contrast, self-assembled block copolymers can lead to well-defined nanostructures where the morphology and domain size are tunable on the nanoscopic length scale.[24,25] Ion-containing block copolymers in which only one of the blocks is sulfonated, or contains other types of tethered ions, are attractive because they conjoin the attributes of regular structure and ion conduction where one of the microdomains contains the ionic moiety and facilitates transport, while the other nonionic microdomain provides mechanical support to the membrane. Sulfonated block copolymers are intriguing materials as fuel cell membranes because the combination of ionic and nonionic blocks provides the potential for highly ordered morphologies where transport properties can be tailored in a reliable fashion. Thus, a detailed study of these types of materials may allow researchers to determine the morphological effects on conductivity that are difficult to elucidate for randomly functionalized systems.

Sulfonated block copolymers were first reported in the patent literature in the 1960s.[26,27] In the academic literature, work on sulfonated block copolymers did not appear until the 1990s, where reports during this decade focused on the sulfonation and structural and thermal characterization of styrene-based block copolymers at low ion exchange capacities (IECs; < 0.5 meq g^{-1}).[28−33] One result of interest on lightly sulfonated block copolymers includes work by Wiess and co-workers[34] on sulfonated poly(styrene-*b*-(ethylene-*r*-butylene)-*b*-styrene) revealing coexisting morphological length scales with ∼3−4 nm spacing for the ionic clusters within block copolymer microdomains with ∼20−30 nm spacing. In general, these early reports on sulfonated block copolymers consisted of low IECs (i.e., lightly sulfonated), and transport properties were not measured.

*Corresponding authors. E-mail: elabd@drexel.edu; hickner@matse.psu.edu.

© 2010 American Chemical Society

Published on Web 11/30/2010

Only during the past decade have sulfonated block copolymers with higher IECs (~1−2 meq g^{-1}) been reported and their transport properties studied. Examples include sulfonated poly(styrene-*b*-(ethylene-*r*-butylene)-*b*-styrene),[35,36] sulfonated poly(styrene-*b*-isobutylene-*b*-styrene),[37] sulfonated poly(vinylidene difluoride-*co*-hexafluoropropylene-*b*-styrene),[38] and sulfonated poly(arylene ether)s.[39] A number of recent studies have demonstrated significant enhancement in proton conductivity in sulfonated block copolymers compared to their sulfonated random copolymer counterparts and have shown conductivities across a wide range of temperatures and relative humidity that are higher than Nafion (DuPont; 0.91 meq g^{-1}), the benchmark polymer used in fuel cells.[38,40−44] In this perspective, we will highlight the morphological development in sulfonated block copolymers and observations from the literature on their solid-state structures. Salient examples are shown in Table 1. We will also review findings on how parameters such as block copolymer chain architecture, microdomain size and orientation, crystallinity, and crosslinking affect morphology and subsequently transport properties in these types of materials. Challenges with obtaining well-ordered equilibrium morphologies at high IECs and strategies to obtain improved transport selectivities will be presented. Also, we will discuss new opportunities for ion-containing block copolymers in alkaline membrane fuel cells.

Yossef (Joe) A. Elabd is an associate professor of Chemical and Biological Engineering at Drexel University. He received his Ph.D. in chemical engineering from Johns Hopkins University under the direction of Professor Timothy A. Barbari. Before joining Drexel University, Elabd was a National Research Council postdoctoral fellow at the Army Research Laboratory from 2001−2003. Among other awards, he has received the National Science Foundation CAREER Award, DuPont Science and Engineering Award, and the Army Research Office Young Investigator Award. His research interests include diffusion in polymers, ion-containing polymers, and fuel cells.

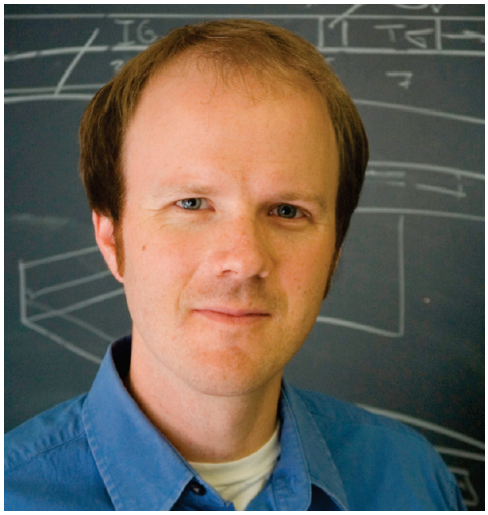

Michael A. Hickner is currently the Virginia S. and Philip L. Walker, Jr. Faculty Fellow and an Assistant Professor of Materials Science and Engineering at The Pennsylvania State University. He earned a B.S. in Chemical Engineering at Michigan Technological University and a Ph.D. in Chemical Engineering at Virginia Tech under the direction of Professor James E. McGrath. He spent time at Los Alamos National Laboratory and Sandia National Laboratories before joining Penn State in 2007. Hickner has received Office of Naval Research and Army Research Office Young Investigator Awards in 2008 and a Presidential Early Career Award in Science and Engineering (PECASE) and 3M Nontenured Faculty Grant in 2009. His research is focused on the synthesis of ion-containing polymers, detailed measurements of water−polymer interactions, and investigations of morphology−transport relationships in polymeric systems.

Sulfonated Block Copolymer Morphology

Flory−Huggins theory and models developed by Helfand and Matsen,[50−53] among others,[54,55] provide accurate predictions of the phase behavior of many block copolymers with a wide variety of chemical constituents. Harnessing the regular arrangement and potential for long-range order of block copolymers to affect fast transport has been a goal for at least the last 20 years.[56] Lately, researchers in the polymer and membrane communities have designed materials with highly ion conductive domains whose size and connectivity are determined by block copolymer phase separated morphology. One early example includes the creation of ion-rich domains in a membrane using a graft copolymer that enhanced the ion conductivity over its random analog (Figure 2).[57] Extensive experimental studies have proven that blocky structures are valuable for enhancing ion transport in many cases, but a fundamental description for rigorously understanding how the presence of tethered ions affects block copolymer morphology has not been worked out. Furthermore, the "ideal" morphological features for creating membranes with the highest attainable ionic conductivity have not yet been determined. Therefore, design of materials with ion-rich domains that transmit ions rapidly across a membrane has been limited to "synthesize and check" strategies and it has been difficult to gauge how close the community has come to achieving the optimized properties of these materials.

Ion clustering and ion repulsion in polymers that have covalently tethered ions to the backbone chain have been studied extensively in ionomers with low ion content[58] and polyelectrolytes with high ion content:[59] the two opposite ends of the ion-containing polymer spectrum. Ionic clusters are known to increase the T_g and mechanical properties of polymers, and ionomers have been used to good effect as structural materials.[60] Generally, morphological observations in ionomers were made on materials with the acid groups neutralized with metal cations.[61,62] Placing ionic moieties on polymer chains in a low dielectric constant medium (such as a polymer melt or nonpolar solvent) has been shown to induce chain aggregation and coil−globule transitions due to ionic monomers exhibiting strong dipolar attraction when the ionic groups are paired.[63,64] Oppositely, soluble polyelectrolytes with high concentrations of ions show expanded conformations, termed the "polyelectrolyte effect," when studied in a high dielectric constant solvent.[65] Sulfonated block copolymers occupy a middle ground between ionomers and polyelectrolytes, where the ion content is reasonably high, but the polymer remains water insoluble. The selective sulfonation of one block and the resulting dipolar and electrostatic interactions

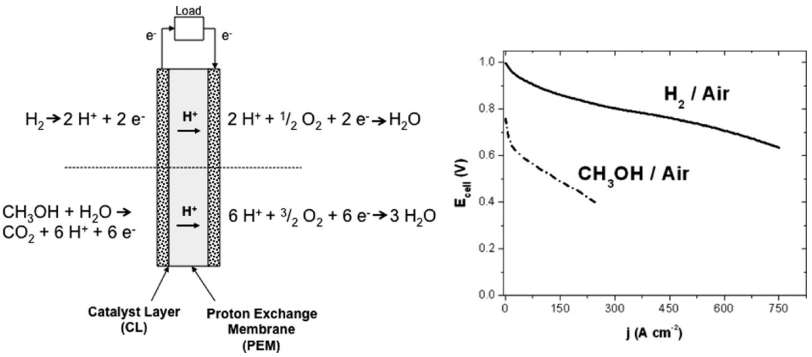

Figure 1. Schematic of PEM fuel cell (left) and polarization curves (cell voltage vs current density; right). Fuel cell schematic shows hydrogen (top) and methanol (bottom) half-cell reactions.

between monomers, depending on the extent of ionization within that block, may cause significant conformational asymmetry in ion-containing block copolymers and, thus, shift the phase diagram in these materials from what one might expect given the volume fractions of the two blocks.[66]

The solubility parameter of styrene sulfonate was measured experimentally by Lu and Weiss[67] to be 34.0 $(J\ cm^{-3})^{-0.5}$, whereas the solubility parameter of styrene is 18.6 $(J\ cm^{-3})^{-0.5}$.[68] This large increase in solubility parameter with sulfonation leads to the formation of very small clusters of ions in lightly sulfonated poly(styrene). The high solubility parameter for sulfonated styrene and the presence of strong dipoles and/or ionized groups calls into question whether Flory−Huggins theory can be used to accurately describe the interactions between the components in the system.

Balsara and co-workers have performed in-depth experimental and simulation studies on sulfonated poly(styrene-*b*-methylbutylene) diblock copolymers to determine the origins of the phase behavior of these polymers in the presence of tethered ions. Through small-angle X-ray scattering (SAXS) order−disorder transition (ODT) measurements and determination of the neutron scattering structure factor of a disordered sample, they estimated the $\chi_{SS\text{-}S}$ (sulfonated styrene−styrene) to be 5.89.[69] They then used this value to describe the phase behavior of sulfonated chains with alternating and blocky sulfonated styrene sequences in modeling studies.[70] The authors did not include dipolar or electrostatic interactions between monomers as the traditional χN description only encompasses dispersion forces and chain length. In the modeling work, they concluded that χ parameters give a general description of the phase behavior of sulfonated block copolymers, but experimentally observed ODTs and order−order transitions (OOT) with $p^2\chi N$ were not replicated in the simulations. The authors postulated that the exact placement of sulfonate groups in the hydrophilic phase may have an effect on the ordering behavior as even small sequences of sulfonated monomers will tend to phase separate from nonionic regions due to their high χ. This work demonstrates, as the authors state, that more sophisticated models incorporating specific ionic and dipolar interactions are needed for quantitative agreement between experiment and simulation for these types of materials.

There are a few studies showing unequivocal evidence of highly ordered ion-containing block copolymers with IECs greater than 1 meq g^{-1}. Examples from Balsara and co-workers[69] include well-ordered phases in sulfonated poly(styrene-*b*-methylbutene). Both microscopy and X-ray scattering provides evidence of microphase separated domains with long-range order in highly sulfonated samples (53 mol % of poly(styrene) block) with high molecular weight (up to 43 kg mol^{-1}). Interestingly, the morphological phases that are predicted by self-consistent mean field theory as a function of volume fraction of the sulfonated phase were not necessarily observed. For instance, sulfonated poly(styrene-*b*-methylbutene) show disordered, lamellar, hexagonal-packed cylinders, hexagonally perforated lammellar, and gyroid phases all within a narrow volume fraction range (0.45−0.5) of sulfonated poly(styrene) as a function of the mol % sulfonation in the styrene phase and molecular weight.[69] In this volume fraction range, conventional block copolmers usually exhibit only lamellae or a disordered morphology. Mauritz et al.[71] observed a morphological transition from hexagonally packed cylinders for an unmodified 70 kg mol^{-1} sulfonated poly(styrene-*b*-(ethylene-*r*-butylene)-*b*-styrene) triblock copolymer with 30 mol % styrene content to lamellae for a 12 mol % sulfonated sample. Mauritz et al.[17] hypothesized a few mechanisms for the morphological shift with sulfonation, including increased interfacial surface tension between the phases resulting from an increase in $\chi_{S\text{-}EB}$. This increase would drive minimization of surface area and thus a transition from cylinders to lamellae. Elabd et al.[42] observed a similar transition in a sulfonated poly(styrene-*b*-isobutylene-*b*-styrene) triblock copolymer (M_n = 48850 g mol^{-1}, 31 wt % styrene) from cylinders to lamellae at low sulfonatation level (degree of sulfonation 13 mol %, ~IEC 0.4 meq g^{-1}) and a second periodic to nonperiodic transition once the IEC reached 1.0 meq g^{-1}, ~40 mol % sulfonation.

Generally, well-ordered morphologies typically observed in nonionic block copolymers have only been demonstrated in sulfonated block copolymers with sulfonation levels at or below 50 mol % and M_n less than 100 kg mol^{-1}.[72] Rubatat et al.[73] and Saito et al.[46] have shown somewhat ordered block copolymer phases in samples with molecular weights of 20−100 kg mol^{-1} and degrees of sulfonation of up to 100 mol %. However, the morphologies obtained in these investigations on high molecular weight systems with high degrees of sulfonation are not as ordered as those discussed above as evidenced by microscopy and scattering studies.

Sulfonated block colymers that do not contain sulfonated styrene moieties, such as aromatic block and segmented copolymers, have also been shown to yield distinct ionic nanophases attributed to phase separation of the hydrophilic and hydrophobic blocks.[49,74,75] These materials are generally synthesized by step-growth polymerization and therefore have polydispersity indices (PDI) that are greater than 2.0. Despite their high PDIs, phase separated morphologies were observed in these materials that could be tuned by altering their chemical composition and the processing conditions during the formation of cast membranes. These types of polymers are more suited for long-term operation in a fuel cell, because the chemical environment (i.e., formation of free radicals) in a fuel cell degrades aliphatic polymers more readily than aromatic polymers. However, their controlled synthesis can be difficult and the lack of highly regular and predictable phases has hampered efforts to quantitatively describe the ordering behavior of these systems. Figure 3 shows examples of microscopy and scattering data from ion-containing block copolymers with varying degrees of order as determined by

Table 1. Examples of Ion-Containing Block Copolymers That Have Been Studied As Proton Exchange Membranes

Chemical Structure	Attributes	Reference
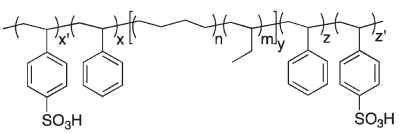	• aliphatic backbone • widely available • low PDI • many unsulfonated reports • extensively studied	Kim et al.[35]
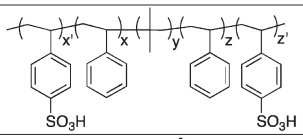	• aliphatic backbone • widely available • low PDI	Elabd et al.[37]
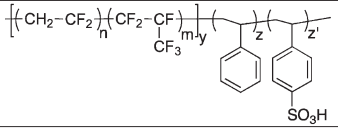	• fluorinated block	Holdcroft et al.[38]
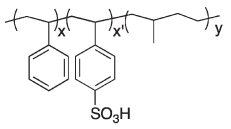	• aliphatic backbone • excellent morphological control • widely tunable synthesis	Balsara et al.[44]
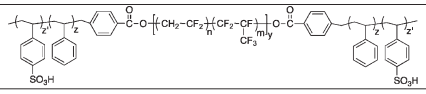	• fluorinated center blocks	Wang et al.[45]
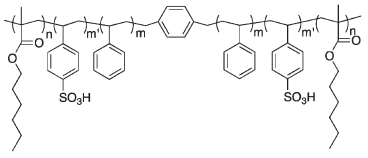	• aliphatic backbone • high molecular weight • sulfonated center blocks	Hickner et al.[46]
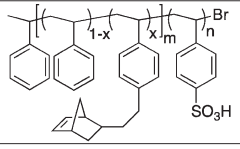	• aliphatic backbone • crosslinkable • latent ionic groups	Hillmyer et al.[47]
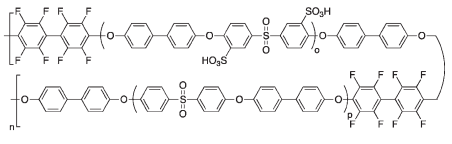	• aromatic backbone • high chemical stability • demonstrated fuel cell performance	McGrath et al.[48]
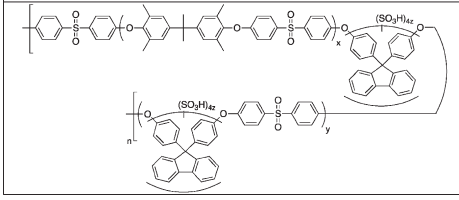	• aromatic backbone • high chemical stability • demonstrated fuel cell performance	Miyatake et al.[49]

transmission electron micrographs and the presence and intensity of higher order SAXS peaks.

Achieving long-range order and testing whether long-range order is necessary for high conductivity in a wide variety of sulfonated block copolymers has proven difficult as most sulfonated polymers show evidence of defects in transmission electron micrographs or have low intensity higher order scattering peaks. Foremost, annealing sulfonated block copolymers to obtain morphologies that approach equilibrium is difficult due to the high T_g of sulfonated poly(styrene). The T_g of poly(styrene) climbs quickly from 105 °C at 0 mol % sulfonation to 160 °C at 20 mol % sulfonation[78] and above 200 °C for high degress of sulfonation. The desulfonation temperature for sulfonated poly(styrene) has been reported to be approximately 220 °C,[79] making it nearly impossible to anneal highly sulfonated block copolymers to an equilibrium morphology without causing chemical degradation. Additionally, aggregation of ion-functionalized chains in solution and limited solubility of hydrophilic−hydrophobic block copolymers can frustrate the development of an equilibrium solid-state morphology during the solution casting process.[80] Thus, observations on the morphological structure of sulfonated block copolymers can be highly sensitive to processing conditions

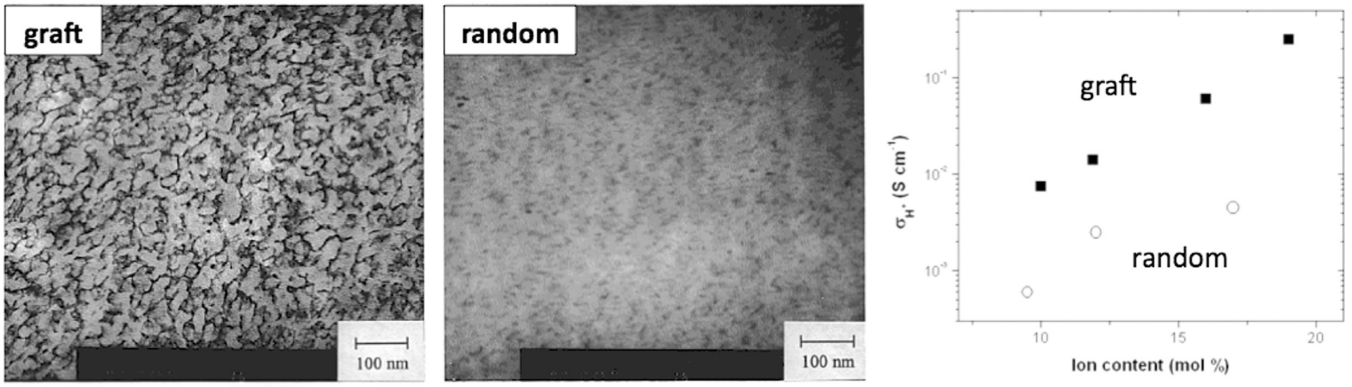

Figure 2. Solid-state morphololgy as evidenced by TEM of Pb^{2+} stained poly(styrene)-*g*-poly(styrene sulfonate) (left) and poly(styrene)-*r*-poly(styrene sulfonate) (center) copolymers and proton conductivity (σ_{H+}; right) for the two copolymers showing that graft copolymers with connected ion-rich nanodomains have increased conductivity.[57]

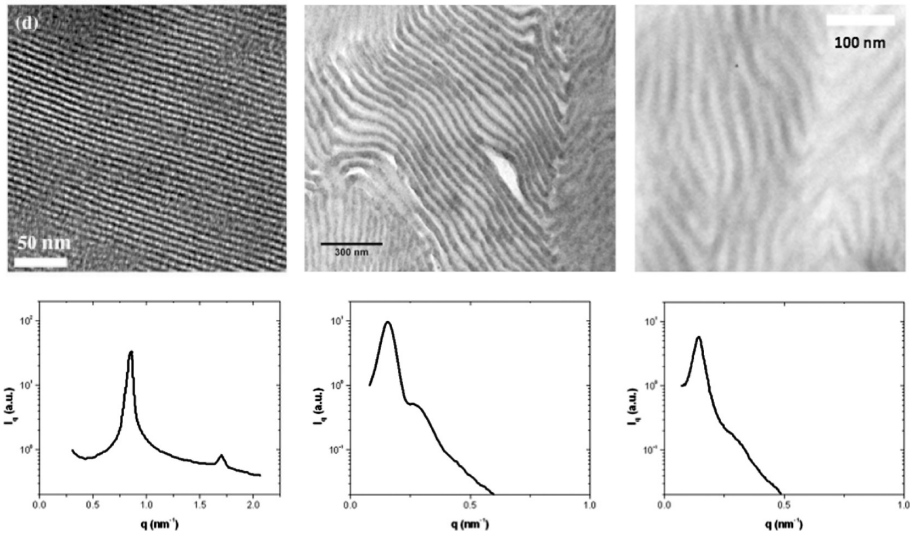

Figure 3. Transmission electron micrographs and small-angle X-ray scattering data for sulfonated poly(styrene-*b*-methylbutene) 3.1−2.6 kg mol^{-1}, 21 mol % sulfonation (left column),[69] sulfonated poly(hexylmethacrylate-*b*-styrene-*b*-hexylmethacrylate) 58.6−69.1−58.6 kg mol^{-1}, 100 mol % sulfonation (middle column), reproduced from ref 76 by permission of The Royal Society of Chemistry, and sulfonated poly(arylene ether sulfone) 15−15 kg mol^{-1} segmented multiblock, 100 mol % sulfonation (right column), reprinted from ref 77 with permission from Elsevier.

and methods such as thermal or vapor annealing have not been widely employed for these materials. While there are still details to uncover to allow for predictive design of sulfonated block copolymers with specific characteristics, the morphologies observed in sulfonated block copolymers do, in some cases, lead to superior transport properties as detailed in the sections below.

Block Copolymers in Hydrogen Fuel Cells

In the hydrogen fuel cell, ion-containing polymer membrane requirements include chemical and mechanical stability over a wide range of temperatures and the membrane must also exhibit sufficient proton conductivity at low water content. The proton conductivity of typical sulfonated polymers is highly dependent on water content, with values on the order of 10^{-1} S cm^{-1} when fully saturated, but decreases by orders of magnitude at lower water contents. There are numerous advantages to operating the fuel cell at higher temperatures and lower humidities, such as increasing catalytic activity, reducing cathode flooding, and eliminating the need for external humidification equipment. At higher temperatures, sulfonated polymers can dehydrate or their domain structure can become phase-mixed or disordered,[81] thus, reducing proton conductivity and cell performance.[82,83] Therefore, understanding water−polymer interactions and developing new ion-containing polymers that can conduct protons at higher temperatures (> 80 °C) and lower humidities is desired.

Similar to most sulfonated polymers, sulfonated block copolymers exhibit increases in proton conductivity with IEC and water content. Due to their distinct ionic domain structure, block copolymers generally have different relationships between IEC, water content, and proton conductivity compared to their random copolymer counterparts. Figure 4 shows proton conductivity as a function of hydration number (λ, the moles of water per moles of sulfonic acid moiety) for Nafion, block, and random copolymers at 80 °C. This data confirms the previous studies of Holdcroft et al. that showed a conductivity increase for blocky polymer architectures.[57] The data also highlights the importance of considering the hydration of the sample, as water uptake is a key determinant of proton conductivity. The figure shows that the block copolymer has a lower conductivity than Nafion at low hydration, but at hydration numbers greater than 4−5, the conductivity of the block copolymer exceeds that of Nafion. This trend is likely due to the higher acidity of the perfluorosulfonic acid groups in Nafion, which promote high conductivity at low hydration numbers, as compared to the aryl sulfonic acid groups in the aromatic block copolymer. At high hydration, where the acidity difference is less important, the ionic domain structure of the block copolymer yields higher conductivity than Nafion.

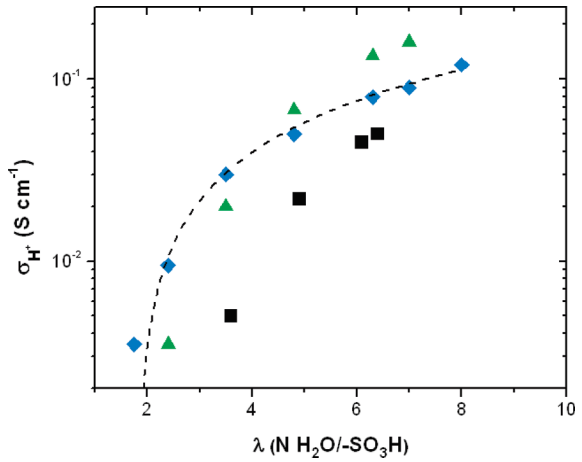

Figure 4. Proton conductivity as a function of hydration number for Nafion (blue diamond) and aromatic random (black square) and block (green triangle) copolymers at 80 °C.[43]

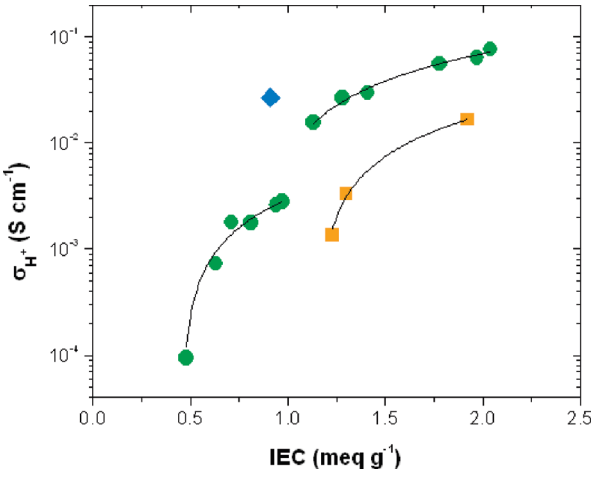

Figure 5. Room-temperature through-plane conductivity for Nafion (blue diamond), sulfonated poly(styrene-*b*-isobutylene-*b*-styrene) (green circle), and sulfonated poly(styrene) (orange square).[42]

Changes in morphology with sulfonation or hydration[44] can lead to large alterations of transport properties. For example, the work of Elabd et al.[42] on sulfonated poly(styrene-*b*-isobutylene-*b*-styrene) revealed morphological transitions from periodic lamellar morphology preferentially oriented in the plane of the membrane (anisotropic) at IECs ranging from 0.5 to 1 meq g^{-1} to a nonperiodic cocontinuous morphology (isotropic) at IECs ranging from 1.1 to 2 meq g^{-1}. This morphological transition resulted in a discontinuous abrupt increase in conductivity with increasing IEC (Figure 5). Similarly, work by Kim et al.[84] revealed a morphological transition in sulfonated poly(styrene-*b*-(ethylene-*r*-butylene)-*b*-styrene) from periodic lamellar to a nonperiodic structure with a change in casting solvent from tetrahydrofuran (THF) to a THF/methanol mixture. The observed transition coincided with a 1 order of magnitude increase in proton conductivity without a change in IEC. Further work by Elabd et al.[42] also showed that proton conductivity can change by 3 orders of magnitude in sulfonated poly(styrene-*b*-isobutylene-*b*-styrene) due to changes in morphology induced by solution casting from different toluene/alcohol mixtures, again, without changing the ion content of the polymer. These results demonstrate that sulfonation of block polymers can disrupt the phase behavior of the nonionic base material, presumedly due to the increase in the effective χ of the sulfonated block and possible changes in the sulfonated block chain conformation. Moreover, these morphologies are sensitive to casting solvent and can result in a variety of nonperiodic kinetically trapped nonequilibrium morphologies that impact transport properties. Morphologies of highly sulfonated block copolymers are difficult to predict and equilibrium states are not readily obtained. But, it is of great interest to understand and control these structures because they have a significant effect on proton conductivity.

Both Figures 4 and 5 highlight that sulfonated block copolymers exhibit enhanced proton conductivity compared to other sulfonated polymer architectures (e.g., random copolymers) at similar IECs and water contents. This connection between morphology and transport properties was also shown by Shi and Holdcroft[38] in their work on sulfonated poly([vinylidene difluoride-*co*-hexafluoropropylene]-*b*-styrene), where higher conductivities were observed compared to both random and graft copolymers of sulfonated poly(styrene) at the same IEC. Also, higher conductivities were reported in the fluorinated block copolymer compared to other nonfluorinated sulfonated block copolymers (e.g., sulfonated poly(styrene-*b*-(ethylene-*r*-butylene)-*b*-styrene)). Transmission electron microscopy (TEM) of these materials showed an interconnected phase-separated morphology with ion channels on the order of 8−15 nm. Many other investigators have reported greater absolute proton conductivities in sulfonated block copolymers and the strategy of creating ionic phase separated morphologies with block copolymers is now considered one of the routes to advanced PEMs.[38,40−44]

McGrath et al.[41,85] have shown that higher water diffusion coefficients in block copolymers is one of the mechanisms by which block copolymers achieve higher conductivity compared to their random analogs. These authors found that NMR pulsed-field gradient water self-diffusion coefficients were not a function of diffusion length at long diffusion times in block systems and in Nafion, whereas random architectures had steadily decreasing water self-diffusion coefficients with diffusion length. Thus, block copolymers, in addition to concentrating ionic groups in a highly sulfonated domain, seem to have an influence on the water behavior, which is intimately tied to their proton conduction properties.

Both the orientation and size of block microdomains have been shown to impact proton conductivity. For example, an order of magnitude difference was observed when comparing in-plane and through-plane conductivities for sulfonated poly(styrene-*b*-isobutylene-*b*-styrene) with anisotropic lamellae oriented in the plane of the membrane.[86] Park and Balsara were able to obtain both lamellar morphologies oriented in the plane (by hot pressing) and perpendicular to the plane (by both E-field and flow alignment) of the membrane.[87] They observed a difference in conductivity measured in two different directions for the samples with lamellae oriented in the plane, but not for those perpedicular to the plane. They suggested a possible lack of connectivity across misaligned microdomains in the samples with lamellae perpedicular to the plane to be the reason for no observed difference in directional conductivity. Park et al.[44] showed that proton conductivity improves under hot (90 °C) and dry (50% RH) conditions in sulfonated poly(styrene-*b*-methylbutene) for microdomain sizes below 5 nm. Chen et al.[47] work on cross-linked poly(norbornenylethylstyrene-*s*-styrene)-poly(*n*-propyl-*p*-styrene-sulfonate) block polymers confirms these results where conductivity improved for microdomains below 5 nm in size. In addition to these microdomain effects, Uehara et al.[88] recently showed that crystallinity in the nonconductive microdomain of sulfonated poly(ethylene-*b*-styrene) can alter the conductivity−water uptake relationship. This last example suggests that changes to the nonionic block microdomain can also affect proton transport.

Block Copolymers in Methanol Fuel Cells

Similar to hydrogen fuel cells, methanol fuel cells produce electrical energy directly from a chemical fuel, but instead of employing hydrogen gas as the fuel, a liquid solution of methanol and water is fed to the anode (see Figure 1). Although methanol fuel cells have energy densities double that of current lithium-ion rechargeable batteries at an overall efficiency of only ~20−25%, there are a number of critical factors that hinder the methanol fuel cell from reaching its maximum theoretical efficiency (100%).[89] One key limitation of methanol fuel cell operation is high methanol flux (also referred to as methanol crossover) in currently employed ion-containing polymer membranes, which contributes to low overall cell power, efficiency, and lifetime.[90,91] Although common sulfonated polymers exhibit the desired high water-saturated proton conductivities, these materials also possess undesired high methanol permeabilities (~10^{-6} cm^2/s). When methanol permeates at this rate across the polymer membrane in the fuel cell, the catalytic reaction of methanol at the cathode competes with oxygen reduction resulting in a mixed potential and a loss of fuel. Therefore, low methanol fuel concentrations of ~1−2 M are typically fed to the anode instead of the desired equimolar (~17 M) anode half-cell reaction concentration, because methanol flux increases significantly with increasing methanol concentration.[92] If the methanol flux across the membrane was drastically reduced, higher methanol fuel concentrations could be used, which would result in significantly higher cell voltages and power densities. In response to the methanol crossover problem, a variety of new ion-containing polymer membranes have been synthesized, with the goal of high proton conductivity coupled with high methanol resistance (i.e., high selectivity).[22]

In regard to transport phenomena in polymers for methanol fuel cells, the transport of protons, water, and methanol occur in the polymer simultaneously, where various gradients (i.e., driving forces) and molecular interactions are present. In practice, generally only two primary experimental measurements are conducted on newly developed ion-containing polymer membranes for methanol fuel cells: proton conductivity and methanol permeability, where the aim is both high proton conductivity and high proton/methanol selectivity. Selectivity, α, has been defined as a ratio of the measured proton conductivity and methanol permeability:[93]

$$\alpha = \frac{\sigma_p}{P_m} = \frac{D_p C_p F^2}{D_m K_m RT} \quad (1)$$

where proton conductivity, σ_p, described by the Nernst−Einstein equation, is linearly proportional to the proton diffusion coefficient, D_p, and the concentration of protons in the polymer, C_p. Methanol permeability is the product of the methanol diffusion coefficient, D_m, and the methanol partition coefficient, K_m. Increasing selectivity in PEMs is a challenge since several of the factors in eq 1 are interdependent and linked through the chemical composition, hydration state, and morphology of the PEM. Equation 1 is a simplified view of the problem, where in reality, the transport of protons, water, and methanol in an ionic polymer membrane in a methanol fuel cell is complex and includes multiple concentration gradients (multicomponent diffusion: the effect of the concentration gradient of each component on the flux of the other), molecular scale interactions (hydrogen bonding and ionic interactions between protons, water, methanol, and the polymer), and an electrical potential gradeint. Although all of the these mechanisms have not yet been fully explored, numerous investigations have reported general transport trends, where increasing ion content (IEC) usually results not only in increased water content and proton conductivity, but also in increased methanol permeability. In other words, most investigations report that proton and methanol transport usually increase or decrease simultaneously in sulfonated polymers due to the coupled nature of IEC and water uptake making it difficult to achieve high selectivities at high proton conductivities.[22]

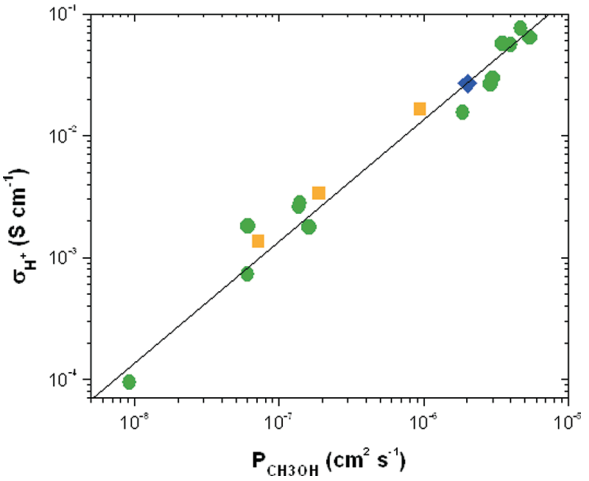

Figure 6. Room-temperature through-plane conductivity vs methanol permeability for Nafion (blue diamond), sulfonated poly(styrene-*b*-isobutylene-*b*-styrene) (green circle), and sulfonated poly(styrene) (orange square).[42]

Several sulfonated block copolymers have been explored in regard to their performance in a methanol fuel cell.[86] Although the morphological benefits of block copolymers have resulted in enhanced proton transport compared to other polymer architectures, these results have usually not translated into higher selectivities. For example, numerous reports on sulfonated styrene-based block copolymers have demonstrated improved proton conductivity with changes to morphology by changing IEC or casting solvent as described in the previous section. However, these changes also coincided with simultaneous increases in methanol permeability with no significant change in selectivity. Figure 6 shows the proton conductivity and methanol permeability of sulfonated poly(styrene-*b*-isobutylene-*b*-styrene) compared to a random copolymer sulfonated poly(styrene) and Nafion. All of the sulfonated polymers have a similar selectivity regardless of IEC, water content, polymer chemistry, chain architecture, or morphology. This conductivity/permeability trade-off has also been observed in many other PEMs, including block and random copolymers.

Recently, Hallinan and Elabd[94] demonstrated the measurement of multicomponent diffusion and sorption of methanol/water mixtures in a sulfonated polymer using time-resolved Fourier transform infrared-attenuated total reflectance spectroscopy. These results quantitatively show that the primary contributing factor to the increase in methanol flux (with increasing methanol solution concentration) is methanol sorption (i.e., partitioning) in the polymer and not methanol diffusion. This suggests that future polymer synthesis strategies should focus on developing ion-containing polymers that sorb less methanol as opposed to creating morphological obstacles to retard methanol diffusivity.

These results were supported by Won et al.[95] in their work on cross-linked sulfonated poly(styrene-*b*-butadiene-*b*-styrene), which demonstrated the combination of high water-saturated proton conductivities and high selectivities. They reported selectivity an order of magnitude higher than un-cross-linked sulfonated block polymer and Nafion. Also, their data demonstrated higher proton conductivities (by orders of magnitude) when compared to a cross-linked random coplymer of sulfonated poly(styrene-*r*-butadiene). They postulated that cross-linking

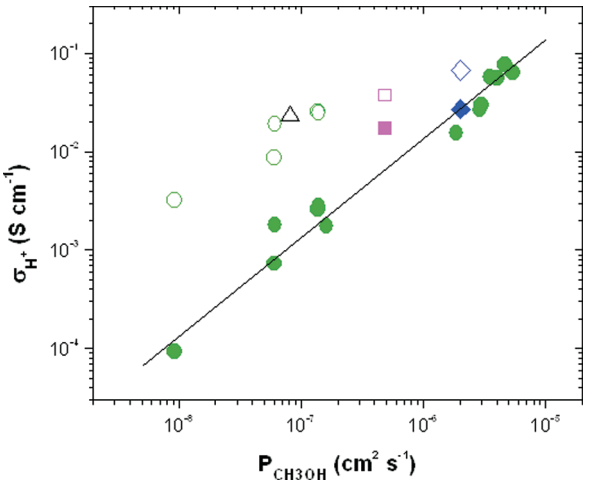

Figure 7. Room-temperature in-plane (open symbols) and through-plane (closed symbols) conductivity vs methanol permeability for Nafion (blue diamond), sulfonated poly(styrene-*b*-isobutylene-*b*-styrene) (green circle),[42] cross-linked sulfonated poly(styrene-*b*-(ethylene-*r*-butylene)-*b*-styrene) (black diamond),[95] and cross-linked poly(norbornenylethylstyrene-*s*-styrene)-poly(*n*-propyl-*p*-styrenesulfonate) (pink square).[47]

the nonconducting block minimized swelling in the conducting block upon exposure to solvents and therefore sorbed less methanol while mainting high water-saturated proton conductivities. Their hypothesis was confirmed with no observable change between dry and wet X-ray scattering, where a change in microdomain spacing was observed for the un-cross-linked sulfonated block copolymer. Also, this study showed a clear advantage compared to a random copolymer, where the cross-linked sulfonated block copolymer exhibited both high selectivity and conductivity, while the random copolymer had significantly reduced proton conductivity.

Ishikawa et al.[96] supported these findings with their studies of cross-linked multiblock copolymers of sulfonated poly(aryl ether ketone), where the methanol crossover rate was reduced without decreasing proton conductivity. Their results also showed improvements over the cross-linked random copolymer. These data were further supported in work by Chen et al.[47] on cross-linked poly(norbornenylethylstyrene-*s*-styrene)-poly(*n*-propyl-*p*-styrenesulfonate) block polymers, where lower methanol permeability was reported, while high proton conductivity was maintained. These results suggest that the combination of an ordered block copolymer morphology with a nonswellable ion conductive block can result in the desired combination of high proton conductivity and high proton/methanol selectivity. Figure 7 shows how the cross-linked sulfonated block copolymers developed by Won et al.[95] and Chen et al.[47] deviate from this proton/methanol trade-off.

Figure 7 also demonstrates the difference between two proton conductivity measurement techniques: in-plane (usually measured using four electrodes in the plane of the membrane; open symbols) and through-plane (measured using two electrodes through the plane of the membrane; solid symbols). There is approximately a 2-fold difference in conductivity for Nafion (isotropic morphology) reported between these measurement techniques, which is likely a product of interfacial resistance being a large fraction of the total resistance in the two-electrode, through-plane measurement.[86,97] However, the through-plane measurement is more applicable to fuel cell operation, where proton transport across the thin dimension of the membrane is most important. Therefore, the differences between these techniques should be considered more carefully when investigating PEMs with anisotropic morphologies. For example, the data in Figure 7 shows in-plane measurements for sulfonated poly-

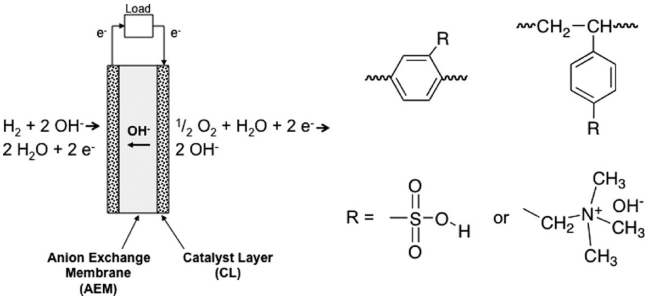

Figure 8. Half reactions of the alkaline fuel cell (left) and chemical motifs for attaching sulfonate or quaternary ammonium moieties onto a main-chain aromatic polymer or incorporating these groups into a polymer through styrene residues.

(styrene-*b*-isobutylene-*b*-styrene) triblock copolymers with lamellar microdomains preferentially oriented in the plane of the membrane, which resulted in proton conductivities and selectivities an order of magnitude higher than through-plane measurements.[86] Won et al.[95] data on cross-linked sulfonated poly(styrene-*b*-(ethylene-*r*-butylene)-*b*-styrene) was similar. They reported only in-plane measurements on cylindrical morphology samples (with no information about microdomain orientation provided). Chen et al.[47] work on cross-linked poly(norbornenylethylstyrene-*s*-styrene)-poly(*n*-propyl-*p*-styrenesulfonate) block polymers showed minimal difference between in-plane and through-plane measurements due to an isotropic bicontinuous microphase-separated morphology. Note that caution should be taken when comparing these two techniques as through-plane measurements on thin membranes will often produce erroneous results. There must be a large enough separation between electrodes for the bulk resistance of the membrane to override the other resistances in the system (e.g., interfacial resistance).

Block Copolymers in Other Aqueous Electrochemical Cells

In the past decade, hydrogen and methanol fuel cells have driven the majority of work in the design and understanding of ion-containing block copolymer membranes. However, other aqueous-based electrochemical cells where these materials could be of significant importance include electrolyzers,[98,99] electrodialysis units,[100,101] and alkaline fuel cells. Here, we will discuss the application of one of the most pressing concerns in our view: the alkaline membrane fuel cell (Figure 8). Traditionally, alkaline fuel cells are the best performing fuel cells at temperatures below 200 °C and can operate with a number of different fuels, such as hydrogen, methanol, and ethanol. Most significant is that alkaline fuel cells do not require the use of precious metal catalysts as with acid-based electrolyte fuel cells, but can operate with cheaper non-noble metal catalysts (e.g., nickel). The main difficulty with traditional liquid electrolyte alkaline fuel cells relates to the use of potassium hydroxide, which can result in leakage, system corrosion, and ionic conductivity degradation by reaction with CO_2. If one could replace the liquid electrolyte with an ion-containing solid polymer membrane that can conduct hydroxide ions (i.e., an anion exchange membrane), the problems with electrolyte leakage and carbonate precipitation would be eliminated.[102] Several research groups have demonstrated a working alkaline fuel cell with an anion exchange membrane, but there is considerable potential to improve the performance of these devices and dramatically lower the cost of fuel cells.[103,104]

To fast-track the alkaline membrane fuel cell device development, several key membrane hurdles must be overcome, namely, improving chemical and mechanical stability and hydroxide conductivity in polymer membranes to produce high power density devices with long operational lifetimes. To date, only a few

hydroxide conducting block copolymers have been reported, such as quaternized poly(styrene-*b*-vinylbenzylchloride-*b*-styrene) and quaternized poly(styrene-*b*-(ethylene-*r*-butylene)-*b*-styrene).[105,106] Although no morphological evidence was reported in these studies, the block structure of these materials may provide opportunities for enhanced conductivity and selectivity in anion-conducting membranes. Figure 8 shows general structures for incorporation of sulfonate or quaternary ammonium groups into polymer backbones through tethering to main-chain aromatic polymers or by employing functionalized styrene moieties, the two most common polymer-ion linkages employed for PEMs and AEMs. As with PEMs, the synthetic control afforded by styrenic moieties in the synthesis of block copolymers has promted the use of these types of monomers for initial studies of block copolymer AEMs. However, the stability of these types of polymers in a fuel cell environment remains under investigation. While there are limited choices for the proton-bearing group in proton exchange membranes, there are many possibilities for the fixed cation in anion exchange membranes. Quaternary ammonium is the most commonly reported cation so far, but phosphonium,[107] guanadinium,[108] and other cations[109] may prove useful in these types of systems.

Outlook

Studies of ion-containing block copolymers have provided clear evidence that the phase segregation between hydrophilic and hydrophobic phases can produce materials with superior ionic conductivity, which is important for performance improvements in fuel cells and other aqueous electrochemical devices. To advance the field further, there must be continued development of theoretical and simulation tools to describe and predict phase separation of these systems with strong dipoles and ionic moieties and gain fundamental insights on their interactions with water. Well-defined block copolymers with low polydispersity indices and controlled placement of sulfonate groups have proven to be useful model systems and observations from various research groups have raised interesting questions as to whether ionic systems can be treated like traditional nonionic block copolymers. The initial work to translate the models developed for nonionic block copolymers to ion-containing materials must be furthered by characterizing equilibrium morphologies of ion-containing block copolymers, if they can be achieved, and continuing to refine the understanding of the mechanisms that determine the morphological development in these systems. Approaching equilibrium morphologies remains a challenge in ion-containing block copolymers and theoretical descriptions of the phase formation in the presence of ions and strong dipoles are needed. The importance of long-range order and the role of grain boundaries in the conduction of ions across micrometer length scales need further attention. Alignment of ordered morphologies improves the conductivity of membranes to a certain extent, but the microscopic details of how protons traverse grain boundaries and tortuosity effects of the ionic domains on proton transport require further study.

Complementary synthetic and simulation studies of materials with greater polydispersity and chemical diversity are needed to advance the basic knowledge surrounding material sets that can withstand the electrochemical stress and high temperatures of fuel cells. Model block copolymers containing sulfonated styrene residues will not withstand the conditions in many fuel cell devices. High molecular weight, highly sulfonated aromatic polymers have shown promising performance in hydrogen and direct methanol fuel cells and display chemical and mechanical stability that may be sufficient for widespread use as proton exchange membranes. Therefore, more fundamental work in understanding the self-assembly and development of long-range, well-ordered morphologies of aromatic ion-containing block copolymers is needed. These types of polymers are difficult to simulate due to the large numbers of atoms involved in a complete description of the material, and so far there is no predictive capability for guiding the design of aromatic block copolymers. Moreover, their synthesis is not as well controlled as with living polymerization methods, which can deter researchers from undertaking complicated synthetic and morphological studies and generating the needed experimental data to prompt theoretical and simulation work. Synthetic methods that combine aspects of controlled monomer/functional group placement and chemical robustness are needed to bring together the superior morphological structure of low PDI styrene-based block copolymers and the device performance advantages of aromatic polymers.

Conclusions

The benefits of the block copolymer strategy for fuel cell membranes have been highlighted. Specifically, the block copolymer sequential chain architecture and microdomain size and orientation have been shown to significantly improve proton conductivity compared to random copolymer analogs. So far, only cross-linking the nonionic block microdomain in ion-containing block copolymers has shown to improve proton/methanol selectivity. This approach has resulted in some of the highest proton/methanol selectivities reported for sulfonated polymer membranes. It is clear that ordered morphologies impact transport properties and the application of these results can impact hydrogen and methanol fuel cell performance. To realize these material advances in devices, a more thorough fundamental understanding of predicting and controlling block copolymer morphology in ion-containing block copolymers should be pursued.

Acknowledgment. Y.A.E. gratefully acknowledges support from the National Science Foundation (CBET-0644593), the U.S. Army Research Office (W911NF-07-1-0452; W911NF-07-1-0149), and the U.S. Army Research Laboratory Materials Center of Excellence (W911NF-06-2-0013). M.A.H. thanks the Penn State Materials Research Institute, the Penn State Institutes of Energy and the Environment, the U.S. Army Research Office (W911NF-08-1-0282), the U.S. Office of Naval Research (N00014-08-1-0730), and the U.S. National Science Foundation (CBET-0932740) for support.

References and Notes

(1) Kreuer, K.-D.; Paddison, S. J.; Spohr, E.; Schuster, M. *Chem. Rev*. **2004**, *104*, 4637–4678.
(2) Kreuer, K.-D. *J. Membr. Sci*. **2001**, *185*, 29–39.
(3) Eisenberg, A.; King, M. *Ion Containing Polymers: Physical Properties and Structure*; Academic Press: New York, 1977.
(4) Hsu, W. Y.; Barkley, J. R.; Meakin, P. *Macromolecules* **1980**, *13*, 198–200.
(5) Yeo, R. S.; Yeager, H. L. Structural and Transport Properties of Perfluorinated Ion-Exchange Membranes. In *Perfluorinated Ionomer Membranes*; Eisenberg, A., Yeager, H. L., Eds.; American Chemical Society: Washington, D.C., 1980; pp 437−505.
(6) Yeager, H. L.; Steck, A. A. *J. Electrochem. Soc*. **1981**, *128*, 1880–1884.
(7) Hsu, W. Y.; Gierke, T. D. *J. Membr. Sci*. **1983**, *13*, 307–326.
(8) Gebel, G. *Polymer* **2000**, *41*, 5829–5838.
(9) Elliott, J. A.; Hanna, S.; Elliot, A. M. S.; Cooley, G. E. *Macromolecules* **2000**, *33*, 4161–4171.
(10) Rubatat, L.; Gebel, G.; Diat, O. *Macromolecules* **2004**, *37*, 7772–7783.
(11) Page, K. A.; Landis, F. A.; Phillips, A. K.; Moore, R. B. *Macromolecules* **2006**, *39*, 3939–3946.
(12) Kim, M.-H.; Glinka, C. J.; Grot, S. A.; Grot, W. G. *Macromolecules* **2006**, *39*, 4775–4787.
(13) Schmidt-Rohr, K.; Chen, Q. *Nat. Mater*. **2008**, *7*, 75–83.

(14) Mauritz, K. A.; Moore, R. B. *Chem. Rev.* **2004**, *104*, 4535–4585.
(15) Gronowski, A. A.; Jiang, M.; Yeager, H. L.; Wu, G.; Eisenberg, A. *J. Membr. Sci.* **1993**, *82*, 83–97.
(16) Matsuyama, H.; Teramoto, M.; Tsuchiya, M. *J. Membr. Sci.* **1996**, *118*, 177–184.
(17) Tongwen, X.; Weihua, Y.; Bingling, H. *Chem. Eng. Sci.* **2001**, *56*, 5343–5350.
(18) Elabd, Y. A.; Napadensky, E.; Sloan, J. M.; Crawford, D. M.; Walker, C. W. *J. Membr. Sci.* **2003**, *217*, 227–242.
(19) Roziere, J.; Jones, D. J. *Annu. Rev. Mater. Res.* **2003**, *33*, 503–555.
(20) Rikukawa, M.; Sanui, K. *Prog. Polym. Sci.* **2000**, *25*, 1463–1502.
(21) Souzv, R.; Ameduri, B. *Prog. Polym. Sci.* **2005**, *30*, 644–687.
(22) Deluca, N. W.; Elabd, Y. A. *J. Polym. Sci., Part B: Polym. Phys.* **2006**, *44*, 2201–2225.
(23) Hickner, M. A.; Ghassemi, H.; Kim, Y. S.; Einsla, B. R.; McGrath, J. E. *Chem. Rev.* **2004**, *104*, 4587–4612.
(24) Bates, F. S.; Fredrickson, G. H. *Phys. Today* **1999**, 32–38.
(25) Ruzette, A.-V.; Leibler, L. *Nat. Mater.* **2005**, *4*, 10–31.
(26) Quisenberry, R. K.; Pacofsky, E. A. U.S. Patent 3,317,632, May 2, 1967.
(27) Winkler, D. E. U.S. Patent 3,577,357, May 4, 1971.
(28) Gouin, J. P.; Williams, C. E.; Eisenberg, A. *Macromolecules* **1989**, *22*, 4573–4578.
(29) Lu, X.; Steckle, W. P.; Weiss, R. A. *Macromolecules* **1993**, *26*, 5876–5884.
(30) Venkateshwaran, L. N.; York, G. A.; DePorter, C. D.; McGrath, J. E.; Wilkes, G. L. *Polymer* **1992**, *33*, 2277–2286.
(31) Storey, R. F.; Chisholm, B. J.; Lee, Y. *Polym. Eng. Sci.* **1997**, *37*, 73–80.
(32) Blackwell, R. I.; Mauritz, K. A. *Polymer* **2004**, *45*, 3457–3463.
(33) Kwee, T.; Taylor, S. J.; Mauritz, K. A.; Story, R. F. *Polymer* **2005**, *46*, 4480–4491.
(34) Weiss, R. A.; Sen, A.; Pottick, L. A.; Willis, C. L. *Polymer* **1991**, *32*, 2785–2792.
(35) Kim, J.; Kim, B.; Jung, B. *J. Membr. Sci.* **2002**, *207*, 129–137.
(36) Edmondson, C. A.; Fontanella, J. J.; Chung, S. H.; Greenbaum, S. G.; Wnek, G. E. *Electrochim. Acta* **2001**, *46*, 1623–1628.
(37) Elabd, Y. A.; Napadensky, E.; Sloan, J. M.; Crawford, D. M.; Walker, C. W. *J. Membr. Sci.* **2003**, *217*, 227–242.
(38) Shi, Z. Q.; Holdcroft, S. *Macromolecules* **2005**, *38*, 4193–4201.
(39) Ghassemi, H.; McGrath, J. E.; Zawodzinski, T. A. *Polymer* **2006**, *47*, 4132–4139.
(40) Yang, Y.; Shi, Z.; Holdcroft, S. *Macromolecules* **2004**, *37*, 1678–1681.
(41) Roy, A.; Hickner, M. A.; Yu, X.; Li, Y.; Glass, T. E.; McGrath, J. E. *J. Polym. Sci., Part B: Polym. Phys.* **2006**, *44*, 2226–2239.
(42) Elabd, Y. A.; Napadensky, E.; Walker, C. W.; Winey, K. I. *Macromolecules* **2006**, *39*, 399–407.
(43) Bae, B.; Miyatake, K.; Watanabe, M. *ACS Appl. Mater. Int.* **2009**, *1*, 1279–1286.
(44) Park, M. J.; Downing, K. H.; Jackson, A.; Gomez, E. D.; Minor, A. M.; Cookson, D.; Weber, A. Z.; Balsara, N. P. *Nano Lett.* **2007**, *7*, 3547–3552.
(45) Xu, K.; Li, K.; Khanchaitit, P.; Wang, Q. *Chem. Mater.* **2007**, *19*, 5937–5945.
(46) Saito, T.; Moore, H. D.; Hickner, M. A. *Macromolecules* **2010**, *43*, 599–601.
(47) Chen, L.; Hallinan, D. T., Jr.; Elabd, Y. A.; Hillmyer, M. A. *Macromolecules* **2009**, *42*, 6075–6085.
(48) Lee, H.-S.; Roy, A.; Lane, O.; Dunn, S.; McGrath, J. E. *Polymer* **2008**, *49*, 715–723.
(49) Bae, B.; Miyatake, K.; Watanabe, M. *Macromolecules* **2010**, *43*, 2684–2691.
(50) Helfand, E.; Wasserman, Z. R. *Macromolecules* **1976**, *9*, 879–888.
(51) Matsen, M. W.; Schick, M. *Macromolecules* **1994**, *27*, 6761–6767.
(52) Matsen, M. W.; Schick, M. *Macromolecules* **1994**, *27*, 7157–7163.
(53) Matsen, M. W.; Schick, M. *Phys. Rev. Lett.* **1994**, *72*, 2660–2663.
(54) Matsen, M. W.; Bates, F. S. *Macromolecules* **1996**, *29*, 1091–1098.
(55) Leibler, L. *Macromolecules* **1980**, *13*, 1602–1617.
(56) Csernica, J.; Baddour, R. F.; Cohen, R. E. *Macromolecules* **1987**, *20*, 2468–2471.
(57) Ding, J.; Chuy, C.; Holdcroft, S. *Chem. Mater.* **2001**, *13*, 2231–2233.
(58) Eisenberg, A.; Kim, J.-S. *Introduction to Ionomers*; John Wiley and Sons: New York, 1998.
(59) *Handbook of Polyelectrolytes and Their Applications*; Tripathy, S. K., Kumar, J., Nalwa, H. S., Eds.; American Scientific Publishers: Los Angeles, 2002.
(60) Tant, M. R.; Wilkes, G. L. *J. Macromol. Sci., Part C: Rev. Macromol. Chem. Phys.* **1988**, *C28*, 1–63.
(61) Laurer, J. H.; Winey, K. I. *Macromolecules* **1998**, *31*, 9106–9108.
(62) Benetatos, N. M.; Heiney, P. A.; Winey, K. I. *Macromolecules* **2006**, *39*, 5174–5176.
(63) Lebedev, V. T.; Orlova, D. N.; Mel'nikov, A. B.; Vinogradova, L. V. *Polym. Sci., Ser. A.* **2009**, *51*, 965–973.
(64) Ganazzoli, F. *J. Chem. Phys.* **1998**, *108*, 9924–9932.
(65) Peiffer, D. G.; Lundberg, R. D. *J. Polym. Sci., Part A: Polym. Chem.* **1984**, *22*, 1757–1773.
(66) Bates, F. S.; Schulz, M. F.; Khandpur, A. K.; Forster, S.; Rosedale, J. H.; Almdal, K.; Mortensen, K. *Faraday Discuss.* **1994**, *98*, 7–18.
(67) Lu, X. Y; Weiss, R. A. *Macromolecules* **1996**, *29*, 1216–1221.
(68) *Polymer Handbook*, 3rd ed.; Brandrup, J., Immergut, E. H., Eds.; Wiley: New York, 1989.
(69) Park, M. J.; Balsara, N. P. *Macromolecules* **2008**, *41*, 3678–3687.
(70) Knychala, P.; Banaszak, M.; Park, M. J.; Balsara, N. P. *Macromolecules* **2009**, *42*, 8925–8932.
(71) Mauritz, K. A.; Blackwell, R. I.; Beyer, F. L. *Polymer* **2004**, *45*, 3001–3016.
(72) Rubatat, L.; Li, C.; Dietsch, H.; Nykänen, A.; Ruokolainen, J.; Mezzenga, R. *Macromolecules* **2008**, *41*, 8130–8137.
(73) Rubatat, L.; Shi, Z.; Diat, O.; Holdcroft, S.; Frisken, B. J. *Macromolecules* **2006**, *39*, 720–730.
(74) Essafi, W.; Gebel, G.; Mercier, R. *Macromolecules* **2004**, *37*, 1431–1440.
(75) Lee, H. S.; Roy, A.; Badami, A. S.; McGrath, J. E. *Macromol. Res.* **2007**, *15*, 160–166.
(76) Moore, H. D.; Saito, T. S.; Hickner, M. A. *J. Mater. Chem.* **2010**, *20*, 6316–6321.
(77) Lee, M.; Park, J. K.; Lee, H.-S.; Lane, O.; Moore, R. B.; McGrath, J. E.; Baird, D. G. *Polymer* **2009**, *50*, 6129–6138.
(78) Yang, S.; Sun, K.; Risen, W. M. *J. Polym. Sci., Part B: Polym. Phys.* **1990**, *28*, 1685–1697.
(79) Suleiman, D.; Elabd, Y. A.; Napadensky, E.; Sloan, J. M.; Crawford, D. M. *Thermochim. Acta* **2005**, *430* (1−2), 149–154.
(80) Gromadzki, D.; Cernoch, P.; Janata, M.; Kudela, V.; Nallet, F.; Diat, O.; Stepánek, P. *Eur. Polym. J.* **2006**, *42*, 2486–2496.
(81) Kim, Y. S.; Dong, L.; Hickner, M. A.; Pivovar, B. S.; McGrath, J. E. *Polymer* **2003**, *44*, 5729–5736.
(82) Zawodzinski, T. A.; Neeman, M.; Sillerud, L. O.; Gottesfeld, S. *J. Phys. Chem.* **1991**, *95*, 6040–6044.
(83) Xu, H.; Song, Y.; Kunz, H. R.; Fenton, J. M. *J. Electrochem. Soc.* **2005**, *152*, A1828–A1836.
(84) Kim, J.; Kim, B.; Jung, B.; Kang, Y. S.; Ha, H. Y.; Oh, I. H.; Ihn, K. J. *Macromol. Rapid Commun.* **2002**, *23*, 753–756.
(85) Roy, A.; Yu, X.; Dunn, S.; McGrath, J. E. *J. Membr. Sci.* **2009**, *327*, 118–124.
(86) Elabd, Y. A.; Beyer, F. L.; Walker, C. W. *J. Membr. Sci.* **2004**, *231*, 181–188.
(87) Park, M. J.; Balsara, N. P. *Macromolecules* **2010**, *43*, 292–298.
(88) Uehara, H.; Kakiage, M.; Sekiya, M.; Yamagishi, T.; Yamanobe, T.; Nakajima, K.; Watanabe, T.; Nomura, K.; Hase, K.; Matsuda, M. *Macromolecules* **2009**, *42*, 7627–7630.
(89) Larminie, J.; Dicks, A. *Fuel Cell Systems Explained*, 2nd ed.; Wiley: New York, 2003.
(90) Ravikumar, M. K.; Shukla, A. K. *J. Electrochem. Soc.* **1996**, *143*, 2601–2606.
(91) Scott, K.; Taama, W.; Cruickshank, J. *J. Appl. Electrochem.* **1998**, *28*, 289–297.
(92) Ge, J.; Liu, H. *J. Power Sources* **2005**, *142*, 56–69.
(93) Pivovar, B. S.; Wang, Y. X.; Cussler, E. L. *J. Membr. Sci.* **1999**, *154*, 155–162.
(94) Hallinan, D. T., Jr.; Elabd, Y. A. *J. Phys. Chem. B* **2007**, *111*, 13221–13230.
(95) Won, J.; Park, H. H.; Kim, Y. J.; Choi, S. W.; Ha, H. Y.; Oh, I. H.; Kim, H. S.; Kang, Y. S.; Ihn, K. J. *Macromolecules* **2003**, *36*, 3228–3234.
(96) Ishikawa, J.; Fujiyama, S.; Inoue, K.; Omi, T.; Tamai, S. *J. Membr. Sci.* **2007**, *298*, 48–55.
(97) Gardner, C. L.; Anantaraman, A. V. *J. Electroanal. Chem.* **1995**, *395*, 67–73.
(98) Kramer, W.; Luke, B. *J. Electrochem. Soc.* **1987**, *134*, C487–C487.
(99) Takenaka, H; Torikai, E.; Kawami, Y.; Wakabayashi, N. *Int. J. Hydrogen Energy* **1982**, *7*, 397–403.

(100) Charcosset, C. *Desalination* **2009**, *245*, 214–231.
(101) Nagarale, R. K.; Gohil, G. S.; Shahi, V. K. *Adv. Colloid Interface Sci.* **2006**, *119*, 97–130.
(102) Adams, L. A.; Poynton, S. D.; Tamain, C.; Slade, R. C. T.; Varcoe, J. R. *ChemSusChem*. **2008**, *1*, 1–3.
(103) Varcoe, J. R.; Slade, R. C. T.; Yee, E. L. H. *Chem. Commun*. **2006**, 1428–1429.
(104) Lu, S.; Pan, J.; Huang, A.; Zhuang, L.; Lu, J. *Proc. Natl. Acad. Sci. U.S.A*. **2008**, *105*, 20611–20614.
(105) Liu, Y.; Cavicchi, K. A.; Mausar, J.; Decker, B. *PMSE Prepr*. **2009**, *100*, 448.
(106) Zeng, Q. H.; Liu, Q. W.; Broadwell, I.; Zhu, A. M.; Xiong, Y.; Tu, X. P. *J. Membr. Sci.* **2010**, *349*, 237–243.
(107) Gu, S.; Cai, R.; Luo, T.; Chen, Z.; Sun, M.; Liu, Y.; He, G.; Yan, Y. *Angew. Chem., Int. Ed.* **2009**, *48*, 6499–6502.
(108) Wang, J. H.; Li, S. H.; Zhang, S. B. *Macromolecules* **2010**, *43*, 3890–3896.
(109) Kong, X.; Wadhwa, K.; Verkade, J. G.; Schmidt-Rohr, K. *Macromolecules* **2009**, *42*, 1659–1664.

DOI: 10.1021/ma102289w

Macromolecules
COMMUNICATION TO THE EDITOR

Poly(tetramethyl glycolide) from Renewable Carbon, a Racemization-Free and Controlled Depolymerizable Polyester

Haruo Nishida,*,† Yoshito Andou,† Kohtaro Watanabe,† Yoshiro Arazoe,† Seiji Ide,‡ and Yoshihito Shirai†

†*Eco-Town Collaborative R&D Center for the Environment and Recycling, Kyushu Institute of Technology, Hibikino 2-4, Wakamatsu, Kitakyushu, Fukuoka 808-0196, Japan, and* ‡*Chemical & Textile Research Institute, Fukuoka Industrial Technology Center, Kamikoga 3-2-1, Tikushino, Fukuoka 818-8540, Japan*

Received October 6, 2010
Revised Manuscript Received November 26, 2010

The development of biomass-based polymers is one strategic step toward achieving a sustainable social system. A typical biomass-based polymer is poly(L-lactic acid) (PLLA), which through a combination of biological fermentation and chemical reaction can be synthesized from naturally abundant biomasses such as starch or cellulose.[1] PLLA shows good physical properties such as crystallinity, thermoplasticity, transparency, and a high melting point (T_m) of around 170 °C.[2] It also has the excellent quality of being easily reproduced from the depolymerization product: L,L-lactide.[3] Hence, the likelihood that PLLA will become the plastic material of choice for sustainable systems has been attracting much interest from researchers. However, in practical applications, PLLA does have some drawbacks, such as slow crystallization,[4] low impact resistance,[2] hydrolyzability,[5] and racemization.[6] PLLA readily causes racemization from an L-unit to a D-unit in a chain under heating.[7] Such racemization proceeds by the mechanism of ester−semiacetal tautomerization, causing a decrease in optical purity and crystallinity.[8] This is a serious problem in the reproduction of practical materials via thermal depolymerization and repolymerization. A fundamental and complete solution to this problem requires a modification of the chemical structure of lactic acid.

In this study, in order to overcome the problems associated with PLLA while preserving its superior properties, a biomass-based and racemization-free polymer: poly(tetramethyl glycolide) (PTMG) possessing superior depolymerizability for the reproduction is developed. Previously, PTMG has been synthesized from petroleum by wholly chemical processes involving the ring-opening polymerization of tetramethyl glycolide (TMG), which is a cyclic dimer of α-hydroxyisobutyric acid (HIBA).[9] HIBA itself has also required preparation over many steps from petroleum using the cyanhydrin method for methyl methacrylate production.[10] The methyl methacrylate production has been improved by some novel production processes such as the AVENEER method. Recently, a biosynthesis method of HIBA from renewable carbons has been achieved.[11] PTMG shows a high T_m at 185−190 °C[9] and a characteristic thermal degradability into methacrylic acid, TMG, acetone, etc.[12] However, the derivation of PTMG from biomass and its controlled depolymerization into monomers, which will become required for many commonly used polymers in a future, are newly proposed in this study.

Scheme 1. Total Synthetic Processes of PTMG and Its Depolymerization

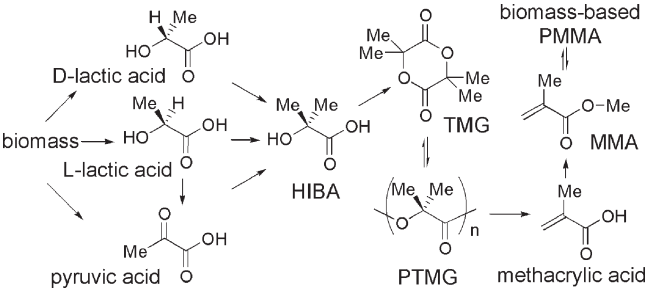

Renewable resources: D-/L-lactic acids and pyruvic acid derived from biomasses are employed as starting materials for the synthesis of HIBA in this study, which is an acyclic monomer of PTMG. The biomass-based HIBA is prepared by methylation of the acids and then converted into the cyclic dimer: TMG by a cyclic esterification. The following synthesis of polymer PTMG is carried out by a ring-opening polymerization of TMG. Moreover, the controlled depolymerization of PTMG is performed either to return to TMG or to convert to methacrylic acid depending on the use of a specific catalyst for each monomeric product.

Two synthetic routes of HIBA from the renewable resources were performed. One was the direct methylation of D-/L-lactic acid derivatives after the abstraction of α-hydrogen on a chiral carbon: the other was the methylation of an α-keto group of a pyruvic acid derivative by the Grignard reaction, which is an oxidized form of corresponding D-/L-lactic acid derivatives. Although the direct methylation has been reported in our recent research,[13] the methylation of the pyruvic acid derivative is a new finding introduced in this study. Results of the methylation are listed in Table 1. The methylation of methyl pyruvate by the Grignard reaction showed a 50% yield at room temperature. On the other hand, the direct methylation of the hydroxyl-group protected ethyl D-/L-lactate (HPEL), with protection provided by a methoxymethyl group, gave relatively high yields of 54−75% at −84 °C. These methylation reactions have the advantage of using multiple renewable resources: pyruvic acid and L-, D-, and D-/L-lactic acids without the need of high optical purity.

HIBA was obtained by the hydrolytic deprotection of methylated products with high yields of >74%. The cyclic dimerization of HIBA proceeded smoothly in the presence of the dehydration catalyst methane: sulfonic acid to isolate the cyclic dimer: TMG in a 67% yield. The ring-opening anionic polymerization of TMG that followed was achieved by using three initiators: EtOLi, *n*-BuLi, and *t*-BuLi, resulting in the preparation of a high molecular weight PTMG (M_n 90 000) as shown in Table S1.

Previously, Deibig et al.[9] showed T_m of PTMG in a range of 180−190 °C, but no glass transition (T_g) temperature was reported. The isolated PTMG showed T_m and T_g at 191 and 70 °C (Figure 1), respectively, about 15 °C higher than those of PLLA. The T_g transition signal was very weak, and the T_m peak shifted into higher temperatures of up to 206 °C with a corresponding increase in the heat treatment temperature. The weak T_g signal and high T_m value of PTMG suggest superior crystallization and heat resistance, respectively.

*Corresponding author: Fax (+81) 93-695-6060; e-mail nishida@lsse.kyutech.ac.jp.

 Published on Web 12/09/2010 © 2010 American Chemical Society

Table 1. Synthesis of α-Hydroxyisobutyric Acid (HIBA) Esters from Methyl Pyruvate and Hydroxyl Group Protected Ethyl Lactate (HPEL)

run	substrate (S)	reagent (R_1/R_2)	$S/R_1/R_2$ [molar ratio]	temp/time [°C/h]	yield[a] [%]
1-1	methyl pyruvate	MeMgBr	1.0/1.0	rt/1	50
1-2	HPEL[c]	LiTMP/MeI	1.0/1.2/2.0	−84/4	54
1-3[b]	HPEL	LDA/MeI	1.0/1.3/2.0	−84/4	75

[a] Calculated from GC. [b] Under the same conditions at ref 13. [c] Ethyl D-/L-lactate protected by a methoxymethyl group.

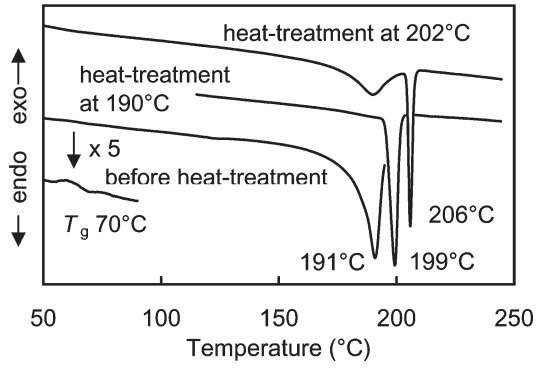

Figure 1. DSC profiles of heat-treated PTMG. Heating rate: 10 °C min^{-1} under a nitrogen flow of 20 mL min^{-1}. Heat treatment: 10 min.

An additional interesting result is the controllable depolymerization behavior of PTMG into TMG and methacrylic acid (MA). In the thermal degradation of PTMG, it has been reported that TMG, methacrylic acid, acetone, etc., are recovered as volatile products without any catalyst needed for the reaction control.[12,14−17] In this study, by using appropriate catalysts for the selective depolymerization, the thermal degradation of PTMG was controlled successfully to generate TMG or methacrylic acid as shown in Table 2. Recovered TMG can be used to reproduce PTMG. Another selectable product: MA was converted into a methacrylic ester: methyl methacrylate (MMA) after an esterification reaction. From the obtained MMA, a biomass-based poly(methyl methacrylate) (PMMA) with high molecular weight (M_n 70 000 and M_w 238 000) was produced by free-radical polymerization in bulk. This is an early report on the preparation of biomass-based PMMA.

These results reveal PTMG as a superior recyclable material by the virtue of its controllable conversion into each monomer.

In conclusion, the biomass-based and racemization-free polyester PTMG was synthesized from lactic and pyruvic acids as renewable resources. The high T_m (∼206 °C) and T_g (70 °C) values of PTMG were confirmed, and the superior resource recyclability of PTMG was demonstrated showing selective reduction to TMG or methacrylic acid. Moreover, the preparation of biomass-based PMMA was reported.

Table 2. Catalytic Thermal Depolymerization of PTMG[a]

			volatile products [%][d]		
run	catalyst[b]	temp[c] [°C]	TMG	methacrylic acid	acetone
2-1		283	2.9	57.1	40.0
2-2	$Sn(Oct)_2$	265	80.8	19.2	0
2-3	MgO	235	17.7	80.6	1.6

[a] PTMG: M_n 22 000, M_w 32 000. [b] Catalyst 1 wt %. [c] Isothermal heating. [d] From ^{1}H NMR analysis.

Supporting Information Available: Experimental details and the characterization data of ^{1}H NMR, GPC, and DSC. The material is available free of charge via the Internet at http://pubs.acs.org.

References and Notes

(1) Lunt, J. *Polym. Degrad. Stab.* **1998**, *59*, 145–152.
(2) Ajioka, M.; Enomoto, K.; Suzuki, K.; Yamaguchi, A.; Environ, J. *Polym. Degrad.* **1995**, *3*, 225–234.
(3) Fan, Y.; Nishida, H.; Shirai, Y.; Endo, T. *Green Chem.* **2003**, *5*, 575–579.
(4) Sanchez, F. H.; Mateo, J. M.; Colomer, F. J. R.; Sanchez, M. S.; Ribelles, J. L. G.; Mano, J. F. *Biomacromolecules* **2005**, *6*, 3283–3290.
(5) Mohd-Adnan, A.-F.; Nishida, H.; Shirai, Y. *Polym. Degrad. Stab.* **2008**, *93*, 1053–1058.
(6) Kopinke, F. D.; Remmler, M.; Mackenzie, K.; Moder, M.; Wachsen, O. *Polym. Degrad. Stab.* **1996**, *53*, 329–342.
(7) Tsukegi, T.; Motoyama, T.; Shirai, Y.; Nishida, H.; Endo, T. *Polym. Degrad. Stab.* **2007**, *92*, 552–559.
(8) Kolstad, J. J. *J. Appl. Polym. Sci.* **1996**, *62*, 1079–1091.
(9) Deibig, H.; Geiger, J.; Sander, M. *Makromol. Chem.* **1971**, *145*, 123–131.
(10) Gross, A. W.; Dobson, J. C. In *Kirk-Othmer Encyclopedia of Chemical Technology*, 4th ed.; Kroschwitz, J. I., Howe-Grant, M., Eds.; John Wiley and Sons: New York, 1955; Vol. *16*, pp 474−506.
(11) Rohwerder, T.; Müller, R. H. *Microb. Cell Fact.* **2010**, *9*, 13.
(12) Sutton, G. J.; Tighe, B. J.; Roberts, M. *J. Polym. Sci., Polym. Chem. Ed.* **1973**, *11*, 1079–1093.
(13) Watanabe, K.; Andou, Y.; Shirai, Y.; Nishida, H. *Chem. Lett.* **2010**, *39*, 698–699.
(14) Deibig, H.; Geiger, J.; Sander, M. *Makromol. Chem.* **1971**, *145*, 133–139.
(15) Lovett, A. J.; O'Donnell, W. G.; Sutton, G. J.; Tighe, B. J. *J. Polym. Sci., Polym. Chem. Ed.* **1973**, *11*, 2031–2043.
(16) Tighe, B. J. In *Developments in Polymer Degradation*, 5th ed.; Grassie, N., Ed.; Applied Science Publishers: London, 1984; pp 31−77.
(17) Golomb, A.; Ritchie, P. D. *J. Chem. Soc.* **1962**, 838–847.

DOI: 10.1021/ma1024945

Macromolecules
COMMUNICATION TO THE EDITOR

Structural Characterization of a Polymer of Intrinsic Microporosity: X-ray Scattering with Interpretation Enhanced by Molecular Dynamics Simulations

Amanda G. McDermott,[†] Gregory S. Larsen,[†] Peter M. Budd,[‡] Coray M. Colina,[†] and James Runt*,[†]

[†]*Department of Materials Science and Engineering, The Pennsylvania State University, University Park, Pennsylvania 16802, United States, and* [‡]*School of Chemistry, The University of Manchester, Manchester M13 9PL, U.K.*

Received November 2, 2010
Revised Manuscript Received December 6, 2010

Materials containing networks of pores smaller than 2 nm in diameter, termed *microporous* by IUPAC convention,[1] are of interest for applications including gas storage and separations, adsorption, and catalysis. Rather than relying on templating or cross-linking to induce microporosity, polymers of intrinsic microporosity (PIMs) feature porosity derived from inefficient packing due to a combination of rigid segments and sites of contortion within the macromolecular backbone.[2]

PIM-1, a polybenzodioxane with a ladder-type structure (see Figure 1), is the most extensively characterized PIM with a Brunauer−Emmett−Teller (BET) surface area of 720−780 m^2/g and pores 5.2−10.7 Å in size.[2−4] The variability in measurements of these key properties is due to the influence of sample processing (thermal history and methanol or gas exposure[3]) as well as assumptions necessary to interpret data from various characterization techniques.

In this paper, we present the first broad scattering vector (q) range X-ray scattering data for PIM-1. We also compare wide-angle X-ray scattering (WAXS) patterns with structure factors calculated from molecular dynamics (MD) simulations. In addition to providing a useful validation of PIM simulations, this greatly enhances our understanding of PIM scattering features, building on previous interpretations of WAXS patterns from microporous polymers.[5−8]

PIM-1 was synthesized as described previously,[9] and 100 μm thick films were cast from chloroform solution under ambient conditions. Powder samples were precipitated by adding a solution of PIM-1 (in tetrahydrofuran) to methanol. Prior to scattering measurements, all samples were degassed in a vacuum oven at 120−130 °C for at least 24 h.

WAXS patterns were collected using a Rigaku DMAX-RAPID instrument with an image-plate detector. Small-angle X-ray scattering (SAXS) patterns were collected using a Molecular Metrology instrument with a pinhole camera, multiwire area detector, and sample-to-detector distances of 1.5 and 0.5 m. Both WAXS and SAXS instruments used Cu Kα radiation (λ = 1.54 Å) and yielded isotropic two-dimensional patterns, which were azimuthally averaged into one-dimensional profiles of intensity $I(q)$ vs scattering vector $q = 4\pi(\sin\theta)/\lambda$. Ultrasmall-angle X-ray scattering (USAXS) patterns were collected with a Bonse-Hart camera using an incident energy of 12 keV (λ = 1 Å) at beamline 32-ID[10] of the Advanced Photon Source; these have been desmeared. Backgrounds were subtracted from all scattering patterns.

To model PIM-1, chains were grown at a low density to a target length of 10 repeat units and then compressed to a 45-Å box with a realistic density using LAMMPS[11] with bonded parameters from GAFF,[12] nonbonded parameters from TraPPE,[13] and charges from *ab initio* calculations with Gaussian 03[14] and RESP.[15] These molecular dynamics simulations are described in detail elsewhere.[16]

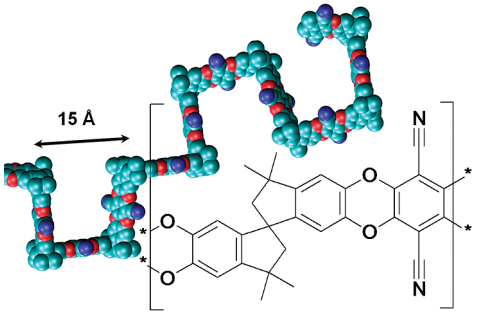

Figure 1. Chemical structure and representative single-chain conformation of PIM-1.

The structure factor $S(q)$ was computed using ISAACS software[17] from 10 snapshots acquired during a 500 ps NVT run following compression. The low-q limit of $S(q)$ is defined by the box size: $2\pi/[(45\ \text{Å})/2] = 0.28\ \text{Å}^{-1}$. Because a united-atom model was used, $S(q)$ does not include contributions from hydrogen atoms; however, hydrogen is present at a low mole fraction and scatters X-rays much more weakly than heavier elements. The total structure factor for an isotropic system is computed from a Fourier transform of the sum of partial radial distribution functions $g_{AB}(r)$ weighted by atomic X-ray scattering lengths b_i and mole fractions c_i:[17−19]

$$S(q) = 1 + 4\pi\rho\int_0^\infty \left[\frac{1}{\langle b^2\rangle}\left(\sum_{A,B} c_A b_A c_B b_B g_{AB}(r)\right) - 1\right]\frac{\sin qr}{qr}\, r^2\, \mathrm{d}r \quad (1)$$

where $g_{AB}(r)$ represents the probability of finding an atom of species B at a distance r from an atom of species A, normalized to 1 at large distances, and

$$\langle b^2\rangle = \left(\sum_i c_i b_i\right)^2$$

with the index i spanning the atom types present in the simulated structure. We also define partial structure factors $S_{AB}(q)$, similar to the Faber−Ziman definition but scaled by mole fractions and scattering lengths:

$$S_{AB}(q) = \frac{c_A b_A c_B b_B}{\langle b^2\rangle}\left(1 + 4\pi\rho\int_0^\infty [g_{AB}(r) - 1]\frac{\sin qr}{qr}\, r^2\, \mathrm{d}r\right) \quad (2)$$

so that

$$S(q) = \sum_{A,B} S_{AB}(q)$$

Low-q intensity is proportional to q^{-3} over several decades (Figure 2), which is consistent with the limiting case of either a dense mass fractal (D = 3) or a rough, space-filling surface fractal

*Corresponding author. E-mail: runt@matse.psu.edu.

 Published on Web 12/09/2010 © 2010 American Chemical Society

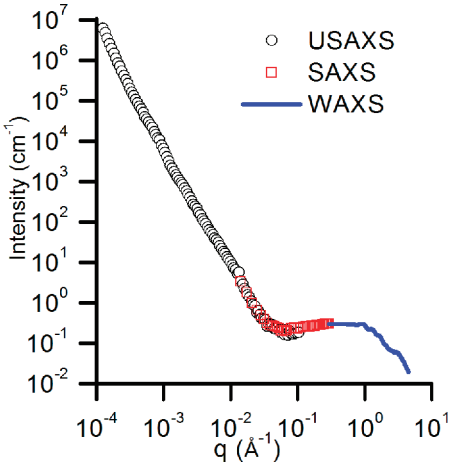

Figure 2. Broad q range X-ray scattering data for a PIM-1 film. SAXS (□) and WAXS (—) patterns were scaled so that overlapping q ranges match USAXS data (○), which was desmeared and calibrated on an absolute-intensity scale. For clarity, only every 8th SAXS data point is shown.

(D_s = 3).[18] If the spatial distribution of voids (pores) in PIMs at these large length scales is fractal, this must be induced by the same unusual chain statistics that give rise to the large concentration of interconnected free volume; chain statistics in PIMs have yet to be directly investigated. The low-q power law, flat SAXS intensity, and shoulder in the WAXS region are also seen in amorphous, nanoporous activated carbons.[20] Although the shoulder or knee feature from 10^{-1} to 2 Å^{-1} should contain information about the pore size distribution, developing a model such as a modified Guinier function to extract this information is complicated by the superimposition of several broad peaks and the presence of a high concentration of pores of poorly defined geometry.

Features in WAXS patterns from amorphous polymers are typically limited to one or two amorphous halos, representing distances of closest approach between segments of different chains. Unlike materials with larger, patterned pores, PIMs have no "bulk" phase, only interconnected unoccupied volume. Pore dimensions in PIMs are therefore defined by intersegmental distances. Figure 3 shows that high-resolution WAXS patterns include characteristic peaks at q = 0.89, 1.25, and 1.63 Å^{-1}. Because these peaks are superimposed on a smooth shoulder not found in nonporous polymers, it is not immediately clear that they should be interpreted as amorphous halos representing intersegmental distances. Weaker features above 2 Å^{-1} are related to correlations on the scale of bond lengths; the exaggeration of these features in the calculated $S(q)$ could arise in part from the approximation of atomic scattering lengths as q-independent.[17]

WAXS patterns from PIMs typically include several broad peaks. Ritter et al. have observed that for polyimide-based PIMs both the degree of microporosity and the relative intensities of amorphous halos, but not their q values, are sensitive to processing conditions.[6] Our data (Figure 3) also indicate that for PIM-1 the 1.25 and 1.63 Å^{-1} peaks are of higher relative intensity in powders than in films. Methanol treatment significantly increases the permeability of a film, and thermogravimetric measurements suggest that this is due to the removal of adsorbed species that persist after degassing.[4] Soaking a film in methanol prior to degassing does not affect the relative peak intensities, but it does increase the low-q intensity of the shoulder. A reduction in the intensity of the scattering shoulder when some pores are occupied is consistent with the idea that scattering in this q range and at smaller q contains information about pore sizes.

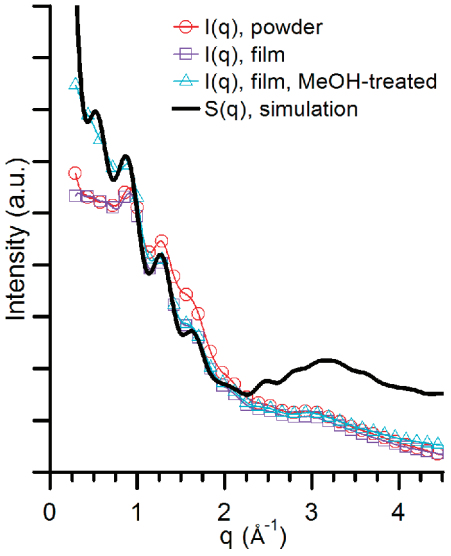

Figure 3. Simulated structure factor $S(q)$ (—) compared to experimental WAXS intensity of PIM-1 samples with three different processing histories: a precipitated powder (○), a solution-cast film (□), and an identical film that was also treated with methanol (Δ). For clarity, only every 50th experimental data point is indicated with a symbol.

$S(q)$ from the simulated sample, which certainly includes no adsorbed species, reproduces the low-q shoulder intensity of a methanol-treated sample and the relative peak intensities of solution-cast films, expected to be closer to equilibrium than precipitated powders. The reproduction of processing-independent WAXS features from the simulated structure indicates that the force-field parameters and structure generation used accurately reproduce intersegmental interactions, crucial in PIMs due to the equivalence of porosity, free volume, and intersegmental distances.

Comparing simulated $S(q)$ to a methanol-treated PIM-1 film, there is some excess intensity at the lowest q; this is likely a box-size effect, an inherent limitation related to periodic boundary conditions. There is also a small, seemingly superfluous peak in $S(q)$ near 0.52 Å^{-1}. Examining the partial structure factors (Figure 4 and Supporting Information) reveals that there are many positive and negative contributions to this portion of the scattering pattern, which in PIM-1 nearly cancel. When the chemical structure of PIM-1 is modified to include larger spirocenter substituents—one or two phenyl groups instead of two methyl groups[21]—an additional peak appears here in experimental scattering patterns (unpublished data). It is reasonable to conclude that this simulated structure does not precisely reproduce the history of these experimental samples, but examining partial structure factors can still clarify the meaning of processing-independent scattering features.

Figure 4 shows the contribution to the total $S(q)$ from several partial structure factors. $S_{R-R}(q)$ is defined as the sum of all $S_{AB}(q)$ (eq 2) such that A and B are atoms located in rigid segments; $S_{S-S}(q)$ includes contributions from atoms in spirocenters, and $S_{R-S}(q)$ includes cross-terms. Note that $S(q) = S_{R-R}(q) + S_{R-S}(q) + S_{S-S}(q)$. Simulations included 10 atom types, and partial structure factors for all pairs are shown in the Supporting Information.

The rigid segments overwhelmingly define the shape of the shoulder, a feature that is not present in nonporous polymers and which we conclude contains information about pore sizes. In contrast, spirocenters contribute mainly to the broad peaks superimposed on the shoulder. The lowest-q peak at 0.52 Å^{-1} contains contributions from both rigid segments and spirocenters; it represents the correlation between adjacent spirocenters

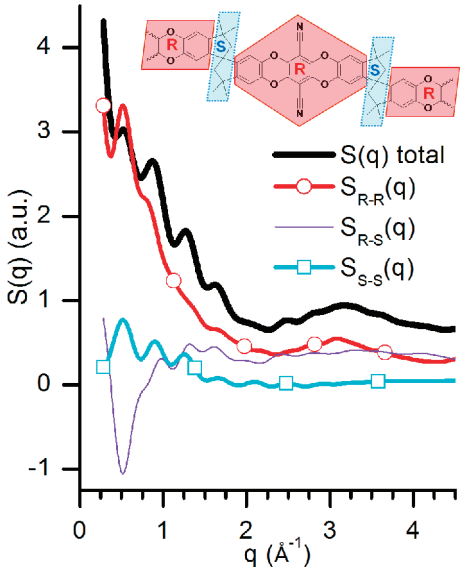

Figure 4. Contributions to the total simulated structure factor $S(q)$ (—) from atoms in rigid segments $S_{R-R}(q)$ (○), atoms in spirocenters $S_{S-S}(q)$ (□), and correlations between atoms in the two groups $S_{R-S}(q)$ (−). For clarity, very few data points are indicated with symbols.

along a single chain ~15 Å apart. Notably, neither of the two strongest experimental features (0.89 and 1.25 $Å^{-1}$) is an integer multiple of 0.52 $Å^{-1}$, suggesting that these represent distances between spirocenters or segments either on different chains or on the same chain, farther apart than the persistence length.

Comparing experimental and simulated scattering patterns serves not only to validate the model structure arising from interchain interactions in simulations but also to guide interpretation of experimentally observed scattering features. While correlations between nearest-neighbor segments in nonporous amorphous polymers give rise to one or two amorphous halos against a relatively flat WAXS background, intersegmental distances in PIMs instead contribute to a scattering shoulder, underscoring the fundamental difference in the organization of free volume in these highly permeable polymers. The broad peaks observed superimposed on this shoulder represent characteristic distances between segments or sites of contortion on different chains. Further study will focus on the development of a model to extract pore size distributions from PIM scattering patterns.

Acknowledgment. The authors acknowledge the support of the Materials World Network via the National Science Foundation, Division of Materials Research, Award 0908781. Use of the Advanced Photon Source at Argonne National Laboratory was supported by the U.S. Department of Energy, Office of Science, Office of Basic Energy Sciences, under Contract DE-AC02-06CH11357; USAXS data were collected at beamline 32-ID by Dr. Jan Ilavsky. We thank Dr. Carin Tattershall, Dr. James Selbie, and Nhamo Chaukura (University of Manchester) for providing samples. A. G. McDermott is supported by a National Science Foundation Graduate Research Fellowship.

Supporting Information Available: Partial structure factors for all 10 atom types in the simulation. This material is available free of charge via the Internet at http://pubs.acs.org.

References and Notes

(1) McNaught, A. D.; Wilkinson, A. *IUPAC Compendium of Chemical Terminology* (*the "Gold Book"*), 2nd ed.; Blackwell Scientific Publications: Oxford, 1997.
(2) McKeown, N. B.; Budd, P. M. *Macromolecules* **2010**, *43* (12), 5163–5176.
(3) Emmler, T.; Heinrich, K.; Fritsch, D.; Budd, P. M.; Chaukura, N.; Ehlers, D.; Rätzke, K.; Faupel, F. *Macromolecules* **2010**, *43* (14), 6075–6084.
(4) Budd, P. M.; McKeown, N. B.; Ghanem, B. S.; Msayib, K. J.; Fritsch, D.; Starannikova, L.; Belov, N.; Sanfirova, O.; Yampolskii, Y.; Shantarovich, V. *J. Membr. Sci.* **2008**, *325* (2), 851–860.
(5) Weber, J.; Su, Q.; Antonietti, M.; Thomas, A. *Macromol. Rapid Commun.* **2007**, *28* (18−19), 1871–1876.
(6) Ritter, N.; Antonietti, M.; Thomas, A.; Senkovska, I.; Kaskel, S.; Weber, J. *Macromolecules* **2009**, *42* (21), 8017–8020.
(7) Du, N.; Robertson, G. P.; Song, J.; Pinnau, I.; Thomas, S.; Guiver, M. D. *Macromolecules* **2008**, *41* (24), 9656–9662.
(8) Du, N.; Robertson, G. P.; Pinnau, I.; Guiver, M. D. *Macromolecules* **2009**, *42* (16), 6023–6030.
(9) Budd, P. M.; Ghanem, B. S.; Makhseed, S.; McKeown, N. B.; Msayib, K. J.; Tattershall, C. E. *Chem. Commun.* **2004**, *2004* (2), 230–231.
(10) Ilavsky, J.; Jemian, P. R.; Allen, A. J.; Zhang, F.; Levine, L. E.; Long, G. G. *J. Appl. Crystallogr.* **2009**, *42* (3), 469–479.
(11) Plimpton, S. *J. Comput. Phys.* **1995**, *117* (1), 1–19.
(12) Wang, J.; Wolf, R. M.; Caldwell, J. W.; Kollman, P. A.; Case, D. A. *J. Comput. Chem.* **2004**, *25* (9), 1157–1174.
(13) Wick, C. D.; Martin, M. G.; Siepmann, J. I. *J. Phys. Chem. B* **2000**, *104* (33), 8008–8016.
(14) Gaussian 03, Revision E.01: Frisch, M. J.; Trucks, G. W.; Schlegel, H. B.; Scuseria, G. E.; Robb, M. A.; Cheeseman, J. R.; Montgomery, J. A.; Vreven, T.; Kudin, K. N.; Burant, J. C.; Millam, J. M.; Iyengar, S. S.; Tomasi, J.; Barone, V.; Mennucci, B.; Cossi, M.; Scalmani, G.; Rega, N.; Petersson, G. A.; Nakatsuji, H.; Hada, M.; Ehara, M.; Toyota, K.; Fukuda, R.; Hasegawa, J.; Ishida, M.; Nakajima, T.; Honda, Y.; Kitao, O.; Nakai, H.; Klene, M.; Li, X.; Knox, J. E.; Hratchian, H. P.; Cross, J. B.; Bakken, V.; Adamo, C.; Jaramillo, J.; Gomperts, R.; Stratmann, R. E.; Yazyev, O.; Austin, A. J.; Cammi, R.; Pomelli, C.; Ochterski, J. W.; Ayala, P. Y.; Morokuma, K.; Voth, G. A.; Salvador, P.; Dannenberg, J. J.; Zakrzewski, V. G.; Dapprich, S.; Daniels, A. D.; Strain, M. C.; Farkas, O.; Malick, D. K.; Rabuck, A. D.; Raghavachari, K.; Foresman, J. B.; Ortiz, J. V.; Cui, Q.; Baboul, A. G.; Clifford, S.; Cioslowski, J.; Stefanov, B. B.; Liu, G.; Liashenko, A.; Piskorz, P.; Komaromi, I.; Martin, R. L.; Fox, D. J.; Keith, T.; Laham, A.; Peng, C. Y.; Nanayakkara, A.; Challacombe, M.; Gill, P. M. W.; Johnson, B.; Chen, W.; Wong, M. W.; Gonzalez, C.; Pople, J. A. Gaussian, Inc., Wallingford, CT, 2004.
(15) Wang, J.; Wang, W.; Kollman, P. A.; Case, D. A. *J. Mol. Graphics Modell.* **2006**, *25* (2), 247–260.
(16) Larsen, G. S.; Lin, P.; Siperstein, F. R.; Colina, C. M. *Adsorption* **2010**, DOI 10.1007/s10450-010-9281-7.
(17) Le Roux, S.; Petkov, V. *J. Appl. Crystallogr.* **2010**, *43* (1), 181−185. See also: http://isaacs.sourcefourge.net/phys/scatt.html.
(18) Roe, R.-J. *Methods of X-Ray and Neutron Scattering in Polymer Science*; Oxford University Press: New York, 2000.
(19) Mondello, M.; Yang, H.-J.; Furuya, H.; Roe, R.-J. *Macromolecules* **1994**, *27* (13), 3566–3574.
(20) Pfeifer, P.; Ehrburger-Dolle, F.; Rieker, T. P.; Gonzalez, M. T.; Hoffman, W. P.; Molina-Sabio, M.; Rodriguez-Reinoso, F.; Schmidt, P. W.; Voss, D. J. *Phys. Rev. Lett.* **2002**, *88* (11), 115502.
(21) Carta, M.; Msayib, K. J.; Budd, P. M.; McKeown, N. B. *Org. Lett.* **2008**, *10* (13), 2641–2643.

Macromolecules
COMMUNICATION TO THE EDITOR

Macromolecules **2011**, *44*, 17–19 **17**
DOI: 10.1021/ma102446b

Highly Efficient and Stable Deep Blue Light Emitting Poly(9,9-dialkoxyphenyl- 2,7-silafluorene): Synthesis and Electroluminescent Properties

Jun Wang,[†] Chang-qing Zhang,[†] Cheng-mei Zhong,[‡] Su-jun Hu,[‡] Xue-yi Chang,[§] Yue-qi Mo,*[,†] Xiwen Chen,*[,⊥] and Hong-bin Wu*[,‡]

[†]*Key Laboratory of Special Functional Materials, South China University of Technology, Guangzhou 510640, P. R. China,* [‡]*Institute of Polymer Optoelectronic Materials and Devices, South China University of Technology, Guangzhou 510640, P. R. China,* [§]*Canton Oledking Optoelectronic Materials Co., ltd, Guangzhou 510640, P. R. China, and* [⊥]*CSIRO Materials Science and Engineering, Bayview Avenue, Clayton, VIC 3168, Australia*

Received October 27, 2010
Revised Manuscript Received December 5, 2010

Introduction. Highly efficient blue emitting polymer with good color purity is one of the key issues of the commercialization of the polymer light emitting diodes (PLEDs)[1] for the next-generation flat-panel displays. Although many efforts have been focused on poly(*p*-phenylene)s, polycarbazoles, polythiophenes, etc., 2,7-fluorene-based polymers[2] are regarded as the most successful blue light emitters. Very recently, Yang et al.[3] and Chen et al.[4] reported highly efficient blue emitting PLEDs based on alkoxyphenyl-substituted poly(2,7-fluorene) derivatives. On the other hand, poly(9,9-dialkylsilafluorene)s are another promising candidate for blue light emitting PLEDs, which was first reported by Holmes' group[5] and us nearly the same time in 2005.[6] In general, polysilafluorenes exhibit even more stable blue emission due to the higher oxidative stability of Si at the 9-position of polysilafluorenes as compared to that of the C-9 carbon of polyfluorenes, which usually result in the formation of the keto defects.[7] Moreover, Si-containing polymers are expected to have higher electron affinity owing to the $\sigma^*-\pi^*$ conjugation.[8] As a result, photovoltaic cells based on 9,9-dialkylsilafluorene-based copolymers have been demonstrated to have higher open voltage circuit as compared to that based on its polyfluorene analogue,[9] and the related PLEDs exhibit very good EL performance,[10,11] which received intense attention.[12] However, we note that the device based on the homopolymer of 9,9-dialkylsilafluorene shows a moderate external quantum efficiency (EQE) of 0.66% and a maximal luminous efficiency of 0.53 cd/A.[10] Given the fact that polymers with aryl side chains usually have higher thermal stability due to higher glass transition temperatures than those with alkyl side chains,[13,14] bulky aryl substitutes were thought to result in more effective suppression of aggregation than alkyl substitutes. As it can lead to the suppression of excimer formation and long-wavelength emission,[15] it is very interesting to develop homopolymers of 9,9-diarylsilafluorene for blue light emitting devices. Although some 9,9-diarylsilafluorene-containing compounds had been reported previously,[16] to the best of our knowledge, processable homopolymers of 9,9-diarylsilafluorene have not appeared in the literature.

*Corresponding authors. E-mail: moyueqi@263.net (Y.M.); hbwu@scut.edu.cn (H.W.); Xiwen.Chen@csiro.au (X.C.).

In this Communication, we report the synthesis a soluble poly(9,9-dialkoxyphenyl-2,7-silafluorene) (PSF) by the Yamamoto reaction. The thermal, photophysical, and EL properties of the obtained polymer were investigated.

Experimental Section. The synthesis of PSF is shown in Scheme 1. 9,9-Dichloro-2,7-dibromosilafluorene[17] is the key intermediate for the synthesis of 9,9-di(4-(3′,7′-dimethyloctyloxy))-2,7-dibromosilafluorene (**1**). We tried another intermediate—9-phenyl-9-chloro-2,7-dibromosilafluorene—but it is difficult to get the objective product (**1**). In order to get high yield of 9,9-dichloro-2,7-dibromosilafluorene, excess $SiCl_4$ was added to suppress the formation of spirosilafluorene[18] and was stripped eventually before the addition of alkoxyphenyllithium. PSF was obtained via the Yamamoto reaction. After the solution of **1** and nickel catalyst was stirred at 85 °C for 2 days, bromobenzene was added to diminish the bromo end groups which may cause formation of green emission aggregates.[19] After purification, PSF with M_n of 23 000 and M_w of 92 000 was obtained. PSF was readily soluble in common organic solvents, including toluene, chlorobenzene, chloroform, and THF.

Results and Discussion. The UV−vis absorption spectra and photoluminescent spectra (PL) of PSF in CH_2Cl_2 and in solid state are shown in Figure 1. It can be seen that the absorption spectrum of PSF in solution are almost identical to that in film, with the absorption maximum at 391−392 nm, implying that the conjugation length does not change upon the film was formed after spin-coating. The absorption onset of PSF is around 438 nm; thus, the optical bandgap (E_g) of PF is estimated at ca. 2.83 eV, slightly smaller than that of poly(9,9-dialkysilafluorene) (2.93 eV).[5] As the onset potential of the oxidation process (p-doping) of PSF occurs at about 1.38 V against Hg/Hg_2Cl_2 (as shown in Figure S5), the HOMO level of PSF was calculated to be −5.78 eV according to the empirical formula $E_{HOMO} = -(E_{ox} + 4.4)$ (eV),[20] which is quite close to that of poly(9,9-dialkysilafluorene) (−5.77 eV).[5] The LUMO level was calculated to be about −2.95 eV from the HOMO level and the optical bandgap (E_g).

As can be seen from the PL spectra of PSF in CH_2Cl_2 (ca. 5 ppm) and in the solid state, which were obtained by a Fluorolog JY luminescence spectrometer under excitation of 340 nm, the PL spectrum of PSF in film shows a 14 nm of red shift as compared with that in CH_2Cl_2 while both PL spectra show strong vibronic structure. The PL maximum of PSF in film is located at 437 nm, which shows about 12 nm of red shift compared with poly(9,9-dialkysilafluorene) film,[5] with two vibronic sidebands at 461 and 495 nm, respectively. The PL quantum yields of PSF in dilute 1,2-dichloroethane and in film were estimated to be ca. 95% and 75% as measured in an integrated sphere, respectively.

To investigate the electroluminescence properties of the PSF, single-active-layer devices with the configuration ITO/PEDOT:PSS/PSF/Ba/Al and ITO/PEDOT:PSS/PVK /PSF/Ba/Al have been fabricated, where poly(*N*-vinylcarbazole) (PVK) was used as hole transporting layer. The EL spectra of the devices and the PL spectra of the PSF are shown in Figure 2. We note that the EL spectra of the devices in both configurations are nearly identical to that of the PL spectrum, with an emission peak at ca. 435 nm and a shoulder at 458 nm, implying that EL and PL have the same origin. Unlike poly(dioctylfluorene), in which pronounced emission in the longer wavelength

© 2010 American Chemical Society
Published on Web 12/15/2010

Scheme 1. Synthesis of the PSF

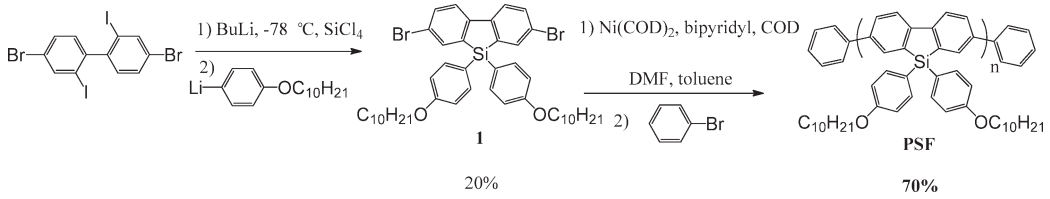

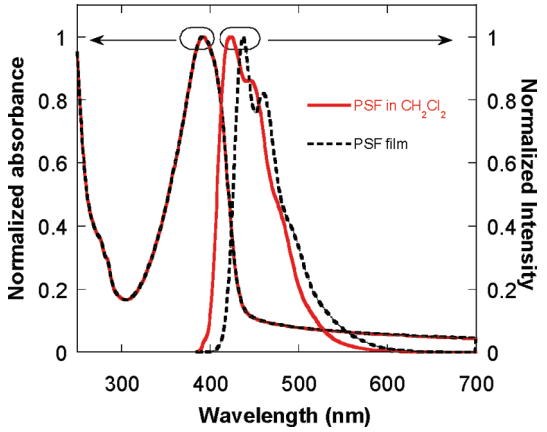

Figure 1. Absorption and PL spectra of PSF in CH_2Cl_2 and in solid state.

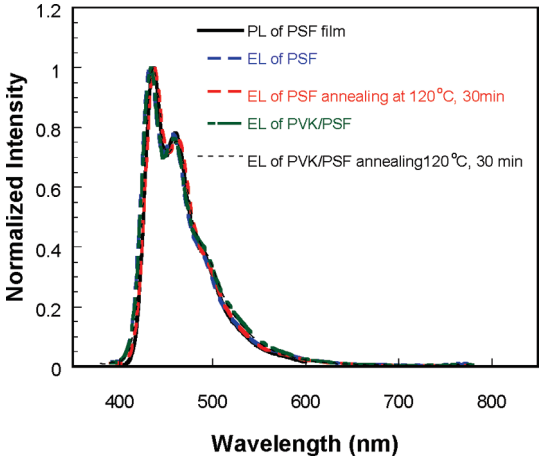

Figure 2. PL and EL spectra of the devices fabricated from PSF in device configuration of ITO/PEDOT:PSS/PSF/Ba/Al and ITO/PEDOT:PSS/PVK/PSF/Ba/Al.

region typically exists and unstable blue emission upon increase of temperature and operation stress,[15] the EL spectra of the PSF devices remain nearly unchanged even the devices were annealed at 120 °C for 30 min. The excellent spectral stabilities of PSF can be attributed to the bulky 9,9-diphenyl substitutes, which could result in the suppression of aggregation and/or excimer formation.

The CIE coordinates of the blue emission were found to be around from (0.17, 0.12) to (0.17,0.13), representing deep blue emission in the 1931 CIE diagram. Table 1 summarizes the performance of the PSF devices fabricated from two device configurations. With a device configuration of ITO/PEDOT:PSS/PSF/Ba/Al, the maximal LE of 0.53 cd/A (corresponding to an EQE of 0.51%.) was obtained after annealing at 120 °C for 0.5 h. Upon the incorporation of a thin layer of PVK (~30 nm), despite the turn-on voltage (defined as the voltage at which a luminance of 1 cd/m^2 was measured) slightly increased, the LE dramatically increased to 2.3 cd/A, while the EQE of the device reached 2.2%. We noticed that the best performance of a

Table 1. Device Performance of the PLEDs Based on PSF[a]

entry	treatment	LE_{max} (cd/A)	EQE_{max} (%)	V_{on} (V)	L_{max} (cd/m^2)	CIE
1		0.32	0.31	3.2	1540	(0.16, 0.12)
2	120 °C, 30 min	0.53	0.51	2.8	2362	(0.16, 0.12)
3		2.1	2.02	3.2	6278	(0.17, 0.13)
4	120 °C, 30 min	2.3	2.21	3.4	6107	(0.17, 0.13)

[a] Configurations of 1 and 2: ITO/PEDOT:PSS/PSF/Ba/Al. Configurations of 3 and 4: ITO/PEDOT:PSS/PVK/PSF/Ba/Al. LE: luminous efficiency; EQE: external quantum efficiency; *L*: luminance; V_{on}: turn-on voltage.

polyfluorene analogue—poly[9,9-bis(4-(2-ethylhexyloxy)phenyl)fluorene-2,7-diyl]—was reported to a luminous efficiency of 1.9 cd/A (corresponding to an EQE of 1.8%) with CIE coordinates of (0.16, 0.12).[3] The current density−luminance−voltage ($J-L-V$) characteristics of device A and the LE−current density ($LE-J$) characteristics of both devices are plotted in the Figures S6 and S7.

The thermal properties of PSF were investigated using thermogravimetric analysis (TGA) and differential scanning calorimetry (DSC) under a nitrogen atmosphere. PSF exhibits excellent thermal stability from the TGA and DSC measurements (shown in Figures S8 and S9). In the DSC trace of heating (10 °C/min), PSF exhibited a glass transition at about 120 °C, which is slightly higher than that of poly(9,9-dialkoxyphenyl-2,7-fluorene) (108 °C)[14] and much higher than that of poly(9,9-dihexyl-3,6-fluorene) (83 °C).[6] TGA curve shows that decomposition temperature of PSF starts at 426 °C (5% weight loss), which is close to that of poly(9,9-dialkysilafluorene).[5] We attribute the excellent thermal stabilities of PSF to the 9,9-diphenyl substitutes.

Conclusion. In conclusion, the soluble poly(9,9-dialkoxyphenyl-2,7-silafluorene) was prepared via Yamamoto reactions. This polymer with high glass transition temperature of 120 °C exhibits a high external quantum efficiency of 75% and a luminous efficiency of 2.1−2.3 cd/A.

Acknowledgment. The authors are grateful for financial support from Fundamental Research Funds for the Central Universities of China (No. 2009ZM0307), Ministry of Science and Technology Project (No. 2009CB623601), and the National Nature Science Foundation of China (No. U0634003). We thank Prof. Hongzhi Wang for help with the PL measurements.

Supporting Information Available: NMR spectra of monomers and PSF, cyclic voltammograms of PSF, DSC heating curves of PSF, TGA of PSF, the current density−luminance−voltage ($J-L-V$) characteristics and the LE−current density ($LE-J$) characteristics of the devices from PSF. This material is available free of charge via the Internet at http://pubs.acs.org.

References and Notes

(1) Burroughes, J. H.; Bradley, D. D. C.; Brown, A. R.; Marks, R. N.; Mackay, K.; Friend, R. H.; Burn, P. L.; Holmes, A. B. *Nature* **1990**, *347*, 539–541.

(2) (a) Ohmori, Y.; Uchida, M.; Muro, K.; Yoshino, K. *Jpn. J. Appl. Phys.* **1991**, *30*, L1941–L1943. (b) Janietz, S.; Bradley, D. D. C.; Grell, M.; Giebeler, C.; Inbasekaran, M.; Woo, E. P. *Appl. Phys. Lett.* **1998**, *73*, 2453–2455.
(3) Liu, J.; Zou, J. H.; Yang, W.; Wu, H. B.; Li, C.; Zhang, B.; Peng, J. B.; Cao, Y. *Chem. Mater.* **2008**, *20*, 4499–4506.
(4) Huang, C. W.; Peng, K. Y.; Liu, C. Y.; Jen, T. H.; Yang, N. J.; Chen, S. A. *Adv. Mater.* **2008**, *20*, 3709–3716.
(5) Chan, K. L.; McKiernan, M. J.; Towns, C. R.; Holmes, A. B. *J. Am. Chem. Soc.* **2005**, *127*, 7662–7663.
(6) (a) Mo, Y. Q.; Tian, R. Y.; Shi, W.; Cao, Y. *Chem. Commun.* **2005**, 4925–4926. (b) Chan, K. L.; Watkins, S. E.; Mak, C. S. K.; McKiernan, M. J.; Towns, C. R.; Pascu, S. I.; Holmes, A. B. *Chem. Commun.* **2005**, 5766–5768.
(7) (a) List, E. J. W.; Guentner, R.; Freitas, P. S.; Scherf, U. *Adv. Mater.* **2002**, *14*, 374–378. (b) Kulkarni, A. P.; Kong, X.; Jenekhe, S. A. *J. Phys. Chem. B* **2004**, *108*, 8689–8701. (c) Liu, L. L.; Tang, S.; Liu, M. R.; Xie, Z. Q.; Zhang, W.; Lu, P.; Hanif, M.; Ma, Y. G. *J. Phys. Chem. B* **2006**, *110*, 13734–13740. (d) Abbel, R.; Wolffs, M.; Bovee, R.; van Dongen, J.; Lou, X.; Henze, O.; Feast, W.; Meijer, E.; Schenning, A. *Adv. Mater.* **2009**, *21*, 597–602.
(8) (a) Palilis, L. C.; Mäkinen, A. J.; Uchida, M.; Kafafi, Z. H. *Appl. Phys. Lett.* **2003**, *82*, 2209. (b) Yamaguchi, S.; Endo, T.; Uchida, M.; Izumizawa, T.; Furukawa, K.; Tamao, K. *Chem.—Eur. J.* **2000**, *6*, 1683–1692.
(9) (a) Duan, C. H.; Cai, W. Z.; Huang, F.; Zhang, J.; Wang, M.; Yang, T. B.; Zhong, C. M.; Gong, X.; Cao, Y. *Macromolecules* **2010**, *43*, 5262–5268. (b) Wang, E. G.; Wang, L.; Lan, L. F.; Luo, C.; Zhuang, W. L.; Peng, J. B.; Cao, Y. *Appl. Phys. Lett.* **2008**, *92*, 033307. (c) Boudreault, P.-L. T.; Michaud, A.; Leclerc, M. *Macromol. Rapid Commun.* **2007**, *28*, 2176–2179.
(10) Wang, E. G.; Li, C.; Peng, J. B.; Cao, Y. *J. Polym. Sci., Part A* **2007**, *45*, 4941–4949.
(11) (a) Mo, Y. Q.; Deng, X. Y.; Jiang, X.; Cui, Q. H. *J. Polym. Sci., Part A* **2009**, *47*, 3286–3296. (b) Wang, E. G.; Li, C.; Mo, Y. Q.; Zhang, Y.; Ma, G.; Shi, W.; Peng, J. B.; Yang, W.; Cao, Y. *J. Mater. Chem.* **2006**, *16*, 4133–4140.
(12) (a) Beaupre, S.; Boudreault, P. L. T.; Leclerc, M. *Adv. Mater.* **2010**, *22*, E6–E27. (b) Cheng, Y. J.; Yang, S. H.; Hsu, C. S. *Chem. Rev.* **2009**, *109*, 5868–5923. (c) Chen, J. W.; Cao, Y. *Macromol. Rapid Commun.* **2007**, *28*, 1714–1742. (d) Zhao, Q.; Liu, S. J.; Huang, W. *Macromol. Chem. Phys.* **2009**, *210*, 1580–1590. (e) Grimsdale, A. C.; Chan, K. L.; Martin, R. E.; Jokisz, P. G.; Holmes, A. B. *Chem. Rev.* **2009**, *109*, 897–1091. (f) Wong, W. W. H.; Holmes, A. B. *Adv. Polym. Sci.* **2008**, *212*, 85–98.
(13) (a) Yu, W. L.; Pei, J.; Huang, W.; Heeger, A. *J. Adv. Mater.* **2000**, *12*, 828–831. (b) Klärner, G.; Davey, M. H.; Chen, W. D.; Scott, J. C.; Miller, R. D. *Adv. Mater.* **1998**, *10*, 993–997.
(14) Lee, J. H.; Hwang, D. H. *Chem. Commun.* **2005**, 2836–2837.
(15) (a) Hung, M. C.; Liao, J. L.; Chen, S. A.; Chen, S. H.; Su, A. C. *J. Am. Chem. Soc.* **2005**, *127*, 14576–14577. (b) Sims, M.; Bradley, D. D. C.; Ariu, M.; Koeberg, M.; Asimakis, A.; Grell, M.; Lidzey, D. G. *Adv. Funct. Mater.* **2004**, *14*, 765–781. (c) Zhou, X. H.; Zhang, Y.; Xie, Y. Q.; Cao, Y.; Pei, J. *Macromolecules* **2006**, *39*, 3830–3840. (d) Zeng, G.; Yu, W. L.; Chua, S. J.; Huang, W. *Macromolecules* **2002**, *35*, 6907–6914.
(16) (a) Chen, R. F.; Fan, Q. L.; Liu, S. J.; Zhu, R.; Pu, K. Y.; Huang, W. *Synth. Met.* **2006**, *156*, 1161–1167. (b) Couzijn, E. P. A.; van den Engel, D. W. F.; Slootweg, J. C.; de Kanter, F. J. J.; Ehlers, A. W.; Schakel, M.; Lammertsma, K. *J. Am. Chem. Soc.* **2009**, *131*, 3741–3751. (c) Yan, D. C.; Mohsseni-Ala, J.; Auner, N.; Bolte, M.; Bats, J. W. *Chem.—Eur. J.* **2007**, *13*, 7204–7214. (d) Shimizu, M.; Mochida, K.; Hiyama, T. *Angew. Chem., Int. Ed.* **2008**, *47*, 9760–9764. (e) Yabusaki, Y.; Ohshima, N.; Kondo, H.; Kusamoto, T.; Yamanoi, Y.; Nishihara, H. *Chem.—Eur. J.* **2010**, *16*, 5581. (f) Li, L.; Xu, C.; Li, S. *Tetrahedron Lett.* **2010**, *51*, 622–624.
(17) Liu, Y. X.; Stringfellow, T. C.; Ballweg, D.; Guzei, I. A.; West, R. *J. Am. Chem. Soc.* **2002**, *124*, 49–57.
(18) Xiao, H. B.; Leng, B.; Tian, H. *Polymer* **2005**, *46*, 5707–5713.
(19) Chen, X. W.; Tseng, H. E.; Liao, J. L.; Chen., S. A. *J. Phys. Chem. B* **2005**, *109*, 17496–17502.
(20) Bredas, J. L.; Silbey, R.; Boudreaux, D. S.; Chance, R. R. *J. Am. Chem. Soc.* **1983**, *105*, 6555–6559.

20 *Macromolecules* **2011**, *44*, 20–28
DOI: 10.1021/ma1018523

Macromolecules
ARTICLE

Initiation of Cavitation of Polypropylene during Tensile Drawing

A. Rozanski,[†] A. Galeski,*[,†] and M. Debowska[‡]

[†]*Centre of Molecular and Macromolecular Studies, Polish Academy of Sciences, 90363 Lodz, Poland, and* [‡]*Institute of Experimental Physics, Wroclaw University, Poland*

Received August 15, 2010; Revised Manuscript Received December 1, 2010

ABSTRACT: The effect of stabilizers, additives, and low molecular weight fractions on cavitation during tensile drawing was studied in polypropylene. The additives were extracted from compression molded samples by critical CO_2 and also by a mixture of nonsolvents. The extract was an oily liquid composed of antioxidant, processing stabilizer, and a spectrum of low molecular weight fractions of polypropylene. Purified polypropylene exhibited surprisingly more intense cavitation than pristine polypropylene as it was determined by small-angle X-ray scattering and volume strain measurements. Intensification of the cavitation process in the purified samples was explained by the changes in the amorphous phase, namely, the changes in free volume by eliminating low fractions and soluble additives. An increase in free volume was probed with positron annihilation lifetime spectroscopy. Intense formation of cavitation pores in purified polypropylene proves that initiation of cavitation in polypropylene has a homogeneous nature.

Introduction

In the simplest kind of deformation, tensile drawing, deformation of most crystalline materials is accompanied by formation of cavities, which manifests itself by strong whitening of the material. For years cavitation was regarded as an artifact accompanying deformation of selected materials, having no considerable influence on the course of material deformation. The research conducted during recent years allowed to understand better many aspects connected with formation of discontinuities in the material and demonstrate that cavitation is actually an important, unignorable phenomenon, which nevertheless frequently masks true mechanisms of deformation. Even though a number of factors influencing the intensity of cavitation are known, such as thickness and orientation of crystals,[1,2] molecular weight of a polymer,[3,4] deformation rate and temperature,[3,5−7] or thickness of interlamellar regions,[1] the nature of nuclei initiating cavitation in polymer materials during their deformation as well as the influence of the physical parameters of amorphous phase on the phenomenon are still not known. It was clearly demonstrated[1] that during plastic deformation there is a kind of "rivalry" between activation of deformation mechanisms of crystalline phase and cavitation occurring in amorphous regions. The competition between crystal plasticity and cavitation during tensile drawing of crystalline polymers was first addressed by us.[1,8] The competition between the two phenomena is best described by the hypothesis of Ludwig−Davidenkov−Orovan (see ref 9) that was adopted to polymers from mechanics of metals and ceramics. In simpler words, easier phenomenon occurs before the one that is more difficult. In the description of cavitation, we used the term "cohesion of the amorphous phase" for the quantitative description of its strength. Its measure is a 3-D stress needed for initiation of cavitation. The 3D stress is important in cavitation of semicrystalline polymers, and we may learn, for example, from the studies by Castagnet et al.[10] We have correlated the strength of amorphous layers against cavitation with their thickness and crystallinity degree and not with the thickness of crystals alone because in the instant of cavity formation the cavity diameter is limited by the amorphous layer thickness, otherwise lamellae have to be broken. The cohesion of the amorphous layers is dependent on their thickness because when crystallinity is higher, most of the entanglements are rejected into the amorphous phase, then the thinner and the stronger is the amorphous phase. We may refer to papers of Bartczak[11−13] in which he has demonstrated that not only crystallinity degree and crystal thickness (amorphous layer thickness) in PE is influencing the amount of tie molecules, permanent entanglements and number of segments between active cross-links but also the molecular characteristics of PE that is used and pressure during PE processing. In addition we have shown that cavities can be stable only if the 3D stress resulting from tensile drawing is sufficient to keep them open. There is a decisive role of surface tension that tends to close a cavity and counteracts with a negative pressure generated during tensile drawing. On the basis of surface tension and thickness of amorphous regions, Pawlak and Galeski[1] estimated the negative pressure necessary to generate stable cavitations, equivalent to the strength of the amorphous phase, for several polymeric materials and also for polypropylene.

Recently cavitation in polyethylene was described by Humbert et al.[14] in terms of "density of stress transmitters". Such elements as tie molecules, entanglements, and partial percolation of the crystalline phase are considered as stress transmitters through stacks of crystalline lamellae, and they are responsible for an increase of elastic modulus of confined amorphous layers above that typical for the bulk rubbery modulus. According to Humbert et al., two parameters are governing cavitation: density of stress transmitters and crystal thickness. Cavitation occurs when the stress in the system exceeds a certain critical stress needed for cavitation. Cavitation in the amorphous phase according to Humbert et al.[14] occurs under tensile stress, unlike in other approaches to cavitation of liquids or rubbers requiring 3D stress (negative pressure) [e.g., refs 15−17]. The conclusion drawn is that cavitation is triggered under certain tensile stress that is related to the strength of the amorphous phase against cavitation governed by the ratio of stress transmitters and crystal thickness.

Low molecular weight liquids show no strength at all because cavitation is immediate due to the presence of residual impurities

*To whom correspondence should be addressed. E-mail: andgal@cbmm.lodz.pl.

 Published on Web 12/15/2010 © 2010 American Chemical Society

and dissolved gases acting as instantaneous heterogeneous nuclei of cavitation. These facts are known since 1672 by Huygens[18] and detailed much later by Reynolds.[19,20] Those studies allowed one to understand better the nature of the phenomenon. Only very pure liquids show strength and can transfer the stress without breaking. In water, cavitation is nucleated by gas or vapor microbubbles or solid, hydrophobic impurities, whose pores are filled with air. Also during crystallization of polymers from the molten state, cavitation is supported by the presence of additives, whose surfaces exhibit weak adhesion to a melt.[21] In both cases, cavitation exhibits properties of a heterogenously nucleated process. The above presented facts indicate that the amorphous phase of crystalline polymers at a temperature above its glass transition temperature differs markedly from low molecular weight analogous liquids. Polymers are not specially purified; it is opposite: they contain various additives such as stabilizers, antioxidants, residue of catalysts, low molecular weight fractions, lubricants, light stabilizer, etc. Despite these impurities and additives, the amorphous phase of crystalline polymers exhibit amazingly high strength in terms of cavitation stress, at the level of 10−20 MPa; for comparison, tap water has no strength at all. It is even more astonishing when considering that all those substances and additives are rejected into amorphous layers during polymer crystallization. Usually additives do not cocrystallize with polymers, also low molecular weight fractions are rejected from crystals to the amorphous phase because of fractionation. Cavitation initiation in polymers seemingly has a complicated nature, unlike in unpurified low molecular weight liquids. The most probable reasons are confinement of amorphous layers between crystalline lamellae and macromolecular chain entanglements, the factors that are absent in low molecular weight liquids. One of the prime objectives of the paper is to examine the influence of impurities on the nucleation of cavities generated during deformation of a polymer. It seems by analogy with low molecular weight liquids that substances present in the amorphous phase of crystalline polymers, such as stabilizers, processing additives, or low molecular weight fractions (oligomers) as well as residues of catalyst can significantly influence the intensity of the cavitation process. In order to determine the role of the mentioned additives in nucleation of cavitation, the material has been subjected to purification and degassing and the influence of the mentioned "impurities" on initiation and intensity of the cavitation process has been examined. The conducted studies should determine if nucleation of cavitation during deformation of polymers takes place in a similar, heterogeneous manner as in the case of liquids of low molecular weight. The obtained results will allow one to better understand the mechanism of cavity formation during deformation of crystalline polymers and thus enable better control of the phenomenon, e.g., elimination of cavitation where it is undesired.

Experimental Section

Materials. Studies presented in the paper have been conducted for a number of crystalline polymers, whose deformation was accompanied by cavitation. The materials used are presented and characterized: polypropylene, Novolen 1100H (M_w = 400 kg/mol, M_n = 80 kg/mol, M_w/M_n = 5; manufacturer data), of melt flow index MFI = 1.8 g/10 min (for 230 °C, 2.16 kg according to ISO 1133), density 0.91 g/cm^3, by BASF.

Purification. The process of polypropylene purification has been performed using the following methods: (1) purification using supercritical CO_2 extraction. Extraction was run for 13 h at the temperature of 60 °C under pressure of 200 bar, very slow decompression of the system was applied to enable slow removal of CO_2 and to avoid changes in the material structure; (2) purification using extraction with a nonsolvent mixture (hexane/chloroform/ethanol 4/1/1, v/v/v)[22,23] in Soxhlet apparatus. Components of the mixture are nonsolvents of the crystalline phase; however, they can permeate into the amorphous regions of polyolefins. The extraction process was run for at least 72 h. After completion of extraction, the purified material was taken out of the nonsolvent mixture and placed in a vacuum drier at the temperature of 50 °C in order to remove nonsolvents. The nonsolvent mixture, after extraction, was evaporated on a vacuum evaporator, so as to perform quality and quantity assessment of substances extracted from the material.

Mechanical Testing. Mechanical properties of the materials examined in the paper were assessed using a testing machine (Instron 5582) of load range 0-100kN. The shape of samples was according to ISO 527-2 standard, with 1 mm thickness and 4 mm width. The gauge length was 25 mm. Tests were performed at room temperature at the rates 6.7×10^{-4} and 3.3×10^{-3} s^{-1}. The actual shape of a sample during deformation was recorded using a Nikon D50 digital camera. In order to determine the local strain, markers of sputter coated gold located along the entire gauge length at a distance of 1 mm from one another, were being placed on surfaces of the samples using an ion sputter coater and a mask obtained with the use of photolithography. A similar measuring technique was used in the papers.[2,3,24−26] Local strain was calculated as a change in distance between the markers according to a relation: $(l - l_0)/l_0$, where l_0 is a distance between markers for the undeformed sample and l is a distance between markers for the deformed sample. Volume strain for local strains was determined using the following relation: $(V - V_0)/V_0$, where V_0 denotes volume of the undeformed sample. To do so, a small mirror was set up during the photographic register of deformation, which directed an image of the sample's thickness to a digital camera. The volume of the sample between markers was determined on the basis of a distance between markers and the thickness of the photographed sample.

Deformation of samples during small-angle synchrotron radiation scattering studies at Hasylab, Hamburg, Germany, was performed on a specially designed testing machine which enabled tension of samples with a simultaneous register of SAXS scattering patterns. Symmetrically stretched samples were monitored with the use of a camera, which enabled precise calculation of local strain of the sample on the basis of change in distance between the markers. Tests were performed at room temperature at a standard rate 3.3×10^{-3} s^{-1}. For selected experiments, a deformation rate of 6.7×10^{-4} s^{-1} was used. Deformation was conducted for 6 s, and next a scattering pattern for a given strain (calculated on the basis of images obtained with a photographic camera, with no tension) was registered. The entire procedure was cyclically repeated up to the rupture of the sample.

Differential Scanning Calorimetry (DSC). Thermal analysis of the examined materials was conducted using an indium-calibrated DSC apparatus (TA 2920, Thermal Analysis). Samples of total mass of 6−8 mg were being placed in aluminum pans and pressed slightly in order to ensure good contact with the DSC cell surface. The data was registered during heating at a constant rate of 10°/min, under nitrogen flow. The degree of crystallinity of the studied samples was determined according to a formula: $X_c = \Delta H_m/\Delta H_m^\circ$, where: ΔH_m is the measured specific heat of melting, ΔH_m° is the heat of fusion of the crystal. For polypropylene, the value of ΔH_m° = 209 J/g has been assumed.[27]

Positron Annihilation Lifetime Spectroscopy (PALS). Positron lifetime spectra measurements were performed using an ORTEC "fast-fast" spectrometer,[28] equipment of The Section of Application of Nuclear Physics, Institute of Experimental Physics, University of Wroclaw. The resolution of the spectrometer was found to be 270 ps.

In this method, positrons emitted by the radioactive source (in this case ^{22}Na) penetrate into two samples surrounding the source and annihilate after thermalization. In the case of

polymers, some positrons create a positronium (hydrogen-like bound state of an electron and a positron) in the free volume regions. A mean lifetime of a triplet positronium (orthopositronium) is related to the size of the free volume regions in which the atoms of the orthopositronium annihilate. Reconstruction of the distribution of the positronium lifetimes, on the basis of the measured lifetime spectrum and determination of shape of the free volume regions, enables one to determine radius or volume distribution of these areas.

Positron lifetime spectra measurements were performed in air at room temperature. Measurement time for one spectrum was 20 min, which corresponds to a total of approximately 1×10^6 counts under the measured spectrum. LIFETIME software was used for the analysis.[29]

Nuclear Magnetic Resonance (NMR). ^{13}C NMR spectra in a liquid phase (deutered chloroform as a solvent) were recorded using Bruker AV 200 apparatus operating at the frequency of 50.33 MHz. Chemical shifts of signals given in parts per million (ppm) were measured relative to chloroform (^{13}C 77.00).

Small-Angle X-ray Scattering (SAXS). The small-angle X-ray scattering technique was used for detection of cavities and for determination of a long period. The 0.5 m long Kiessig-type camera was equipped with a tapered capillary collimator combined with additional pinholes (300 μm in diameter) forming the beam and imaging plates as a detector and recording medium (Kodak). The camera was coupled to an X-ray source (sealed-tube, fine point Cu Kα filtered radiation, operating at 50 kV and 40 mA; Philips). The time of collection of the pattern was usually around 3 h. Exposed imaging plates were read with Phosphor Imager SI scanner and ImageQuant software (Molecular Dynamics).

In situ studies with the use of synchrotron radiation, λ = 0.1542 nm, were performed at the A2 beamline in Hasylab (Hamburg, Germany). Two-dimensional scattering patterns were registered with the use of a MarCCD 165 detector (Mar Research, Norderstedt, Niemcy) with a resolution of 2048 $\times$ 2048 pixels. The distance between the sample and the detector was 2513 mm. The exposure time was 12 s.

Long periods were determined from one-dimensional sections of the 2-D pattern. Background and Lorentz corrections were applied to the curves. A long period was then calculated from the position of the maximum of the corrected curves using Braggs law.

Wide-Angle X-ray Scattering (WAXS). Analysis of the crystalline structure of the materials and assessment of the degree of their crystallinity was performed using wide-angle X-ray scattering measurements by means of a computer controlled goniometer coupled to a sealed-tube source of Cu Kα radiation (Philips), operating at 50 kV and 30 mA. The Cu Kα line was filtered using electronic filtering and the usual thin Ni filter. The degree of crystallinity was calculated on the basis of diffractograms registered at a step $2\theta = 0.05°$ by means of sufficiently thin diaphragms. Since reflections from the crystalline phase and the amorphous halo frequently overlap each other, it was necessary to separate them. Analysis of diffraction profiles of the examined samples and separation of peaks was performed using WAXSFit software designed by M. Rabiej of the University of Bielsko-Biała (AHT).[30] The software allows one to approximate the shape of the peaks with a linear combination of Gauss and Lorentz or Gauss and Cauchy functions and adjusts their settings and magnitudes to the experimental curve with a "genetic" minimizing algorithm. Such calculated surfaces of peaks, corresponding to given crystallographic planes, and an amorphous halo allowed one to determine the degree of crystallinity of the sample.

Results

The presence of impurities, both in liquids of low molecular weight and in a melt of the crystallizing material, encourages formation of cavitation bubbles. Stabilizers present in the material (added by manufacturers to improve thermal parameters and material processing), catalyst residue, crystallization nucleants, and low molecular weight fractions, oligomers (result of an imperfect process of synthesis), can act as impurities, which are substances that affect the intensity of the cavitation process. The above-mentioned substances do not cocrystallize with a polymer and are preferentially located in the amorphous phase of the material. In order to assess their impact on cavitation accompanying tensile drawing, commercial polypropylene was subjected to purification using supercritical CO_2 extraction and extraction with a nonsolvent mixture (hexane/chloroform/ethanol 4/1/1, v/v/v) in Soxhlet apparatus. Both methods of purification of the amorphous phase led to very similar results; hence, only the detailed results obtained for the polypropylene purified using extraction with the nonsolvent mixture will be presented further. This type of extraction is used in research on thermal and thermooxidative degradation and stability of polyolefin materials[22,23] as it does not cause any changes to the crystalline phase. The samples in the form appropriate for mechanical and X-ray studies were cut out from a film, 1 mm thick, prepared by compression molding at the temperature of 220 °C.

In order to test the efficiency of the applied purification method, an oily liquid extracted from the material (extraction process was run for at least 72 h, oily residue constituted 0.5−0.9% by weight) has been analyzed. Figure 1 presents a ^{13}C spectrum of nuclear magnetic resonance performed for the extracted substance, dissolved in deutereted chloroform. The presented spectrum allowed one to identify carbon atoms (marked in the figure) forming a molecule of the material acting as a stabilizer (pentaerythritol tetrakis(3-(3,5-ditert-butyl-4-hydroxyphenyl)propionate), corresponding to the trade name Irganox 1010) and molecules of propylene oligomers of various size and architecture, overlapped with signals from stearate. Therefore, the applied method allowed one to remove molecules of the stabilizer, processing aid, and low molecular weight fractions from the examined material, substances whose presence should influence the intensity of the cavitation process. In order to assess the influence of the extracted substances (impurities) on cavitation during tensile drawing, the purification process should not influence parameters of the crystalline phase of the material.

Hence, with the use of X-ray techniques and differential scanning calorimetry, selected parameters of the crystalline phase of the examined material prior to and after extraction were determined. Once the extraction process has been completed, the samples were being dried at the temperature of 50 °C in order to remove the residues of nonsolvents. Samples of the reference material were subjected to an analogous procedure. Table 1 presents selected parameters of the crystalline phase determined for samples prior to and after the purification process. Reference and purified samples consist of only the α form crystals as it can be judged from the X-ray diffraction reflexes from (110), (040), (130), (060), and (113) crystallographic planes of monoclinic iPP crystals (α form). No other crystals such as cocrystals with additives were detected. SAXS patterns for both samples are characteristic for stacking of crystalline lamellae interspersed with amorphous layers with clear periodicity. Since the crystals are free from additives, it is concluded that the additives are concentrated in amorphous layers. Also low molecular weight fractions are embeded in crystals as it can be deduced from a high and sharp melting temperature (167.1 °C $\pm$ 0.1 °C). The presented data indicate a lack of substantial changes in the crystalline structure of the material as a result of the extraction process. Therefore, the applied method of material purification allows one to obtain a desired effect without markedly influencing other parameters of the material. Figure 2 illustrates the engineering stress−strain curve of pristine polypropylene with polypropylene

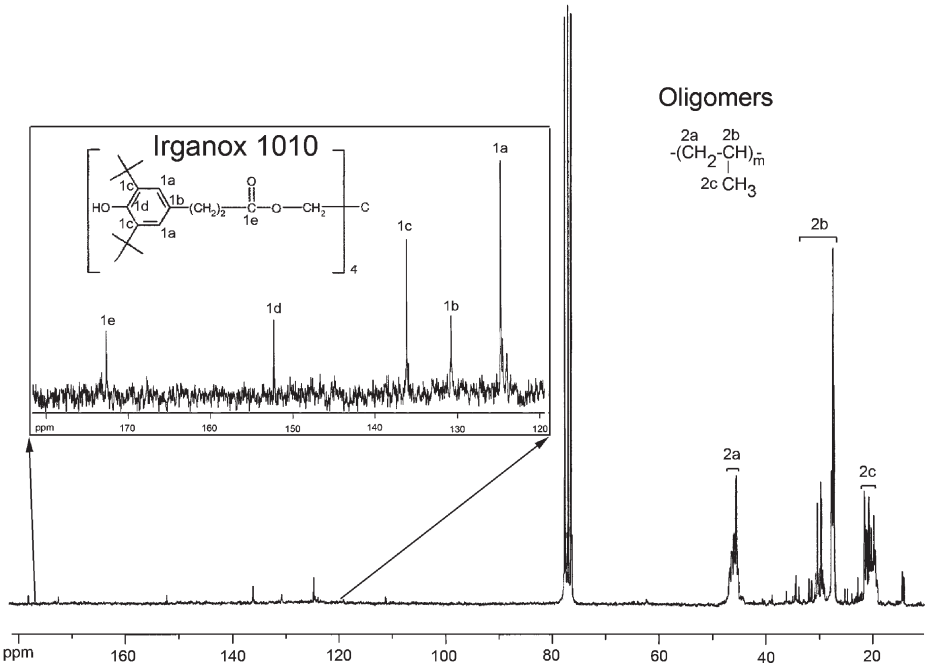

Figure 1. ^{13}C NMR spectrum of a substance extracted from the examined polypropylene.

Table 1. Parameters of Crystalline Phase of Polypropylene Samples Prior to and after the Purification Process

sample	long period [nm]	crystallinity degree [%] (DSC)	crystallinity degree [%] (WAXS)
reference (RS)	13.3 ± 0.2	47.8 ± 0.1	46.3 ± 0.5
purified (PS)	13.6 ± 0.2	48.0 ± 0.1	46.6 ± 0.5

purified by extraction with the nonsolvent mixture. There is not many changes caused by extraction except a slightly lower strain to break. Very similar stress−strain curves for reference and purified samples presented in Figure 2 prove that nothing serious happened to the entanglement density and the number of taut molecules spanning neighboring lamellae during purification. They remained untouched as it can be judged from the lack of changes in strain hardening behavior. The evident difference between the two samples was that the purified sample during tensile drawing exhibited even stronger stress whitening than pristine sample.

In order to assess the influence of the purification process of the material on the phenomenon of cavitation accompanying tensile drawing, in situ small-angle X-ray scattering studies using synchrotron radiation were performed. X-ray scattering is much stronger from cavities than from the structural elements of the material due to a difference in the electron density. The SAXS method is therefore a very useful tool for examination of the cavitation process in the material. Figure 3 presents SAXS scattering patterns recorded for the reference and purified polypropylene deformed at a rate 3.3×10^{-3} s^{-1}, up to the local strain of 4.5.

In the case of the reference sample (RS), signals indicating formation of cavities in the material, on SAXS scattering patterns, are already observed at the local strain equal to 0.13. The obtained scattering pattern indicates that cavities at this stage of deformation are of ellipsoidal shape and are oriented by their long axis perpendicularly to the direction of deformation (signal in the meridional region on a scattering pattern). The specific arrangement and shape of cavities is forced by the lamellar structure of the material. On further deformation stages, an increase in the intensity of the registered signal is observed in the aforementioned region of a scattering pattern, up to the strain of 0.8. At this stage of deformation, a signal in the equatorial region of a scattering pattern is also registered, which indicates the presence of the second population of cavities oriented parallel to the direction of the applied force. Signal appearing in this region of the scattering pattern at the cost of intensity in the meridional region demonstrates that subsequent plastic deformation mechanisms of the material (lamellar fragmentation) activated at this stage of deformation also force reorganization of the shape of cavities.

Further stages of deformation (>0.8) are accompanied by a substantial decrease in size of cavitation pores perpendicularly to the direction of deformation and their strong orientation toward the direction of deformation. For a local strain equal to 4.5, one observes a decrease in the intensity of signal coming from the cavities. The reason for this effect is that cavities enlarge with deformation, and finally most of them scatter X-rays outside of the SAXS detection limit.

Deformation of the purified samples is also accompanied by cavitation. It proceeds almost identically as in the case of reference material; however, a significant difference concerns the intensity of scattering signals coming from cavities at subsequent stages of deformation. Analysis of the presented scattering patterns indicates that the intensity of the cavitation process has increased in the purified material. The extraction process, which resulted in the removal of substances capable of nucleating cavitation, not only did not decrease the intensity of cavitation but produced a reverse effect, an increase in the number of cavitation pores formed during deformation of the material.

Analogous conclusions can be drawn while analyzing volume strain measurements performed for the examined material prior to and after the purification process. Figure 4 presents the relevant data. Deformation of the unmodified polypropylene sample (RS) is accompanied by a strong increase in volume (of around 70%), an effect of discontinuities occurring in the material. The purification process leads to an increase in the intensity of cavitation, whose effect is a volume strain increase, presented in Figure 4, up to around 95%. Removing stabilizers and additives filling the amorphous phase of the material and low

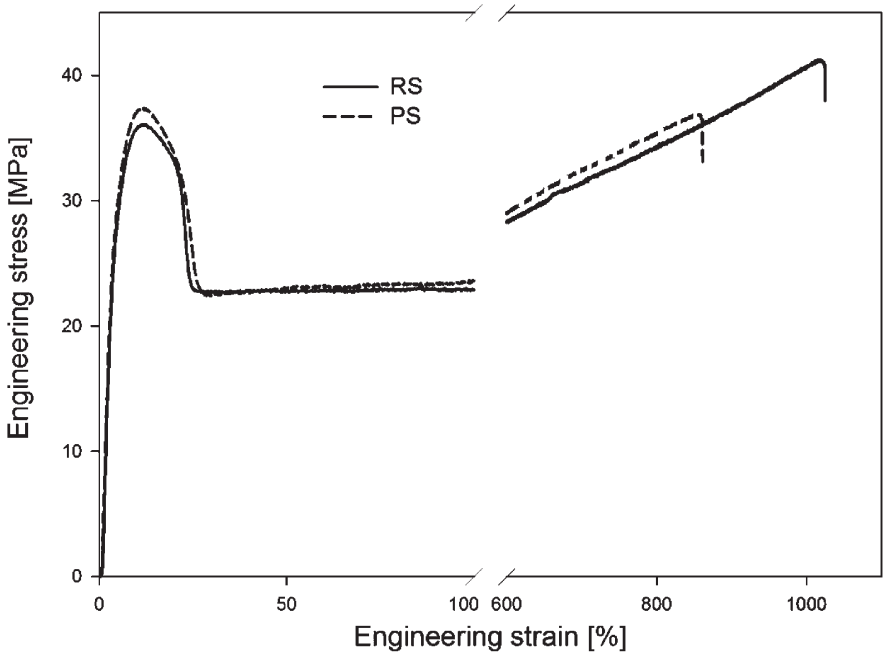

Figure 2. Engineering stress−strain curve of the polypropylene sample subjected to purification and degassing compared with the stress−strain curve for the reference sample.

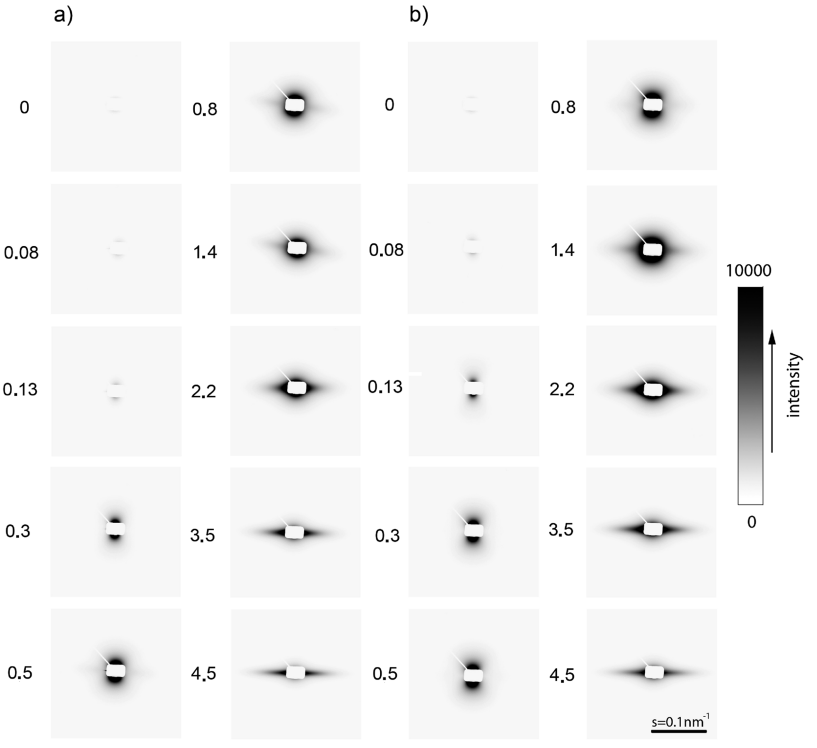

Figure 3. Small-angle X-ray scattering patterns of a series of polypropylene samples: (a) RS and (b) PS. Patterns correspond to the local strain of samples. Deformation rate, 3.3×10^{-3} s^{-1}; direction of deformation, vertical.

molecular weight fractions resulted in an increase of approximately 30% in the intensity of cavity formation in the material.

Intensity of cavitation accompanying tensile drawing of crystalline polymers is affected by numerous factors connected with parameters of the material and conditions under which deformation takes place. One of such factors is the deformation rate. Therefore, additional examinations of polypropylene were conducted before and after purification for a lower deformation rate (6.7×10^{-4} s^{-1}).

Decreasing the deformation rate should decrease the intensity of cavitation in both materials and at the same time intensify the difference between them. Figure 5 presents SAXS scattering patterns recorded during in situ studies using synchrotron radiation for reference and purified polypropylene deformed at a rate of 6.7×10^{-4} s^{-1} up to a local strain of 4.5. Deformation of polypropylene samples prior to and after the purification process is accompanied by cavitation; however, the intensity of the phenomenon is significantly higher for materials after extraction of

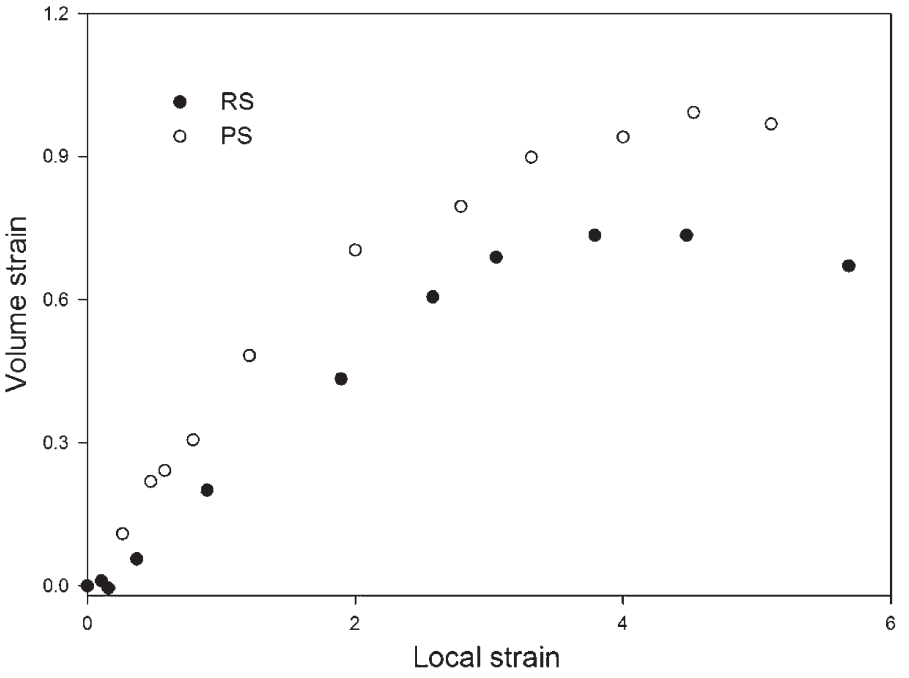

Figure 4. Volume strain as a function of local strain for reference polypropylene (RS) and purified polypropylene (PS). Deformation rate $3.3 \times 10^{-3}\ s^{-1}$.

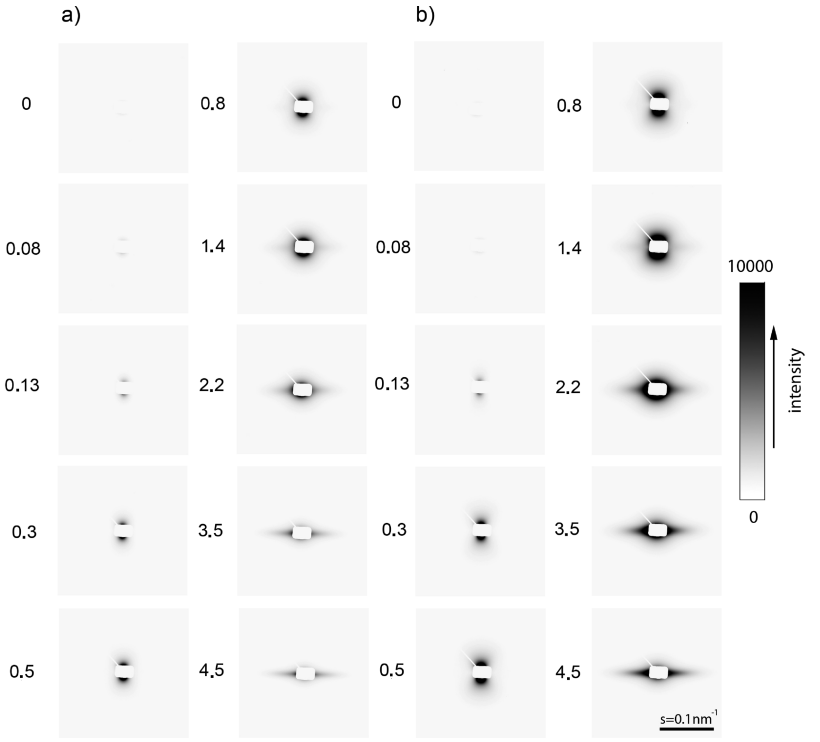

Figure 5. Small-angle X-ray scattering patterns of a series of polypropylene samples: (a) RS and (b) PS. Numbers correspond to the local strain of samples. Deformation rate, $6.7 \times 10^{-4}\ s^{-1}$; direction of deformation, vertical.

stabilizers and low molecular weight substances. At each stage of deformation of the examined materials, one observes a substantial difference in the intensity of the scattering signal between the reference and the purified sample.

Figure 6 presents volume strain measurements for samples prior to and after the purification process, deformed at a rate of $6.7 \times 10^{-4}\ s^{-1}$. Tensile drawing of the unmodified polypropylene sample (RS) is accompanied by a substantial volume increase (up to 50%), resulting from cavities generated in the material. Purification of the material increases the intensity of cavitation, whose effect is an increase in volume strain by approximately 70%, presented in Figure 6. Extraction leading to removal of impurities from the amorphous phase of the material, i.e., stabilizers and low molecular weight fractions, results in an increase in cavity formation in the material by around 40%.

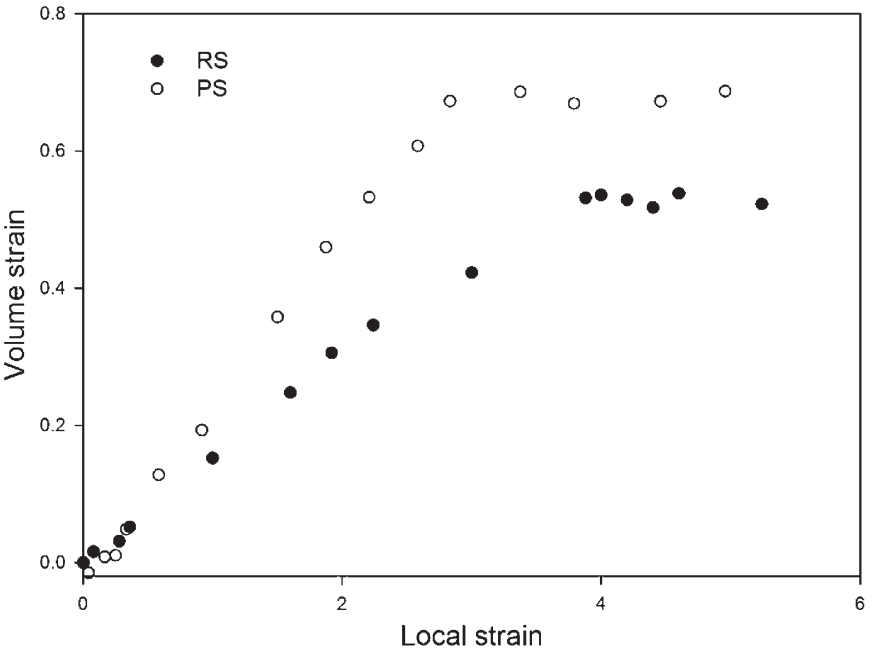

Figure 6. Volume strain as a function of local strain for reference polypropylene (RS) and purified polypropylene (PS). Deformation rate $6.7 \times 10^{-4}\ s^{-1}$.

Table 2. Results of Positron Lifetime Spectra Analysis

	mean lifetime					component intensity	
sample	τ_1[ps]	$\langle\tau_2\rangle$ [ps]	$\langle\tau_3\rangle$ [ns]	σ_2 [ps]	σ_3 [ns]	$I_1 + I_3$ [%]	I_2 [%]
reference sample (RS)	125	357.4 ± 1.6	2.37 ± 0.07	61.9 ± 0.6	0.95 ± 0.09	22.2 ± 0.4	77.8 ± 0.4
purified sample (PS)	125	371.9 ± 1.2	2.57 ± 0.02	72.2 ± 0.4	0.83 ± 0.04	19.7 ± 0.1	80.3 ± 0.1

The above results are astonishing and against expectation. There is no direct analogy between amorphous phase of crystalline polymers above Tg and low molecular weight liquid: it is not the impurities that nucleate cavitation in the amorphous phase during tensile drawing. There must be an inherent property of the amorphous phase that upon purification intensifies nucleation of cavitation.

The packing of the amorphous phase of the material, which is a consequence of the chemical structure of macromolecules and organization of the supermolecular structure, naturally generates the free volume pores, whose size and dynamics of reorganization caused by thermal movements of polymer chains may have a direct influence on initiation of cavitation during deformation of the material. The amorphous phase of polymers is characterized by a more unordered structure than amorphous low molecular weight materials due to steric hindrances introduced by chemical bonds of long chains. Hence, an intrinsic element of the polymer's amorphous phase is a fraction of so-called "free volume" resulting from its incomplete packing. This results in a difference in density between well-packed polymer crystals and the amorphous phase. At the temperatures above the glass transition, the amorphous phase exhibits certain dynamics of free volume, "empty" spaces change in time as a result of thermal movements of the polymer chains. The presence of "empty" spaces (vapor or gas bubbles) in low molecular weight liquids is conducive to formation of cavities. In polymers, the dynamic "empty" spaces may also initiate nucleation of cavitation. The size of these empty spaces is considerably smaller than the thickness of amorphous layers, though it can increase under the influence of mechanical stress during tensile drawing of a polymer, which is when they may become cavitation nuclei.

In order to assess the influence of the extraction process on parameters of the amorphous phase of the material (size of the free volume of the amorphous phase), positron-lifetime spectra measurements were performed. The choice of the model for spectra analysis is extremely important. Results presented further in the paper correspond to the model of spectra analysis, which assumes (1) the intensity ratio of anihilating para- and orthopositronium of 1:3, (2) lifetime of annihilating parapositronium, τ_1, of 125 ps, (3) the presence of the log-normal distribution of mean lifetimes corresponding to free annihilation of positrons and annihilation of ortho-positrons by "pick off". In the analyzed spectrum, this corresponds to components of mean values $\langle\tau_2\rangle$ and $\langle\tau_3\rangle$, of mean lifetimes τ_2 and τ_3. Distribution of mean lifetimes τ_2 and τ_3 are characterized by dispersion values σ_2 and σ_3. The results of the obtained spectra are presented in Table 2.

A simple quantum-mechanical model allows one to relate a mean lifetime τ_3 with the size of the free volume region. In analysis of the results, as in the case of a model proposed by Tao and Eldrup,[31,32] the spherical shape of these regions has been assumed. On the basis of the distribution of τ_3 values, normalized volume distributions of the free volume regions, V, were determined as presented in Figure 7.

The extracted mass amounted to 0.9 wt %. All of it was localized in the amorphous phase before purification. The volume of purified polypropylene was not decreased due to purification as it is concluded from the long period values: 13.3 and 13.6 Å for the reference and purified samples, respectively. Also the X-ray absorption coefficients 0.3295 and 0.3251 nm^{-1} for the reference and purified samples, respectively, measured in WAXS apparatus indicate that purified sample is less absorbing of X-rays. So, the compaction, if any, that occurred during purification was very low. Apparently the sample shrinkage was very limited because of a stiff crate construction that is made up from crystalline lamellae. It leads to the conclusion that the

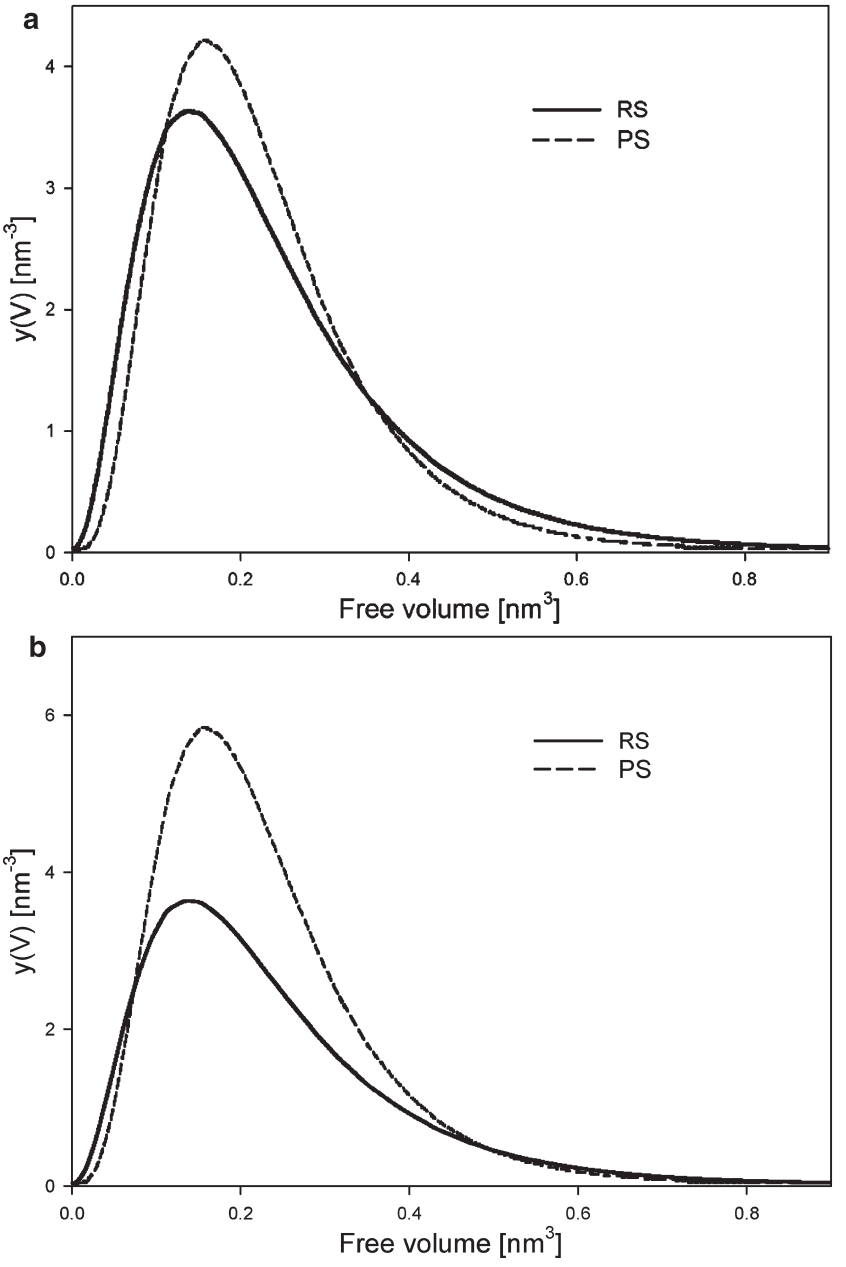

Figure 7. (a) Normalized size distributions of free volume pores of the amorphous phase of reference (RS) and purified polypropylene (PS), probed by positronium. (b) Relative size distributions of free volume pores of the amorphous phase of reference (RS) and purified polypropylene (PS), probed by positronium.

free volume in the amorphous phase was increased by a significant amount. In order to estimate the increase in free volume due to purification, we assumed the number of free volume holes at 5.2×10^{20} g^{-1} for the amorphous phase of polypropylene in the rubbery state based on the studies by Baer et al.[33] The mean free volume hole size in the reference sample is 0.139 nm^3 as it follows from our PALS measurements. The fraction of free volume of amorphous PP layers at room temperature is then $N\rho D \approx 0.065$, where N is the number of free volume holes in 1 g of amorphous phase, ρ is the density of the amorphous phase, and D is the mean size of free volume holes (0.139 nm^3). The additional free volume generated by purification is 0.9 wt %/0.9 g/cm^3 = 0.01 vol of a sample. Considering that the new free volume is concentrated only in the amorphous phase, we arrive at a total free volume fraction of 0.09 in the amorphous phase. Since Figure7a illustrates normalized size distributions of free volume holes, the curves should be corrected considering that the total free volume for the reference sample is 0.065, while for the purified sample it is 0.09. The new plot is presented in Figure 7b.

Analysis of the presented data clearly indicates an increase in the mean size and number of the free volume regions in the purified material. Removal, as a result of extraction, of stabilizers, other additives, and low-molecular weight fractions filling the amorphous part of the material leads to changes in the interlamellar regions, which results in the size increase of empty spaces constituting an integral part of the unordered phase.

Intensification of the cavitation process in the purified samples can only be explained by the changes in the amorphous phase, namely, the changes in free volume by eliminating low fractions and soluble additives. The scheme illustrating the enlargement of free volume pores in solidified polypropylene upon extraction of stabilizers, additives, and low molecular weight fractions is presented in Figure.8.

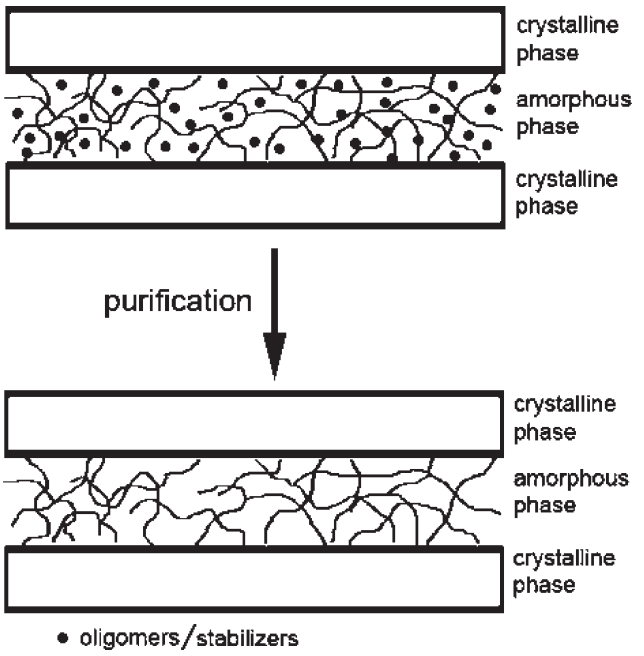

Figure 8. Schematics illustrating formation of larger and more numerous free volume pores in amorphous layer of polypropylene upon extraction of stabilizers, additives, and low molecular weight fractions.

Conclusions

Extraction of additives and the low molecular weight fraction from solidified polypropylene by a mixture of nonsolvents or by supercritical CO_2 does not cause any detectable changes to its crystalline phase. Neither the long period, as measured by SAXS, nor the crystallinity of the samples have changed. Changes introduced to the amorphous phase by extraction was limited to a significant increase in the free volume; however, the entanglement density and number of taut molecules spanning neighboring lamellae remained untouched as it can be judged from the lack of changes in strain hardening behavior. Also, the natural draw ratio of samples before extraction and after extraction is very similar if the contribution to the cross section area in the purified sample of additional cavities was taken into account (see Figure 4 showing an increase in the volume of deformed samples due to additional cavities).

Purification caused two detectable effects: increase in free volume (by PALS) and increase in cavitation intensity (volume strain, SAXS). Since all other parameters of the material were not changed significantly, it is evident that there is a strong dependence between free volume, which increased by extraction of additives and low molecular weight oligomers, and intensification of cavitation.

The dominant role of the free volume of the amorphous phase, which is an integral part of unordered regions of all crystalline polymers, in formation of cavitation pores proves that initiation of the phenomenon is of a homogeneous nature. We mean by the term "homogeneous nucleation" a nucleation from the material itself in contrast to heterogeneous nucleation on foreign substances. That was proven by removing most of the heterogeneous nuclei: impurities, additives, and gas. It appears that in crystalline polymers a heterogeneous nucleation of cavitation is nearly inactive. The observation of heterogeneous nucleation of cavitation at the level of stress of 0.5 MPa by chalk particles by Nowacki et al.[21] concerned the decohesion of polymer melt at much larger sizes than the amorphous layers in polypropylene: 1−3 μm against 10−20 nm and assuring weak bounding between polymer melt and filler particles. In polypropylene, the homogeneous nucleation of cavitation occurs under a negative stress of 10−20 MPa. We expect similar behavior connected with extraction of additives and the low molecular weight fraction in other crystalline cavitating polymers.

Acknowledgment. We wish to express thanks to the Hamburg Synchrotron Radiation Laboratory (HASYLAB) for the beam time granted within the Project I 20090069 EC. Also the Grant N N508 468834 from the Polish Ministry of Science and Higher Education is acknowledged for the financial support of the work.

References and Notes

(1) Pawlak, A.; Galeski, A. *Macromolecules* **2005**, *38*, 9688–9697.
(2) Pawlak, A. *Polymer* **2007**, *48*, 1397–1409.
(3) Pawlak, A; Galeski, A. *Macromolecules* **2008**, *41*, 2839–2851.
(4) Butler, M. F.; Donald, A. M.; Ryan, A. J. *Polymer* **1998**, *39*, 39–52.
(5) Liu, Y.; Truss, R. W. *J. Polym. Sci., Part B: Polym. Phys.* **1994**, *32*, 2037.
(6) Zhang, X. C.; Butler, M. F.; Cameron, R. E. *Polymer* **2000**, *41*, 37973807.
(7) Pawlak, A.; Galeski, A. *J. Polym. Sci., Part B: Polym. Phys.* **2010**, *48*, 1271–1280.
(8) Galeski, A. Strength and Toughness of Crystalline Polymer Systems. In *Mechanical Properties of Polymers Based on Nanostructure and Morphology*; Michler, G. H., Balta-Calleja, F. J., Eds.; CRC Taylor-Francis: Boca Raton, FL, 2005; pp 159−214.
(9) Ward, I. M.; Hadley, D. W. *An Introduction to the Mechanical Properties of Solid Polymers*; Wiley: New York, 1993; pp 232−245.
(10) Castagnet, S.; Deburk, Y. *Mater. Sci. Eng.* **2007**, *A 448*, 56–66.
(11) Bartczak, Z. *Macromolecules* **2005**, *38*, 7702–7713.
(12) Bartczak, Z.; Kozanecki, A. *Polymer* **2005**, *46*, 8210–8221.
(13) Lezak, E.; Bartczak, Z. *J. Appl. Polym. Sci.* **2007**, *105*, 14–24.
(14) Humbert, S.; Lame, O.; Chenal, J. M.; Rochas, C.; Vigier, G. *Macromolecules* **2010**, *43*, 7212–7221.
(15) Bucknall, C. B. *Toughened Plastics*; Applied Science Publishers: London, 1977.
(16) Frenkel, J. *Kinetic Theory of Liquids*; Clarendon Press: Oxford, U.K., 1946.
(17) Brennen, Ch. E. *Cavitation and Bubble Dynamics*; Oxford University Press: New York, 1995.
(18) Huygens, C. *Phil. Trans.* **1672**, *7*, 5027–5030.
(19) Reynolds, O. In *Scientific Papers on Mechanical and Physical Subject*; Cambridge University Press, 1900−1903; Vol. *I*, pp 231−243.
(20) Reynolds, O. In *Scientific Papers on Mechanical and Physical Subject*; Cambridge University Press, 1900−1903; Vol. *I*, pp 394−398.
(21) Nowacki, R.; Piorkowska, E. *J. Appl. Polym. Sci.* **2007**, *105*, 1053–1062.
(22) Audouin, L.; Girois, S.; Achimsky, L.; Verdu, J. *Polym. Degrad. Stab.* **1998**, *60*, 137–143.
(23) Khelidj, N.; Colin, X.; Audouin, L.; Verdu, J.; Monchy-Leroy, C.; Prunier, V. *Polym. Degrad. Stab.* **2006**, *91*, 1598–1605.
(24) G'Sell, C.; Hiver, J.-M.; Dahoun, A. *Int. J. Solids Struct.* **2002**, *39*, 3857–3872.
(25) Samuels, R. J. *J. Polym. Sci., Part C* **1967**, *20*, 253–265.
(26) Kryszewski, M.; Galeski, A.; Pakula, T.; Szylhabel, R. *Polimery (Polish)* **1971**, *16*, 8–11.
(27) Brandrup, J.; Immergut, E. H.; Grulke, E. A. *Polymer Handbook*; John Wiley & Sons, Inc.: New York, 1999.
(28) Coleman, P. G. In *Principles and Applications of Positron and Positronium Chemistry*; Jean, Y. C., Mallon, P. E., Schrader, D. M., Eds.; World Scientific: New York, 2003.
(29) Kansy, J. J. *Nucl. Instrum. Methods Phys. Res.* **1996**, *A374*, 235.
(30) Rabiej, M. *Polimery (Polish)* **2003**, *48*, 288–295.
(31) Tao, S. J. *J. Chem. Phys.* **1972**, *56*, 5499–5507.
(32) Eldrup, M.; Lightbody, D.; Sherwood, J. N. *Chem. Phys.* **1981**, *63*, 51–58.
(33) Wang, H. P.; Ansems, P.; Chum, S. P.; Hiltner, A.; Baer, E. *Macromolecules* **2006**, *39*, 1488–1495.

Macromolecules
ARTICLE

Macromolecules **2011**, *44*, 29–38 **29**
DOI: 10.1021/ma102366d

Free Volumes, Glass Transitions, and Cross-Links in Zinc Oxide/Waterborne Polyurethane Nanocomposites

Somia Awad,[†,‡] Hongmin Chen,[†] Guodong Chen,[§] Xiaohong Gu,[†,§] James L. Lee,[⊥] E. E. Abdel-Hady,[‡] and Y. C. Jean*[,†]

[†]*Department of Chemistry, University of Missouri—Kansas City, Kansas City, Missouri 64110, United States*, [‡]*Department of Physics, Faculty of Science, Minia University, Minia, Egypt*, [§]*Materials and Construction Research Division, National Institute of Standards and Technology, Gaithersburg, Maryland 20899, United States*, and [⊥]*Department of Chemical and Biomolecular Engineering, The Ohio State University, Columbus, Ohio 43210, United States*

Received October 18, 2010; Revised Manuscript Received November 30, 2010

ABSTRACT: The free-volume properties in a system of zinc oxide (ZnO) nanoparticles (20 nm) dispersed in waterborne polyurethane (WBPU) were measured using positron annihilation lifetime spectroscopy. Two glass-transition temperatures (T_g), lower $T_g \sim 220$ K and higher $T_g \sim 380$ K of the ZnO/WBPU nanocomposites, were found and both increase with increasing zinc oxide content from 0% to 5%. These two glass transitions are interpreted from two segmental domains of WBPU; the lower T_g is due to soft aliphatic chains and high T_g is due to polar hard microdomains, respectively. The increase in T_g with the addition of ZnO fillers is mainly attributed to interfacial interactions through hydrogen bonding, van der Walls forces, and electrostatic forces between the polymer matrix and zinc oxide nanoparticles. These results are supported by the data from the dynamic mechanical thermal analysis (DMTA). The relationship between the free volume obtained from nanoscopic positron method and the physical cross-link density from macroscopic DMTA method as a result of microphase separation of hard and soft segments in polyurethane is found to follow an exponential function. Chemical properties and surface morphology of nanocomposites were examined by Fourier transform infrared spectroscopy (FTIR) and by atomic force microscopy (AFM).

1. Introduction

Nanoparticles are a class of materials with unique chemical and physical properties and wide application potential to diverse areas.[1−3] Dispersion of nanoscale inorganic fillers into organic polymers to form polymer nanocomposites has gained increasing interest in recent years.[4−9] Controlling the nanostructure, composition, and morphology of nanocomposites plays an essential role in their diverse applications. Novel properties and advantages of nanocomposites can be obtained by successful imparting of the characteristics of parent constituents to a single material, such as increased mechanical strength, improved gas permeaselectivity, and enhanced thermal and electrical properties.[10−14]

Zinc oxide (ZnO) is an important semiconductive material and has drawn much attention due to its characteristics in optics, photonics, electronics, and biological applications.[15−23] For example, ZnO has a special UV absorption with the band gap of 3.4 eV, it also shows a marked antibacterial activity at pH values in the range from 7 to 8 without the presence of light.[15,16] ZnO nanoparticles can be obtained by various methods including thermal evaporation, electrochemical deposition, sonochemical method, sol−gel, hydrothermal synthesis and so forth.[17] Various one-dimensional (1D) ZnO nanostructures have been realized, such as nanorods, nanowires, nanobelts, nanosheets, nanotubes, nanonails, etc.[19−23] Among the 1D ZnO nanostructures, nanorods have been widely studied because of their easy preparation and wide applications.[19] In the existing studies, ZnO nanoparticles were blended with various types of polymers, such as polyethylene,[24] polypropolyene,[25,26] poly(methyl methacrylate) (PMMA),[27,28] polystyrene,[29] polyamide,[30] polyacrylonitrile,[31] polyacrylate,[32] and recently polyurethane,[33−35] to achieve specific materials properties and performance.

Waterborne polyurethanes (WBPU), namely polyurethanes dispersed in water, are a new generation of polyurethane (PU) in manufacturing electronic, adhesive, coatings, membranes, and biological applications.[36−47] They represent a major trend in the PU development because of the increasing interest about the environmental pollution, the health and safety risks. A wide variety of aqueous systems can be tailored with properties based on polyurethane chemistry and technology and related to conventional solvent-borne coatings, and with several technological advantages, including low viscosity and good applicability as coatings for different types of substrates (such as wood, concrete, leather, metal, textiles, and some polymers).[48−57] The WBPU synthesis is based on a polymerization process which involves di- or polyisocyanates and di- or polyols, which are essentially the same used for the preparation of conventional PU.[58] The large applicability of WBPU results from the fact that their performances can be modified by selecting appropriate raw materials, catalysts, and auxiliary compounds, by employing various production methods, and/or by using various methods for further processing and/or for shaping the final products.

Polyurethanes offer good elasticity because of their specific microstructure, which contains two parts: a rigid chain segments (hard) and a flexible chain segments (soft).[48−58] The soft segments originate from the polyol and impart elastomeric characteristics to the polymer and the hard segments contain the highly polar urethane linkages and act as a high modulus "filler". The thermodynamic incompatibility of the polar hard segments with the nonpolar soft segments produces microphase-separated

*Corresponding author. jeany@umkc.edu.

© 2010 American Chemical Society
Published on Web 12/09/2010

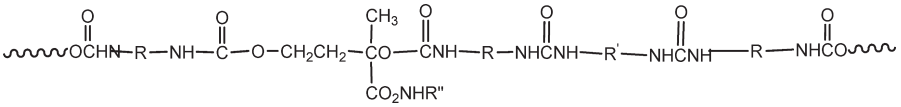

Figure 1. General chemical structure of waterborne polyurethane (WBPU).

structures, forming microdomains. The properties of WBPU depend on the relative amount of the soft and hard segments.

The diisocyanate residues and the chain extenders aggregate into hard domains due to the intersegment hydrogen bonding between N−H and C═O groups. The hard domains are dispersed throughout the soft segment matrix and impart mechanical strength to the WBPU acting as physical cross-links. As a consequence, the physical,[59] mechanical,[60−62] and adhesive[41] properties strongly depend on the degree of phase separation and on the interconnectivity of the hard domains.

Existing physical methods, such as NMR, FTIR, DMTA, neutron diffraction, X-rays, AFM, SEM, XPS, etc.[63−68] have been employed to investigate basic properties polymer nanocomposites. Only recently, a novel method, positron annihilation spectroscopy (PAS) has been used to investigate atomic and molecular defects and interfacial properties.[69−97] One of PAS techniques, positron annihilation lifetime spectroscopy (PALS), is capable of determining the free-volume and hole properties directly at the atomic and nonoscales.[98,99] This capability arises from the fact that positronium (bound state of positron and electron, Ps) is preferentially localized in regions of low electron density sites, such as free volumes, holes, interfaces, and pores. The primary mechanism of annihilation of triplet positronium (o-Ps) is by pick-off with electrons of the polymeric materials under study. Thus, the intrinsic o-Ps lifetime (142 ns) is shortened to a few ns (1−10 ns) by two-γ annihilation processes. Generally, the lifetime of o-Ps is determined by an overlap integral between the positron and the electron densities in the free volumes of molecular systems. Therefore, the o-Ps lifetime is expected to correlate directly with the dimensions where Ps is localized. A larger hole, which contains a lower mean electron density, results in a longer Ps lifetime. A simple quantum mechanical model, where o-Ps resides in a spherical well having an infinite potential barrier of radius R_o with a homogeneous electron layer in the region $R < r < R_o$, ($R_o = R + \Delta R$) has been proposed to derive the relationship.[100] Such a model provides a simple relation between the o-Ps lifetime, usually denoted as τ_3, the third mean lifetime as analyzed from experimental PALS data and the mean free-volume radius (R). A semiempirical equation by fitting the measured o-Ps lifetime (τ_3) in a spherical infinitive potential model with known cavity sizes is established as:[100−102]

$$1/\tau_3 = 2[1 - R/R_0 + (1/2\pi)\sin(2\pi R/R_0)] \quad (1)$$

where τ_3 and R are expressed in the units of ns, and Å, respectively and ΔR was calibrated to be 1.656 Å.

In this paper, we use PALS to measure free-volume sizes, distributions, and relative fractions in ZnO/WBPU nanocomposites with different % of ZnO nanoparticles and correlate chemical, physical, and mechanical properties obtained by conventional methods, FTIR, AFM, and DMTA.

2. Experimental Section

2.1. Materials and Sample Preparation. A waterborne dispersion of ZnO nanoparticles (NANOBYK, BYK) and a waterborne dispersion of polyurethane (WBPU, Bayhydrol, Bayer Material Science) were selected for this study. The chemical structure of waterborne polyurethane (WBPU) is shown in Figure 1. The WBPU was composed of long-chain aliphatic polyester segments (R, R′), which form a low-melting-point elastomeric matrix (soft) and of polar urea (−NHCONH−) and urethane (−NHCOO−) groups, which aggregate into glassy (hard) microdomains. This microphase separation is resulted from the intersegmental hydrogen bonding between N−H and C═O groups and due to the incomparability of the nonpolar soft segments and the polar hard segments. The hard segmental microdomains were winded throughout the soft segments and behave as physical cross-linking, which contributes to the mechanical strengths of the WBPU.[59−68]

The ZnO nanoparticle dispersion contains 45% by mass of nonvolatile substance, in which 86% is ZnO (measured by thermogravimetry analysis). The nominal diameter of the ZnO nanoparticles is 20 nm (provided by the manufacturer). This nanoparticle dispersion is designed by the manufacturer to improve the long-term UV stability of coatings for wood and furniture, as well as architectural applications. The WBPU is a one component anionic dispersion of an aliphatic polyester urethane resin in water/*n*-methyl-2-pyrrolidone. ZnO nanoparticle/WBPU films (hereafter referred to as ZnO/WBPU) were prepared by mixing the WBPU dispersion with different loadings of ZnO dispersion using a mechanical stirrer (Dispermat, VMA) at 315 rad/s (3000 rpm) for 20 min. After degassing for 1 h in vacuum, the mixture was then applied to the substrates. Thick films having a thickness of 100 μm were prepared by drawdown technique on the glass substrate that was pretreated with a releasing agent. All films were dried overnight under ambient conditions, followed by an oven postcure at 423 K for 10 min. Freestanding ZnO/WBPU films were obtained by removing the thick films from the glass substrates. Thin films having a thickness of approximately 6 or 100 μm were prepared by spin coating onto calcium fluoride (CaF_2) substrates at 209 rad/s (2000 rpm) for 30 s. In addition, WBPU films without ZnO nanoparticles also were prepared for comparison.

2.2. Measurements. *2.2.1. Dynamic Mechanical Thermal Analysis (DMTA).* The thermal mechanical properties of the ZnO/WBPU films, such as storage module (G'), the loss module (G''), and the loss tangent or dissipation (damping) factor (tan δ):

$$\tan\delta = G''/G' \quad (2)$$

were measured on an RSA III (TA Instruments) dynamic mechanical thermal analyzer (DMTA). Figure 2 shows the modules' results from DMTA measurements.

The glass transition temperature (T_g) measurements were determined from the peak positions of tan δ vs temperature from ~170 to 420 K at a temperature ramp of 3 °C/min, with a frequency of 1.0 Hz and a strain of 0.5% and were the average of three measurements.

2.2.2. Fourier Transform Infrared Spectroscopy (FTIR). Chemical structures of the ZnO/WBPU films coated on CaF_2 were measured by FTIR transmission using a PIKE autosampling accessory (PIKE Technologies). The autosampler accessory was placed in an FTIR spectrometer compartment (Nicolet 560x) equipped with a liquid nitrogen-cooled mercury cadmium telluride (MCT) detector. Spectra were recorded at a resolution of 4 cm^{-1} and were averaged over 128 scans. The peak height was used to represent IR intensity, which was expressed in absorbance. Four characteristic peaks are seen: 1250 cm^{-1} due to ether C−O−C or C−N−C stretching, 1732 cm^{-1} due to carbonyl stretching C═O, and 2928 cm^{-1} due to C−H stretching of soft segment, and the longer ~3330 cm^{-1} due to the stretching vibration of N−H or O−H in hydrogen bonding.[103,104] The FTIR spectra (Figure 3) show no new covalent bonding between ZnO and WBPU.

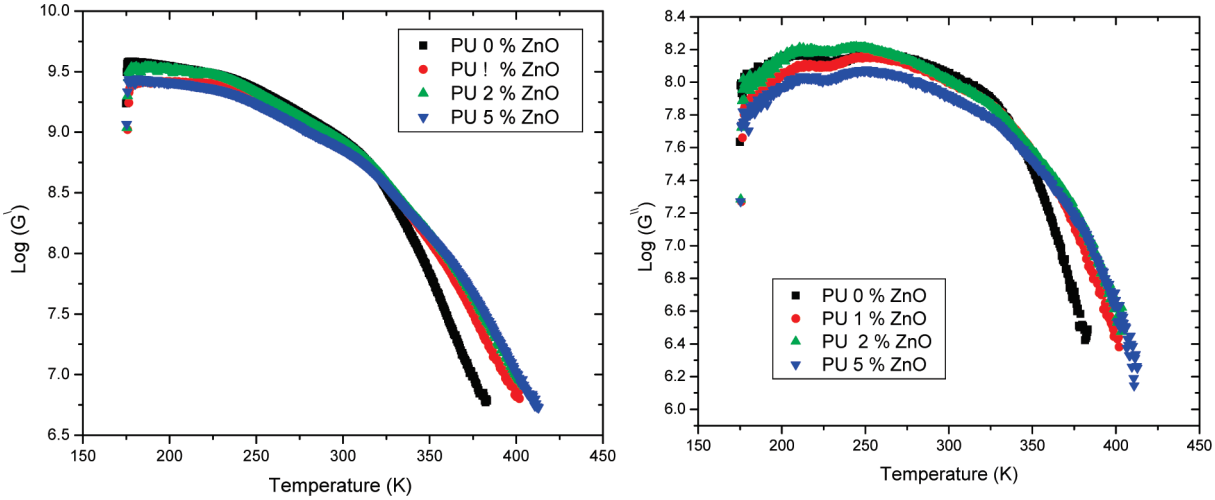

Figure 2. Log_{10} of storage and loss modules (G' and G'' in the unit of Pa) of DMTA vs temperature in ZnO/WBPU nanocomposites.

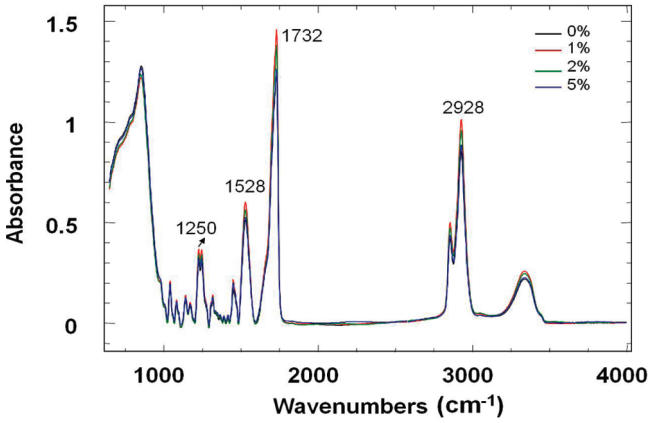

Figure 3. FTIR transmission spectra of pristine WBPU and ZnO/WBPU films containing 1%, 2%, and 5% ZnO loadings by mass. The specimens are spin-coated films on CaF_2 substrates.

2.2.3. Atomic Force Microscopy (AFM) Measurements. In recent years, AFM has been successfully used to image the microdomains in polymers.[105−107] A Dimension 3100 AFM (Veeco Metrology) was used to image the morphology and the microstructure of the nano-ZnO filled WBPU. The AFM was operated in the tapping mode using commercial silicon probes (TESP 70, Veeco Metrology). A resonance frequency of approximately 300 kHz and a free-oscillation amplitude of 62 nm ±2 nm were used. The set-point ratio (the ratio of set point amplitude to the free amplitude) ranged from 0.60 to 0.80. Figure 4 shows the AFM images of ZnO/WBPU systems.

The phase contrast image shown in Figure 4 reveals that the WBPU films have a two-phase heterogeneous nanostructure with bright domains about 10−20 nm in diameter. This can be attributed to the microphase separation of the hard and soft segments in the WBPU. No distinct differences are observed in the phase contrast for the films with different ZnO loadings. Note that these nonstructural domains are independent of their surface topography and the phase contrast and the size of the bright domains are similar. A number of particles that show relatively bright contrast in the phase images are likely ZnO nanoparticles; the diameters of these particles are around 30−50 nm. Considering the AFM tip effect, it is reasonable to suggest that these particles are monodispersed ZnO nanoparticles; a WBPU rich layer exists on the film surface.

2.2.4. Positron Annihilation Lifetime Spectroscopy (PALS). A conventional fast−fast coincidence spectrometer with a time resolution 280 ps was used for PALS measurements.[98] WBPU and ZnO/WBPU films (about 100 μm thickness) were staked together to obtain a suitable thickness of the sample. The positron source (10 μCi) ^{22}Na was deposited in an envelope of KAPTON foils (6 μm thick) and then sandwiched in between eight identical pieces of the samples. This sandwich was completely enclosed in a copper sample holder at the end of the coldfinger of a close-cycle helium gas refrigerator (ADP). Each selected temperature was kept constant within ±1 K during data acquisition. The entire source-sample assembly was placed under high vacuum. The following sequence of measurements was carried out: first, the measurements were performed at r.t. (293 K) on samples immediately after source installation. Second, the temperature was lowered to 20 K and then the experiments from low temperature to 420 K and then down and then up for three cycles at a temperature interval of 5−20 K. One or two million (some selected temperatures) counts were recorded at each temperature for a typical period of acquisition 3−5 h. In conventional analysis the PATFIT-88 program[108] was employed. And the PALS spectra were analyzed into three components (τ_1, τ_2 and τ_3) with their intensities (I_1, I_2, and I_3). Source correction terms were made from each spectrum in data analysis. We further used LT.9 program[109] to obtain the lifetime distribution. Four-lifetime analyses were attempted and the results did not show as systematic as from three-lifetime analysis. We only present three-lifetime analysis results here.

3. Results and Discussions

3.1. Dependence of Positron Annihilation Lifetime on Nanofiller. We performed the PALS experiment as a function of ZnO concentration at room temperature. Figure 5 shows the o-Ps lifetime, τ_3, (also free-volume radius, R) and o-Ps formation intensity, I_3, as a function of ZnO concentration. It is observed that the o-Ps lifetime decreases with increasing ZnO concentration which indicates the decrease of the mean free-volume size. Similarly, I_3 decreases with increasing ZnO nanofiller concentration.

The relationship between free-volume parameters and ZnO concentration is observed in addition by taking the product of I_3 and $V_h = 4\pi R^3/3$, where R is calculated from eq 1 from τ_3 data shown in Figure 5 and by a scaling factor,[98] which refers as the relative fractional free volume (FFV) as shown in Figure 6. As expected, the free volume (V_h in Figure 6) as a function of ZnO concentration has the similar behavior as τ_3 (Figure 5) does. However, the relative fractional free volume (FFV) can be well fitted into a linear equation with a good correlation factor $r^2 = 0.987$ while the free volume (V_h) could not fit well. The linear relationship

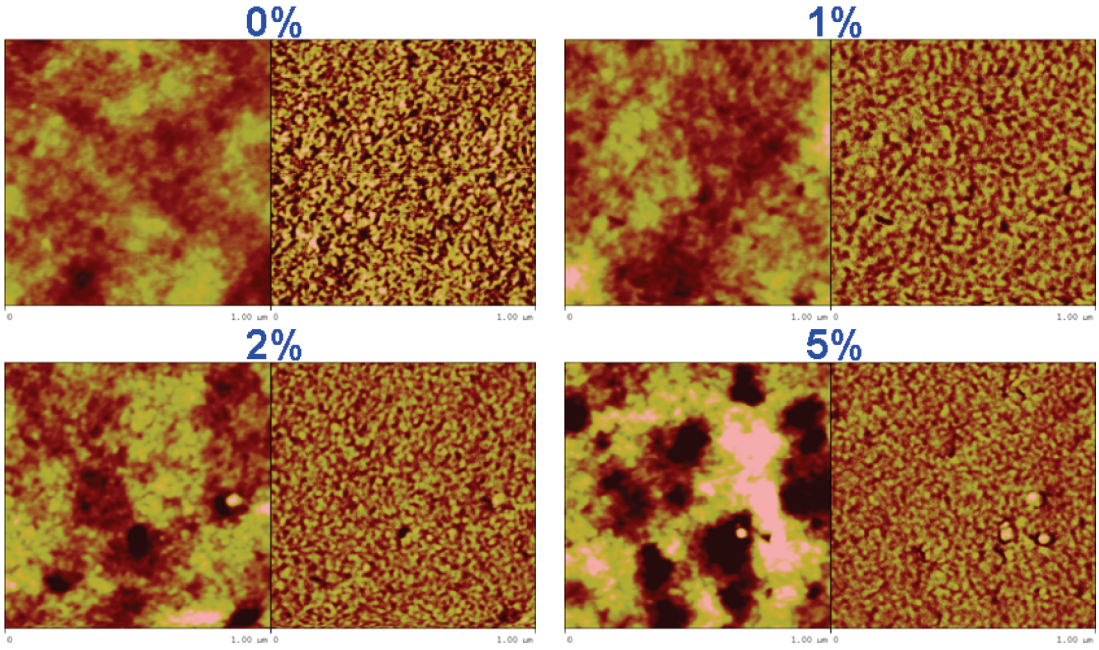

Figure 4. High magnification AFM height (left) and phase (right) images of the surfaces of pure WBPU and ZnO/WBPU films containing 0%, 1%, 2%, and 5% ZnO by mass. Lateral dimensions of the images are 1 μm × 1 μm. The height scale is 5 nm and the phase is 5°.

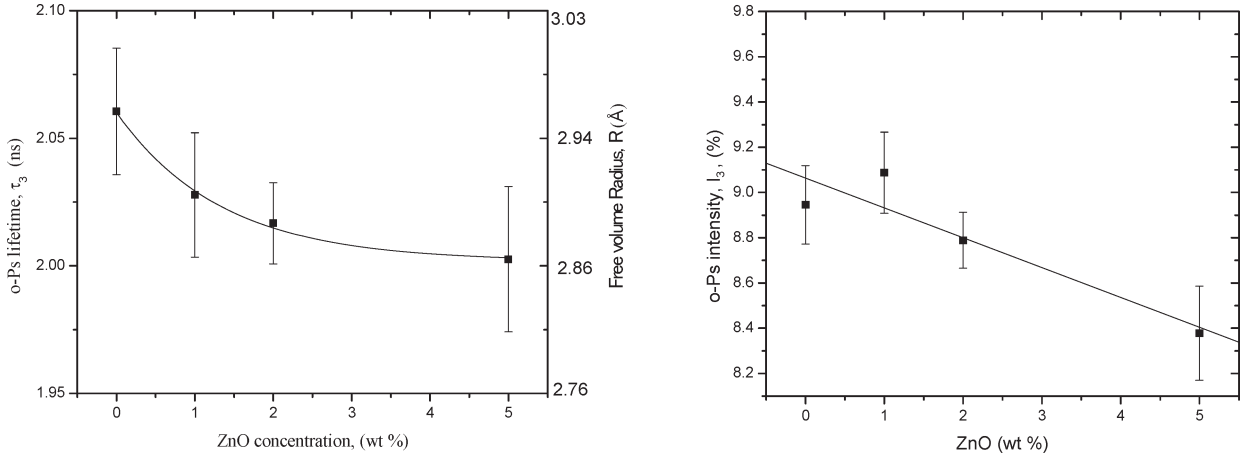

Figure 5. o-Ps lifetime and intensity as a function of ZnO concentration (Lines were smoothly drawn for eye-guide purpose only).

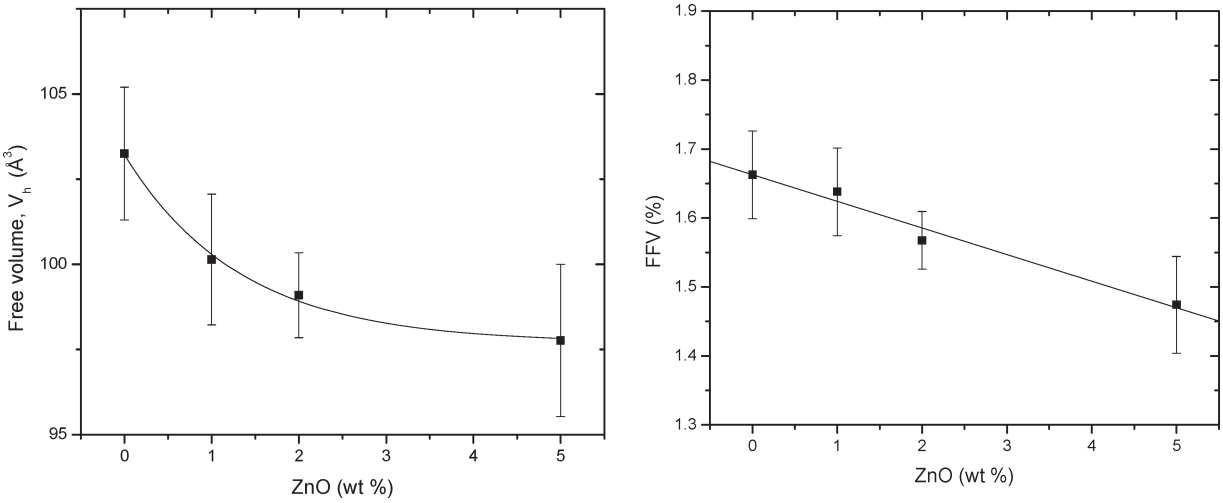

Figure 6. Free volume and relative fractional free volume as a function of ZnO concentration at room temperature. The line in free volume plot (left) was drawn through data points and the line for FFV (right) is from linear regression.

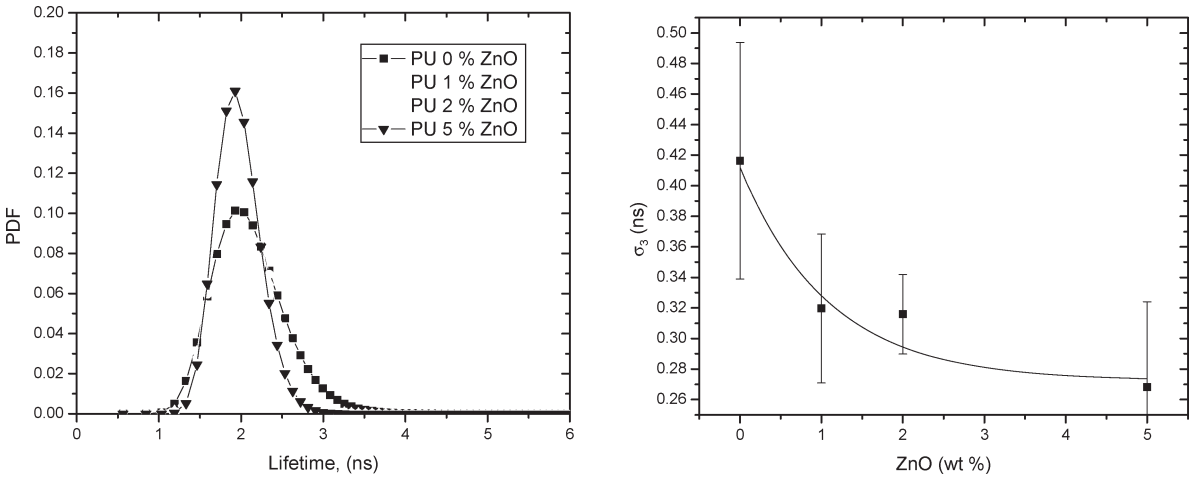

Figure 7. o-Ps lifetime distributions and the dispersion of the o-Ps lifetime in different ZnO concentrations of WBPU matrices. Lines were smoothly drawn for eye-guide only.

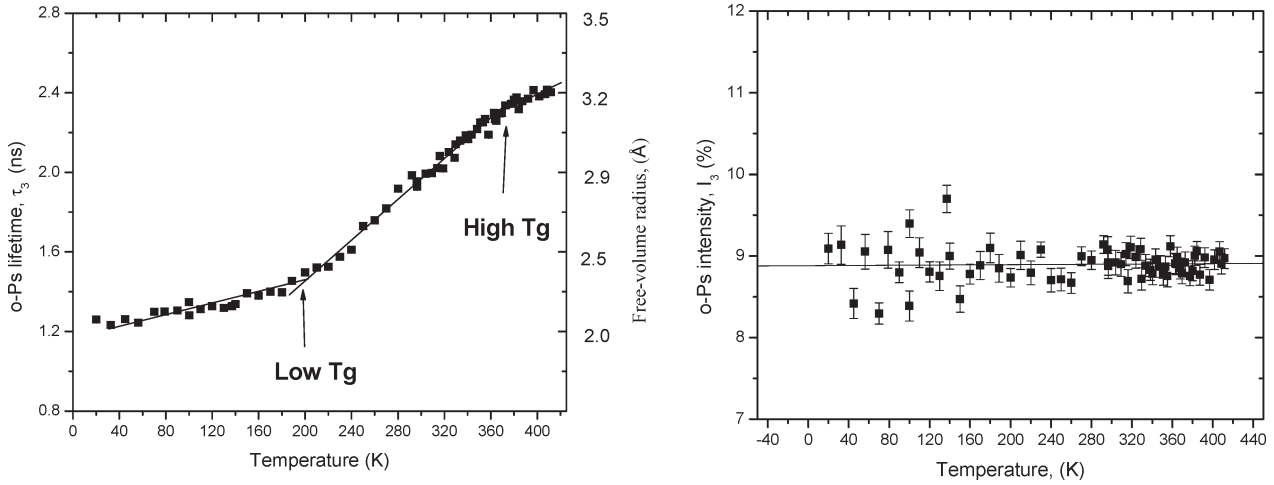

Figure 8. o-Ps lifetime (free-volume radius) and its intensity vs temperature in the pristine WBPU. Lines for o-Ps lifetime (left plot) were from linear regression and for intensity (right) was drawn for eye-guide.

between relative FFV vs ZnO (%) may be understood that ZnO has no o-Ps[110−112] and the correlation between τ_3 and I_3 (typical correlation coefficients = −0.7 to −0.8) in the PATFIT analysis. It should be noted that FFV here in nanocomposites is not referring to the number density of free volume holes in polymer matrix itself.

The PALS data were further fitted into lifetime distribution using the LT program. Figure 7 shows the results of o-Ps (τ_3 or free-volume radius) distributions and the dispersions of the distributions (σ_3) from LT analysis. It is interesting to observe a narrowing of distributions due to the addition of nano fillers into polymers. This may be resulted from the interfacial interactions between the surface of nanoparticles and polymers.

3.2. Dependence of Positron Annihilation Lifetime on Temperature. The temperature dependence of the o-Ps lifetime and its intensity for pristine WBPU is shown in Figure 8. As shown in this figure, while the o-Ps intensity (right plot) scatters around at 8.9 ± 0.8% but no systematic variation with the temperature (T), the o-Ps lifetime (left plot) increases systematically with T. They compose of three regions: the low temperature (T < 210 K); the intermediate (210 < T < 380 K) and the high temperature T > 380 K, respectively. These three-region variation from PALS is consistent with the reported results obtained by different techniques in similar polyurethane systems.[113−117] We therefore fitted three regions' data in three linear regressions and obtained three lines as shown in Figure 8. Then we calculated the two intercept temperatures, one at 210.25 ± 2.82 K, and the other at 363.48 ± 9.91 K, respectively. We interpret these results and the intercepts as two transition temperatures (T_g) as follow.

First, cycling temperature up, down, and up three times, the PALS results do not show any hysteresis that indicates that there is no significant physical or chemical aging in the temperatures between 20 to 420 K during a period of 3 months of PALS experiments. Therefore, we proceed to interpret the increase of o-Ps lifetime or free-volume size as a thermal expansion of free volume. Second, at the very low T region (<210 K), we interpret that the increase of free volume is dominantly contributed from the motion of the soft segment of -O−$(CH_2)_n$− of R and R′ in WBPU (Figure 1 of chemical structure) and we observe an onset of o-Ps lifetime (free-volume radius) as shown in Figure 8. The first on-set temperature (210 K) is assigned as the commonly known T_g for WBPU and is consistent with the literature T_g (215 K) obtained from DSC[118] and DMTA[119,120] methods. Third, further increasing temperature above 360 K, the slope of o-Ps becomes less steep as shown in Figure 8. In homogeneous polymeric systems, this often occurs at $T > T_g +$ ~ 100 K, where o-Ps lifetime reaches a plateau or very small temperature dependence.[93,98,99] This nearly temperature

Table 1. Glass Transition Temperatures from Various Methods in ZnO/WBPU Nanocomposites

samples	existing T_g (K) [118−120]	T_g from this DMTA work	T_g (low) from PALS	T_g (high) from PALS
0% ZnO/WBPU	215 [DSC], 356 [DMTA]	364.5 ± 1.2 K	210.25 ± 2.82 K	363.48 ± 9.91 K
1% ZnO/WBPU		387 ± 4.8 K	215.40 ± 2.19 K	368.97 ± 6.86 K
2% ZnO/WBPU		392 ± 1.5K	220.90 ± 3.23 K	371.85 ± 9.79 K
5% ZnO/WBPU		396 ± 1.3 K	236.61 ± 2.75 K	382.01 ± 5.55 K

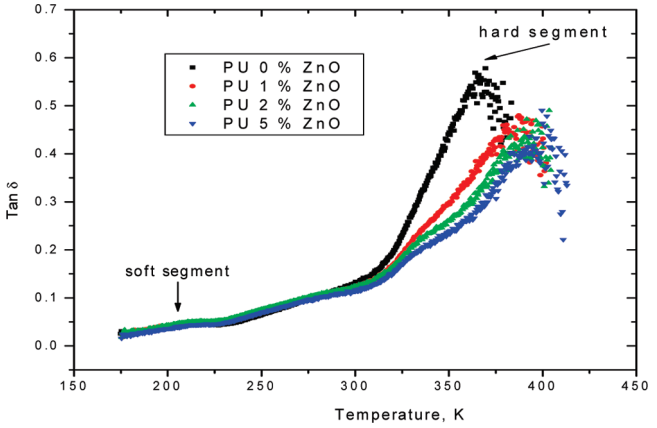

Figure 9. DMTA result: plots of tan δ vs temperature for WBPU/ZnO nanocomposites.

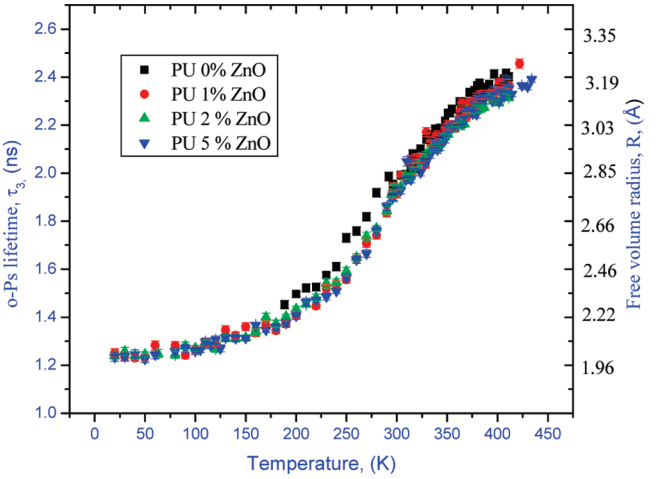

Figure 10. Temperature dependence of o-Ps lifetime in ZnO/WBPU composites.

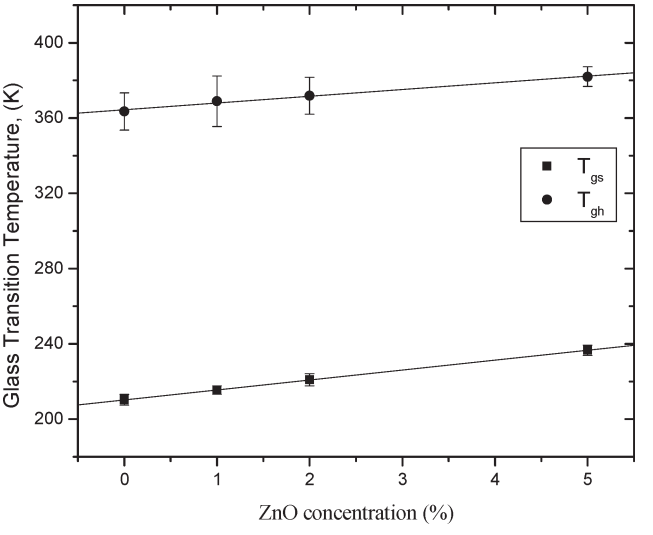

Figure 11. Glass transition temperatures as a function of ZnO concentration in the WBPU matrix.

independence region has been explained by the Ps-bubble formation in low viscosity fluids such that an artificial bubble is created due to the zero-point energy when Ps is localized in liquids.[98−100] In the current WBPU polymer which contains two phases or domains, a soft segment and a hard microdomain, the o-Ps lifetime variation needs further consideration. At $T > 360$ K, the soft segmental region is in the liquid state, where Ps-bubble formation will contribute no or insignificant lifetime expansion as been observed in most polymers.[93,98,99] However, the hard segments become a dominant contribution to the increase of o-Ps lifetime particularly when the glass transition temperature of the hard segmental microdomains is reached. This hard microdomain is responsible for the mechanical behavior of WBPU and its T_g has been observed better by DMTA method. The dissipation factor (tan δ) plot of DMTA data (Figure 9) clearly shows a predominate peak at $T = 364$ K, which agrees well with the reported value of hard segmental T_g (364.5 K).[119,120] Therefore, we assigned the high temperature onset (364 K) from PALS as the second T_g of WBPU. It is noted that the low T_g (210 K) is also seen as a shoulder peak in Figure 9 but not a remarkable peak. This is because the intrinsic property of DMTA mainly for dynamic mechanical responses, at this low temperature, the mobility of the soft domains is restricted by the glassy hard domains. On the other hand, the DSC results[118] only clearly show the soft segment motion since the heat capacity change for the hard segmental transition is much less than the soft segmental motion and normally escape from the DSC test. It appears that PALS can clearly detect both soft (low T_g) and hard segmental (high T_g) motions in terms of free volume. The T_g results from this work are compared with others in Table 1.

3.3. Glass Transitions as a Function of ZnO Concentrations. The results of o-Ps lifetimes vs temperature for WBPU with different ZnO (%) nancomposites are shown in Figure 10. Similarly, we observed: (1) o-Ps intensity scatters at a constant value (data similar to Figure 8 and not shown) for each of three ZnO concentrations similar to that as in Figure 8 except the absolute value decreases with the addition of ZnO; (2) three regions of o-Ps lifetime variations vs T are seen as in pristine WBPU; and (3) two intercept temperatures are obtained from linear regression as T_g (low) and T_g (high) due to soft and hard segmental motions, respectively. It is interesting to further observe that the glass transition temperatures of both soft and hard regions increase with the increase of the concentration of ZnO. The obtained two T_g values from the intercepted temperatures among three regions are listed in Table 1.

The increase of T_g's vs % ZnO in WBPU is plotted in Figure 11. As noticed from the Table 1 and Figure 11 that T_g increases with increasing ZnO content for both soft and hard segments. While the trend of the increase in high T_g is consistent with the DMTA data, the amount of T_g increase by PALS is slightly less than that by DMTA, as shown in the Table 1. This is typical due to a much longer time of data collection in each PALS spectrum (10^3−10^4 s).[98]

The increase in T_g with increasing ZnO nanoparticle loading indicates that the mobility of the WBPU polymer

Table 2. Thermal expansion coefficients of WBPU and ZnO/WBPU composites

samples	α_{fv1} (K^{-1})[a]	α_{fv2} (K^{-1})[b]	α_{fv3} (K^{-1})[c]	α_{bulk} at 293 K (K^{-1}) [121−124]
0% ZnO/WBPU	2.33×10^{-3}	7.34×10^{-3}	3.06×10^{-3}	6.04×10^{-4}
1% ZnO/WBPU	1.90×10^{-3}	7.12×10^{-3}	2.76×10^{-3}	
2% ZnO/WBPU	2.30×10^{-3}	6.96×10^{-3}	2.40×10^{-3}	
5% ZnO/WBPU	2.28×10^{-3}	8.86×10^{-3}	2.31×10^{-3}	

[a] Glassy state of soft segments (< 210 K). [b] Rubbery state of soft segments. [c] Rubbery state of hard segments (> 360 K).

chains has been reduced after introducing nanoparticles into the polymer, suggesting interfacial interactions could exist between ZnO nanoparticles and WBPU molecules. Note that the ZnO nanoparticles used in this study were modified with wetting agents/surfactants by the manufacturer for the dispersion and designed to be compatible with the waterborne polymer matrix. Possible interfacial integrations are hydrogen bonding, van der Walls forces, and electrostatic forces. The hydroxyl groups on the surface of the ZnO nanoparticles tend to form hydrogen bonding with the urethane linkage in the hard segments and the ester linkage in the soft segments of WBPU. The FTIR spectra (Figure 3) show a slight variation of intensity in major bands of WBPU that mainly due to thickness variation, but no new peaks from covalent bonding between ZnO and WBPU were observed. An increase of T_g due to ZnO concentration can be attributed to overall increased interfacial interactions between nanoparticles and polymers that is because no substantial differences in the degree of nanoparticle dispersion were observed for nanocomposites with different amounts of ZnO nanoparticles (data not shown).

Next, from the o-Ps lifetime data of Figure 10 and their corresponding free volume ($V_h = 4\pi R^3/3$), we calculated the thermal expansion coefficient of the free volume, α_{fv} using the equation $\alpha_{fv} = (1/V_h)(\Delta V_h/\Delta T)$.[98,99] The results of the free-volume thermal expansion coefficients in three regions α_{fv1} (glassy state of soft segments), α_{fv2} (rubbery state of soft segments), and α_{fv3} (rubbery state of hard segments, assuming insignificant Ps-bubble expansion) are listed in Table 2. These values (on the order of 10^{-3} K^{-1}), which are significantly larger than the thermal expansion coefficient of the bulk of WBPU of 6.04×10^{-4} K^{-1}.[121−124] This large difference comes from the fact that PALS probes only the free volume while the bulk α_{bulk} is contributed from a fraction of free-volume expansion.[98,99] Furthermore, it is observed that the free-volume thermal expansion coefficient in the hard segment is only about one-third of the soft segments in the rubbery state. This may explain why the thermal expansion below the second T_g is dominated by the soft segmental motions. The addition of the ZnO nanoparticles appears to decrease the hard segment's expansivity while it does not affect systematically for the soft segmental free volumes.

3.4. Relationship between Free Volumes and Mechanical Properties. Information about the molecular motions of WBPU chains can be obtained from the analysis of DMTA data, which should have some links with the molecular level free volumes from PALS. First, the plots of dissipation loss factor, tan δ, versus temperature for the WBPU/ZnO samples shown in Figure 9 display a similar variation as the free-volume (o-Ps lifetime) variation in Figure 10. Two peaks were observed from DMTA: a very small peak for the glass-transition temperature of the amorphous soft segments (T_{gs}) at a lower temperature and a large peak corresponding to the glass-transition temperature of the amorphous hard segments (T_{gh}) at a higher temperature in WBPU. In PALS, two intercepting temperatures were detected as glass transition temperatures, corresponding to soft and hard segments. However, DMTA is more sensitive to the hard segmental motion than the soft segmental while the free-volume change from PALS is more pronounced for the soft segments than the hard segmental part of WBPU. Second, the trend observed for the shift of the peak position in the plot of tan δ vs temperature is consistent with the plot of the free volume vs temperature when the amount of the ZnO nanoparticles increases. For PALS, the addition of ZnO decreases o-Ps lifetime (free volumes) as shown in Figures 8 and 10 and its intensity as ZnO has no Ps formation.

Corresponding to the two glass transition temperatures observed in DMTA tan δ vs temperature plot, the storage module, G', vs temperature (Figure 2) shows three general regions: glassy state of soft segments ($T < 220$ K), rubbery state of soft segments (220 K $< T <$ 330 K), and rubbery state of hard segments ($T > 330$ K). This is consistent with the PALS results. It is well-known[116,125] that the value of G', at the rubbery region can be used to estimate cross-link density of the polymer network. Because the glassy hard segments can act as physical cross-linkers for the soft segments in the WBPU, we attempt to estimate such physical cross-link density from rubbery state of soft segments in the DMTA. Here the physical cross-link density arising from hydrogen bonding between hard segments in WBPU is used in the estimation to replace the chemical cross-linking in rubbery state. The hydrogen bonding may dissociate as the temperature increases, resulting a loss of physical cross-linkers.

The physical cross-link density (X_c) in WBPU can be expressed in the following equation:[125]

$$X_c = A \exp(E_a/RT) \tag{3}$$

where X_c is the physical cross-linking density (mol/cm^3), A is a constant, R, the gas constant, T, the absolute temperature, and E_a is the apparent activation energy for hydrogen bonding dissociation. According to the kinetic theory of elasticity, the storage modulus in the rubbery state of soft segments can be expressed as the following equation:[116]

$$G' = X_c RT = ART \exp(E_a/RT) \tag{4}$$

Thus, the above equation can be rewritten as

$$\ln G'/T = \ln AR + E_a/RT \tag{5}$$

Then, E_a and A are obtained from the slope and intersection of plotting ln G'/T versus $1/T$, as shown in Figure 12. The values of E_a from the slope of the straight line are found to be 76.23 kJ/mol for WBPU 0% ZnO; 55.07 kJ/mol for WBPU/1% ZnO, 48.68 kJ/mol for WBPU/2% ZnO, and 45.57 kJ/mol for WBPU/5% ZnO, respectively. A decrease of E_a vs % ZnO is observed as shown in Figure 13. This decrease may be due to a strong interfacial interaction between ZnO and WBPU that reduces the hard segmental hydrogen bonding dissociation.

The ln of physical cross-link densities (X_c), calculated from eq 3 vs $1/T$, are shown in Figure 14. It follows a linear relationship with respect to $1/T$ as plotted in Figure 14. We also observe that physical cross-link density increases with increasing ZnO content in the plateau temperature region.

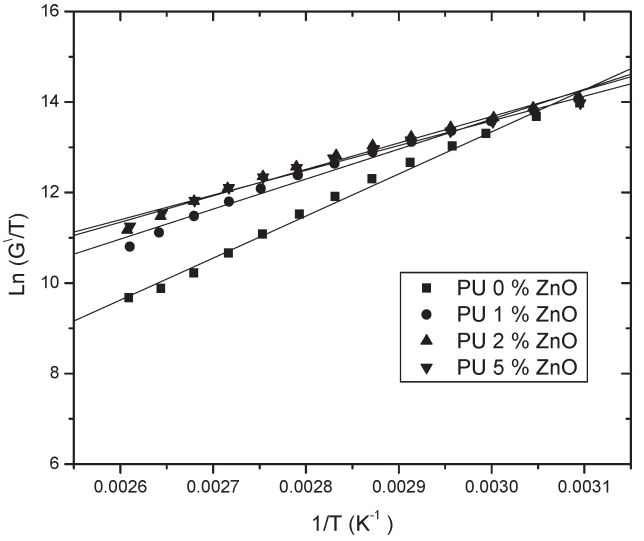

Figure 12. Plots of ln G'/T and $1/T$ for ZnO/WBPU nanocomposites.

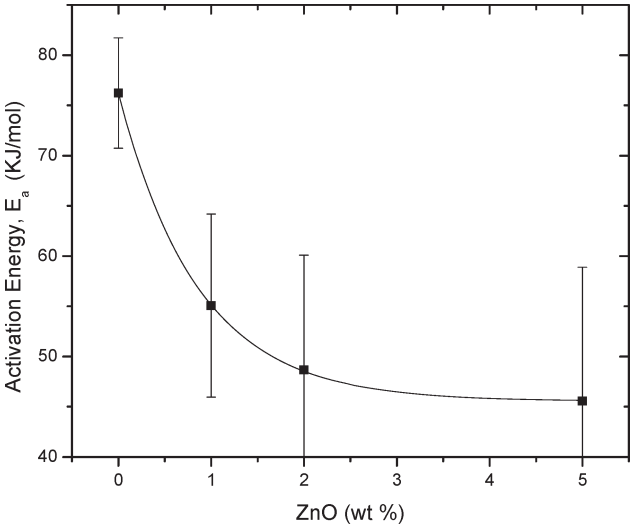

Figure 13. Variations of E_a for hydrogen bonding vs % ZnO in ZnO/WBPU nanocomposites. The line was smoothly drawn through data points.

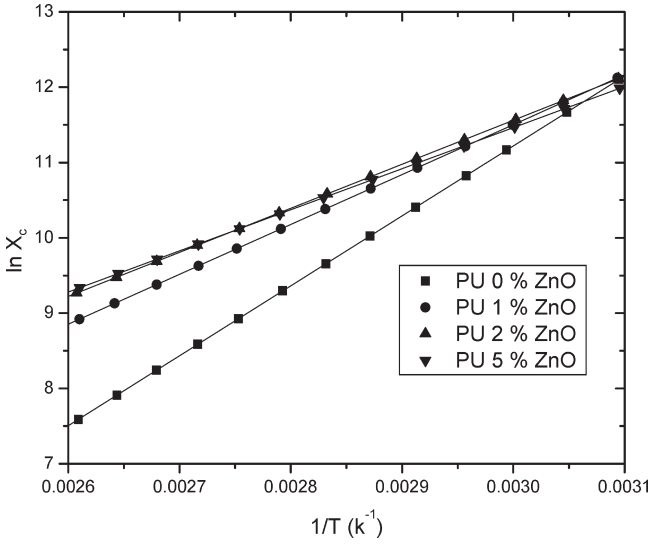

Figure 14. Plots of ln(X_c, physical cross-link density) of WBPU/ZnO nanocomposite as a function of reciprocal of temperature. Lines were linearly fitted.

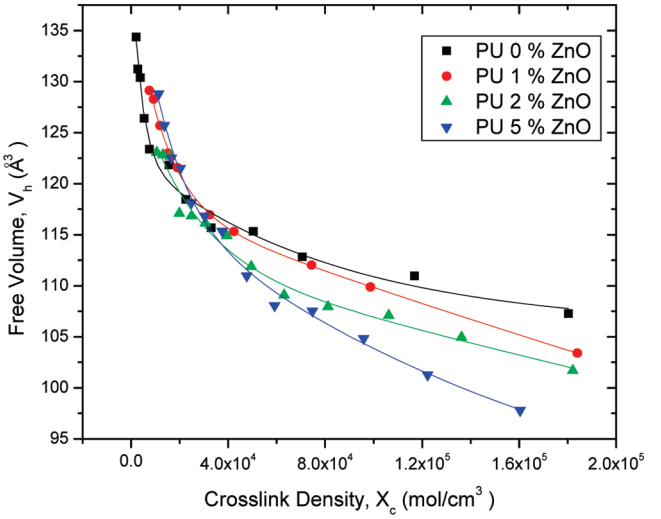

Figure 15. Relation between free volume (V_h) from PALS and the cross-link density (X_c) for ZnO/WBPU nanocomposite. Lines fit well with an exponential eq 6 .

It indicates that the addition of ZnO increases the physical cross-link density in the WBPU matrix.

Since the free volume and cross-link density has an anti-correlation, we plot the free volumes obtained by PALS vs the cross-link density obtained from DMTA in Figure 15. We fitted the free volume (V_h) and X_c and found that it follows nicely in an exponential equation as below:

$$V_h = C \exp(-DX_c) \quad (6)$$

where C and D are fitting parameters. It is interesting to observe this negative exponential relationship, which is different from chemical cross-link density, that usually shows a reciprocal relationship with free-volume parameters.[98,126] This result shows a direct link between the nanoscopic free volumes obtained from PALS and the cross-link density derived from macroscopic DMTA tests for these ZnO filled nanocomposites.

4. Conclusion

We have reported a systematic study of free volumes in a series of ZnO dispersed waterborne polyurethane matrix as a function of temperature between 20 and 420 K. We found the addition of ZnO nanoparticles decreases the free volumes of ZnO/WBPU systems. A systematic increase of free volume and distributions was observed as a function of temperature. From the free volume-temperature data, we observed two glass transition temperatures in ZnO/WBPU systems: low T_g (~220 K) and high T_g (~380 K) due to the two segmental motions in WBPU, soft segments and hard microdomains, respectively. This observation is consistent with the DSC, and DMTA results. The increase in the both glass transition temperatures with the increase of ZnO content can be attributed to hydrogen bonding, van der Walls forces, and electrostatic forces between surfaces of ZnO nanoparticles and WBPU. We also observe an exponential relationship between the free volumes from nanoscopic PALS probe and the physical cross-link density from macroscopic DMTA method.

Acknowledgment. S.A. wishes to express thanks for the financial support of the channel system and mission department of Egypt. This research is supported by the NSF-sponsored Nanoscale Science and Engineering Center for Affordable Nanoengineering of Polymeric Biomedical Devices (NSEC-CANPBD), the National Institute of Standards and Technology, and the Army Research Office (W911NF-10-1-0476).

References and Notes

(1) Wong, E. W.; Sheehan, P. E.; Lieleer, C. M. *Science* **1997**, *227*, 1971–1975.
(2) Schaefer, H.-E. In *Mechanical Properties and Deformation Behavior of Materials Having Ultra-Fine Microstructures*; Nastasi, M., Parkin, D., Gleiter, H., Eds.; Kluwer Academic Publishers: The Netherlands, 1993; p 81.
(3) Balazs, A .C.; Emrick, T.; Russell, T. P. *Science* **2006**, *314*, 1107–1110.
(4) Guo, C.; Zheng, Z.; Zhu, Q.; Wang, X. *Polym. Plastics Technol. Eng.* **2007**, *46*, 1161–1166.
(5) Kwak, G. H.; Inoue, K.; Tominga, Y.; Asai, S.; Sumita, M. *J. Appl. Polym. Sci.* **2001**, *82*, 3058–3066.
(6) Alexandre, M.; Dubois, P. *Mater. Sci. Eng. R-Rep.* **2000**, *28*, 1–63.
(7) Gilman, J. W.; Jackson, C. L.; Morgan, A. B.; Harris, R.; Manias, E.; Giannelis, E. P.; Wuthenow, M.; Hilton, D.; Phillips, S. H. *Chem. Mater.* **2000**, *12*, 1866–1873.
(8) Hegedus, C.; Pepe, F.; Lindenmuth, D.; Burgard, D. *JCT Coatings Technol.* **2008**, *5*, 42–52.
(9) Giannelis, E. P. *Appl. Organomet. Chem.* **1998**, *12*, 675–680.
(10) Soo, P. P.; Huang, B.; Jang, Y. I.; Chiang, Y. M.; Sadoway, D. R.; Mayers, A. M. *J. Electrochem. Soc.* **1999**, *146*, 32–37.
(11) Balazs, A. C. *Curr. Opin. Colloid Interface Sci.* **1999**, *4*, 443–448.
(12) Cho, H. Y.; Bae, C. Y.; Kim, B. K. *Prog. Org. Coat.* **2010**, *68*, 356–362.
(13) Rittigstein, P.; Torkelson, J. M. *J. Polym. Sci., Part B: Polym. Phys.* **2006**, *44*, 2935–2943.
(14) Krishnamoorti, R.; Vaia, R. A. *J. Polym. Sci., Part B: Polymer Phys.* **2007**, *45*, 3252–3256.
(15) Lin, Y.; Boker, A.; He, J. B.; Sill, K.; Xiang, H. Q.; Abetz, C.; Li, X. F.; Wang, J.; Emrick, T.; Long, S.; Wang, Q.; Balas, A.; Russell, T. P. *Nature* **2005**, *434*, 55–59.
(16) Schmidt-Mende, L.; Macmanus-Driscoll, L. *J. Mater. Today* **2007**, *10*, 40.
(17) Yamamoto, O. *Int. J. Inorg. Mater.* **2001**, *3*, 643–646.
(18) Tam, K. H.; Djurisic, A. B.; Chan, C. M. N.; Xi, Y. Y.; Tse, C. W.; Leung, Y. H.; Chan, W. K.; Leung, F. C. C.; Au, D. W. T. *Thin Solid Films* **2008**, *516*, 6167–6174.
(19) Chen, Y. W.; Liu, Y. C.; Lu, S. X.; Xu, C. S.; Shao, C. L.; Wang, C.; Zhang, J. Y.; Lu, Y. M.; Shen, D. Z.; Fan, X. W. *J. Chem. Phys.* **2005**, *123*, 134701–134705.
(20) Zhang, Y.; Jia, H. B.; Luo, X. H.; Chen, X. H.; Yu, D. P.; Wang, R. M. *J. Phys. Chem. B* **2003**, *107*, 8289–8293.
(21) Chen, S. J.; Liu, Y. C.; Shao, C. L.; Mu, R.; Lu, Y. M.; Zhang, J. Y.; Shen, D. Z.; Fan, X. W. *Adv. Mater.* **2005**, *17*, 586–590.
(22) Wang, C.; Mao, B.; Wang, E.; Kang, Z.; Tian, C. *Solid State Commun.* **2007**, *141*, 620–623.
(23) Kong, X. Y.; Wang, Z. L. *Nano Lett.* **2003**, *3*, 1625–1631.
(24) Yang, R.; Li, Y.; Yu, J. *Polym. Degrad. Stab.* **2005**, *88*, 168–174.
(25) Chandramouleeswaran, S.; Mhaske, S. T.; Kathe, A. A.; Varadarajan, P. V.; Prasad, V.; Vigneshwaran, N. *Nanotechnology* **2007**, *18*, 385702–385709.
(26) Zhao, H.; Li, R. *Polymer* **2006**, *47*, 3217.
(27) Sun, D.; Miyatake, N.; Sue, H. J. *Nanotechnology* **2007**, *18*, 215606–215611.
(28) Demir, M. M.; Memesa, M.; Castignolles, P.; Wegner, G. *Macromol. Rapid Commun.* **2006**, *27*, 763–770.
(29) Ma, C.; Chen, Y. J.; Kuan, H. C. *J. Appl. Polym. Sci.* **2005**, *98*, 2266–2273.
(30) Wu, M.; Yang, G. Z.; Wang, M.; Wang, W. Z.; Zhang, W. D.; Feng, J. C. *Mater. Chem. Phys.* **2008**, *109*, 547–555.
(31) Chae, D. W.; Kim, B. C. *J. Appl. Polym. Sci.* **2006**, *99*, 1854–1858.
(32) Liufu, S. C.; Xiao, H. N.; Li, Y. P. *Polym. Degrad. Stab.* **2005**, *87*, 103–110.
(33) Wang, Z.; Pinnavaia, T. J. *Chem. Mater.* **1998**, *10*, 3768–3771.
(34) Zheng, J.; Ozisik, R.; Siegel, R. W. *Polymer* **2005**, *46*, 10873–10882.
(35) Zheng, J.; Ozisik, R.; Siegel, R. W. *Polymer* **2006**, *47*, 7786–7794.
(36) Chen, J. -J.; Zhu, C.-F.; Deng, H. -T.; Qin, Z. -N.; Bai, Y. Q. *J. Polym. Res.* **2009**, *16*, 375–380.
(37) Gunes, I. S.; Cao, F.; Jana, S. C. *Polymer* **2008**, *49*, 2223–2234.
(38) Razzaq, M. Y.; Anhalt, M.; Frormann, L.; Weidenfeller, B. *Mater. Sci. Eng.* **2007**, *471*, 57–62.
(39) Seil, J. T.; Webster, T. J. *Int. J. Nanomed.* **2008**, *3*, 523–531.
(40) Guo, C.; Zheng, Z.; Zhu, Q.; Wang, X. *Polym. Plastics Tech. Eng.* **2007**, *46*, 1161–1166.
(41) Hepburn, C. *Polyurethane Elastomers*; Elsevier Applied Science: London and New York, 1992; p 85.
(42) David, D. J.; Stanley, H. B. *Analytical Chemistry of the Polyurethane*; Wiley-Interscience: New York, 1969; Vol. *XVI*.
(43) Szychert, M. *Szycher's Handbook of Polyurethane*; CRC Press: Boca Raton, FL, 1999.
(44) Hatakeyama, T.; Matsumoto, Y.; Asano, Y.; Hatakeyama, H. *Thermochim. Acta* **2004**, *416*, 29–33.
(45) Chattopadhyay, D. K.; Webster, D. C. *Prog. Polym. Sci.* **2009**, *34*, 1068–1133.
(46) Hsieh, K. H.; Liao, D. C.; Chern, Y. C. *Thermoplastic Polyurethane*. In *Handbook of Thermoplastics*; Olabisi, O., Eds; Marcel Dekker Inc.: New York, 1997; Chapter 6, p 381.
(47) Ramanathan, L. S.; Sivaram, S.; Mishira, M. K. In *Polymer Data Hand Book*; Mark, J. E., Eds.; Oxford University Press: New York, 1999; p 870.
(48) Vermette, P.; Griesser, H. J.; Laroche, G.; Guido, R. *Biomedical Applications of Polyurethane*; Eureka Com: Georgetown TX, 2001.
(49) Lamba, N. M. K.; Woodhouse, K. A.; Cooper, S. L. *Polyurethane in Biomedical Applications*; CRC press: Boca Raton FL, 1998.
(50) Coutinho, F. M. B.; Delpech, M. C.; Garcia, M. E. F. *Polym. Test.* **2002**, *21*, 719–723.
(51) Coutinho, F. M. B.; Delpech, M. C.; Alves, L. S. *J. Appl. Polym. Sci.* **2001**, *80*, 566–572.
(52) Coutinho, F. M. B.; Delpech, M. C. *Polym. Degrad. Stab.* **2000**, *70*, 49–57.
(53) Delpech, M. C.; Coutinho, F. M. B. *Polym. Test.* **2000**, *19*, 939–952.
(54) Shao, C. H.; Huang, J. J.; Chen, G. N.; Yeh, J. T.; Chen, K. N. *Polym. Degrad. Stab.* **1999**, *65*, 359–371.
(55) Coutinho, F. M. B.; Delpech, M. C.; Moura, P. M. Q.; Mello, S. D. S. *Polym. Bull.* **1996**, *37*, 1–5.
(56) Coutinho, F. M. B.; Delpech, M. C. *Polym. Test.* **1996**, *15*, 103–113.
(57) Satguru, R.; McMahon, J.; Padget, J. C.; Coogan, R. G. *J. Coat. Technol.* **1994**, *66*, 47–55.
(58) Krol, P. *Prog. Mater. Sci.* **2007**, *52*, 915–1015.
(59) Yang, C. Z.; Grasel, T. G.; Bell, J. L.; Register, R. A.; Cooper, S. L. *J. Polym. Sci., Part B: Polym. Phys.* **1991**, *29*, 581–588.
(60) Lu, X.; Hou, M.; Gao, X.; Chen, S. *Polymer* **1994**, *35*, 2510–2515.
(61) Lai, Y. C.; Quinn, E. T.; Valint, P. L. *Polym. Prepr.* **1992**, *33*, 1058–1059.
(62) Sun, H. *Polym. Prepr.* **1992**, *33*, 556–557.
(63) Liaw, D. J. *J. Appl. Polym. Sci.* **1997**, *66*, 1251–1265.
(64) Koberstein, J. T.; Stein, R. S. *J. Polym. Sci., Polym. Phys. Ed.* **1983**, *21*, 1439–1472.
(65) Wang, C. B.; Cooper, S. L. *Macromolecules* **1983**, *16*, 775–786.
(66) Hsieh, K. H.; Tsai, C. C.; Tseng, S. M. *J. Membr. Sci.* **1990**, *49*, 341–350.
(67) Huang, S. L.; Lai, J. Y. *J. Membr. Sci.* **1995**, *105*, 137–145.
(68) Ponangi, R.; Pintauro, P. N.; Dekee, D. *J. Membr. Sci.* **2000**, *178*, 151–164.
(69) Chen, H. M.; Jean, Y. C.; James Lee, L.; Yang, J.; Huang, J. *Phys. Status Solidi* **2009**, *6*, 2397–2400.
(70) Chen, H. M.; Lee, J. L.; Yang, J.; Gu, X.; Jean, Y. C. *Mater. Sci. Forum* **2009**, *607*, 177–179.
(71) Zheng, Y.; Zheng, Y.; Ning, R. *Mater. Lett.* **2003**, *57*, 2940–2944.
(72) Merkel, T. C.; Freeman, B. D.; Spontak, R. J.; He, Z.; Pinnau, I.; Meakin, P.; Hill, A. J. *Science* **2002**, *296*, 519–522.
(73) Becker, O.; Cheng, Y. B.; Varley, R. J.; Simon, G. P. *Macromolecules* **2003**, *36*, 1616–1625.
(74) Wang, Z. F.; Wang, B.; Qi, N.; Zhang, H. F.; Zhang, L. Q. *Polymer* **2005**, *46*, 719–724.
(75) Zhang, M.; Fang, P. F.; Zhang, S. P.; Wang, B.; Wang, S. J. *Radiat. Phys. Chem.* **2003**, *68*, 565–567.
(76) Forsyth, M.; MacFarlane, D. R.; Best, A.; Adebahr, J.; Jacobsson, P.; Hill, A. J. *Solid State Ionics* **2002**, *147*, 203–211.
(77) Yu, D. H.; Wang, B.; Feng, Y.; Fang, Z. P. *J. Appl. Polym. Sci.* **2006**, *102*, 1509–1515.
(78) Wang, B.; Qi, N.; Gong, W.; Li, X. W.; Zhen, Y. P. *Radiat. Phys. Chem.* **2007**, *76*, 146–149.
(79) Zhang, M.; Wang, S. J.; Liu, L. M.; Fang, P. F. *Mater. Sci. Forum* **2009**, *607*, 210–212.
(80) Yao, X. F.; Yeh, H. Y.; Zhou, D.; Zhang, Y. H. *J. Comp. Mater.* **2006**, *40*, 371–381.
(81) Merkel, T. C.; Freeman, B. D.; Spontak, R. J.; He, Z.; Pinnau, I.; Meakin, P.; Hill, A. J. *Chem. Mater.* **2003**, *15*, 109–123.
(82) Liu, L. M.; Fang, P. F.; Zhang, S. P.; Wang, S. J. *Mater. Chem. Phys.* **2005**, *92*, 361–365.
(83) Mukherjee, M.; Charkravorty, D.; Nambissan, P. M. G. *Phys. Rev. B* **1998**, *5* (7), 848–856.

(84) Jessie Lue, S.; Lee, D. T.; Chen, J. Y.; Chiu, C. H.; Hu, C. C.; Jean, Y. C.; Lai, J. Y. *J. Membr. Sci.* **2008**, *325*, 831–839.
(85) De Sitter, K.; Winberg, P.; D'Haen, J.; Dotremont, C.; Leysen, R.; A. Martens, J.; Mullens, S.; Maurer, F. H. J.; Vankelecom, I. *J. Membr. Sci.* **2006**, *278*, 83–91.
(86) De Sitter, K.; Andersson, A.; D'Haen, J.; Leysen, R.; Mullens, S.; Maurer, F. H.J.; Vankelecom, I. *J. Membr. Sci.* **2008**, *321*, 284–292.
(87) Anilkumar, S.; Kumaran, M. G.; Thomas, S. *J. Phys. Chem. B* **2008**, *112*, 4009–4015.
(88) Kruse, J.; Kanzow, J.; Ratzke, K.; Faupel, F.; Sterescu, D. M.; Stamatialis, D. F.; Wessling, M. *J. Phys. Chem. B* **2007**, *111*, 13914–13918.
(89) Peng, F.; Pan, F.; Sun, H.; Lu, L.; Jiang, Z. *J. Membr. Sci.* **2007**, *300*, 13–19.
(90) Ladewig, B. P.; Knott, R. B.; Hill, A. J.; Riches, J. D.; White, J. W.; Martin, D. J.; Diniz da Costa, J. C.; Lu, G. Q. *Chem. Mater.* **2007**, *19*, 2372–2381.
(91) Park, I.; Peng, H. G.; Gidley, D. W.; Xue, S. Q.; Pinnavaia, T. J. *Chem. Mater.* **2006**, *18*, 650–656.
(92) Garcia, M.; Barsema, J.; Galindo, R. E.; Cangialosi, D.; Garcia-Turiel, J.; Van Zyl, W. E.; Verweij, H.; Blank, D. H. A. *Polym. Eng. Sci.* **2004**, *44*, 1240–1246.
(93) Ngai, K. L.; Bao, L.-R.; Yee, A. F.; Soles, C. L. *Phys. Rev. Lett.* **2001**, *87*, 21501–4.
(94) Kim, S. H.; Chung, J. W.; Kang, T. J.; Kwak, S. Y.; Suzuki, T. *Polymer* **2007**, *48*, 4271–4277.
(95) Zheng, Y.; Ning, R.; Zheng, Y. *J. Reinf. Plast. Comp.* **2005**, *24*, 223–233.
(96) Winberg, P.; Eldrup, M.; Maurer, F. H. J. *Polymer* **2004**, *45*, 8253–8264.
(97) Winberg, P.; DeSitter, K.; Dotremont, C.; Mullens, S.; Vankelecom, I. F J.; Maurer, F. H. *Macromolecules* **2005**, *38*, 3776–3782.
(98) Jean, Y. C. *Microchem. J.* **1990**, *42*, 72–102.
(99) Jean, Y. C.; Mallon, P. E.; Schrader, D. M., Eds.; *Principles and Applications of Positron and Positronium Chemistry*; World Scientific: Singapore, 2003.
(100) Tao, S. J. *J. Phys. Chem.* **1972**, *56*, 5499–5510.
(101) Eldrup, M.; Lightbody, D.; Sherwood, J. N. *Chem. Phys.* **1981**, *63*, 51–58.
(102) Nakanishi, N.; Wang, S. J.; Jean, Y. C. In *International Symposium on Positron Annihilation Studies of Fluids*; Sharma, S. C., Ed.; World Scientific: Singapore, 1988; pp 292−298.
(103) Nguyen, T.; Jasmin, J.; Sung, L.; Gu, X.; Rezig, A.; Martin, D.; Martin, J. W. In *Service Life Prediction: Challenge the Status Quo*; Martin, J. W., Ryntz, R. A., Dickie, R. A., Eds.; Federation of Societies for Coatings Technology, FSCT: Blue Bell: PA, 2005; p 13.
(104) Nakanishi, K. *Infrared Absorption Spectroscopy-Practical*; Holden-Day Inc: San Francisco, CA, 1962.
(105) Garrett, J. T.; Siedlecki, C. A.; Runt, J. P. *Macromolecules* **2001**, *34*, 7066–7070.
(106) McLean, R. S.; Sauer, B. B. *Macromolecules* **1997**, *30*, 8314–8317.
(107) Takahashi, A.; Kita, R.; Kaibara, M. *J. Mater. Sci.: Mater. Med.* **2002**, *13*, 259–264.
(108) PATFIT package (1989) purchased from Riso National Laboratory, Denmark.
(109) Kansy, J. *Nucl. Instrum. Methods Phys. Res. A* **1996**, *374*, 235–244.
(110) Wang, D.; Chen, Z. Q.; Wang, D. D.; Qi, N.; Gong, J.; Cao, C. Y.; Tang, Z. *J. Appl. Phys.* **2010**, *107*, 023524–023531.
(111) Koida, T.; Chichibu, S. F.; Uedono, A.; Tsukazaki, A.; Kawasaki, M.; Sota, T.; Segawa, Y.; Koinuma, H. *Appl. Phys. Lett.* **2003**, *82*, 532–534.
(112) Brauer, G.; Anwand, W.; Grambole, D.; Grenzer, J.; Skorupa, W.; Čížek, J.; Kuriplach, J.; Procházka, I.; Ling, C. C.; So, C. K.; Schulz, D.; Klimm, D. *Phys. Rev. B* **2009**, *79*, 115212–15.
(113) Kwon, J. Y.; Kim, H. D. *J. Appl. Polym. Sci.* **2005**, *96*, 595–604.
(114) Orgiles-Calpena, E.; Aran-Ais, F.; Torro −Palau, A. M.; Orgiles-Barcelo, C.; Martın-Martınez, J. M. *Int. J. Adhes. Adhes.* **2009**, *29*, 309–318.
(115) Seo, J. W.; Kim, B. K. *Polym. Bull.* **2005**, *54*, 123–128.
(116) Pan, H.; Chen, D. *Eur. Polym. J.* **2007**, *43*, 3766–3772.
(117) Wetton, R. E. *Thermal Analysis.* In *Polymer Characterization*; Hunt, B. J., James, M. I., Eds.; Blackie: London, 1993.
(118) Schneider, N. S.; Sung, C. S. P. *Polym. Eng. Sci.* **1977**, *17*, 73–80.
(119) Kwon, J.; Kim, H. *J. Polym. Sci., Part A: Polym. Chem.* **2005**, *43*, 3973–3985.
(120) Princi, E.; Vicini, S.; Castro, K.; Capitani, D.; Proietti, N.; Mannina, L. *Macromol. Chem. Phys.* **2009**, *210*, 879–889.
(121) Gunes, I. S.; Cao, F.; Jana, S. C. *J. Polym. Sci., Part B: Polym. Phys.* **2008**, *46*, 1437–1449.
(122) Morimoto, K.; Suzuki, T.; Yosomiya, R. *Polym. Eng. Sci.* **1984**, *24*, 1000–1006.
(123) Kia, H. G. *Polym. Comp.* **1988**, *9*, 237–241.
(124) Mateen, A.; Shamim, A. *J. Mater. Sci. Lett.* **1989**, *8*, 927–930.
(125) Weisfeld, L. B.; Little, J. R.; Wolstenholme, W. E. *J. Polym. Sci.* **1962**, *56*, 455–463.
(126) Zhang, R.; Mallon, P. E.; Chen, H.; Huang, C. M.; Zhang, J.; Li, Y.; Wu, Y. C.; Jean, Y. C. *Prog. Org. Coatings* **2001**, *43*, 244–252.

Macromolecules
ARTICLE

Macromolecules **2011**, *44*, 39–45 **39**
DOI: 10.1021/ma102438k

High Ionic Liquid Content Polymeric Gel Membranes: Preparation and Performance

Johannes Carolus Jansen*

Institute on Membrane Technology, ITM-CNR, c/o University of Calabria, Via P. Bucci 17/C, 87030 Rende (CS), Italy

Karel Friess

Institute of Chemical Technology Prague, Department of Physical Chemistry, Technická 5, Prague 6-Dejvice, 166 28 Czech Republic

Gabriele Clarizia

Institute on Membrane Technology, ITM-CNR, c/o University of Calabria, Via P. Bucci 17/C, 87030 Rende (CS), Italy

Jan Schauer

Institute of Macromolecular Chemistry, Heyrovského nám. 2, 162 06 Prague 6-Břevnov, Czech Republic

Pavel Izák

Institute of Chemical Process Fundamentals, Rozvojová 135, 165 02 Prague 6-Suchdol, Czech Republic

Received October 25, 2010; Revised Manuscript Received December 2, 2010

ABSTRACT: Ionic liquid polymeric gel membranes containing from 20 wt % to 80 wt % of the ionic liquid 1-ethyl-3-methylimidazolium bis(trifluoromethylsulfonyl)imide ([EMIM][TFSI]) in poly(vinylidene fluoride-*co*-hexafluoropropylene) (p(VDF-HFP)) were prepared by solvent casting from a solution in acetone. The effect of the ionic liquid on the performance and properties of the membranes was discussed and compared with the neat polymer. In the presence of an excess of ionic liquid, p(VDF-HFP) membranes swell in a significant way, especially above 70 °C, becoming completely soluble above 90 °C. DSC analysis shows a gradual decrease of the melting point of the gel and a decrease in the overall melting enthalpy with increasing IL content, whereas the melting enthalpy normalized for the polymer fraction shows an initial drop and then a gradual increase. In the presence of the ionic liquid, the elastic modulus and break strength decrease dramatically, while the maximum deformation first increases due to higher flexibility of the plasticized polymer and then rapidly decreases above 40 wt % of IL as a consequence of the progressive decrease of the number of entanglements. X-ray studies demonstrate a reduction in the overall crystal content. The position of the strongest diffraction peak remains unaltered in all samples, suggesting that only the polymer chains crystallize and that no cocrystallization of ionic liquid and polymer takes place. Preliminary gas permeation measurements show a significant increase of the permeability in the presence of [EMIM][TFSI], especially for carbon dioxide. This suggests a potential application in gas separation membranes, for instance for natural gas treatment or for CO_2 sequestration from flue gas.

Introduction

During the past few years, ionic liquids (IL) have been recognized as a possible environmentally benign alternative to the classical organic solvents, mainly due to their good thermal stability and ability to dissolve a large range of organic molecules.[1] Ionic liquids have also been successfully applied in a wide range of applications, for instance in asymmetric synthesis, electrochemical applications, extractive separation in biotechnology,[2−4] and also in membrane gas separations[5] and pervaporation.[6] Their successful use is based on their extremely low volatility and consequent stability of the membrane compared to traditional supported liquid membranes.

*Corresponding author. E-mail: jc.jansen@itm.cnr.it.

Ionic liquid membranes are usually prepared in the form of supported liquid membranes, in which the pores of a porous membrane are saturated with the room temperature ionic liquid (RTIL).[7] In such membranes, the ionic liquid is trapped inside the pores by capillary forces. Although evaporation of IL can be excluded, if such membranes come in contact with a liquid phase, for instance in pervaporation, they can loose the ionic liquid from inside the polymer network due to swelling and leaching into the liquid phase.

To avoid this problem, in other cases membranes were prepared from polymerized room-temperature ionic liquids.[8,9] These RTILs are more stable but they require particular polymerizable groups and sophisticated membrane preparation techniques.

© 2010 American Chemical Society

Published on Web 12/14/2010

IL Gels/Membrane Preparation and Their Use. Numerous polymers may form thermoreversible gels from dilute or concentrated solution in the proper solvent.[10] A continuous physical network structure extending throughout the volume of the system is formed when at a certain reduced solvent power of the medium the polymeric chains form association complexes at widely separated points. In the majority of the cases these gels derive from the existence of a crystalline network structure, formed upon cooling from the homogeneous solution.

Such gels may also be formed starting from the polymer solution in a solvent mixture, in which "the good solvent" is allowed to evaporate and the second poor solvent is nonvolatile. Upon evaporation of "the good solvent", the polymer will phase separate. Under the proper conditions, and if the polymer is far enough below its nominal melting temperature, phase separation may take place as solid−liquid demixing. In this case, the free energy minimization favors the formation of small crystals as a solid phase in the liquid mixture. In this process, the polymer chains in solution form bridges between different crystals, diminishing chain mobility so much as to preclude subsequent macroscopic phase separation. In other cases the crystallization may be preceded by liquid−liquid phase separation, if a poor solvent or a solvent mixture is used and the process takes place not too far below the polymer melting point.

Very few cases have been reported where the thermoreversible gels are based on ILs as the poor solvent for the polymer. Recently Harner and Hoagland reported thermoreversible poly(ethylene glycol)/1-ethyl-3-methylimidazolium ethylsulfate [EMIM][$EtSO_4$] ionic liquid gels.[11] He and Lodge reported gels of 1-ethyl-3-methylimidazolium bis(trifluoromethylsulfonyl)imide [EMIM][TFSI] in acrylamide and ethylene oxide-based triblock or pentablock copolymers.[12] Kawauchi et al. reported thermoreversible ion gels based on poly(methyl methacrylate)s in 1-butyl-3-methylbenzimidazolium hexafluorophosphate.[13]

The supported liquid membranes have been tested for targeted gas/gas separations and especially for separation from air of volatile organic compounds,[14,15] leaking from gasoline during its storage, transportation and handling. In comparison with frequently used polymers like polydimethylsiloxane (PDMS),[16−18] polyether−polyamide block copolymer (PEBA), poly(vinylidene fluoride) (PVDF), high-free volume amorphous glassy perfluoropolymers,[19] or cross-linked fluorinated or poly(amide-imide) polymers,[20,21] RTIL supported membranes are, highly absorbing for alkanes and aromates without enormous material swelling. They also provide higher mass fluxes of separated substances or high separation factors.[22]

Scope. The aim of the present work is to develop, using a simple solution casting technique, stable RTIL membranes in which the IL is trapped inside a polymer gel phase. A further aim is to gain insight into the thermal, mechanical and structural properties of the gel phase and their correlation with the transport properties, in view of the potential use of such membranes in gas separation processes.

Experimental Part

Materials. Acetone (analytical grade, Lachner, Czech Republic) and ionic liquid 1-ethyl-3-methylimidazolium bis(trifluoromethylsulfonyl)imide (puriss., 99%, Solvent Innovation, mp −20 °C) were used without further purification. The ionic liquid (see Figure 1) will further be abbreviated as [EMIM][TFSI].

Poly(vinylidene fluoride-*co*-hexafluoropropylene) *fluoroelastomer*, further abbreviated as p(VDF-HFP), with nominal M_n = 130 000 g/mol, M_w = 400 000 g/mol, melting point 140−145 °C and molecular structure $-[CH_2-CF_2]_n-[CF_2-CF(CF_3)]_m-$ was supplied by Sigma-Aldrich.

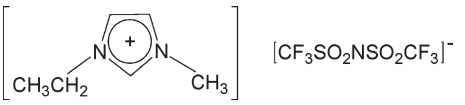

Figure 1. Structure of the ionic liquid 1-ethyl-3-methylimidazolium bis(trifluoromethylsulfonyl)imide ([EMIM][TFSI]).

The gases for the permeation tests (nitrogen, oxygen, methane, helium, hydrogen, and carbon dioxide, all with purity 99.99+%) were supplied by Pirossigeno, Italy.

Membrane Preparation. The polymer solution was prepared by dissolving 10 wt % of p(VDF-HFP) in acetone at room temperature under magnetic stirring for at least 1 h until a clear homogeneous solution was obtained. Different amounts of the ionic liquid [EMIM][TFSI] were added to the polymer solution under magnetic stirring and they dissolved completely in a few minutes.

The membranes were prepared by solution casting of the polymer/ionic liquid mixture in acetone on a Petri dish and by subsequent solvent evaporation at room temperature for 24 h. The membranes were further dried at 70 °C for 4 h to guarantee complete removal of the volatile solvent.

Membrane Swelling and Solubility Tests in [EMIM][TFSI]. Films of pure p(VDF-HFP) with a thickness of 0.15 mm were dried under vacuum at 80 °C, weighed, and immersed in an excess of pure [EMIM][TFSI] ionic liquid. After 48 h the films were removed from the liquid, wiped with tissue paper, and weighed again to determine the amount of ionic liquid absorbed. The experiments were carried out at different temperatures from 25 to 85 °C.

DSC. The thermal properties of the membranes were determined by DSC analysis, using a Pyris Diamond differential scanning calorimeter (Perkin-Elmer) equipped with Intracooler refrigeration system. Samples of 10−16 mg were wrapped in a small disk of aluminum foil (< 5 mg) and were subjected to a heating/cooling/heating cycle in the range from −50 to +200 °C at a rate of 20 °C/min. Given the low weight of the sample holder, no reference was used. Baseline subtraction was used to reduce the curvature of the baseline. The temperature and heat flow were calibrated with indium and zinc standards.

Mechanical Properties. Tensile tests on the membranes were carried out at room temperature on a Zwick/Roell single column Universal Testing Machine, model Z2.5, equipped with a 50 N load cell and flat pneumatic clamps. The clamp surface was covered with adhesive rubber to avoid slipping or damage of the softer samples with high IL content.

Specimens with an effective length of 40 mm (distance between the clamps) and a width of 5 mm were tested at a deformation rate of 20 mm min^{-1} (= 50% min^{-1}), with exception of the sample without IL, which was tested at a deformation rate of 8 mm min^{-1} (= 20% min^{-1}) to avoid early rupture due to its higher stiffness and fragility. The average value and the standard deviation of the Young's modulus, the break strength and the maximum deformation were determined on a series of 4−6 samples.

X-ray. The XRD data of sample films (20 × 15 mm) were collected at room temperature by an X'Pert PRO $\theta-\theta$ diffractometer (PANanalytical, The Netherlands) using Cu Kα radiation (λ = 1.5418 Å, U = 40 kV, I = 30 mA) in parafocusing Bragg−Brentano geometry. The data were scanned with an ultrafast X'Celerator detector over the angular range 5−70° (2θ) with a step size of 0.033° (2θ) and time per step 20.32 s. Data evaluation was performed by the software package HighScore Plus.

Gas Permeability Measurements. Gas permeation rate tests on flat dense membranes were carried out at room temperature (25 °C) by fixed-volume pressure increase instrument, described in detail elsewhere.[23] After thorough evacuation of the membrane

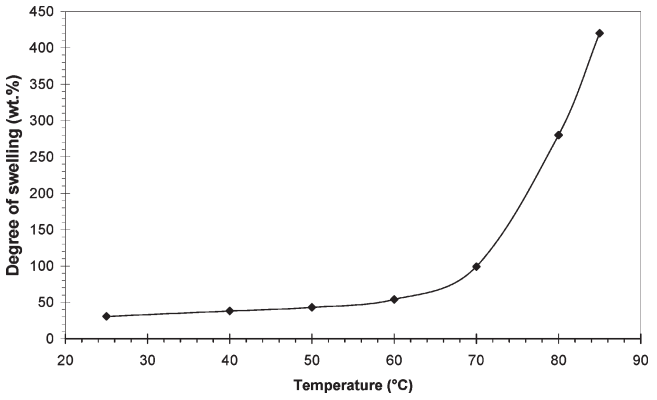

Figure 2. Temperature dependence of the swelling degree of the p(VDF-HFP) fluoroelastomer in excess ionic liquid [EMIM][TFSI].

to remove all previously dissolved species, the membrane is exposed to the feed gas and from that moment the pressure in the fixed permeate volume is monitored. Measurements were carried out with six permanent gases (He, H_2, CH_4, N_2, O_2, and CO_2). Permeability coefficients, P, were calculated from the slope of time-pressure curve in steady state condition:[24]

$$p_t = p_0 + (\mathrm{d}p/dt)_0 t + \frac{RTA}{V_p V_m}\frac{p_f P}{l} t \quad (1)$$

in which p_t is the permeate pressure at time t, p_0 is the starting pressure, $(\mathrm{d}p/\mathrm{d}t)_0$ is the baseline slope. R is the universal gas constant, T is the absolute temperature, A is the exposed membrane area, V_P is the permeate volume, V_m is the molar volume of a gas at standard temperature and pressure [0 °C and 1 atm], and p_f is the feed pressure. The transport properties of the gases were determined at the feed pressure of 1 bar. A total membrane area of 11.3 or 34.2 cm^2 was used.

Results and Discussion

Membrane Preparation. All membranes in this work were cast from solutions in acetone, a good common solvent for both the fluoroelastomer and the ionic liquid [EMIM]-[TFSI]. The membranes were prepared by controlled solvent evaporation. As a result of the evaporation of acetone ("the good solvent") the relative concentration of IL ("the less good solvent") and polymer increased. In this way, the deteriorating solvent quality leads to gelation of the solution by crystallization of the polymer and to the gradual formation of a solid film. Upon complete drying at higher temperature, mechanically resistant transparent self-supported membranes were obtained for all ratios of polymer and ionic liquid. Often a small amount of IL exudate appeared on the surface of the membranes as tiny droplets or as a thin film.

Membrane Swelling and Solubility Tests in [EMIM][TFSI]. Swelling of pure p(VDF-HFP) films in excess IL was carried out at different temperatures. The degree of swelling (DS) of the neat polymer films after 48 h was calculated using the relationship:

$$\mathrm{DS} = (W_S - W_0)/W_0 \quad (2)$$

where W_S is the weight of the swollen sample and W_0 is the weight of the same film before immersion.

It was found that at room temperature (25 °C) the neat p(VDF-HFP) film swells about 30 wt % in [EMIM][TFSI]. The swelling increases more or less linearly with temperature up to about 60 °C and then increases dramatically above 70 °C (Figure 2). Above 90 °C, the polymer becomes completely

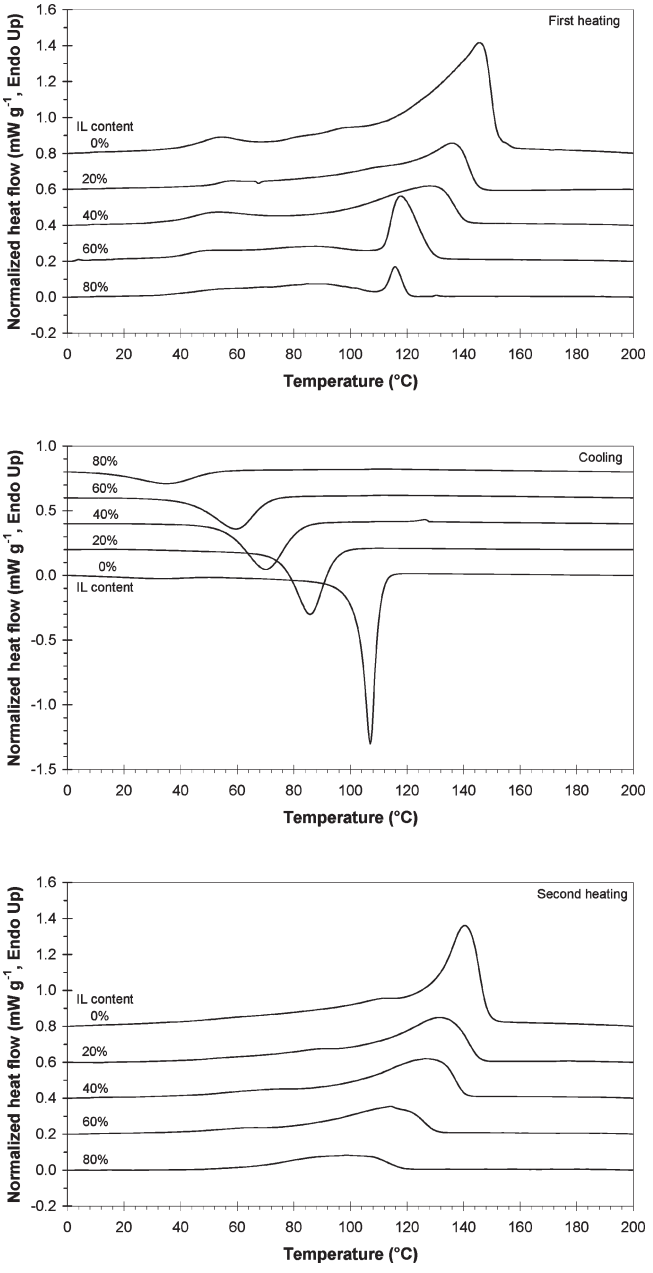

Figure 3. DSC thermograms of the freshly prepared samples during heating (top), the successive cooling run (middle), and the second heating run (bottom). Curves are shifted vertically for clarity.

soluble. Once dissolved, the polymer remains in solution even upon cooling down to room temperature. This behavior confirms the good compatibility of the polymer with the ionic liquid. The complete dissolution of the polymer above 90 °C is in accordance with the strong melting point depression of the membranes with the highest IL content observed by DSC analysis. Obviously the melting of the crystalline phase of the polymer corresponds with the point where the polymer becomes soluble. In this light, swelling of a neat polymer film in the IL could be a successful alternative method to prepare IL-containing membranes. However, this is not suitable to reach high IL concentrations because the membrane is easily deformed or damaged during the swelling as a result of the dissolution and extraction of the low molar mass fraction of the polymer.

Thermal Analysis of the Gel Membranes. The thermal properties of the membranes were investigated by DSC

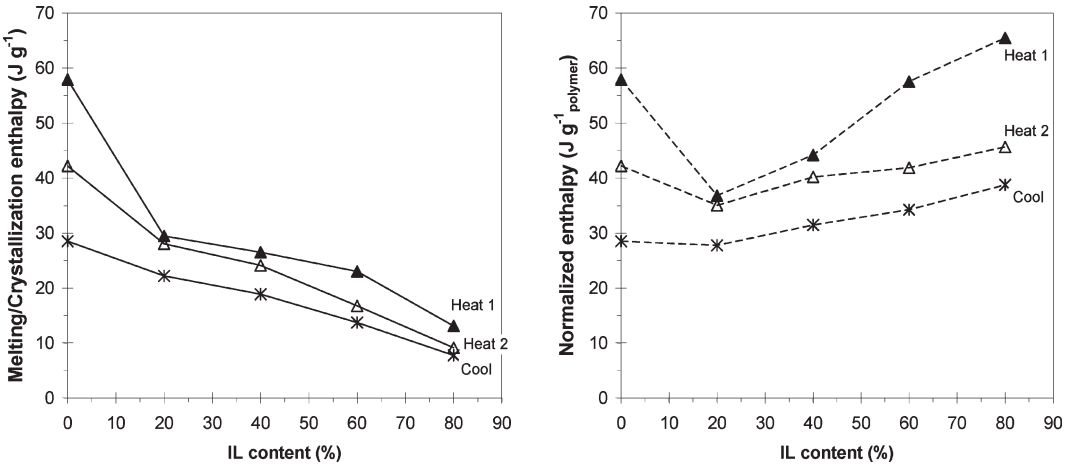

Figure 4. Total melting and crystallization enthalpy of the overall membranes (left) and after normalization for the polymer content (right). Heat 1, Heat 2, and Cool indicate the first and second heating run and the cooling run, respectively.

analysis. The results are displayed in Figure 3. With increasing IL content there is a strong decrease of the melting temperature of the gel in comparison with the pure polymer. At the same time the strong and relatively sharp peak makes place for a much weaker and broader melting peak, suggesting a reduction of the average crystal size and/or purity. The differences in the melting and crystallization peak temperature are related to the kinetics of the crystallization process. In the present case the degree of supercooling depends on the viscosity of the system (related among others to the molar mass, chain flexibility and polymer concentration) and on the probability that polymer chains approach one another to form a stable nucleus (related again to the polymer concentration in the ionic liquid).

Up to 80% of IL in the membrane the gelation is thermally reversible above room temperature, as can be seen from the strong endothermal crystallization peak in the cooling curves. Both the crystallization temperature and the enthalpy decrease markedly with increasing IL content.

The stable solution obtained during the swelling and solubility tests of the polymer in the IL is apparently only possible at very low polymer concentrations. The dissolution temperature of 90 °C observed in the swelling tests in excess IL corresponds approximately to the melting point of the gels, if we extrapolate the data from Figure 3 to higher IL content and to lower polymer concentration.

Given the thermal reversibility of the gel formation also the thermally induced phase separation process (TIPS) should in principle be a possible alternative for the current solution-casting membrane formation process. Nevertheless, from the viewpoint of practical applicability the solution casting is the better process because it is easier to obtain thin films, thus limiting the consumption of expensive ionic liquid.

The overall melting enthalpy of the films decreases almost linearly with increasing IL content, obviously due to the lower polymer concentration (Figure 4). However, if this value is normalized for the polymer concentration, a different trend is found: after an initial decrease, going from neat polymer to 20 wt % of IL, with a further increase of the IL content the normalized melting enthalpy also slightly increases. This is even more evident in the freshly prepared sample, in which crystallization has taken place during evaporation of the solvent, and it is an indication that crystallization is more efficient due to higher freedom of motion of single chains in the diluted phase. The measured crystallization enthalpy is somewhat lower than the melting enthalpy

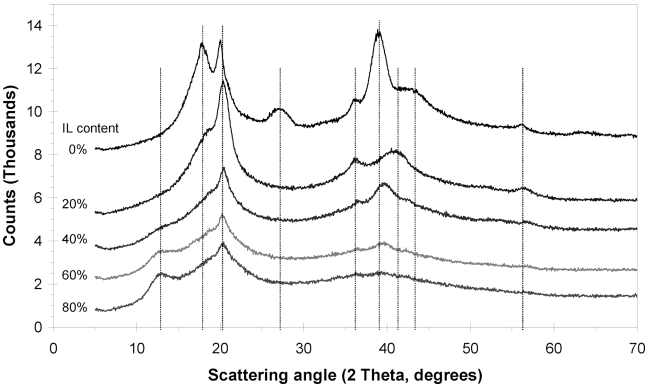

Figure 5. Wide-angle X-ray diffraction patterns of the membrane samples (*x*-axis °2θ, *y*-axis counts or arbitrary units). The lines are shifted vertically for better comparison.

in the second run. This indicates that at the given cooling rate of 20 °C/min crystallization is not totally complete in the measurement window shown in Figure 3. Evidently some further crystallization takes place when the sample is cooled to −50 °C before the next measurement.

In this light it is interesting to note that the samples with 60 and 80 wt % IL show a quite unique and remarkably sharp melting peak just below 120 °C in the fresh sample. In the case of PVDF, which has different crystal polymorphs, it is known that in solution-cast films the type of solvent can influence which polymorph will be formed predominantly,[25] Also in the present p(VDF-HFP) copolymer we believe that mainly the short VDF sequences are responsible for the crystal fraction. Therefore, it is not unlikely that different polymorphs may have been formed also in the most "diluted" samples of the present series. Indeed, the X-ray diffraction pattern shows a significant peak at $2\theta = 12°$ only in the samples with 60 and 80 wt % IL (Figure 5 and the text below). More detailed studies, such as temperature dependent X-ray diffraction, could confirm this presumption but this is out of the scope of the present manuscript.

Membrane Structural Properties by X-ray Diffraction Studies. The wide-angle X-ray diffraction patterns of the IL gel membranes and the reference membrane of pure polymer are displayed in Figure 5. The main diffraction peaks are listed in Table 1. The diffraction patterns confirm the general trend of decreasing crystallinity with increasing IL content observed by DSC analysis. In all samples one of the strongest peaks is located at $2\theta = 20°$. The diffraction

pattern of the pure polymer shows some remarkable similarities with that of PVDF, which has two intermediate peaks close together at $2\theta = 18$ and 18.5°, related to the (100) plane and the (020) plane of the α-polymorph, a very strong peak at 20° related to the (110) plane of the α-polymorph, and finally another moderate peak at 27°, due to the (021) plane of the α-polymorph. Upon addition of the IL, the peaks around 18 degrees and 27 degrees disappear completely and the peak at 20° shifts to a slightly higher value. This is the typical position for the (101) plane of the γ-polymorph of PVDF. The only significant novel peak formed at higher IL content appears in the samples with 60% and 80% of IL at ca. 13°, corresponding to a *d*-spacing of 6.78 Å. Its origin is not clear, but given the low polymer concentration, it should presumably involve the IL itself. In these two samples also the DSC first heating run shows a distinct melting peak which is absent in the other samples.

The VDF/HFP ratio in the polymer is approximately 4:1 and statistically VDF sequences with an average of 4 monomeric units should be present, The signals are not sufficiently resolved for a positive identification of the crystal structure but from the low HFP content and the above evaluation it seems likely that short VDF sequences in the copolymer are responsible for a PVDF-like crystal phase and that the presence of the IL favors the formation of one polymorph rather than the other, in the present case probably γ instead of α. The effect of solvents or additives on the polymorph of solution-cast PVDF films is well-known.[26] Also the melting enthalpy of our copolymer (42 J/g) is quite close to that of PVDF (ca. 50 J/g in the second heating run[27]), justifying the hypothesis of a PVDF-like crystal phase.

Table 1. Diffraction Angles (2θ) of the Main Diffraction Peaks of the IL Gel Membranes with the Corresponding Interplanar Distances (*d*-Spacing)

	IL content (wt %)					
diffraction angle, 2θ (deg)	0%	20%	40%	60%	80%	*d*-spacing (Å)
13.0			~	+	+	6.78
17.8	++	~				4.97
20	+++	+++	+++	++	++	4.43
27.1	++					3.28
36	+	++	~	~	~	2.49
38.9	+++					2.32
39.6			++	~	~	2.27
40.9		+				2.20
42.1	+		~			2.14
56	~	~	~			1.64

Mechanical Properties. All membranes were obtained as flexible dense films with sufficient mechanical resistance to be handled without difficulties. The tensile tests were performed on small strips of the films and the results are given in Figure 6 as a function of the ionic liquid content. The ionic liquid has a very strong plasticizing effect on the polymer, causing already at only 20 wt % of IL a decrease of the elastic modulus of an order of magnitude. This is also due to the decrease in crystallinity compared to the neat polymer, as confirmed by DSC. At the same time the break strength of the polymer decreases as a result of the incorporation of the IL. With further increasing IL content both the Young's modulus and the break strength decrease to about 3 and 2 MPa, respectively.

In contrast, the maximum deformation first increases with increasing IL content because of the reduced rigidity and the increased flexibility of the plasticized polymer, and then it rapidly decreases again above 40% of IL, when the gel becomes too weak to undergo a strong plastic deformation. At high IL content, the polymer is more diluted. Under these conditions there is less overlap of the polymer coils in solution and as a consequence the intrachain crystallization becomes relatively more important than interchain crystallization. The latter is responsible for the formation of the physically cross-linked network, and as a consequence the sample loses its mechanical strength and its elasticity.

Gas Transport Properties. The presence of the ionic liquid strongly affects the transport properties of the polymer, but up to about 60 wt % of ionic liquid the membranes still behave more as a glassy polymer rather than as a rubbery polymer. Thus, as the IL content in membrane samples rises, the permeability of all gases investigated increases dramatically (Figure 7). However, the less permeable species (nitrogen and methane) and the most soluble carbon dioxide increase their permeation rate much more than small molecules like helium and hydrogen. Indeed, due to its very stiff nature and the relatively high crystallinity, the neat polymer behaves as a barrier material and its selectivity is mainly determined by its size sieving properties. With increasing IL content the samples become more flexible and this favors the transport of the originally slow species, such as methane and nitrogen, as well as the species with high solubility, such as CO_2. The much higher solubility of CO_2 in comparison with N_2 and H_2 determines the difference in the absolute value of

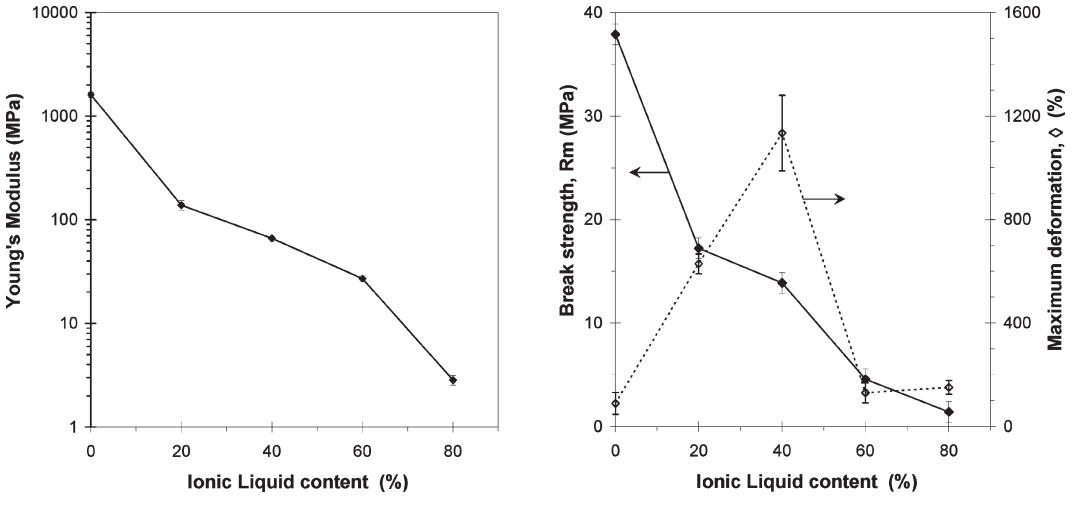

Figure 6. Young's modulus, *E* (left) and the maximum break strength, R_m, and maximum deformation, ε (right), as a function of the IL content.

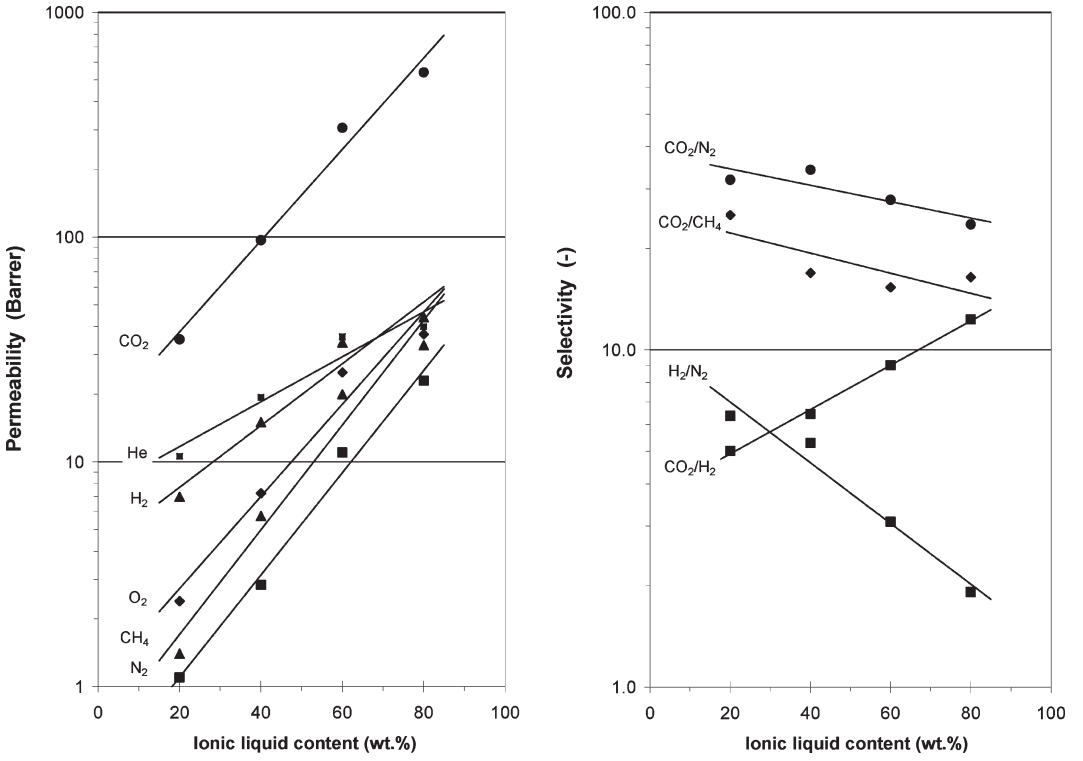

Figure 7. Permeability of six permanent gases as a function of the IL content (left) and corresponding selectivity between selected gas pairs (right). Lines are plotted as a guide to the eye.

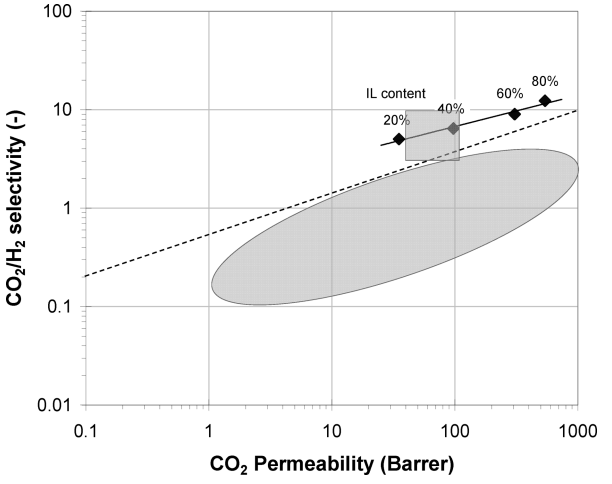

Figure 8. Robeson diagram for the gas pair CO_2/H_2 indicating the experimental points of the present work (♦). The approximate range for common homopolymers (ellipse) and for poly(ethylene glycol) and poly(propylene glycol) derivatives (square), adapted from Patel et al.,[29] are indicated as a reference.

the permeability but does not influence to a large extent the trend as a function of the IL content.

As a consequence the CO_2/N_2 and the CO_2/CH_4 selectivity values undergo only a slight decrease, while the H_2/N_2 selectivity decreases rather strongly with increasing IL content (Figure 7).

On the contrary, as the IL concentration rises, the CO_2/H_2 selectivity shows a remarkable increase, because of the significantly higher positive effect of the IL on the CO_2 permeability than on the hydrogen permeability. The relatively high CO_2 permeability is probably an effect of the affinity of CO_2 for the ionic liquid, and thus of the high solubility of this gas in the membrane. If this is generally applicable, then the presented type of membranes can be successfully used in the separation of those mixtures where species with a significantly different affinity for the ionic liquid are present.

Membranes with such a large CO_2/H_2 selectivity are quite uncommon because hydrogen is usually the faster permeating species. Indeed, in his famous diagrams, Robeson represents the permeation data for the CO_2 and H_2 gas pair as the H_2/CO_2 selectivity against the H_2 permeability.[28] Thus, whereas one usually searches for membranes with a high H_2/CO_2 selectivity, the present membranes behave in the opposite way and might be interesting for those applications where CO_2 must be removed from a hydrogen stream and where hydrogen should remain at high pressure. An alternative Robeson diagram of the CO_2/H_2 selectivity against the CO_2 permeability was presented by Patel et al.[29] (Figure 8). The increase of the upper bound line in this diagram corresponds with the trend in our own experimental data. It is interesting to note that all our data are significantly above the general trend in the data, indicating that IL gel membranes are indeed promising candidates for the given separation.

Conclusions

The fluoroelastomeric polymer p(VDF-HFP) forms stable gels in the ionic liquid [EMIM][TFSI], enabling the successful preparation of resistant free-standing membranes by solution casting of the polymer/ionic liquid mixture, followed by controlled solvent evaporation. The membranes consist of a thermoreversible polymeric gel in which crystallization of p(VDF-HFP) is responsible for the network structure, as supported by DSC and X-ray diffraction analysis. The polymer shows a good compatibility with the IL and may swell up to 30% at room temperature, while it becomes soluble at 90 °C or higher, depending on the concentration of IL.

The presence of IL in the polymer causes a decrease of the elastic modulus of several orders of magnitude and a significant

reduction of the break strength over the entire concentration range. On the other hand, the maximum deformation initially increases to over 1000% and then decreases for an IL content above 40%. This is due to a compromise between the increased elasticity of the gel (lower Young's modulus), leading to higher elongations, and the reduced break strength, leading to lower elongations.

DSC analysis shows a strong decrease of the polymer melting point in the gel as a function of the IL content and a decrease of the overall melting enthalpy. However, normalized for the polymer concentration, the melting enthalpy tends to increase at the higher IL concentrations, presumably due to more efficient chain folding as a result of the lower viscosity and higher mobility of the polymer chains in the IL solution.

The gas permeability strongly rises with the IL concentration and the transport of larger and more condensable species is favored over that of the smaller molecules. The separation thus changes from a diffusion-controlled process to a solubility-controlled one. The CO_2/H_2 selectivity is unusually high for this reason, offering perspectives for application of these membranes in environments where carbon dioxide must be separated from hydrogen while the latter remains at high pressure.

Acknowledgment. This research was supported by the CNR-CAS bilateral agreement 2010-2012 (Novel composite membranes containing selected ionic liquids and polymers for gas and vapour separations). The authors are also thankful for the financial support of the Czech Ministry of Education, Sports and Youth MSM (Grant No. 6046137307) and of the Czech Science Foundation (Grant No. P106/10/1194) and the Grant Agency of the Czech Republic (Grant No. 203/08/0465). Alessio Fuoco, Fabio Bazzarelli, and Paola Bernardo are gratefully acknowledged for their assistance in the tensile tests and in the gas permeation measurements. Alena Randová and Lidmila Bartovská are also gratefully acknowledged for their assistance in the swelling measurements.

References and Notes

(1) Freemantle, M. New Horizons for Ionic Liquids. *Chem. Eng. News* **2001**, 21–25.
(2) Fadeev, A. G.; Meagher, M. M. Opportunities for ionic liquids in recovery of biofuels. *Chem. Commun.* **2001**, 295–296.
(3) Kohoutová, M.; Sikora, A.; Hovorka, Š.; Randová, A.; Schauer, J.; Tišma, M.; Setničková, K.; Guernik, S.; Greenspoon, N.; Izák, P. Influence of ionic liquid content on properties of dense polymer membranes. *Eur. Polym. J.* **2009**, *45*, 813–819.
(4) Izák, P.; Schwarz, K.; Ruth, W.; Bahl, H.; Dyson, P. J.; Kragl, U. Increased productivity of Clostridium acetobutylicum fermentation of acetone, butanol, and ethanol by pervaporation through supported ionic liquid membrane. *Appl. Microbiol. Biotechnol.* **2008**, *78*, 597–602.
(5) Scovazzo, P. Determination of the upper limits, benchmarks and critical properties for gas separations using stabilized room temperature ionic liquid membranes (SILMs) for the purpose of guiding future research. *J. Membr. Sci.* **2009**, *343*, 199–211.
(6) Izák, P.; Friess, K.; Šípek, M. Pervaporation and Permeation Taking Advantage of Ionic Liquids. in *Handbook of Membrane Research: Properties, Performance and Applications*; Gorley, S. V., Ed.; Nova Science Publishers: Hauppauge, NY, 2009; Chapter 12.
(7) Branco, L. C.; Crespo, J. G.; Afonso, C. A. M. Studies on the Selective Transport of Organic Compounds by Using Ionic Liquids as Novel Supported Liquid Membranes. *Chem.—Eur. J.* **2002**, *8*, 3865–3871.
(8) Bara, J. E.; Lessmann, S.; Gabriel, C. J.; Hatakeyama, E. S.; Noble, R. D.; Gin, D. L. Synthesis and performance of polymerizable room temperature ionic liquids as gas separation membranes. *Ind. Eng. Chem. Res.* **2007**, *46*, 5397–5404.
(9) Bara, J. E.; Hatakeyama, S. E.; Gin, D. L.; Noble, R. D. Improving CO_2 permeability in polymerized room-temperature ionic liquid gas separation membranes through the formation of a solid composite with a room-temperature ionic liquid. *Polym. Adv. Technol.* **2008**, *19*, 1415–1420.
(10) Hiltner, A. Gelation Properties of Polymer Solutions. In *Polymer Handbook*, 4th ed.; Brandrup, J., Immergut, E. H., Grulke, E. A., Eds.; John Wiley & Sons: New York, 1999; Chapter 7.
(11) Harner, J. M.; Hoagland, D. A. Thermoreversible gelation of an ionic liquid by crystallization of a dissolved polymer. *J. Phys. Chem. B* **2010**, *114*, 3411–3418.
(12) He, Y.; Lodge, T. P. Thermoreversible ion gels with tunable melting temperatures from triblock and pentablock copolymers. *Macromolecules* **2008**, *41*, 167–174.
(13) Kawauchi, T.; Kumaki, J.; Okoshi, K.; Yashima, E. Stereocomplex formation of isotactic and syndiotactic poly(methyl methacrylate)s in ionic liquids leading to thermoreversible ion gels. *Macromolecules* **2005**, *38*, 9155–9160.
(14) Krull, F. F.; Fritmann, C.; Melin, T. Liquid Membranes for Gas/Vapor Separations. *J. Membr. Sci.* **2008**, *325*, 509–519.
(15) Mehnert, C. P. Supported Ionic Liquid Phases. *Chem.—Eur. J.* **2005**, *11*, 50–56.
(16) Kim, H. J.; Nah, S.S..; Min., B. R. A new technique for preparation of PDMS pervaporation membrane for VOC removal. *Adv. Env. Res.* **2002**, *6*, 255–264.
(17) Majumdar, S.; Bhaumik, D.; Sirkar, K. K. Performance of commercial-size plasmapolymerized PDMS-coated hollow fiber modules in removing VOCs from N_2/air. *J. Membr. Sci.* **2003**, *214*, 323–330.
(18) Sohn, W. I.; Ryu, D. H.; Oh, S. J.; Koo, J. K. A study on the development of composite membranes for the separation of organic vapors. *J. Membr. Sci.* **2000**, *175*, 163–170.
(19) Yampolskii, Y.; Pinnau, I.; Freeman, B. *Materials Science of Membranes for Gas and Vapor Separation*: John Wiley & Sons: Chichester, England, 2006.
(20) Šindelář, V.; Sysel, P.; Hynek, V.; Friess, K.; Šípek, M.; Castaneda, N. Transport of Gases and Organic Vapors Through Membrane Made of Poly(amide-imide)s Crosslinked With Poly(ethyleneadipate). *Collect. Chech Chem. Commun.* **2001**, *66*, 533–540.
(21) Guizard, C.; Boutevin, B.; Guida, F.; Ratsimihety, A.; Amblard, P.; Lasere, J. C.; Naiglin, S. VOC Vapor Transport Properties of New Membranes Based on Cross-linked Fluorinated Elastomers. *Sep. Purif. Technol.* **2001**, *22*, 23–30.
(22) Obuskovic, G.; Majumdar, S.; Sirkar, K. K. Highly VOC-selective hollow fiber membranes for separation by vapor permeation. *J. Membr. Sci.* **2003**, *217*, 99–116.
(23) (a) Clarizia, G.; Algieri, C.; Drioli, E. Filler-polymer combination: a route to modify gas transport properties of a polymeric membrane. *Polymer* **2004**, *45*, 5671–5681. (b) Macchione, M.; Jansen, J. C.; De Luca, G.; Tocci, E.; Longeri, M.; Drioli, E. Experimental analysis and simulation of the gas transport in dense Hyflon AD60X membranes. Influence of residual solvent. *Polymer* **2007**, *48*, 2619–2635.
(24) Jansen, J. C.; Friess, K.; Drioli, E. Organic vapour transport in glassy perfluoropolymer membranes. A simple semi-quantitative approach to analyze clustering phenomena by time lag measurements, *J. Membr. Sci.* **2011**, *367*, 141−151.
(25) Lovinger, A. J. Poly(vinylidene fluoride). In *Developments in crystalline polymers-1*; Bassett, D. C., Ed.; Applied Science Publishers: London, England, 1982; pp 195−273.
(26) Benz, M.; Euler, W. B. Determination of the crystalline phases of poly(vinylidene fluoride) under different preparation conditions using differential scanning calorimetry and infrared spectroscopy. *J. Appl. Polym. Sci.* **2003**, *89*, 1093–1100.
(27) Choi, S.-H.; Tasselli, F.; Jansen, J. C.; Barbieri, G.; Drioli, E. Effect of the preparation conditions on the formation of asymmetric poly(vinylidene fluoride) hollow fibre membranes with a dense skin. *Eur. Polym. J.* **2010**, *46*, 1713–1725.
(28) Robeson, L. M. The upper bound revisited. *J. Membr. Sci.* **2008**, *320*, 390–400.
(29) Patel, N. P.; Hunt, M. A.; Lin-Gibson, S.; Bencherif, S.; Spontak, R. J. Tunable CO_2 transport through mixed polyether membranes. *J. Membr. Sci.* **2005**, *251*, 51–57.

46 *Macromolecules* **2011**, *44*, 46–59
DOI: 10.1021/ma1022378

Macromolecules
ARTICLE

Well-Defined Polyamide Synthesis from Diisocyanates and Diacids Involving Hindered Carbodiimide Intermediates

An-Liu Chen,[†] Kuan-Liang Wei,[†] Ru-Jong Jeng,[†] Jiang-Jen Lin,*[,‡] and Shenghong A. Dai*[,†]

[†]*Department of Chemical Engineering, National Chung Hsing University, Taichung 402, Taiwan, and* [‡]*Institute of Polymer Science and Engineering, National Taiwan University, Taipei 106, Taiwan*

Received May 6, 2010; Revised Manuscript Received November 26, 2010

ABSTRACT: We have uncovered a novel polycondensation strategy for the synthesis of well-defined polyamides of narrow molecular weight distributions based on modifications of our sequential self-repetitive reaction ("SSRR") previously developed for diisocyanate−dicarboxylic acid polymerization. In our newly discovered SSRR polyamide formation mechanism, a small amount of hindered carbodiimide, *N*,*N*′-bis(2,6-diisopropylphenyl)carbodiimide (iPr-CDI) or a hindered isocyanate such as 2,6-diisopropylphenyl isocyanate (iPr-NCO), was introduced to the polymerization as an initiator, followed by simultaneous addition of diisocyanates and diacids monomers. By using this new reaction mode, the SSRR mechanism produces polyamide products of narrow molecular weight distributions with their dispersities reduced to 1.2−1.4, which is far lower than a range of >2.5 found in regular SSRR reactions. Significantly different from a conventional step-growth or standard SSRR reaction, the formation of a polymer backbone is preferential when the diacid is added to the requisite iPr-CDI in the first step, followed by a rearrangement to form amide and fragmented components for SSRR. The control of molecular weight is mainly attributed to the acid addition favoring the unhindered poly-CDI intermediates in the middle of the growing chains over the hindered-CDI at the chain terminals. It appears that the formation of a "hindered isocyanate" and the subsequent formation of a "new hindered-CDI" at the terminal end of growing amide-chains in each SSRR cycle force the acid again toward the preferred unhindered CDI sites dictating the observed outcome. This simple polyamide synthesis methodology is unique and unconventional, and it could significantly facilitate the development of tailored-made polyamides from a variety of diisocyanates and diacids.

Introduction

In recent years, synthesis of structurally well-defined polymers has been one of the most active areas of polymer research. Particularly, living free radical polymerizations such as atom-transfer radical polymerization (ATRP),[1,2] nitroxide-mediated free radical polymerization (NMRP),[3,4] and reversible addition−fragmentation chain transfer polymerization (RAFT)[5−7] have been extensively developed to synthesize polymers with narrow molecular weight distributions. All of these synthetic methods are based on vinyl monomer addition to the terminal active sites of the growing backbones. This vinyl monomer addition polymerization differs from the conventional condensation polymerizations which proceed through a step-growth mechanism that allows monomers and the growing oligomers to react randomly with each other simultaneously. This random step-growth mechanism in the condensation polymerization produces polymers with a wide range of molecular weight distributions. However, Yokozawa et al.[8−16] have recently demonstrated the ability to control molecular weights and dispersities of condensation polymers such as polyamides, polyesters, and polyethers by "chain-growth condensation" of para-substituted AB-type aromatic monomers. They manipulated the condensation reaction through introduction of an activated functional group in the polymerization steps; thereby creating a preferred site and thus a sequence for the new monomer addition. This general principle has inspired and ushered in new efforts for finding "controlled" condensation polymerization.[17]

In our previous paper in this series, we described a "sequential self-repetitive reaction (SSRR)" for the synthesis of polyamide through condensation of diisocyanate with diacid in the presence of a carbodiimide (CDI) catalyst.[18,19] The standard "SSRR" reaction involves three basic repetitive yet sequential reactions including: (i) condensation of two isocyanates into a CDI in the presence of a CDI catalyst (DMPO)[20] (ii) addition of acid to the CDI to yield *N*-acylurea and (iii) thermal fragmentation of the *N*-acylurea to form amide and isocyanate fragments both in half of the original molar amount, (Scheme 1). It was observed that step i and step ii were very facile even at a ambient temperature, whereas step iii could only be effective at a temperature of greater than 140 °C.[21−23] However, when this three-step cycle repeats under heated conditions with sufficient acid, all of the isocyanate and CDI are converted into amide as the final product in excellent conversion and selectivity.[18,19] By extending this unique methodology, we have devised a new twist to the SSRR process by addition of small amount of a hindered carbodiimide (CDI) such as *N*,*N*′-bis(2,6-diisopropylphenyl)carbodiimide, iPr-CDI **1**, or a hindered isocyanate such as 2,6-diisopropylphenyl isocyanate, iPr-NCO **7**. Doing so creates terminally new hindered-CDIs (PiPr-CDI type **10**, Scheme 4) on the growing polymer chains. Introduction of the terminally new hindered-CDIs has been found to form "less-reactive" CDI-sites than those of the unhindered CDI counterparts on the regular polymer chains for the "SSRR" cycles. These sterically new hindered-CDIs were found to control the site and sequence of the acid addition. As the consequence, polyamides **4a**′**−4f**′ of low dispersities were prepared from varieties of diacids **2a−2f** and methylene diphenylene diisocyanate (MDI) **3** as shown in Scheme 2.

Results and Discussion

The new DMPO-catalyzed polycondensations from diisocyanates and dicarboxylic acids are basically the same as those of the regular SSRR,[18,19,24−26] where both intermediates were added

*Corresponding authors. (S.A.H.) E-mail: shdai@dragon.nchu.edu.tw. (J.J.L.) E-mail: jianglin@ntu.edu.tw. Telephone: + 886-4-2285-1283. Fax: + 886-4-2287-4159.

 Published on Web 12/15/2010 © 2010 American Chemical Society

Scheme 1. The Standard "SSRR" Reaction

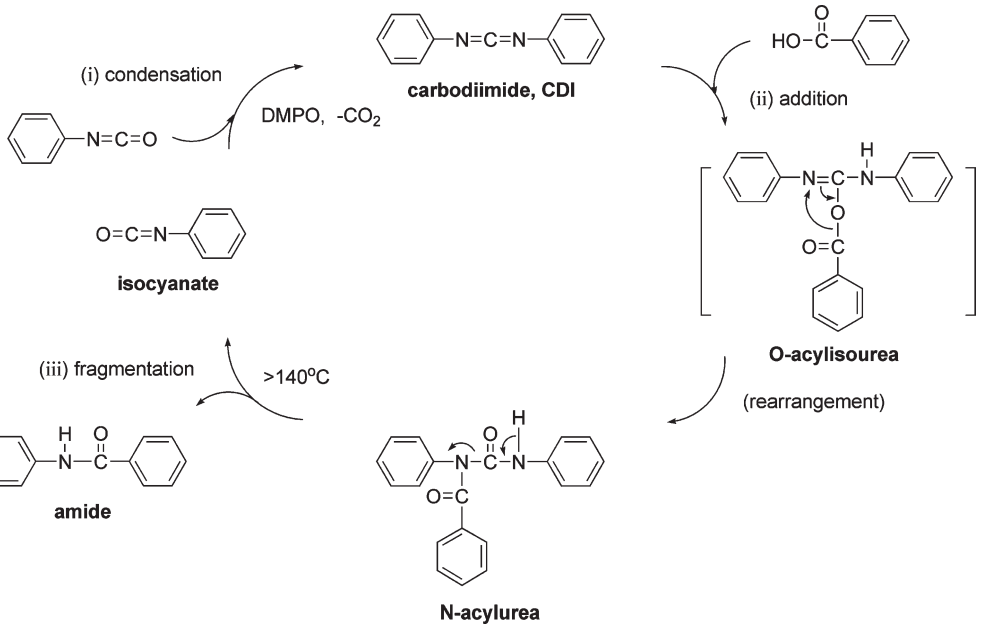

Scheme 2. New "SSRR" Polyamide Synthesis with a Hindered Carbodiimide Initiated Polymerization of Diisocyanate and Diacid

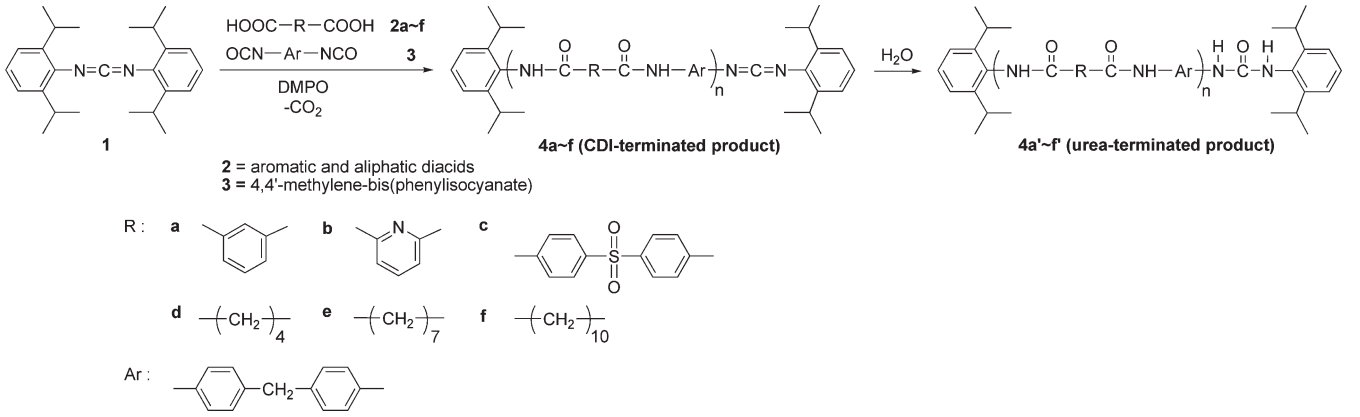

into a solution containing a catalyst at about 180−200 °C. However, due to the new addition of iPr-CDI **1** in the beginning of the new reaction, iPr-CDI **1** reacted with diacid **2** forming an amide terminated monoacid **6** as one of the initiation steps of the polymerization (Scheme 3). In the meantime, 2,6-diisopropylphenyl isocyanate (iPr-NCO, **7**) generated was found to slowly create new hindered-CDI at the terminal end of the growing polymer chains as shown in Scheme 4, Scheme 5 and Scheme 6. Therefore, two types of CDIs, the diisopropyl-phenyl containing new hindered-CDI type at the terminal ends of the polymer chains and the unhindered CDIs type, such as **10**, **13** or **16** at the midportions of their growing chains were both created in the new SSRR polymerization process mainly through cross-condensation involving iPr-NCO **7**.

First, condensation of MDI **3** monomer under the catalyst of DMPO was converted into poly-CDI products **8** at a rapid rate. iPr-NCO **7** being the "less-reactive" isocyanate serves as a regulator in the polymerization by facilitating the capping of poly-CDI **8** and residual isocyanates **9** slowly under the catalytic action of DMPO (Scheme 4). Both condensation reactions create unsymmetrically new hindered-CDI groups at the terminal end of poly-CDI-chains **10**. PiPr-CDI terminated poly-CDI **10** was found to go forward with the chain-growth reaction with the monoacid 6 in formation of acylureas **11** thereby starting the SSRR sequence as shown in Scheme 5. By this mechanism, the propagation of the growing polyamide chains takes place preferentially at the unhindered CDI-sites (such as **13**) through SSRR. Overall as shown in Schemes 5 and 6, the mode of polymerization constitutes controlled insertions of diacid **2** onto unhindered polyamide-CDIs sites at the midportions of the polymer chains followed by fragmentation of the resulting acylureas to form polyamide **16** and new isocyanates **12** for further repetitive reactions leading to **4** as the final product.

The proof of the proposed mechanism operative in this new SSRR is shown in the isolated polyamides which all possess diisopropyl-phenyl groups at their terminal ends as evidenced by the NMR spectroscopy of polymer products featured either in part a or part b of Figure 1 as a urea-terminated PA due to water treatment. This result confirms that iPr-CDI **1** indeed was involved in the major polymerization process. The FT-IR monitoring of the reaction mixture provided additional evidence of the proposed reaction mechanism. Our FT-IR spectral analysis based on authentic and synthesized model compounds, Figure 2 revealed that the initial CDI absorption at 2169 cm^{-1} of iPr-CDI **1** disappeared rapidly upon addition of diacid **2**, indicating that iPr-CDI **1** was consumed readily. Coinciding with the disappearance of the iPr-CDI **1** absorption is the emergence of a new isocyanate absorption of iPr-NCO **7** at 2290 cm^{-1} confirming the initiation reaction of iPr-CDI **1** (Figure 2a). Meanwhile, at the

Scheme 3. Initiation Mechanism of New SSRR through iPr-CDI 1 and Diacid 2

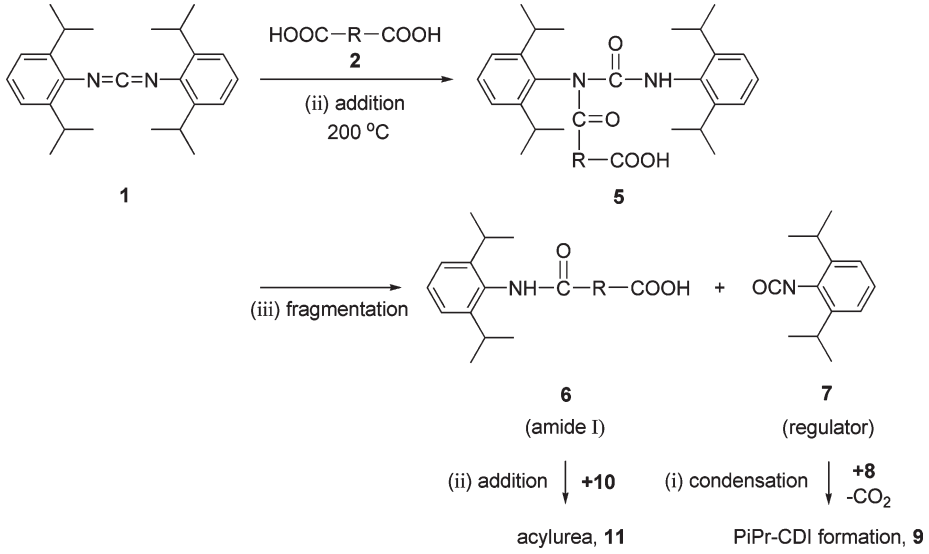

Scheme 4. Propagation Mechanism of PiPr-CDI Terminated 10 Formation through Capping of 8 and 9 by iPr-NCO 7

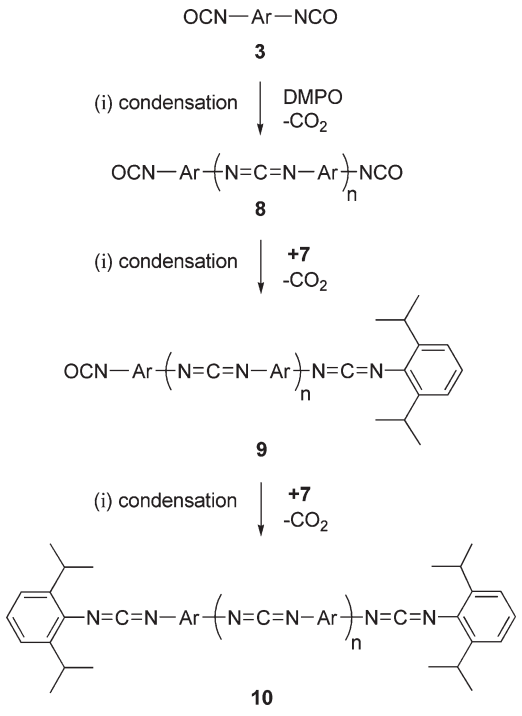

early stage of adding MDI **3**/diacid **2** monomers to the reaction mixture, the isocyanate IR absorption at 2260 cm^{-1} corresponding to MDI **3** though visible, was converted into poly-CDI products **8** at a rapid rate, evidenced by the appearance of strong IR doublet absorptions at 2136 and 2112 cm^{-1} (Figure 2a). This observation is indicative of a rapid conversion of MDI **3** into unhindered poly-CDI oligomers **8**. Upon further propagation between MDI **3** and diacids **2** at 190 °C, the hindered isocyanate absorption of iPr-NCO **7** at 2290 cm^{-1} became gradually diminished as shown in Figure 2d. Toward the end of the reaction, twin CDI peaks at 2136 and 2112 cm^{-1} which both correspond to the poly-CDI **8** absorptions originating from MDI **3** merged gradually into one new peak at 2152 cm^{-1}. This absorption was attributed to polymers such as **10**, **13**, **16** or **4** with unsymmetrically new hindered-CDI type at the terminal of the polymer chains. This IR spectral assignment is consistent with that of the model unsymmetrical *N*′-phenyl-*N*-(2,6-diisopropylphenyl) CDI, (PiPr-CDI) **20** as shown in Figure 3b, and this model unsymmetrical *N*′-phenyl-*N*-(2,6-diisopropylphenyl) CDI (PiPr-CDI) **20**, and this model unsymmetrical *N*′-phenyl-*N*-(2,6-diisopropylphenyl) CDI, (PiPr-CDI) **20**, was synthesized and isolated in 58% according to the reactions shown in Scheme 7.[27] The new hindered-CDI absorption at 2151 cm^{-1} (Figure 2, parts c−f) persists in the polymeric solution toward the end of polymerization at 200 °C. These observations are consistent with our proposed new SSRR mechanism shown in Schemes 3, 4, 5, and 6 showing the initiation, CDI active-site formations, propagation, and then the termination.

Most unexpectedly, the generated polyamides **4**′ by this new SSRR process were found to have narrow molecular weight (MW) distributions of less than 1.40 in molar ratios of iPr-CDI/MDI/IA of 1/5/5 and 1/10/10 respectively by GPC analysis shown in Figure 4, parts a and b. The molecular weights increased linearly indicating that the controlled mechanism is operative from 3838 molecular weight for 1/5/5 for iPr-CDI/MDI/PA up to 6424 for 1/20/20 (Figure 5, parts a and b). These dispersities of less than 1.40 are substantially different from those without the use of hindered CDI **1** as the initiator such as in part c of Figure 4 showing a dispersity of >2.5. This general synthetic procedure has been successfully extended to synthesize polyamides **4**′ with a variety of diacids **2** including isophthalic acid (IA), 2,6-pyridinedicarboxylic acid (PA) and 4,4′-sulfonyldibenzoic acid (SA), adipic acid (AA), azelaic acid (AZA), and 1,10-decanedicarboxylic acid (DA), all with MDI **3** as the common diisocyanate, and all producing well-defined polyamides **4a**′−**4f**′ with narrow MW distributions of less than 1.4 as shown in Table 1.[28]

Other pieces of data supporting the proposed mechanism were found through our model study shown in Scheme 8a where benzoic acid **22** was added to a mixed solution containing five molar excess of both unhindered diphenyl carbodiimide (diphenyl CDI) **21** and the hindered iPr-CDI **1** in a competitive reaction. Through the amide product analyses in HPLC after the reaction, it was found that the relative addition rates of benzoic acid **22** to these two CDIs was determined to be in a ratio of as large as 4 to 1 at 140 °C in favor of unhindered phenyl CDI **21** in formation of the amides **23**. Furthermore, in a similar model competitive study for Scheme 8b between two addition sites of internal unsymmetrical PiPr-CDI **20**, the preferred addition site to form acylurea is also shown to favor the unhindered side of intermolecular dissymmetrical PiPr-CDI **20** by a ratio of 2.4 to 1.0 in formation

Scheme 5. Propagation Mechanism of iPr-amide Terminated Poly-CDI Formation 13 through Addition of Monoacid 6

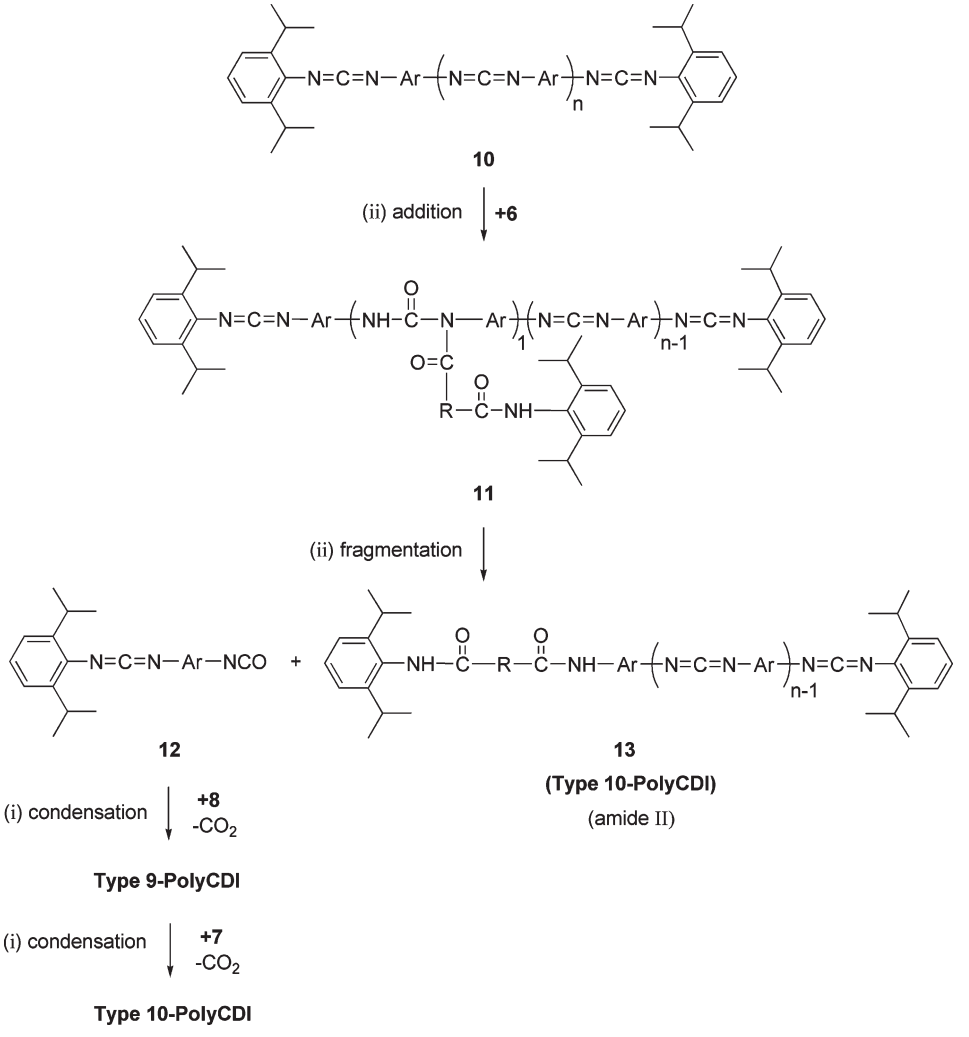

of their respective amides.[29] Thus, both these data support our proposed mechanism that the unhindered CDIs are favored kinetically in the addition reaction in Schemes 5 and 6.

Moreover, DMPO catalyzed trans-CDI disproportion reaction shown in Scheme 9a should also be taken into account in overall mechanism because this disproportion reaction will also lead to the formation of new hindered-CDI **20**.[30] This model study shown in Scheme 9a was carried out by addition of DMPO catalyst into the 1:1 molar mixture of mixed iPr-CDI **1** and diphenyl CDI **21** solution at 140 °C. It was found that 32% of PiPr-CDI **20**, the trans-CDI disproportion product, was found in the reaction solution after 4 h of equilibration. Furthermore, mixing of iPr-NCO **7** and diphenyl CDI **21** in mole ratio of 2 to 1 at 140 °C for an hour has also resulted in an isocyanate-CDI exchange reaction in formation of unsymmetrical CDI **20** as the major product (83%) in the mixture shown in Scheme 9b.[31] Therefore, this trans-CDI disproportion reaction along with the isocyanate-CDI exchange reaction are capable of shifting the long poly-CDI chains **8** toward terminally hindered-CDI compounds such as **10**. In another words, these reactions are alternative paths of forming intermediates of new hindered-CDI type **10** with two discernible CDI-reaction sites.

Finally, proof of our proposed mechanism was further reinforced by a controlled polymerization experiment, where high molecular weight unhindered poly-CDI containing polyamides **26** was prepared first by mixing excess MDI **3** and diacids **2c** in the molar ratio of 10 to 8 at 180 °C in solution with DMPO. As indicated by GPC in Figure 6a, several high molecular unhindered poly-CDI containing polyamide components **26** were observed, but the major fraction is the one having a molecular weight of 52 373 and a dispersity of 2.15. After the reaction was stabilized, a small amount of iPr-CDI initiator **1** together with the rest of requisite diacid **2c** were added to the reaction mixture as the second step. We observed the reshuffling of the product distribution in the ensuing reactions at 180 °C, and after 3 h of stirring, a new polyamide **4c′-2** with M_n = 18,538 with dispersity of 1.22 (shown in Figure 6b) was isolated. On the basis of the results revealed in GPC analysis in Figure 6, we could postulate reaction sequences of the change in Scheme 10 and this result reinforces the fact that iPr-CDI **1** is essential and critical in our controlled polyamide formation. However, it is important to point out that the addition of iPr-CDI **1** works in those cases, only when polyamides still possess CDI or isocyanate groups in its main chains. This is due to the need for the regulator to operate through trans-CDI disproportion reaction and isocyanate-CDI exchange reaction. We also found that this controlled polymerization could be also accomplished by replacing iPr-CDI **1** by iPr-NCO **7** as the initiator which achieves the same result (see example polyamide **4c′-3**) because interconversion of iPr-NCO **7** and PiPr-CDI **20** is rapid as shown in Scheme 9b.

Conclusions

A unique and simple methodology has been found for synthesizing well-defined polyamides from diisocyanates such as MDI

Scheme 6. Polyamide 4 Formation through Selective Addition of Diacid 2 to iPr-amide Terminated Poly-CDI 13 in The New SSRR Cycles

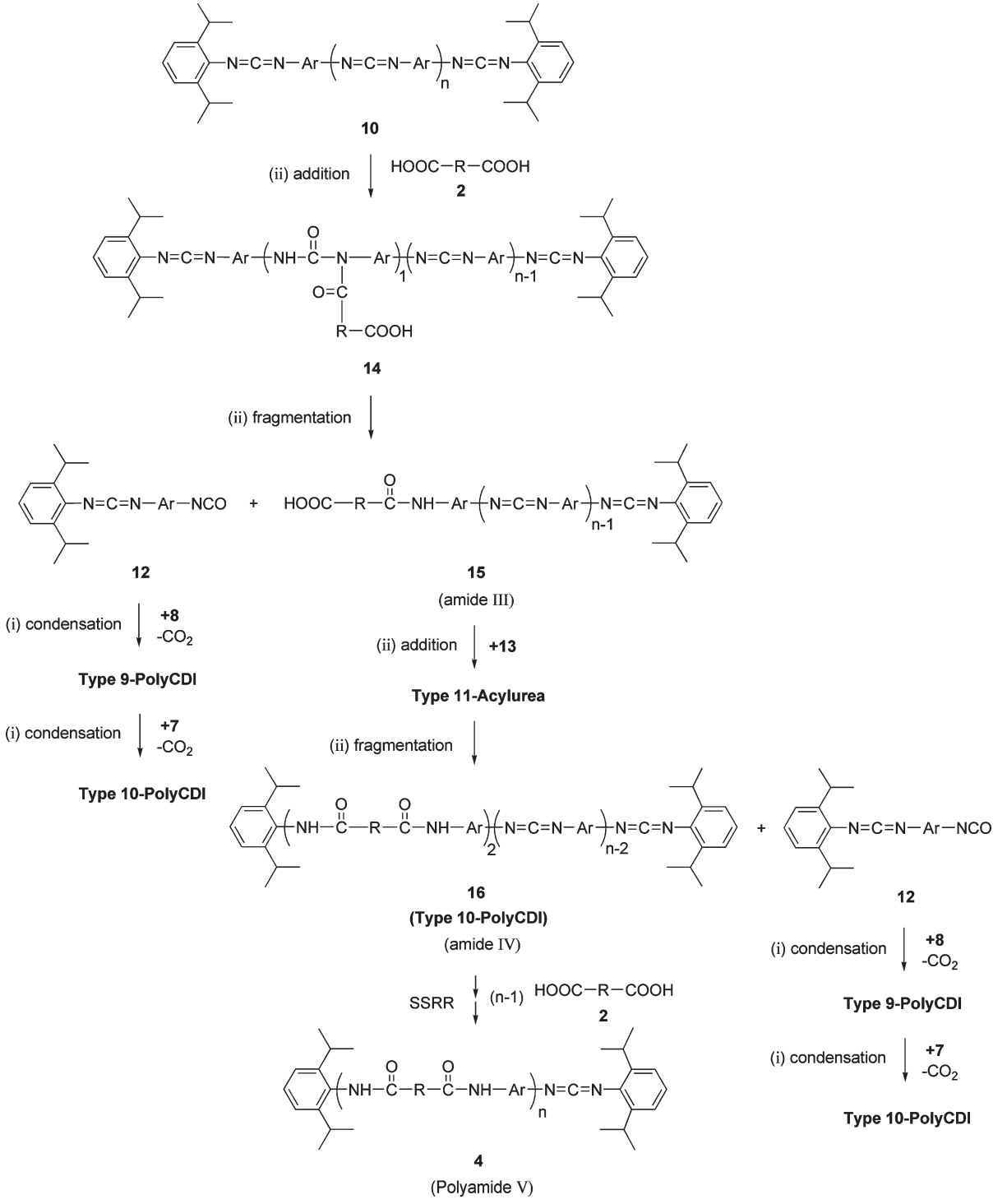

and diacids to form polyamides of narrow molecular weight distributions (dispersity < 1.4). The new SSRR mechanism involves creation of two types of CDIs of different reactivity toward carboxylic acid, i.e. the new hindered-CDI and unhindered CDIs, through the introduction of iPr-CDI, followed by sterically controlled addition of carboxylic acid to the preferred unhindered CDI initially. In this new process, the new hindered-CDI sites play a regulating role until unhindered CDIs are consumed preferentially. This preferred reaction at center each time will generate intermediates and products of type **10** and type **13** of approximately the same lengths, and thus it results in the formation of controlled polyamides with low dispersities. The chemistry behind the new mechanism seems complex; however, the process itself is straightforward, with high-yield and versatility for making final well-defined polyamides. More results of this developed polymerization strategies in other polymer applications will be reported shortly.

Experimental Section

Materials. *N*,*N*′-Bis(2,6-diisopropylphenyl)carbodiimide (iPr-CDI) **1** was supplied under the trade name of Stabaxol 1 by Rhein Chemie Rheinau GmbH and used without further purification. Isophthalic acid (IA) **2a** was purchased from Lancaster,

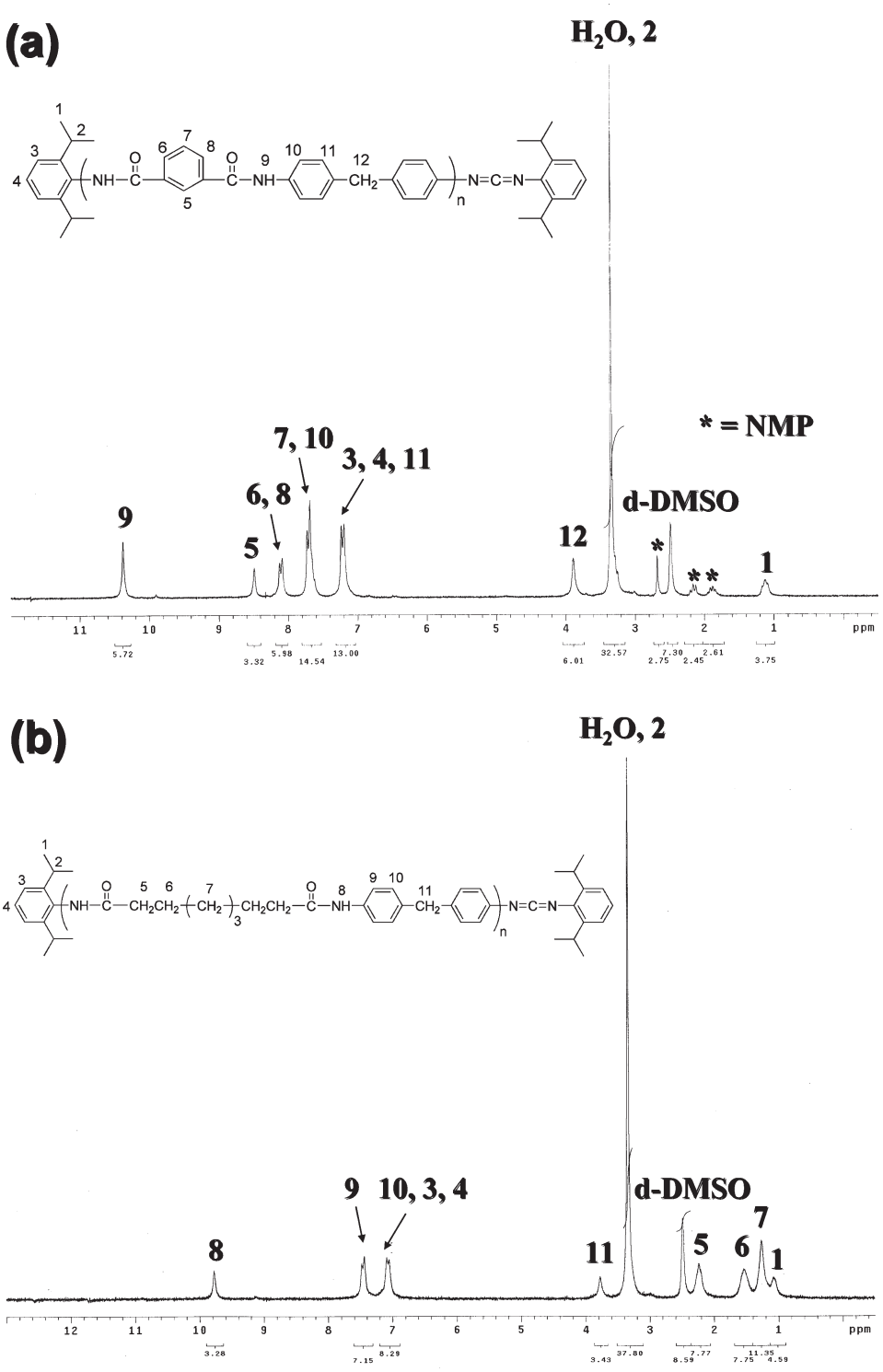

Figure 1. ^{1}H NMR spectra for (a) aromatic polyamide **4a′-2** (iPr-CDI/MDI/IA = 1/10/10) and (b) aryl-aliphatic polyamide **4e′** (iPr-CDI/MDI/AZA = 1/10/10).

2,6-pyridinedicarboxylic acid (PA) **2b** from Aldrich, 4,4′-sulfonyldibenzoic acid (SA) **2c** from Acros, adipic acid (AA) **2d** from Showa, azelaic acid (AZA) **2e** from Aldrich, and 1,10-decanedicarboxylic acid (DA) **2f** from Alfa. All of the above chemicals were used without further purification. 4,4′-Methylenebis(phenyl isocyanate) (4,4′-MDI) **3** was received from BASF, and freshly distilled under reduced pressure before use. 1,3-Dimethyl-3-phospholene oxide (DMPO) was received from GRECO of Taichung, Taiwan. 2,6-Diisopropylphenyl isocyanate **7**, phenyl isothiocyanate **17**, and 2,6-diisopropylaniline **18** were purchased from Acros and used without further purification. Sodium hydroxide was purchased from Fisher Chemical and tetra-*n*-butylammonium bromide was received from Alfa. Benzoic acid **22** and sodium hypochlorite solution (12%) were purchased from Showa and used as received. Phenyl isocyanate **25** was purchased from Fluka and used without further purification. Acetonitrile (AN) and dichloromethane (DCM) were purchased from Tedia. Tetrahydrofuran (THF) and chloroform were purchased from Tedia, distilled over calcium hydride and stored on molecular sieves. *N*-Methyl-2-pyrrolidone (NMP) was received from Tedia, distilled

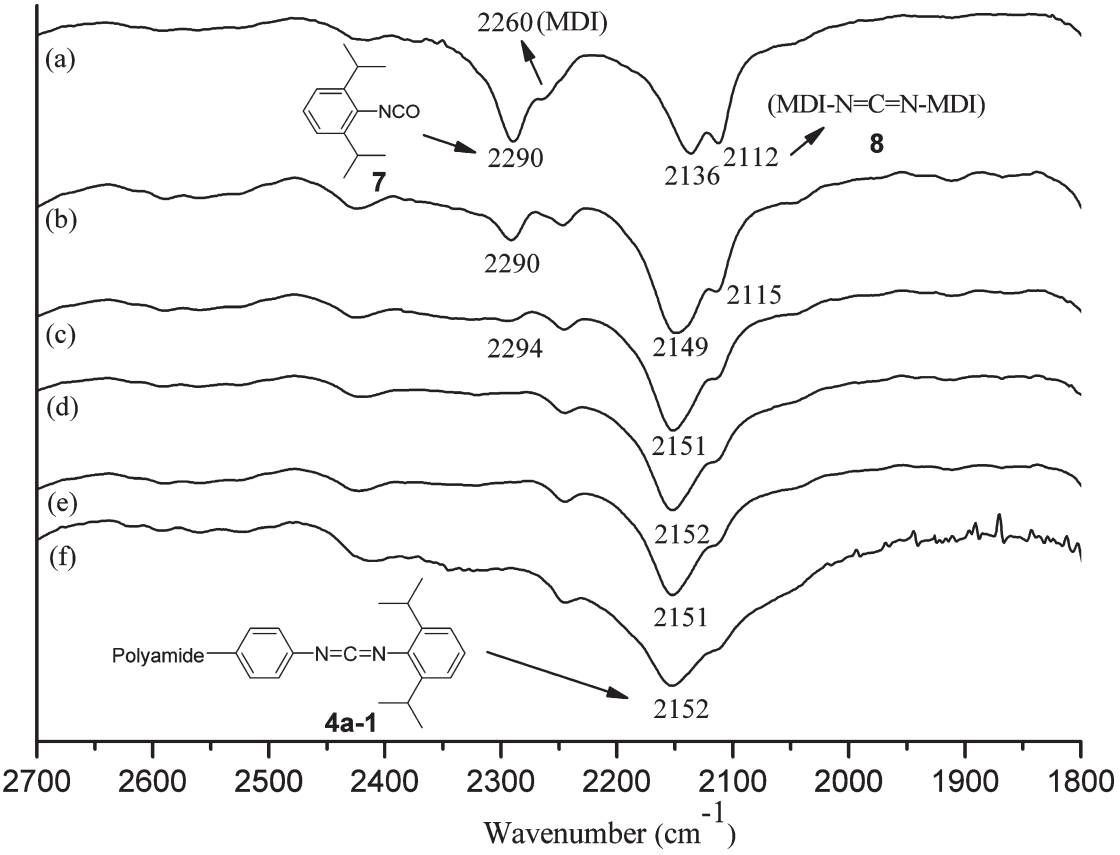

Figure 2. FT-IR monitoring of spectra of polyamides **4a-1** (iPr-CDI/MDI/IA = 1/5/5) after completing addition of monomers at 200 °C: (a) 0 min; (b) 7 min; (c) 15 min; (d) 30 min; (e) 1 h (f) 3 h.

over calcium hydride and stored on molecular sieves before use. *N,N*-Dimethylformamide (DMF) was received from Mallinckrodt Chemicals, distilled over calcium hydride, and stored on molecular sieves before use.

Measurements. ^{1}H NMR spectra was recorded on Varian Inova 200 MHz. Chemical shifts were given in δ, and the coupling constants J were given in Hz. The spectra were recorded in solvents such as $CDCl_3$ or DMSO-d_6 at room temperature, and chemical shifts were given relative to the solvent signals. FT-IR was carried out using a Perkin-Elmer Spectrum One FT-IR spectrometer. Elemental CHN analysis was performed on a Heraeus CHN-OS rapid analyzer. Electron ionization mass (EIMS) analysis was performed on a ThermoQuest MAT 95XL apparatus. The molecular weights (M_n) were determined by gel permeation chromatography (Shodex GPC with a Shodex RI detector) and calibrated by polystyrene standards. In the GPC analysis, both degassed *N,N*-dimethylformamide (DMF) and *N*-methyl-2-pyrrolidone (NMP) were used as the eluent and performed at a flow rate of 1.0 mL min^{-1}. NMP was used partly in the cases where less soluble polyamide and analyzed. HPLC was performed using a 5 m spherical particle/100 Å pore size column (Hypersil-100 C18, Thermo Electron Corporation) using a UV detector with its UV band set at 254 nm with 50% or 100% of AN/water as an eluent at a flow rate of 0.5 mL/min. The resulting polyamide products were quenched by pouring into water followed by filtration. Polyamide products were purified by low-polar solvent (chloroform or THF) and were vacuum-dried into polyamide powder before testing.

Synthesis of Polyamides 4a′−4f′ (Scheme 2). *Synthesis of Aromatic Polyamides* ***4a′−4c′***. Reaction of *N,N′*-bis(2,6-diisopropylphenyl)carbodiimide (iPr-CDI) **1** with 4,4′-methylenebis(phenylisocyanate) (MDI) **3** and isophthalic acid (IA) **2a** in the molar ratio of iPr-CDI/MDI/IA = 1/10/10 is given here as a typical example. Into a 100 mL, three-necked, round-bottomed flask equipped with a thermometer, a nitrogen gas inlet tube, a reflux condenser, an oil bath, and a magnetic stirrer, was placed 10 mL of dry NMP and was heated to 180 °C. 1,3-Dimethyl-3-phospholene oxide (DMPO, 0.050 g) and iPr-CDI **1** (0.363 g, 1 mmol) were added into the hot NMP solution and stirred for 30 s. Freshly distilled MDI **3** (2.500 g, 10 mmol) and IA **2a** (1.660 g, 10 mmol) were dissolved in 20 mL of dry NMP and were then added dropwise into the NMP solution in 6 min at 180 °C. The reaction was further heated to 202 °C for 3 h. The reaction was monitored by FT-IR. The peak absorption at 2112, 2136, 2260, and 2290 cm^{-1} disappeared and was replaced by new hindered-CDI absorption at 2151 cm^{-1} in approximate 30 min. The new peak absorption at 2151 cm^{-1} was persisted to the rest of 2.5 h. The resulting product **4a-2** solution was quenched by 500 mL of water, filtered and dried, to yield 3.582 g (99%) of crude polyamide **4a′-2** (light yellow solid). FT-IR analysis of the crude product showed the CDI peak absorption at 2151 cm^{-1} disappeared and was replaced by urea/amide complex absorption at 1668 cm^{-1}. A small portion of product (0.5 g) was further purified by dissolving in about 5 mL of NMP solvent, following by precipitating from 50 mL of chloroform (70% yields). The detail results of FT-IR, ^{1}H NMR, and GPC for aromatic polyamides were described below.

Synthesis of Aromatic Polyamide ***4a′-1***. Reaction of *N,N′*-bis(2,6-diisopropylphenyl)carbodiimide (iPr-CDI) **1** with 4,4′-methylenebis(phenylisocyanate) (MDI) **3** and isophthalic acid (IA) **2a** in the molar ratio of iPr-CDI/MDI/IA = 1/5/5. Yield = 98% of a light yellow solid. FT-IR (KBr cm^{-1}): 1668 (amide, C=O), 3288 (amide, N−H). ^{1}H NMR (200 MHz, DMSO-d_6, δ, ppm): 1.05−1.18 (t, 24H, iPr−CH_3), 3.25−3.43 (t, 4H, iPr−CH), 3.90 (s, 2*n*H, Ph−CH_2), 7.20−7.24 (d, (4*n* + 6)H, Ar−H), 7.66−7.73 (t, 5*n*H, Ar−H), 8.10−8.13 (d, 2*n*H, Ar−H), 8.50 (s, 1*n*H, Ar−H), 10.37 (s, 2*n*H, N−H). GPC (DMF): dispersity = 1.27, M_w = 18923, M_n = 14900.

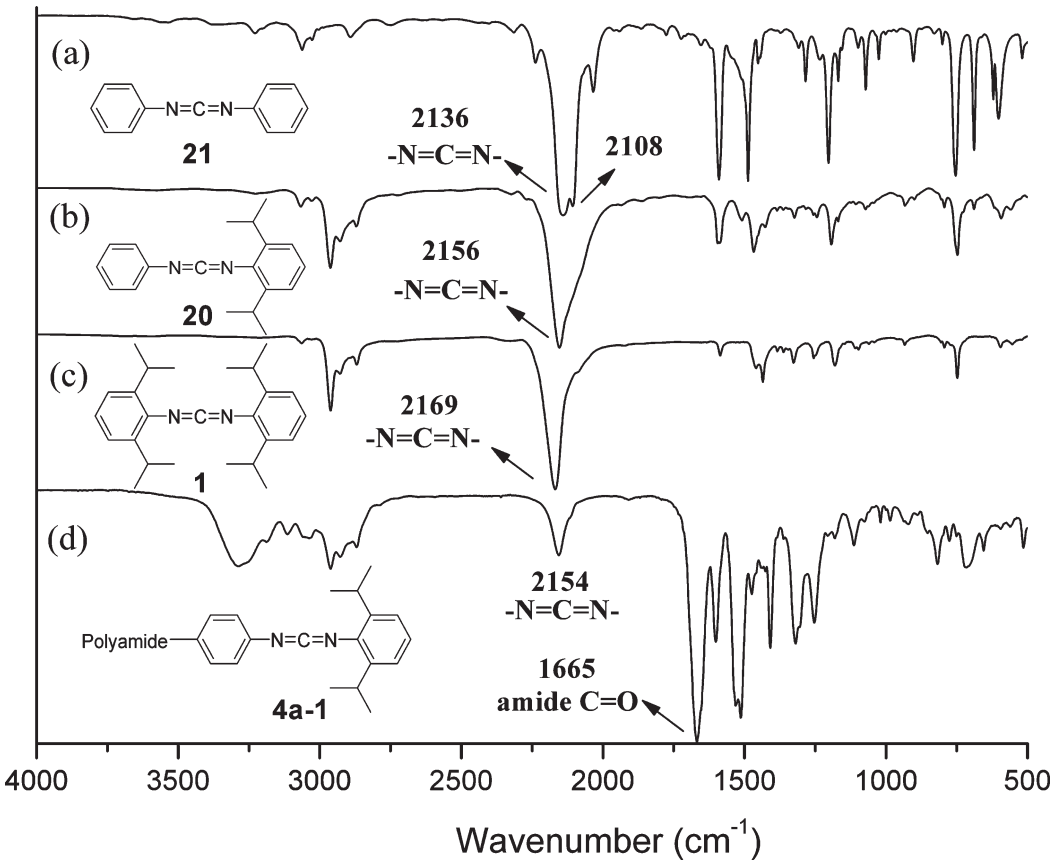

Figure 3. Model FT-IR spectrum of (a) diphenyl carbodiimide **21**; (b) *N*′-phenyl-*N*-(2,6-diisopropylphenyl) carbodiimide **20**; (c) *N*,*N*′-bis(2,6-diisopropylphenyl) carbodiimide **1**; and (d) hindered CDI-capped polyamide **4a-1** (iPr-CDI/MDI/IA = 1/5/5).

Scheme 7. Synthesis of Model Unsymmetrical *N*′-Phenyl-*N*-(2,6-diisopropylphenyl) Carbodiimide (PiPr-CDI) 20: (a) Synthesis of *N*′-Phenyl-*N*-(2,6-diisopropylphenyl) Thiourea 19; (b) Synthesis of Model *N*′-Phenyl-*N*-(2,6-diisopropylphenyl) Carbodiimide (PiPr-CDI) 20

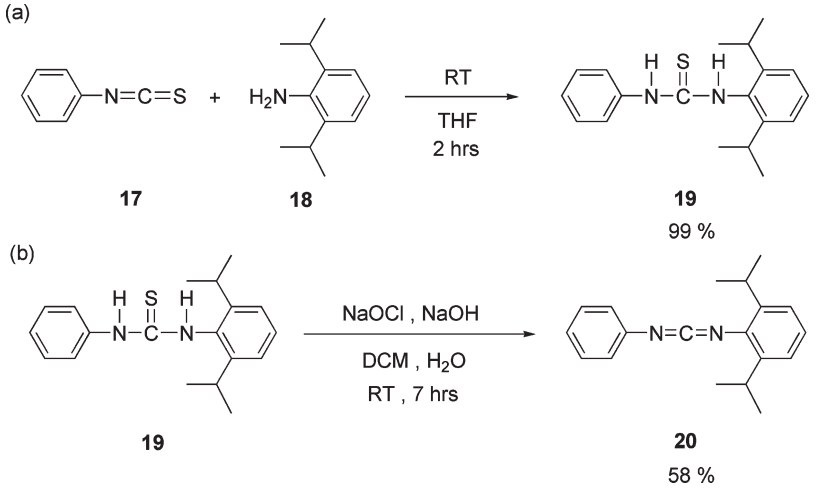

*Synthesis of Aromatic Polyamide **4a′-2***. Reaction of *N*,*N*′-bis(2,6-diisopropylphenyl)carbodiimide (iPr-CDI) **1** with 4,4′-methylenebis(phenylisocyanate) (MDI) **3** and isophthalic acid (IA) **2a** in the molar ratio of iPr-CDI/MDI/IA = 1/10/10. Yield = 99% of a light yellow solid. FT-IR (KBr cm^{-1}): 1668 (amide, C=O), 3288 (amide, N−H). ^{1}H NMR (200 MHz, DMSO-d_6, δ, ppm): 1.05−1.18 (t, 24H, iPr−CH_3), 3.26−3.32 (t, 4H, iPr−CH), 3.90 (s, 2*n*H, Ph−CH_2), 7.19−7.24 (d, (4*n* + 6)H, Ar−H), 7.66−7.72 (d, 5*n*H, Ar−H), 8.10−8.14 (d, 2*n*H, Ar−H), 8.50 (s, 1*n*H, Ar−H), 10.37 (s, 2*n*H, N−H). GPC (DMF): dispersity = 1.30, M_w = 22880, M_n = 17600.

*Synthesis of Aromatic Polyamide **4a′-3***. Reaction of 4,4′-methylenebis(phenylisocyanate) (MDI) **3** with isophthalic acid (IA) **2a** in the molar ratio of iPr-CDI/MDI/IA = 0/1/1. The detail procedure for preparing polyamide **4a′-3** was described below. Yield = 98% of a light yellow solid. FT-IR (KBr cm^{-1}): 1668 (amide, C=O), 3288 (amide, N−H). ^{1}H NMR (200 MHz, DMSO-d_6, δ, ppm): 3.90 (s, 2*n*H, Ph−CH_2), 7.20−7.24 (d, (4*n* + 6)H, Ar−H), 7.62−7.73 (m, 5*n*H, Ar−H), 8.10−8.13 (d, 2*n*H, Ar−H), 8.50 (s, 1*n*H, Ar−H), 10.37 (s, 2*n*H, N−H). GPC (DMF): dispersity = 6.06, M_w = 122419, M_n = 20201.

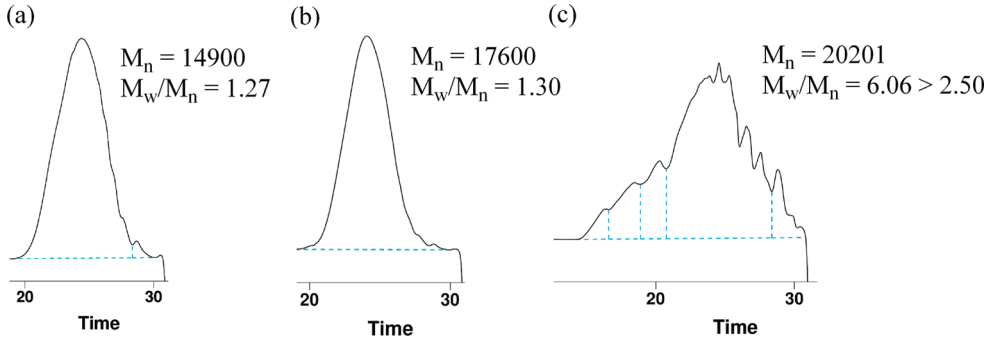

Figure 4. GPC profiles (DMF) of polyamides **4a′-1**−**4a′-3** prepared by new SSRR: (a) polyamide **4a′-1** of iPr-CDI/MDI/IA = 1/5/5; (b) polyamide **4a′-2** of iPr-CDI/MDI/IA = 1/10/10; (c) polyamide **4a′-3** of iPr-CDI/MDI/IA = 0/1/1 (no iPr-CDI **1** as initiator).

*Synthesis of Aromatic Polyamide **4b′-1***. Reaction of *N*,*N*′-bis(2,6-diisopropylphenyl)carbodiimide (iPr-CDI) **1** with 4,4′-methylenebis(phenylisocyanate) (MDI) **3** and 2,6-pyridinedicarboxylic acid (PA) **2b** in the molar ratio of iPr-CDI/MDI/PA = 1/5/5. Yield = 91%of a light red brown solid. FT-IR (KBr cm^{-1}): 1677 (amide, C=O), 3297 (amide, N−H). ^{1}H NMR (200 MHz, DMSO-d_6, δ, ppm): 1.13−1.15 (s, 24H, iPr−CH_3), 3.23−3.42 (t, 4H, iPr−CH), 3.95 (s, 2*n*H, Ph−CH_2), 7.27−7.30 (d, (4*n* + 6)H, Ar−H), 7.79−7.83 (d, 4*n*H, Ar−H), 8.28−8.34 (t, 3nH, Ar−H), 10.97 (s, 2*n*H, N−H). GPC (NMP): dispersity = 1.29, M_w = 4951, M_n = 3838.

*Synthesis of Aromatic Polyamide **4b′-2***. Reaction of *N*,*N*′-bis(2,6-diisopropylphenyl)carbodiimide (iPr-CDI) **1** with 4,4′-methylenebis(phenylisocyanate) (MDI) **3** and 2,6-pyridinedicarboxylic acid (PA) **2b** in the molar ratio of iPr-CDI/MDI/PA = 1/7.5/7.5. Yield = 93% of a light red brown solid. FT-IR (KBr cm^{-1}): 1677 (amide, C=O), 3297 (amide, N−H). ^{1}H NMR (200 MHz, DMSO-d_6, δ, ppm): 1.12−1.15 (d, 24H, iPr−CH_3), 3.23−3.42 (t, 4H, iPr−CH), 3.95 (s, 2*n*H, Ph−CH_2), 7.27−7.30 (d, (4*n* + 6)H, Ar−H), 7.79−7.83 (d, 4*n*H, Ar−H), 8.29−8.34 (t, 3nH, Ar−H), 10.97 (s, 2*n*H, N−H). GPC (NMP): dispersity = 1.29, M_w = 5270, M_n = 4085.

*Synthesis of Aromatic Polyamide **4b′-3***. Reaction of *N*,*N*′-bis(2,6-diisopropylphenyl)carbodiimide (iPr-CDI) **1** with 4,4′-methylenebis(phenylisocyanate) (MDI) **3** and 2,6-pyridinedicarboxylic acid (PA) **2b** in the molar ratio of iPr-CDI/MDI/PA = 1/10/10. Yield = 96% of a light red brown solid. FT-IR (KBr cm^{-1}): 1677 (amide, C=O), 3297 (amide, N−H). ^{1}H NMR (200 MHz, DMSO-d_6, δ, ppm): 11.11−1.14 (d, 24H, iPr−CH_3), 3.30−3.38 (t, 4H, iPr−CH), 3.93 (s, 2*n*H, Ph−CH_2), 7.25−7.28 (d, (4*n* + 6)H, Ar−H), 7.78−7.82 (d, 4*n*H, Ar−H), 8.28−8.32 (d, 3nH, Ar−H), 10.96 (s, 2*n*H, N−H). GPC (NMP): dispersity = 1.30, M_w = 6042, M_n = 4648.

*Synthesis of Aromatic Polyamide **4b′-4***. Reaction of *N*,*N*′-bis(2,6-diisopropylphenyl)carbodiimide (iPr-CDI) **1** with 4,4′-methylenebis(phenylisocyanate) (MDI) **3** and 2,6-pyridinedicarboxylic acid (PA) **2b** in the molar ratio of iPr-CDI/MDI/PA = 1/12.5/12.5. Yield = 95% of a light red brown solid. FT-IR (KBr cm^{-1}): 1677 (amide, C=O), 3297 (amide, N−H). ^{1}H NMR (200 MHz, DMSO-d_6, δ, ppm): 1.13 (s, 24H, iPr−CH_3), 3.26−3.40 (t, 4H, iPr−CH), 3.94 (s, 2*n*H, Ph−CH_2), 7.26−7.29 (d, (4*n* + 6)H, Ar−H), 7.78−7.82 (d, 4*n*H, Ar−H), 8.33 (s, 3nH, Ar−H), 10.96 (s, 2*n*H, N−H). GPC (NMP): dispersity = 1.35, M_w = 6817, M_n = 5049.

*Synthesis of Aromatic Polyamide **4b′-5***. Reaction of *N*,*N*′-bis(2,6-diisopropylphenyl)carbodiimide (iPr-CDI) **1** with 4,4′-methylenebis(phenylisocyanate) (MDI) **3** and 2,6-pyridinedicarboxylic acid (PA) **2b** in the molar ratio of iPr-CDI/MDI/PA = 1/15/15. Yield = 94% of a light red brown solid. FT-IR (KBr cm^{-1}): 1677 (amide, C=O), 3297 (amide, N−H). ^{1}H NMR (200 MHz, DMSO-d_6, δ, ppm): 1.13 (s, 24H, iPr−CH_3), 3.36 (s, 4H, iPr−CH), 3.94 (s, 2*n*H, Ph−CH_2), 7.29 (s, (4*n* + 6)H, Ar−H), 7.78−7.82 (d, 4*n*H, Ar−H), 8.33 (s, 3nH, Ar−H), 10.96 (s, 2*n*H, N−H). GPC (NMP): dispersity = 1.38, M_w = 7176, M_n = 5200.

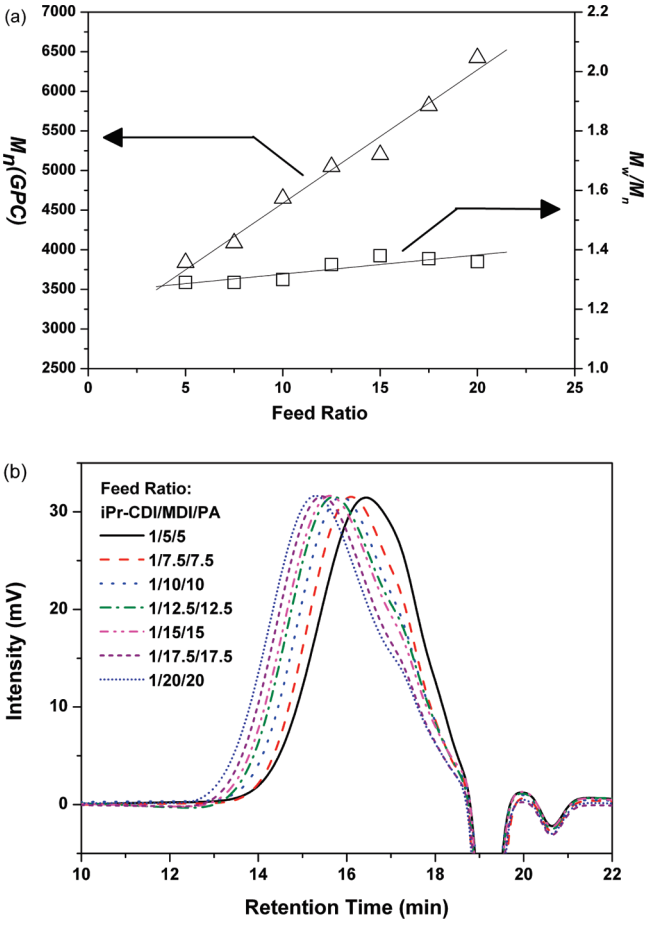

Figure 5. GPC results (NMP) of polyamides **4b′-1**∼**b′-7**: (a) M_n and M_w/M_n values as a function of the feed ratio of MDI/PA to iPr-CDI; (b) GPC profiles obtained as a function of the feed ratio of iPr-CDI/MDI/PA.

*Synthesis of Aromatic Polyamide **4b′-6***. Reaction of *N*,*N*′-bis(2,6-diisopropylphenyl)carbodiimide (iPr-CDI) **1** with 4,4′-methylenebis(phenylisocyanate) (MDI) **3** and 2,6-pyridinedicarboxylic acid (PA) **2b** in the molar ratio of iPr-CDI/MDI/PA = 1/17.5/17.5. Yield = 93% of a light red brown solid. FT-IR (KBr cm^{-1}): 1677 (amide, C=O), 3297 (amide, N−H). ^{1}H NMR (200 MHz, DMSO-d_6, δ, ppm): 1.08−1.13 (d, 24H, iPr−CH_3), 3.35−3.38 (d, 4H, iPr−CH), 3.93 (s, 2*n*H, Ph−CH_2), 7.25−7.28 (d, (4*n* + 6)H, Ar−H), 7.78−7.81 (d, 4*n*H, Ar−H), 8.28−8.32 (d, 3nH, Ar−H), 10.95 (s, 2*n*H, N−H). GPC (NMP): dispersity = 1.37, M_w = 7971, M_n = 5818.

Table 1. Molecular Weights and Polydispersities of Polyamides 4a′−4j′[a]

entry	composition	molar ratio	feed [min]	M_w	M_n	dispersity [M_w/M_n]
4d′	iPr-CDI/MDI/AA[b]	1/10/10	7	17 650	14 355	1.23
4e′	iPr-CDI/MDI/AZA[b]	1/10/10	7	13 621	12 197	1.11
4f′	iPr-CDI/MDI/DA[b]	1/10/10	7	11 264	10 444	1.08
4a′-2	iPr-CDI/MDI/IA[b]	1/10/10	7	22 800	17 600	1.30
4c′-1	iPr-CDI/MDI/SA[b]	1/10/10	7	22 821	18 860	1.21
4b′-1	iPr-CDI/MDI/PA[c]	1/5/5	7	4951	3838	1.29
4b′-3	iPr-CDI/MDI/PA[c]	1/10/10	7	6042	4648	1.30
4b′-5	iPr-CDI/MDI/PA[c]	1/15/15	7	7176	5200	1.38
4b′-7	iPr-CDI/MDI/PA[c]	1/20/20	7	8737	6424	1.36

[a] Aliphatic diacids **2d**−**2f**: AA = adipic acid **2d**, AZA = azelaic acid **2e**, DA = 1,10-decanedicarboxylic acid **2f**. Aromatic diacids **2a**−**2c**: IA = isophthalic acid **2a**, SA = 4,4′-sulfonyldibenzoic acid **2c**, PA = 2,6-pyridinedicarboxylic acid **2b**. [b] Measured by GPC of *N*-dimethylformamide (DMF) was used as the eluent. [c] Measured by GPC of *N*-methyl-2-pyrrolidone (NMP) was used as the eluent for less soluble polyamide.

*Synthesis of Aromatic Polyamide **4b′-7***. Reaction of *N*,*N*′-bis(2,6-diisopropylphenyl)carbodiimide (iPr-CDI) **1** with 4,4′-methylenebis(phenylisocyanate) (MDI) **3** and 2,6-pyridinedicarboxylic acid (PA) **2b** in the molar ratio of iPr-CDI/MDI/PA = 1/20/20. Yield = 96% of a light red brown solid. FT-IR (KBr cm^{-1}): 1677 (amide, C═O), 3297 (amide, N−H). ^{1}H NMR (200 MHz, DMSO-d_6, δ, ppm): 1.12−1.14 (d, 24H, iPr−CH$_3$), 3.25−3.43 (m, 4H, iPr−CH), 3.93 (s, 2*n*H, Ph−CH$_2$), 7.25−7.28 (d, (4*n* + 6)H, Ar−H), 7.78−7.81 (d, 4*n*H, Ar−H), 8.27−8.32 (d, 3nH, Ar−H), 10.95 (s, 2*n*H, N−H). GPC (NMP): dispersity = 1.36, M_w = 8737, M_n = 6424.

*Synthesis of Aromatic Polyamide **4c′-1***. Reaction of *N*,*N*′-bis(2,6-diisopropylphenyl)carbodiimide (iPr-CDI) **1** with 4,4′-methylenebis(phenylisocyanate) (MDI) **3** and 4,4′-sulfonyldibenzoic acid (SA) **2c** in the molar ratio of iPr-CDI/MDI/SA = 1/10/10. Yield = 95% of a light yellow solid. FT-IR (KBr cm^{-1}): 1668 (amide, C═O), 3288 (amide, N−H). ^{1}H NMR (200 MHz, DMSO-d_6, δ, ppm): 1.06−1.14 (t, 24H, iPr−CH$_3$), 3.28−3.40 (m, 4H, iPr−CH), 3.87 (s, 2*n*H, Ph−CH$_2$), 7.16−7.20 (d, (4*n* + 6)H, Ar−H), 7.62−7.66 (d, 4*n*H, Ar−H), 8.07−8.17 (t, 9nH, Ar−H), 10.40 (s, 2*n*H, N−H). GPC (DMF): dispersity = 1.21, M_w = 22821, M_n = 18860.

*Synthesis of Aromatic Polyamide **4c′-2***. Reaction of *N*,*N*′-bis(2,6-diisopropylphgenyl)carbodiimide (iPr-CDI) **1** with 4,4′-methylenebis(phenylisocyanate) (MDI) **3** and 4,4′-sulfonyldibenzoic acid (SA) **2c** in the overall molar ratio of iPr-CDI/MDI/SA = 1/10/10. The detail procedure for preparing polyamide **4c′-2** was described below. Yield = 92% of a light yellow solid. FT-IR (KBr cm^{-1}): 1668 (amide, C═O), 3288 (amide, N−H). ^{1}H NMR (200 MHz, DMSO-d_6, δ, ppm): 1.05−1.13 (t, 24H, iPr−CH$_3$), 3.31−3.35 (d, 4H, iPr−CH), 3.87 (s, 2*n*H, Ph−CH$_2$), 7.17−7.21 (d, (4*n* + 6)H, Ar−H), 7.62−7.66 (d, 4*n*H, Ar−H), 8.09−8.17 (t, 8nH, Ar−H), 10.40 (s, 2*n*H, N−H). GPC (DMF): dispersity = 1.22, M_w = 22617, M_n = 18538.

*Synthesis of Aromatic Polyamide **4c′-3***. Reaction of 2,6-diisopropylphenyl isocyanate **7** with 4,4′-methylenebis(phenylisocyanate) (MDI) **3** and 4,4′-sulfonyldibenzoic acid (SA) **2c** in the molar ratio of iPr-NCO/MDI/SA = 2/10/10. The detail procedure for preparing polyamide **4c′-3** was described below. Yield = 95% of a light yellow solid. FT-IR (KBr cm^{-1}): 1668 (amide, C═O), 3288 (amide, N−H). ^{1}H NMR (200 MHz, DMSO-d_6, δ, ppm): 1.06−1.14 (t, 24H, iPr−CH$_3$), 3.44 (s, 4H, iPr−CH), 3.88 (s, 2*n*H, Ph−CH$_2$), 7.17−7.21 (d, (4*n* + 6)H, Ar−H), 7.63−7.66 (d, 4*n*H, Ar−H), 8.12 (s, 8nH, Ar−H), 10.42 (s, 2*n*H, N−H). GPC (DMF): dispersity = 1.27, M_w = 22275, M_n = 17466.

*Synthesis of Aliphatic Polyamides **4d′−4f′***. Reaction of *N*,*N*′-bis(2,6-diisopropylphenyl)carbodiimide (iPr-CDI) **1** with 4,4′-methylenebis(phenylisocyanate) (MDI) **3** and azelaic acid (AZA) **2e** in the molar ratio of iPr-CDI/MDI/AZA = 1/10/10 is given here as a typical example. Into a 100 mL, three-necked, round-bottomed flask equipped with a thermometer, a nitrogen gas inlet tube, a reflux condenser, an oil bath, and a magnetic stirrer, was placed 10 mL of dry NMP and was heated to 180 °C.

Scheme 8. Model Competitive Studies: (a) Reaction of iPr-CDI 1 and Diphenyl CDI 21 with Benzoic Acid 22; (b) Reaction of PiPr-CDI 20 with Benzoic Acid 22

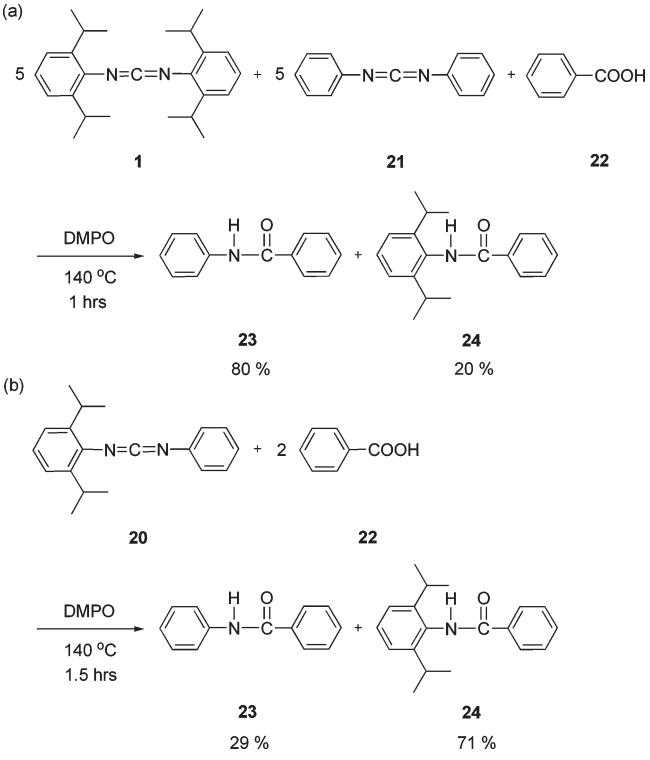

1,3-Dimethyl-3-phospholene oxide (DMPO, 0.050 g) and iPr-CDI **1** (0.363 g, 1 mmol) were added into the hot NMP solution and stirred for 30 s. Freshly distilled MDI **3** (2.500 g, 10 mmol) and AZA **2e** (1.880 g, 10 mmol) were dissolved in 20 mL of dry NMP and were then added dropwise into the NMP solution in 6 min at 180 °C. The reaction was further heated to 202 °C for 3 h. The reaction was monitored by FT-IR. The peak absorption at 2112, 2136, 2260, and 2290 cm^{-1} disappeared and was replaced by new hindered-CDI absorption at 2151 cm^{-1} in approximate 30 min. The new peak absorption at 2151 cm^{-1} was persisted to the rest of 2.5 h. The resulting product **4e** solution was quenched by 500 mL of water, filtered, and dried, to yield 3.752 g (98%) of crude polyamide **4e′** (white solid). FT-IR analysis of the crude product showed the CDI peak absorption at 2151 cm^{-1} disappeared and was replaced by urea/amide complex absorption at 1660 cm^{-1}. A small portion of product (0.5 g) was further purified by dissolving in about 5 mL of NMP solvent, following by precipitating from 50 mL of chloroform (80% yields). The detailed results of FT-IR, ^{1}H NMR, and GPC studies for aliphatic polyamides were described below.

Scheme 9. Trans-CDI Disproportion and Isocyanate-CDI Exchange Reactions: (a) Reaction of iPr-CDI 1 with Diphenyl CDI 21; (b) Reaction of iPr-NCO 7 with Diphenyl CDI 21; (c) Reaction of iPr-NCO 7 with Phenyl Isocyanate 25

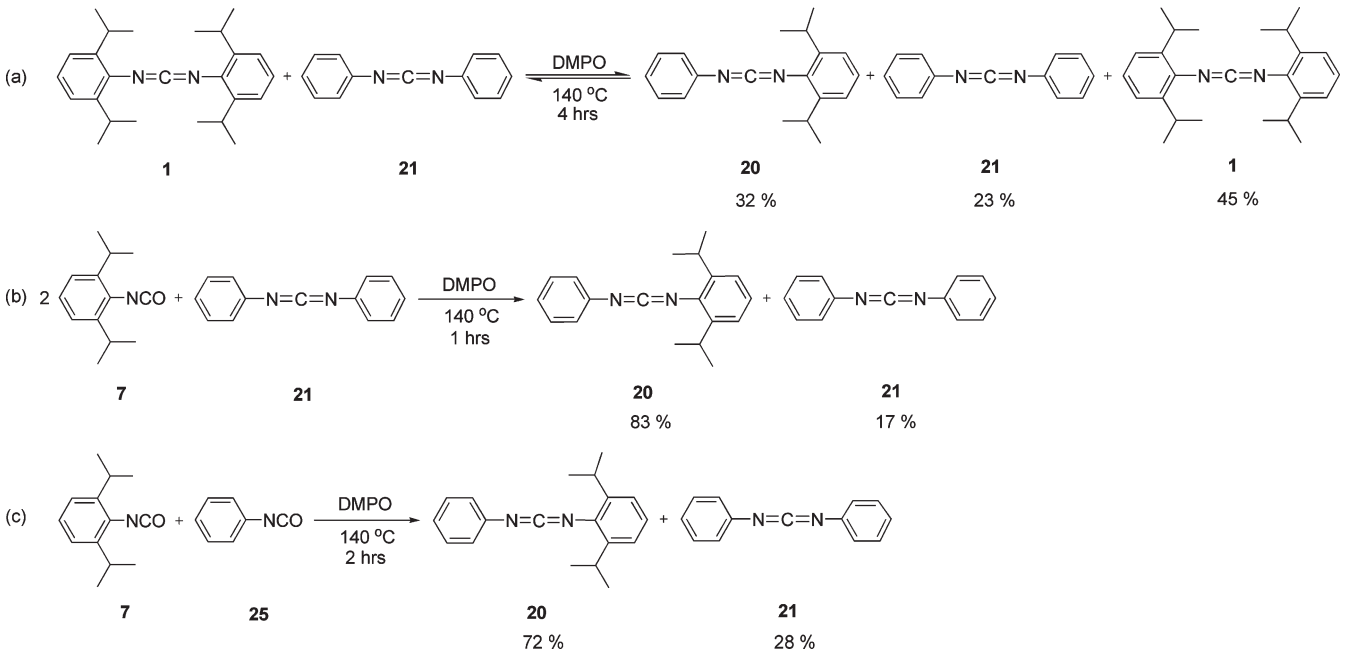

Synthesis of Aliphatic Polyamide ***4d′***. Reaction of *N*,*N*′-bis-(2,6-diisopropylphenyl)carbodiimide (iPr-CDI) **1** with 4,4′-methylenebis(phenylisocyanate) (MDI) **3** and adipic acid (AA) **2d** in the molar ratio of iPr-CDI/MDI/AA = 1/10/10. Yield = 91% of a white solid. FT-IR (KBr cm^{-1}): 1658 (amide, C═O), 3301 (amide, N−H). ^{1}H NMR (200 MHz, DMSO-d_6, δ, ppm): 1.05−1.08 (d, 24H, iPr−CH_3), 1.58 (s, 4*n*H, −CH_2−), 2.27 (s, 4*n*H, −CH_2−), 3.34 (s, 4H, iPr−CH), 3.78 (s, 2*n*H, Ph−CH_2), 7.05−7.09 (d, 4*n*H, Ar−H), 7.44−7.48 (d, 4*n*H, Ar−H), 9.78 (s, 2*n*H, N−H). GPC (DMF): dispersity = 1.23, M_w = 17650, M_n = 14355.

Synthesis of Aliphatic Polyamide ***4e′***. Reaction of *N*,*N*′-bis-(2,6-diisopropylphenyl)carbodiimide (iPr-CDI) **1** with 4,4′-methylenebis(phenylisocyanate) (MDI) **3** and azelaic acid (AZA) **2e** in the molar ratio of iPr-CDI/MDI/AZA = 1/10/10. Yield = 98% of a white solid. FT-IR (KBr cm^{-1}): 1660 (amide, C═O), 3301 (amide, N−H). ^{1}H NMR (200 MHz, DMSO-d_6, δ, ppm): 1.07 (s, 24H, iPr−CH_3), 1.27 (s, 6nH, −CH_2−), 1.55 (s, 4*n*H, −CH_2−), 2.25 (s, 4*n*H, −CH_2−), 3.34 (s, 4H, iPr−CH), 3.78 (s, 2*n*H, Ph−CH_2), 7.06−7.10 (d, 4*n*H, Ar−H), 7.45−7.49 (d, 4*n*H, Ar−H), 9.76 (s, 2*n*H, N−H). GPC (DMF): dispersity = 1.11, M_n = 12197, M_w = 13621.

Synthesis of aliphatic polyamide ***4f′***. Reaction of *N*,*N*′-bis(2,6-diisopropylphenyl)carbodiimide (iPr-CDI) **1** with 4,4′-methylenebis(phenylisocyanate) (MDI) **3** and 1,10-decanedicarboxylic acid (DA) **2f** in the molar ratio of iPr-CDI/MDI/DA = 1/10/10. Yield = 92% of a white solid. FT-IR (KBr cm^{-1}): 1660 (amide, C═O), 3301 (amide, N−H). ^{1}H NMR (200 MHz, DMSO-d_6, δ, ppm): 1.10 (s, 24H, iPr−CH_3), 1.24 (s, 12*n*H, −CH_2−), 1.54 (s, 4*n*H, −CH_2−), 2.24 (s, 4*n*H, −CH_2−), 3.20−3.42 (t, 4H, iPr−CH), 3.78 (s, 2*n*H, Ph−CH_2), 7.05−7.09 (d, 4*n*H, Ar−H), 7.44−7.48 (d, 4*n*H, Ar−H), 9.75 (s, 2*n*H, N−H). GPC (DMF): dispersity = 1.08, M_w = 11264, M_n = 10444.

Synthesis of Model Unsymmetrical *N*′-Phenyl-*N*-(2,6-diisopropylphenyl) Carbodiimide (PiPr-CDI) (Scheme 7). *Synthesis of N*′*-Phenyl-N-(2,6-diisopropylphenyl) Thiourea* ***19*** *(Scheme 7a).* Into a 250 mL three-necked round-bottomed flask equipped with a thermometer, a nitrogen gas inlet, an ice bath, and a magnetic stirrer were placed phenyl isothiocyanate **17** (8.03 g, 58 mmol) and 10 mL of dry THF. After the mixture was cooled to 0−4 °C, 2,6-diisopropylaniline **18** (10.19 g, 52 mmol) dissolved in 10 mL of dry THF was added dropwise to the stirred solution. After the addition, the reaction was continued at room temperature for 2 h. The resulting solution was then poured into 100 mL of petroleum ether. The precipitated product was filtered and dried at room temperature under vacuum. The yield of *N*′-phenyl-*N*-(2,6-diisopropylphenyl) thiourea **19** was 99% (16.36 g). Mp = 173−174 °C. FT-IR (KBr cm^{-1}): 1330 (thiourea, C═S), 3340 (thiourea, N−H). ^{1}H NMR (200 MHz, DMSO-d_6, δ, ppm): 1.12−1.23 (m, 12H, iPr−CH_3), 3.06−3.13 (t, 2H, iPr−CH), 7.17−7.35 (m, 6H, Ar−H), 7.59−7.62 (d, 2H, Ar−H), 8.41,9.00 (s, 2H, N−H), 9.60,9.84 (s, 2H, N−H). Anal. Calcd for $C_{19}H_{24}N_2S$: C, 73.03; H, 7.74; N, 8.97; S, 10.26. Found: C, 73.07; H, 7.73; N, 8.92; S, 10.25. Mass spectrum (*m*/*e*): 312 (M^+, 100% relative abundance).

Synthesis of N′*-Phenyl-N-(2,6-diisopropylphenyl) Carbodiimide (PiPr-CDI)* ***20*** *(Scheme 7(b)).* Into a 100 mL three-necked round-bottomed flask equipped with a thermometer, a nitrogen gas inlet tube, and a magnetic stirrer were added *N*′-phenyl-*N*-(2,6-diisopropylphenyl) thiourea **19** (9.36 g, 30 mmol) and 50 mL of DCM. After the mixture was cooled to 0−4 °C in an ice bath, sodium hydroxide (2.40 g, 60 mmol) and tetra-*n*-butylammonium bromide (0.10 g, 3 mmol) dissolved in 50 mL of H_2O were added dropwise to the stirred solution. To this solution was then added 12% of sodium hypochlorite solution (55.83 g, 90 mmol), and the combined solution was maintained at room temperature with stirring for 7 h until the color of the solution changing from deep orange to light yellow. The reaction mixture was extracted three times with dichloromethane (DCM). The organic layer was dried with $MgSO_4$. The crude product was purified by rapidly passing through a short chromatograph column packed with silica gel with DCM as the eluent. After evaporation of DCM, *N*′-phenyl-*N*-(2,6-diisopropylphenyl) carbodiimide (PiPr-CDI) **20** (4.84 g; 58%) was isolated as a colorless viscose liquid. FT-IR (KBr cm^{-1}): 2156, (carbodiimide, −NCN−). ^{1}H NMR (200 MHz, DMSO-d_6, δ, ppm): 1.17−1.20 (d, 12H, iPr−CH_3), 3.23−3.39 (m, 2H, iPr−CH), 7.16 (s, 6H, Ar−H), 7.31−7.38 (t, 2H, Ar−H). Mass spectrum (*m*/*e*): 278 (M^+, 100% relative abundance).

Experiments on Model Competitive Study (Scheme 8). *Diphenyl Carbodiimide (Phenyl-CDI)* ***21*** *and N,N*′*-Bis(2,6-diisopropylphenyl)-Carbodiimide (iPr-CDI)* ***1*** *Reacted with Benzoic Acid* ***22*** *(Scheme 8a).* Into a 100 mL three-necked round-bottomed flask equipped with a thermometer, a nitrogen gas inlet tube, an oil

bath, and a magnetic stirrer was placed 4 mL of dry NMP, and the flask was heated to 140 °C. 1,3-Dimethyl-3-phospholene oxide (DMPO, 0.050 g) and benzoic acid **22** (0.12 g, 1.0 mmol) were added into the solution and stirred for 5 min. *N*,*N*′-Bis(2,6-diisopropylphenyl)carbodiimide **1** (1.81 g, 5.0 mmol) and diphenyl carbodiimide **21** (0.97 g, 5.0 mmol) dissolved in 6 mL of dry NMP and were then added into the reaction mixture at 140 °C. The reaction was monitored by FT-IR. The peak of CDI absorption at 2102, 2137, and 2166 cm^{-1} did not diminish in 60 min. The resulting mixture was quenched by concentrated H_2SO_4 (1 mL) and H_2O (4 mL) and poured into 200 mL of water, filtered, and dried, to yield 2.75 g of crude amide product. FT-IR analysis of the crude product showed the CDI peak absorptions at 2102, 2137, and 2166 cm^{-1} have been converted into urea absorption at 1641 cm^{-1}. HPLC analysis of the crude reaction products showed the yields ratios of 80:20 for phenyl benzamide **23** and *N*-(2,6-diisopropylphenyl) benzamide **24** respectively.

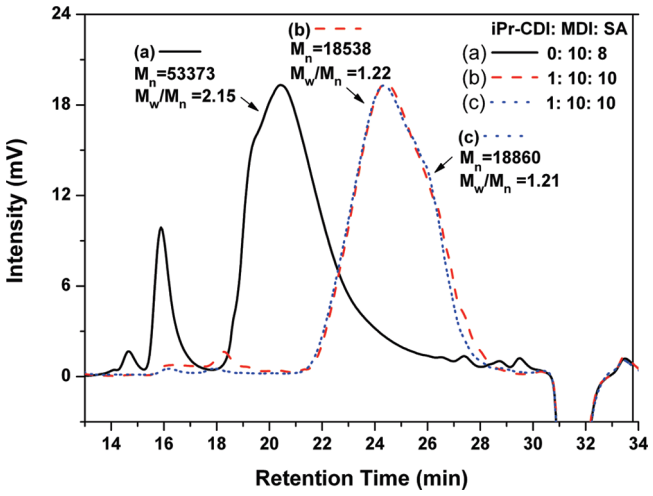

Figure 6. GPC spectra (DMF) of polyamide **4c′-2** (iPr-CDI/MDI/SA = 1/10/10) prepared by a two step method: (a) the first step: synthesis of polyamides **26** with unhindered poly-CDI containing (iPr-CDI/MDI/SA = 0/10/8); (b) second step: addition of iPr-CDI initiator **1** and SA diacids **2c** to control the molecular weight (iPr-CDI/MDI/SA = 1/10/10). (c) One step method by new SSRR for polyamide **4c′-1** (iPr-CDI/MDI/SA = 1/10/10).

*N′-Phenyl-N-(2,6-diisopropylphenyl) Carbodiimide (PiPr-CDI) **20** Reacted with Benzoic Acid **22** (Scheme 8(b))*. Into a 100 mL three-necked round-bottomed flask equipped with a thermometer, a nitrogen gas inlet tube, an oil bath, and a magnetic stirrer was placed 3 mL of dry NMP, and the flask was heated to 140 °C. 1,3-Dimethyl-3-phospholene oxide (DMPO, 0.050 g) and *N*′-phenyl-*N*-(2,6-diisopropylphenyl) carbodiimide (PiPr-CDI) **20** (1.01 g, 3.63 mmol) were added into the solution and stirred for 5 min. Benzoic acid **22** (3.63 g, 7.26 mmol) dissolved in 2 mL of dry NMP and was then added into the reaction mixture at 140 °C. The reaction was monitored by FT-IR. The peak of PiPr-CDI absorption at 2156 cm^{-1} and isocyanate absorption at 2260 and 2290 cm^{-1} disappeared to finish reaction in 90 min. The resulting mixture was quenched by the addition of concentrated H_2SO_4 (0.5 mL) and H_2O (2 mL) and poured into 200 mL of water, filtered, and dried, to yield 5.56 g of crude amide product. FT-IR analysis of the crude product showed amide absorption at 1653 cm^{-1}. HPLC analysis of the crude reaction products showed yield ratios of 29:71 for phenyl benzamide **23** and *N*-(2,6-diisopropylphenyl) benzamide **24**, respectively.

Experiments on Trans-CDI Disproportion and Isocyanate-CDI Exchange Reactions (Scheme 9). *Reaction of N,N′-Bis-(2,6-diisopropylphenyl)Carbodiimide (iPr-CDI) **1** with Diphenyl Carbodiimide (diphenyl CDI) **21** (Scheme 9a)*. Into a 100 mL three-necked round-bottomed flask equipped with a thermometer, a nitrogen gas inlet tube, an oil bath, and a magnetic stirrer was placed 8 mL of dry NMP, and the flask was heated

Scheme 10. Mechanism of the Two Step Method: (a) First Step, Synthesis of Polyamides 26 Containing Unhindered Poly-CDI; (b) Second Step, Addition of iPr-CDI Initiator 1 and Residual Diacids 2c To Control The Molecular Weight and Finish the Reaction

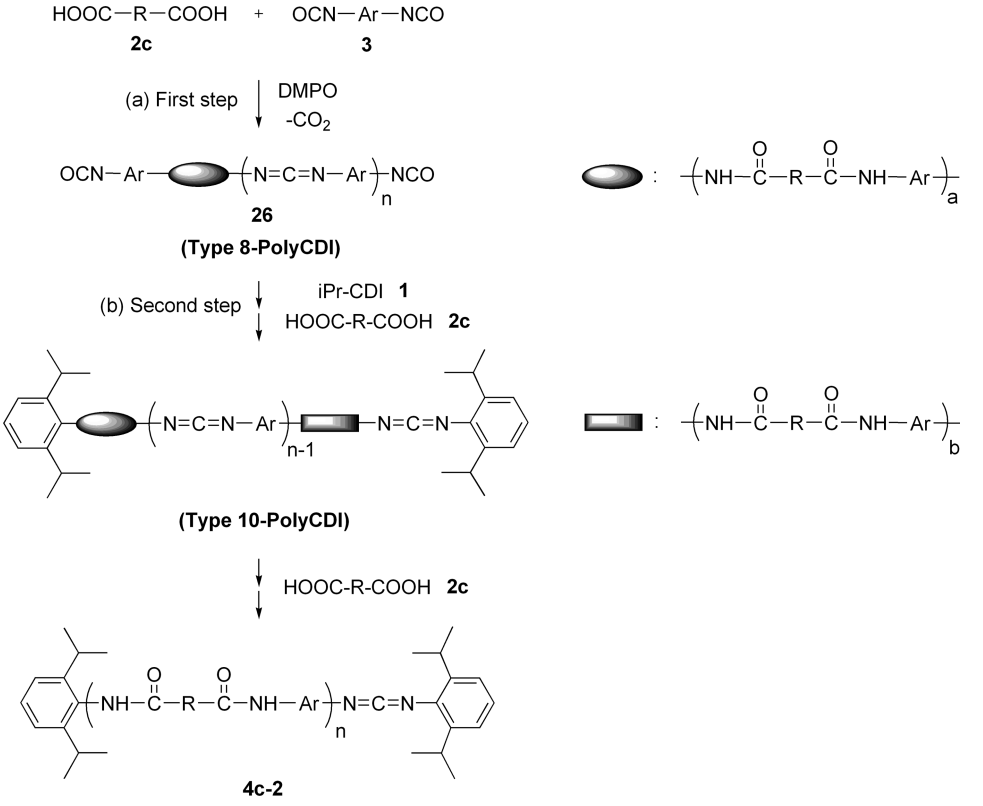

to 140 °C. 1,3-Dimethyl-3-phospholene oxide (DMPO, 0.050 g) and diphenyl carbodiimide **21** (2.02 g, 10.4 mmol) were added into the solution and stirred for 5 min. *N*,*N*′-Bis(2,6-diisopropylphenyl)carbodiimide **1** (3.77 g, 10.4 mmol) dissolved in 12 mL of dry NMP and was then added into the reaction mixture at 140 °C. The reaction was monitored by FT-IR. The peak absorption at 2107, 2137, and 2166 cm^{-1} were converted into new CDI absorption at 2156 cm^{-1} in 240 min. The resulting mixture was quenched by concentrated H_2SO_4 (1 mL) and H_2O (4 mL) and poured into 200 mL of water, filtered and dried, to yield 4.89 g of crude urea product. FT-IR analysis of the crude product showed the new CDI peak absorption at 2156 cm^{-1} have been converted into urea absorption at 1643 cm^{-1}. The urea product ratios of 32:23:45 for *N*′-phenyl-*N*-(2,6-diisopropylphenyl) urea, diphenyl urea, and *N*,*N*′-bis-(2,6-diisopropylphenyl) urea respectively were measured by HPLC analysis. This ratio of 32:23:45 was assumed to be the ratio of the corresponding CDIs for *N*′-phenyl-*N*-(2,6-diisopropylphenyl) carbodiimide (PiPr-CDI) **20**, diphenyl carbodiimide **21** and *N*,*N*′-bis(2,6-diisopropylphenyl)carbodiimide **1** respectively before their hydrolysis.

Reaction of 2,6-Diisopropylphenyl Isocyanate (*iPr-NCO*) *7 with Diphenyl Carbodiimide* (*diphenyl CDI*) ***21*** (*Scheme 9b*). Into a 100 mL three-necked round-bottomed flask equipped with a thermometer, a nitrogen gas inlet tube, and a magnetic stirrer was placed 6 mL of dry NMP and was heated to 140 °C. 1, 3-Dimethyl-3-phospholene oxide (DMPO, 0.050 g) and diphenyl carbodiimide **21** (0.51 g, 2.64 mmol) were added into the solution and stirred for 5 min. 2,6-Diisopropylphenyl isocyanate **7** (1.07 g, 5.28 mmol) was dissolved in 7 mL of dry NMP and was then added into the reaction mixture at 140 °C. The reaction was monitored by FT-IR. The peak absorption at 2290 cm^{-1} rapidly diminished and disappeared, while a new CDI IR absorption at 2156 cm^{-1} became the major absorption in 60 min. The resulting mixture was quenched by the addition of concentrated H_2SO_4 (0.5 mL) and H_2O (2 mL) to convert all CDIs in the solution into urea derivitives. The resulting solution was poured into 200 mL of water, filtered and dried, to yield 1.22 g of crude urea product. FT-IR analysis of the crude product showed the new CDI peak absorption at 2156 cm^{-1} have been converted into urea absorption at 1643 cm^{-1}. The composition of this urea product mixture was analyzed through HPLC where the relative ratio of ureas were determined to be 83:17 for *N*′-phenyl-*N*-(2,6-diisopropylphenyl) urea and diphenyl urea. This ratio of 83:17 was assumed to be the ratio of the corresponding CDIs for *N*′-phenyl-*N*-(2,6-diisopropylphenyl) carbodiimide (PiPr-CDI) **20** and diphenyl carbodiimide **21** respectively before their hydrolysis.

Reaction of 2,6-Diisopropylphenyl Isocyanate (*iPr-NCO*) *7 with Phenyl Isocyanate* (*Phenyl NCO*) ***25*** (*Scheme 9c*). Into a 100 mL three-necked round-bottomed flask equipped with a thermometer, a nitrogen gas inlet tube, and a magnetic stirrer was placed 5 mL of dry NMP, and heated to 140 °C. 1,3-Dimethyl-3-phospholene oxide (DMPO, 0.05 g) and phenyl isocyanate **25** (0.29 g, 2.43 mmol) were added into the solution and stirred for 5 min. 2,6-Diisopropylphenyl isocyanate **7** (0.50 g, 2.43 mmol) dissolved in 5 mL of dry NMP was then added into the reaction mixture at 140 °C. The reaction was monitored by FT-IR. The peak absorption at 2260 and 2290 cm^{-1} disappeared and was replaced by new CDI absorption at 2156 cm^{-1} in 120 min. The resulting mixture was quenched by concentrated H_2SO_4 (0.5 mL) and H_2O (2 mL) and poured into 200 mL of water, filtered, and dried, to yield 0.51 g of crude urea product. FT-IR analysis of the crude product showed the new CDI peak absorption at 2156 cm^{-1} has been converted into urea absorption at 1643 cm^{-1}. The composition of this urea product mixture was analyzed through HPLC where the relative ratio of urea was determined to be 72:28 for *N*′-phenyl-*N*-(2,6-diisopropylphenyl) urea and diphenyl urea, respectively. This ratio of 72:28 was assumed to be the ratio of the corresponding CDIs for *N*′-phenyl-*N*-(2,6-diisopropylphenyl) carbodiimide (PiPr-CDI) **20** and diphenyl carbodiimide **21** respectively before their hydrolysis.

Synthesis of Polyamide 4a-3 with No iPr-CDI Initiator in Regular SSRR (Figure 4c). *Synthesis of Aromatic Polyamide* ***4a′-3*** *with No iPr-CDI Initiator* ***1*** (*Figure 4c*). Reaction of 4,4′-methylenebis(phenylisocyanate) (MDI) **3** with isophthalic acid (IA) **2a** in the molar ratio of iPr-CDI/MDI/IA = 0/1/1 is given here as a typical example. Into a 100 mL, three-necked, round-bottomed flask equipped with a thermometer, a nitrogen gas inlet tube, a reflux condenser, an oil bath, and a magnetic stirrer was placed 10 mL of dry NMP, and the flask was heated to 180 °C. 1,3-Dimethyl-3-phospholene oxide (DMPO, 0.050 g) was added into the hot NMP solution and stirred for 30 s. Freshly distilled MDI **3** (2.500 g, 10 mmol) and IA **2a** (1.660 g, 10 mmol) were dissolved in 20 mL of dry NMP and were then added dropwise into the NMP solution in 6 min at 180 °C. The reaction was further heated to 202 °C for 3 h. The reaction was monitored by FT-IR. The peak absorption at 2112 and 2136 cm^{-1} disappeared in 10 min. No CDI peak absorption was generated and persisted to the rest of 170 min. The resulting product **4a-3** solution was poured into 500 mL of water, filtered and dried, to yield 3.214 g (98%) of crude polyamide **4a′-3** (light yellow solid). FT-IR analysis of the crude product showed amide absorption at 1668 cm^{-1} and no CDI peak absorption at 2112 and 2136 cm^{-1}. A small portion of product (0.5 g) was further purified by dissolving in about 5 mL of NMP solvent, following by precipitating from 50 mL of chloroform (78% yields). The detail results of FT-IR, ^1H NMR, and GPC for aromatic polyamides **4a′-3** were described above.

Demonstration of the Importance of iPr-CDI to Control The Molecular Weight in New SSRR (Scheme 10). *First Step: Synthesis of Polyamides* ***26*** *with Unhindered Poly-CDI Containing* (*Scheme 10a*). Reaction of 4,4′-methylenebis(phenylisocyanate) (MDI) **3** with 4,4′-sulfonyldibenzoic acid (SA) **2c** in the molar ratio of iPr-CDI/MDI/SA = 0/10/8 is given here. Into a 100 mL, three-necked, round-bottomed flask equipped with a thermometer, a nitrogen gas inlet tube, a reflux condenser, an oil bath, and a magnetic stirrer, was placed 6 mL of dry NMP, and the flask was heated to 180 °C. 1,3-Dimethyl-3-phospholene oxide (DMPO, 0.050 g) was added into the hot NMP solution and stirred for 30 s. Freshly distilled MDI **3** (2.500 g, 10 mmol) and SA **2c** (2.450 g, 8 mmol) were dissolved in 15 mL of dry NMP and were then added dropwise into the NMP solution in 10 s at 180 °C. The reaction was further heated to 202 °C for 2 min. The resulting product solution became viscous and sticky in the process. The resulting product solution was monitored by FT-IR. The peak absorption was converted into poly-CDI absorption at 2112 and 2136 cm^{-1} in 2 min. Taking small resulting product solution (about ~2 mL) was quenched by 50 mL of water, filtered and dried, to yield 0.008 g of high molecular weight polyamide **26** product with unhindered poly-CDI containing (yellow and viscous solid). GPC (DMF): dispersity = 2.15, M_w = 114752, M_n = 52373.

Second Step: Synthesis of Aromatic Polyamide ***4c-2*** *with Adding iPr-CDI Initiator* ***1*** *and SA Diacids* ***2c*** *To Control The Molecular Weight and Finish The Reaction* (*Scheme 10b*). Reaction of *N*,*N*′-bis(2,6-diisopropylphenyl)carbodiimide (iPr-CDI) **1** and 4,4′-sulfonyldibenzoic acid (SA) **2c** with the first step of the resulting product in the overall molar ratio of iPr-CDI/MDI/SA = 1/10/10 is given here. The first step of the resulting product solution was carried onto the second step. Initiator iPr-CDI **1** (0.363 g, 1 mmol) and residual SA **2c** (0.612 g, 2 mmol) were dissolved in 9 mL of dry NMP and were then added dropwise into the NMP solution in 6 min at 202 °C. The reaction was further heated to 202 °C for 3 h. The viscous resulting product solution clarified immediately in the process. The reaction was monitored by FT-IR. The peak absorption at 2112, 2136, and 2290 cm^{-1} disappeared and was replaced by the new hindered-CDI of absorption at 2151 cm^{-1} in 30 min. The new peak absorption at 2151 cm^{-1} was persisted to the rest of 2.5 h.

The resulting product **4c-2** solution was quenched by 500 mL of water, filtered and dried, to yield 4.60 g (92%) of crude polyamide **4c′-2** (light yellow solid). FT-IR analysis of the crude product showed the CDI peak absorption at 2151 cm^{-1} disappeared and was replaced by urea/amide complex absorption at 1668 cm^{-1}. A small portion of product (0.5 g) was further purified by dissolving in about 5 mL of NMP solvent, following by precipitating from 50 mL of THF (80% yields). The detail results of FT-IR, ^{1}H NMR, and GPC for aromatic polyamides **4c′-2** were described above.

Demonstration of iPr-NCO as the Initiator To Control The Molecular Weight in New SSRR (Example Polyamide 4c-3). *Synthesis Aromatic Polyamide 4c′-3 with iPr-NCO 7 as the Initiator*. Reaction of 2,6-diisopropylphenyl isocyanate (iPr-NCO) **7** with 4,4′-methylenebis(phenylisocyanate) (MDI) **3** and 4,4′-sulfonyldibenzoic acid (SA) **2c** in the molar ratio of iPr-NCO/MDI/SA = 2/10/10 is given here. Into a 100 mL, three-necked, round-bottomed flask equipped with a thermometer, a nitrogen gas inlet tube, a reflux condenser, an oil bath, and a magnetic stirrer, was placed 10 mL of dry NMP and was heated to 180 °C. 1,3-Dimethyl-3-phospholene oxide (DMPO, 0.050 g) and iPr-NCO **7** (0.203 g, 2 mmol) were added into the hot NMP solution and stirred for 30 s. Freshly distilled MDI **3** (2.500 g, 10 mmol) and SA **2c** (3.063 g, 10 mmol) were dissolved in 20 mL of dry NMP and were then added dropwise into the NMP solution in 6 min at 180 °C The reaction was further heated to 202 °C for 3 h. The reaction was monitored by FT-IR. The peak absorption at 2112, 2136, 2260, and 2290 cm^{-1} disappeared and was replaced by new hindered-CDI of absorption at 2151 cm^{-1} in 30 min. The new peak absorption at 2151 cm^{-1} was persisted to the rest of 2.5 h. The resulting product **4c-3** solution was quenched by 500 mL of water, filtered, and dried, to yield 4.72 g (95%) of crude polyamide **4c′-3** (light yellow solid). FT-IR analysis of the crude product showed the CDI peak absorption at 2151 cm^{-1} disappeared and was replaced by urea/amide complex absorption at 1668 cm^{-1}. A small portion of product (0.5 g) was further purified by dissolving in about 5 mL of NMP solvent, following by precipitating from 50 mL of THF (78% yields). The detail results of FT-IR, ^{1}H NMR, and GPC for aromatic polyamides **4c′-3** were described above.

Acknowledgment. This work was financially supported in parts by GRECO of Taichung, Taiwan, by a grant (98-EC-17-A-17-S1-111) from the Ministry of Economics Affairs and by the Ministry of Education under ATU plan, executive Yuan, Taiwan. We also thank Ms. Karin D. Kelly for advising our manuscript.

Supporting Information Available: Figures showing NMR spectra for polyamides and model compounds and HPLC spectra for model reactions (including model competitive study, trans-CDI disproportion and isocyanate-CDI exchange reactions). This material is available free of charge via the Internet at http://pubs.acs.org.

References and Notes

(1) Klaikherd, A.; Ghosh, S.; Thayumanavan, S. *Macromolecules* **2007**, *40*, 8518–8520.
(2) Dong, H.; Tang, W.; Matyjaszewski, K. *Macromolecules* **2007**, *40*, 2974–2977.
(3) Dire, C.; Charleux, B.; Magnet, S.; Couvreur, L. *Macromolecules* **2007**, *40*, 1897–1903.
(4) Phan, T. N. T.; Bertin, D. *Macromolecules* **2008**, *41*, 1886–1895.
(5) Rzayev, J.; Penelle, J. *Angew. Chem., Int. Ed.* **2004**, *43*, 1691–1694.
(6) Cheng, C.; Sun, G.; Khoshdel, E.; Wooley, K. L. *J. Am. Chem. Soc.* **2007**, *129*, 10086–10087.
(7) You, Y. Z.; Zhou, Q. H.; Manickam, S. D.; Wan, L.; Mao, G. Z.; Oupicky, D. *Macromolecules* **2007**, *40*, 8617–8624.
(8) Yokozawa, T.; Asai, T.; Sugi, R.; Ishigooka, S.; Hiraoka, S. *J. Am. Chem. Soc.* **2000**, *122*, 8313–8314.
(9) Yokozawa, T.; Ogawa, M.; Sekino, A.; Sugi, R.; Yokoyama, A. *J. Am. Chem. Soc.* **2002**, *124*, 15158–15159.
(10) Yokoyama, A.; Yokozawa, T. *Macromolecules* **2007**, *40*, 4093–4101.
(11) Yokozawa, T.; Yokoyama, A. *Prog. Polym. Sci.* **2007**, *32*, 147–172.
(12) Yokoyama, A.; Masukawa, T.; Yamazaki, Y.; Yokozawa, T. *Macromol. Rapid Commun.* **2009**, *30*, 24–28.
(13) Yokozawa, T.; Yokoyama, A. *Chem. Rev.* **2009**, *109*, 5595–5619.
(14) Yoshino, K.; Yokoyama, A.; Yokozawa, T. *J. Polym. Sci., Part A: Polym. Chem.* **2009**, *47*, 6328–6332.
(15) Ohishi, T.; Masukawa, T.; Fujii, S.; Yokoyama, A.; Yokozawa, T. *Macromolecules* **2010**, *43*, 3206–3214.
(16) Yoshino, K.; Hachiman, K.; Yokoyama, A.; Yokozawa, T. *J. Polym. Sci., Part A: Polym. Chem.* **2010**, *48*, 1357–1363.
(17) Kim, Y. J.; Seo, M.; Kim, S. Y. *J. Polym. Sci., Part A: Polym. Chem.* **2010**, *48*, 1049–1057.
(18) Wei, K. L.; Wu, C. H.; Huang, W. H.; Lin, J. J.; Dai, S. A. *Macromolecules* **2006**, *39*, 12–14.
(19) Chen, C. W.; Cheng, C. C.; Dai, S. A. *Macromolecules* **2007**, *40*, 8139–8141.
(20) Campbell, T. W.; Monagle, J. J. *J. Am. Chem. Soc.* **1962**, *84*, 1493.
(21) Schotman, A. H. M. *Trav. Chim. Pays-Bas* **1991**, *110*, 319–324.
(22) Schotman, A. H. M.; Mijs, W. J. *Trav. Chim. Pays-Bas* **1992**, *111*, 88–91.
(23) Schotman, A. H. M.; Weber, T. M. J.; Mijs, W. J. *Macromol. Chem. Phys.* **1999**, *200*, 635–641.
(24) Chang, H. L.; Lin, H. L.; Wang, Y. C.; Dai, S. A.; Su, W. C.; Jeng, R. J. *Polymer* **2007**, *48*, 2046–2055.
(25) Lin, H. L.; Chao, T. Y.; Shih, Y. F.; Dai, S. A.; Su, W. C.; Jeng, R. J. *Polym. Adv. Technol.* **2008**, *19*, 984–992.
(26) Lin, H. L.; Chang, H. L.; Juang, R. H.; Dai, S. A.; Liu, Y. L.; Jeng, R. J. *Dyes Pigm.* **2009**, *82*, 76–83.
(27) Note: ^{1}H NMR characterization of model unsymmetrical *N*′-phenyl-*N*-(2,6-diisopropylphenyl) CDI (PiPr-CDI) **20** for Scheme 7 were shown in the Supporting Information, Figure S18 and S19.
(28) Note: ^{1}H NMR characterization for polyamides **4a′**−**4f′** were shown in the Supporting Information, Figures S2−S17.
(29) Note: HPLC analysis of model competitive studies for Scheme 8 were shown in the Supporting Information, Figures S20 and S21.
(30) Ulrich, H. In *Chemistry and Technology of Carbodiimides*: John Wiley & Sons Publishers: England, 2007; p 30 and p 60.
(31) Note: HPLC analysis of trans-CDI disproportion and isocyanate-CDI exchange reactions for Scheme 9 were shown in the Supporting Information, Figures S22−S24.

60 *Macromolecules* **2011**, *44*, 60–67
DOI: 10.1021/ma101514c

Macromolecules
ARTICLE

Controlling the *m*-Poly(phenylene ethynylene) Helical Cavity Environment: Hydrogen Bond Stabilized Helical Structures

Ha H. Nguyen, James H. McAliley, and David A. Bruce*

Department of Chemical and Biomolecular Engineering, Clemson University Clemson, South Carolina 29634-0909, United States

Received July 7, 2010; Revised Manuscript Received November 26, 2010

ABSTRACT: Replica exchange molecular dynamics (REMD) simulations using explicit solvents were used to study the folding behaviors of a group of *m*-poly(phenylene ethynylene)s (mPPEs), which are being actively investigated for a variety of biological and catalysis applications. The mPPEs considered in this study have different *endohelix* functional groups, which in the helical conformation of the polymer are localized within the helical cavity. The results showed that, for mPPEs with ester functional groups arranged on the exohelix of the helical polymer, altering the endohelix functional groups did not significantly affect folding behaviors in acetonitrile. This result is consistent with experimental data and indicates that the properties of the helical cavity may be tailored for certain applications without destabilizing the helix conformation, so long as the exohelix functional groups are esters. We also present simulation results for a set of mPPEs with endohelix functional groups that enhance the stability of the helical conformation via the formation of intra- and interturn hydrogen bonds (HBs). If mPPE folding is viewed as a nucleation/growth process, intraturn HB interactions facilitate both nucleation events and growth, while interturn HBs and π-stacking interactions affect only the growth process. These mPPEs, which lack exohelix functional groups, were shown to fold into stable helical secondary structures in acetonitrile, methanol, and even chloroform, although chlorinated solvents have previously been known to denature mPPE helical structures. Our results predict that this stabilization occurs to the extent that a variety of exohelix functional groups can be incorporated into mPPE backbones, while maintaining a stable helical secondary structure, including many functional groups that are known to destabilize the helix in non-hydrogen-bonded mPPEs.

Introduction

m-Poly(phenylene ethynylene)s or mPPEs are a class of polymers known for their ability to form helical secondary structure in suitable solvent conditions.[1] This special ability not only invites the opportunity for many different applications but also provides a simple and interesting platform for studying the conformational behavior of macromolecules. Thus, understanding and controlling the factors that affect their folding behavior is crucial in designing an effective functionalized mPPE for a given application. It is especially important to understand the impact of functional groups on the polymer backbone, as such knowledge is extremely useful in studying secondary structure formation of macromolecules in general.

Primarily, two types of functional groups can be employed to modify the properties of a given mPPE, as shown in Figure 1. On the basis of their locations on the expected helical structures, we refer to those in position R_1 as *exohelix* functional groups. These groups are at *meta* positions to the ethynylene linkages and arranged on the outer wall of the helical conformation. Similarly, we refer to groups at position R_2 as *endohelix* functional groups. These are located at the position that is *ortho* to both ethynylene linkages on a phenyl ring, and they are encased inside the cavity of the mPPE in its helical conformation.

The exohelix functional groups of mPPEs have been shown by many experimental and modeling studies to directly affect the solubility and folding behaviors of their respective mPPEs.[1−10] The endohelix functional groups, on the other hand, have been employed mostly to control the environment inside the helix cavity. For example, Tanatani et al.[11] employed methyl functional groups to reduce the size of the helix cavity of an mPPE, effectively blocking the entrance of small molecules into the cavity. In another study, Prince et al.[12] used nitrile endohelix functional groups to form a silver ion complex within the helix cavity. The bonds between the ion and the nitrile functional groups of the complex provided an additional stabilizing effect for the helical structure in tetrahydrofuran solution.

Aside from their ability to change the environment inside the mPPE helix cavity, endohelix functional groups may also influence helix stability by enhancing the π-stacking of overlapping aromatic rings. This effect is brought about because, in general, substituted benzyl rings have stronger π-stacking interactions in comparison to benzene.[13,14] On the other hand, they could also inhibit helical formation through steric interactions. The steric effect was shown by Arnt and Tew[2] with an mPPE having large ether endohelix functional groups and by Adisa and Bruce[4] in a modeling study with similar mPPE structures. Steric interactions of course depend on the size of the functional groups, and in our previous study,[10] the folding behavior of an mPPE having small endohelix functional groups was found to be similar to that of an mPPE with only hydrogen endohelix functional groups.

In this study, we examine how the stability of the mPPE helical structure is affected by endohelix functional groups, including those that are capable of forming hydrogen bonds. The idea of incorporating hydrogen bonds into an mPPE structure was previously explored by Cary and Moore,[15] by placing suitable functional groups at the position that is *ortho* to the ethynylene

*Corresponding author. Address: Department of Chemical & Biomolecular Engineering, Clemson University, 127 Earle Hall, Clemson, SC 29634-0909. E-mail: dbruce@clemson.edu.

 Published on Web 12/13/2010 © 2010 American Chemical Society

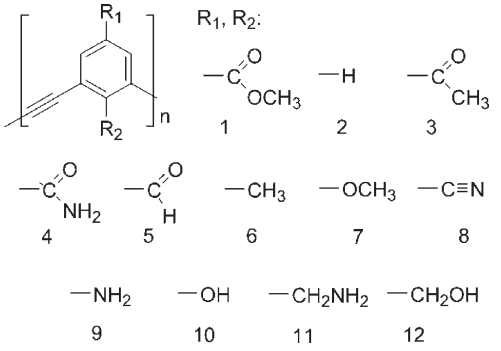

Figure 1. Structure of functionalized mPPEs. R_1: exohelix functional group, which would be on the outer wall of the helical structure. R_2: endohelix functional group, which would be encased inside the cavity of the helical structure.

linkages as well as on the outer wall of the mPPE helical structures. In that study, hydrogen bonds between the functional groups significantly improved the stability of helical structures, allowing them to withstand a higher ratio of chlorinated solvent in solvent mixtures. Because hydrogen bonds are far stronger than the π-stacking effect, they would presumably lead to more stable helical structures and bring the mPPE secondary conformations a step closer to those of biological macromolecules, which are primarily stabilized by a series of hydrogen bonds.

In an earlier study,[10] we employed a replica exchange molecular dynamics (REMD) simulation protocol to examine the effect of exohelix functional groups on the folding behaviors of a wide range of functionalized mPPEs. While experimental results have shown that the factors affecting secondary structure in mPPEs are so exceedingly complex that they preclude classification by simple heuristics, we found that our simulation results proved an accurate indicator of whether a given mPPE will fold under given conditions.

The excellent agreement of our previous simulation results with numerous published experimental results as well as the results from other published modeling works indicate that molecular simulation is a useful tool for exploring the folding behavior of mPPEs, presenting a cost-effective alternative to laboratory synthesis and characterization. Thus, in this study, we employed our REMD protocol as well as classical molecular dynamics (MD) to study the effect of the aforementioned endohelix functional groups on the folding behaviors of their respective mPPEs.

Methods

The REMD protocol employed in this paper is identical to that described in earlier work[3,10] and, as such, is only briefly described here. All constant volume REMD and MD simulations were conducted using Gromacs, version 3.3.1,[16−22] on the *Palmetto* supercomputer[23] at Clemson University. The starting mPPE structures, which contained 12 monomer units (from Figure 1, $n = 12$), were built in Materials Studio 4.4,[24] then transferred to Gromacs. Isothermal conditions for all simulations were maintained using Berendsen temperature coupling[25] ($T = 300$ K, $\tau_T = 0.1$ ps), whereas Parrinello−Rahman pressure coupling[26] ($P = 1$ bar, $\tau_P = 1$ ps) was used to maintain system pressure during 200 ns isothermal−isobaric simulations that were used to equilibrate the solvated mPPE systems prior to REMD and MD simulations. The LINCS algorithm[20] was employed to hold constant all mPPE bond lengths. Finally, Visual Molecular Dynamics[27] was used to render graphics of mPPE structures.

To evaluate the folding behaviors of a given mPPE system, we used Gromacs to conduct two REMD simulations, one initialized with the mPPE in a random extended structure and the other with the polymer in a helical conformation. Results were used to categorize the various mPPEs into groups, based on the time evolution of the radius of gyration (R_g) observed during simulations of the polymers. These groups are designated by a number, 1 to 4, and indicate the likelihood that the mPPE will form a stable helix in the given solvent (group 1 being least likely and group 4 being most likely). Refer to our previous work[10] for a detailed description of the method and classification system. In order to monitor the mPPE conformation changes during the simulation, we employed several different parameters including the radius of gyration, the Lennard-Jones interactions between mPPE and solvent molecules, the Lennard-Jones interactions between mPPE atoms, the solvent accessible surface area, the average distances between overlapping aromatics rings as well as visual inspection of the trajectories. All of these parameters show similar correlation with the folding process. Thus, only the time evolution of the radius of gyration is reported in the text.

The mPPE and solvent models were taken from the Optimized Potentials for Liquid Simulations (OPLS),[28−30] following the procedure described earlier.[3,4] The endohelix functional groups, numbered 6 to 10 in Figure 1, were selected to represent a range of size, polarity, and their ability to form hydrogen bonds. Furthermore, we selected only groups whose sizes were small enough to fit inside the helix cavity to avoid any steric effects, as such interactions could severely hinder formation of the helical structure.[4] Three explicit solvents were used for this study: acetonitrile, methanol, and chloroform. Hydrogen bond analyses were performed using Gromacs, with a cut off distance of 0.35 nm and an angle cut off of 30°, as in a previous study.[31]

For this study, 12 different exohelix functional groups were investigated. Among them, $R_1 = -COOCH_3$ and H were fully studied for all seven endohelix functional groups, R_2 from 6 to 12 (see Figure 1). The others were only studied with $R_2 = -CH_2NH_2$ and $-CH_2OH$. REMD and MD simulations for mPPEs with $R_1 = -COOCH_3$ and H and $R_2 = -CH_2NH_2$ and $-CH_2OH$ were conducted in explicit acetonitrile, methanol and chloroform. For the other mPPEs, only REMD simulations in explicit acetonitrile were conducted.

Results and Discussion

In addition to the predictive value of the REMD simulations, the results of this work provide insight into the folding process of mPPEs, and of macromolecules in general. Particularly, we offer new observations for mPPEs that are capable of forming hydrogen bonds, elucidating the role that such hydrogen bonds play in the folding process. In what follows, we present simulation results which will be of use to researchers designing mPPE architectures with tailored properties and stable helical secondary structure.

Secondary Structure of mPPEs with Ester Exohelix Functional Groups ($R_1 = 1$). The ester-functionalized mPPE ($R_1 = 1$) is one of the few mPPEs that maintains a stable helical structure independent of the nature of endohelix functional groups attached to the aromatic rings of the polymer. This allows for control over the environment within the helical cavity without disrupting polymer structure. In this section, we report REMD simulation results for several ester-functionalized mPPE structures having different endohelix functional groups, including those reported in the literature.[11,12]

Simulations were conducted in explicit acetonitrile for seven mPPE systems with ester exohelix functional groups ($R_1 = 1$). The time evolution of R_g is shown in Figure 2 for each of these simulations. Among them, six mPPEs were observed to have similar folding behaviors to that of the hydrogen functionalized ester mPPE ($R_1 = 1$, $R_2 = 2$). That is, the simulations indicated the polymers would be fully folded in acetonitrile. The only exception to this is the mPPE having $R_2 = -CN$, which was observed to only partially fold. This exception is similar to results from our previous

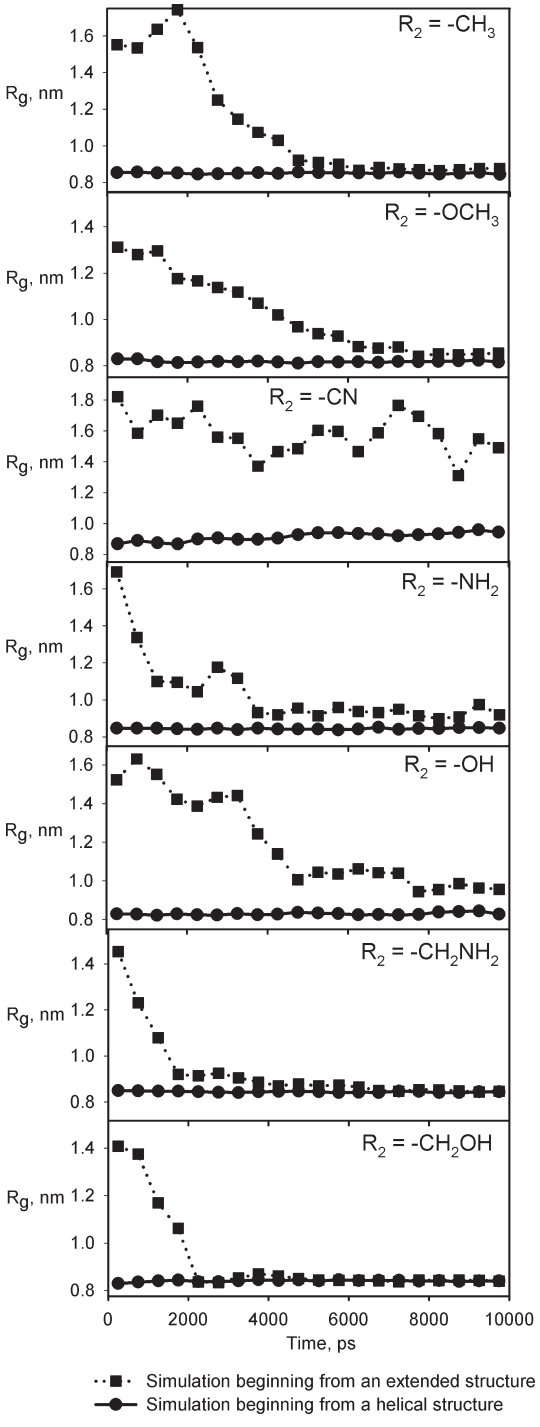

Figure 2. Time evolutions of R_g for seven mPPEs in acetonitrile containing ester exohelix groups (R_1 = $-COOCH_3$) but differing endohelix functional groups (R_2). Data points are averages over 500 ps, placed at the middle of the time range.

simulation study[10] in which an mPPE with the same functional group in the exohelix position (R_1 = $-CN$) only partially folded in acetonitrile and other solvents.

Of the endohelix functional groups considered in Figure 2, two are nonpolar (R_2 = 6 and 7), one has a moderate dipole moment (R_2 = 8), and four are strongly polar (R_2 = 9, 10, 11, 12). Because each of these substituents bear essentially the same results in Figure 2, it is reasonable to conclude that the polarities of endohelix functional groups are unlikely to have a strong effect on the folding behavior of mPPEs functionalized with ester exohelix groups. These results

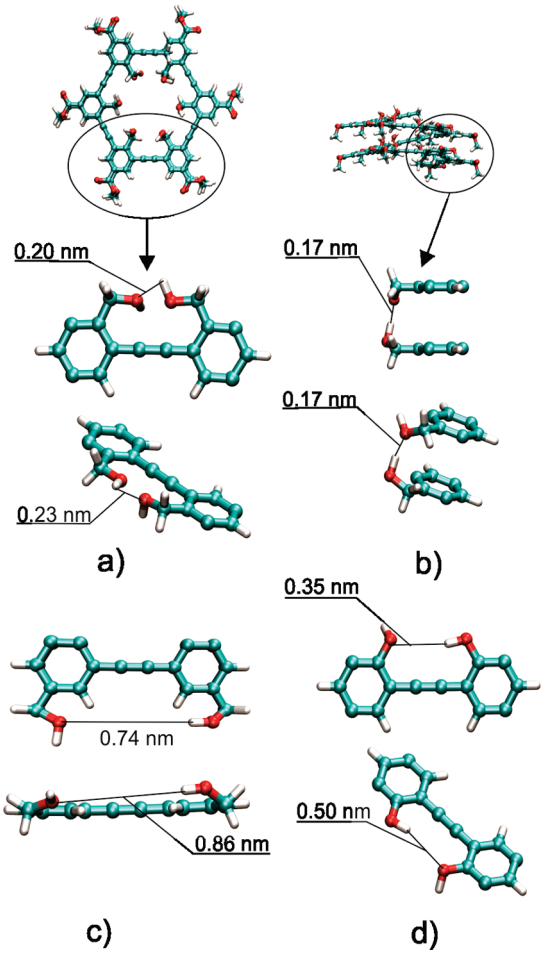

Figure 3. Representative distances between hydrogen bond (HB) donors and acceptors attached to the exohelix of helical mPPEs: HB distances between (a) adjacent and (b) overlapping residues for an mPPE with endohelix functional groups R_2 = $-CH_2OH$. Also pictured are HB distances for (c) an mPPE with exterior functional groups R_1 = $-CH_2OH$, and (d) an mPPE with endohelix functional groups R_2 = $-OH$. Atom colors for oxygen, hydrogen, and carbon are red, white, and cyan, respectively.

further indicate that the helix cavity of an mPPE can be tailored to be polar or nonpolar as needed for a given application without compromising the mPPE's ability to fold, so long as the exohelix functional group is an ester.

Hydrogen bonding in mPPEs with R_1 = $-COOCH_3$. Further analysis of the REMD simulations for mPPEs with ester exohelix functional groups (R_1 = $-COOCH_3$) and polar endohelix functional groups (R_2 = 9, 10, 11 or 12) showed that hydrogen bonds were formed between the endohelix functional groups. Specifically, two kinds of hydrogen bonds were observed: (*i*) those between functional groups of adjacent residues, i.e., between residues numbered *n* and *n*+1. We refer to this type of interaction as an *intraturn* hydrogen bond (intraturn HB), an example of which is pictured in Figure 3a; and (*ii*) those between functional groups of overlapping residues, i.e., between residues numbered *n* and *n*+*x*, with $x \geq 5$. Such an interaction is referred to as an *interturn* hydrogen bond (interturn HB), an example of which is depicted in Figure 3b.

The geometries of mPPEs are such that both intraturn and interturn hydrogen bonds are possible, depending on the functional groups and their positions on the phenylene rings. For example, in a typical mPPE helical conformation with endohelix functional groups R_2 = $-CH_2NH_2$ or $-CH_2OH$,

the distances between hydrogen donors ($-NH_2$ or $-OH$) and hydrogen acceptors ($-N$ or $-O$) are approximately 0.2 to 0.25 nm for groups on adjacent phenylene rings and approximately 0.17 nm for groups on overlapping rings. These values are within the normal range for hydrogen bonds. On the other hand, when these groups ($-CH_2NH_2$ or $-CH_2OH$) are at the R_1 exohelix positions, we see a donor−acceptor separation of more than 0.3 nm between adjacent rings, indicating that intraturn HBs are not likely to form in such mPPEs (Figure 3c). A similar conclusion could be made for mPPEs containing endohelix groups $R_2 = -NH_2$ or $-OH$ (see Figure 3d); the distance between neighboring functional groups is too far to allow intraturn HBs to form.

When analyzing hydrogen bond formation in REMD simulations of mPPEs containing endohelix functional groups $R_2 = -NH_2$ or $-OH$, only interturn HBs were observed, while for mPPEs having $R_2 = -CH_2NH_2$ or $-CH_2OH$, both interturn HBs and intraturn HBs were present. These observations are consistent with the donor−acceptor distance analysis described above.

Effect of Hydrogen Bonds on Folding Behavior. Hydrogen bonds are far stronger than π-stacking interactions, which are the primary contributor to stabilization of the helical conformation in most mPPEs. A typical nonionic hydrogen bond in an organic molecule has a bond dissociation energy of about 4−5 kcal/mol,[31] which is stronger than the π-stacking interaction (dissociation energy of about 1.5−2.5 kcal/mol[13,32−34]). The strong stabilizing effect of hydrogen bonds on mPPE helical structures was experimentally confirmed by Cary and Moore[15] for a mPPE having hydrogen bonds formed between exohelix functional groups. Thus, it is logical to conclude that the presence of hydrogen bonds would make the helical structures significantly more stable than those without hydrogen bonds. Further, the quick convergence of the folding process observed in simulations initialized with extended structures (e.g., Figure 2, parts f and g) suggests that hydrogen bond formation may significantly increase the rate of mPPE folding, although the Monte Carlo exchange moves incorporated into REMD prevent a quantitative comparison of kinetics from these simulations.

When examining the role that hydrogen bonds play in the folding process, several scenarios are possible. In one scenario, the hydrogen bonds form prior to the onset of folding, possibly playing a role in initializing the folding process. Alternatively, the hydrogen bonds may form consecutively as folding progresses, indicating that hydrogen bond formation is a possible driver of the folding process. A third possibility is that the mPPE helical structures form due to the usual π-stacking interactions, as they would in non-hydrogen-bonded mPPEs, with the hydrogen bonds formed only after the required proximity is obtained through π-stacking. This information is easily gathered from the REMD simulations, and may be different for intraturn HBs and interturn HBs.

Results from the simulations initialized with the respective mPPE in an extended structure showed that interturn HBs formed only while the mPPEs folded, inversely correlating with the decrease in R_g of the mPPE (as shown in Figure 4). This is expected, since interturn HBs can only form once the position advantage of an overlap is available to them. On the other hand, for mPPEs having $R_2 = -CH_2NH_2$ or $-CH_2OH$, where both interturn HB and intraturn HB hydrogen bonds were observed, results indicate the presence of intraturn HBs prior to the onset of folding, with the number increasing as folding progresses.

By their nature, intraturn hydrogen bonds between endohelix functional groups promote *cissoid* conformations

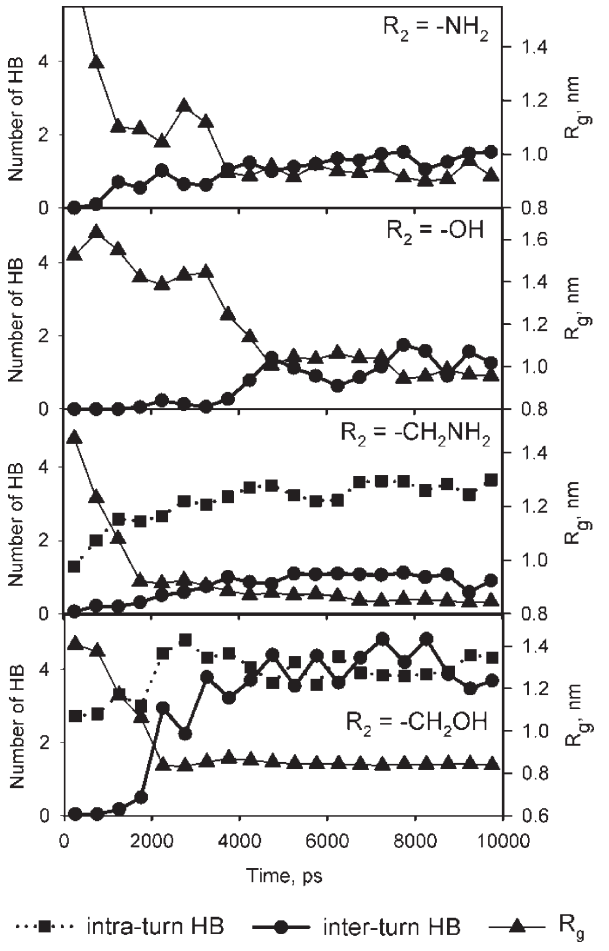

Figure 4. Time evolutions of the numbers of hydrogen bonds (interturn HBs and intraturn HBs) during simulations initialized with extended structures for mPPEs having exohelix functional group $R_1 = -COOCH_3$ in acetonitrile. Data points are averages over 500 ps, placed at the middle of the time range. The absence of intraturn HBs in parts a and b is expected, as the small size of endohelix groups $R_2 = -NH_2$ or $-OH$ prohibits their formation.

within mPPE chains, which is a necessity for helix formation. Furthermore, *cissoid* conformations are stabilized by intraturn HBs in a single step—that is, bond rotation about a single ethynylene linkage. This situation is considerably different in mPPEs that cannot form intraturn HBs, because stabilization occurs only when an overlap interaction is formed, either through π-stacking of aromatic rings or through the formation of interturn hydrogen bonds. However, a set of coordinated rearrangements is required before the first overlap forms. Therefore, intraturn HBs accelerate the folding process in two ways: by facilitating the initial overlap interaction, and by providing an additional driving force for the formation of each subsequent *cissoid* conformation. If mPPE folding is viewed as a nucleation/growth process, intraturn HB interactions facilitate both nucleation events and growth, while interturn HBs and π-stacking interactions affect only the growth process. Therefore, the additional effect of nucleation due to intraturn HBs is likely responsible for the enhanced folding rates evident in Figure 2, parts f and g.

Secondary Structure of mPPEs without Exohelix Functional Groups ($R_1 = -H$). In order to clarify the effect of the endohelix functional groups on the folding behavior of mPPEs, and to explore the role of hydrogen bonds in helix formation, we conducted a series of REMD simulations for

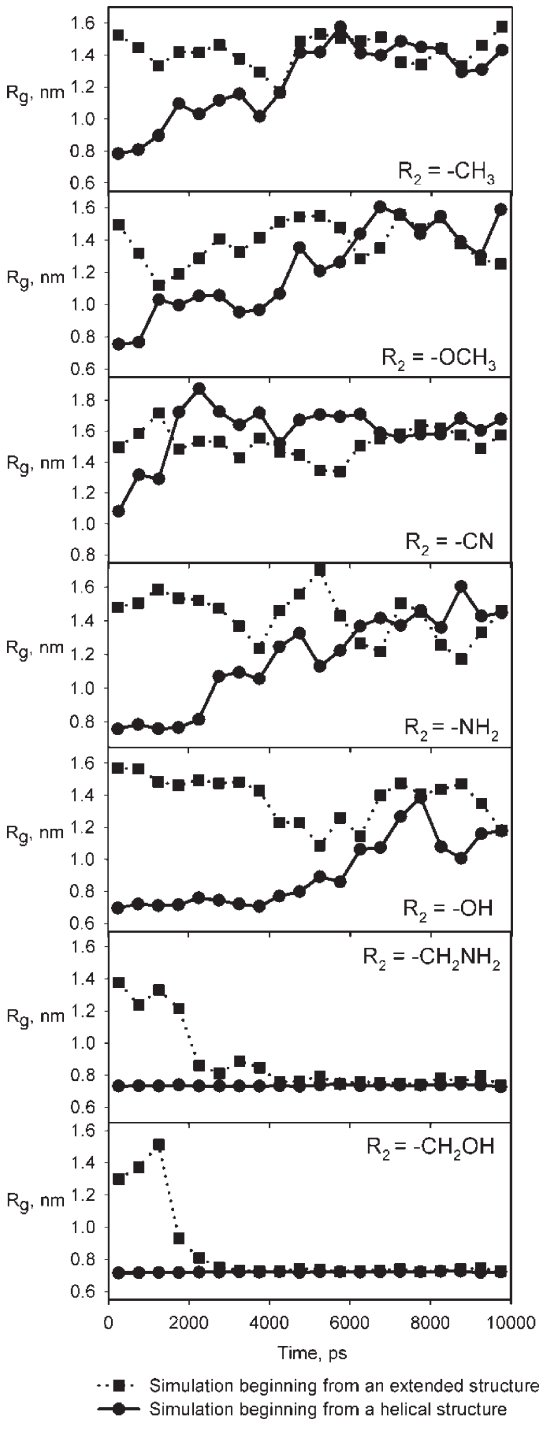

Figure 5. Time evolutions of R_g for seven mPPEs having hydrogen as the exohelix functional group (R_1 = −H) in acetonitrile. Data points are averaged over 500 ps and placed at the middle of the time range.

several mPPEs having only hydrogen in the exohelix functional group position (R_1 = H). The absence of exohelix functional groups in these oligomers allows for a better examination of the effect of the endohelix functional groups on their respective mPPE folding behaviors. Further, these may be compared to previous work in which we considered mPPEs with similar functional groups in the R_1 position instead of the R_2 position.[10] The simulation results for these mPPEs are shown in Figure 5 and summarized in Table 1.

Simulation results showed that five in seven mPPEs, those having functional groups R_2 = 6, 7, 8, 9, and 10 at the endohelix positions, were similar to those mPPEs with the same groups placed at exohelix positions (R_1). This indicates that the positions of the functional groups do not have a significant effect on their respective mPPE folding behaviors, suggesting that the effect of functional groups on π-stacking has stronger implications for secondary structure formation than does the placement of solvophobic and solvophilic interactions along the chains.

Table 1. REMD Simulation Results for Various Functionalized mPPEs in Acetonitrile[a]

	mPPE[b] folding behavior in acetonitrile	
functional group	(*endohelix*)[c] R_1 = H, R_2 = specified group	(*exohelix*)[d] R_1 = specified group, R_2 = H
6 (−CH_3)	1	1
7 (−OCH_3)	1	1
8 (−CN)	1	2
9 (−NH_2)	1	1
10 (−OH)	2	1
11 (−CH_2NH_2)	4	1
12 (−CH_2OH)	4	1

[a] Folding behaviors range from 1 to 4, with 1 indicating the least likelihood of folding into a helical conformation and 4 indicating the greatest. [b] The reported mPPE structures having specified functional groups either at *endohelix* (R_2) or *exohelix* (R_1) positions. Hydrogens were placed at the remaining functional group positions. [c] Based on REMD simulation results in this study. [d] On the basis of results in a previous study.[10]

The results for mPPEs having R_2 = −NH_2 and −OH demonstrate that the interturn HBs present in the helical mPPE structures at the beginning of the simulations were not sufficient to maintain the stability of the helices, causing the polymers to transition to less ordered conformations. Further, the absence of any helical secondary structure in simulations initialized with extended conformations demonstrates that the interturn HBs in these mPPEs are not able to stabilize the π-stacking pairs, should any occur.

As shown in Table 1, the two mPPEs capable of forming endohelix intraturn HBs (those with R_2 = −CH_2NH_2 or −CH_2OH) have completely different folding behaviors when compared to mPPEs with these groups at the exohelix position R_1, where group spacing prohibits the formation of intraturn HBs. At the exohelix position, these groups resulted in nonfolding (group 1) behavior, while at the endohelix position, they resulted in fully folding (group 4) behavior. These results again suggest that the ability to form intraturn HBs is a significant advantage in terms of secondary structure formation, when compared to interturn HBs.

For further investigation of the effect of intraturn HBs on secondary structure formation, REMD simulations were conducted for mPPEs having R_2 = −CH_2NH_2 or −CH_2OH in two additional solvents. We chose to examine their behavior in methanol, as this solvent is capable of forming hydrogen bonds that may disrupt the intraturn HBs, and in chloroform, which is known to deter helical structure formation in most mPPEs. The results are given in Figure 6, showing that the mPPEs were indeed able to fold in both methanol and chloroform. Although the transitions from extended conformations to helical conformations in chloroform were slower than those observed in acetonitrile or in methanol, results clearly show that the helical structure is stable and that the extended structure has a tendency to fold into the helix. Should this prediction be correct, we feel that an mPPE with the ability to fold in chloroform is a significant finding, since chloroform generally acts as a denaturing solvent for most known mPPEs.[1,10,35] Further, the polymers often have low solubility in solvents that promote folding into helical structures, and this result shows that it may be

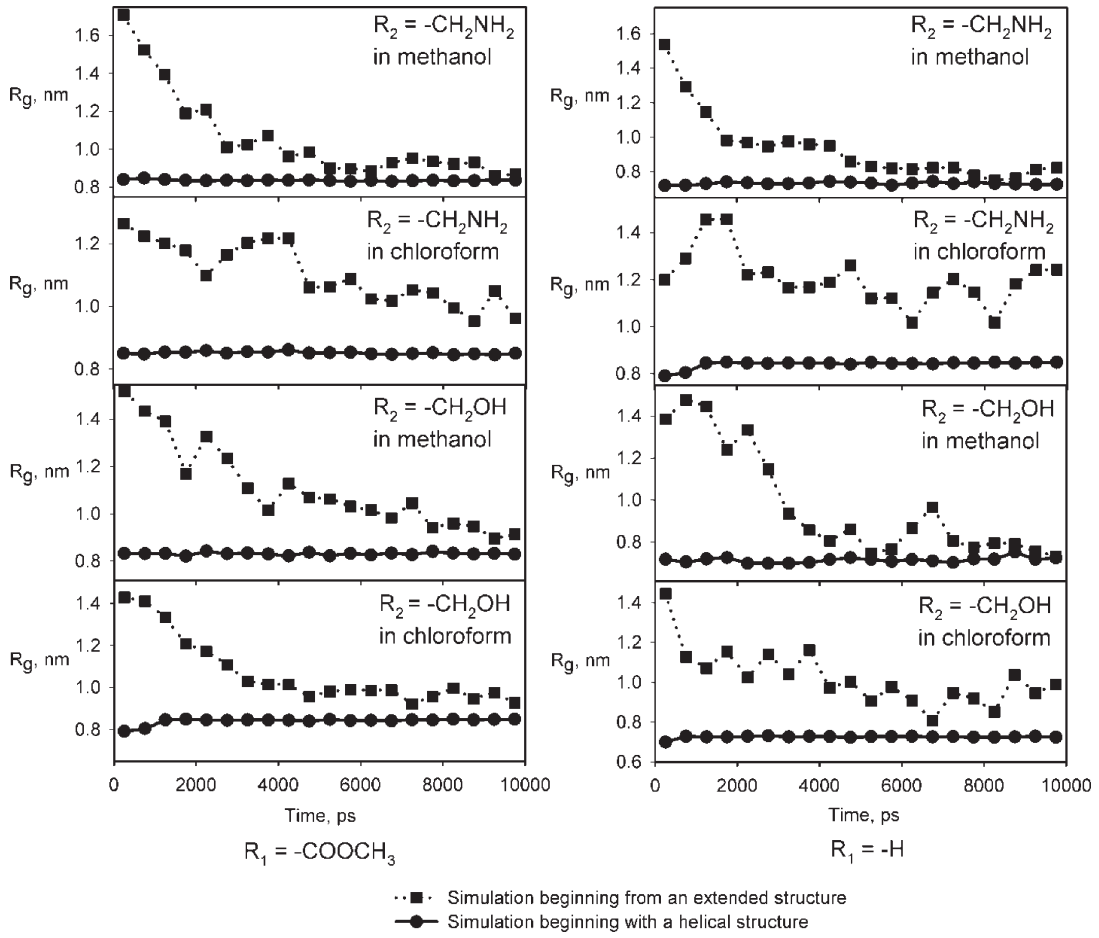

Figure 6. Time evolutions of R_g for mPPEs having $R_2 = -CH_2NH_2$ or $-CH_2OH$ in methanol and in chloroform. Plots on the left are for mPPEs with $R_1 = -COOCH3$, while plots on the right are for mPPEs with $R_1 = -H$. Data points are average over 500 ps and placed at the middle of the time range.

possible to obtain an mPPE/solvent system that exhibits high solubility in addition to secondary structure. Our result is not without precedent. An earlier study by Cary and Moore[15] showed that mPPE helices stabilized by hydrogen bonds are much more resistant to denaturation than similar mPPEs without hydrogen bonds. Our finding suggests that additional hydrogen bonds could strongly stabilize the mPPE helical structure even in denaturing solvents such as pure chloroform.

Analysis of Hydrogen Bonds for R_2 = 11 and 12. Time averages of the number of hydrogen bonds during REMD simulations are shown in Table 2. The average number of hydrogen bonds in mPPEs with $R_2 = -CH_2OH$ are always higher than those in mPPEs with $R_2 = -CH_2NH_2$, consistent with the higher level of electron affinity of oxygen (3.5) as compared to nitrogen (3.0). These affinities also reflect the strength of hydrogen bonds in those cases: hydrogen bonds between −OH and O are stronger than those between −NH and N. In most of the cases, we observed that the average numbers of intraturn HBs are higher than those for interturn HBs. This latter observation results from the interturn HBs being dependent on the distances between overlapping aromatic rings, meaning any disturbance in these distances could easily lead to interturn HB breaking. There is one exception to this rule, observed for mPPEs having $R_2 = -CH_2OH$ in acetonitrile. For this case, there are more interturn HBs than intraturn HBs, indicating the hydrogen bonds of mPPE helical structures are less likely to be disturbed than in methanol or chloroform.

When the exohelix (R_1) functional groups attached to these polymers are changed from −H to $-COOCH_3$, there is a significant change in the number of hydrogen bonds formed between the endohelix (R_2) functional groups in acetonitrile, methanol, and chloroform. Additionally, in acetonitrile and chloroform, which do not have the ability to form hydrogen bonds, the difference between the average number of intraturn HB and interturn HB is less apparent; on the other hand, in methanol, we observed a clear decrease in the number of interturn HBs, probably resulting from the competition between intramolecular hydrogen bonds between mPPE functional groups and intermolecular hydrogen bonds between mPPE functional groups and solvent molecules. When the exohelix functional group is set to hydrogen (R_1 = -H), this same trend is observed for the mPPE having $R_2 = -CH_2OH$. However, the mPPE having $R_1 = -H$ and $R_2 = -CH_2NH_2$ exhibited the opposite behavior, with the number of mPPE hydrogen bonds in methanol being slightly greater than in the other solvents.

Effect of Hydrogen Bonds on mPPE Folding Kinetics. To determine the effect of hydrogen bonds on folding kinetics, which cannot be obtained from REMD simulations, we conducted MD simulations initialized from the extended structures of the mPPEs having hydrogen bonds. These were carried out in three explicit solvents: acetonitrile, chloroform, and methanol. During these MD simulations, helical structures were observed after significantly shorter times than those reported in earlier studies[5,7] (see Table 2). In all cases studied, the mPPEs folded into a helical conformation

Table 2. Hydrogen Bond Analysis from MD Simulations of Four mPPEs (R_1 = $-COOCH_3$ or $-H$, R_2 = $-CH_2NH_2$ or $-CH_2OH$) in Three Solvents (Acetonitrile, Methanol, and Chloroform)[a]

	mPPE, R_1 = $-COOCH_3$, R_2 = $-CH_2NH_2$			mPPE, R_1 = $-COOCH_3$, R_2 = $-CH_2OH$		
property	acetonitrile	methanol	chloroform	acetonitrile	methanol	chloroform
total hydrogen bonds[b]	4.46	4.00	4.53	8.25	4.02	7.99
intraturn HBs	3.41	3.18	3.49	4.00	3.28	4.82
interturn HBs	1.00	0.70	0.95	4.09	0.54	2.76
bond length (nm)	0.22	0.22	0.22	0.20	0.20	0.20
average angles (deg)[c]	16.1	16.0	15.5	13.1	13.0	13.0
folding time (ns)[d]	10	8	< 5	17	35	10
	mPPE, R_1 = $-H$, R_2 = $-CH_2NH_2$			mPPE, R_1 = $-H$, R_2 = $-CH_2OH$		
property	acetonitrile	methanol	chloroform	acetonitrile	methanol	chloroform
total hydrogen bonds[b]	2.47	3.05	2.75	7.50	4.96	6.31
intraturn HBs	1.47	2.87	2.54	3.08	3.19	4.58
interturn HBs	0.99	0.16	0.20	4.39	1.74	1.56
bond length (nm)	0.23	0.22	0.23	0.20	0.20	0.21
average angles (deg)[c]	18.3	15.7	15.2	13.9	13.2	13.2
folding time (ns)[d]	23	12	10	18	9	< 5

[a] Values are averaged over 1 ns of REMD simulation. [b] The total number of hydrogen bonds includes all types of intraturn HBs and interturn HBs, but does not account for mPPE-solvent hydrogen bonding. [c] The HB angles are reported as donor−hydrogen−acceptor. [d] Time at which the first helical structure was observed during MD simulation.

in less than 35 ns, even less than 5 ns in several cases, especially for simulations in chloroform. Though these simulations were not repeated for multiple initial conformations of the uncoiled polymers, we do believe that the observed folding times are representative of average values based upon observations from the REMD simulations. Further, after the helical structure formed in each simulation, it was stable for the remainder of the simulation without any unfolding event, even when the total time was extended up to 100 ns, demonstrating that the helical structure is highly stable for these mPPEs.

Effect of Hydrogen Bonds on the Geometry of mPPE Helical Structures. Comparing the helical structures of mPPEs that form intramolecular hydrogen bonds to those that do not, there is an apparent difference: the former show much less regularity in the overlap of aromatic rings on adjacent turns as compared to the latter (see Figure 7). The regular helical structures formed by mPPE systems lacking the ability to form intramolecular hydrogen bonds are stabilized by a series of π-stacking interactions, leading to conformations in which the aromatics rings overlap directly upon one another. On the other hand, the mPPE systems that readily form intramolecular hydrogen bonds often do not maintain perfect overlap of the aromatic rings on adjacent turns. This results from it being more energetically favored for the mPPE to form hydrogen bonds between neighboring functional groups than to orient the polymer backbone in such a way as to optimize the weak π-stacking interactions between overlapping aromatic rings. In these polymers, a slight structural variation in the helical arrangement of the polymer backbone can significantly increase the number of intramolecular hydrogen bonds, which leads to a lower energy mPPE conformation and simultaneously maximizes the stability of the helical structure.

The difference in the mPPE helical structures with and without intramolecular hydrogen bonds is apparent when comparing the geometries of the two polymer types. The distance between adjacent helical turns is approximately 0.37 nm for the hydrogen bonded mPPE polymers, whereas the interturn distance increases to nearly 0.45 nm for mPPEs unable to form intramolecular hydrogen bonds. While the non-hydrogen bonded mPPEs have exactly six aromatics rings per turn, the studied hydrogen bonded structures have slightly less than this. Such a change in pitch allows for the formation of a small number of interturn HBs between functional groups attached to residues numbered n and $n + 5$ along the chain, whereas a non-hydrogen bonded mPPE with six rings per turn has π-stacking interactions only between residues numbered n and $n + 6$. The internal diameter of the hydrogen bonded helical mPPEs is 1.27 nm on average, as measured by the distance between two endohelix carbon atoms of two opposite aromatics rings in the helix. This is smaller than the internal diameter of the helical structures without hydrogen bonds, 1.35 nm, giving a further indication of a more compact structure for the hydrogen bonded polymers.

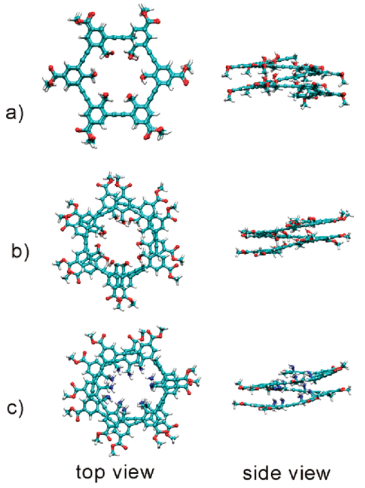

Figure 7. Representative helical structures of mPPEs functionalized with hydrogen bonding groups: (a) a hypothetical helical structure for an mPPE with R_1 = $-COOCH_3$ and R_2 = $-CH_2OH$, where there is optimal overlap of aromatic rings from adjacent turns; (b) the energy-minimized helical structure from REMD for the same oligomer as in part a; and (c) the energy-minimized structure from REMD for an mPPE with R_1 = $-COOCH_3$ and R_2 = $-CH_2NH_2$. Atom colors for oxygen, hydrogen, nitrogen and carbon are red, white, blue and cyan, respectively.

REMD Simulations for Hydrogen-Bonded mPPEs with Other Exohelix Functional Groups. As shown in our REMD results for mPPEs with R_2 = $-CH_2NH_2$ (11) and $-CH_2OH$ (12), the presence of hydrogen bonds can significantly stabilize the helical structure of mPPEs, such that they will fold under conditions in which folding would otherwise not be

expected to occur. Thus, in this section, we revisit some of our previous simulations study,[10] in which we considered different exohelix functional groups (R_1), by incorporating the endohelix functional groups R_2 = 11 and 12 in those polymers. These simulations were performed to ascertain whether hydrogen bonded endohelix functional groups can induce folding in mPPEs having exohelix functional groups that are known to inhibit folding.

REMD simulations of nine mPPEs (R_1 = 3 to 12, R_2 = $-CH_2-NH_2$ as shown in Figure 1) were conducted in explicit acetonitrile. Nearly identical results were observed for all of these mPPEs: all of them were predicted to fold into stable helices (group 4). These results suggest that mPPEs with endohelix hydrogen bonding may be modified using different exohelix functional groups—allowing them to be compatible with a wide range of solvents—while maintaining their stable helical structure.

Conclusion

The simulation results in this work present several insights into secondary structure formation in mPPEs, which may also have significant impact on the study of secondary structure in macromolecules in general. Our results indicate that the folding behavior of a given mPPE should be relatively unaltered by moving its external functional groups to positions inside the helical core. This suggests that the placement of solvophobic and solvophilic sites on the polymer is less important for mPPEs than the effect of aromatic substituents on π-stacking interactions. This finding differs substantially from our current understanding of secondary structure in biopolymers, for example, in which solvophobic/solvophilic interactions play a major role.

Our simulations also identified two general approaches that will aid in designing mPPEs for specific applications. First, we demonstrated that choosing an exohelix functional group with a known propensity to induce folding will result in considerable freedom when choosing an endohelix functional group. When the ester group was used (R_1 = 1), results showed that small endohelix (R_2) functional groups did not significantly change the folding behavior of their respective mPPEs. This indicates the feasibility of tailoring the environment inside the cavity of an mPPE, whether in terms of polarity, size, or other factors, without altering its folding behaviors. Second, we found that choosing hydrogen bonded endohelix (R_2) functional groups gives the same level of freedom in selecting exohelix (R_1) functional groups, without disrupting the helical secondary structure. Thus, prudent selection of the appropriate endohelix functional groups would ensure that an mPPE with desired exohelix functionality would exhibit a helical conformation in a wide range of solvents, as dictated by a given application.

Acknowledgment. This study was supported by the National Science Foundation, under award number CTS-0626143. The authors would like to acknowledge the support of the staff from Clemson University's Cyber Infrastructure Technology Integration (CITI) group, for administration and maintenance of the computers used in the work.

References and Notes

(1) Nelson, J. C.; Saven, J. G.; Moore, J. S.; Wolynes, P. G. *Science* **1997**, *277*, 1793–1796.
(2) Arnt, L.; Tew, G. N. *J. Am. Chem. Soc.* **2002**, *124*, 7664–7665.
(3) Adisa, B.; Bruce, D. A. *J. Phys. Chem. B* **2005**, *109*, 7548–7556.
(4) Adisa, B.; Bruce, D. A. *J. Phys. Chem. B* **2005**, *109*, 19952–19959.
(5) Elmer, S. P.; Park, S.; Pande, V. S., *J. Chem. Phys.* **2005**, *123*, 114902(0−14).
(6) Elmer, S. P.; Park, S.; Pande, V. S., *J. Chem. Phys.* **2005**, *123*, 114903(0−7).
(7) Elmer, S. P.; Pande, V. S. *J. Chem. Phys.* **2004**, *121*, 12760–12771.
(8) Elmer, S.; Pande, V. S. *J. Phys. Chem. B* **2001**, *105*, 482–485.
(9) Lee, O. S.; Saven, J. G. *J. Phys. Chem. B* **2004**, *108*, 11988–11994.
(10) Nguyen, H. H.; McAliley, J. H.; Batson, W. A.; Bruce, D. A. *Macromolecules* **2010**, *14*, 5232–5242.
(11) Tanatani, A.; Hughes, T. S.; Moore, J. S. *Angew. Chem., Int. Ed.* **2002**, *42*, 325–328.
(12) Prince, R. B.; Okada, T.; Moore, J. S. *Angew. Chem., Int. Ed.* **1999**, *38*, 233–236.
(13) Sinnokrot, M. O.; Sherrill, C. D. *J. Phys. Chem. A* **2003**, *107*, 8377–8379.
(14) Sherrill, D. C. Computations of Noncovalent pi-interactions. In *Reviews in computational chemistry*; Lipkowitz, K. B., Boyd, D. B., Eds.; Wiley: New York, 2009; Vol. *26*, pp 1−30.
(15) Cary, J. M.; Moore, J. S. *Org. Lett.* **2002**, *4*, 4663–4666.
(16) van der Spoel, D.; Lindahl, E.; Hess, B.; Groenhof, G.; Mark, A. E.; Berendsen, H. J. C. *J. Comput. Chem.* **2005**, *26*, 1701–1718.
(17) Lindahl, E.; Hess, B.; van der Spoel, D. *J. Mol. Model* **2001**, *7*, 306–317.
(18) Berendsen, H. J. C.; van der Spoel, D.; Vandrunen, R. *Comput. Phys. Commun.* **1995**, *91* (1−3), 43–56.
(19) Bekker, H.; Dijkstra, E. J.; Berendsen, H. J. C. *Supercomputer* **1993**, *10* (2), 4–10.
(20) Hess, B.; Bekker, H.; Berendsen, H. J. C.; Fraaije, J. *J. Comput. Chem.* **1997**, *18*, 1463–1472.
(21) Hukushima, K.; Nemoto, K. *J. Phys. Soc. Jpn.* **1996**, *65*, 1604–1608.
(22) GROMACS USER MANUAL. http://www.gromacs.org/Documentation/Manual.
(23) *High performance computing*. http:/citi.clemson.edu/hpc.
(24) Materials Studio, v 4.4, Accelrys Software Inc: San Diego, CA, 2008.
(25) Berendsen, H. J. C.; Postma, J. P. M.; Vangunsteren, W. F.; Dinola, A.; Haak, J. R. *J. Chem. Phys.* **1984**, *81*, 3684–3690.
(26) Parrinello, M.; Rahman, A. *J. Appl. Phys.* **1981**, *52*, 7182–7190.
(27) Humphrey, W.; Dalke, A.; Schulten, K. *J. Mol. Graphics* **1996**, *14*, 33–38.
(28) Jorgensen, W. L.; Maxwell, D. S.; Tirado-Rives, J. *J. Am. Chem. Soc.* **1996**, *118*, 11225–11236.
(29) Jorgensen, W. L. *J. Phys. Chem.* **1986**, *90*, 1276–1284.
(30) Jorgensen, W. L.; Madura, J. D.; Swenson, C. J. *J. Am. Chem. Soc.* **1984**, *106*, 6638–6646.
(31) van der Spoel, D.; van Maaren, P. J.; Larsson, P.; Timneanu, N. *J. Phys. Chem. B* **2006**, *110*, 4393–4398.
(32) Tsuzuki, S.; Fujii, A. *Phys. Chem. Chem. Phys.* **2008**, *10*, 2584–2594.
(33) Sinnokrot, M. O.; Sherrill, C. D. *J. Am. Chem. Soc.* **2004**, *126*, 7690–7697.
(34) Sinnokrot, M. O.; Valeev, E. F.; Sherrill, C. D. *J. Am. Chem. Soc.* **2002**, *124*, 10887–10893.
(35) Lahiri, S.; Thompson, J. L.; Moore, J. S. *J. Am. Chem. Soc.* **2000**, *122*, 11315–11319.

DOI: 10.1021/ma1023473

Macromolecules
ARTICLE

Thiol−Yne Click Polymerization: Regio- and Stereoselective Synthesis of Sulfur-Rich Acetylenic Polymers with Controllable Chain Conformations and Tunable Optical Properties

Jianzhao Liu,[†,#] Jacky W. Y. Lam,[†,#] Cathy K. W. Jim,[†,#] Jason C. Y. Ng,[†] Jianbing Shi,[†] Huimin Su,[‡] Kwok Fai Yeung,[‡] Yuning Hong,[†,#] Mahtab Faisal,[†,#] Yong Yu,[†,#] Kam Sing Wong,[‡] and Ben Zhong Tang*[,†,#,§]

[†]*Fok Ying Tung Research Institute, The Hong Kong University of Science & Technology (HKUST), Nansha, Guangzhou, China,* [‡]*Department of Chemistry, Institute of Molecular Functional Materials, and* [#]*Department of Physics, HKUST, Clear Water Bay, Kowloon, Hong Kong, China, and* [§]*Department of Polymer Science and Engineering, Zhejiang University, Hangzhou 310027, China*

Received October 14, 2010; Revised Manuscript Received November 22, 2010

ABSTRACT: The atom-economical alkyne polyhydrothiolations of aromatic diynes (**1**) and dithiol (**2**) catalyzed by rhodium complexes proceed smoothly under mild conditions at room temperature in a regioselective manner, producing sole anti-Markovnikov products of poly(vinylene sulfide)s (**3**) with high molecular weights (M_w up to 31500) and stereoregularities (*E* content up to 100%) in high yields (up to 95.2%). The stereostructures of the polymers are readily tuned by engineering control on the sequential addition of monomers during the polymerization process and postmanipulation by light irradiation. All the poly(vinylene sulfide)s are soluble in common organic solvents and exhibit good film-forming ability and high optical transparency. The functional pendants in **1** have endowed **3** with novel properties such as aggregation-enhanced emission characteristics, optical limiting to harsh laser pulses, and ceramization capability to semiconducting nanoparticles. The polymers are thermal and UV curable, enabling the fabrication of fluorescent photopatterns. Their thin films show high refractive indices (n_D = 1.75−1.70) and low optical dispersions (down to 0.006) at telecom important wavelengths. Their refractive indices vary with their stereostructures and can be modulated by UV irradiation.

Introduction

Synthesis of electronically active conjugated polymers (CPs) is a hot research topic because they offer great economic advantages as low-cost electronic conducting materials for the production of large-area flexible optoelectronic devices such as light-emitting diodes,[1] organic photovoltaic cells (OPVs),[2] and field-effect transistors.[3] The majority of the CPs are featured with a pure carbon backbone (Chart 1), examples of which include polyacetylene (**I**),[4] polyyne (**II**),[5] polyphenylene (**III**),[6] poly(phenylenevinylene) (**IV**),[1a] poly(phenyleneethynylene) (**V**),[7] and their miscellaneous derivatives. Integrations of heteroatoms, such as S and N, into the backbone of CPs may create new functionalities that are difficult, if not impossible, to access by the polymers with pure carbon-based skeletons. Particular interest is the synthesis of sulfur-containing CPs. Heretofore among all the CPs, polythiophene (**VI**) based organic OPVs have been found to exhibit outstanding performances in the conversion of light energy into electricity.[2,8] Poly(phenylene sulfide) (**VII**) is industrially important as both an engineering plastic and precursor to conducting polymer.[9] However, the variety of this kind of polymers is limited. Synthesis of new electronically active sulfur-rich polymers with novel structures and unique properties will be highly rewarding. It is envisioned that incorporation of carbon−carbon double bond in between the aromatic ring and the sulfur atom in the polymer repeat unit will generate new types of electronically active poly(vinylene sulfide)s [PVS's, **VIII**], in which the delocalization of π−electrons through the sulfur bridge will endow the polymers with an array of remarkable characteristics, such as light refractivity, nonlinear optical property, and so on.

Chart 1

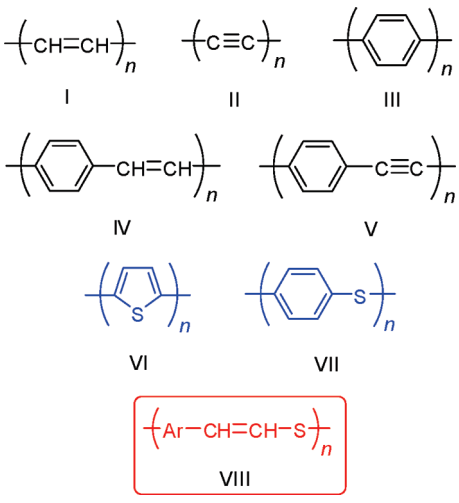

How to synthesize these PVS's is a challenging aspect. Retrostructural analysis leads us to find that alkyne hydrothiolation is a potential methodology for the synthesis of PVS's. The extensive studies on utilizing alkyne hydrothiolations for the construction of low molecular weight compounds in the past half century have

*Corresponding author. Telephone: +852-2358-7375. Fax: +852-2358-1594. E-mail: tangbenz@ust.hk.

 Published on Web 12/10/2010 © 2010 American Chemical Society

revealed that the reactions proceed through Markovnikov and anti-Markovnikov addition routes to produce regio- and stereoisomers with branched and linear structures (Scheme 1).[10−12] It is not an easy task to develop this atom-economic organic reaction into a successful polymerization technique for the synthesis of new functional PVS's. Several important issues should be carefully taken into consideration: choice of an efficient catalyst system, monomer scope and functional group tolerance, optimum reaction conditions, control of molecular weights, control of regio- and stereostructures, and solubility and processability of the resultant polymers. An ideal polymerization reaction is expected to be conducted in an efficient, precise, modular, and reliable manner under mild conditions. In other words, a click-type polymerization is the most desirable.

Our groups are interested in developing alkyne reactions into useful tools for the preparation of functional polymers. Employing monoynes, diynes, and triynes as monomers, we have successfully synthesized a large variety of polyacetylenes, polyarylenes, polydiynes, and polytriazoles with linear and hyperbranched structures and regio- and stereoregularities by metathesis, cyclotrimerization, coupling, and click polymerizations.[4d,g,13] Azide−alkyne polycycloaddition or "azido-click" polymerizations are of our particular interests because of their important roles in both polymer chemistry and macromolecular engineering. We have systematically investigated this click polymerization system in our previous work.[14] Inspired by the discovery of thiol−ene click reaction[15] and new endeavors to acetylenic polymer chemistry, the unexploited thiol−yne polyaddition or alkyne polyhydrothiolation becomes our current research focus because it has the potential to be developed into a new "thio-click" polymerization technique for the preparation of new electronically active sulfur-containing polymers.[16]

With these issues in mind, in this work, we devote our efforts to developing the rhodium-catalyzed alkyne hydrothiolation into an efficient polymerization technique for the preparation of new sulfur-rich polymers. The polymerizations of functional diynes (**1**) with dithiol (**2**) (Scheme 2) proceed in a regioselective manner under mild conditions at room temperature to give linear PVS's (**3**) with high molecular weights in high yields. The PVS's are rich in *E*-vinylene structure up to 100%. The stereostructures or chain conformations of the polymers not only can be in situ controlled by sequential addition of monomers but also postmanipulated by light irradiation. The resultant PVS's show excellent and tunable optical properties. This is the first example of transition metal-catalyzed regio- and stereoselective alkyne polyhydrothiolation or thiol−yne click polymerization reaction.

Scheme 1

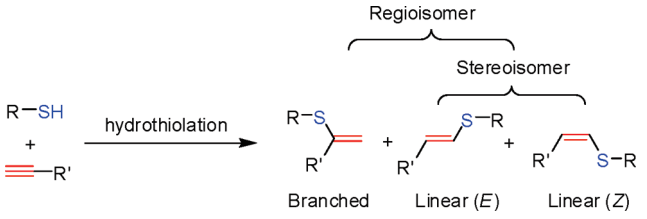

Results and Discussion

Polymer Synthesis. For a widely used catalytic polymerization system, the catalytic efficiency, functional group tolerance, and structural tunability are of the primary concerns. Unlike the limited monomer scope and low structural selectivity of the radical- and nucleophile-initiated alkyne hydrothiolations, the rhodium-catalyzed system is expected to work efficiently for a wide variety of functional monomers and possess high regio- and stereoselectivities. An $A_2 + B_2$ strategy was employed for the construction of linear PVS's. Four types of diyne monomers with different functionalities, viz. bis(4-ethynylphenyl)dimethylsilane (**1a**),[17] 4,4′-isopropylidenediphenyl bipropiolate (**1b**),[18] 1,1-dimethyl-2,5-bis(4-ethynylphenyl)-3,4-diphenylsilole (**1c**),[19] and (*E*,*E*)-1,1′-bis[2-(4-ethynylphenyl)vinyl]ferrocene (**1d**)[20] (Scheme 2), were synthesized and utilized to investigate the polymerization behavior. Aromatic dithiol 4,4′-thiodibenzenethiol (**2**) was commercially available and used as comonomer.

We first investigated the catalytic efficiencies of $Rh(PPh_3)_3Cl$ (C**1**), $[Rh(nbd)Cl]_2$ (C**2**), and $[Rh(nbd)(PPh_3)_2]^+PF_6^-$ (C**3**) for the polymerizations of model monomers **1a** and **2**. Table 1 lists the polymerization results. Under the same experimental conditions, all the Rh complexes can catalyze the alkyne polyhydrothiolation to give polymers with excellent solubility in common organic solvents. Among them, Wilkinson catalyst C**1** reveals the best result, producing a polymer with the highest molecular weight in the highest yield (Table 1, no. 1). The rhodium dimer C**2** and zwitterionic complex C**3** also work well for the polymerization and generate polymers with modest molecular weights in good yields (Table 1, nos. 2 and 3). All the polymers are synthesized in a regioselective manner to give PVS's with solely linear vinylene structures. Of particular interest is the polymer prepared by C**1**, which possesses 100% *E*-vinylene structure. On the contrary, polymers with *Z*-rich isomeric structures are obtained in C**2** and C**3**-catalyzed systems, but their *E*/*Z* ratios (34/66 and 39/61) are far from satisfactory. It can be seen that the stereoregularity of

Scheme 2

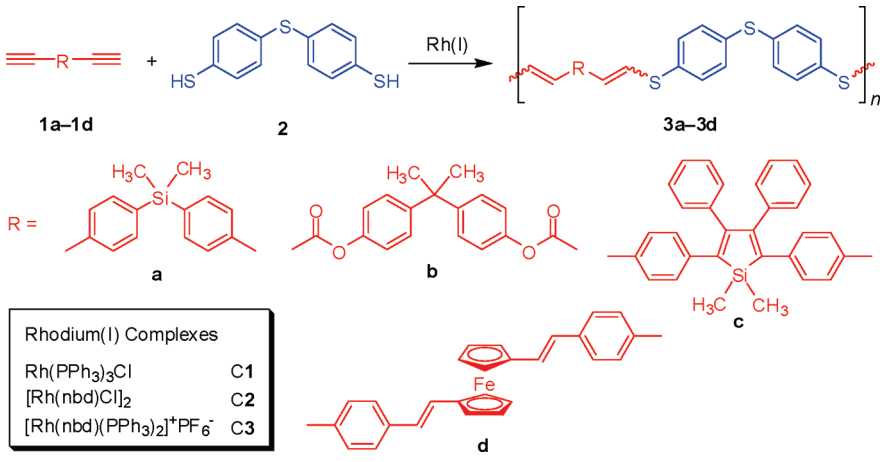

the PVS's can be readily tuned by the choice of different catalysts.

Since C**1** gives the best polymerization results, we thus utilized it to systematically study the polymerization behaviors of other monomer pairs. Delightfully, C**1** also performs well for the polymerizations of **1b**−**1d** and **2** and exhibits high tolerance to functional groups such as ester and metal moiety in the monomers. Increasing the monomer concentration from 50 to 100 mM and catalyst concentration from 1 to 2 mM help shorten the polymerization time by one-third and give polymers with comparable molecular weights (M_w's 22500 and 19500) and polydispersities (3.0 and 2.6) (Table 2, nos. One and 2). From the results given in Table 2, a general trend can be concluded that increasing the monomer concentration and the catalyst loading, and prolonging the reaction time play positive roles in producing polymers with higher molecular weights in higher yields. However, polymerizations at relatively high catalyst and monomer concentrations can lead to the formation of partially soluble or insoluble polymeric products (Table 2, nos. 5 and 8).

Control of stereoselectivity in the polymerization process is very important for the synthesis of polymers with precise structures. When monomers **1a** and **2** and catalyst **C1** are added simultaneously, PVS with 100% *E*-isomer structure was obtained. On the contrary, when one of the monomers and C**1** are first aged for 1 h followed by addition of another monomer, the resultant PVS's possess mixed stereostructures with *E*/*Z* ratios of 50/50 and 65/35 (Table 2, nos. 3 and 4). This finding offers a good strategy to control the stereoregularity of the PVS's. Interestingly, variation of the diyne from **1a** to **1b** and **1c** leads to no stereoselectivity and gives polymers **3b** and **3c** with *E*/*Z* ratios of 50/50. When the ferrocene-containing diyne (**1d**) was employed for the polymerization, PVS with high *E*-isomeric unit (90%) was obtained. Systematic study of the electronic and steric effects of the monomers on the regio- and stereoselectivities of the polymerizations is currently underway in our group.

The Rh-catalyzed alkyne polyhydrothiolation shows high efficiency and functionality tolerances, enabling us to synthesize different PVS's with high molecular weights in high yields under mild conditions. The polymerizations can proceed in regio- and stereoselective manners and PVS's with perfect *E*-isomeric structures can be produced. The sequence of monomer addition during the polymerization process is first used to control the stereoregularity of the PVS's. All these features meet the criteria of a click-type polymerization. Thus, this thiol−yne polymerization has enriched the family of click polymerization.

Structural Characterization. The polymers are characterized by spectroscopic methods and satisfactory results corresponding to their molecular structures are obtained (see Experimental Section for detailed analysis data). An example of the IR spectra of polymer **3a** and its monomers **1a** and **2** is given in Figure S1 in the Supporting Information. The S−H stretching vibration of **2** is observed at 2557 cm^{-1}, while the ≡C−H stretching of **1a** occurs at 3271 cm^{-1}. These peaks are also observed in the spectrum of **3a** but their intensities become much weaker. Instead, a new peak associated with C=C stretching vibration is emerged at 1594 cm^{-1}, indicating that the triple bonds of **1a** and the mercapto groups of **2** have been transformed to vinyl sulfide units in **3a** by the polymerization reaction.

To provide spectroscopic evidence that the stereoregularity of the polymers can be tuned by engineering control, we analyzed the NMR spectra of the associated polymers and their monomers. Figure 1 shows the ^{1}H NMR spectra of monomers **1a** and **2** and their polymers **3a** prepared via different modes of monomer addition. The acetylene and thiol protons of monomers **1a** and **2** resonate at δ 3.18 and 3.46, respectively, which almost or completely disappear in the spectrum of **3a**. New peaks assigned to the proton resonances of the linear vinylene structures are observed. Because of the different chemical envirorments in different stereoisomers, the *E*- and *Z*-vinylene protons can be discerned and the *E*/*Z* ratio can be calculated from their integrals. Simultaneous feeding of monomers **1a** and **2** and catalyst C**1** leads to the formation of 100% *E*-**3a** exhibiting characteristic olefin proton signals at δ 6.86 and 6.73 (Figure 1E). On the contrary, polymers prepared by sequential addition of monomers show resonance at δ 6.86 and 6.73, and δ 6.59 and 6.46 for the *E*- and *Z*-olefin protons, respectively (Figure 1, parts C and D). The *E*/*Z* ratio is

Table 1. Polymerizations of Monomers 1a and 2 with Different Rhodium Catalysts[a]

no.	catalyst	yield (%)	*E*/*Z*	*S*[b]	M_w[c]	M_w/M_n[c]
1	C**1**	90.3	100/0	√	19 500	2.6
2	C**2**	71.3	34/66	√	11 900	3.3
3	C**3**	72.5	39/61	√	8 700	2.4

[a] Carried out in 1,2-dichloroethane at room temperature under nitrogen for 24 h; $[M]_o$ = 100 mM, [cat] = 2 mM. [b] Solubility (*S*) tested in common organic solvents such as THF, toluene, DCM, and chloroform; √ = completely soluble. [c] Estimated by gel-permeation chromatography (GPC) in THF on the basis of a polystyrene calibration; M_w = weight-average molecular weight; M_n = number-average molecular weight; M_w/M_n = polydispersity index.

Table 2. Polymerizations of Monomers 1 and 2 Using $Rh(PPh_3)_3Cl$ as Catalyst [a]

no.	polymer	$[M]_o$ (mM)	[cat] (mM)	*t* (h)	yield (%)	*E*/*Z*	*S*[b]	M_w[c]	M_w/M_n[c]
1	**3a**	50	1	36	88.2	100/0	√	22 500	3.0
2	**3a**	100	2	24	90.3	100/0	√	19 500	2.6
3	**3a**[d]	100	2	24	93.2	50/50	√	13 900	3.2
4	**3a**[e]	100	2	24	95.2	65/35	√	13 500	3.5
5	**3a**	100	4	24	91.7	100/0	Δ	31 500	3.3
6	**3b**	50	1	36	92.3	50/50	√	9500	3.3
7	**3b**	50	2	36	91.6	50/50	√	16 400	5.0
8	**3b**	100	1	18	96.5		×		
9	**3c**	50	1	4	83.8	50/50	√	4000	1.6
10	**3c**	50	1	18	91.6	50/50	√	13 300	3.4
11	**3d**	50	1	18	82.5	87/13	√	5300	2.2
12	**3d**	50	1	36	85.6	86/14	√	7000	3.2

[a] Carried out in 1,2-dichloroethane at room temperature under nitrogen. [b] Solubility (*S*) tested in common organic solvents such as THF, toluene, DCM, and chloroform; √ = completely soluble, Δ = partially soluble, × = insoluble. [c] Estimated by gel-permeation chromatography (GPC) in THF on the basis of a polystyrene calibration; M_w = weight-average molecular weight; M_n = number-average molecular weight; M_w/M_n = polydispersity index. [d] Monomer **2** and catalyst were first aged for 1 h and then reacted with **1a** for 23 h. [e] Monomer **1a** and catalyst were first aged for 1 h and then reacted with **2** for 23 h.

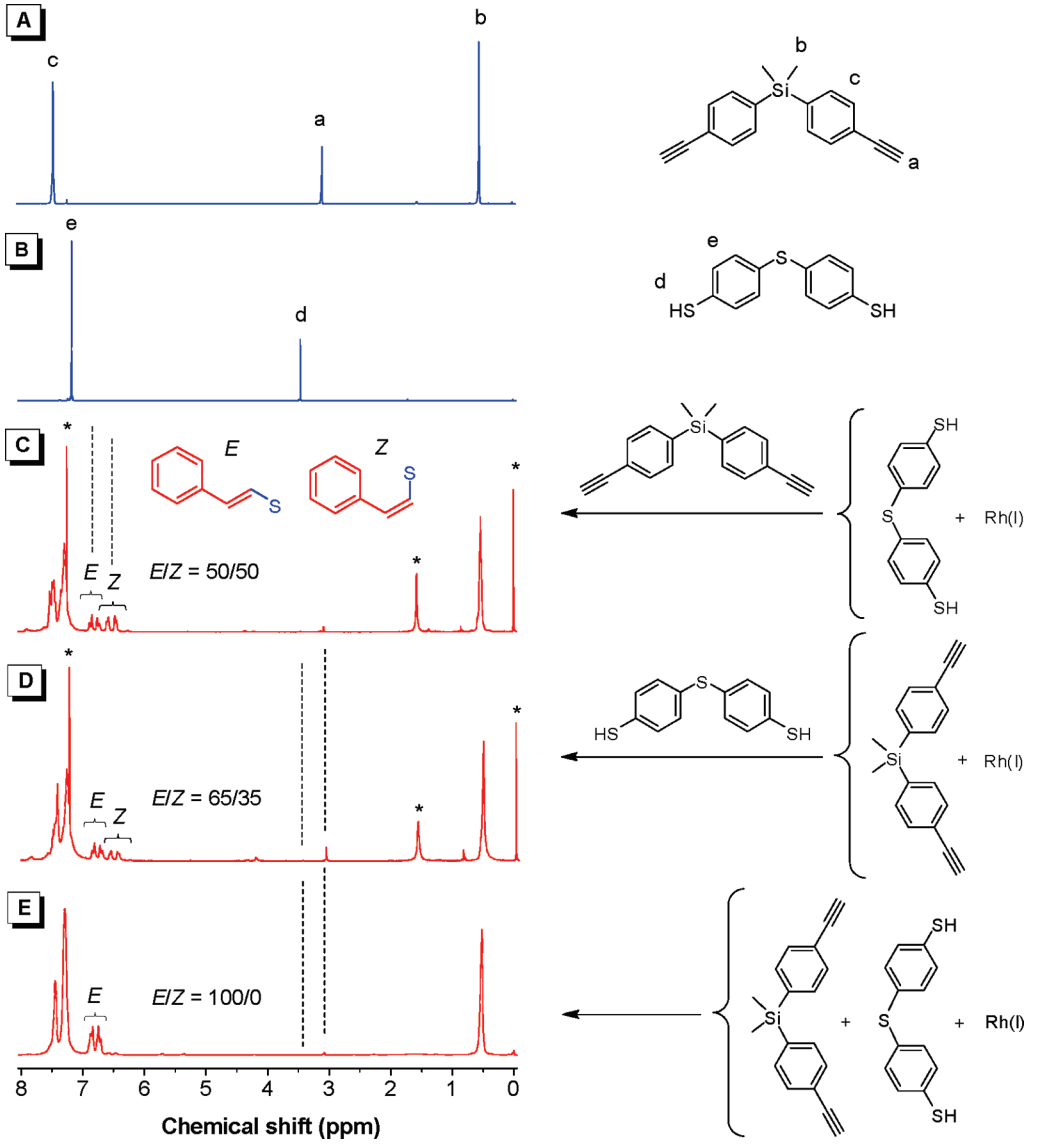

Figure 1. ^{1}H NMR spectra of monomers (A) **1a** and (B) **2** and (C−E) polymers **3a** in $CDCl_3$ (samples taken from Table 2, nos. 2−4). The solvent peaks are marked with asterisks. Abbreviation: Rh(I) = $Rh(PPh_3)_3Cl$.

calculated to be 50/50 when **2** is added prior to **1a**, while a ratio of 65/35 is obtained under the opposite condition.

The ^{13}C NMR spectrum of polymer **3a** shows no resonance peaks of the acetylenic carbons of monomer **1a** at δ 83.8 and 78.1 (Figure 2). New peaks corresponding to the resonances of the olefinic carbons are observed at low fields, due to the conversion of the acetylene triple bonds of **1a** into the double bonds in **3a**. This result is well consistent with that from the ^{1}H NMR analysis, further confirming the occurrence of the alkyne polyhydrothiolation.

Switchable *E*−*Z* Photoisomerization. Structure and function are closely related in the fields of polymer chemistry and physics. Subtle manipulation of the chain conformation can give rise to new materials with dramatically different properties. The main chains of PVS's contain many carbon−carbon double bonds, which offer the possibility to tune the chain conformation by *E*−*Z* isomerization. We have already shown that the stereostructures of the PVS's can be manipulated by varying the addition mode of monomers during the polymerization. Furthermore, we are able to postmanipulate the chain conformation by external stimuli.

Since light irradiation is a convenient technique for the isomerizations of carbon−carbon[21] and nitrogen−nitrogen[22] double bonds, we thus intended to induce the isomerization of **3a** by UV and visible lights. The isomerization process was monitored by measuring the change in the ^{1}H NMR spectrum with time and 100% *E*-**3a** was selected as the starting polymer. As shown in Figure 3, the *E*−*Z* isomerization occurs upon UV irradiation. With an increase of the irradiation time, the *E* content of the polymer decreases. The isomerization process proceeds quickly and comes to equilibrium at an *E*/*Z* ratio of 42/58. Afterward, visible light was applied to induce the reverse *Z*−*E* isomerization. It can be seen that the content of *E*-isomer gradually recovers with lengthening the irradiation time. Although the *E*-content cannot be fully reinstalled, this *E*−*Z* isomerization is switchable from the *E*/*Z* ratio of ~90/10 to 40/60 and vice versa. It is noteworthy to mention that **3a** exhibits good stability and does not suffer from side reactions and chain scission during the whole isomerization cycle. This switchable *E*−*Z* photoisomerization provides us a convenient tool to tune the stereostructures and further the chain conformations of the polymers. The properties of the polymers, especially the optoelectronic properties, will be altered significantly accompanying

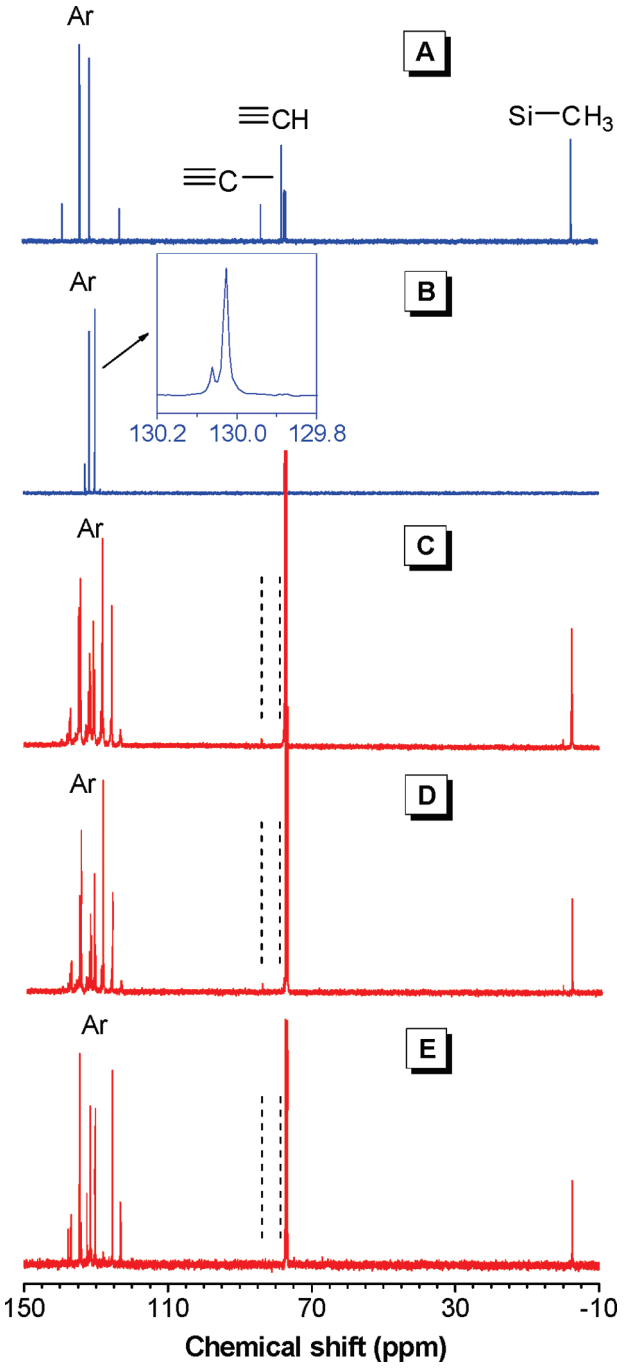

Figure 2. ^{13}C NMR spectra of monomers (A) **1a** and (B) **2** and (C−E) polymers **3a** in $CDCl_3$ (samples taken from Table 2, nos. 2−4). The solvent peaks are marked with asterisks.

the conformational change. This methodology is expected to provide us a gating tool in manipulating the functional properties of the polymers. For example, the *E*−*Z* photoisomerization of a helical PVS will vary its helical pitch and related potential mechanical response, such as axial expansion/contraction. This finding stimulates us to further develop optically active PVS-based foldamers.

Thermal Properties. The thermal properties of the PVS's are evaluated by thermogravimetric (TGA) and differential scanning calorimetric (DSC) analyses. All the polymers exhibit excellent thermal stability. As can be seen from Figure 4, the temperatures for 5% weight loss or the degradation temperatures (T_d) of the polymers are in the range from 310 to 432 °C under nitrogen, indicative of their strong resistance to thermolysis. Except for **3b**, all the polymers carbonize in yields higher than 25 wt % when pyrolyzed at 800 °C. We are interested in utilizing metal-containing polymer as precursors for ceramics by thermal pyrolysis. Pyrolysis of ferrocene-functionalized **3d** gives ceramic C**3d** in a good yield. Analyses by SEM, TEM, XPS, EDX, and XRD demonstrate that the ceramics comprise Fe_7S_8 nanocrystallites wrapped by carboneous shell (Figures S2 and S3 and Table S2, Supporting Information). As an alternative to the inorganic synthetic methods, this serves as a new path to make uniform semiconducting Fe_7S_8 nanoparticles. Additionally, polymer **3d** possesses the advantage of good solution processability, which offers low shape fabrication cost.

The DSC thermograms of all the polymers (Figure 5) recorded during the first heating cycle exhibit broad exothermic peaks centered at ~170 and ~340 °C. Since PVS's contain many carbon−carbon double bonds, the peak spanning from 100 to 200 °C should be ascribed to thermally induced olefin polymerization of the polymers. To confirm this, we have done control experiments in which the polymers were heated to 200 °C. We found that the resultant polymers suffer no degradation and become insoluble. Additionally, no such peak was detected during the second heating scan, indicating that all the polymers have been cured after the first heating cycle. Since the T_d's of PVS's occur at 310−432 °C, it is thus reasonable to assign the second transition peak at ~340 °C to the thermal decomposition of the polymers.

Optical Properties. The monomeric units of **3c** and **3d** are linked together through vinylsulfide bridge, which has enhanced their electronic communications and hence the conjugation of the polymers. Indeed, **3c** and **3d** absorb lights well extended to the visible spectral region and their transmission spectra are bathochromically shifted from their diyne monomers (Figure 6).[19,20] On the contrary, **1a** and **1b** are weakly conjugated due to the presence of electronically saturated dimethylsilylene and isopropylene linkages. Thus, their polymers **3a** and **3b** absorb little visible light and allow almost all the light at wavelengths longer than 400 nm to transmit through. This suggests that they possess high optical transparency and are thus promising candidate materials for advanced photonic applications.

Previous studies have shown that acetylenic polymers with numerous aromatic rings[23] and ferrocene groups[24] show optical limiting responses to harsh laser pulses. It is thus worthy to investigate how our polymers, particularly **3c** and **3d**, response to harsh optical pulses. Figure 7 shows the optical limiting performances of **3c** and **3d** in $CHCl_3$ with different concentrations. The transmitted fluence of the solution of **3d** with a concentration of 0.1 mg/mL increases linearly with the incident fluence but starts to deviate at a value of 0.54 J/cm^2 (defined as limiting threshold; that is, the incident fluence at which the output fluence starts to deviate from linearity). With a further increment of the incident fluence, the transmitted fluence reaches a plateau and is saturated at ~0.41 J/cm^2 (defined as limiting amplitude; that is, the maximum output intensity). At the same linear transmittance, its optical limiting threshold and limiting amplitude are comparable to those of C_{60}, a well-known optical limiter.[25] The limiting effect is affected by concentration and solutions with higher concentrations exhibit better performances. For example, the limiting threshold of the sample decreases from 0.54 to 0.29 J/cm^2 and the limiting amplitude changes from 0.41 to 0.23 J/cm^2 when the solution concentration is increased from 0.1 to 0.2 mg/mL. Accordingly, the solutions of **3d** with concentrations of 0.2 and 0.3 mg/mL show superior optical limiting performances to that of C_{60}. Polymer **3c** exhibits a similar

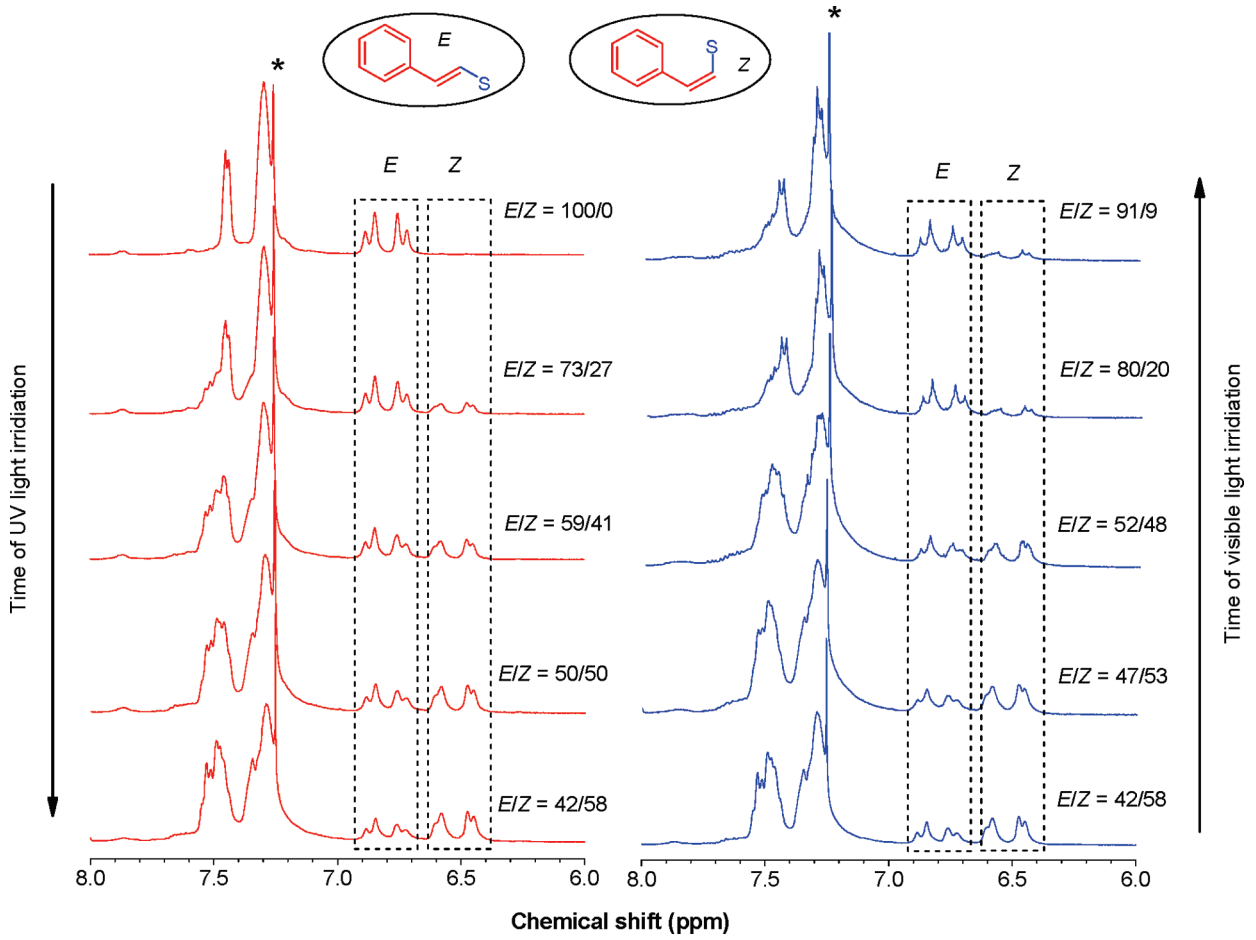

Figure 3. Time course study on the isomerization of polymer **3a** induced by UV and visible lights in $CDCl_3$ (sample taken from Table 2, no. 2). The solvent peaks are marked with asterisks.

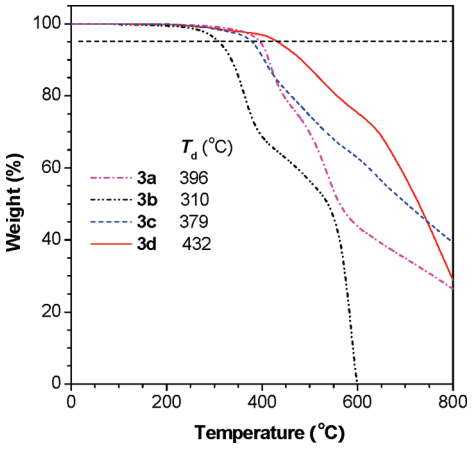

Figure 4. TGA thermograms of polymers **3a**−**3d** (samples taken from Table 2, nos. 2, 6, 9, and 11). T_d denotes the temperature for 5% weight loss.

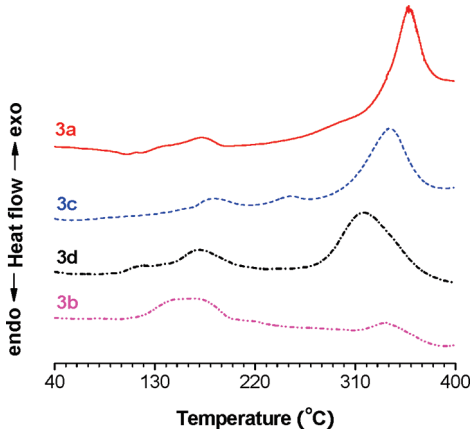

Figure 5. DSC thermograms of polymers **3a**−**3d** recorded during the first heating cycle at a scan rate 10 °C/min under nitrogen (samples taken from Table 2, nos. 2, 6, 9, and 11).

concentration-dependent optical limiting behavior but does not behave as well as **3d**.

Aggregation-Enhanced Emission. Development of highly efficient light-emitting conjugated polymers in the solid state is of great value. However, many of the conventional conjugated polymers suffer from the notorious effect of aggregation-caused quenching in the condensed phase. We have recently observed an exactly opposite effect, namely aggregation-induced emission (AIE): propeller-shaped molecules such as siloles and tetraphenylethenes are nonemissive in the solution state but are induced to emit intensively by aggregate formation.[26] To extend our AIE research program from low molecular weight to polymeric systems, we incorporated AIE-active monomeric building blocks into the polymer skeletons by acetylenic polymerization techniques. Silole diyne monomer **1c** is an AIE luminogen and its polymer **3c** is thus expected to be AIE-active.

Figure 8 shows the photoluminescence (PL) spectra of **3c** in THF and THF/water mixtures with different volume fractions of water. In pure THF, **3c** is somewhat luminescent

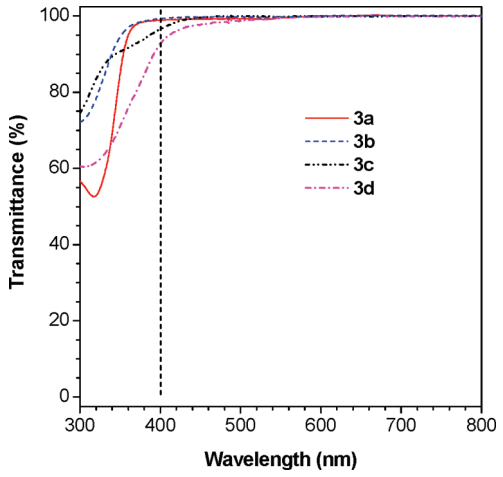

Figure 6. Light transmission spectra of polymers **3a**−**3d** (samples taken from Table 2, nos. 2, 6, 9, and 11). Concentrations (μM): 9.7 (**3a**), 8.6 (**3b**), 7.0 (**3c**), and 7.3 (**3d**).

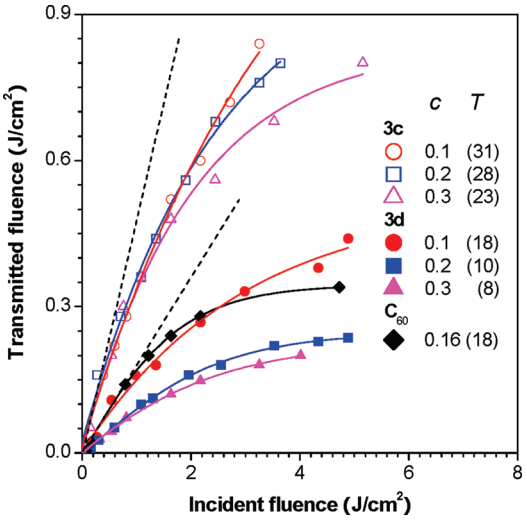

Figure 7. Optical limiting responses to 35 ps, 532 nm optical pulses, of $CHCl_3$ solutions of **3c** and **3d** with different concentrations (samples taken from Table 2, nos. 9 and 11). Abbreviations: c = concentration (mg/mL); T = transmittance (%).

and emits at ~520 nm, which is red-shifted from that of **1c** by ~30 nm.[19] This indicates the extensive conjugation in the polymer due to the electronic communication between the electron-accepting silole and the electron-donating phenylsulfide units through the newly formed carbon−carbon double bond bridge. Addition of water into the THF solution of **3c** has induced its chains to aggregate, which redshifts and enhances its light emission. The higher the water content, the stronger is the light emission, showing a novel phenomenon of aggregation-enhanced emission (AEE) characteristic. The highest emission intensity is recorded at 80 vol % water fraction, which is ~2.6-fold higher than that in pure THF. The emission intensity decreases slightly when the water fraction is changed from 80 to 90 vol %. This may be attributed to the reduction of the effective polymer concentration induced by the precipitation of the large aggregates.

The AEE effect is rationalized by the restriction of energy-dissipating intramolecular motions of the luminogens in the condensed phase. The somewhat luminescence of polymer **3c** in pure THF solution can be interpreted from the fact that its silole units are knitted together by covalent bonds, which

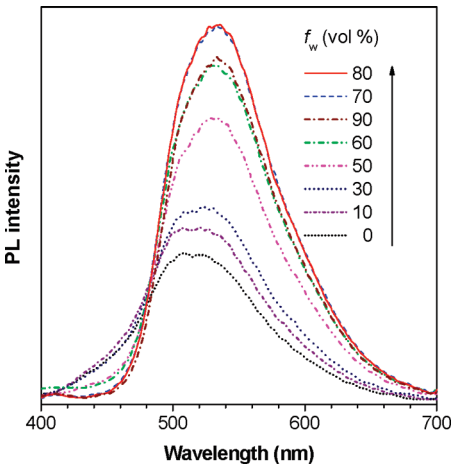

Figure 8. PL spectra of **3c** (sample taken from Table 2, nos. 9) in THF/water mixtures with different volume fractions of water (f_w). Polymer concentration: 5 μg/mL. Excitation wavelength (nm): 370.

have restricted their motions to some extent and activated the radiative decay in the solution state. The intramolecular motions of the luminogens are further restricted in the aggregate state due to the physical constraint, which blocks the nonradiative path and thus strengthens the light emission. It is important to mention here that aggregation will induce short-range excitonic coupling or charge transfer and quench the light emission. Whether the aggregation weakens or strengthens light emission is decided by the competition between these two antagonistic physical effects. Clearly, the positive factor dominates in the light emission process of **3c**. We believe that the intrinsic propeller-shaped silole unit has efficiently hampered the close packing of the polymer chains, which greatly reduces the events of the negative intermolecular excitonic coupling.

Fluorescent Photopatterning. As an alternative to thermal curing method, the UV light-directed curing technique can be operated flexibly and may be a convenient way to precisely control the curing reaction and facilitate the fabrication of patterns. Since polymer **3c** possesses a good film-forming ability and is both photosensitive and highly emissive in the solid state, it is thus an excellent candidate for the fabrication of luminescent patterns. The generation of fluorescent patterns is of great importance for the constructions of photonic and electronic devices and biological sensing and probing systems such as LCD, OLED, and medicinal diagnostic biochip.[27] When a thin film of **3c** spin-coated on a silicon wafer was irradiated with UV light for 15 min through a copper mask, the exposed region was cross-linked and hence insoluble. Without any development, a two-dimensional photoresist pattern was fabricated. The good quality of the pattern (sharp line edges, uniform film thickness, etc.) is clearly seen under normal laboratory lighting (Figure 9A), although the photolithography process has yet been optimized. Upon photoexcitation, the unexposed square parts of the pattern emit bright green light, while the exposed patterned lines suffer from strong photo-oxidative bleaching and are thus not emissive (Figure 9B).

Light Refractivity. Macroscopically processable polymers with high refractive indices (RI's) are promising candidate materials for an array of practical applications, including lenses, prisms, optical waveguides, memories, and holographic image recording systems.[28] The RI values for most of conventional polymers lie in between ~1.40 and ~1.65, with the majority located in a very narrow range of ~1.5−1.6. For example, the RI values of poly(methyl

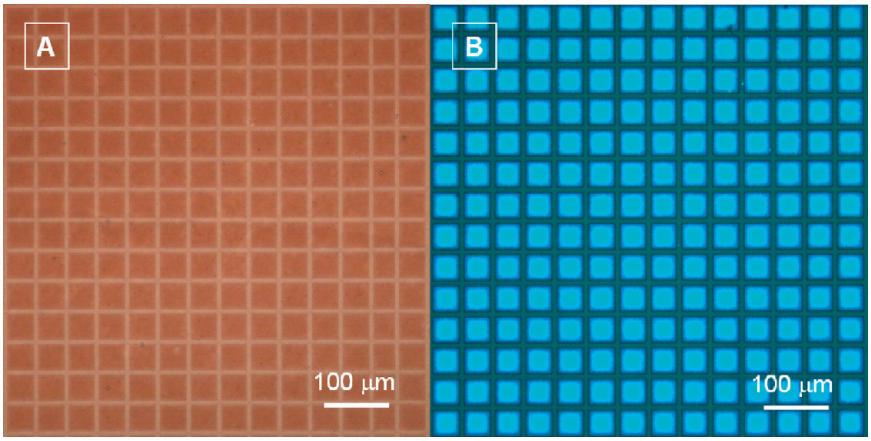

Figure 9. Two-dimensional photoresist pattern generated by UV irradiation of a thin film of **3c** on a silicon wafer through a copper mask. The photographs were taken under (A) normal laboratory lighting and (B) UV illumination.

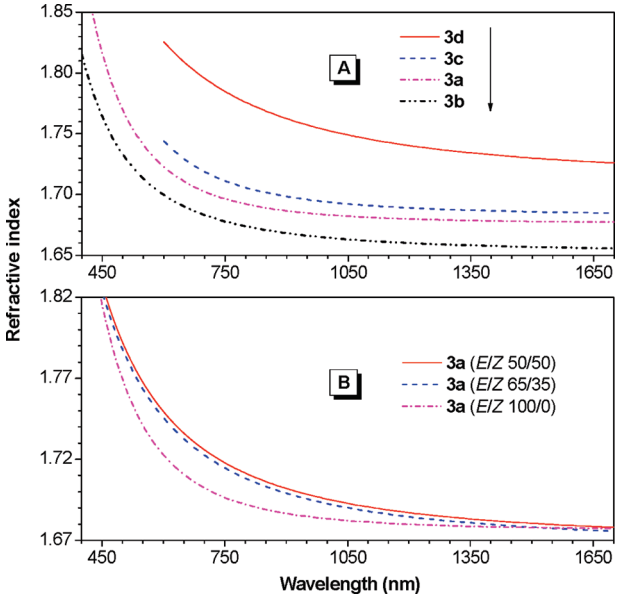

Figure 10. Light refraction spectra of thin solid films of (A) polymers **3a**−**3d** (samples taken from Table 2, nos. 2, 6, 9, and 11, respectively) and (B) polymers **3b** with different *E*/*Z* ratios (samples taken from Table 2, nos. 2−4).

methacrylate), polycarbonate, and polystyrene at 589.3 nm are 1.491, 1.581, and 1.590, respectively.[29] Very few polymers exhibit RI values higher than 1.70. The low refractivities of the existing polymers have greatly limited the scope of their photonic applications and largely retarded the progress in the development of organic photonic systems.

Theory predicts that macromolecules containing groups or units with high polarizabilities and small molecular volumes may show high light refractivities. From the structural point of view, our PVS's comprise polarizable aromatic rings, ester groups, metal elements, and sulfur atoms and thus may show high refractive indices. Indeed, polymers **3a** and **3b** show high RI values of 1.8971−1.6773 and 1.8150−1.6557 in a wide spectral region 400−1700 nm, respectively (Figure 10A). Because of their long conjugation and hence absorption at the visible spectral region, we have difficulty in fitting the light refraction curves of **3c** and **3d** at wavelengths less than 600 nm. Their RI values in the spectral region 600−1700 nm are measured to be 1.7440−1.6848 and 1.8258−1.7260, respectively. All the polymers show RI values higher than 1.65 from visible to infrared light region, which are much higher than those of the conventional polymers mentioned above. Pure organic polymers with such high RI values are very rare. The RI data of the polymers are summarized in Table 3. The RI values of polymers **3a** and **3b** at 589.3 nm or Fraunhofer D line (n_D) are 1.7262 and 1.7023, respectively. At the telecommunication wavelength of 1550 nm, the PVS's show RI values (> 1.65) with an order of **3d** (1.7289) > **3c** (1.6856) > **3a** (1.6777) > **3b** (1.6565). Such trend is correlated with the order of their electronic unsaturation, revealing that PVS's with high higher conjugation show higher RI values due to their stronger polarizabilities. The difference between the RI values of **3d** and **3b** is as large as 0.0742, thanks to the additional contribution of its metal-containing ferrocene units. These results highlight the feature of high refractivity of our PVS's and manifest their manipulability by molecular engineering endeavors of their molecular structures. No or little birefringence is detected, indicative of the amorphous nature of their thin solid films.

Interestingly, the RI value of **3a** is sensitive to its stereoregularity. Polymers **3a** with *E*/*Z* ratios of 50/50 and 65/35 gives n_D's of 1.7530 and 1.7492, respectively, which are higher than that (n_D = 1.7262) of pure *E*-isomer (Figure 10B). This result offers the possibility to tune the RI values of PVS's by controlling their stereoregularities through both engineering control during the polymerization process and postmanipulation by light irradiation.

RI Modulation. RI modulation is a key technology in optical data storage devices, such as compact discs, digital versatile discs, blue ray discs, and holographic recording materials.[30] Development of photosensitive polymers with tunable refractive index is highly rewarding due to the increasing demand for such materials.[31] Since our PVS's contain many photosensitive groups, such as vinyl and ester groups, their RI values are anticipated to be tuned by UV irradiation and thermal treatment, which may result in cross-linking reactions of the photoreactive double bonds in the PVS's. For polymer **3b** with ester groups, photo-Fries rearrangement will also be involved in its cross-linking mechanism. In other words, we can transform these processable linear PVS's into thermosets. Indeed, the polymers become insoluble upon UV irradiation, confirming the occurrence of the cross-linking reactions. Because of the structural variation, the RI values of the polymers will be changed accordingly. The contrast difference between the exposed and unexposed parts of the fluorescent photopattern of **3c** is a typical example demonstrating its RI tunability. Figure 11 gives a quantitative picture to reveal the RI changes of polymers **3a**−**3d** before and after UV irradiation for 15 min.

Table 3. Refractive Indices (n_D and n_{1550}), Abbé Numbers (ν_D), Revised Abbé Numbers (ν'), and Optical Dispersions (D and D') of Thin Films of Polymer 3a−3d [a]

no.	polymer	n_D	Δn_D [b]	n_{1550}	Δn_{1550} [b]	ν_D	D	ν'	D'
1	**3a** (E/Z 50/50)	1.7530		1.6798		11.7	0.0854	55.2	0.0181
2	**3a** (E/Z 65/35)	1.7492		1.6774		16.5	0.0606	56.3	0.0178
3	**3a** (E/Z 100/0)	1.7262		1.6777		10.3	0.0971	161.6	0.0062
4	**3a** (E/Z 65/35) (UV)[c]	1.6437	−0.1055	1.5943	−0.0831	16.9	0.0592	64.2	0.0156
5	**3b**	1.7023		1.6565		13.7	0.0730	104.5	0.0096
6	**3b** (UV)[c]	1.6608	−0.0415	1.6198	−0.0367	17.7	0.0565	90.2	0.0111
7	**3c**			1.6856				109.1	0.0092
8	**3c** (UV)[c]			1.5635	−0.1221			117.7	0.0085
9	**3d**			1.7289				38.5	0.0260
10	**3d** (UV)[c]			1.7012	−0.0277			45.9	0.0218

[a] Data taken from Figures 10 and 11. n_D = RI value at Fraunhofer D line or 589.3 nm; ν_D, ν' = Abbé numbers and D, D' = optical dispersions defined by eqs 1−4. [b] RI change at Fraunhofer D line or 1550 nm. For example, in polymer **3a**, $\Delta n_D = n_{D(UV)} - n_D$. [c] UV photolysis product.

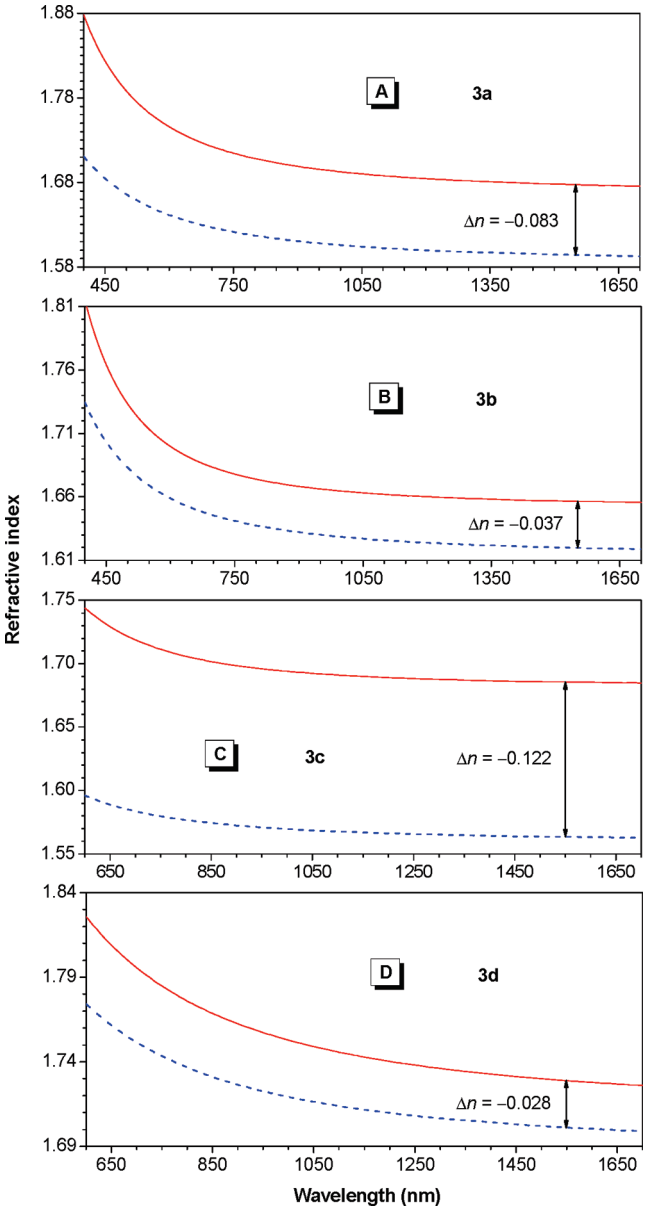

Figure 11. Tuning the refractive indices of thin solid films of (A−D) **3a**−**3d** by light irradiation (samples taken from Table 2, nos. 4, 6, 9, and 11, respectively).

All the polymers reveal a decrease of their RI values in the whole spectral region after UV irradiation, presumably due to the decrease in their electronic conjugations and corresponding polarizabilities caused by the photopolymerizations of their vinyl units to saturated single bonds. The Δn values at the Fraunhofer D line for **3a** and **3b** are as large as −0.1055 and −0.0415, respectively, while those at 1550 nm (Δn_{1550}) for **3a**−**3d** are ranged from −0.0277 to −0.1221 (Table 3). Among the polymers, **3c** shows the largest RI change (Δn_{1550} = −0.1221), which is very rare in organic polymer systems. These polymers will find an array of application for modulated RI pattern in the optical data storage devices. We are now actively pursuing the detailed study for these highly refractive and readily tunable RI materials.

Chromatic Dispersion. For an optical material to be useful for technological applications, its chromatic aberration, that is, the variation of its RI value with wavelengths, should be small. For a conventional optical material working in the visible spectral region, its chromatic aberration is adversely associated with the Abbé number (ν_D) or constringence defined by the following equation

$$\nu_D = \frac{n_D - 1}{n_F - n_C} \tag{1}$$

where n_D, n_F, and n_C are the RI values at 589.3, 486.1, and 656.3 nm, known as Fraunhofer D, F, and C lines, respectively.[32] A modified Abbé number (ν') has been proposed to evaluate the application potential of an optical material, using its RI values at the nonabsorbing infrared wavelengths of 1064, 1319, and 1550 nm. The first two wavelengths are chosen in view of the practical interest of commercial laser wavelengths (Nd:YAG), while the last one is the wavelength of telecom importance.[33] The modified Abbé number is defined as

$$\nu' = \frac{n_{1319} - 1}{n_{1064} - n_{1550}} \tag{2}$$

where n_{1319}, n_{1064}, and n_{1550} are the RI values at 1319, 1064, and 1550 nm, respectively. The optical dispersions D and D' in the visible and infrared regions are the reciprocals of ν_D and ν':

$$D = \frac{1}{\nu_D} \tag{3}$$

$$D' = \frac{1}{\nu'} \tag{4}$$

The ν_D and ν' values of **3a**−**3d** lie in ∼10−14 and ∼39−162, corresponding to D and D' values of 0.097−0.073 and 0.026−0.006, respectively (Table 3). Notably, the ν' value (161.6) of **3a** with perfect E-isomeric structure is ∼3 times higher than those of its cousins with low E/Z ratios (55.2 and 56.3). Generally, an optical

material with a high light refractivity exhibits a low Abbé number and vice versa.[32,34] It is noteworthy that our polymers show both high RI values (n_D > 1.70) and Abbé numbers (ν' up to ~162). After UV irradiation, the ν_D and ν' values of the PVS's except for **3b** are increased by 0.4−4.0 and 7.4−8.6, respectively. In other words, most of our polymers show good performances in optical dispersion. In terms of light refraction behavior and its modulation capacity, these results demonstrate the great potential of our PVS's as optical materials for photonic applications, such as antireflective coatings, optical adhesives or encapsulants for organic light-emitting diodes, microlens components for charge-coupled devices, and high-performance CMOS image sensors.[28]

Conclusions

In this work, we have developed a thio-click polymerization technique for the synthesis of new electronically active sulfur-containing acetylenic polymers. The Rh-catalyzed alkyne polyhydrothiolations of diynes (**1**) and dithiol (**2**) are carried out under mild conditions at room temperature, producing PVS's (**3**) with high molecular weights in high yields. The polymerizations are functionality-tolerant and can proceed in regio- and stereoselective manners. Both engineering control on the sequential addition of monomers during the polymerization process and postmanipulation by light irradiation are capable of tuning the stereostructures of the PVS's. All these attributes make this Rh-catalyzed alkyne polyhydrothiolation a new type of click polymerization.

The PVS is a new member of the family of electronically conjugated polymers. Polymers **3** enjoy good solubility, film-forming ability, and optical transparency. They can be readily cured both by thermal treatment and UV irradiation. Polymer **3c** shows an aggregation-enhanced emission characteristic and can be readily cross-linked by UV irradiation to generate fluorescent photoresist patterns. Polymer **3d** reveals a superior optical limiting property to C_{60} and works as a precursor to prepare semiconducting Fe_7S_8 ceramic. All the polymer films exhibit higher refractive indices than conventional organic polymers. The PVS's with different stereostructures have distinct refractive indices and chromatic aberrations. Their refractivities can be further modulated by UV irradiation. All these hallmarks make these new functional PVS's promising optoelectronic materials for real-world high-tech applications.

Experimental Section

General Information. $Rh(PPh_3)_3Cl$,[35] $[Rh(nbd)Cl]_2$,[36] and $Rh(nbd)(PPh_3)_2{}^+PF_6{}^-$[37] complexes were prepared according to the literatures. Monomer 4,4′-thiodibenzenethiol (**2**), 1,2-dichloroethane (DCE) and other chemicals and reagents were all purchased from Aldrich and used as received without further purification.

M_n, M_w, and PDI (M_w/M_n) values of the polymers were estimated by GPC using a Waters Associates liquid chromatograph equipped with a Waters 515 HPLC pump, a set of Styragel columns (HT3, HT4, and HT6; molecular weight range 10^2-10^7), a column temperature controller, a Waters 486 wavelength-tunable UV−vis detector, a Waters 2414 differential refractometer, and a Waters 2475 fluorescence detector. The polymer solutions in THF (~2 mg/mL) were filtered through 0.45-μm PTFE syringe-type filters before being injected into the GPC system. THF was used as eluent at a flow rate of 1.0 mL/min. The column temperature was maintained at 40 °C, and the working wavelength of the UV−vis detector was set at 254 nm. A set of monodisperse polystyrene standards (Waters) covering the molecular weight range of 10^3-10^7 were used for the molecular weight calibration.

IR spectra were recorded on a Perkin-Elmer 16 PC FTIR spectrophotometer. ^1H and ^{13}C NMR spectra were measured on Bruker ARX 300 or 400 NMR spectrometers using chloroform-*d* as solvent and tetramethylsilane (TMS) as internal reference. Mass spectra were recorded on a GCT Premier CAB 048 mass spectrometer operating in a TOF mode. UV spectra were measured on a Milton Ray Spectronic 3000 array spectrophotometer. PL spectra were recorded on a Perkin-Elmer LS 55 spectrofluorometer. The thermal stability of the polymers was evaluated on a TA Instruments TGA Q5000 under nitrogen at a heating rate of 10 °C/min. The thermal transitions were investigated by differential scanning colorimeter (DSC) using a TA Instruments DSC Q1000 at a heating rate of 10 °C/min. Refractive indices were determined on a J A Woollam Variable Angle Ellipsometry System with a wavelength tunability from 300 to 1700 nm. To fit the acquired Ψ and Δ curves with the data obtained from the 3-layer optical model consisting of crystalline silicon substrate, 2 nm SiO_2 layer and a uniform polymer film, the Levenberg−Marquardt regression algorithm was employed. The cauchy dispersion law was applied to describe the polymer layer from visible to IR region. The X-ray photoelectron spectroscopy (XPS) experiments were conducted on a PHI 5600 spectrometer (Physical Electronics), and the core level spectra were measured using a monochromatic Al Kα X-ray source ($h\nu$ = 1486.6 eV). The analyzer was operated at 23.5 eV pass energy and the analyzed area was 800 μm in diameter. Morphologies of the ceramics were imaged on a JEOL-6300 scanning electron microscope (SEM) operating at an accelerating voltage of 15 kV. Structures of the ceramics were investigated by high-resolution transmission electron microscopy JEOL 2010F TEM. The energy-dispersion X-ray (EDX) analyses were performed on a JEOL 2010F TEM system with quantitative elemental mapping and line scan capacities. The X-ray diffraction (XRD) diagrams were recorded on a Philips PW 1830 powder diffractometer using the monochromatized X-ray beam from a nickel-filtered Cu Kα radiation (λ = 1.5406 Å). The optical limiting properties of the samples were investigated by using a frequency doubled, Q-switched, mode-locked Continuum ns/ps Nd:YAG laser, which provides 35 ps pulses at 532 nm with a repetition rate of 10 Hz. The input laser pulses were split into two parts by a beam splitter. The first part was used to measure the incident laser energy and the second part was focused onto the sample using a lens with 100 mm focal length. The experimental arrangement was similar to that described in the literature.[38] The samples were housed in glass cells with a path of 1 cm. The input laser pulses adjusted by an attenuator (Newport) were split into two beams. One was employed as a reference to monitor the incident laser energy, and the other was focused onto the sample cell by using a lens with a 100 mm focal length. The samples were positioned at the focus. The incident and transmitted laser pulses were monitored by two energy detectors, D1 and D2 (Rjp-735 energy probes, Laser Precision).

Photopatterning and RI tuning of the polymer films were conducted on a Spectroline ENF-280C/F UV lamp at a distance of 1 cm as light source. The incident light intensity was ~18.5 mW/cm^2. UV and visible lights were obtained through filters BG 39 and GG400 placed between the lamp and the polymer film, respectively. The films were prepared by spin-coating the polymer solution (10% w/w in DCE) at 800 rpm for 10 s and then 1500 rpm for 1 min on silicon wafers. The wafers had been cleaned prior to use by sequential treatments for 10 min with dichloromethane, 2-propanol, piranha solution (30 vol % H_2O_2/H_2SO_4), and deionized water in an ultrasonic bath. The polymer film was dried in a vacuum oven at room temperature overnight. The photoresist patterns ware generated using a copper photomask and taken on an optical microscopy (Olympus B202) using a normal light source.

Monomer Synthesis. Monomers **1a**,[17] **1b**,[18] **1c**,[19] and **1d**[20] were synthesized according to our previously published procedures.

*Characterization Data for **1a***. White powder; yield 86%. IR (thin film), ν (cm^{-1}): 3271 (≡C−H stretching), 2105 (weak C≡C

stretching). ^{1}H NMR (300 MHz, $CDCl_3$), δ (TMS, ppm): 7.50 (s, 8H, Ar−H), 3.18 (s, 2H, ≡C−H), 0.58 [s, 6H, $Si(CH_3)_2$]. ^{13}C NMR (75 MHz, $CDCl_3$), δ (ppm): 139.4, 134.3, 131.5, 123.1, 83.8, 78.1, −2.57. MS (TOF), m/z 261.1084 [$(M+1)^+$, calcd 261.1021]. Crystal data for **1a** is given in the Supporting Information.

*Characterization data for **1b**−**1d*** are available in our previously published papers.[17−20]

Polymer Synthesis. All the polymerization reactions were carried out under nitrogen atmosphere using a standard Schlenk technique. A typical procedure for the polymerization of **1a** and **2** is given below as an example.

To a 15 mL Schlenk tube with a three-way stopcock on the side arm was placed 4 mg (0.004 mmol) of $Rh(PPh_3)_3Cl$ (**C1**) under nitrogen in a glovebox. 2.0 mL of DCE was then injected into the tube using a hypodermic syringe. After stirring for 5 min, a solution of 52.1 mg (0.2 mmol) of monomer **1a** and 50.1 mg (0.2 mmol) of **2** in 2.0 mL of DCE was injected. The resultant mixture was stirred at room temperature under nitrogen for 24 h. The resultant solution was diluted with DCE and then added dropwise to 300 mL of hexane via a cotton filter under stirring. The precipitate was allowed to stand overnight and then collected by filtration. The polymer was washed with hexane and dried under vacuum at room temperature to a constant weight. Gray-white powder of polymer **3a** with 100% *E* isomer structure was obtained in 90.3% yield. M_w 19500; M_w/M_n 2.6 (Table 2, no. 2). IR (thin film), ν (cm^{-1}): 3295 (≡C−H stretching), 1594 (*C*=*C*−S stretching). ^{1}H NMR (400 MHz, $CDCl_3$), δ (TMS, ppm): 7.60−7.10 (Ar−H), 6.86 (d, J = 14.8 Hz, =C−H proton from the *E*-vinylene unit), 6.73 (d, J = 14.8 Hz, =C−H proton from the *E*-vinylene unit), 3.08 (≡C−H), 0.52 (CH_3). ^{13}C NMR (100 MHz, $CDCl_3$), δ (TMS, ppm): 137.7, 136.7, 134.6, 134.5, 134.2, 132.5, 131.6, 130.2, 125.4, 123.1, −2.5.

Sequential addition of monomers **1a** and **2** during the polymerization generates polymers **3a** with different *E*/*Z* ratios. Characterization data for **3a** with an *E*/*Z* ratio of 50/50: Gray-white powder; yield 93.2%. M_w 13900; M_w/M_n 3.2 (Table 2, no. 3). IR (thin film), ν (cm^{-1}): 3295 (≡C−H stretching), 1594 (*C*=*C*−S stretching). ^{1}H NMR (400 MHz, $CDCl_3$), δ (TMS, ppm): 7.60−7.10 (Ar−H), 6.87 (d, J = 14.8 Hz, =C−H proton from the *E*-vinylene unit), 6.74 (d, J = 14.8 Hz, =C−H proton from the *E*-vinylene unit), 6.59 (d, J = 9.6 Hz, =C−H proton from the *Z*-vinylene unit), 6.46 (d, J = 9.6 Hz, =C−H proton from the *Z*-vinylene unit), 3.08 (≡C−H), 0.52 (CH_3). ^{13}C NMR (100 MHz, $CDCl_3$), δ (TMS, ppm): 138−137, 136−134, 133−130, 129−127, 126−125, 124−122, −2.5.

*Characterization Data for Polymer **3b***. Gray-white powder; yield 92.3%; *E*/*Z* = 50/50. M_w 9500; M_w/M_n 3.3 (Table 2, no. 6). IR (thin film), ν (cm^{-1}): 3279 (≡C−H stretching), 2125 (C≡C stretching), 1726 (C=O stretching), 1574 (*C*=*C*−S stretching). ^{1}H NMR (400 MHz, $CDCl_3$), δ (TMS, ppm): 7.95−7.90 (=C−H proton from the *E*-vinylene unit), 6.90−7.50 (Ar−H and =C−H proton from the *Z*-vinylene unit), 6.20−6.05 (=C−H proton from the *Z*-vinylene unit), 5.90−5.70 (=C−H proton from the *E*-vinylene unit), 3.06 (≡C−H), 1.9−1.4 (CH_3). ^{13}C NMR (100 MHz, $CDCl_3$), δ (TMS, ppm): 164.8, 163.5, 152.0−150.8, 149.0−147.6, 135.0−127.0, 121.0, 120.9, 120.6, 114.8, 112.7, 77.2, 74.3, 42.5, 30.9.

*Characterization Data for Polymer **3c***. Yellow powder; yield 83.8%; *E*/*Z* = 50/50. M_w 4000; M_w/M_n 1.6 (Table 2, no. 9). IR (thin film), ν (cm^{-1}): 3282 (≡C−H stretching), 1598 (*C*=*C*−S stretching). ^{1}H NMR (400 MHz, $CDCl_3$), δ (TMS, ppm): 7.50−6.70 (Ar−H and =C−H proton from the *E*-vinylene unit), 6.71 (d, J = 9.2 Hz, =C−H proton from the *E*-vinylene unit), 6.50 (d, J = 10.8 Hz, =C−H proton from *Z*-vinylene unit), 6.36 (d, J = 10.8 Hz, =C−H proton from *Z*-vinylene unit), 3.02 (≡C−H), 0.60−0.40 (CH_3). ^{13}C NMR (100 MHz, $CDCl_3$), δ (TMS, ppm): 154.2, 141.3, 139.0−137.0, 136.0−125.0, 124.1, 121.2, −3.6.

*Characterization Data for Polymer **3d***. Red powder; yield 82.5%; *E*/*Z* = 87/13. M_w 5300; M_w/M_n 2.2 (Table 2, no. 11). IR (thin film), ν (cm^{-1}): 3276 (≡C−H stretching), 1595 (*C*=*C*−S stretching). ^{1}H NMR (400 MHz, $CDCl_3$), δ (TMS, ppm): 7.50−7.00 (Ar−H), 6.90−6.40 (=C−H proton from the original *E*- and newly formed *E*-vinylene units), 6.38−6.31 (=C−H proton from the newly formed *Z*-vinylene unit), 6.07−6.00 (=C−H proton from the newly formed *Z*-vinylene unit), 4.43 (H from ferrocene), 4.27 (H from ferrocene), 3.07 (≡C−H). ^{13}C NMR (100 MHz, $CDCl_3$), δ (TMS, ppm): 140−120, 77.2, 70.2, 68.1.

Acknowledgment. This work was partially supported by the Research Grants Council of Hong Kong (603509, 603008, 601608, 602707, AoE/P-03/08-1, and ITP/008/09/NP), the National Science Foundation of China (20974028 and 20634020), and the Ministry of Science & Technology of China (2009CB623605). BZT thanks the support from the Cao Guangbiao Foundation of Zhejiang University.

Supporting Information Available: Crystal data for monomer **1a** (Table S1), IR spectra of monomers **1a** and **2** and polymer **3a** (Figure S11), powder XRD diffractogram of ceramic C**3d** (Figure S2), SEM and TEM images of ceramic C**3d** (Figure S3), atomic compositions of ceramic C**3d** estimated by XPS and EDX analyses (Table S2) and a cif file for C**3d**. This material is available free of charge via the Internet at http://pubs.acs.org.

References and Notes

(1) (a) Grimsdale, A. C.; Chan, K. L.; Martin, R. E.; Jokisz, P. G.; Holmes, A. B. *Chem. Rev.* **2009**, *109*, 897. (b) Lo, S. C.; Burn, P. L. *Chem. Rev.* **2007**, *107*, 1097. (c) Friend, R. H.; Gymer, R. W.; Holmes, A. B.; Burroughes, J. H.; Marks, R. N.; Taliani, C.; Bradley, D. D. C.; Dos Santos, D. A.; Bredas, J. L.; Logdlund, M.; Salaneck, W. R. *Nature* **1999**, *397*, 121.

(2) (a) Cheng, Y. J.; Yang, S. H.; Hsu, C. S. *Chem. Rev.* **2009**, *109*, 5868. (b) Dennler, G.; Scharber, M. C.; Brabec, C. *J. Adv. Mater.* **2009**, *21*, 1323. (c) Chen, L. M.; Hong, Z. R.; Li, G.; Yang, Y. *Adv. Mater.* **2009**, *21*, 1434. (d) Gunes, S.; Neugebauer, H.; Sariciftci, N. S. *Chem. Rev.* **2007**, *107*, 1324. (e) Thompson, B. C.; Frechét, J. M. J. *Angew. Chem., Int. Ed.* **2008**, *47*, 58.

(3) (a) Allard, S.; Forster, M.; Souharce, B.; Thiem, H.; Scherf, U. *Angew. Chem., Int. Ed.* **2008**, *47*, 4070. (b) Murphy, A. R.; Frechét, J. M. *J. Chem. Rev.* **2007**, *107*, 1066.

(4) (a) Shirakara, H. *Angew. Chem., Int. Ed.* **2001**, *40*, 2575. (b) MacDiarmid, A. G. *Angew. Chem., Int. Ed.* **2001**, *40*, 2581. (c) Heeger, A. J. *Angew. Chem., Int. Ed.* **2001**, *40*, 2591. (d) Liu, J.; Lam, J. W. Y.; Tang, B. Z. *Chem. Rev.* **2009**, *109*, 5799. (e) Akagi, K. *Chem. Rev.* **2009**, *109*, 5354. (f) Masuda, T. *J. Polym. Sci., Part A: Polym. Chem.* **2007**, *45*, 165. (g) Lam, J. W. Y.; Tang, B. Z. *Acc. Chem. Res.* **2005**, *38*, 745. (h) Simionescu, C. I.; Percec, V. *Prog. Polym. Sci.* **1982**, *8*, 133.

(5) (a) Nielsen, M. B.; Diederich, F. *Chem. Rev.* **2005**, *105*, 1837. (b) Diederich, F. *Nature* **1994**, *369*, 199. (c) Diederich, F.; Kivala, M. *Adv. Mater.* **2010**, *22*, 803.

(6) (a) Schmaltz, B.; Weil, T.; Mullen, K. *Adv. Mater.* **2009**, *21*, 1067. (b) Wu, J.; Pisula, W.; Mullen, K. *Chem. Rev.* **2007**, *107*, 718. (c) Cianga, I.; Yagci, Y. *Prog. Polym. Sci.* **2004**, *29*, 387. (d) Scherf, U.; List, E. J. W. *Adv. Mater.* **2002**, *14*, 477.

(7) (a) Bunz, H. F. *Acc. Chem. Res.* **2001**, *34*, 998. (b) Thomas, S. W.; Joly, G. D.; Swager, T. *Chem. Rev.* **2007**, *107*, 1339. (c) Morisaki, Y.; Chujo, Y. *Prog. Polym. Sci.* **2008**, *33*, 346.

(8) (a) Ma, W.; Yang, C.; Gong, X.; Lee, K.; Heeger, A. J. *Adv. Funct. Mater.* **2005**, *15*, 1617. (b) Li, G.; Shrotriya, V.; Huang, J.; Yao, Y.; Moriarty, T.; Emery, K.; Yang, Y. *Nat. Mater.* **2005**, *4*, 864. (c) Kim, Y.; Cook, S.; Tuladhar, S. M.; Choulis, S. A.; Nelson, J.; Durrant, J. R.; Bradley, D. D. C.; Giles, M.; McCulloch, I.; Ha, C. S.; Ree, M. *Nat. Mater.* **2006**, *5*, 197. (d) Park, S. H.; Roy, A.; Beaupre, S.; Cho, S.; Coates, N.; Moon, J. S.; Moses, D.; Leclerc, M.; Lee, K.; Heeger, A. J. *Nature Photon* **2009**, *3*, 297.

(9) (a) Gies, A. P.; Geibel, J. F.; Hercules, D. M. *Macromolecules* **2010**, *43*, 943. (b) Cebe, P. *Polym Polym. Compos.* **1995**, *3*, 239. (c) Edmonds, J. T.; Hill, H. W. (Phillips Petroleum Co.). U.S. Patent 3,354,129, 1967. (d) Perng, L. H. *Polym. Degrad. Stab.* **2000**, *69*,

323. (e) Piaggio, P.; Giribone, D.; Musso, G. F.; Cuniberti, C.; Dellepiane, G.; Borghesi, A. *Synth. Met*. **1991**, *41*, 1359.
(10) Truce, W. E.; Simms, J. A. *J. Am. Chem. Soc*. **1956**, *12*, 2756.
(11) (a) Griesbaum, K. *Angew. Chem., Int. Ed*. **1970**, *9*, 273. (b) Patai, S. In *The Chemistry of the Thiol Group*; Wiley: London, 1974; Vol. *2*. (c) Ananikov, V. P.; Malyshev, D. A.; Beletskaya, I. P.; Aleksandrov, G. G.; Eremenko, I. L. *Adv. Synth. Catal*. **2005**, *347*, 1993.
(12) (a) Ichinose, Y.; Wakamatsu, K.; Nozaki, K.; Birbaum, J. L.; Oshima, K.; Utimata, K. *Chem. Lett*. **1987**, 1671. (b) MaDonald, J. W.; Corbin, J. L.; Newton, W. E. *Inorg. Chem*. **1976**, *15*, 9. (c) Kuniyasu, H.; Ogawa, A.; Sato, K. I.; Ryu, I.; Kambe, N.; Sonoda, N. *J. Am. Chem. Soc*. **1992**, *114*, 5902. (d) Bäckvall, J. E.; Ericcson, A. *J. Org. Chem*. **1994**, *59*, 5850. (e) Han, L. B.; Zhang, C.; Yazawa, H.; Shimada, S. *J. Am. Chem. Soc*. **2004**, *126*, 5080. (f) Ogawa, A.; Ikeda, T.; Kimura, K.; Hirao, T. *J. Am. Chem. Soc*. **1999**, *121*, 5108. (g) Burling, S.; Field, L. D.; Messerle, B. A.; Vuong, K. Q.; Turner, P. *J. Chem. Soc., Dalton Trans*. **2003**, 4181. (h) Munro-Leighton, C.; Delp, S. A.; Alsop, N. M.; Blue, E. D.; Gunnoe, T. B. *Chem. Commun*. **2008**, 111. (i) Cao, C.; Fraser, L. R.; Love, J. A. *J. Am. Chem. Soc*. **2005**, *127*, 17614. (j) Kondoh, A.; Yorimitsu, H.; Oshima, K. *Org. Lett*. **2008**, *9*, 1383. (k) Malyshev, D. A.; Scott, N. M.; Marion, N.; Stevens, E. D.; Ananikov, V. P.; Beleskaya, I. P.; Nolan, S. P. *Organometallics* **2006**, *25*, 5562. (l) Sabarre, A.; Love, J. A. *Org. Lett*. **2008**, *10*, 3941. (m) Cao, C.; Wang, T.; Patrick, B. O.; Love, J. A. *Organometallic* **2006**, *25*, 1321. (n) Ananikov, V. P.; Gayduk, K. A.; Orlov, N. V.; Beletskaya, I. P.; Khrustalev, V. N.; Antipin, M. Y. *Chem.—Eur. J*. **2010**, *16*, 2063.
(13) (a) Häu*β*ler, M.; Tang, B. Z. *Adv. Polym. Sci*. **2007**, *209*, 1. (b) Häu*β*ler, M.; Qin, A.; Tang, B. Z. *Polymer* **2007**, *48*, 6181.
(14) (a) Qin, A.; Lam, J. W. Y.; Tang, B. Z. *Chem. Soc. Rev*. **2010**, *39*, 2522. (b) Qin, A.; Lam, J. W. Y.; Tang, B. Z. *Macromolecules* **2010**, *43*, 8693.
(15) (a) Iha, R. K.; Wooley, K. L.; Nystrom, A. M.; Burke, D. J.; Kade, M. J.; Hawker, C. J. *Chem. Rev*. **2009**, *109*, 5620. (b) Hoyle, C. E.; Bowman, C. N. *Angew. Chem., Int. Ed*. **2010**, *49*, 1540. (c) Lower, A. B. *Polym. Chem*. **2010**, *1*, 17. (d) Sumerlin, B. S.; Vogt, A. P. *Macromolecules* **2010**, *43*, 1. (e) Rim, C.; Son, D. Y. *Tetrahedron Lett*. **2009**, *50*, 4161.
(16) (a) Lowe, A. B.; Hoyle, C. E.; Bowman, C. N. *J. Mater. Chem*. **2010**, *20*, 4745. (b) Hoogenboom, R. *Angew. Chem., Int. Ed*. **2010**, *49*, 3415. (c) Fairbanks, B. D.; Scott, T. F.; Kloxin, C. J.; Anseth, K. S.; Bowman, C. N. *Macromolecules* **2009**, *42*, 211. (d) Chen, G.; Kumar, J.; Gregory, A.; Stenzel, M. H. *Chem. Commun*. **2009**, 6291. (e) Konkolewicz, D.; Gray-Weale, A.; Perrier, S. *J. Am. Chem. Soc*. **2009**, *131*, 18075. (f) Chan, J. W.; Hoyle, C. E.; Lowe, A. B. *J. Am. Chem. Soc*. **2009**, *131*, 5751. (g) Hensarling, R. M.; Doughty., V. A.; Chan, J. W.; Patton, D. L. *J. Am. Chem. Soc*. **2009**, *131*, 14673.
(17) Liu, J.; Zheng, R.; Tang, Y.; Häussler, M.; Lam, J. W. Y.; Qin, A.; Ye, M.; Hong, Y.; Gao, P.; Tang, B. Z. *Macromolecules* **2007**, *40*, 7473.
(18) Liu, J.; Zhang, L.; Lam, J. W. Y.; Jim, C. K. W.; Yue, Y.; Deng, R.; Hong, Y.; Qin, A.; Sung, H. H. Y.; Williams, I. D.; Jia, G. C.; Tang, B. Z. *Macromolecules* **2009**, *42*, 7367.
(19) Liu, J.; Zhong, Y.; Lam, J. W. Y.; Lu, P.; Hong, Y.; Yu, Y.; Yue, Y.; Faisal, M.; Sung, H. H. Y.; Williams, I. D.; Wong, K. S.; Tang, B. Z. *Macromolecules* **2010**, *43*, 4921.
(20) Shi, J. B.; Tong, B.; Li, Z.; Shen, J. B.; Zhao, W.; Fu, H. H.; Zhi, J.; Dong, Y. P.; Häussler, M.; Lam, J. W. Y.; Tang, B. Z. *Macromolecules* **2007**, *40*, 8195.
(21) (a) Waldeck, D. H. *Chem. Rev*. **1991**, *91*, 415. (b) Jiang, C.; Xie, R.; Li, F.; Allen, R. E. *Chem. Phys. Lett*. **2009**, *474*, 263.
(22) (a) Sudesh Kumar, G.; Neckers, D. C. *Chem. Rev*. **1989**, *89*, 1915. (b) Xie, S.; Natansohn, A.; Rochon, P. *Chem. Mater*. **1993**, *5*, 403.
(23) (a) Häussler, M.; Liu, J.; Zheng, R.; Lam, J. W. Y.; Qin, A.; Tang, B. Z. *Macromolecules* **2007**, *40*, 1914. (b) Peng, H.; Cheng, L.; Luo, J. D.; Xu, K. T.; Sun, Q. H.; Dong, Y. P.; Salhi, F.; Lee, P. P. S.; Chen, J. W.; Tang, B. Z. *Macromolecules* **2002**, *35*, 5349. (c) Tang, B. Z.; Xu, H. *Macromolecules* **1999**, *32*, 2569.
(24) Yuan, W.; Sun, J. Z.; Liu, J. Z.; Dong, Y.; Li, Z.; Xu, H.; Qin, A.; Häussler, M.; Jin, J.; Zheng, Q.; Tang, B. Z. *J. Phys. Chem. B*. **2008**, *112*, 8896.
(25) Tutt, L. W.; Kost, A. *Nature* **1992**, *356*, 225.
(26) (a) Hong, Y.; Lam, J. W. Y.; Tang, B. Z. *Chem. Commun*. **2009**, 4332. (b) Liu, J.; Lam, J. W. Y.; Tang, B. Z. *J. Inorg. Organomet. Polym. Mater*. **2009**, *19*, 249.
(27) (a) Campbell, L.; Sharp, D. N.; Harrison, M. T.; Denning, R. G.; Turberfield, A. J. *Nature* **2000**, *404*, 53. (b) Kim, J. M. *Macromol. Rapid Commun*. **2007**, *28*, 1191.
(28) (a) Liu, J.; Ueda, M. *J. Mater. Chem*. **2009**, *19*, 8907and references therein. (b) You, N.; Chueh, C.; Liu, C.; Ueda, M.; Chen, W. C. *Macromolecules* **2009**, *42*, 4456.
(29) Seferis, J. C. In *Polymer Handbook*, 3rd ed.; Brandrup, J., Immergut, E. H., Eds.; Wiley: New York, 1989; pp VI/451−VI/461.
(30) (a) Moshrefzadeh, R. S.; Misemer, D. K.; Radcliffe, M. D.; Francis, C. V.; Mohapatra, S. K. *Appl. Phys. Lett*. **1993**, *62*, 16. (b) Tanio, N.; Irie, M. *Jpn. J. Appl. Phys*. **1994**, *33*, 3942. (c) Irie, M.; Sakemura, K.; Okinaka, M.; Uchida, K. *J. Org. Chem*. **1995**, *60*, 8305. (d) Hanazawa, M.; Sumiya, R.; Horika, Y.; Irie, M. *J. Chem. Soc. Chem. Commun*. **1992**, 206.
(31) Griesser, T.; Hofler, T.; Jakopic, G.; Belzik, M.; Kern, W.; Trimmel, G. *J. Mater. Chem*. **2009**, *19*, 4557.
(32) Hecht, E. *Optics*, 4th ed.; Addison Wesley: San Francisco, CA, 2002.
(33) (a) Yang, C. J.; Jenekhe, S. A. *Chem. Mater*. **1994**, *6*, 196. (b) Kim, D. Y.; Sundheimer, M.; Otomo, A.; Stegman, G. I.; Winfried, H. G. H.; Mohlhaupt, G. R. *Appl. Phys. Lett*. **1993**, *63*, 290.
(34) Dislich, H. *Angew. Chem., Int. Ed*. **1979**, *18*, 49.
(35) Osborn, J. A.; Jardine, F. H.; Young, J. F.; Wilkinson, G. *J. Chem. Soc. A* **1966**, 1711.
(36) Tang, B. Z.; Poon, W. H.; Leung, S. M.; Leung, W. H.; Peng, H. *Macromolecules* **1997**, *30*, 2209and references therein.
(37) Schrock, R. R.; Osborn, J. A. *J. Am. Chem. Soc*. **1976**, *98*, 2134.
(38) Yin, S.; Xu, H.; Su, X.; Li, G.; Song, Y.; Lam, J. W. Y.; Tang, B. Z. *J. Polym. Sci., Part A: Polym. Chem*. **2006**, *44*, 2346.

80 *Macromolecules* **2011**, *44*, 80–86
DOI: 10.1021/ma102189n

Macromolecules
ARTICLE

BODIPY-Conjugated Thermo-Sensitive Fluorescent Polymers Based On 2-(2-methoxyethoxy)ethyl methacrylate

R. París,[†] I. Quijada-Garrido,[†] O. García,[‡] and M. Liras*[,‡]

[†]*Departamento de Química-Física de Polímeros and* [‡]*Departamento de Fotoquímica de Polímeros, Instituto de Ciencia y Tecnología de Polímeros (ICTP), Consejo Superior de Investigaciones Científicas (CSIC), c/Juan de la Cierva, 3, E-28006 Madrid. Spain*

Received September 22, 2010; Revised Manuscript Received December 2, 2010

ABSTRACT: A methacrylic monomer containing the dye 4,4-difluoro-4-bora-3a,4a-diaza-*s*-indacene (BODIPYMA) was synthesized to provide fluorescence properties to three different thermo-sensitive families of polymers based on 2-(2-methoxyethoxy)ethyl methacrylate (MEO_2MA). Initially, linear random terpolymers of MEO_2MA, oligo(ethylene glycol) methyl ether methacrylate ($OEG_{8-9}MA$) with M_n = 475 g mol^{-1}, and a very low proportion of BODIPYMA were synthesized by atom transfer radical polymerization (ATRP). These terpolymers showed lower critical solution temperature (LCST), which values were easily tuned by changing the monomeric composition, and fluorescence, which intensity increases significantly after this thermal transition. Second, a family of diblock copolymers was formed by the ATRP of MEO_2MA and a very short block of BODIPYMA. They also behave as a fluorescent thermometer in water but, in this case, the fluorescence quantum yield decreased due to the intermolecular $\pi-\pi$ stacking of BODIPY dyes. In addition, a MEO_2MA-BODIPYMA based hydrogel was prepared to show that the optical and fluorescence properties also exhibit a sudden and reversible change at the volume transition temperature (VTT) of the hydrogel.

Introduction

In the last few years, the number of contributions where the 4,4-difluoro-4-bora-3a,4a-diaza-*s*-indacene (BODIPY) dyes appear is exponentially increasing.[1,2] Recently, the BODIPY dyes have been used as optical sensitivity compounds for biochemical labeling,[3] solar cells,[4] or luminescent ionic liquid crystals.[5] These dyes present advantageous characteristics versus other chromophores, such as high extinction coefficients, high quantum yields, low triplet−triplet absorption and the fact that its excitation wavelength lies in the visible-wavelength range.[6,7]

The covalent incorporation of BODIPY dyes into a polymer main chain,[8−13] side chain,[14,15] or initial end[16] has drawn attention during the last years. In fact, our research group has demonstrated that novel BODIPY-based polymers prepared by the free radical copolymerization of methyl methacrylate (MMA) with methacrylic BODIPY monomers,[17,18] exhibited efficient and high photostability toward laser in liquid and in solid polymeric matrices. Besides, BODIPY cross-linker monomer has showed better results than the former.[19] Although BODIPY-based polymers are being investigated, just few articles report the use of thermo-sensitive polymers to obtain fluorescent temperature sensors.[20,21] On the one hand, Wang et al.[20] synthesized by free radical random copolymerization a system composed of *N*-isopropylacrylamide (*N*-iPAAm) and BODIPY monomer having a meso-pyridinium group. These polymers act as a fluorescence-enhancement-type thermometer and displayed reversible fluorescence enhancement/quenching at the lower critical solution temperature (LCST) of P(*N*-iPAAm), due to the inhibition of the rotation of the mesopyridinium group in the BODIPY after the polymer collapse.[20] On the other hand, Nagai et al.[21a] studied random copolymers based on 2-dimethylaminoethyl methacrylate (DMAEMA) and a BODIPY-based monomer synthesized by reversible addition−fragmentation chain transfer polymerization (RAFT). This is also a very interesting work in which the luminescent intensity of the obtained also depends on the temperature.

In the present contribution, we propose fluorescent thermo-sensitive polymers with controlled molecular weigh and structure, based on 2-(2-methoxyethoxy)ethyl methacrylate (MEO_2MA) with a very low proportion of BODIPY methacrylic monomer (BODIPYMA). This system is going to present reversible change in the fluorescence intensity with the temperature but also, some advantages that clearly improve the properties of the system in comparison to the previous works.[20,21a] Thus, MEO_2MA-based polymers present thermo-responsive behavior generally comparable to P(*N*-iPAAm),[28] showing a LCST at around 26 °C,[22] but they show the advantage that this transition temperature can be easily modulated by copolymerization of MEO_2MA with longer oligo(ethylene glycol) (OEG) methacrylates without losing the sharpness of the transition.[23−27] Another remarkable aspect in comparison with the previous compounds is that our system shows good biorelated properties (i.e., nontoxicity, anti-immunogenicity) since they are formed by oligo(ethylene glycol) side chains. In addition, they can be successfully obtained from controlled/living polymerizations techniques, such as atom transfer radical polymerization (ATRP),[23−25,29,30] that will allow a control over the molecular weight and the molecular weight distribution. Moreover, MEO_2MA has demonstrated to be a good monomer in order to synthesize thermo- and pH-sensitive hydrogels, which has been the focus of our more recently investigations.[31,32] Furthermore, the last novelty of this work is that the chromophore group in BODIPYMA is tethered to the methacrylic group by a short methylene chain which will allow a better coupling to the dynamics of the thermo-sensitive polymer, increasing the expected thermal fluorescent response.

*Corresponding author. Telephone: (34) 91 258 74 04 and (34) 91 562 29 00. Fax: (34) 91 564 48 53. E-mail: martaliras@ictp.csic.es.

 Published on Web 12/14/2010 © 2010 American Chemical Society

Scheme 1

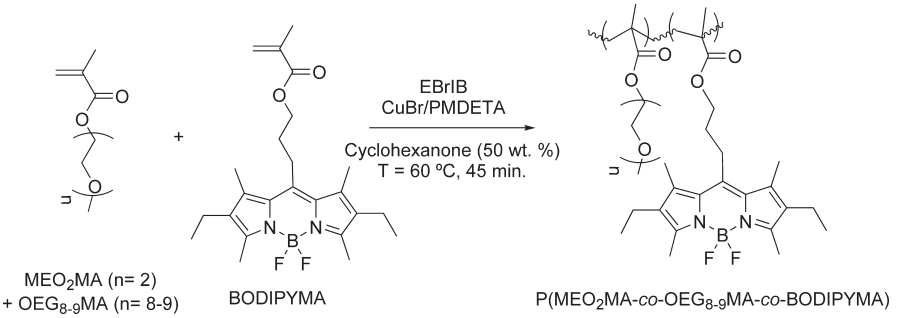

Scheme 2

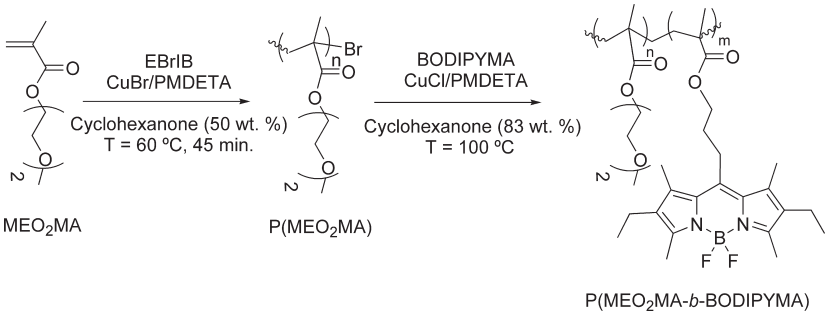

Taking all these facts into account, linear random terpolymers of MEO_2MA, oligo(ethylene glycol) methyl ether methacrylate ($OEG_{8-9}MA$) with M_n = 475 g mol^{-1} and a very low proportion of BODIPYMA were synthesized by ATRP, according with Scheme 1. The main aim of this strategy was to modulate the temperature at which the increase of the fluorescence occurs by tuning the LCST of the terpolymers, which can be easily done by changing the ratio of the two OEG monomers.[23−27] A second aim was to evaluate if the luminescent properties of these fluorescent thermometers in water depend on the $\pi-\pi$ stacking interactions originated from the planar structure of BODIPY. Thus, a two step ATRP synthesis (Scheme 2) was employed to obtain diblock copolymers. To the best of our knowledge this is the first example of the study of thermo-sensitive block copolymer based on BODIPY dyes. Thus, the fluorescent properties were studied as a function of the temperature and compared with the properties of the statistical copolymers. In addition, a BODIPY-based hydrogel, where the dye is covalent bound to a thermo-sensitive network, was synthesized for the first time to show that this relevant combination of thermo-sensitivity and luminescence can also be used in cross-linked structures. The reduction of void or free volume surrounding the dye at the volume transition temperature (VTT) is going to restrict the molecular motions giving rise to nonradiative decay, and thus enhances the emission intensity.

Experiments

Materials. The monomers 2-(2-methoxyethoxy)ethyl methacrylate (MEO_2MA, Aldrich 95%) and oligo(ethylene glycol) methyl ether methacrylate with M_n = 475 g mol^{-1} ($OEG_{8-9}MA$, Aldrich) were purified by passing by neutral alumina column to remove the inhibitor. The ligand *N*,*N*,*N*′,*N*″,*N*″-pentamethyldiethylenetriamine (PMDETA, Aldrich 99%) was purified by vacuum distillation. The initiator ethyl 2-bromoisobutyrate (EBrIB, Aldrich 99%), the catalyst precursors copper bromide (CuBr, Aldrich 99.999%) and copper chloride (CuCl, Aldrich 99.99%), the solvents cyclohexanone (Scharlau 99.5%), *n*-hexane (Panreac 98%), acetone (Carlo Ebra 99.8%), toluene (Merck 99.9%), dichloromethane (DCM, Merck 99.8%), ethanol (Normapur, analytical reagent) and chloroform (Sds 99.9%) were used as received. The BODIPY derivative 4,4-difluoro-1,3,5,7,8-pentamethyl-2,6-diethyl-4-bora-3a,4a-diaza-*s*-indacene (PM567, laser grade from Exciton, OH) used as reference in the measurement of the photophysical properties was also used without previous purification. The chemicals used for the synthesis of the monomer BODIPYMA[17] were purchased from Aldrich (Steinheim, Germany) and were used without further purification, except 3-ethyl-2,4-dimethylpyrrole, which was distilled.

For the synthesis of the hydrogel, the activator *N*,*N*,*N*′,*N*′-tetramethylethylenediamine (TEMED, Fluka 99%), the conventional cross-linker tetraethylene glycol dimethacrylate (TEGDMA, Fluka 90%) and the initiator ammonium peroxodisulfate (APS, Fluka 98%) were also used as received. Phosphate buffer solutions (PBS) were prepared employing water (Milli-Q) from water purification facility (Millipore Milli-U10), sodium dihydrogen phosphate anhydrous (Fluka ≥99%), disodium hydrogen phosphate (Panreac ≥98%), ortho-phosphoric acid (Panreac 85%), and sodium chloride (Panreac ≥99.5%) to keep constant the ionic strength (μ).

Synthesis of the Monomer BODIPYMA. The synthesis of BODIPYMA, a methacrylic monomer with a BODIPY dye (analogous to PM567) tethered by a spacer of three methylene groups, was made according with the procedure described previously by our research group.[17] Its structure can be observed in Scheme 1.

Syntheses of P(MEO_2MA-*co*-$OEG_{8-9}MA$-*co*-BODIPYMA) Terpolymers. Terpolymerizations were carried out by ATRP at 60 °C in cyclohexanone solution (50 wt %) with a constant monomer/initiator concentration ratio of 100:1 and with the monomeric compositions showed in Table 1, being in all cases $[MEO_2MA+OEG_{8-9}MA]_0/[BODIPYMA]_0$ = 1400:1. Amine ligand (PMDETA) (46 mg, 0.266 mmol), degassed monomers ($[MEO_2MA]_0+[OEG_{8-9}MA]_0$ = 26.6 mmol), BODIPYMA (8 mg, 0.019 mmol), CuBr (38 mg, 0.266 mmol), and solvent (previously bubbled with nitrogen for at least 15 min) were all added to dry Pyrex tube

Table 1. Experimental Synthetic Conditions, Polymer Characterization, and Photophysical Properties of P(MEO_2MA-*co*-$OEG_{8-9}MA$-*co*-BODIPYMA) Terpolymers[a]

								photophysical properties			
entry	f_{MEO2MA}	F_{MEO2MA}	conv (%)	$M_{n,theor.}$ (g mol^{-1})	$M_{n,SEC}$ (g mol^{-1})	M_w/M_n	cloud point (°C)	solvent	λ_{abs} (nm)	λ_{em} (nm)	ε (M^{-1} cm^{-1})	Φ_{flu}
T1	1.00	1.00	60.4	11 570	19 655	1.39	27.2	acetone	521	535	4900	0.86
								toluene	525	539	5600	0.70
								ethanol	522	535	5600	0.87
								DCM	524	536	2600	0.56
								PBS[b]	524	535	4950	0.67
T2	0.95	0.95_6	63.6	12 950	20 846	1.50	34.8	PBS[b]	524	535	4950	0.67
T3	0.85	0.87_1	59.7	13 640	24 476	1.57	46.1	PBS[b]	524	535	5900	0.67

[a] The photophysical properties were measured in 0.36 mg mL^{-1} solutions at 10 °C. [b] pH = 7, μ = 0.1 M.

Table 2. Experimental Synthetic Conditions, Polymer Characterization, and Photophysical Properties of P(MEO_2MA-*b*-BODIPYMA) Block Copolymers Synthesized by ATRP Using a P(MEO_2MA) Macroinitiator Previously Synthesized by ATRP (Conv = 72%, $M_{n,SEC}$ = 19686 g mol^{-1}, M_w/M_n = 1.41, LCST = 27.6 °C)

						photophysical properties in PBS (pH 7)			
entry	time (min)	$[M]_0/[I]_0$	$M_{n,SEC}$ (g mol^{-1})	M_w/M_n	cloud point (°C)	λ_{abs} (nm)	λ_{em} (nm)	ε (M^{-1} cm^{-1})	Φ_{flu}
B1	60	45	20 889	1.41	26.4	524	532	52 800	0.10
B2	20	10	20 423	1.42	27.8	524	534	26 300	0.08

ampules. Next, the polymerization mixtures were carefully degassed by bubbling nitrogen during 20 min, and then the initiator (EBrIB) (39 μL, 0.266 mmol) dissolved in cyclohexanone (2 mL) was introduced into the ampules using degassed syringes in order to start the polymerization. The ampules were immediately placed in a thermostatic oil bath, regulated with a precision of ±0.1 °C. When the desired time (45 min) was up, the reaction mixture was quenched opening the ampule and exposing the content to air, cooled in an ice/water bath and adding chloroform (30 mL). Then, the reaction product solution was passed through a neutral alumina column to remove the catalyst. The solution was concentrated by rotary-evaporation, and the polymer solution was poured into a large excess of *n*-hexane (600 mL). The precipitated products were decanted and dried until a constant weight was reached. Total monomer conversions were measured gravimetrically.

Syntheses of P(MEO_2MA-*b*-BODIPYMA) Copolymers. The synthesis of these diblock copolymers was made in two steps. Initially, a P(MEO_2MA) homopolymer was synthesized using the procedure described in the last section but without BODIPYMA. Then, it was used as macroinitiator for the polymerization of BODIPYMA in a second step. These chain extensions were carried at 100 °C, in cyclohexanone solution (1:5 wt./wt.) and with a constant macroinitiator/CuCl/PMDETA concentration ratio of 1:1:1. The synthetic procedure was the same previously described for the statistical terpolymers. The relationship between macroinitiator and BODIPYMA monomer and the time of reaction are detailed in Table 2.

Synthesis of P(MEO_2MA-*co*-BODIPYMA) Hydrogel. A P(MEO_2MA-*co*-BODIPYMA) hydrogel was synthesized by free radical cross-linking random polymerization in solution using $[MEO_2MA]_0/[BODIPYMA]_0$ = 1400:1. Polymerization was carried out in a mixture water/ethanol 1:1 (v/v) as solvent with TEGDMA. In all cases the monomers/solvent ratio was 1:1 (w/w). Cross-linker TEGDMA, activator TEMED, and initiator APS were used with an initial ratio of 0.5 wt % of the total monomer amount. The procedure to obtain the hydrogels in the desired shape is described elsewhere.[31]

Characterization. ^{1}H and ^{13}C NMR spectra were recorded on a Bruker 300 MHz spectrometer in $CDCl_3$ at room temperature. Molecular weights (M_n) and molecular weight distributions (MWD) were determined by SEC with a GPC Perkin-Elmer (mobile phase: DMF with LiBr (0.1 wt %) at 0.3 mL min^{-1} and 70 °C) with a differential refractometer Waters 410 detector. Poly(methyl methacrylate) (PMMA) standards were employed for the calibration. The LCST was studied by determining the optical transmittance at 600 nm of the copolymers in PBS as a function of temperature. The analysis was made using a Cary 3 BIO-Varian UV−visible spectrophotometer. The temperature was raised from 5 to 80 °C at a rate of 1 °C min^{-1}. The LCST (cloud point) was defined as the temperature at the inflection point of the absorbance vs temperature curve. UV−vis absorption and fluorescence spectra were recorded on a Perkin−Elmer Lambda-16 and on a Perkin-Elmer LS5OB spectrophotometer, respectively. Fluorescence signals (excitation at 490 nm) were recorded in the front-face mode by orienting the sample at 35° and 55° with respect to the excitation and emission beams, respectively when the measures were done at different temperatures. The recorded fluorescence spectra were the average of at least three independent measurements made until reproducible fluorescence intensity was reached. The fluorescence quantum yield (Φ) (excitation at 490 nm) was evaluated relative to the PM567 dye in ethanol solution (Φ = 0.86).[33] The samples were thermostatized using a Huber-polycat cc1 cryostat system or a Julabo-paratherm U5-electronic thermostatized bath. For the hydrogel, the equilibrium swelling (Q_∞) was calculated in grams of solvent incorporated per grams of dry gel (xerogel) at 24 h of swelling.

Results and Discussion

P(MEO_2MA-*co*-$OEG_{8-9}MA$-*co*-BODIPYMA) Terpolymers. ATRP was used to synthesize random terpolymers based on MEO_2MA (Scheme 1), in which $OEG_{8-9}MA$ was used as comonomer to modulate the LCST,[22−25,34−40] and BODIPYMA was used in a constant and low proportion to produce luminescent compounds.[17,18] Experimental synthetic conditions and properties of the obtained copolymers are summarized in Table 1. It should be noted that, in all cases, a high feed molar ratio of MEO_2MA (f_{MEO2MA}) was used to obtain polymers with low LCST, since the LCSTs of P(MEO_2MA) and P($OEG_{8-9}MA$) are of ∼26 and ∼90 °C, respectively.[23]

The chemical structure of the obtained polymers was analyzed by ^{1}H NMR (Figure S1 in the Supporting Information),

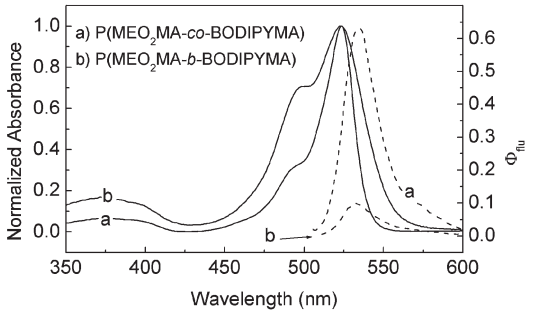

Figure 1. UV−vis normalized absorption (solid lines) and fluorescence spectra (dashed lines) of (a) P(MEO_2MA-*co*-BODIPYMA) copolymer (sample **T1**) and (b) P(MEO_2MA-*b*-BODIPYMA) diblock copolymer (sample **B1**) both dissolved in PBS (pH 7, μ = 0.1 M) at 10 °C.

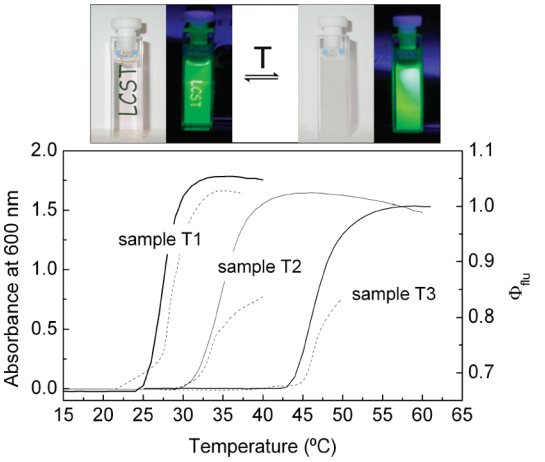

Figure 2. Absorbance at 600 nm (solid lines) and fluorescence quantum yield (dashed lines) vs temperature of the P(MEO_2MA-*co*-OEG_{8-9}MA-*co*-BODIPYMA) terpolymers dissolved (0.36 mg mL^{-1}) in PBS (pH 7, μ = 0.1 M). Photographs under visible and UV irradiation taken at temperatures below LCST (left part) and above LCST (right part) of sample **T1** are included.

mainly observing those proton signals of the oligo(ethylene glycol) macromonomer units.[25] Thus, the experimental molar ratios of MEO_2MA in the copolymer (F_{MEO2MA}), which values are shown in Table 1, could be estimated from the ratio between the intensity of the signal corresponding to the protons of the central OCH_2 groups and the intensity of the rest of signals. These experimental values are quite close to those used in the feed. This, together with the fact that conversions achieved are quite similar for all monomeric compositions, indicates that the two main monomers present similar reactivity ratios under these conditions, as it could be expected from their similar chemical structure. This is also a relevant result since it allows to easily obtain the desired composition in the polymers. The SEC analysis of the copolymers established that the polymerization was well controlled (Figure S2 in the Supporting Information). The molecular weight distributions were narrow and therefore, relatively low polydispersity indices were obtained. Moreover, the number-average molecular weights ($M_{n,SEC}$) increased coherently with the conversion achieved in the range under study.

Because of the incorporated BODIPY groups, the terpolymers are fluorescents. As an example, Figure 1 shows the absorption and emission spectra of sample **T1** in water. According with a BODIPY-based compound, the maximum of absorption (λ_{abs}) is around 524 nm, independently on the composition and the solvent employed in its determination. This fact can be observed from the photophysical data showed in Table 1. Moreover, a good relationship could be determined between the intensity of the absorption at this wavelength and the concentration of the solution, according with the Lambert−Beer's law. Therefore, the extinction molar coefficient (ε) values in aqueous solution, collected in the table, could be estimated. These ε values are similar in the three cases and, compared with the ε value of the parent dye PM567 (77000 M^{-1} cm^{-1} in water/ethanol 90 vol. %),[33] they are low. Thus, it can be estimated that only around 5−10% of the polymer chains have covalently bounded to a molecule of dye. In addition, distinctive fluorescence, assigned to the BODIPY units, appears at 500−650 nm. The maximum emission (λ_{em}) takes place at around 535 nm. Moreover, the quantum yields (Φ_{flu}) are quite high, according with the typical values obtained for BODIPY-based polymers.[41,42] We can conclude that the photophysical properties of the new P(MEO_2MA-*co*-OEG_{8-9}MA-*co*-BODIPYMA) terpolymers are not affected by the differences in the terpolymer composition at low temperature (around 10 °C), observing similar values for λ_{abs}, ε and λ_{em} in water (PBS pH = 7, μ = 0.1 M).

The methacrylic polymers with oligo(ethylene glycol) side chains under study are thermo-sensitive.[22−25,34−40] They undergo a thermal transition in water solution, becoming reversibly nonsoluble when the solution temperature is higher than the LCST. The LCST values (cloud points) of each polymer were determined by turbidimetry and they are collected in Table 1. As it is well-known, these values linearly increase when the MEO_2MA ratio in the polymer decreases.[23−27] But the most important issue here is that the system shows a remarkable increase in the fluorescent intensity when the polymer collapses, which means at temperatures above the LCST. Thus, Figure 2 shows the dependence of the absorbance at 600 nm (cloud point determinations) and the quantum yield of fluorescence on the temperature for each polymer water solution. At low temperature, the polymers are soluble (transparent) and only relative weak fluorescence is observed. However, the fluorescence intensity increases drastically when the thermal transition is achieved. According with Wang et al.,[20] this fluorescence enhancement is due to the aggregation properties of the thermo-sensitive polymer and moreover, a covalent bond between the BODIPY units and the polymeric chains is necessary for the heat-induced fluorescence enhancement. The difference in the quantum yield above the cloud point between the sample **T1** (Φ_{flu} close to the unit) and the rest of samples could be explained from the differences between the macromolecular mobility. Thus, polymers with longer ethylene glycol side chains (samples **T2** and **T3**) exhibit higher mobility above this transition.

Apart from the relevant change in the optical and luminescent properties of the polymers in water solution at the LCST, it is also important to point out that this change is reversible. In order to prove this fact, Figure 3 shows the change in absorption at 600 nm and quantum yield emission of sample **T1** for different heating/cooling cycles. The changes in absorbance (transparent/opaque) and in fluorescence (enhancement/quenching) occurred reversibly at least six times. In summary, a relevant increase in the fluorescence intensity can be achieved at the desired temperature in a reversible way. This fact is due to the LCST of these terpolymers can be tuned just varying the feed monomer composition in the synthesis.

P(MEO_2MA-*b*-BODIPYMA) Block Copolymers. In the previous terpolymeric system, the ratio of [MEO_2MA+$OEG_{8-9}MA]_0$ /$[BODIPYMA]_0$ was 1400:1 in all cases. This

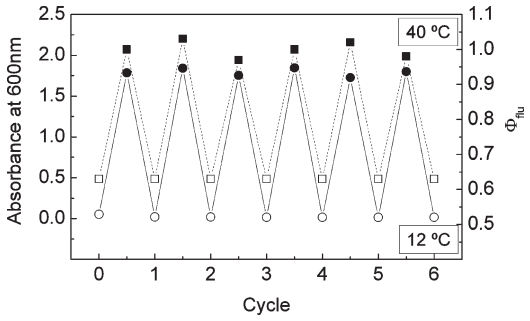

Figure 3. Change in absorbance at 600 nm (circles) and in fluorescence quantum yield (squares) of sample **T1** dissolved (0.36 mg mL^{-1}) in PBS (pH 7, μ = 0.1 M), where the temperature was changed repeatedly between 12 °C (< LCST, open symbols) and 40 °C (> LCST, full symbols).

suggests that inter- or intramolecular association of the BODIPY units scarcely occurs and therefore, BODIPY units should be isolated from each other. However, it was demonstrated that $\pi-\pi$ stacked BODIPY units can play an important role in the emission properties.[15] In order to study this effect in the thermo-sensitive system under study, P(MEO_2MA-*b*-BODIPYMA) diblock copolymers were synthesized in two steps, according to the procedure described in the experimental part and shown in Scheme 2. In the first step, a thermo-sensitive segment of P(MEO_2MA) was prepared in a controlled way ($M_{n,SEC}$ = 19686 g mol^{-1}, M_w/M_n = 1.41) and used as macroinitiator for the ATRP of BODIPYMA in a second step. The synthetic conditions and the properties of the obtained diblock copolymers are summarized in Table 2. It should be noted that copolymers were mainly and deliberately constituted by MEO_2MA. Therefore, their cloud point values almost do not change because the BODIPY blocks are very short in comparison. In fact, monomer conversions could not be determined gravimetrically. In addition, the ^1H NMR signals corresponding to the chromophore units are not visible in their spectra due to its low relation proportion. However, the incorporation of BODIPY units could be observed from the color of the polymers but also, by SEC determinations. An increment in the molecular weights was observed without apparent detriment of the narrow polydispersity indices. Thus, the BODIPYMA content in samples **B1** and **B2** was estimated, using SEC measurements, as 1.7 and 2.8%, respectively. These values were confirmed from the experimentally calculated molar extinction coefficients.

The photophysical properties of the diblock copolymers were evaluated and some relevant differences in comparison with the terpolymers were observed (Table 2), taking into account that the dye content in the block copolymers is higher than in the terpolymers. The typical absorption spectrum of BODIPY dyes has a main absorption band, attributed to the 0−0 vibrational band of a strong S_0-S_1 transition (~520 nm), and a shoulder assigned to the 0−1 vibrational band of the same transition (~490 nm). As can be seen in Figure 1, the relative intensity of these absorption bands in PBS is different in the block copolymers where the 0−1 vibrational band increases. In addition, that change in the absorption band is accompanied by a strong decrease in the fluorescence quantum yield until Φ_{flu} = 0.1. This fact was first observed by Johansson et al.[43] and was interpreted as a rare example of aggregation in BODIPY dyes. The H aggregate with a main band around 477 nm was confirmed later by Nagai et al.[21a,15] in nonthermo-sensitive diblock copolymers based on a BODIPY monomer and in random

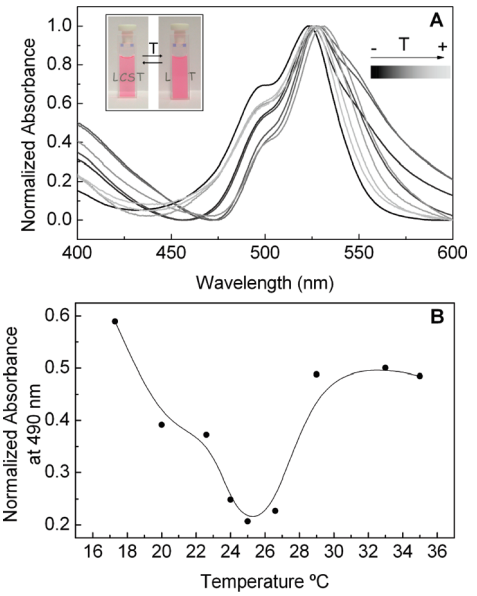

Figure 4. (A) Normalized UV−vis absorption spectra of the P(MEO_2MA-*b*-BODIPYMA) diblock copolymer (sample **B1**) dissolved (0.36 mg mL^{-1}) in PBS (pH 7, μ = 0.1 M) at different temperatures and (B) evolution of the absorbance intensity at 490 nm with the temperature. Photographs taken at temperature below the LCST (left part) and above the LCST (right part) of sample **B1** are included.

copolymers based on DMAEMA and BODIPY. There are two kinds of aggregates in chromophores depending of the molecular orientation, J-aggregates and H-aggregates. The J-aggregate is a one-dimensional molecular arrangement, in which the transition moments of individual monomers are aligned parallel to the line joining their centers (end-to-end arrangement). The most characteristic feature of J-aggregate is that it exhibits a narrow peak (J-band) red-shifted in the absorption spectrum with respect to the monomer absorption. The H-aggregate is also a one-dimensional array of molecules in which the transition moments of individual monomers are aligned parallel to each other but perpendicular to the line joining their centers (face-to-face arrangement). The absorption spectrum of the H-aggregate consists of a blue-shifted band (generally is not as narrow as the J-band) with respect to the monomer absorption. In both cases, the fluorescence decreases with the formation of aggregates.

Figure 4 shows how the intensity of the peak at 490 nm in normalized spectra (H-aggregates) changes with the temperature. It decreases with temperature until to a value close to the LCST, increasing again with a further increase of temperature. The first decrease could be explained assuming the formation of a micellar solution, at low temperature, that is progressively destroyed with the increase of temperature until the LCST. The last increment could be attributed to the thermal collapse of the P(MEO_2MA) chains in the same way as it was explained in the previous section for the random terpolymers. The hydrophobic character of the BODIPY block makes possible the formation of micelles at temperatures below the LCST. However, the whole polymer becomes non soluble above the LCST, the $\pi-\pi$ stacking between the chromophores disappears and the absorption spectrum changes.

The variation of the fluorescence spectrum and the evolution of Φ_{flu} with the temperature are plotted in Figure 5. It can be observed that the fluorescence displays the same behavior with temperature as the absorption at 490 nm. This is logical since the excitation wavelength used was exactly 490 nm. The low emission together with the characteristic

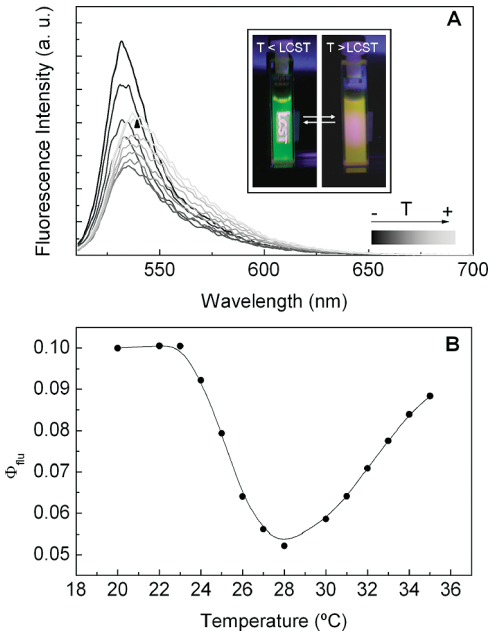

Figure 5. (A) Emission spectra (exciting at 490 nm) of the P(MEO_2MA-*b*-BODIPYMA) diblock copolymer (sample **B1**) dissolved (0.36 mg mL^{-1}) in PBS (pH 7, μ = 0.1 M) at different temperatures and (B) evolution of its emission quantum yield with the temperature. Photographs under UV irradiation taken at temperature below LCST (left part) and above LCST (right part) of sample **B1** are included.

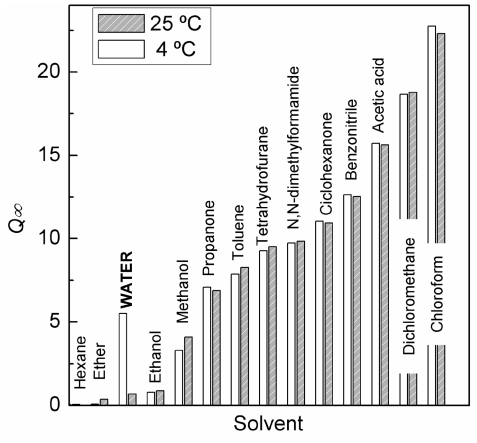

Figure 6. Equilibrium swelling of the P(MEO_2MA-*co*-BODIPYMA) hydrogel in several solvents at 4 and 25 °C.

short BODIPY's Stokes shift made impossible the measurement of the fluorescence exciting at the main absorption band.

P(MEO_2MA-*co*-BODIPYMA) Hydrogel. In order to show that the MEO_2MA-BODIPYMA system can also be interesting for other polymeric structures, a hydrogel of MEO_2MA was synthesized under the same experimental conditions previously described by our research group,[31] but adding a very low proportion of BODIPYMA (1400:1). Figure 6 shows that the equilibrium swelling of this compound depends on the solvent. It can be observed that it is not function of the temperature, with the exception of the solvent water, where a relevant variation with this parameter takes place.

This dependence is shown in detail in Figure 7, in which the equilibrium swelling (Q_∞), the emission (excited at 490 nm) and the absorbance at 600 nm spectra are plotted versus temperature. In this kind of hydrogels, a radical change in the volume and an increase in the opacity are observed above

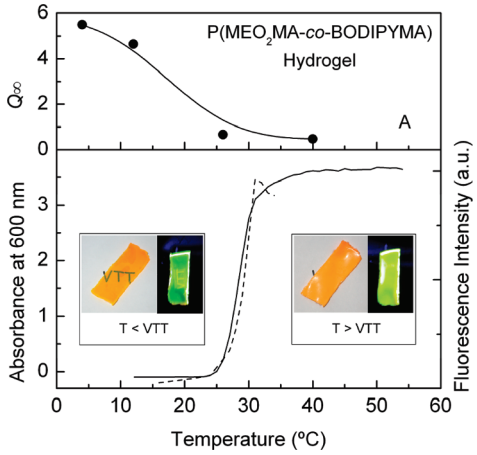

Figure 7. (A) Equilibrium swelling and (B) evolution of absorbance at 600 nm (solid line) and emission (excited at 490 nm, dashed line) of the P(MEO_2MA-*co*-BODIPYMA) hydrogel in PBS (pH 7, μ = 0.1 M) vs temperature. Photographs under visible and UV irradiation taken at temperature below VTT (left part) and above VTT (right part) are included.

a temperature value, called volume transition temperature (VTT), in the same way that the LCST in the noncross-linker polymers.[31] In this case, this transition takes place independently on the BODIPYMA units. However, the novelty of the present system is again that the hydrogel is fluorescent due to the presence of BODIPY side groups. Analogous to their homologues linear polymers, the intensity of the fluorescence depends on the temperature, as it can also be observed in Figure 7. Thus, for temperatures higher than the VTT (around 26 °C) the equilibrium swelling decreases, the system becomes opaque and the fluorescence emission intensity increases. Therefore, it is experimentally demonstrated that the cross-linked structures show the same interesting results of fluorescence observed for the linear polymers. It is important to mention that the VTT of this kind of hydrogels can also be easily modulated by the incorporation of low proportion of other oligo(ethylene glycol) side chain macromonomers, as it was found previously by our research group.[31]

Conclusions

Three different families of thermo-sensitive polymers based on MEO_2MA with a very low proportion of a fluorescent monomer based on BODIPY have been synthesized to study their thermosensitive/fluorescent behavior in aqueous solution: (i) Well-controlled random P(MEO_2MA-*co*-OEG_{8-9}MA-*co*-BODIPYMA) terpolymers, in which the monomeric feed ratio establishes the values of the LCST. In this system, the intensity of the fluorescence strongly increases in a reversible way at the LCST. (ii) Well-controlled diblock P(MEO_2MA-*b*-BODIPYMA) copolymers, in which the H-aggregation between the BODIPY units reduces the emission properties. (iii) A random P(MEO_2MA-*co*-BODIPYMA) hydrogel that becomes opaque and exhibits an increase of the fluorescence intensity rising the VTT, in the same way that its linear homologues.

Acknowledgment. The authors express thanks for the financial support of the Consejo Superior de Investigaciones Científicas (CSIC), Ministerio de Ciencia e Innovación, Ministerio de Sanidad y Consumo and Comunidad Autónoma de Madrid through Projects CTQ 2008-03229, FIS-PI081677, and CAM S 0505/MAT/0227. R.P. thanks the Ministerio de Ciencia e Innovación for a Juan de la Cierva contract and M.L. thanks the CSIC for a JAE-Doc contract.

Supporting Information Available: Figures S1 (NMR spectra) and S2 (SEC traces). This material is available free of charge via the Internet at http://pubs.acs.org.

References and Notes

(1) Ulrich, G.; Ziessel, R.; Harriman, A. *Angew. Chem., Int. Ed.* **2008**, *47*, 1184–1201.
(2) Loudet, A.; Burgess, K. *Chem. Rev.* **2007**, *107*, 4891–4932.
(3) Raymer, B.; Kavana, M.; Price, A.; Wang, B.; Corcoran, L.; Kulathila, R.; Groarke, J.; Mann, T. *Bioorg. Med. Chem. Lett.* **2009**, *19*, 2804–2807.
(4) Rousseau, T.; Cravino, A.; Ripaud, E.; Leriche, P.; Rihn, S.; De Nicola, A.; Ziessel, R.; Roncali, J. *Chem. Commun* **2010**, *46*, 5082–5084.
(5) Olivier, J.-H.; Camerel, F.; Ulrich, G.; Barberá, J.; Ziessel, R. *Chem.—Eur. J.* **2010**, *16*, 7134–7142.
(6) Karolin, J.; Johansson, L. B. A.; Strandberg, L.; Ny, T. *J. Am. Chem. Soc.* **1994**, *116*, 7801–7806.
(7) Treibs, A.; Kreuzer, F. H. *Liebigs Ann. Chem.* **1968**, *718*, 208.
(8) (a) Donuro, V. R.; Vegesna, G. K.; Velayudham, S.; Meng, G.; Lioj, H. *J. Polym. Sci., Polym. Chem.* **2009**, *47*, 5354–5366. (b) Donuro, V. R.; Vegesna, G. K.; Velayudham, S.; Green, S.; Liu, H. *Chem. Mater.* **2009**, *21*, 2130–2138.
(9) Nagai, A.; Miyake, J.; Kokado, K.; Nagata, Y.; Chujo, Y. *J. Am. Chem. Soc.* **2008**, *130*, 15276–15278.
(10) Nagai, A.; Kokado, K.; Miyake, J.; Chujo, Y. *Polym. J.* **2010**, *42*, 37–42.
(11) Nagai, A.; Chujo, Y. *Macromolecules* **2010**, *43*, 193–200.
(12) Nagai, A.; Chujo, Y. *Chem. Lett.* **2010**, *39*, 430–435.
(13) (a) Forgie, J. C.; Skabara, P. J.; Stibor, I.; Vilela, F.; Vobecka, Z. *Chem. Mater.* **2009**, *21*, 1784–1786. (b) Algı, F.; Cihaner, A. *Org. Electron* **2009**, *10*, 453–458. (c) Cihaner, A.; Algı, F. *React. Funct. Polym.* **2009**, *69*, 62–67.
(14) Kajiwara, Y.; Nagai, A.; Chujo, Y. *J. Mater. Chem.* **2009**, *20*, 2985–2992.
(15) Nagai, A.; Kokado, K.; Miyake, J.; Chujo, Y. *Macromolecules* **2009**, *42*, 5446–5452.
(16) Janjic, J. M.; Srinivas, M.; Kadayakkara, D. K. K.; Ahrens, E. T. *J. Am. Chem. Soc.* **2008**, *130*, 2832–2841.
(17) Amat-Guerri, F.; Liras, M.; Carrascoso, M. L.; Sastre, R. *Photochem. Photobiol.* **2003**, *77*, 577–584.
(18) García-Moreno, I.; Costela, A.; Campo, L.; Sastre, R.; Amat-Guerri, F.; Liras, M.; López Arbeloa, F.; Bañuelos Prieto, J.; López Arbeloa, I. *J. Phys. Chem. A* **2004**, *108*, 3315–3323.
(19) García-Moreno, I.; Amat-Guerri, F.; Liras, M.; Costela, A.; Infantes, L.; Sastre, R.; López Arbeloa, F.; Bañuelos Prieto, J.; López Arbeloa, I. *Adv. Funct. Mater.* **2007**, *17*, 3088–3098.
(20) Wang, D.; Miyamoto, R.; Shiraishi, Y.; Hirai, T. *Langmuir* **2009**, *25*, 13176–13182.
(21) (a) Nagai, A.; Kokado, K.; Miyake, J.; Cyujo, Y. *J. Polym. Sci., Polym. Chem.* **2010**, *48*, 627–634. (b) Nagai, A.; Kokado, K.; Miyake, J.; Chujo, Y. *J. Polym. Sci., Polym. Chem.* **2010**, *48*, 1849. (c) Nagai, A.; Yoshii, R.; Otsuka, T.; Kokado, K.; Chujo, Y. *Langmuir* **2010**, *26*, 15644–15649.
(22) Han, S.; Hagiwara, M.; Ishizone, T. *Macromolecules* **2003**, *36*, 8312–8319.
(23) Lutz, J. F. *J. Polym. Sci., Polym. Chem.* **2008**, *46*, 3459–3470.
(24) Lutz, J. F.; Hoth, A. *Macromolecules* **2006**, *39*, 893–896.
(25) Lutz, J. F.; Weichenhan, K.; Akdemir, O.; Hoth, A. *Macromolecules* **2007**, *40*, 2503–2508.
(26) Cai, T.; Marquez, M.; Hu, Z. *Langmuir* **2007**, *23*, 8663–8666.
(27) Yamamoto, S. I.; Pietrasik, J.; Matyjaszewski, K. *J. Polym. Sci., Polym. Chem.* **2008**, *46*, 194–202.
(28) Lutz, J. F.; Akdemir, O.; Hoth, A. *J. Am. Chem. Soc.* **2006**, *128*, 13046–13047.
(29) Yamamoto, S. I.; Pietrasik, J.; Matyjaszewski, K. *Macromolecules* **2008**, *41*, 7013–7020.
(30) Jiang, X.; Zhao, B. *Macromolecules* **2008**, *41*, 9366–9375.
(31) París, R.; Quijada-Garrido, I. *Eur. Polym. J.* **2009**, *45*, 3418–3425.
(32) París, R.; García, J. M.; I. Quijada-Garrido, I. *Polym. Int.* **2010**, (DOI 10.1002/pi.2924)
(33) López Arbeloa, F.; López Arbeloa, T.; López Arbeloa, I.; García-Moreno, I.; Costela, A.; Sastre, R. *Chem. Phys.* **1998**, *236*, 331–341.
(34) Aoshima, S.; Oda, H.; Kobayashi, E. *J. Polym. Sci., Polym. Chem.* **1992**, *30*, 2407–2413.
(35) Aoshima, S.; Sugihara, S. *J. Polym. Sci., Polym. Chem.* **2000**, *38*, 3962–3965.
(36) Kitano, H.; Hirabayashi, T.; Gemmei-Ide, M.; Kyogoku, M. *Macromol. Chem. Phys.* **2004**, *205*, 1651–1659.
(37) Sugihara, S.; Kanaoka, S.; Aoshima, S. *Macromolecules* **2005**, *38*, 1919–1927.
(38) Zhang, D.; Macias, C.; Ortiz, C. *Macromolecules* **2005**, *38*, 2530–2534.
(39) Fechler, N.; Badi, N.; Schade, K.; Pfeifer, S.; Lutz, J. F. *Macromolecules* **2009**, *42*, 33–36.
(40) Badi, N.; Lutz, J. F. *J. Controlled Release* **2009**, *140*, 224–229.
(41) Costela, A.; García-Moreno, I.; Sastre, R.; López Arbeloa, F.; López Arbeloa, T.; López Arbeloa, I. *Appl. Phys. B: Laser Opt.* **2001**, *73*, 19–24.
(42) López Arbeloa, F.; Bañuelos, J.; Martínez, V.; Arbeloa, T.; López Arbeloa, I. *Int. Rev. Phys. Chem.* **2005**, *24*, 339–374.
(43) Bergström, F.; Mikhalyov, I.; Hägglöf, P.; Wortmann, R.; Ny, T.; Johansson, L. B.-Å. *J. Am. Chem. Soc.* **2002**, *124*, 196–204.

Macromolecules
ARTICLE

Macromolecules **2011**, *44*, 87–94 **87**
DOI: 10.1021/ma102216d

Pressure-Sensitive Adhesives from Renewable Triblock Copolymers

Jihoon Shin, Mark T. Martello, Mona Shrestha, Jane E. Wissinger, William B. Tolman,* and Marc A. Hillmyer*

Department of Chemistry and Center for Sustainable Polymers University of Minnesota, 207 Pleasant Street SE, Minneapolis, Minnesota 55455-0431, United States

Received September 24, 2010; Revised Manuscript Received November 18, 2010

ABSTRACT: ABA triblock copolymers were prepared using the renewable monomers menthide and lactide, by sequential ring-opening polymerizations. Initially, hydroxy telechelic polymenthide was synthesized by the diethylene glycol-initiated and tin(II) ethylhexanoate-catalyzed polymerization of menthide. The resulting 100 kg mol^{-1} polymer was used as a macroinitiator for the tin(II) ethylhexanoate-catalyzed ring-opening polymerization of D,L-lactide. Two polylactide−polymenthide−polylactide triblock copolymers were prepared with 5 and 10 kg mol^{-1} polylactide end blocks. Transesterification between the two blocks, and polylactide homopolymer formation were minimized, and triblock copolymers with narrow molecular weight distributions were produced. Microphase separation in these systems was corroborated by differential scanning calorimetry and small-angle X-ray scattering measurements. The triblocks were combined with up to 60 wt % of a renewable tackifier, and the resulting mixtures were evaluated using probe tack, 180° peel adhesion, and shear strength tests. Maximum values of peel adhesion (3.2 N cm^{-1}) and tack (1.1 N) were obtained at 40 wt % of tackifier. These new materials hold promise as renewable and hydrolytically degradable pressure-sensitive adhesives.

Polymeric materials derived from renewable resources have received significant attention due to environmental and other concerns associated with the use of petroleum-based products.[1−3] Currently, renewable resource polymers are used for biomedical applications, food packing, and disposable items, but their somewhat limited property profiles limit their widespread application. Pressure-sensitive adhesives (PSAs) represent a potential application (e.g., tapes, labels, stamps, and sticky notes) that would benefit from the use of renewable materials.[4−6] A distinctive characteristic of PSAs is that they exhibit permanent tackiness and the ability to wet surfaces on contact. PSAs are typically formulated with tackifiers, plasticizers, and fillers mixed with an elastomeric polymer such as a polyacrylate, natural rubber, a silicone, or a styrenic block copolymer (SBC).[7,8] Commonly used SBCs[9,10] have an ABA architecture comprised of a soft, rubbery, low-T_g segment (B) flanked by two hard (high-T_g) end blocks (A).[11] At ambient temperature when microphase separated, the end blocks can act as physical cross-links to form a network of elastically effective B-strands responsible for superior resistance to flow.[12] For removable PSAs this property is essential to minimize residue after the adhesive is removed. Tackifying resins miscible with the midblock improve PSA performance,[13] while plasticizers reduce cost, decrease hardness, and improve low-temperature flexibility.[14] PSAs include solvent-based, hot-melt, and emulsion-based formulations.[15]

In paper recycling PSAs attached to the paper can break down into small pieces during repulping, resulting in a so-called "stickies" problem for the recycling industry.[16] Macrostickies are effectively removed during screening and cleaning processes, but microstickies are still left in the aqueous pulp solution, leading to deposition on equipment and reduced paper quality. To address these problems, two types of PSAs have been studied: screenable/removable PSAs which are broken into relatively large particles and dispersible/soluble PSAs which could be dissolved in the recycling process. Recently, polymeric materials from cationic butyl acrylates[17] and sugar-based acrylates[18,19] have been explored as water-soluble PSAs.

Herein, we report the preparation and characterization of a new PSA system composed of all renewable polylactide−polymenthide−polylactide (PLA-PM-PLA) triblock copolymers combined with a renewable rosin ester tackifier. In previous work, the ring-opening polymerization of menthide (**M**) was demonstrated,[20] and PLA-PM-PLA triblocks containing 20−50 wt % PLA were synthesized using $ZnEt_2$ and $AlEt_3$ catalysts in a two-step polymerization process.[21] These microphase-separated triblocks behaved as thermoplastic elastomers and were shown to be susceptible to hydrolytic degradation.[22,23] On the basis of previous literature, we hypothesized that materials suitable as elastomers for PSA formulations could be attained if the **PM** segment were lengthened and the PLA content minimized.[12,24] We also sought to improve the protocol for synthesis of such triblocks to render the process greener and amenable to large-scale preparations needed for property testing of PSA formulations. Herein we report (a) new methods for preparing PLA-PM-PLA triblocks with 100 kg mol^{-1} **PM** segments with narrow molecular weight distributions, (b) characterization of these triblocks using ^{1}H and ^{13}C NMR spectroscopy, size exclusion chromatography (SEC) coupled with multiangle light scattering (MALS), differential scanning calorimetry (DSC), tensile testing, and small-angle X-ray scattering (SAXS), and (c) combination of these triblocks with variable amounts of a renewable rosin ester tackifier to yield all-renewable PSA formulations with excellent adhesive performance as shown by peel adhesion, probe tack, and shear strength tests.

Results and Discussion

Synthesis of Triblock Copolymers. *a. Synthesis of Menthide.* In previous studies we showed that (−)-menthone could be effectively oxidized to **M** using *m*-chloroperbenzoic acid (*m*-CPBA) in a chlorinated solvent.[20,21,25] We now report

*Corresponding authors. E-mail: wtolman@umn.edu (W.B.T.); hillmyer@umn.edu (M.A.H.).

© 2010 American Chemical Society

Published on Web 12/07/2010

Scheme 1

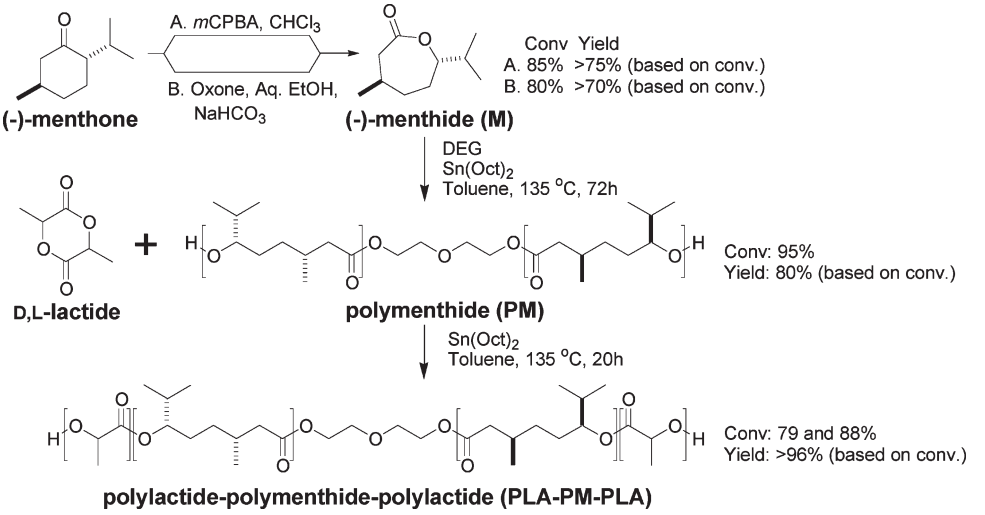

the Baeyer−Villiger oxidation of (−)-menthone using Oxone (potassium peroxymonosulfate) in an ethanol/water mixture as a potentially greener alternative to the *m*-CPBA/$CHCl_3$ (Scheme 1) process with ~80% conversion of starting material; following distillation and sublimation, **M** was obtained in greater than 70% isolated yield.[26] Characterization data for **M** were consistent with previous literature reports.[20,27]

b. Preparation of Telechelic Polymenthide Midblock. α,ω-Hydroxyl-functionalized polymenthide (**PM**) was prepared from the ring-opening polymerization of **M** using tin(II) ethylhexanoate ($Sn(Oct)_2$) as the catalyst and diethylene glycol (DEG) as a bifunctional initiator (Scheme 1). The polymerization was carried out in the presence of a minimal amount of toluene at 135 °C under an inert atmosphere for 72 h on a 50 g scale (see Experimental Section). ^{1}H NMR spectroscopy was used to monitor monomer conversion (typically ≈95%), determine DEG chain connectivity, and calculate M_n for **PM**.[20,21] Conversion of the DEG into the corresponding ester upon addition of **M** resulted in the quantitative downfield shift of both sets of methylene resonances (H_b and H_c, Figure 1). The methine protons at the termini of the **PM** chains were also observed (H_a). Comparison of the integration values for the methylene resonances from the DEG initiator to the methine protons at the **PM** chain ends gave a ratio of about 4 to 1, consistent with two hydroxyl groups per chain and indicative of suppression of adventitious initiation. On the basis of conversion (95%) and the initial monomer-to-initiator content (635:1), the theoretical M_n for **PM**(100)A was 103 kg mol^{-1} (Table 1). A M_n value of 100 kg mol^{-1}, in good agreement with the theoretical value, was determined by ^{1}H NMR spectroscopy using the relative integration between the methylene protons of the DEG initiator fragment (8 protons in total) and the methine protons from the polymenthide repeat units, assuming one DEG moiety per chain. A similar result was obtained if the integration values for the methine protons from the hydroxyl end groups were used in the calculation. By SEC using PS standards, the M_n = 95 kg mol^{-1} (PDI = 1.07) (Table 1 and Figure 2a). The absolute M_n was measured by SEC equipped with a MALS detector which gave a value of 91 kg mol^{-1}. The molecular weight distribution was monomodal and narrow with a PDI of 1.03 (Table 1). In sum, this simple method for the preparation of **PM** with $Sn(Oct)_2$ represents a significant advance over our previously reported synthetic scheme that relied on the use of diethylzinc.[20,21]

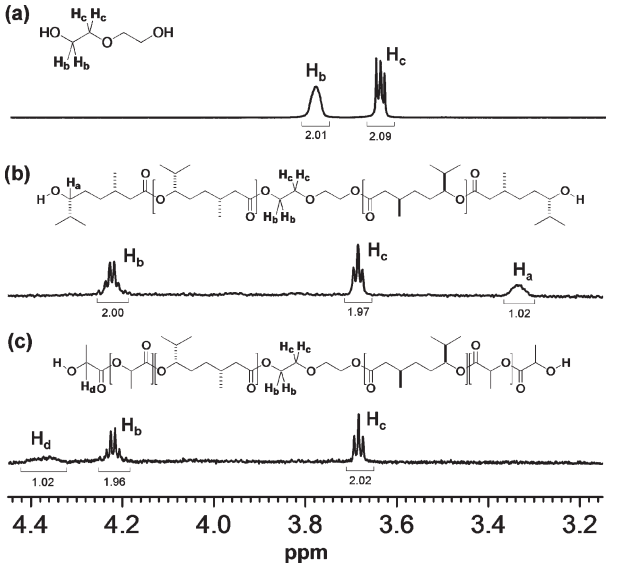

Figure 1. Expanded ^{1}H NMR spectra (500 MHz, $CDCl_3$) of (a) diethylene glycol (DEG), (b) **PM**(100)A, and (c) PLA-PM-PLA-(10-100-10)A.

c. Synthesis and Characterization of PLA-PM-PLA Triblock Copolymers. Typical SBCs used in PSA formulations contain 10−30 wt % polystyrene (PS) as the minority component.[12,24] This requires the overall molecular weight, and the PS block length, be large enough such that the PS domains form hard physical cross-links. Accordingly, PLA end blocks with M_n values of 5 and 10 kg mol^{-1} were targeted. **PM**(100)A was used as a macroinitiator in the ring-opening polymerization of DL-lactide (LA) catalyzed by $Sn(Oct)_2$ at 135 °C (20 h) in a minimal amount of toluene under an inert atmosphere on a 20 g scale (Scheme 1). Upon completion of the reaction, the signal for the terminal methine protons of **PM** at δ 3.33 ppm was no longer present in the ^{1}H NMR spectrum, and a signal for the new terminal methine protons of the PLA end blocks appeared at δ 4.36 ppm (H_d, Figure 1), consistent with efficient initiation by the **PM** chain ends. As illustrated in Figure 1C, the relative integration between the terminal PLA methine protons and the DEG methylene protons corroborates the ABA architecture and suggests that contamination by PLA homopolymer is insignificant.

Table 1. Characterization Data for PM and PLA-PM-PLA[a]

polymer	$[M]_0/[I]_0$	M_n(theo) (kg/mol)[d]	M_n(NMR) (kg/mol)[e]	M_n(SEC) (kg/mol) (PDI)[f]	M_n(SEC-LS) (kg/mol) (PDI)[g]	f_{PLA}[h]
PM(100)A	635[b]	103	100	95 (1.07)	91 (1.03)	
PM(100)B[i]	635[b]	102	105	101 (1.09)		
PLA-PM-PLA(5-100-5)A	104[c]	112	111	102 (1.07)	95 (1.04)	0.08
PLA-PM-PLA(10-100-10)A	190[c]	124	122	109 (1.09)	102 (1.04)	0.15
PLA-PM-PLA(10-100-10)B[i]	190[c]	126	123	112 (1.13)	96 (1.05)	0.13

[a] See Experimental Section for details. [b] M is menthide and I is diethylene glycol (DEG) as a initiator. [c] **M** is D,L-lactide and I is polymenthide (**PM**) as a macroinitiator. [d] Calculated on conversion from monomer to polymer on ^{1}H NMR spectroscopy. [e] Calculated from relative integrations of **PM** repeating units and DEG for **PM** and relative integrations of PLA and **PM** repeating units for PLA-PM-PLA by ^{1}H NMR spectroscopy. [f] Determined with size exclusion chromatography (SEC) in $CHCl_3$ at 35 °C relative to polystyrene standards. [g] Determined by SEC with multiangle laser light scattering (MALS). [h] Calculated volume fraction of PLA using the density of PLA and **PM** as 1.248 and 0.975 g/cm^3 at 25 °C, respectively. [i] Performed by one-pot, two-step polymerization (sequential addition).

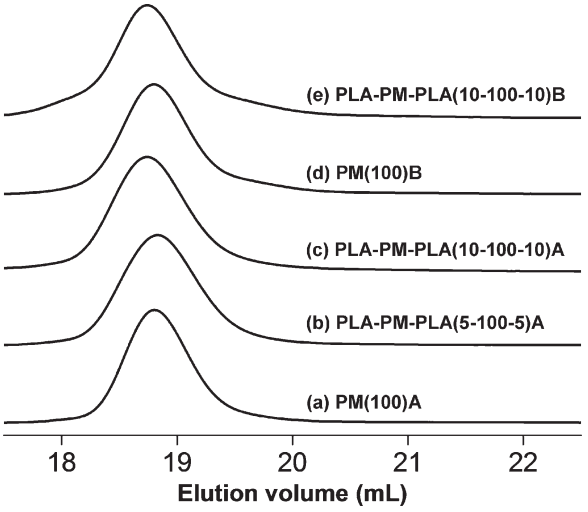

Figure 2. Size exclusion chromatography data (1 mg/mL $CDCl_3$) for **PM** samples and PLA-PM-PLA triblock copolymers.

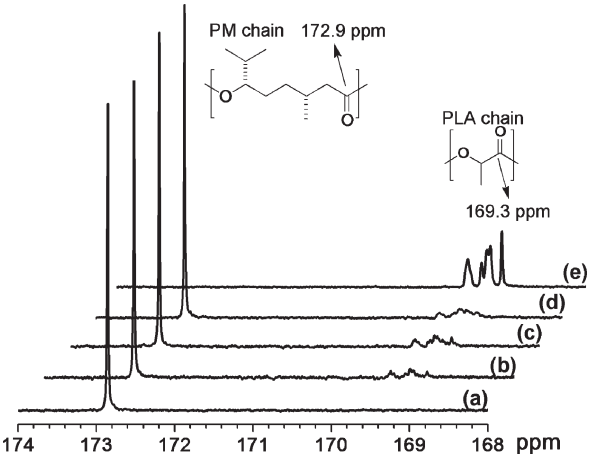

Figure 3. ^{13}C NMR spectra for carbonyl carbons of (a) PM(100)A, (b) PLA-PM-PLA(5-100-5)A, (c) PLA-PM-PLA(10-100-10)A, (d) PLA-PM-PLA(10-100-10)B by one-pot, two synthetic process, and (e) PLA (as a reference; poly(D,L-lactide)).

Prior to purification, ^{1}H NMR spectroscopy of the crude reaction mixture showed 79% and 88% conversion of LA corresponding to a triblock composition of 11.5 wt % PLA and 19.7 wt % PLA for PLA-PM-PLA(5-100-5)A and PLA-PM-PLA(10-100-10)A, respectively. The purified triblock compositions were 10.1 wt % PLA and 18.2 wt % PLA, respectively. The theoretical total PLA M_n based on 79% conversion of LA for PLA-PM-PLA(5-100-5)A was 12 kg mol^{-1}, which compares well to a measured PLA M_n of 11 kg mol^{-1} calculated using the integration values for the PLA and **PM** backbone methine protons. For PLA-PM-PLA(10-100-10)A, the theoretical total PLA M_n values based on 88% conversion of LA and the measured PLA M_n were 24 and 22 kg mol^{-1}, respectively. Analysis of the triblocks by SEC/SEC-LS showed a shift toward lower elution volumes compared to the **PM** homopolymer, and the absence of low molecular weight material that would be indicative of PLA homopolymer (Figure 2).

Transesterification between the PLA end blocks and the **PM** midblock would compromise the ABA triblock architecture.[28] To evaluate this possibility, ^{13}C NMR spectra of PM(100)A, PLA-PM-PLA(5-100-5)A, PLA-PM-PLA(10-100-10)A, PLA-PM-PLA(10-100-10)B, and a PLA homopolymer (M_n = 19.4 kg mol^{-1} and PDI = 1.08) were compared (Figure 3). The triblock copolymers possess only two distinct resonances (172.9 and 169.3 ppm) associated with the carbonyl groups of the **PM** and PLA blocks, consistent with minimal transesterification (additional **PM** carbonyl peaks would be observed if transesterification were significant).[29] This conclusion is also supported by with the observed narrow molecular weight distributions (Figure 2).

To simplify the triblock synthesis further, we developed a one-pot two-step method. As shown in Scheme 1, **M** was first polymerized using the DEG/Sn(Oct)$_2$/toluene system to give the corresponding macroinitiator, which was not isolated. Instead, LA and additional toluene were then added to the reaction mixture, and heating was continued. The conversion of **M** by ^{1}H NMR spectroscopy just prior to the addition of LA was 94%; this observation is consistent with the **M** polymerization reaching its equilibrium conversion (95% at 135 °C).[20] The conversion of LA reached 87% after 20 h at 135 °C. Similarly, the preparation of PLA-PM-PLA(10-100-10)A reached 88% conversion under nearly identical conditions. The residual **M** content was a constant ~5% before and after the polymerization of LA, suggesting that **M** present during the polymerization of LA is not incorporated in the PLA end blocks. These results are similar to those reported for ε-caprolactone/LA copolymerizations where significant ε-caprolactone conversion does not take place until almost all of the LA has been depleted.[30] PLA-PM-PLA(10-100-10)B also possessed only two distinct resonances for **PM** and PLA at 172.9 and 169.3 ppm in the ^{13}C NMR spectrum, indicating minimal transesterification (Figure 3d) and little incorporation of unreacted **M** into the PLA end blocks.[30] The M_n and PDI values (SEC, PS standards) of **PM**and PLA-PM-PLA by the one-pot method were determined to be 101 kg mol^{-1} (PDI 1.09) and 112 kg mol^{-1} (PDI 1.13) (Figure 2d,e), respectively. These values are nearly identical to those obtained by the "two pot, two step procedure" described above. Furthermore, the SEC data are consistent with negligible PLA homopolymer byproducts from fortuitous initiators.

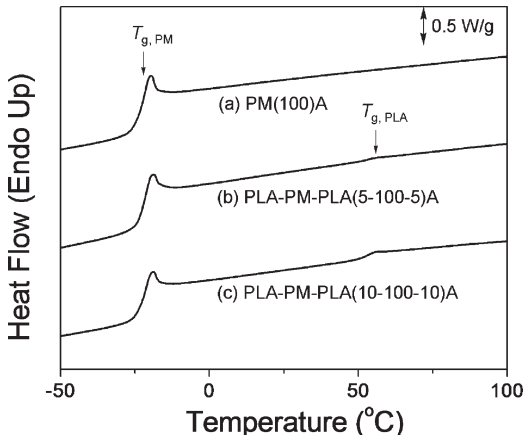

Figure 4. DSC analysis for **PM** and PLA-PM-PLA triblock copolymers.

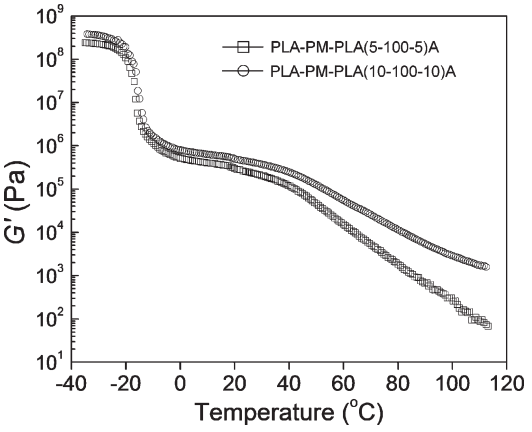

Figure 5. Expanded storage moduli (G') for PLA-PM-PLA triblock copolymers at 1 rad s^{-1}, a strain around 1%, and a ramp rate of 3 °C min^{-1}.

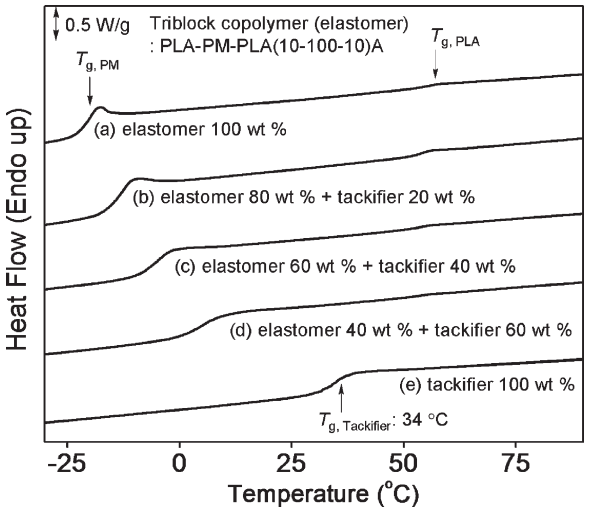

Figure 6. DSC analysis for PLA-PM-PLA(10-100-10)A/rosin ester (RE) tackifier blends.

In a separate experiment, the reaction mixture was held at 135 °C for 1 week after the addition of LA. Although some broadening of the molecular weight distribution was observed relative to the above experiment (PDI = 1.14), no transesterification was evident by ^{13}C NMR spectroscopy (Figure S1). After the 1 week at 135 °C, a second aliquot of LA was added to the reaction mixture and allowed to react for an additional 20 h. The PLA end blocks increased in molecular weight, confirming that the tin catalyst was still active. Again there was some broadening of the molecular weight distribution (PDI = 1.18), but no evidence for transesterification between the **PM** midblock and the PLA end blocks. The reaction was then held at 135 °C for another week, and no evidence for transesterification or incorporation of unreacted **M** into the PLA chains was observed (PDI = 1.18). Collectively, these results are consistent with no reaction of the propagating PLA chains with either **M** or **PM**.

Thermal Properties and Morphology. The microstructures adopted by the triblock copolymers were studied by differential scanning calorimetry (DSC) and small-angle X-ray scattering (SAXS). DSC analyses (Figure 4) of the triblock copolymers show two glass transition temperatures at −22 and 53 °C, corresponding to the **PM** midblock and the PLA end blocks, respectively. This suggests that the PLA end blocks are not mixed in the **PM** phase. SAXS analysis (Figure S2) at room temperature exhibited a weak principal reflection that was also consistent with microphase separation of the triblock copolymer. The principal domain spacings for PLA-PM-PLA(5-100-5)A and PLA-PM-PLA(10-100-10)A were determined to be 59 and 62 nm, respectively.[21] Evidence from both DSC and SAXS support a microphase-separated structure lacking long-range order, where the PLA segments form discrete glassy domains embedded in a rubbery **PM** matrix at room temperature.

Dynamic Mechanical Properties. An important property for PSAs is the dynamic elastic modulus. To promote wetting and contact between adhesive and substrate at the use temperature PSAs should exhibit a dynamic elastic modulus below the Dahlquist criterion (shear modulus $G' \leq 3 \times 10^5$ Pa at 1 s^{-1} or alternatively tensile (Young's) modulus, $E \leq 1 \times 10^5$ Pa).[31] The storage moduli (G') of the two triblock copolymers as a function of temperature at low strain (1%) are shown in Figure 5. The precipitous drop in G' at ∼ −20 °C occurs around the T_g of the **PM** phase. As the temperature is raised, a plateau in the storage modulus is observed until the onset of a more gradual drop in G' due to the glass to rubber transition in the PLA block. The plateau moduli (although not established with great precision)[32] at 25 °C for the two PLA-PM-PLA(5-100-5 and 10-100-10)A samples are 2.0×10^5 and 3.5×10^5 Pa, respectively. From the plateau modulus values at 25 °C, the entanglement molecular weight $M_e \approx 11-14$ kg mol^{-1} for **PM** was approximated using the Guth−Smallwood equation.[33,34] These values are larger than the M_e reported for PI (∼7 kg mol^{-1}), the midblock in SIS block copolymers, and thus less additive would be necessary to achieve even further reduction in the plateau modulus and comparable PSA properties.[35,36] To access more effective PSA's, the use of tackifiers was explored in order to dilute the entanglements and thus lower the modulus further.[12,13,37]

Adhesive Behavior. Through simple compatibility tests, we determined that the rosin ester (RE) tackifier (Sylvalite 2E 80HP) was miscible with the triblocks (Figure S3). Eight PSA formulations were prepared by the combination of PLA-PM-PLA(5-100-5)A and PLA-PM-PLA(10-100-10)A with 0, 20, 40, and 60 wt % RE tackifier. DSC measurements showed two glass transitions for these mixtures (Figure 6 and Figure S4). Adding more tackifier led to broadening of the glass transition temperatures and an increase in the T_g of the **PM** midblock in the blends, relative to that of the pure triblock copolymer. However, there was little change in the T_g of the PLA end blocks in the blends (Figure S4). This is consistent with our conclusion that the tackifier is miscible with only the **PM** midblock, as expected given the more hydrophobic nature of the **PM** midblock.[37,38]

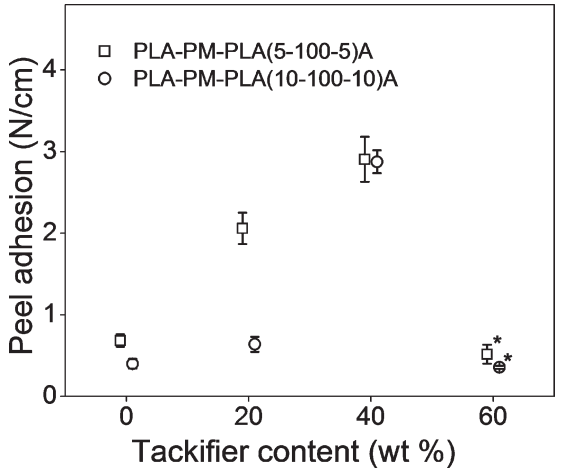

Figure 7. Effect of RE tackifier content on the peel adhesion of the PSA systems. In the case marked by an asterisk, the adhesive separated from the backing (i.e., interfacial or adhesive failure occurred).

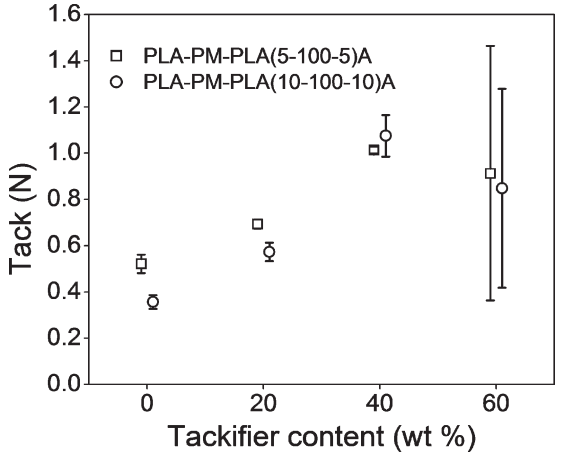

Figure 8. Effect of RE tackifier content on the tack of the PSA systems.

Tack is the property that controls the instant formation of a bonding interaction between adhesive and substrate when they are brought into contact, peel strength is the force needed to remove an adhesive from a substrate, and shear strength is the internal resistance of an adhesive to flow under an applied load.[4,7] Results of these three types of adhesive tests for the eight PSA systems are shown in Figures 7−9 (see Supporting Information for details and comparisons to commercial PSA tapes).[39−41] The triblock copolymers exhibited some degree of peel adhesion and tack without adding tackifier (consistent with the low modulus values show in Figure 5), and the adhesive properties increased with increasing RE tackifier content, ultimately reaching values of peel adhesion = 3.2 N cm^{-1}, tack = 1.1 N, and shear strength ≈ 2500 min at 40 wt % tackifier. By comparison, tests on commercial duct, paper, and electrical tapes under identical conditions gave values of peel adhesion = 1.9−4.2 N cm^{-1}, tack = 0.4−0.6 N, and shear strength ≈ 1500 min (for most samples) as shown in Figures S5−S7. These results for the adhesive properties of our renewable PSA show that they are comparable to commercial samples.

After the peel test of samples with 60% RE, interfacial failure (adhesive failure) was evident (residue left on the stainless steel test plate). Also, the probe tack test results for this blend showed a large standard deviation. Evidently, while tackifiers can improve the cohesive strength in PSAs by the formation of a tackifier-rich soft phase,[12,37,38] too much tackifier (60 wt %) can lead to increases in the T_g of the PSA, actually reducing tack.[42] Finally, similar values from the shear tests were observed regardless of the amount of tackifier (Figure 9). Taken together, the probe tack, peel adhesion, and shear strength test data demonstrate that mixtures of PLA-PM-PLA triblock copolymers and commercially available (and renewable) tackifiers are not only effective PSAs but also exhibit adhesive properties that are competitive with commercial samples (see Figures S5−S7).

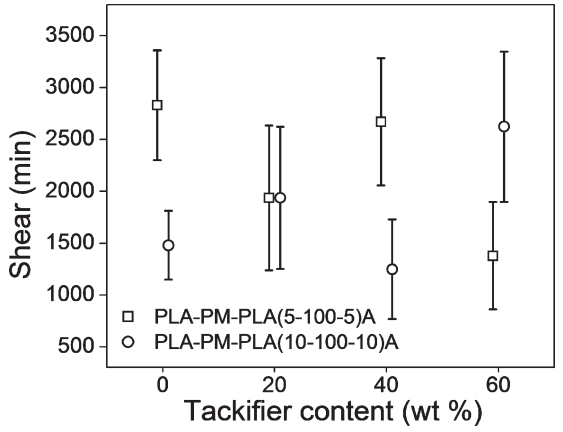

Figure 9. Effect of RE tackifier content on the shear strength of the PSA systems.

Conclusions

A pressure-sensitive adhesives system was designed using renewable triblock copolymers derived from natural products. Using a green chemical approach, **M** was prepared using Oxone and aqueous ethanol. The synthesis of the end-functionalized **PM** with controlled molar mass involved the ring-opening polymerization of **M** by $Sn(Oct)_2$ as the catalyst, giving the corresponding macroinitiator. Subsequently, PLA-PM-PLA triblock copolymers were synthesized as elastomer bases for PSA formulations, using the same catalyst. The polymers were characterized by NMR spectroscopy and size exclusion chromatography. All polymers showed narrow molecular weight distributions. Phase separation was elucidated with small-angle X-ray scattering and differential scanning calorimetry. We determined that transesterification was minimized during polymerization of lactide from a polymenthide macroinitiator, thus providing well-defined block polymers. We also reported the one-pot, two-step polymerization for the triblock copolymers. The elastomers were formulated with a renewable rosin ester tackifier, and probe tack, peel adhesion, and shear strength tests were carried out to evaluate the adhesive properties. The adhesion results were consistent with excellent adhesive performance, thus demonstrating a new application for the all-renewable PLA-PM-PLA triblock copolymers.

Experimental Section

Materials. All air- or moisture-sensitive compounds were handled under a nitrogen atmosphere in a glovebox, as indicated. Toluene was dried using sodium and benzophenone, distilled under reduced pressure, and stored in a nitrogen-filled glovebox. Diethylene glycol (Aldrich) used for polymerizations was distilled under reduced pressure over sodium and stored in a glovebox. Tin(II) 2-ethylhexanoate (Aldrich) used for polymerization was also distilled using a Kugelrohr apparatus followed by storage in a glovebox. D,L-Lactide (Purac) was recrystallized twice from toluene prior to being stored in a glovebox. (−)-Menthone (90%), Oxone, and *m*-chloroperoxybenzoic acid (*m*-CPBA, ≤77%) were used as received from Aldrich without further purification. The rosin ester tackifier, Sylvalite 2E 80HP, and the polyterpene tackifier, Sylvares TR B115, were obtained

from Arizona Chemical. All other solvents and reagents were used as received from the commercial source without further purification. The backing for the adhesive testing was poly(ethylene terephthalate) sheet (PET, thickness: 50 μm).

Measurements. ^{1}H and ^{13}C NMR spectra were recorded using Varian Inova-500 spectrometer at room temperature. The samples of the polymers were prepared at a concentration of approximately 10 and 100 mg/mL, respectively, in $CDCl_3$ (Cambridge). Molecular weights (M_n and M_w) were determined by size exclusion chromatography (SEC) using polystyrene standards. Chloroform was the mobile phase, and the flow rate was set at 1.0 mL/min at 35 °C using a Hewlett-Packard high-pressure liquid chromatography equipped with three Jordi poly(divinylbenzene) columns of 10^4, 10^3, and 500 Å pore size and a HP1047A differential refractometer. To measure the absolute molecular weights of the polymers, SEC coupled with MALS was also performed in THF at ambient temperature with an eluent flow rate of 1 mL/min using an Alltech 426 HPLC pump with a 100 μL injection loop, a Wyatt Technology Corp. Dawn DSP-F laser photometer, and a Wyatt Technology Corp. Optilab DSP interferometric refractometer with three Phenomonex Phenogel columns (pore sizes 5×10^3, 5×10^4, and 5×10^5 Å). The differential refractive index increment (dn/dc) was determined by pumping THF solutions of the polymers of known concentration through the Wyatt Technology Corp. Optilab DSP interferometric refractometer, with a wavelength of 633 nm and a temperature of 25 °C throughout the measurement. All GC-MS experiments were conducted on an Agilent Technologies 7890A GC system and 5975C VL MSD. Differential scanning calorimetry (DSC) measurements were performed using a TA Instruments Q1000 under a nitrogen atmosphere. The polymer samples were heated to 120 °C, held there for 1 min to avoid the influence of thermal history, cooled to −100 °C, held there for 1 min, and then reheated to 120 °C. The rates of heating and cooling were 10 °C/min. The values reported were obtained from the second heating cycle. An indium standard was used for calibration. Samples weighing 7.0−9.0 mg were loaded into aluminum pans. SAXS measurements for samples of PLA-PM-PLA(5-100-5 and 10-100-10)A were performed at the Advanced Photon Source (APS) on beamline 5 ID-D, which is maintained by the DuPont−Northwestern−Dow Collaborative Access Team (DND-CAT). The X-ray source operated at a wavelength of 0.8856 Å with a sample-to-detector distance of 8552 mm calibrated with silver behenate. The flight tube was evacuated. Two-dimensional diffraction images were recorded using a Mar 165 mm CCD X-ray detector at a resolution of 2048 × 2048. The two-dimensional images were azimuthally integrated and reduced to the one-dimensional form of scattered intensity versus the spatial frequency q. Rheological testing was performed on the as-synthesized samples with an ARES (Rheometric Scientific, Piscataway, NJ) with 8 mm parallel plates. The dynamic moduli were measured as a function of temperature at a frequency of 1 rad s^{-1}, a strain around 1%, and a ramp rate of 3 °C min^{-1}. Low-temperature measurements were performed by heating the sample above the glass transition of the PLA, increasing the distance between the parallel plates to ca. 7 mm, thereby stretching the sample, and subsequently cooling to the test temperature. This allowed for the measurement of the moduli in the glassy region, in which the stiffness of the sample would have otherwise caused compliance errors and transducer resonance.

Synthesis of (−)-Menthide (M). Two Baeyer−Villiger reaction protocols were employed to prepare **M** in one step starting from (−)-menthone. As previously reported by Zhang et al.,[20] *m*-chloroperbenzoic acid in chloroform converted the starting material to **M** with 85% conversion determined by ^{1}H NMR spectroscopy. Following isolation and purification, **M** was obtained in > 75% gravimetric yield on a 50 g scale. The following procedure has been developed for the preparation of **M** using Oxone in an aqueous ethanol solution. A round-bottom flask (1 L) was loaded with (−)-menthone (6.170 g, 40 mmol), sodium bicarbonate (26.9 g, 320 mmol), and ethanol (200 mL). The reaction was stirred at room temperature as a solution of Oxone (49.2 g, 160 mmol) in water (200 mL) was added via syringe pump over 48 h. After the addition was complete, the reaction was allowed to stir for an additional 8 h. The reaction mixture was vacuum filtered through Celite to remove the solids. The filtrate was concentrated to ~10 mL via rotary evaporation under reduced pressure. The product was diluted with ethyl acetate (100 mL), dried over anhydrous magnesium sulfate, and vacuum filtered through Celite. The product was purified by vacuum distillation (65−70 °C, 0.6 mmHg) followed by sublimation (40−42 °C, 0.3 mmHg) to yield **M**, which is a white crystalline solid (4.0 g, 23.5 mmol and overall yield of 58.8%). GC/MS (m/z): 56, 69, 81, 98, 128. ^{1}H NMR ($CDCl_3$): δ 4.04 (dd, J = 9.2 and 4.4 Hz, 1H), 2.57−2.45 (m, 2H), 1.97−1.81 (m, 4H), 1.64−1.56 (m, 1H), 1.33−1.25 (m, 1H), 1.04 (d, J = 6.7 Hz, 3H), 0.97 (t, 6.8 Hz, 6H). ^{13}C{^{1}H} NMR ($CDCl_3$) δ 174.0, 83.8, 42.1, 36.8, 32.9, 30.7, 30.1, 23.6, 18.1, 16.6.

Synthesis of PM(100)A. In a nitrogen-filled glovebox, **M** (48.0 g, 282 mmol) was dissolved in toluene (22.4 mL). The menthide solution was passed through activated basic alumina (Fisher Scientific). Without passing **M** through the alumina column, attempts to prepare high molecular weight **PM** polymers resulted in an apparent bimodal molecular distribution and a reduction in the molecular weight determined by SEC. Employing the alumina column resulted in a unimodal molecular weight distribution. We attribute the bimodal distribution to an impurity in the monomer feed, possibly the hydrolysis product, that acts as an adventitious monofunctional initiator during the polymerization. The filtered solution was quantitatively transferred to a pressure vessel (350 mL) equipped with a stir bar. Diethylene glycol (42.1 μL, 0.444 mmol) was injected into the reaction vessel followed by the addition of tin(II) 2-ethylhexanoate (180 mg, 0.444 mmol). The reaction vessel was sealed, taken out of the glovebox, and placed in a thermostatic oil bath at 135 °C for 72 h (95% conversion of monomer). The reaction was quenched by exposure to the air. The crude product was diluted with chloroform (ca. 400 mL). The polymer solution was precipitated into methanol at −78 °C in order to recover **PM** and remove the remaining monomers. It was dried at 90 °C in a vacuum oven (36.5 g recovered, 80% isolated yield based on product weight calculated by conversion). Density: 0.975 g/cm^3. dn/dc: 0.064 mL/g in THF at 25 °C. ^{1}H NMR ($CDCl_3$): δ 4.72 (m, 589H, H_a from the repeating unit of **PM**), 4.22 (q, J = 4.5 Hz, 4H, H_b from the incorporated initiator), 3.68 (t, J = 4.5 Hz, 4H, H_c from incorporated initiator), 3.33 (br, 2H, $H_{a\ terminal}$ from the end unit of **PM**), 2.30 (dd, J = 15.3 and 5.5 Hz, 589H from the repeating unit of **PM**), 2.07 (dd, J = 14.4 and 8.5 Hz, 589H from the repeating unit of **PM**), 1.94 (m, 589H from the repeating unit of **PM**), 1.82 (m, 589H from the repeating unit of **PM**), 1.53 (m, 1178H from the repeating unit of **PM**), 1.33 (m, 589H from the repeating unit of **PM**), 1.18 (m, 589H from the repeating unit of **PM**), 0.94 (d, J = 6.6 Hz, 1767H from the repeating unit of **PM**), 0.88 (dd, J = 6.8 and 2.0 Hz, 3534H from the repeating unit of **PM**). ^{13}C{^{1}H} NMR ($CDCl_3$): δ 172.9, 78.2, 41.9, 32.6, 31.1, 30.3, 28.4, 19.7, 18.6, 17.5.

Synthesis of PLA-PM-PLA(5-100-5)A. In a nitrogen-filled glovebox, a pressure vessel (350 mL) was charged with PM(100)A (17.7 g, 0.177 mmol), tin(II) 2-ethylhexanoate (71.5 mg, 0.177 mmol), and toluene (35.0 mL). The reaction vessel was sealed and taken out of the glovebox to dissolve the mixture at 135 °C for 30 min. The vessel was cooled to room temperature and again brought into the glovebox. D,L-Lactide (2.65 g, 18.4 mmol) was added into the reaction vessel. It was sealed and taken out of the glovebox to stir at 135 °C for 20 h (79% conversion of monomer). The reaction was quenched by exposure to the air, diluted with chloroform (ca. 100 mL), and precipitated into methanol at −78 °C. The recovered PLA-PM-PLA was dried at 90 °C in a vacuum oven (19.4 g recovered, 98% isolated yield based on product weight calculated by conversion). dn/dc: 0.058 mL/g in THF at 25 °C. ^{1}H NMR ($CDCl_3$): δ 5.20 (m, 78H, H_d from the repeating unit of PLA) 4.72 (m, 589H, H_a from the repeating unit of **PM**), 4.36 (br, 2H, $H_{d\ terminal}$ from the end unit of PLA), 4.22 (q, J = 4.5 Hz,

4H, H_b from the incorporated initiator), 3.68 (t, J = 4.5 Hz, 4H, H_c from incorporated initiator), 2.30 (dd, J = 15.3 and 5.5 Hz, 589H from the repeating unit of **PM**), 2.07 (dd, J = 14.4 and 8.5 Hz, 589H from the repeating unit of **PM**), 1.94 (m, 589H from the repeating unit of **PM**), 1.82 (m, 589H from the repeating unit of **PM**), 1.53 (m, 1178H from the repeating unit of **PM** and 234H from the repeating unit of PLA), 1.33 (m, 589H from the repeating unit of **PM**), 1.18 (m, 589H from the repeating unit of **PM**), 0.94 (d, J = 6.6 Hz, 1767H from the repeating unit of **PM**), 0.88 (dd, J = 6.8 and 2.1 Hz, 3534H from the repeating unit of **PM**). $^{13}C\{^1H\}$ NMR ($CDCl_3$): δ 172.9, 169.3, 78.2, 69.2, 41.9, 32.6, 31.1, 30.3, 28.4, 19.7, 18.6, 17.5, 16.7.

Synthesis of PLA-PM-PLA(10-100-10)A. In a nitrogen-filled glovebox, a pressure vessel (350 mL) was charged with PM-(100)A (17.1 g, 0.171 mmol), tin(II) 2-ethylhexanoate (69.2 mg, 0.177 mmol), and toluene (34.0 mL). The reaction vessel was sealed and taken out of the glovebox to dissolve the mixture at 135 °C for 30 min. The vessel was cooled to room temperature and again brought into the glovebox. D,L-Lactide (4.68 g, 32.5 mmol) was added into the reaction vessel. It was sealed and taken out of the glovebox to stir at 135 °C for 20 h (88% conversion of monomer). The reaction was quenched by exposure to the air. The crude product was diluted with chloroform (ca. 100 mL). The polymer solution was precipitated into methanol at −78 °C in order to recover the PLA-PM-PLA and remove the remained monomers. It was dried at 90 °C in a vacuum oven (20.3 g recovered, 96% isolated yield based on product weight calculated by conversion). dn/dc: 0.065 mL/g in THF at 25 °C. ^1H NMR ($CDCl_3$): δ 5.20 (m, 153H, H_d from the repeating unit of PLA) 4.72 (m, 589H, H_a from the repeating unit of **PM**), 4.36 (br, 2H, $H_{d\ terminal}$ from the end unit of PLA), 4.22 (q, J = 4.5 Hz, 4H, H_b from the incorporated initiator), 3.68 (t, J = 4.5 Hz, 4H, H_c from incorporated initiator), 2.30 (dd, J = 15.3 and 5.5 Hz, 589H from the repeating unit of **PM**), 2.07 (dd, J = 14.4 and 8.5 Hz, 589H from the repeating unit of **PM**), 1.94 (m, 589H from the repeating unit of **PM**), 1.82 (m, 589H from the repeating unit of **PM**), 1.53 (m, 1178H from the repeating unit of **PM** and 459H from the repeating unit of PLA), 1.33 (m, 589H from the repeating unit of **PM**), 1.18 (m, 589H from the repeating unit of **PM**), 0.94 (d, J = 6.6 Hz, 1767H from the repeating unit of **PM**), 0,88 (dd, J = 6.8 and 2.1 Hz, 3534H from the repeating unit of **PM**). $^{13}C\{^1H\}$ NMR ($CDCl_3$): δ 172.9, 169.3, 78.2, 69.2, 41.9, 32.6, 31.1, 30.3, 28.4, 19.7, 18.6, 17.5, 16.7.

One-Pot, Two-Step Polymerization for Synthesis of PLA-PM-PLA(10-100-10)B. In a nitrogen-filled glovebox, **M** (2.50 g, 14.7 mmol) was dissolved in toluene (1.2 mL) and filtered through activated basic alumina. The filtered solution was transferred to a pressure vessel (35 mL) with a stir bar. Diethylene glycol (2.20 μL, 0.023 mmol) was injected into the reaction vessel followed by the addition of tin(II) 2-ethylhexanoate (9.30 mg, 0.023 mol). The reaction vessel was sealed and taken out of the glovebox and heated to 135 °C for 72 h (94% conversion of monomer). After cooling the vessel to room temperature, it was brought into the glovebox. The vessel was charged with toluene (3.8 mL) and reheated to 135 °C for 30 min to dissolve the polymer. The vessel was cooled to room temperature, and D,L-lactide (634 mg, 4.40 mmol) was added into the reaction vessel in the glovebox. The vessel was sealed and returned to 135 °C for 20 h (87% conversion of monomer). The reaction was quenched by exposure to the air, diluted with chloroform (ca. 5 mL), and precipitated into methanol at −78 °C. The recovered PLA-PM-PLA was dried at 90 °C in a vacuum oven (2.3 g recovered, 78% recovery based on product weight calculated by conversion).

Adhesive Behaviors. *a. Compatibility Tests*. The compatibility of the tackifier and the elastomer was estimated by the following simple tests. First, the liquid phase separation of the adhesive solution in toluene was examined. Individual solutions of PLA-PM-PLA(10-100-10)A in toluene (40 wt %) and rosin ester or polyterpene in toluene (40 wt %) were prepared, to make the tackifier content 50 wt % based on the total solid content. The same amounts of two solutions were mixed in a vial using a stir bar for 3 h. The solution was transferred to a test tube, allowed to stand for 10 days at room temperature, and then observed visually. Second, the 40 wt % toluene solutions of the adhesive systems were cast on a PET sheet. After evaporating toluene at room temperature, the transparency of the films was observed visually. The resulting thickness of the adhesive systems layer was ca. 20 μm. The 50 wt % of tackifier content was used.

b. Samples Preparation for Adhesive Tests. Eight samples from our PSAs system were prepared for performing adhesive tests and measuring the thermal properties. PLA-PM-PLA(5-100-5 and 10-100-10)A were used as elastomers and the rosin ester was used as a tackifier. The concentration of PLA-PM-PLA/tackifier toluene solution was 30 wt %. The tackifier concentration was 0, 20, 40, and 60 wt % based on the total solid content. Selected amounts of eight solution samples were dried at 90 °C in a vacuum oven to completely evaporate toluene and anneal overnight. They were used for preparing DSC samples. The solutions of the PSAs in toluene were coated on the PET sheets (thickness: 50 μm), using a drawdown caster and a wire wound rod, and were dried in a 100 °C oven for 10 min. The cast films were transferred to a room with controlled temperature and humidity of 22 ± 1.5 °C and 50 ± 2% room humidity and remained in the room for at least 12 h before testing. The target thickness of the cast adhesive after drying was ca. 20 μm. PSA sample performance was evaluated using the following adhesive tests.

c. Peel 180° Test. The peel strength of the PSAs was measured in the controlled room, using an IMASS SP101B slip/peel tester at a peel rate of 12 in. min^{-1}. One inch wide PET backed films were peeled from Pressure-Sensitive Tape Council, PSTC-grade polished stainless steel panels as an adherend. The strip on the stainless steel was pressed with a 5.0 lb ASTM quality manual roller to develop good contact between the adhesive and the steel plate. The average peel force and standard deviation from at least three tests were reported for each sample.

d. Probe Tack Test. Tack was also measured in the controlled room, using the IMASS SP101B slip/peel tester with a 10 N load cell. A stainless steel probe with a diameter of 5 mm contacted the film, was held at a constant force for 15 s, and then raised from the surface at a fixed rate. The resulting maximum force was recorded. The probe was cleaned before each test. The average tack force and standard deviation from at least 10 tests were reported for each sample.

e. Shear Test. Shear test strips were prepared with a contact area of 0.5 × 0.5 in. between PSTC-grade polished stainless steel panels and the adhesive. Samples were rolled with a 5 lb ASTM quality manual roller. 500 g weights were attached to the bottom of the test strips. The average time in minutes for the weight to pull the PET-backed films from the plate for at least three tests was reported for each sample.

Acknowledgment. This work was supported by the Center for Sustainable Polymers at the University of Minnesota through a grant from the Institute for Renewable Energy and the Environment (IREE RL-0009-09). The authors greatly appreciate Arizona Chemical for samples of the tackifiers, Dr. Carolyn L. Wanamaker for helpful discussions and for some experimental support, and Dr. Steve Severtson and Dr. Jiguang Zhang for help with adhesive testing.

Supporting Information Available: ^{13}C NMR spectra for sequential additions, SAXS profiles for PLA-PM-PLA triblock copolymers, compatibility tests details with rosin ester and polyterpene tackifiers, and adhesive test details and comparisons to commercial PSA tapes. This material is available free of charge via the Internet at http://pubs.acs.org.

References and Notes

(1) Yu, L.; Dean, K.; Li, L. *Prog. Polym. Sci.* **2006**, *31*, 576–602.
(2) *Monomers, Polymers and Composites from Renewable Resources*; Belgacem, M. N., Gandini, A., Eds.; Elsevier: Amsterdam, 2008.
(3) Meier, M. A. R.; Metzger, J. O.; Schubert, U. S. *Chem. Soc. Rev.* **2007**, *36*, 1788–1802.
(4) Pocius, A. V. *Adhesion and Adhesives Technology: An Introduction*, 1st ed.; Hanser-Gardner: Cincinnati, 1997; pp 251−259.
(5) Yuan, B.; McGlinchey, C.; Pearce, E. M. *J. Appl. Polym. Sci.* **2006**, *99*, 2408–2413.
(6) Paiva, A.; Sheller, N.; Foster, M. D.; Crosby, A. J.; Shull, K. R. *Macromolecules* **2001**, *34*, 2269–2276.
(7) Benedek, I. *Pressure-Sensitive Adhesives and Applications*, 2nd ed.; Marcel Dekker: New York, 2004; pp 429−477.
(8) (a) Creton, C.; Fabre, P. T. In *Adhesion Science and Engineering*; Dillard, D. A., Pocius, A. V., Eds.; Elsevier: Amsterdam, 2002; Vol. *1*, pp 535−576. (b) Creton, C.; Roos, A.; Chiche, A. In *Adhesion: Current Research and Applications: Effect of the Diblock Content on the Adhesive and Deformation Properties of PSAs Based on Styrenic Block Copolymers*; Possart, W. G., Ed.; Wiley-VCH: Weinheim, 2005; pp 337−364.
(9) Lewis, P. R.; Price, C. *Polymer* **1971**, *13*, 20–26.
(10) (a) McIntyre, D.; Campos-Lopez, E. *Macromolecules* **1970**, *3*, 322–327. (b) Campos-Lopez, E.; McIntyre, D.; Fetters, L. J. *Macromolecules* **1973**, *6*, 415–423. (c) Creton, C.; Hu, G. J.; Deplace, F.; Morgret, L.; Shull, K. R. *Macromolecules* **2009**, *42*, 7605–7615.
(11) Kraus, G.; Rollman, K. W.; Gruver, J. T. *Macromolecules* **1970**, *3*, 92–96.
(12) (a) Creton, C. *MRS Bull.* **2003**, *28*, 434–439. (b) Daoulas, K. Ch.; Theodorou, D. N.; Roos, A.; Creton, C. *Macromolecules* **2004**, *37*, 5093–5109.
(13) (a) Kraus, G.; Rollman, K. W.; Gray, R. A. *J. Adhes.* **1979**, *10*, 221–236. (b) Lim, D.-H.; Do, H.-S.; Kim, H.-J. *J. Appl. Polym. Sci.* **2006**, *102*, 2839–2846.
(14) Martin-Martínez, J. M. Rubber-Based Pressure-Sensitive Adhesives. In *Technology of Pressure-Sensitive Adhesives and Products*; Benedek, I., Feildstein, M. M., Eds.; CRC Press: Boca Raton, FL, 2009; pp 2-40−2-41.
(15) Goulding, T. M. Pressure-Sensitive Adhesive. In *Handbook of Adhesive Technology*; Pizzi, A., Mittal, K. L., Eds.; Marcel Dekker: New York, 1994; pp 549−564.
(16) (a) Cathie, K. *Int. J. Adhes. Adhes.* **1994**, *14*, 63–67. (b) Nowak, M. J.; Severtson, S. J.; Wang, X. P.; Kroll, M. S. *Ind. Eng. Chem. Res.* **2003**, *42*, 1681–1687. (c) Severtson, S. J.; Wang, X. P.; Kroll, M. S. *Ind. Eng. Chem. Res.* **2002**, *41*, 5668–5675.
(17) Yan, Z.; Deng, Y. *J. Appl. Polym. Sci.* **2003**, *90*, 1624–1630.
(18) Bloembergen, S.; Mclennan, I. J.; Schmaltz, C. S. *Adhes. Technol.* **1999**, *9*, 10–13.
(19) Bloembergen, S.; Mclennan, I. J.; Cassar, S. E.; Narayan, R. *Adhes. Age* **1998**, *41*, 20–24.
(20) Zhang, D.; Hillmyer, M. A.; Tolman, W. B. *Biomacromolecules* **2005**, *6*, 2091–2095.
(21) Wanamaker, C. L.; O'Leary, L. E.; Lynd, N. A.; Hillmyer, M. A.; Tolman, W. B. *Biomacromolecules* **2007**, *8*, 3634–3640.
(22) Wanamaker, C. L.; Bluemle, M. J.; Pitet, L. M.; O'Leary, L. E.; Tolman, W. B.; Hillmyer, M. A. *Biomacromolecules* **2009**, *10*, 2904–2911.
(23) Wanamaker, C. L.; Hillmyer, M. A.; Tolman, W. B. *Biomacromolecules* **2009**, *10*, 443–448.
(24) Gibert, F. X.; Marin, G.; Derail, C.; Allal, A.; Lechat *J. Adhes.* **2003**, *79*, 825–852.
(25) Canan Koch, S. S.; Chamberlin, A. R. *Synth. Commun.* **1989**, *19*, 829–833.
(26) Shrestha, M.; Martello, M. T.; Wissinger, J. E.; Hillmyer, M. A. Abstract of Papers, 239th ACS National Meeting, San Francisco, CA, Mar 21−25, **2010**.
(27) Kaneda, K.; Ueno, S.; Imanaka, T.; Shimotsuma, E.; Nishiyama, Y.; Ishii, Y. *J. Org. Chem.* **1994**, *59*, 2915–2917.
(28) Dechy-Cararet, O.; Martin-Vaca, B.; Bourissou, D. *Chem. Rev.* **2004**, *104*, 6147–6176.
(29) Agarwal, S.; Xie, X. *Macromolecules* **2003**, *36*, 3545–3549.
(30) (a) Vanhoorne, P.; Dubois, Ph.; Jerome, R.; Teyssie, Ph. *Macromolecules* **1992**, *25*, 37–44. (b) Grijpma, D. W.; Pennings, A. J. *Polym. Bull.* **1991**, *25*, 335–341. (c) Kricheldorf, H. R.; Bornhorst, K.; Hachmann-Thiessen, H. *Macromolecules* **2005**, *38*, 5017–5024. (d) Mosnáček, J.; Duda, A.; Libiszowski, J.; Penczek, S. *Macromolecules* **2005**, *38*, 2027–2029.
(31) (a) Dahlquist, C. A. Pressure-Sensitive Adhesive. In *Treatise on Adhesion and Adhesives*; Patrick, R. L., Ed.; Dekker: New York, 1969; Vol. *2*, p 219. (b) Yarsso, D. J. Effect of Rheology on PSA performance. In *Adhesion Science and Engineering*; Dillard, D. A., Pocious, A. V., Eds.; Elsevier: Amsterdam, 2002; Vol. *1*, pp 505−506.(c) Autumn, K.; Majidi, C.; Groff, R. E.; Dittmore, A.; Fearing, R. *J. Exp. Biol.* **2006**, *209*, 3558–3568.
(32) In the case of polystyrene−polyisoprene−polystyrene (SIS), because the difference between the T_g values for the soft and hard phases is large (∼150 °C), the plateau is readily distinguished. However, because PLA-PM-PLA has a relatively small difference between the two T_g values (∼70 °C), the plateau is less clearly established.
(33) Guth, E. *J. Appl. Phys.* **1945**, *16*, 20–25.
(34) Tse, M. F. *J. Adhes. Sci. Technol.* **1989**, *3*, 551–570.
(35) Holden, G.; Kricheldorf, H. R.; Quirk, R. P. *Thermoplastic Elastomers*, 3rd ed.; Hanser-Gardner: Cincinnati, 2004; pp 51−56.
(36) Hiemenz, P. C.; Lodge, T. P. *Polymer Chemistry*, 2nd ed.; CRC Press: Boca Raton, FL, 2007; pp 444−450.
(37) Nakamura, Y.; Sasaki, Y.; Adachi, M.; Fuji, S.; Sasaki, M.; Urahama, Y. *J. Adhes. Sci. Technol.* **2008**, *22*, 1313–1331.
(38) Sasaki, M.; Nakamura, Y.; Fujita, K.; Kinugawa, Y.; Iida, T.; Urahama, Y. *J. Adhes. Sci. Technol.* **2005**, *19*, 1445–1457.
(39) Czech, Z. *J. Appl. Polym. Sci.* **2005**, *97*, 886–892.
(40) Urban, D.; Ilosa, J. M. T.; Wulff, D.; Weiss, A.; Arisandy, C. Carrier for Cold Seal Coated Face and Back. U.S. Pat. Appl. 0277560, 2009.
(41) Fry, A. L. Repositionable Pressure-Sensitive Adhesive Sheet Material. U.S. Patent 5,194,299, Mar 13, 1993.
(42) Brown, K.; Hooker, J. C.; Creton, C. *Macromol. Mater. Eng.* **2002**, *287*, 163–179.

Macromolecules
ARTICLE

Macromolecules **2011**, *44*, 95–103 **95**
DOI: 10.1021/ma1023654

Synthesis and Electronic Structure of Ferrocenylborane-Modified Quaterthiophenes and Polythiophenes

Haiyan Li,[†] Anand Sundararaman,[†] Thilagar Pakkirisamy,[†] Krishnan Venkatasubbaiah,[†] Frauke Schödel,[‡] and Frieder Jäkle*,[†]

[†]*Department of Chemistry, Rutgers University—Newark, 73 Warren Street, Newark, New Jersey 07102, United States, and* [‡]*Institut für Anorganische und Analytische Chemie, Johann Wolfgang Goethe-Universität Frankfurt am Main, Max-von-Laue-Strasse 7, D-60438 Frankfurt, Germany*

Received October 16, 2010; Revised Manuscript Received November 23, 2010

ABSTRACT: Polythiophene was functionalized with redox-active ferrocenylborane pendent groups. A postpolymerization modification procedure was applied, in which silylated polythiophene was reacted with BBr_3 to give a polymer with pendent BBr_2 groups. The dibromoboryl functionalities were then further elaborated by first treating the intermediate with $FcSnMe_3$ to introduce the ferrocenyl moieties and then with an arylcopper derivative ArCu (Ar = 2,4,6-trimethylphenyl (Mes), 2,4,6-triisopropylphenyl (Tip)) to sterically stabilize the boron centers. Using similar methods, two quaterthiophene derivatives were also prepared. The number-average molecular weight (M_n) of the polymers was determined by gel permeation chromatography (GPC) relative to narrow PS standards to range from 9400 to 14 600 Da. The polymer structure was further confirmed by MALDI-TOF mass spectrometry and by multinuclear NMR spectroscopy. H,H-NOESY spectroscopy and single crystal X-ray diffraction experiments on the quaterthiophene derivatives were used to gain insight into the conformation of the oligomers and polymers in solution and the solid state. The electronic structure of the oligo- and polythiophenes was studied in detail by UV−vis spectroscopy and electrochemical measurements.

Introduction

Polythiophenes are among the most thoroughly investigated classes of conjugated polymers and stand out due to their interesting optical and electronic properties which can easily be fine-tuned thanks to an exceptional degree of synthetic flexibility. Applications in organic light-emitting devices, photovoltaics, organic field effect transistors, and sensor materials have been extensively studied.[1] The incorporation of organoborane groups into conjugated polymer structures, on the other hand, has recently attracted considerable research efforts.[2] These studies take advantage of the fact that the empty p orbital of boron shows a strong tendency for p−π interactions with extended organic π-systems, which results in interesting photophysical and electronic properties.[3,4] Most of the work in the area of conjugated organoborane polymers to date has focused on the incorporation of the borane moieties into the polymer main chain.[5]

We have recently reported an alternative approach that entails the lateral functionalization of oligo- and polythiophenes with electron-deficient dimesitylborane groups.[6,7] One of the advantages of such an approach is that the conjugated polymer main chain is uninterrupted, while its electronic properties are modified through electronic coupling with the pendent boryl groups.[8] For instance, we have demonstrated that functionalization of polythiophene with $-BMes_2$ groups (PT-$BMes_2$) leads to red-shifted absorption and emission bands, and according to cyclic voltammetry studies, PT-$BMes_2$ is more easily reduced than the respective trimethylsilyl-substituted analogue (PT-$SiMe_3$).[6]

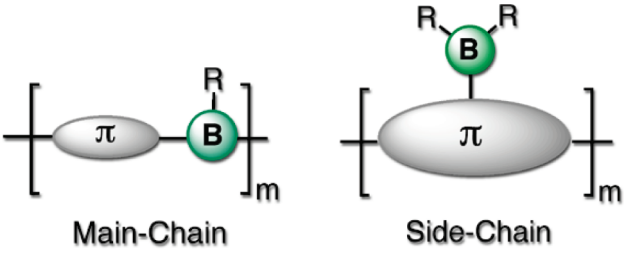

An interesting challenge is to further increase the electron-deficient character of the pendent boryl groups and thereby to enhance the electronic effect on the conjugated polymer main chain. In other work we have demonstrated that the relative Lewis acidity of ferrocenylboranes can be enhanced through oxidation of ferrocenyl substituents that are directly attached to boron, an effect that is related to an increase in the electron-deficient character of the tricoordinate boron sites.[9,10] With this in mind we set out to prepare a new type of conjugated metallopolymer[11] that contains lateral boryl groups to which redox-active ferrocenyl substituents are attached.[12,13] If reversible oxidation of the ferrocenyl groups is possible, this might allow us to tune the interaction between the boryl groups and the conjugated polythiophene backbone and ultimately to address the electronic properties of the conjugated polymer itself.

Results and Discussion

Our strategy for the synthesis of ferrocenylborane modified quater- and polythiophenes is shown in Scheme 1. The compounds

*To whom correspondence should be addressed. E-mail: fjaekle@rutgers.edu.

© 2010 American Chemical Society

Published on Web 12/13/2010

Scheme 1. Synthesis of QT-BFcAr and PT-BFcAr (Ar = 2,4,6-Trimethylphenyl (Mes), 2,4,6-Triisopropylphenyl (Tip))

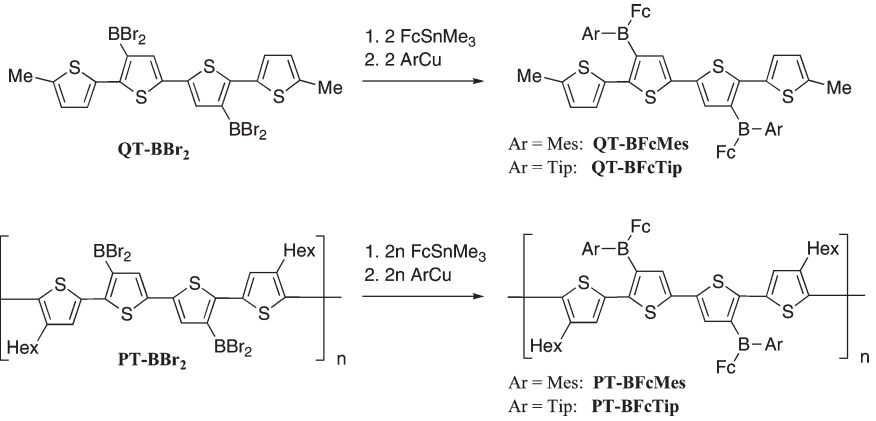

$QT\text{-}BBr_2$ and $PT\text{-}BBr_2$ were prepared according to a previously published procedure, in which the respective trimethylsilylated precursors were reacted with BBr_3 at ambient temperature.[6] Treatment of these BBr_2-functionalized oligo- and polythiophenes with 2 equiv of $FcSnMe_3$ (Fc = ferrocenyl) at room temperature for 12 h in CH_2Cl_2 led, under the conditions applied, to attachment of only one ferrocenyl group to each boryl moiety. The excellent selectivity of this reaction was confirmed by ^1H NMR of the intermediate B(Br)Fc-substituted oligo- and polythiophenes. In a second step, 2,4,6-trimethylphenylcopper (MesCu) or 2,4,6-triisopropylphenylcopper (TipCu) was added, and the mixture was kept at 110 °C for 48 h. The purpose of installing the bulky aryl group as a second substituent is to increase the stability of the polymer toward air and moisture.[3]

The polymers were analyzed by gel permeation chromatography (GPC) and MALDI-TOF mass spectrometry. The molecular weights of PT-BFcMes and PT-BFcTip were determined by GPC equipped with a refractive index (RI) detector. Number-average molecular weights of $M_n = 9440$ with a polydispersity of $M_w/M_n = 1.54$ for PT-BFcMes and $M_n = 14\,600$ with a polydispersity of $M_w/M_n = 1.65$ for PT-BFcTip were recorded. MALDI-TOF analysis with benzo[*a*]pyrene as the matrix further confirmed the polymer structure and provided insights into nature of the end groups. The spectrum of PT-BFcMes shows three major series of peaks that correspond to linear oligomers with the expected $\{Th_2Hx_2\text{-}Th_2(BFcMes)_2\}$ (Hx = *n*-hexyl) repeating units (Figure 1 and Table 1). Oligomers with up to 9 repeating units could be clearly identified in the spectrum. (The lower molecular weight in comparison to the GPC results is likely in part due to less effective ionization of the higher molecular weight polymer chains.) The most intense peaks (series A, Figure 1) correspond to chains with H− and $-CH_3$ termini, where the dihexylbithiophene end group is capped with a proton and the diborylbithiophene end group is capped with a methyl group. This is consistent with the structure of the precursor polymer, for which we found series with H−, $-CH_3$ (and a smaller amount of CH_3Th_2Si-, $-CH_3$) end groups as a result of methyl group transfer as a mode of polymer termination in the Stille-type polycondensation reaction.[6] The other two less intense series are due to (i) the presence of an additional boryl group (BMesFc) instead of a proton, presumably at the 2-position of the terminal thiophene group (series B, Figure 1), and (ii) the loss of one boryl group within the polymer chain (series C, Figure 1). We rationalize this result by reaction of the terminal acidic thiophene proton with BBr_3 under generation of a $-BBr_2$ terminus, which leads to polymers with one additional functional group. The concomitant release of HBr may in turn induce protiodesilylation at one of the disilylbithiophene fragments of the same or another polymer with formation of Me_3SiBr and a polymer chain that is lacking one of the functional groups.

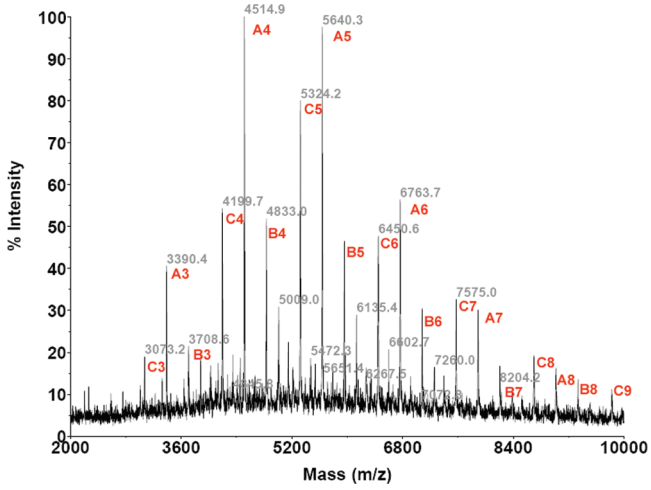

Figure 1. MALDI-TOF spectrum of PT-BFcMes recorded in (+)-reflector mode. Series A*n* corresponds to ions $[H\text{-}(RU)_n\text{-}CH_3]^+$; series B*n* corresponds to ions $[Mes(Fc)B\text{-}(RU)_n\text{-}CH_3]^+$; series C*n* corresponds to $[H\text{-}(RU)_n\text{-}CH_3 - B(Fc)Mes]^+$ with RU = $Th_2Hx_2\text{-}Th_2(B(Fc)Mes)_2$ repeating unit.

The polymers and the respective quaterthiophene model compounds were also examined by multinuclear NMR spectroscopy (Table 2). The observation of a broad ^{11}B NMR resonance in the range from 58 to 67 ppm for each of the compounds is consistent with formation of triarylborane functional groups. The attachment of two different aryl groups to boron is reflected in the ^1H NMR spectra. They show three signals in the region of 4−5 ppm in a 5:2:2 intensity ratio, in agreement with attachment of the monosubstituted ferrocenyl groups. The phenyl proton signals are found at about 6.6 ppm for QT-BFcMes and PT-BFcMes, while they resonate at about 6.9 ppm for QT-BFcTip and PT-BFcTip. Peak integration of the methyl and isopropyl groups in the region from 3.0 to 0.8 ppm supports the attachment of one Mes or Tip and one ferrocenyl group to each boryl moiety. The protons on the borylated thiophene rings are downfield shifted to about 8.20 ppm for QT-BFcMes/PT-BFcMes and even 8.40 ppm for QT-BFcTip/PT-BFcTip, in stark contrast to the $BMes_2$-functionalized compounds (ca. 6.9 ppm). A slight upfield shift of the protons on the adjacent alkylthiophene moieties for QT-BFcMes/PT-BFcMes (6.24 to 6.33 ppm) and a stronger shift for QT-BFcTip/PT-BFcTip (5.77 to 6.22 ppm) are also noticeable. Pronounced ring current effects must be responsible, which suggests that distinct conformational changes occur upon variation of the substitution pattern on boron.

To further examine these conformational peculiarities, we acquired H,H-NOESY NMR data for all new compounds (Figure 2).

Table 1. MALDI-TOF Mass Spectrometry Results for PT-BFcMes

structure		n = 3	4	5	6	7	8
H-(RU)$_n$-CH$_3$ (A)[a]	calcd	3390.0	4515.3	5639.7	6765.0	7890.3	9014.7
	obsd	3390.4	4514.9	5640.3	6763.7	7890.2	9017.4
Mes(Fc)B-(RU)$_n$-CH$_3$ (B)[a]	calcd	3704.1	4829.4	5953.8	7079.1	8203.4	9329.8
	obsd	3703.2	4833.0	5958.5	7083.9	8204.2	9334.0
H-(RU)$_n$-CH$_3$ - loss of B(Fc)Mes (C)[a]	calcd	3074.9	4200.2	5324.6	6449.9	7574.3	8699.5
	obsd	3073.2	4199.7	5324.2	6450.6	7574.9	8697.5

[a] RU = Th_2Hx_2-Th_2(B(Fc)Mes)$_2$ repeating unit.

Table 2. Comparison of Selected ^{11}B and ^{1}H NMR Data

	δ (^{11}B) (ppm)	δ (^{1}H) Th^B (ppm)	δ (^{1}H) Th$^{Me/Hex}$ (ppm)	δ (^{1}H) *m*-Ph (ppm)
QT-BFcMes	67	8.21	6.33, 6.28	6.63
PT-BFcMes	60	8.27	6.24	6.65
QT-BFcTip	67	8.40	6.22, 5.77	6.91
PT-BFcTip	58	8.44	5.90	6.92
QT-BMes$_2$[6]	69	6.89	6.53	6.68
PT-BMes$_2$[6]	62	6.94	6.48	6.69

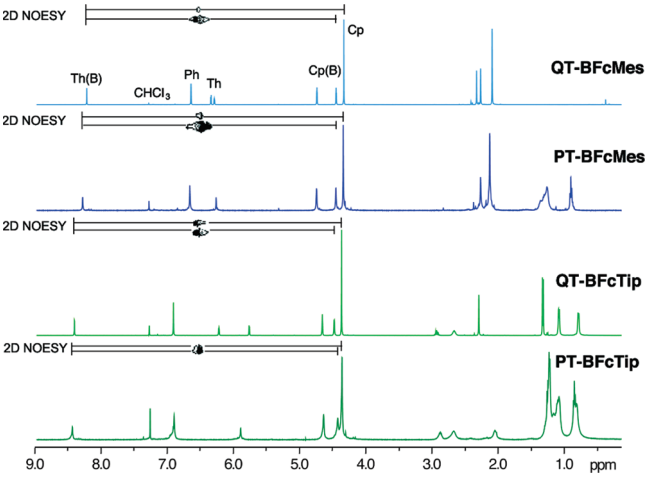

Figure 2. Comparison of 1D ^{1}H NMR and 2D H,H-NOESY NMR data in $CDCl_3$.

Similar chemical shifts and cross-coupling patterns were observed for each of the individual polymers and their respective model compounds, suggesting that the polythiophenes adopt similar conformations as the quaterthiophene model compounds (Table 2). Cross-peaks between the ortho protons of the boron-substituted Cp ring (Cp^B) and the protons on the free Cp rings with those of the boron-substituted thiophene rings (Th^B) are observed in all cases. For QT-BFcTip/PT-BFcTip, these cross-peaks are of similar intensity. However, in contrast, the cross-peak between the Cp^B and Th^B protons for QT-BFcMes/PT-BFcMes is much more intense than that between the protons of the free Cp and Th^B rings. This suggests that the thiophene protons are closer to the substituted Cp rings than the free Cp rings. No cross-peak was observed between the free Cp protons and the terminal thiophene protons, which indicates that the ferrocenyl groups are facing to the center of each molecule. These observations are consistent with two distinct conformations for QT-BFcMes and QT-BFcTip as illustrated in Figure 3.

To compare the conformations adopted by the oligothiophenes in solution with those in the solid state, we acquired single crystal X-ray diffraction data for both QT-BFcMes and QT-BFcTip. The crystal structure of QT-BFcMes in Figure 4 shows a surprisingly different conformation in comparison to that previously found for QT-BMes$_2$.[6] In stark contrast to the almost coplanar arrangement of all four thiophene rings in QT-BMes$_2$, the terminal rings for QT-BFcMes are strongly twisted with respect to the (coplanar) internal

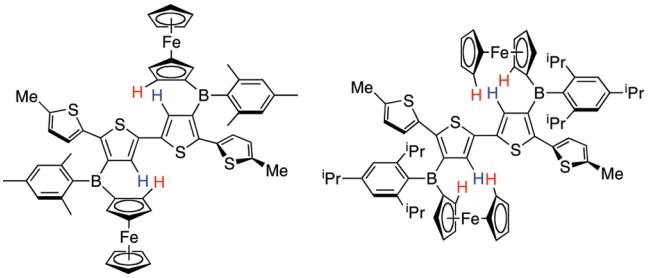

Figure 3. Different conformations adopted by QT-BFcMes and QT-BFcTip; thiophene and ferrocene protons that show strong NOE signals are emphasized.

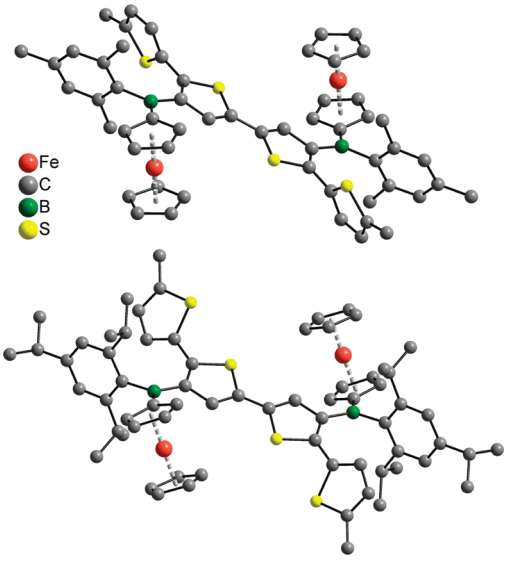

Figure 4. Plots of the single crystal X-ray structures of QT-BFcMes (top) and QT-BFcTip (bottom). Hydrogen atoms are omitted for clarity.

bithiophene unit (dihedral angles Th^B//Th^{Me} 61.0°). The arrangement of the aryl groups on boron is also quite different: The bulky mesityl groups in QT-BFcMes stand almost orthogonal to the thiophene (69.9°) and Cp rings (78.1°). However, the Cp rings of the ferrocenyl moieties make a rather small angle of only 30.2° with the internal thiophene rings, consistent with the conformation deduced from our solution NMR studies. This conformation should favor cross-conjugation through the Cp rings rather than the terminal thiophene rings. To estimate the possible overlap between the empty p-orbital on boron and the conjugated Cp^B and Th^B rings, we determined the dihedral angles with the best plane made of boron and the three boron-bound ipso-carbon atoms (BC_3); relatively small interplanar angles of BC_3//Th^B 15.2° and BC_3//Cp^B 19.1° suggest that extended conjugation through the tricoordinate boron center is favorable. This conjugation in turn is likely further extended to the iron centers as the boryl groups are slightly bent out of the Cp plane toward the Fe atoms (tilt angle Cp$^B_{CENT}$−C19−B1 172.6°). Such a tilting effect has been shown

Table 3. Selected Interplanar and Tilt Angles (deg) for QT-BFcMes and QT-BFcTip[a]

	QT-BFcMes	QT-BFcTip	QT-BMes$_2$[6]
$Th^B//Th^B$	0	0	0
$Th^B//Th^{Me}$	61.0	46.3	15.2
Th^B//Mes or Tip	69.9	81.9	79.6
$Th^B//Cp^B$	30.2	44.7	70.2 (Th^B//Mes)
Mes of Tip//Cp^B	78.1	89.6	84.3 (Mes//Mes)
$BC_3//Th^B$	15.2	25.7	41.1
$BC_3//Cp^B$	19.1	24.9	52.63 (BC_3//Mes)
BC_3//Mes or Tip	65.0	82.1	45.8
Th^{Me}//Mes or Tip	29.9	41.3	65.4
$Cp^B{}_{CENT}-{}^iC-B$	172.6	174.7	N/A

[a] Mes = mesityl ring, Tip = triisopropylphenyl ring, BC_3 = best plane made of boron and the three boron-bound ipso-carbon atoms, Th^B = boron-substituted thiophene ring, Th^{Me} = methyl-substituted thiophene ring, Cp^B = boron-substitutend Cp ring.

by Wagner and Holthausen in a density functional theory (DFT) study of $FcBH_2$ to be due to a delocalized interaction between the electron-deficient boron, the Cp ring, and the electron-rich iron.[10] Consistent with strong electronic coupling between boron and the ferrocenyl moiety is also that the B−C bond length to the Cp ring of B1−C19 1.553(3) Å is relatively short in comparison to that to the thiophene ring (B1−C3 1.570(3) Å) and even more so the long distance to the mesityl group (B1−C10 1.580(3) Å). Another unusual feature of the structure of QT-BFcMes is the almost coplanar arrangement of the terminal thiophene rings and the B-Mes substituents.

Substitution with the even bulkier Tip groups in QT-BFcTip leads to three significant changes to the molecular conformation (Table 3): (i) The four thiophene rings adopt a more coplanar conformation with a smaller dihedral angle $Th^B//Th^{Me}$ of 46.3° between the terminal and internal thiophenes. This effect should favor extended conjugation through the oligothiophene chain. (ii) The dihedral angles between the planes describing the Cp^B, Th^B, and Tip rings on the same boron atom are considerably larger than those for QT-BFcMes; remarkably, the Tip group stands almost orthogonal to both the Th^B and the Cp^B rings, and the ferrocene moieties rotate into a position that places the free Cp rings close to the internal thiophene rings as already deduced from the solution NOE experiments. (iii) The dihedral angle between each of the aromatic rings attached to boron relative to the BC_3 plane becomes larger. These observations suggest that the empty p orbital on boron participates less effectively in extended p−π conjugation in the presence of the bulkier Tip substituent in QT-BFcTip than in QT-BFcMes.

We conclude that the lower steric demand of only one mesityl group in QT-BFcMes allows for alignment of the Fc-B-Th-Th-B-Fc fragment, which should favor cross-conjugation with electronic delocalization between the Cp rings and the central bithiophene moiety via the empty p orbital on boron. Replacement of the Mes groups with the even bulkier Tip groups in QT-BFcTip disfavors this conjugation pathway but leads to a more planar structure of the quaterthiophene backbone. This trend is taken one step further when two Mes groups are attached to each boron in QT-BMes$_2$, which leads to an almost coplanar arrangement of the entire oligothiophene chain but a strong twist of the boron substituents.

An obvious feature of the ferrocenyl derivatives is their deep red color, which is due to relatively intense absorption bands at around 494 to ca. 515 nm ($\varepsilon > 1000$ M^{-1} cm^{-1}; cf. $\varepsilon = 96$ M^{-1} cm^{-1} at $\lambda_{max} = 442$ nm for ferrocene in cyclohexane) (Table 4 and Figure 5). These absorptions are not observed for QT-BMes$_2$ and PT-BMes$_2$,[6] and they are in a typical region of bands for ferrocenylboranes that are generally attributed to d−d transitions with considerable charge transfer character.[14] In the case of the polymers this band overlaps with one of several more intense higher energy absorptions, the origin of which could be the ferrocene and/or

Table 4. Comparison of UV−Vis Absorption and Cyclic Voltammetry (CV) Data

	λ_{max}/nm (ε/M^{-1} cm^{-1})[a]	$E_{1/2}$/mV (ΔE_p/mV) (oxidation)[b]	$E_{1/2}$/mV (ΔE_p/mV) (reduction)[c]
QT-BFcMes	287 (38300)		
	326 (26900)	120 (170)	−2480 (100)
	376 sh (21700)	890 (320)	−2610 (140)
	490 (3900)		
PT-BFcMes	289 (45200)	150 (130)	−2410 (220)
	334 (31000)	880[d]	−2610 (190)
	401 (31000)		
	498 sh (2900)		
QT-BFcTip	290 (34800)	140 (150)	−2480 (110)
	386 (24300)	960 (170)	−2660 (170)
	501 (8200)	1150 (140)	
PT-BFcTip	290 (37700)	160 (150)	−2360 (160)
	416 (34000)	990 (280)	−2600 (180)
	511 sh (5100)		

[a] In CH_2Cl_2; for the polymers ε corresponds to quaterthiophene repeating units. [b] In CH_2Cl_2/0.05 M $Bu_4N[B(C_6F_5)_4]$, 100 mV/s, referenced vs $Cp^*{}_2Fe^{0/+}$ couple (−610 mV). [c] In THF/0.1 M $Bu_4N[PF_6]$, 100 mV/s, referenced vs $Cp^*{}_2Fe^{0/+}$ (−550 mV). [d] From square-wave voltammogram (100 mV/s).

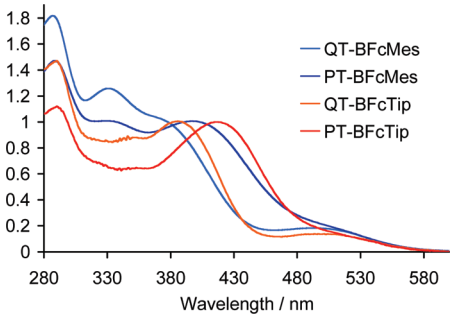

Figure 5. UV−vis absorption spectra (CH_2Cl_2, normalized to second lowest energy band).

oligothiophene moieties. We find the second-lowest energy band at longer wavelength for the polymers than for the quaterthiophenes (by about 25−30 nm), which suggests that it is primarily due to the conjugated oligo-/polythiophene chromophores, consistent with our earlier observations for the silylated precursors (QT-SiMe$_3$, 357 nm; PT-SiMe$_3$, 382 nm) and the BMes$_2$-substituted species (QT-BMes$_2$, 412 nm; PT-BMes$_2$, 441 nm).[6] This band is slightly more intense and red-shifted by ca. 10−15 nm for the derivatives with the bulkier Tip groups in comparison to the systems with Mes substituents. While the effect is subtle and it is difficult to draw quantitative conclusions, the more planar structure adopted by the quaterthiophene backbone in the case of the Tip derivative seen in the X-ray structure of QT-BFcTip may be responsible in part.[15]

The electronic structure of the oligo- and polythiophenes was further studied by cyclic voltammetry. For all of the compounds two well-separated quasi-reversible redox waves were found at around $E_{1/2} = -2.4$ and −2.6 V, which correspond to reduction of the two boron centers attached to the adjacent thiophenes (Figure 6). The redox splitting is in the range of $\Delta E = 130-240$ mV, suggesting significant electronic communication across the bithiophene bridge. The polymers show consistently larger redox splittings than the quaterthiophene derivatives, and the first reduction takes place at comparatively lower potential (by 70 mV for PT-BFcMes and 120 mV for PT-BFcTip). A tentative explanation for the observed differences is that extended conjugation through the polymer main chain affects the orbital levels on the thiophene π-systems, which in turn would lead to subtle differences in the π-overlap with the boron-centered p-orbital. If this is the case, for the polymer, the presence of the additional

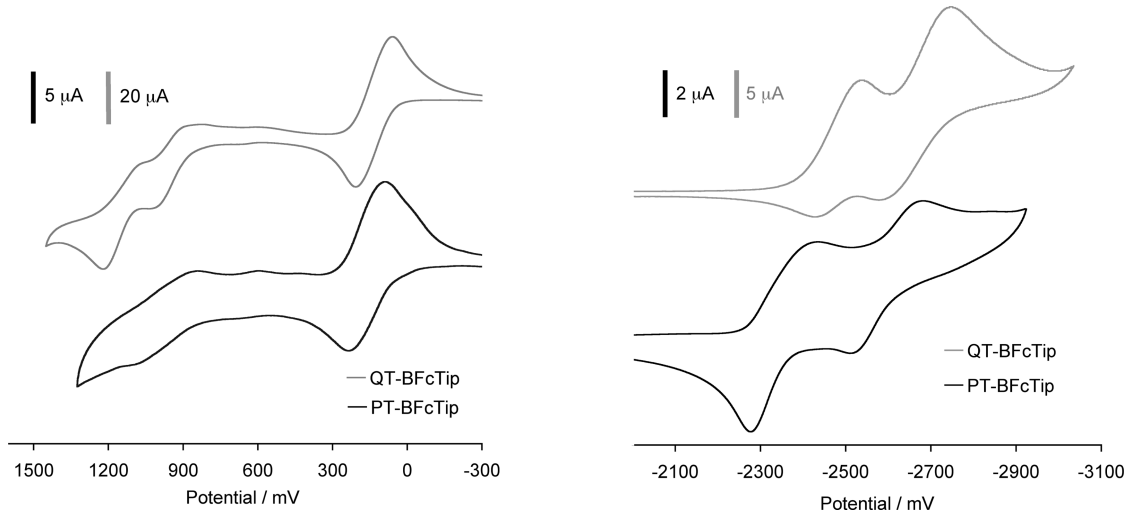

Figure 6. Cyclic voltammograms of QT-BFcTip and PT-BFcTip (a) in CH_2Cl_2/0.05 M $Bu_4N[B(C_6F_5)_4]$ and (b) in THF/0.1 M $Bu_4N[PF_6]$ (100 mV/s, referenced with Cp^*_2Fe and reported vs $Cp_2Fe^{0/+}$ couple).

boryl groups on the adjacent repeating units may have an influence through the conjugated Th_2Hx_2 linker. One would then expect that in the first reduction step the boryl groups are reduced at less cathodic potentials in the presence of the additional organoborane π-acceptors attached to the adjacent repeating units (which are not present in the quaterthiophene model system). Upon reduction of one of the boryl groups on each of the diboryl-bithiophene moieties, however, this effect should be less pronounced, or the opposite effect might be observed in that the presence of a boron-centered radical anion in the next repeating unit leads to a more cathodic second reduction step.

In addition to these boron-centered processes, we find a reversible two-electron process at ca. 120−160 mV that is attributed to oxidation of the ferrocene moieties based on spectroelectrochemistry data discussed in detail later. In contrast to the boron redox, two separate waves could not be resolved (Table 4). In the case of QT-BFcTip, two additional quasi-reversible oxidation peaks are detected at higher potentials ($E_{1/2}$ = +960 and +1150 mV), while for the other compounds only one irreversible process is clearly observed. This process corresponds to oxidation of the thiophene main chain, and the better reversibility observed for the Tip derivative indicates that the bulkier Tip groups help to stabilize the polycationic species formed. A comparison with literature data on quaterthiophenes reveals that the presence of the ferroceniumborane moieties leads to a significant increase in the oxidation potentials (e.g., for cyclohexyl end-capped quaterthiophene;[16] $E_{1/2}$ = +320 and +640 mV). The effect of oxidation of the ferrocene moiety is also evident from comparison of the potentials for oxidation of the thiophene main chain in QT-BFcTip ($E_{1/2}$ = +960 and +1150 mV) with those for QT-$BMes_2$ ($E_{1/2}$ = +510 and +760 mV in CH_2Cl_2/0.1 M $Bu_4N[PF_6]$).

Spectroelectrochemical measurements were performed to further confirm the assignment of the redox events observed in the cyclic voltammograms and to gain additional insight into the electronic structure of the oxidized species. For this purpose a solution of QT-BFcTip in CH_2Cl_2 containing 0.05 M $Bu_4N[B(C_6F_5)_4]$ was filled into an OTTLE (optical transparent thin-layer electrochemical) cell[17] under N_2 protection. Initially, we looked at the first redox process by scanning within the potential range from −0.4 to +0.8 V (Figure 7A,B). A clear change of the absorption spectrum with three distinct isosbestic points is consistent with a reversible oxidation process. The original absorption bands at 386 and 501 nm gradually decrease, and a new band at ca. 370 nm emerges. At the same time, a very broad low-intensity absorption appears in the range of ca. 500−700 nm, which is consistent with formation of a ferrocenium-type species ($[Cp_2Fe]^+[PF_6]^-$: λ_{max} = 617 nm). The observation of a blue shift of the higher energy band to 370 nm might suggest that the quaterthiophene moiety adopts a less coplanar conformation after oxidation of the ferrocene pendent groups. It is also possible that this blue shift is a result of the ferrocenium moiety exerting an electron-withdrawing effect through the boron p orbital, or both of these factors may contribute. However, in that case, we would have expected to see a red-shifted rather than blue-shifted absorption (see ref 15). We then decided to scan the entire range from −0.4 to +1.7 V, and the corresponding UV traces are displayed in Figure 7C,D. After the initial changes described above, a new very strong band develops at 675 nm, which is accompanied by an even stronger band at 737 nm at higher potentials. These can be assigned to products from mono- and dioxidation, respectively, of the quaterthiophene main chain based on comparison with literature data. For instance, Bäuerle and co-workers found absorption maxima of 693 nm for the monocation and 775 nm for the dication of a cyclohexyl end-capped quaterthiophene,[16] while Hotta et al. recorded absorptions at 670 and 726 nm, respectively, upon oxidation of α,ω-dimethylquaterthiophene.[18] However, as seen in Figure 7D, scanning back to −0.4 V results in an absorption spectrum that is significantly different from that of the neutral starting material. This indicates that at higher potentials partial degradation occurs, possibly involving cleavage of the organoborane substituents.

Conclusions

The attachment of redox-active ferrocenylborane moieties to quater- and polythiophene was accomplished using a postpolymerization modification procedure, in which BBr_2 groups were first attached and the bromines on boron were then selectively replaced with the ferrocenyl groups. In the last step bulky aryl groups were introduced for steric stabilization. The attachment of the relatively more sterically demanding Tip groups led to better stability than Mes groups. Of particular interest was the question of how the relatively bulky side groups affect the conformation of the polythiophene main chain. On the basis of NOESY NMR spectroscopy and single crystal X-ray diffraction on the quaterthiophenes, we find that in the case of −B(Fc)Mes substituents the thiophenes in the main chain are significantly twisted, but a new conjugation path to the substituted Cp ring of the ferrocenyl moieties becomes more favorable. Introduction of the even bulkier −B(Fc)Tip groups disfavors this conjugation pathway,

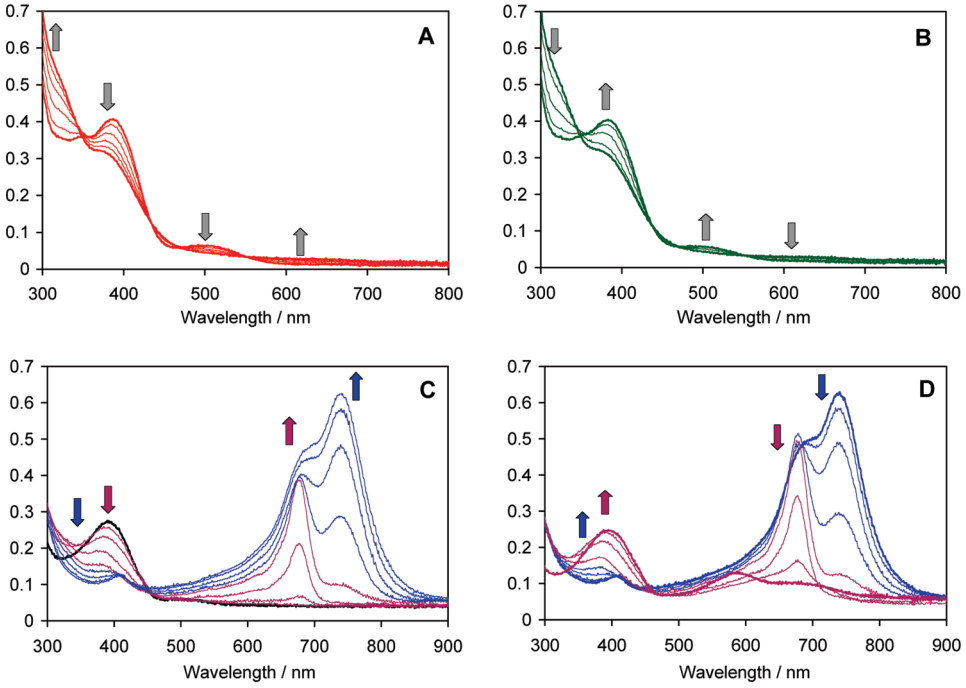

Figure 7. Spectroelectrochemistry data for QT-BFcTip in CH_2Cl_2/0.05 M $Bu_4N[B(C_6F_5)_4]$; scan rate 15 mV/s. (A) Oxidation within potential range from −0.4 to +0.8 V. (B) Reduction within potential range from +0.8 to −0.4 V. (C) Oxidation within potential range from −0.4 to +1.7 V. (D) Oxidation within potential range from +1.7 to −0.4 V.

and surprisingly, a more coplanar structure of the quaterthiophene main chain is achieved. Thus, while steric effects of pendent groups can strongly influence the conjugation in these materials, bulkier groups do not necessarily result in a more twisted main chain of the conjugated polymer as one might assume. That the more planar structure of the main chain in QT-BFcTip and PT-BFcTip favors extended conjugation is also suggested by a bathochromic shift of the second-lowest energy absorption, which is assigned to an oligothiophene-centered $\pi-\pi^*$ transition. Cyclic voltammetry revealed that initial, reversible oxidation of these materials occurs at the ferrocene moieties, followed by mono- and dioxidation of the polythiophene backbone. The assignment of the individual redox processes was confirmed by spectroelectrochemical measurements performed on QT-BFcTip. The latter also indicated that at higher potentials certain degradation processes occur. These most likely involve reactivity at the ferrocenylborane moieties. Future work will therefore involve the development of polymers that are more stable also in their oxidized state, featuring, for example, sterically more demanding and also more electron-rich pentamethylferrocene substituents.

Experimental Section

Materials and General Methods. BBr_3 was purchased from Aldrich and benzo[*a*]pyrene from TCI Chemicals. Compounds QT-BBr_2[6] and PT-BBr_2,[6] trimethylstannylferrocene,[19] and mesitylcopper[20] (recrystallized from toluene) were prepared according to literature procedures. All reactions and manipulations were carried out under an atmosphere of prepurified nitrogen using either Schlenk techniques or an inert-atmosphere glovebox (Innovative Technologies). Ether solvents were distilled from Na/benzophenone prior to use. Hydrocarbon and chlorinated solvents were purified using a solvent purification system (Innovative Technologies; alumina/copper columns for hydrocarbon solvents), and the chlorinated solvents were subsequently distilled from CaH_2 and degassed via several freeze−pump−thaw cycles.

All 499.893 MHz ^{1}H, 125.7 MHz ^{13}C, and 160.4 MHz ^{11}B NMR spectra were recorded at ambient temperature on a Varian INOVA spectrometer equipped with a boron-free 5 mm dual broadband gradient probe (Nalorac, Varian Inc., Martinez, CA). Solution ^{1}H and ^{13}C NMR spectra were referenced internally to solvent signals. ^{11}B NMR spectra were acquired with boron-free quartz NMR tubes and referenced externally to $BF_3\cdot Et_2O$ (δ = 0). The abbreviations Th (2-thienyl), Hx_2Th_2 (3,3′-dihexyl-2,2′-bithiophenediyl), Mes (2,4,6-trimethylphenyl), Fc (ferrocenyl), and Hx (*n*-hexyl) are used for the peak assignments.

GPC analyses were performed in THF (1 mL/min) using a Waters Breeze system equipped with a 717plus autosampler, a 1525 binary HPLC pump, a 2487 dual λ absorbance detector, and a 2414 refractive index detector. For separation the samples were passed through a series of styragel columns (Polymer Laboratories; two columns 5 μm/Mixed-C), which were kept in a column heater at 35 °C. The columns were calibrated with polystyrene standards (Polymer Laboratories).

MALDI-TOF measurements of the polymers were performed on an Applied Biosystems 4800 Proteomics Analyzer in reflectron (+) mode with delayed extraction. Benzo[*a*]pyrene was used as the matrix (10 mg/mL in toluene). Samples were prepared in toluene (10 mg/mL), mixed with the matrix in a 1:10 ratio, and then spotted on the wells of a sample plate inside a glovebox. Peptides were used for calibration (Des-Arg-Bradykinin (904.4681), Angiotensin I (1296.6853), Glu-Fibrinopeptide B (1570.6774), ACTH (clip 1-17) (2093.0867), ACTH (clip 18-39) (2465.1989), ACTH (clip 7-38) (3657.9294) with α-hydroxy-4-cyanocinnamic acid as the matrix). High-resolution mass spectral data for the quaterthiophenes were obtained on an Apex-ultra 70 Hybrid FT-MS (Bruker Daltonics).

UV−vis absorption data were acquired on a Varian Cary 500 UV−vis/NIR spectrophotometer. Sample solutions were prepared using a microbalance (±0.1 mg) and volumetric glassware. Cyclic voltammetry was carried out on a CV-50W analyzer from BAS. The three-electrode system consisted of an Au disk as working electrode, a Pt wire as secondary electrode, and a Ag wire as the reference electrode. The voltammograms were recorded with ca. 10^{-3} M solutions in THF containing 0.1 M $Bu_4N[PF_6]$ (reductions scans) or CH_2Cl_2 containing 0.05 M $Bu_4N[B(C_6F_5)_4]$ (oxidation scans) as the supporting electrolyte. The scans were referenced after the addition of a small amount of decamethylferrocene as internal standard. The potentials are reported relative to

the ferrocene/ferrocenium couple (−610 mV for $Cp^*_2Fe/Cp^*_2Fe^+$ in CH_2Cl_2/0.5 M $Bu_4N[(B(C_6F_5)_4]$; −550 mV for $Cp^*_2Fe/Cp^*_2Fe^+$ in THF/0.1 M $Bu_4N[PF_6]$). Spectroelectrochemistry was performed using a home-built OTTLE (optical transparent thin-layer electrochemical) cell,[17] a Perkin-Elmer Lambda 16 UV/vis spectrometer, and an EG&G Princeton Applied Research 263A potentiostat. The measurements were recorded on ca. $10^{-3}-10^{-4}$ M solutions in CH_2Cl_2 containing $Bu_4N[B(C_6F_5)_4]$ (0.05 M) as the supporting electrolyte. Elemental analyses were obtained from Quantitative Technologies Inc., Whitehouse, NJ.

X-ray diffraction intensities of QT-BFcMes and QT-BFcTip were collected on a Bruker SMART APEX CCD diffractometer. Crystallographic data and details of the X-ray diffraction experiment and crystal structure refinement are given in Table S2. SADABS[21] absorption correction was applied, and the structures were solved using direct methods and completed by subsequent difference Fourier syntheses and refined by full matrix least-squares procedures on reflection intensities (F^2). All non-hydrogen atoms were refined with anisotropic displacement coefficients. The H atoms were placed at calculated positions and were refined as riding atoms. All software and sources scattering factors are contained in the SHELXTL (6.14) program package.[22] Crystallographic data for the structures of QT-BFcMes and QT-BFcTip have been deposited with the Cambridge Crystallographic Data Center as supplementary publications CCDC-796548 and CCDC-796549, respectively.

Caution! BBr_3 is toxic and corrosive and should be handled appropriately with great care. Fluorinated grease was used for ground glass joints in reactions involving BBr_3.

Synthesis of QT-BFcMes. QT-BBr_2 (100 mg, 0.143 mmol) in 5 mL of CH_2Cl_2 was treated with $FcSnMe_3$ (100 mg, 0.29 mmol) in 5 mL of CH_2Cl_2 and kept stirring for 12 h. Me_3SnBr was removed by repeatedly dissolving the crude material in toluene and drying under high vacuum. Selective attachment of the ferrocenyl groups was confirmed by ^{1}H NMR ($CDCl_3$, 499.9 MHz): δ = 7.56 (s, 2H, Th-H8,8′), 6.95 (d, ^3J = 2.5 Hz, 2H, Th-H3,3′), 6.58 (br d, 2H, Th-H4,4′), 4.76 (br, 4H, Cp-H2,5), 4.37 (br, 4H, Cp-H3,4), 4.20 (s, 10H, C_5H_5), 2.42 (s, 6H, Me). Without further purification, the product was redissolved in 8 mL of toluene, $(MesCu)_5\cdot$toluene (63 mg, 0.31 mmol "MesCu") in 5 mL of toluene was added slowly, and the reaction mixture was kept stirring at 100 °C for 24 h. A precipitate (CuBr) formed, which was removed by filtration through a fritted glass disk. All volatile components were removed under high vacuum, and the product was crystallized from toluene at −35 °C. Yield: 82 mg (58%). For QT-BFcMes: ^{1}H NMR ($CDCl_3$, 499.893 MHz): δ = 8.21 (s, 2H, Th^B-H), 6.63 (s, 4H, Mes-H), 6.33 (d, ^3J = 3.0 Hz, 2H, Th^{Me}-H), 6.28 (d, ^3J = 3.0 Hz, 2H, Th^{Me}-H), 4.73 (pst, ^3J = 2.0 Hz, 4H, Cp-H2,5), 4.44 (pst, ^3J = 2.0 Hz, 4H, Cp-H3,4), 4.32 (s, 10H, C_5H_5), 2.32 (s, 6H, Me), 2.26 (s, 6H, *p*-Me), 2.08 (s, 12H, *o*-Me). ^{13}C NMR ($CDCl_3$, 125.7 MHz): δ = 145.9, 145.5, 142.7, 141.1, 139.0, 137.0, 136.1, 133.5, 132.9, 128.5, 127.2, 124.8 (Th-C, Mes-C), 77.9 (Cp-C), 76.7 (Cp-C_i), 74.7 (Cp-C), 69.7 (C_5H_5), 23.6 (*o*-Me), 21.3 (*p*-Me), 15.2 (Me). ^{11}B NMR ($CDCl_3$, 160.3 MHz): δ = 67 ($w_{1/2}$ = 3000 Hz); MALDI-TOF: m/z = 986.1840 (calcd for $^{12}C_{56}{}^1H_{52}{}^{11}B_2{}^{32}S_4{}^{56}Fe_2$ 986.1837). Analysis calcd for $C_{56}H_{52}B_2Fe_2S_4$: C 68.18, H 5.31; found C 67.90, H 5.38%.

Synthesis of Polymer PT-BFcMes. A solution of PT-BBr_2 prepared from BBr_3 (324 mg, 1.3 mmol) and PT-$SiMe_3$ (320 mg, 1.0 mmol of $SiMe_3$ groups) in 15 mL of CH_2Cl_2 was treated with $FcSnMe_3$ (506 mg, 1.45 mmol) in 5 mL of CH_2Cl_2 and kept stirring for 12 h. The reaction solution was concentrated under high vacuum to 3 mL and then precipitated into 500 mL of hexanes and washed twice with hexanes. Selective formation of the ferrocenyl-substituted product was confirmed by ^{1}H NMR ($CDCl_3$, 499.9 MHz): δ = 7.60 (s, 2H, B_2Th_2-H3,3′), 6.92 (s, 2H, Hx_2Th_2-H7,7′), 4.72 (br, 4H, Cp-H2,5), 4.35 (br, 4H, Cp-H3,4), 4.19 (br, 10H, C_5H_5), 2.29 (br, 4H, Hex), 1.4−1.2 (m, 8H, Hex), 1.2−1.1 (m, 4H, Hex), 1.1−1.0 (m, 4H, Hex), 0.87 (t, ^3J = 6.5 Hz, 6H, Hex-CH_3). Without further purification, the product was redissolved in 15 mL of toluene, $(MesCu)_5\cdot$toluene (302 mg, 1.48 mmol "MesCu") in 5 mL of toluene was added slowly, and the reaction mixture was kept stirring at 100 °C for 24 h. A solid precipitate (CuBr) formed and was removed by filtration through a fritted glass disk. The reaction solution was concentrated under high vacuum to 2 mL and then precipitated into 500 mL of cold hexanes. The red powdery product was washed with cold hexanes and dried under high vacuum for 12 h. Yield: 0.32 g (57%). For PT-BFcMes: ^{1}H NMR ($CDCl_3$, 499.893 MHz): δ = 8.27 (s, 2H, Th^B-H), 6.65 (s, 4H, Mes-H), 6.24 (s, 2H, Th^{Hex}-H), 4.74 (br, 4H, Cp-H2,5), 4.45 (br, 4H, Cp-H3,4), 4.34 (br, 10H, C_5H_5), 2.20 (br s, 6H, *p*-Me), 2.12 (br s, 12H, *o*-Me), 1.4−1.2 (m, 20H, Th-CH_2), 0.80 (t, ^3J = 6.5 Hz, 4H, Hexyl-Me). ^{13}C NMR ($CDCl_3$, 125.7 MHz): δ = 145.6, 142.8, 142.0, 139.1, 137.0, 136.2, 135.0, 133.6, 129.36, 129.55, 127.50 (Th-C, Mes-C), 77.9 (Cp-C), 74.7 (Cp-C), 69.68 (C_5H_5), Cp-C_i not observed, 23.7 (*o*-Me), 21.6 (*p*-Me), 32.0, 30.4, 29.5, 28.6, 22.9, 14.4 (hexyl). ^{11}B NMR ($CDCl_3$, 160.3 MHz): δ = 60 ($w_{1/2}$ = 4000 Hz). GPC-RI (in THF against PS standards) M_n = 9440, M_w = 14 500, PDI = 1.54. TGA (N_2, 20 °C/min): T_{dec} = 220 °C (onset, 80% weight loss at 900 °C). Anal. Calcd for $(C_{33}H_{35}B_1Fe_1S_2)_n$: C 70.22, H 6.61; found C 69.26, H 6.38%.

Synthesis of QT-BFcTip. $FcSnMe_3$ (100 mg, 0.29 mmol) in 5 mL of CH_2Cl_2 was added to QT-BBr_2 (100 mg, 0.14 mmol) in 5 mL of CH_2Cl_2. The solution turned red immediately and was kept stirring for 12 h at RT. After the solvent was evaporated, the crude materials were repeatedly dissolved in toluene and dried under high vacuum to remove completely Me_3SnBr. Formation of the ferrocene-substituted intermediate was confirmed by ^{1}H NMR. Without further purification, the crude product was redissolved in 8 mL of toluene, and a solution of 2,4,6-triisoproylphenylcopper (TipCu) (92 mg, 0.35 mmol) in 5 mL of toluene was added. The reaction mixture was kept stirring at 110 °C for 48 h. The solid byproduct CuBr was removed by filtration through a fritted glass disk. All volatile components were removed under high vacuum, and the crude product was crystallized from a mixture of toluene and hexanes at −35 °C to afford a red microcrystalline solid. Yield: 121 mg (73%). Single crystals for X-ray diffraction were obtained by recrystallization from toluene at −35 °C. For QT-BFcTip: ^{1}H NMR ($CDCl_3$, 499.9 MHz): δ = 8.40 (s, 2H, Th^B-H), 6.91 (s, 4H, Mes-H), 6.22 (br d, 2H, Th^{Me}-H), 5.77 (d, ^3J = 3.5 Hz, 2H, Th^{Me}-H), 4.66 (br, 4H, Cp-H2,5), 4.48 (br, 4H, Cp-H3,4), 4.37 (s, 10H, C_5H_5), 2.93 (septet, 2H, *p*-C*H*Me $_2$), 2.67 (m, 4H, *o*-C*H*Me_2), 2.30 (s, 6H, Me), 1.33 (d, ^3J = 7.0 Hz, 12H, *p*-CH*Me*$_2$), 1.09 (d, ^3J = 6.0 Hz, 12H, *o*-CH*Me*$_2$), 0.80 (d, ^3J = 6.0 Hz, 12H, *o*-CH*Me*$_2$). ^{13}C NMR ($CDCl_3$, 125.7 MHz): δ = 149.2, 148.9, 146.2, 144.6, 143.9, 141.2, 135.3, 134.4, 133.5, 129.0, 125.6, 120.7 (aromatic C), 78.4 (Cp-C), 78.1 (Cp-C), 73.7 (Cp-C), 69.7 (C_5H_5), 35.4 (*o*-*C*HMe_2), 34.7 (*p*-*C*HMe_2), 25.1 (*o*-CH*Me*$_2$), 24.7 (*p*-CH*Me*$_2$), 15.2 (Th-Me). ^{11}B NMR ($CDCl_3$, 160.3 MHz): δ = 67 ($w_{1/2}$ = 4800 Hz); MALDI-TOF: m/z = 1154.3741 (calcd for $^{12}C_{68}{}^1H_{76}{}^{11}B_2{}^{32}S_4{}^{56}Fe_2$ 1154.3734). Anal. Calcd for $C_{68}H_{76}B_2Fe_2S_4$: C 70.72, H 6.63; found: C 70.81, H 6.19.

Synthesis of Polymer PT-BFcTip. A solution of PT-BFcBr was prepared from BBr_3 (100 mg, 0.39 mmol), PT-$SiMe_3$ (100 mg, 0.31 mmol of $SiMe_3$ groups), and $FcSnMe_3$ (158 mg, 0.45 mmol) in 5 mL of CH_2Cl_2 as described above. The crude product was redissolved in 5 mL of toluene, a solution of TipCu (123 mg, 0.46 mmol) in 3 mL of toluene was added, and the reaction mixture was kept stirring at 110 °C for 48 h. A solid precipitate (CuBr) formed and was removed by filtration through a fritted glass disk. The filtrate was concentrated under high vacuum to 1 mL and then precipitated into 100 mL of cold hexanes. A red precipitate formed, which was washed with hexanes twice and freeze-dried from benzene to afford a powdery red product. Yield: 120 mg (60%). For PT-BFcTip: ^{1}H NMR ($CDCl_3$, 499.9 MHz): δ = 8.44 (s, 2H, B_2Th_2-H3,3′), 6.91 (s, 4H, Mes-H), 5.90 (s, 2H, Hx_2Th_2-H7,7′), 4.65 (br, 4H, Cp-H2,5), 4.43 (br, 4H, Cp-H3,4), 4.37 (br, 10H, C_5H_5), 2.88 (br, 2H, *p*-C*H*Me_2), 2.67 (br, 4H, *o*-C*H*Me_2), 2.05 (br, 4H, Hex), 1.4−0.9 (m, 40H, Hex, *o*-CH*Me*$_2$), 0.90−0.75 (m, 18H, Hex, *p*-CH*Me*$_2$). ^{13}C NMR ($CDCl_3$, 125.7 MHz): δ = 149.0, 148.8, 145.5, 144.6, 144.0, 142.6, 135.8, 135.5, 134.7, 130.8, 130.0, 120.8

(aromatic C), 78.4 (Cp-C), 73.7 (Cp-C), 69.7 (C_5H_5), Cp-C_i not observed, 35.5, 34.4 ($CHMe_2$), 32.1, 30.8, 29.2, 28.9 (Hex), 25.0, 24.3 ($CH\mathit{Me}_2$), 22.8, 14.4 (Hex). ^{11}B NMR ($CDCl_3$, 160.3 MHz): δ = 58 ($w_{1/2}$ = 5120 Hz); GPC-RI (in THF against PS standards) M_n = 14 600, M_w = 24100, PDI = 1.65. TGA (N_2, 10 °C/min): T_{dec} = 236 °C (onset, 87% weight loss at 800 °C). Anal. calcd for $\{C_{78}H_{94}B_2Fe_2S_4\}_n$: C 69.98, H 6.84; found: C 72.45, H 7.33.

Acknowledgment. Acknowledgment is made to the National Science Foundation (CHE-0809642, MRI 0116066, and CRIF 0443538) for support of this research. F.J. thanks the Alexander von Humboldt Foundation for a Friedrich Wilhelm Bessel Research Award. We are deeply grateful to Prof. Dr. M. Wagner at the Johann-Wolfgang-Goethe Universität Frankfurt for many scientific discussions and for providing access to the spectroelectrochemistry equipment. We also thank Jose Medina for his contributions to the synthesis of QT-$SiMe_3$.

Supporting Information Available: Additional cyclic voltammetry data, crystal structure plots, and details of the X-ray structure determinations. This material is available free of charge via the Internet at http://pubs.acs.org.

References and Notes

(1) (a) *Handbook of Oligo- and Polythiophenes*; Fichou, D., Ed.; Wiley-VCH: Weinheim, 1999. (b) *Semiconducting Polymers*; Hadziioannou, G., van Hutten, P. F., Eds.; Wiley-VCH: Weinheim, 2000.

(2) (a) Jäkle, F. *Chem. Rev.* **2010**, *110*, 3985–4022. (b) Matsumi, N.; Chujo, Y. *Polym. J.* **2008**, *40*, 77–89. (c) Nagata, Y.; Chujo, Y. In *Macromolecules Containing Metal and Metal-Like Elements*; Abd-El-Aziz, A. S., Carraher, C. E., Jr., Pittman, C. U., Jr., Zeldin, M., Eds.; John Wiley & Sons, Inc.: Hoboken, NJ, 2007; Vol. *8*, pp 121−147. (d) Jäkle, F. *Coord. Chem. Rev.* **2006**, *250*, 1107–1121.

(3) (a) Entwistle, C. D.; Marder, T. B. *Angew. Chem., Int. Ed.* **2002**, *41*, 2927–2931. (b) Entwistle, C. D.; Marder, T. B. *Chem. Mater.* **2004**, *16*, 4574–4585.

(4) (a) Jäkle, F. Boron: Organoboranes. In *Encyclopedia of Inorganic Chemistry*; Crabtree, R. H., Ed.; John Wiley: Chichester, 2006; pp 560−598, DOI: 10.1002/0470862106.ia028. (b) Yamaguchi, S.; Wakamiya, A. *Pure Appl. Chem.* **2006**, *78*, 1413–1424. (c) Lee, B. Y.; Wang, S.; Putzer, M.; Bartholomew, G. P.; Bu, X.; Bazan, G. C. *J. Am. Chem. Soc.* **2000**, *122*, 3969–3970. (d) Jia, W. L.; Feng, X. D.; Bai, D. R.; Lu, Z. H.; Wang, S.; Vamvounis, G. *Chem. Mater.* **2005**, *17*, 164–170. (e) Yuan, Z.; Entwistle, C. D.; Collings, J. C.; Albesa-Jové, D.; Batsanov, A. S.; Howard, J. A. K.; Taylor, N. J.; Kaiser, H. M.; Kaufmann, D. E.; Poon, S.-Y.; Wong, W.-Y.; Jardin, C.; Fathallah, S.; Boucekkine, A.; Halet, J.-F.; Marder, T. B. *Chem.—Eur. J.* **2006**, *12*, 2758–2771. (f) Sundararaman, A.; Venkatasubbaiah, K.; Victor, M.; Zakharov, L. N.; Rheingold, A. L.; Jäkle, F. *J. Am. Chem. Soc.* **2006**, *128*, 16554–16565. (g) Yuan, M. S.; Fang, Q.; Liu, Z. Q.; Guo, J. P.; Chen, H. Y.; Yu, W. T.; Xue, G.; Liu, D. S. *J. Org. Chem.* **2006**, *71*, 7858–7861. (h) Zhao, C. H.; Wakamiya, A.; Inukai, Y.; Yamaguchi, S. *J. Am. Chem. Soc.* **2006**, *128*, 15934–15935. (i) Wakamiya, A.; Mori, K.; Yamaguchi, S. *Angew. Chem., Int. Ed.* **2007**, *46*, 4273–4276. (j) Chiu, C. W.; Gabbai, F. P. *Angew. Chem., Int. Ed.* **2007**, *46*, 1723–1725. (k) Zhao, G.; Baumgarten, M.; Müllen, K. *J. Am. Chem. Soc.* **2008**, *130*, 12477–12484. (l) Weber, L.; Werner, V.; Fox, M. A.; Marder, T. B.; Schwedler, S.; Brockhinke, A.; Stammler, H.-G.; Neumann, B. *Dalton Trans.* **2009**, 2823–2831. (m) Braunschweig, H.; Herbst, T.; Rais, D.; Ghosh, S.; Kupfer, T.; Radacki, K.; Crawford, A. G.; Ward, R. M.; Marder, T. B.; Fernández, I.; Frenking, G. *J. Am. Chem. Soc.* **2009**, *131*, 8989–8999. (n) Collings, J. C.; Poon, S. Y.; Le Droumaguet, C.; Charlot, M.; Katan, C.; Pålsson, L. O.; Beeby, A.; Mosely, J. A.; Kaiser, H. M.; Kaufmann, D.; Wong, W. Y.; Blanchard-Desce, M.; Marder, T. B. *Chem.—Eur. J.* **2009**, *15*, 198–208. (o) Cao, D.; Liu, Z.; Li, G.; Liu, G.; Zhang, G. *J. Mol. Struct.* **2008**, *874*, 46–50. (p) Zhao, C.; Sakuda, E.; Wakamiya, A.; Yamaguchi, S. *Chem.—Eur. J.* **2009**, *15*, 10603–10612.

(5) (a) Matsumi, N.; Naka, K.; Chujo, Y. *J. Am. Chem. Soc.* **1998**, *120*, 5112–5113. (b) Matsumi, N.; Naka, K.; Chujo, Y. *J. Am. Chem. Soc.* **1998**, *120*, 10776–10777. (c) Matsumi, N.; Miyata, M.; Chujo, Y. *Macromolecules* **1999**, *32*, 4467–4469. (d) Matsumi, N.; Chujo, Y. *Macromolecules* **2000**, *33*, 8146–8148. (e) Matsumi, N.; Umeyama, T.; Chujo, Y. *Polym. Bull.* **2000**, *44*, 431–436. (f) Miyata, M.; Meyer, F.; Chujo, Y. *Polym. Bull.* **2001**, *46*, 23–28. (g) Sato, N.; Ogawa, H.; Matsumoto, F.; Chujo, Y.; Matsuyama, T. *Synth. Met.* **2005**, *154*, 113–116. (h) Matsumoto, F.; Chujo, Y. *Pure Appl. Chem.* **2009**, *81*, 433–437. (i) Nagai, A.; Murakami, T.; Nagata, Y.; Kokado, K.; Chujo, Y. *Macromolecules* **2009**, *42*, 7217–7220. (j) Nagai, A.; Miyake, J.; Kokado, K.; Nagata, Y.; Chujo, Y. *Macromolecules* **2009**, *42*, 1560–1564. (k) Corriu, R. J. P.; Deforth, T.; Douglas, W. E.; Guerrero, G.; Siebert, W. S. *Chem. Commun.* **1998**, 963–964. (l) Sundararaman, A.; Victor, M.; Varughese, R.; Jäkle, F. *J. Am. Chem. Soc.* **2005**, *127*, 13748–13749. (m) Li, H.; Jäkle, F. *Angew. Chem., Int. Ed.* **2009**, *48*, 2313–2316. (n) Li, H.; Jäkle, F. *Macromol. Rapid Commun.* **2010**, *31*, 915–920. (o) Lorbach, A.; Bolte, M.; Li, H.; Lerner, H.-W.; Holthausen, M. C.; Jäkle, F.; Wagner, M. *Angew. Chem., Int. Ed.* **2009**, *48*, 4584–4588. (p) Niu, W. J.; Smith, M. D.; Lavigne, J. J. *J. Am. Chem. Soc.* **2006**, *128*, 16466–16467. (q) Chai, J.; Wang, C.; Jia, L.; Pang, Y.; Graham, M.; Cheng, S. Z. D. *Synth. Met.* **2009**, *159*, 1443–1449. (r) Liu, W.; Pink, M.; Lee, D. *J. Am. Chem. Soc.* **2009**, *131*, 8703–8707. (s) Bonifacio, V. D. B.; Morgado, J.; Scherf, U. *J. Polym. Sci., Part A: Polym. Chem.* **2008**, *46*, 2878–2883.

(6) Li, H.; Sundararaman, A.; Venkatasubbaiah, K.; Jäkle, F. *J. Am. Chem. Soc.* **2007**, *129*, 5792–5793.

(7) For related work by Yamaguchi et al. on the lateral functionalization of poly(phenyleneethynylene)s and by Lambert et al. on the functionalization of poly(carbazole)s, see: (a) Zhao, C. H.; Wakamiya, A.; Yamaguchi, S. *Macromolecules* **2007**, *40*, 3898–3900. (b) Reitzenstein, D.; Lambert, C. *Macromolecules* **2009**, *42*, 773–782.

(8) Elbing, M.; Bazan, G. C. *Angew. Chem., Int. Ed.* **2008**, *47*, 834–838.

(9) (a) Venkatasubbaiah, K.; Nowik, I.; Herber, R. H.; Jäkle, F. *Chem. Commun.* **2007**, 2154–2156. (b) Venkatasubbaiah, K.; Doshi, A.; Nowik, I.; Herber, R. H.; Rheingold, A. L.; Jäkle, F. *Chem.—Eur. J.* **2008**, *14*, 444–458. (c) Braunschweig, H.; Fernández, I.; Frenking, G.; Kupfer, T. *Angew. Chem., Int. Ed.* **2008**, *47*, 1951–1954. (d) Broomsgrove, A. E. J.; Addy, D. A.; Di Paolo, A.; Morgan, I. R.; Bresner, C.; Chislett, V.; Fallis, I. A.; Thompson, A. L.; Vidovic, D.; Aldridge, S. *Inorg. Chem.* **2010**, *49*, 157–173. For related studies on organoborane-functionalized transition metal complexes see, for example: (e) Sun, Y.; Ross, N.; Zhao, S. B.; Huszarik, K.; Jia, W. L.; Wang, R. Y.; Macartney, D.; Wang, S. N. *J. Am. Chem. Soc.* **2007**, *129*, 7510–7511. (f) Hudson, Z. M.; Zhao, S. B.; Wang, R. Y.; Wang, S. *Chem.—Eur. J.* **2009**, *15*, 6131–6137. (g) Kitamura, N.; Sakuda, E.; Ando, Y. *Chem. Lett.* **2009**, *38*, 938–943. (h) Zhou, G.; Ho, C.-L.; Wong, W.-Y.; Wang, Q.; Ma, D.; Wang, L.; Lin, Z.; Marder, T. B.; Beeby, A. *Adv. Funct. Mater.* **2008**, *18*, 499–511.

(10) Scheibitz, M.; Bolte, M.; Bats, J. W.; Lerner, H.-W.; Nowik, I.; Herber, R. H.; Krapp, A.; Lein, M.; Holthausen, M.; Wagner, M. *Chem.—Eur. J.* **2005**, *11*, 584–603.

(11) (a) Pickup, P. G. *J. Mater. Chem.* **1999**, *9*, 1641–1653. (b) Wolf, M. O. *Adv. Mater.* **2001**, *13*, 545–553. (c) Stott, T. L.; Wolf, M. O. *Coord. Chem. Rev.* **2003**, *246*, 89–101. (d) Manners, I. *Synthetic Metal-Containing Polymers*; Wiley-VCH: Hoboken, NJ, 2004.

(12) Polymers that contain ferrocenyl moieties attached directly to the conjugated backbone or through a π-conjugated organic linker: (a) Vorotyntsev, M. A.; Vasilyeva, S. V. *Adv. Colloid Interface Sci.* **2008**, *139*, 97–149. (b) Higgins, S. J.; Jones, C. L.; Francis, S. M. *Synth. Met.* **1999**, *98*, 211–214. (c) Zotti, G.; Schiavon, G.; Zecchin, S.; Berlin, A.; Pagani, G.; Canavesi, A. *Synth. Met.* **1996**, *76*, 255. (d) Zhu, Y.; Wolf, M. O. *Chem. Mater.* **1999**, *11*, 2995–3001. (e) Zhu, Y.; Wolf, M. O. *J. Am. Chem. Soc.* **2000**, *122*, 10121–10125. (f) Naka, K.; Uemura, T.; Chujo, Y. *Macromolecules* **2000**, *33*, 6965–6969. (g) Tan, L.; Curtis, M. D.; Francis, A. H. *Macromolecules* **2002**, *35*, 4628–4635.

(13) Examples of metal-containing organoborane polymers: (a) Berenbaum, A.; Braunschweig, H.; Dirk, R.; Englert, U.; Green, J. C.; Jäkle, F.; Lough, A. J.; Manners, I. *J. Am. Chem. Soc.* **2000**, *122*, 5765–5774. (b) Matsumoto, F.; Matsumi, N.; Chujo, Y. *Polym. Bull.* **2001**, *46*, 257–262. (c) Matsumi, N.; Chujo, Y.; Lavastre, O.; Dixneuf, P. H. *Organometallics* **2001**, *20*, 2425–2427. (d) Matsumoto, F.; Matsumi, N.; Chujo, Y. *Polym. Bull.* **2002**, *48*, 119–125. (e) Matsumoto, F.; Chujo, Y. *Pure Appl. Chem.* **2006**, *78*, 1407–1411. (f) Heilmann, J. B.; Scheibitz, M.; Qin, Y.; Sundararaman, A.; Jäkle, F.; Kretz, T.; Bolte, M.; Lerner, H.-W.; Holthausen, M. C.; Wagner, M. *Angew. Chem., Int. Ed.* **2006**, *45*, 920–925. (g) Heilmann, J. B.; Qin, Y.; Jäkle, F.; Lerner, H. W.; Wagner, M. *Inorg. Chim. Acta* **2006**, *359*, 4802–4806. (h) Scheibitz, M.; Li, H.; Schnorr, J.; Sánchez Perucha, A.; Bolte, M.; Lerner, H.-W.; Jäkle, F.; Wagner, M. *J. Am. Chem. Soc.* **2009**, *131*, 16319–16329. (i) Parab, K.; Jäkle, F. *Macromolecules* **2009**, *42*, 4002–4007. (j) Cui, C.; Heilmann-Brohl, J.; Perucha, A. S.; Thomson, M. D.; Roskos, H. G.; Wagner, M.; Jäkle, F. *Macromolecules* **2010**, *43*, 5256–5261.

(14) (a) Gamboa, J. A.; Sundararaman, A.; Kakalis, L.; Lough, A. J.; Jäkle, F. *Organometallics* **2002**, *21*, 4169–4181. (b) Carpenter, B. E.; Piers, W. E.; Parvez, M.; Yap, G. P. A.; Rettig, S. J. *Can. J. Chem.* **2001**, *79*, 857–867.
(15) As pointed out by a reviewer, another possible reason might be that the contribution from the empty p-orbital on boron to the conjugation decreases as a result of the stronger twist of the Tip-substituted borane moiety relative to the thiophene π-system. However, it is typically increasing rather than decreasing overlap of the empty p-orbital on boron with organic π-systems that leads to lowering of the LUMO levels and a concurrent red shift of the absorption.
(16) Bäuerle, P.; Segelbacher, U.; Maier, A.; Mehring, M. *J. Am. Chem. Soc.* **1993**, *115*, 10217–10223.
(17) Krejčik, M.; Daněk, M.; Hartl, F. *J. Electroanal. Chem.* **1991**, *317*, 179–187.
(18) (a) Hotta, S.; Waragai, K. *J. Mater. Chem.* **1991**, *1*, 835. (b) Hotta, S.; Waragai, K. *J. Phys. Chem.* **1993**, *97*, 1421–1434.
(19) Guillaneux, D.; Kagan, H. B. *J. Org. Chem.* **1995**, *60*, 2502–2505.
(20) (a) Tsuda, T.; Yazawa, T.; Watanabe, K.; Fujii, T.; Saegusa, T. *J. Org. Chem.* **1981**, *46*, 192–194. (b) Eriksson, H.; Håkansson, M. *Organometallics* **1997**, *16*, 4243–4244. (c) Sundararaman, A.; Jäkle, F. *J. Organomet. Chem.* **2003**, *681*, 134–142.
(21) Sheldrick, G. M. SADABS, Version 2; Multi-Scan Absorption Correction Program University of Göttingen, Germany, 2001.
(22) Sheldrick, G. M. SHELXTL, Version 6.14; Bruker AXS Inc., Madison, WI, 2004.

104 *Macromolecules* **2011**, *44*, 104–111
DOI: 10.1021/ma102223y

Macromolecules
ARTICLE

Well-Defined Poly(sulfobetaine) Brushes Prepared by Surface-Initiated ATRP Using a Fluoroalcohol and Ionic Liquids as the Solvents

Yuki Terayama,[†] Moriya Kikuchi,[‡,§] Motoyasu Kobayashi,[*,‡,§] and Atsushi Takahara[*,†,‡,§]

[†]*Graduate School of Engineering, Kyushu University,* [‡]*Japan Science and Technology Agency, ERATO, Takahara Soft Interfaces Project, and* [§]*Institute for Materials Chemistry and Engineering, Kyushu University, 744 Motooka, Nishi-ku, Fukuoka 819-0395, Japan*

Received September 26, 2010; Revised Manuscript Received November 21, 2010

ABSTRACT: Surface-initiated atom transfer radical polymerization (ATRP) of 2-(*N*-2-methacryloyloxyethyl-*N*,*N*-dimethyl) ammonatoethanesulfonate) (MAES), 3-(*N*-2-methacryloyloxyethyl-*N*,*N*-dimethyl) ammonatopropanesulfonate) (MAPS), and 4-(*N*-2-methacryloyloxyethyl-*N*,*N*-dimethyl) ammonatobutanesulfonate) (MABS) was carried out in 2,2,2-trifluoroethanol (TFE) containing a small amount of 1-hexyl-3-methylimidazolium chloride at 60 °C to produce well-defined poly(sulfobetaine) brushes and the corresponding free polymers with predictable number-average molecular weight (M_n, 1×10^4 to 3×10^5 g mol^{-1}) and narrow molecular weight distributions ($M_w/M_n < 1.2$). A first-order kinetic plot for ATRP of MAPS revealed a linear relationship between the monomer conversion index ($\ln([M]_0/[M])$) and polymerization time. The polymerization rates decreased with increasing ionic liquid concentration. The M_n of poly(MAPS) increased in proportion to the conversion. The sequential polymerization of MAPS initiated with the chain ends of poly(MAPS) produced the postpolymer with quantitative efficiency. The thickness of the polymer brush was controllable from 5 to 100 nm based on the M_n of the polymer. The polymer brush was cleaved from the silicon substrate under the acidic condition to measure the molecular weight by size exclusion chromatography equipped with a multiangle light scattering detector (SEC-MALS). We have confirmed that the molecular weight distribution of polymer brush was also narrow (M_n = 150 000, M_w/M_n = 1.26) as well as the corresponding free polymer. These results suggest the successful control of the polymerization of sulfobetaine-type methacrylates owing to the TFE and ionic liquids. In particular, the high affinity of TFE for the sulfobetaine monomers and polymers yielded a homogeneous polymerization media to improve surface-initiated polymerization generating the polymer brushes on the substrate surface as well as the free polymers formed in the solution. The effect on ATRP of the chemical structure of ionic liquids and ligands for copper catalyst was also investigated.

Introduction

Interfacial polyelectrolyte brushes are attracting considerable attention due to their various useful functionalities such as superhydrophilicity, protein antifouling effect, and water lubrication.[1−4] Researchers have investigated the interface structure of swollen polyelectrolyte brushes in solution by means of X-ray (or neutron) reflectivity,[5−7] ellipsometry,[8] or light scattering[9] measurements in order to understand the interaction between polyelectrolyte brush and hydrated ions or proteins. However, the swollen polyelectrolyte brushes with large molecular weight distribution (MWD) in solution cause large gradient layer at the interface between the brushes and solution media, making the structural analysis difficult. Therefore, precise analysis of swollen polyelectrolyte brushes in aqueous media requires the brushes with narrow MWDs.

Various polymers with well-controlled number-average molecular weights (M_n) and narrow MWDs were recently prepared by controlled/living radical polymerization. However, it is still difficult to prepare the polymer with larger M_n than 100 000 g mol^{-1} and narrow MWD ($M_w/M_n < 1.2$) by direct ATRP of zwitterionic vinyl monomers having carboxybetaine, sulfobetaine, and phosphobetaine groups, because the zwitterionic monomers and polymers are insoluble in nonpolar organic solvents and only soluble in specific protonic solvents such as aqueous solution, which usually induces deactivation of the propagation center or catalyst resulting in poor control.

Polysulfobetaine, such as poly(3-(*N*-2-methacryloyloxyethyl-*N*,*N*-dimethyl) ammonatopropanesulfonate) (MAPS), has attracted considerable attention due to the various unique solution properties attributed to the strong electrostatic interaction among the sulfobetaine groups, ionic strength dependence of chain expansion,[10] and an upper critical solution temperature (UCST) behavior.[11] Therefore, poly(MAPS) brush can be applicable to prepare the stimulus-responsible wet surfaces with various levels of hydrophilicity, protein resistance surface, tribocontrol surface, and adhesion control surfaces.

Conventional free radical polymerization has been widely used for the synthesis of MAPS,[12,13] however, its polydispersity index M_w/M_n is larger than 1.5. The first synthesis of well-defined poly(MAPS) was reported by Armes et al., who carried out group transfer polymerization of 2-(dimethylamino)ethyl methacrylate (DMAEMA) to produce a well-defined polymer with MWD narrower than 1.25 and efficiently converted dimethylamino groups in the side chain to sulfobetaine groups using 1,3-propane sultone.[14] However, this polymer reaction cannot be applied to a densely-grafted poly(DMAEMA) brush because the surface-tethered polymer chains are so crowded that the sulfonation reaction does not proceed quantitatively in the internal part of the brush.

*Corresponding authors. E-mail: (M.K.) motokoba@cstf.kyushu-u.ac.jp; (A.T.) takahara@cstf.kyushu-u.ac.jp. Telephone: +81-92-802-2517. Fax: +81-92-802-2518.

 Published on Web 12/13/2010 © 2010 American Chemical Society

Reversible addition−fragmentation chain transfer (RAFT) polymerization often achieves good control over the M_n of hydrophilic polymers with polar functional groups.[15] McCormick et al. investigated direct synthesis of poly(MAPS) by the RAFT technique,[16] using sodium 4-cyanopentanoic acid dithiobenzoate as a chain transfer agent and 4,4′-azobis(4-cyanopentanoic acid) in 0.5 M NaBr aqueous solution at 70 °C, which gave successfully controlled molecular weight and narrow MWD (M_w/M_n < 1.1). Surface-initiated RAFT polymerization of MAPS was conducted by Kang et al. to produce poly(MAPS) brushes on silicon wafers.[17] The dry thickness of the poly(MAPS) brush film estimated by ellipsometry linearly increased from 5 to 11 nm with the polymerization time from 0.5 to 18 h, although the M_n and MWD of the brush were not described.

Copper-based atom transfer radical polymerization (ATRP) is a well-established controlled/living radical polymerization approach for various types of vinyl monomers. Jiang et al. reported poly(MAPS) with narrow MWD (M_n = 4764, M_w/M_n = 1.26) by direct ATRP of MAPS with catechol-type initiator using CuBr and 2,2-dipyridyl complex in methanol/water mixture (4/1, v/v). However, poly(MAPS) with high molecular weight and narrow MWD could not be synthesized (M_n = 90 340 M_w/M_n = 1.47) by their method because water or aqueous media usually induces deactivation of the copper catalyst and too fast propagating rate to control the polymerization affording a polymer with broad MWD. Nevertheless, research groups have reported that surface-initiated ATRP of MAPS in the methanol/water mixture from alkyl halide-immobilized substrate without any sacrificial free initiator produced a polymer brush.[18,19] The thickness of the poly(MAPS) brush drastically increased to be 300 nm within 10 h. However surface-initiated ATRP of MAPS could not be controlled due to the poor control in aqueous media to yield the polymer brush with broad MWD. Another difficulty of control of surface-initiated ATRP is related to the solubility of MAPS. MAPS monomer is soluble in methanol and water but poly(MAPS) is insoluble in methanol and water due to the strong electrostatic attractive interaction among the sulfobetaine groups. Therefore, polymerization in methanol/water solution was assumed to proceed in a heterogeneous system to result in large MWD and nonuniform brush thickness on the substrate. A homogeneous polymerization state might be preferable for obtaining uniform polymer brushes.

We attempted to develop a homogeneous ATRP system using 2,2,2-trifluoroethanol (TFE), which is known to be a good solvent for poly(MAPS).[20] Well-defined cationic-, carbobetaine- and sulfobetaine types *exo*-7-oxanorbornene polymers with M_n of 21 000 and polydispersity index of 1.12 were recently synthesized via ring-opening metathesis polymerization (ROMP) of *exo*-7-oxanorbornene monomer using Grubbs' catalyst $RuCl_2(PCy_3)_2CHPh$ in a mixture of TFE/dichloromethane (1/1, v/v).[21,22] The controllable polymerization manner and linear relationship of first-order plot were observed by ROMP in TFE/dichloromethane homogeneous solution. Lowe and Ishihara et al. reported that RAFT polymerization of *N*,*N*-di-*n*-propyl-4-vinylbenzylamine (DnPBVA) initiated from poly((methacryloxy)ethyl phosphorylcholine) (MPC) prepolymer in TFE yielded well-defined poly(MPC) -*b*- poly(DnPBMA) with M_n of 11700 and polydispersity index of 1.18.[23] Recently, we reported the successfully controlled ATRP of methacrylate bearing an ammonium chloride group in the side chain of TFE/2-propanol.[24] In addition, ionic liquid is also a good candidate for the ATRP solvent due to its chemical stability and nonvolatile property. Haddleton and co-workers reported that ATRP of methyl methacrylate (MMA) in 1-butyl-3-methylimidazolium hexafluorophosphate showed a higher propagation rate constant than that in bulk or other organic solvents.[25] Various types of ionic liquid have already been applied in ATRP,[26−29] reverse ATRP,[30] and activators generated by electron transfer (AGET) ATRP.[31] Most of them demonstrated polymerization of nonionic monomers in ionic liquid, however, improved control can be expected for the polymerization of electrolyte monomers because ionic liquids have high affinity for polar monomers and polymers, forming a homogeneous reaction media.

In this work, we carried out direct ATRP of methacrylates bearing sulfobetaine side chains in TFE combined with imidazolium type ionic liquids. The effect of fluoroalcohol and the chemical structure of ionic liquids and ligands were investigated to produce well-defined sulfobetaine polymers and polymer brushes.

Experiments

Materials. Copper(I) bromide (CuBr, Wako Pure Chemicals, 99.9%) was purified by successive washing with acetic acid and ethanol and then dried under vacuum. Ethyl 2-bromoisobutylate (EBiB, Tokyo Chemical Inc., 98%) was distilled before use. 2-(Dimethylamino)ethyl methacrylate (DMAEMA, Wako Pure Chemicals, 98%), 2,2′-dipyridyl (bpy, Wako Pure Chemicals, 99.5%), *N*,*N*,*N*′,*N*′-tetramethylethylenediamine (TMEDA, Tokyo Chemical Inc., 98%), *N*,*N*,*N*′,*N*″,*N*″-pentamethyldiethylenetriamine (PMDETA, Tokyo Chemical Inc., 98%), 1-hexyl-3-methylimidazolium chloride (HMImCl, Merck, 98%), 1-ethyl-3-methylimidazolium chloride (EMImCl, Merck, 98%), 1-butyl-3-methylimidazolium chloride (BMImCl, Merck, 98%), 1-butyl-3-methylimidazolium bromide (BMImBr, Merck, 98%), 1-butyl-3-methylimidazolium iodide (BMImI, Merck, 98%), 1,3-propane sultone (Aldrich, 99%), sodium isethionate (Tokyo Chemical Inc., 97.5%), thionyl chloride ($SOCl_2$, Wako Pure Chemicals, 95.0%), 2,6-dimethylpyridine (Wako Pure Chemicals, 97.5%), 1,3-dinitrobenzene (Tokyo Chemical Inc., 99.0%), 1,4-butane sultone (Wako Pure Chemicals, 99.0%) were used as received. 2,2,2-Trifluoroethanol (TFE, Tokyo Chemical Inc., 99.0%) was carefully degassed by a freeze−pump−thaw process before dilution of CuBr, bpy, and EBiB. Surface-initiator (2-bromo-2-methyl)propionyloxyhexyltriethoxysilane (BHE)[32,33] and tris(2-(dimethyl)aminoethyl)amine (Me_6TREN)[34] were synthesized using previously reported procedures. Silicon wafers were washed with piranha solution at 155 °C for 1 h and subsequently exposed to vacuum ultraviolet-rays for 10 min under 30 Pa. BHE was immobilized on the substrates by means of chemical vapor adsorption.[35] Sulfobetaine monomers, such as MAPS,[36] 2-(*N*-2-methacryloyloxyethyl-*N*,*N*-dimethyl) ammonatoethanesulfonate (MAES),[37] and 4-(*N*-2-methacryloyloxyethyl-*N*,*N*-dimethyl) ammonatobutanesulfonate (MABS)[37] were synthesized and purified just before use. Details were described in the Supporting Information.

Surface-Initiated (SI)-ATRP of MAES, MAPS, and MABS in TFE Containing HMImCl. The typical protocol for the SI-ATRP of MAPS (MAES and MABS) in degassed TFE was as follows. Several sheets of the BHE-immobilized silicon wafers, 1.0 mL of MAPS/TFE solution, and the various amounts of HMImCl were charged in a well-dried glass tube with a stopcock, and degassed three times by the freeze−thaw process. CuBr (0.022 mmol) and bpy (0.042 mmol) diluted with TFE were introduced into another glass tube, which was degassed by seven cycles of vacuum pumping and flushing with argon. A free initiator EBiB (0.021 mmol) diluted with TFE was added to the catalyst to immediately give a homogeneous solution with characteristic red color. The copper catalyst solution was degassed by repeated freeze−thaw cycles and then injected into the monomer solution. The resulting reaction mixture was again degassed by repeated freeze−thaw cycles to remove the oxygen and then was stirred in an oil bath at 60 °C for 18 h under argon to simultaneously generate a poly(MAPS) brush from the substrate and free (unbound) poly(MAPS) from EBiB. The reaction was stopped by opening the glass vessel to

Scheme 1

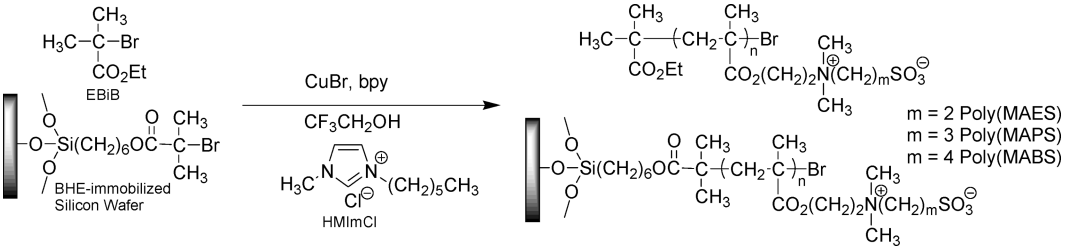

air at 0 °C. The reaction mixture was poured into methanol to precipitate the free polymer and unreacted MAPS. The silicon wafers were washed with TFE using a Soxhlet apparatus for 12 h to remove the free polymer adsorbed on the surface, and were dried under reduced pressure.

Size Exclusion Chromatography (SEC) Measurement of Poly(MAPS) Brush on Substrate. To measure the M_n of the surface-grafted poly(MAPS) on a flat substrate by SEC, the polymer brush was prepared on a larger silicon wafer compared with the general-use silicon plates. A sheet of the BHE-immobilized silicon wafer (65 × 65 × 0.5 mm^3), 30.0 mL of MAPS/TFE/HMImCl solution (1.0 M) were charged in a specially designed separable flask with a stopcock and degassed by the freeze−thaw process three times. Copper catalyst solution containing CuBr (0.060 mmol), bpy (0.125 mmol), and EBiB (0.060 mmol) diluted with TFE was prepared in another glass tube and injected to the MAPS solution. The resulting reaction mixture was degassed by repeated freeze−thaw to remove the oxygen and stirred at 60 °C for 15 h under argon. The resulting silicon wafers were washed with TFE using a Soxhlet apparatus overnight to remove the free polymer adsorbed on their surface and were dried under reduced pressure. The brush-immobilized flat silicon wafers were immersed in the solution mixture of 10 wt % hydrogen fluoride aqueous solution (5 mL) and 200 mM NaCl aqueous solution (10 mL) for 3 days in a plastic vessel and carefully and slowly neutralized by sodium hydrogen carbonate aqueous solution. The resulting solution was collected in a dialysis membrane tube (Spectra/Por 3, Standard regulated cellulose membrane, M_w = 3500 g mol^{-1}) and dialyzed in water to remove inorganic salt ions for 3 days, and was dried using freeze and dry process to remove water. The obtained poly(MAPS) was diluted in 200 mM NaCl aqueous solution and injected to SEC.

Measurements. SEC of the free soluble poly(MAPS) was applied to determine M_n, weight-average molecular weight (M_w), z-average mean-square radius of gyration, and MWD using a Shimadzu HPLC system connected to three polymethacrylate-based TSKgel columns (Tosoh Bioscience): G6000PWXL (pore size >100 nm, bead size 20 μm) + G5000WXL (pore size 100 nm, bead size 10 μm) + G3000WXL (pore size 20 nm, bead size 7 μm) and equipped with a multiangle light scattering detector (MALS; Wyatt Technology DAWN -EOS, 30 mW GaAs linearly polarized laser, wavelength: λ = 690 nm) and refractive index detector (Shimadzu RID-10A, tungsten lamp (wavelength 470 - 950 nm), 40 °C) using 200 mM NaCl aqueous solution as an eluent at a rate of 0.8 mL min^{-1}. The Rayleigh ratio at a scattering angle of 90° was based on that of pure toluene at a wavelength of 632.8 nm at 25 °C. The sensitivities of 17 detectors at angles other than 90° and the dead volume for each detector were determined by the scattering intensities of 0.30 wt % aqueous solution of poly(ethylene oxide) standard with 2.22×10^4 g mol^{-1} and M_w/M_n = 1.08. The specific refractive index increments (dn/dc) of poly(MAES), poly(MAPS), and poly(MABS) in 200 mM NaCl aqueous solution was determined as 0.119, 0.120, and 0.121 mL g^{-1} by aqueous solution differential refractometer (Otsuka Electronics DRM-3000, wavelength λ = 632.8 nm). The thickness of the brush was determined by spectroscopic ellipsometer (Five Lab Co. MASS-102) with an Xenon arc lamp (wavelength 380−890 nm) at a fixed incident angle of 70°. The assumed refractive index and density values were 1.50[17] and 1.34 g cm^{-3},[38] respectively, as referenced from literatures. Atomic force microscopy (AFM) observation was conducted in AC tapping mode using an Agilent5000 (Agilent Technologies, Inc.) in air at room temperature. The polymer brush surface was scanned at a rate of 10 μm s^{-1} using a silicon nitride integrated tip on a commercial rectangular cantilever (Nanosensors, Type PPP-NCHR-20) with a normal force constant of 42 N m^{-1} at a driving frequency of 317 kHz in air (relative humidity 30%). XPS measurements were carried out on an XPS-APEX (Physical Electronics Co. Ltd.) at 1×10^{-6} Pa using a monochromatic Al-KR X-ray source of 300 W. All of the XPS data were collected at a takeoff-angle of 45° and a low-energy (25 eV) electron flood gun was used to minimize sample charging. The survey spectra (0−1000 eV) and high-resolution spectra of the C_{1s}, O_{1s}, N_{1s}, and S_{2p} regions were acquired at pass energies for the analyzer of 100.0 and 25.0 eV, respectively. An X-ray beam was focused onto an area with a diameter of ca. 0.2 mm. Scheme 1 shows the reactions used.

Results and Discussion

ATRP of MAPS in TFE in the Presence of Ionic Liquids. In general, polymers with predictable M_n's and narrow MWDs can be prepared by ATRP in either homogeneous solution or heterogeneous media, however, homogeneous polymerization solution is preferable for the preparation of well-defined polymer brushes because heterogeneous diffusion of monomers and catalysts into the substrate surface results in nonuniform propagation reaction from the surface-immobilized initiators. Therefore, surface-initiated controlled polymerization should be conducted in a good solvent for both the monomer and its polymer. MAES, MAPS, and MABS monomers are soluble in water and methanol, while poly(MAES), poly(MAPS), and poly(MABS) are insoluble in water and methanol, indicating that aqueous solutions is a poor solvent for poly(sulfobetaine)s, although water and methanol have been used in the conventional radical polymerization of MAPS. Since the commercially available MAPS monomers sometimes contain the polymers, in this study, all monomers were freshly synthesized and purified just before use.

Surface-initiated ATRP of MAPS was carried out in the presence of free initiator EBiB and the initiator-immobilized substrate to produce the free poly(MAPS) and the corresponding polymer brushes on the substrates. Table 1 shows the M_n's and MWDs of the free polymers determined by SEC-MALS and the thickness of the polymer brush measured by ellipsometer. Significant differences were not observed in M_n's and MWDs of free poly(MAPS) prepared by ATRP in the presence and absence of initiator-immobilized silicon wafers. ATRP of MAPS in methanol/water (1/1, v/v) proceeded quickly, completing within 0.1 h, but this led to phase separation at high conversion. The reaction mixture became heterogeneous, and the substrate surface was

Table 1. Surface-Initiated ATRP of MAPS at 60 °C.[a]

run	ligands	solvents (weight ratio)	time (h)	yield[b] (%)	M_n calcd[c]	M_n SEC[d]	M_w/M_n	thickness[e] (nm)
1	bpy	MeOH/H_2O (1/1)[f]	0.1	99	147 000	365 000	1.74	70.0
2	bpy	TFE	1	95	153 000	205 000	1.40	24.8
3	bpy	HMImCl/TFE (1/20)	1	26	36 200	54 900	1.29	9.1
4	bpy	HMImCl/TFE (1/20)	6	99	150 000	168 000	1.31	26.5
5	bpy	HMImCl/TFE (1/10)	6	65	92 900	123 000	1.22	20.6
6	bpy	HMImCl/TFE (1/10)[g]	18	99	76 500	82 600	1.18	11.6
7	bpy	HMImCl/TFE (1/10)[h]	12	99	235 000	240 000	1.25	40.4
8	bpy	HMImCl/TFE (1/6.7)	6	48	65 900	94 600	1.19	14.9
9	bpy	HMImCl/TFE (1/5)	6	34	47 900	67 100	1.22	11.7
10	TMEDA	TFE	0.5	40	48 400	146 000	1.74	-
11	TMEDA	HMImCl/TFE (1/10)	12	1	15 800	19 500	1.71	3.0
12	PMDETA	TFE	0.5	67	78 900	184 000	1.65	-
13	PMDETA	HMImCl/TFE (1/10)	12	99	169 000	265 000	1.28	50.5
14	Me_6TREN	TFE	0.5	39	46 300	612 000	1.37	-
15	Me_6TREN	HMImCl/TFE (1/10)	12	90	133 000	638 000	1.24	102.0
16	bpy	EMImCl/TFE (1/10)	12	93	70 800	137 000	1.15	11.5
17	bpy	BMImCl/TFE (1/10)	12	99	70 700	110 000	1.17	8.8
18	bpy	HMImCl/TFE (1/10)	12	99	131 000	134 000	1.20	22.8
19	bpy	BMImBr/TFE (1/10)	12	99	142 000	162 000	1.36	15.2
20	bpy	BMImI/TFE (1/10)	12	20	26 300	46 900	1.55	6.8

[a] MAPS = 3-(*N*-2-methacryloyloxyethyl-*N*,*N*-dimethyl)ammonatopropanesulfonate, TFE = 2,2,2-trifluoroethanol, EMImCl = 1-ethyl-3-methylimidazorium chloride, BMImCl = 1-butyl-3-methylimidazorium chloride, HMImCl = 1-hexyl-3-methylimidazorium chloride, BMImBr = 1-butyl-3-methylimidazorium bromide, BMImI = 1-butyl-3-methylimidazorium iodide, bpy = 2,2-dipyridyl, TMEDA = *N*,*N*,*N*′,*N*′-tetramethylethylenediamine, PMDETA = *N*,*N*,*N*′,*N*′,*N*″-pentamethyldiethylenetriamine, Me_6TREN = tris(2-(dimethyl)aminoethyl)amine, and EBiB = ethyl 2-bromoisobutylate. ATRP condition: [CuBr]/[bpy]/[EBiB]/[MAPS] = 1.05/2/1/550. [b] Gravity. [c] M_n(calcd) = [MAPS]/[EBiB] × Yield/100 × [MW of MAPS]. M_n = number-average molecular weight, M_w = weight-average molecular weight. [d] The M_n(obsd) of free poly(MAPS) was determined by SEC-MALS using a 200 mM NaCl aqueous solution as an eluent. [e] Ellipsometry (refractive index = 1.50). [f] Volume ratio. [g] [CuBr]/[bpy]/[EBiB]/[MAPS] = 2/4/1/270. [h] [CuBr]/[bpy]/[EBiB]/[MAPS] = 2/4/1/850.

covered with the precipitated polymers. The obtained polymer had a broad MWD (M_w/M_n = 1.74) and much higher M_n than the theoretical value calculated by the molar ratio of monomer to free initiator in the feed, suggesting poor control of MAPS polymerization in aqueous solution. The relatively fast polymerization rate and poor control might be attributed to the hydrolysis of Cu−X bonds in the Cu(II) deactivator species.[39]

Huglin et al. demonstrated that TFE and 1.0 M aqueous NaCl solution are good solvents for the poly(MAPS) by the light scattering, membrane osmometry and viscosity measurements.[20] TFE was previously used as a solvent for ROMP of norbornene derivatives bearing sulfobetaine, carbobetaine, and ammonium bromide groups,[21,22] and RAFT of MPC copolymer[23] due to the excellent affinity of TFE for the sulfopropylbetaine monomer and the polymers, yielding a homogeneous reaction mixture. ATRP of MAPS in TFE at 60 °C proceeded in characteristic red colored homogeneous solution (run 2) and produced the polymer at 95% yield within 1 h to give a polymer with narrower MWD (M_w/M_n = 1.40) than that obtained in the aqueous solvent system.

Further improvement in controlled polymerization might be achieved by the addition of halide anions in the reaction mixture for ATRP of electrolyte monomers. Armes et al. reported that the MWD of poly(2-(methacryloxy)ethyltrimethylammonium chloride) (MTAC) prepared by ATRP in the presence of sodium chloride was slightly reduced compared with that obtained in the absence of salt, although they concluded that the improvement was within the range of experimental error.[40] Since inorganic salts are normally insoluble in TFE, we attempted to use imidazolium type ionic liquid HMImCl as an added salt. ATRP of MAPS in TFE in the presence of HMImCl (HMImCl/TFE = 1/20, wt/wt) at 60 °C also yielded a homogeneous solution to give a polymer with narrower MWD (M_w/M_n = 1.29) at 26% yield (run 3). The observed M_n of free poly(MAPS) was relatively close value to the theoretical value. The yield of the polymer eventually reached 99% by prolonging the experiment to 6 h maintaining relatively narrow MWD (run 4), suggesting that polymerization in the presence of ionic liquid proceeded very slowly in a satisfactorily controlled manner. With increasing the additive ratio of HMImCl/TFE by weight from 1/20 to 1/5, the yield of the polymer obtained by ATRP for 6 h decreased from 99 to 34% (runs 4,5,8,9). The polymerization rate was found to be largely dependent on the additive ratio of HMImCl.

The observed M_n's of runs 3−7 determined by SEC-MALS were slightly larger than the theoretical values by yield and the molar ratio of MAPS to free initiator EBiB in the feed. In general, a larger M_n than the theoretical value is caused by undesired deactivation or side reactions during the polymerization reaction. However, the SEC curves of all polymers in this study showed relatively sharp unimodal peaks without tails in the lower molecular weight region, maintaining MWD around 1.19−1.22 independent of the HMImCl concentration. In addition, the difference ratio between the observed M_n and theoretical value was constant at M_n(calcd)/ M_n(obsd) = 0.72 in every batch for ATRP of MAPS in the HMImCl/TFE system. Therefore, deactivation of the initiator might have taken place at the initial stage of polymerization when the initiator/catalyst solution was injected into the monomer solution by the syringe technique. One of the technical difficulties encountered in the experiment was dissolving the MAPS monomer in the high concentration ionic liquid in TFE due to the high viscosity, thus, the preferred controlled polymerization conditions were found to be a HMImCl/TFE mixture of 1/10, (wt/wt) MAPS concentration of around 1.0 M, and catalysts ratio of [CuBr]/[bpy]/[EBiB] = 1.05/2/1. As an exception, a better controlled polymer was obtained by ATRP at the ratio of [CuBr]/[bpy]/[EBiB] = 2.1/4/1 in order to synthesize a polymer with molecular weight higher than $M_n > 200\,000$ g mol^{-1} (run 7).

Figure 1 shows the first-order kinetic plots for ATRP of MAPS in HMImCl/TFE (1/10, wt/wt) at 60 °C. The logarithmic monomer conversion index given by $\ln([M]_0/[M])$

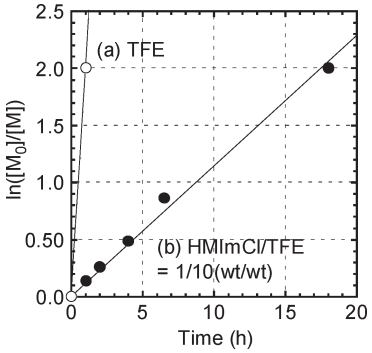

Figure 1. First-order kinetic plots of $\ln([M]_0/[M])$ versus time for the ATRP of MAPS at 60 °C (a) in 2,2,2-trifluoroethanol (TFE) (open circle) and (b) in 1-hexyl-3-methylimidazorium chloride (HMImCl)/TFE (1/10, wt/wt) (filled circle); [CuBr]/[bpy]/[MAPS]/[EBiB] = 1.05/2/250/1 (molar ratio), [EBiB] = 0.0021 mM, where bpy, MAPS, and EBiB are 2,2′-dipyridyl, 3-(*N*-2-methacryloyloxyethyl-*N*,*N*-dimethyl) ammonatopropanesulfonate), and ethyl 2-bromoisobutyrate, respectively. $\ln[M]_0/[M]$ was calculated by the gravities of synthesized poly(MAPS)s.

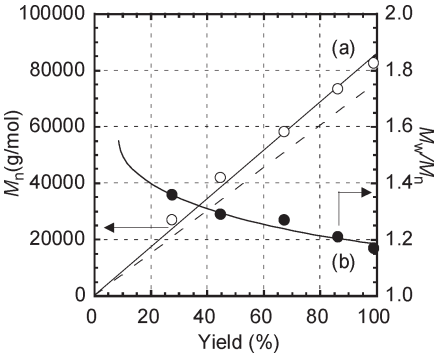

Figure 2. Evolution of (a) the number-averaged molecular weight (M_n) (open circle and straight line) and theoretical line (dash line), and (b) molecular weight distribution (M_w/M_n) (filled circle) with conversion of atom transfer radical polymerization of 3-(*N*-2-methacryloyloxyethyl-*N*,*N*-dimethyl) ammonatopropanesulfonate) in 2,2,2-trifluoroethanol/1-hexyl-3-methylimidazorium chloride (1/10, wt/wt) at 60 °C. M_n and M_w/M_n of the poly(MAPS) were estimated by SEC-MALS measurement using 200 mM NaCl aqueous solution.

increased linearly with polymerization time from the initial stage up to 95% conversion at 18 h, indicating that polymerization proceeded without crucial side reactions or deactivation. In comparison, polymerization in TFE without ionic liquid was completed within 1 h. The apparent propagation rate constants k_p^{app} of ATRP in the absence and presence of HMImCl were 2.8×10^{-1} and 8.3×10^{-3} mol^{-1} L s^{-1}, respectively. As shown in Figure 2, as the monomer conversion increased, the M_n of poly(MAPS) also linearly increased maintaining narrow MWD. The polydispersity index leveled off at around $M_w/M_n = 1.18$ (run 6).

The formation of poly(MAPS) brush was confirmed by XPS measurement, as shown in Figure 3. The four peaks at 532.0, 402.0, 285.0, and 167.0 eV were observed corresponding to oxygen, nitrogen, carbon, and sulfur, respectively. The atomic ratios of C/O/N/S in the poly(MAPS) brush were estimated to be 0.64/0.26/0.05/0.05, which was relatively close to the theoretical values calculated from the atomic composition of MAPS. The carbon ratio was slightly larger than theoretical value probably because of some impurities adsorbed on poly(MAPS) brush surface.

Figure 4a shows the topographic AFM image of poly(MAPS) brush (M_n = 123 000, M_w/M_n = 1.22) using tapping

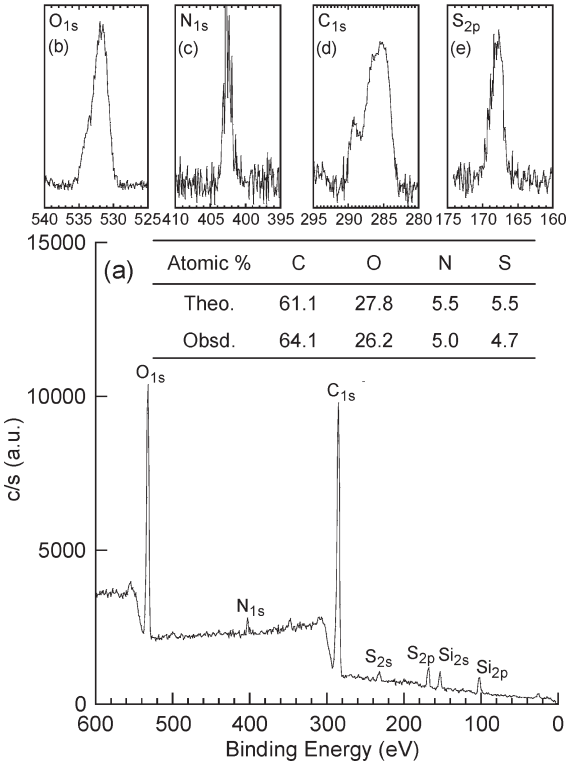

Figure 3. XPS spectra of poly(MAPS) brush prepared by surface-initaited ATRP of MAPS in 2,2,2-trifluoroethanol/1-hexyl-3-methylimidazorium chloride (10/1, wt/wt) on silicon wafer: (a) survey scan spectrum; high-resolution spectra of (b) O_{1s}, (c) N_{1s}, (d) C_{1s}, and (e) S_{2p} peak region.

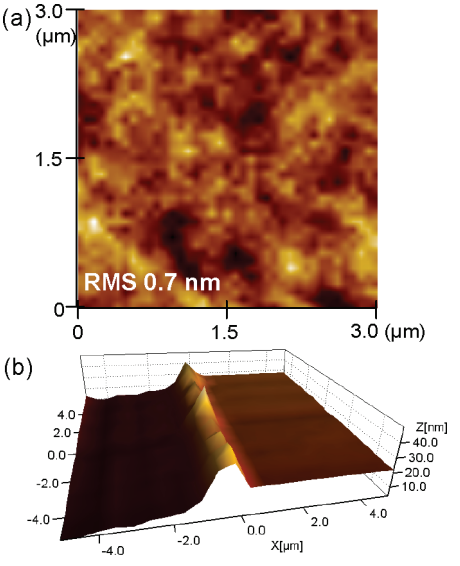

Figure 4. AFM image of poly(MAPS) brush on silicon wafer (M_n 150000 M_w/M_n = 1.20) prepared by surface-initiated ATRP in 2,2,2-trifluoroethanol/1-hexyl-3-methylimidazorium chloride (10/1, wt/wt) using tapping mode in air. (a) Topographic image of poly(MAPS) brush and (b) three-dimensional image of scratched poly(MAPS) brush by sharp needle edge. The height of boundary layer of poly(MAPS) brush was calculated to be 20.3 nm.

mode. The root-mean-square (rms) of the surface roughness was approximately 0.7 nm in a 3 × 3 μm^2 scanning area. Poly(MAPS) brush with large MWD (M_w/M_n = 1.80) prepared by ATRP in water/methanol mixture showed 0.9 nm of rms in a 3 × 3 μm^2. Therefore, no significant difference in

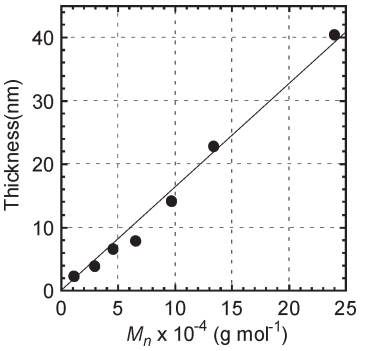

Figure 5. Thickness of poly(MAPS) brushes estimated by ellipsometry as a function of the number-averaged molecular weight (M_n) of the corresponding free polymer produced by ATRP in 2,2,2-trifluoroethanol/1-hexyl-3-methylimidazorium chloride (filled circle).

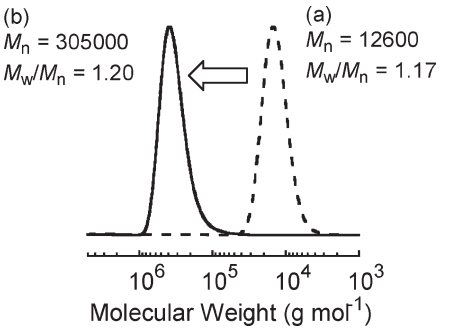

Figure 6. SEC curves of (a: dot line) original poly(MAPS) produced by ATRP in 2,2,2-trifluoroethanol/1-hexyl-3-methylimidazorium chloride (1/10, wt/wt) at 60 °C (M_n(obsd) = 1.26×10^4, M_w/M_n = 1.17), and (b: solid line) postpoly(MAPS) generated from the original polymer by ATRP (M_n(obsd) = 30.5×10^4, M_w/M_n = 1.20).

roughness was observed on the surface of brushes with different MWD by AFM under air. Figure 4b showed three-dimensional image of scratched poly(MAPS) brush surface by sharp needle edge. Although the bank was formed at the boundary scratched region, the gap between flat brush layer and scratched bottom area was 20.3 nm, which well agreed with 20.6 nm of the thickness estimated by ellipsometry. The AFM observation revealed that a homogeneous polymer layer was formed on the substrate.

In order to estimate the molecular weight and MWD of surface-grafted poly(MAPS), the surface-grafted poly(MAPS) was cleaved from the silicon wafer ($65 \times 65 \times 0.5$ mm^3) by acidic hydrolysis using a 3% hydrogen fluoride aqueous solution containing sodium chloride, and was collected to measure SEC-MALS. The surface-grafted poly(MAPS) synthesized by SI-ATRP in methanol/water (1/1, v/v) showed the broad MWD (M_n = 176 000, M_w/M_n = 1.80), while the surface-grafted polymer prepared by SI-ATRP in TFE/HMImCl (1/10, wt/wt) had relatively narrow MWD (M_n = 150 000, M_w/M_n = 1.26). These results indicated that the polymerization of MAPS from surface-tethered initiator proceeded in similar controlled manner as well as the polymerization from sacrificial free initiator.

The thickness of the obtained poly(MAPS) brushes on silicon wafers in air (temperature 298 K, relative humidity 30%) was estimated by ellipsometry. Figure 5 shows the relationship between thickness of poly(MAPS) brush and M_n of corresponding free polymer. The brush thickness increased linearly from 2 to 40 nm with increasing M_n of the free polymer. Provided that the free polymer and brush chain generated in the same reaction batch have the same M_n, the graft density σ of the polymer brush can be estimated to be 0.080 chains nm^{-2} based on the relationship between the thickness L (nm) and M_n as follows:[41]

$$\sigma = \rho L N_A \times 10^{-21}/M_n \quad (1)$$

where ρ and N_A are the assumed density of bulk polymer 1.34 g cm^{-3} [38] and Avogadro's number, respectively. This value is lower than the typical graft density of a PMMA brush (0.60−0.70 chains nm^{-2}) prepared by the "grafting-from" method, because of the larger molecular size of the sulfobetaine group in the side chain compared with MMA. The cross-sectional radius of gyration (R_c) of free poly(MAPS) in TFE solution was estimated to be 0.59 nm by SAXS analysis. The cross-sectional area of a poly(MAPS) chain can be calculated to be 8.87 nm^2 by $d^2/8 = \langle R_c \rangle^2$, where the d is a diameter of polymer chain bearing a sulfobetaine unit. Then, the grafting density σ was estimated to be 0.112 chains nm^{-2}, which was close to the previously mentioned σ value of 0.080 chains nm^{-2}. Therefore, the graft density of the polymer brush was relatively high and was produced by SI-ATRP in this study.

Postpolymerization experiments were conducted in HMImCl/TFE in order to evaluate the living characteristics of the chain ends. First-stage polymerization of MAPS was carried out in HMImCl/TFE (1/10, wt/wt) with free EBiB and BHE-immobilized silicon wafer at 60 °C for 24 h to produce a polymer with M_n of 12 600 and M_w/M_n of 1.17, and a polymer brush with 2.0 nm thickness. The resulting free polymer was carefully purified by reprecipitation two times to remove the unreacted monomers and catalysts, and then dried under vacuum at 50 °C for 12 h. The purified free poly(MAPS) and the brush substrate were loaded in a glass tube together with a fresh MAPS and HMImCl/TFE solution and then the second-stage polymerization was carried out at 60 °C for 18 h. Figure 6 shows the SEC curves for the free poly(MAPS) obtained in the first- and second-stage polymerization. The curve in the second-stage polymerization clearly shifted to a higher molecular region to M_n = 305 000 maintaining relatively narrow MWD (M_w/M_n = 1.20), indicating that most of the polymer chain ends efficiently initiated ATRP of MAPS without any crucial termination reactions. The thickness of the polymer brush was also increased from 2.0 to 24.4 nm.

Effect of Ligand and Ionic Liquid Structure on ATRP. To compare the polymerization control by copper complexes containing various nitrogen-based ligands, such as TMEDA, PMDETA, and Me_6TREN, polymerization was carried out in TFE and HMImCl/TFE (1/10, wt/wt) with EBiB at 60 °C. In general, the activity of the Cu(I)/ligand complexes decreases in the following order: teradentate ligands > tridentate ligands > bidentate ligands.[42] All ATRP in TFE gave polymers with rather broad MWDs independently on the chemical structure of the ligand (runs 10, 12, 14). On the other hand, the MWDs of the polymer synthesized in HMImCl/TFE (1/10, wt/wt) was lower than that in TFE except for the result with TMEDA. Polymerization using the copper complex of TMEDA hardly proceeded in HMImCl/TFE (run 11). Although TMEDA is a bidentate ligand forming a Cu(I)/ligand complex as well as bpy, its catalytic activity was very low. In contrast, tridentate-type PMDETA and tetradentate-type Me_6TREN showed high catalytic activity to give the polymers almost quantitatively within 12 h even in HMImCl/TFE (runs 13 and 15). Although Cu(I)/PMDETA and Me_6TREN produced polymers with relatively narrow MWDs, the M_n determined by SEC-MALS was much higher than the theoretical value, especially in the case of synthesizing high-molecular-weight

Table 2. Surface-Initiated ATRP of MAES and MABS in BMImCl/TFE at 60 °C[a]

run	monomer	time (h)	yield[b] (%)	M_n calcd[c]	M_n SEC[d]	M_w/M_n	thickness[e] (nm)
20	MAES	15	99	123 000	233 000	1.17	29.9
21	MABS	12	99	136 000	193 000	1.16	17.2
22[f]	MABS	12	99	149 000	229 000	1.30	21.6

[a] MAES = 2-(*N*-2-methacryloyloxyethyl-*N*,*N*-dimethyl)ammonatoethanesulfonate), MABS = 4-(*N*-2-methacryloyloxyethyl-*N*,*N*-dimethyl)ammonatobutanesulfonate, TFE = 2,2,2-trifluoroethanol, BMImCl = 1-butyl-3-methylimidazorium chloride, bpy = 2,2-dipyridyl, and EBiB = ethyl 2-bromoisobutylate. ATRP conditions: [CuBr]/[bpy]/[EBiB]/[MAPS] = 1.05/2/1/550; BMImCl/TFE = 1/10 wt/wt. [b] Gravity. [c] M_n(calcd) = [MAES (or MABS)]/[EBiB] × yield/100 × [MW of MAES (or MABS)]. M_n = number-average molecular weight; M_w = weight-average molecular weight. [d] The M_n(obsd) of free polymer was determined by SEC-MALS using a 200 mM NaCl aqueous solution as an eluent. [e] Ellipsometry (Refractive index = 1.50). [f] 1-butyl-3-methylimidazorium bromide was used.

polymer. These results indicate low initiator efficiency in ATRP using a copper complex of PMDETA and Me_6TREN. Therefore, we concluded that bpy was a suitable ligand for copper-catalyzed ATRP of MAPS to give a polymer with predictable molecular weight and narrow MWDs.

The effect of the chemical structure of ionic liquid on controlled polymerization was investigated using 1-substituted-3-methylimidazolium halides with ethyl, butyl, and hexyl groups and counteranions, such as chloride, bromide, and iodide. The polymers obtained by ATRP in TFE solution containing EMImCl and BMImCl also had relatively narrow MWDs of 1.15−1.20 (runs 16−18). No significant difference was observed in ATRP using 1-substituted-3-methylimidazolium chloride with ethyl, butyl, and hexyl groups. On the other hand, poorly controlled polymerization took place when ionic liquid with bromide and iodide counteranions was used. ATRP of MAPS in TFE containing BMImBr and BMImI (runs 19, 20) yielded polymers with broader MWD of 1.36 and 1.50, respectively, in contrast with the case of BMImCl (run 17). The chloride anion was a suitable agent among various counteranions to control the polymerization of MAPS.

The effect of ionic liquid on controlled polymerization of MAPS has not yet been clearly revealed. We suppose that the imidazolium ionic liquid behaved as an electron-donating solvent enhancing the reducing power of the Cu^{II} complex. The polymerization rate depends on the value of the ATRP equilibrium constant, which is the ratio of the rate constants for activation and deactivation established through homolytic cleavage of a C−X bond of a dormant species by a Cu^{I}/ligand complex that generates the corresponding higher oxidation state Cu^{II}/ligand complex deactivator and active species with an organic radical.[43] As a result, for ATRP equilibrium might be shifted to the dormant species side to result in a slow polymerization rate. In the case of BMImI, iodide radicals might be more easily liberated from imidazolium cation compared with BMImCl and BMImBr to trap the propagating radicals, eventually leading to a termination or radical transfer reaction and poorly controlled polymerization. On the other hand, not only the coordination of the ionic liquid to copper catalyst but also the interaction between MAPS monomer and ionic liquid could occur during the polymerization. Coordination of ionic liquids to MAPS were reported by Laschewski et al., who carried out the free radical polymerization of MAPS in 1-butyl-3-methylimidazolium hexafluorophosphate and 1-butyl-3-methylimidazolium tetrafluoroborate to give high molecular weight polymer, although the phase separation occurred during the polymerization.[44] In this study, the interaction between MAPS and ionic liquid was supposed to be moderated by TFE solvent to afford homogeneous polymerization.

ATRP of MAES and MABS in TFE/Ionic Liquid. ATRP in TFE/ionic liquid cosolvent system was applied for controlled polymerization of the other types of sulfobetaine monomers. MAES and MABS are sulfobetaine methacrylates having a different number of methylene units (m) between ammonium cation and sulfonate anion in the side chains: m of MAES and MABS is 2 and 4, respectively. ATRP of these monomers was conducted under the same conditions as that of MAPS (Table 2). ATRP of MAES and MABS in BMImCl/TFE mixture of 1/10 yielded poly(MAPS) and poly(MAES) with M_n's of 233 000 and 193 000 g mol^{-1}, and narrow MWDs of 1.17 and 1.16, respectively (run 21, 22), though the observed M_n's were much larger than theoretical values. We supposed that some impurities in monomers deactivated the initiator at the initial stage of polymerization to decrease the initiator efficiency. On the other hand, poly(MABS) obtained by ATRP in BImBr/TFE mixture had broader MWD of 1.30 (run 23) compared with ATRP of MABS in BMImCl/TFE. As mentioned previous paragraph, chloride counteranion of the imidazolium salt gave better control in ATRP of MAES and MABS compared with bromide counteranion. The graft density values of poly(MAES) and poly(MABS) brushes were calculated to be 0.093 and 0.064 chains nm^{-2}, respectively, by the thickness of brushes and the M_n of the corresponding free polymers. These values might be reasonable considering that the σ of poly(MAPS) (m = 3) was 0.080 chains nm^{-2}. Increasing the methylene spacer m from 2 to 4, the sulfobetaine monomers occupy a larger cross-sectional area on a flat surface to result in smaller graft density of polymer brushes.

Conclusions

We found that (surface-initiated) direct ATRP of MAPS in TFE containing a small portion of 1-alkyl-3-methylimidazolium chloride proceeded in a satisfactorily controlled manner to produce well-defined poly(MAPS) brushes and the corresponding free polymer with predictable M_n of about 200 000 g mol^{-1} and relatively narrow MWD of 1.15−1.25. We assumed that improved control was achieved by homogeneous reaction media given by the affinity of TFE and imidazolium chloride for sulfobetaine monomers. Well-defined free polymers can be prepared even in a heterogeneous reaction mixture; however, it would be difficult to generate the polymer brushes with uniform thickness and M_n on the substrate surface. In general, sulfobetaine monomers and polymers in water with low ionic strength self-aggregate due to the strong attractive electrostatic interaction. The polarity of TFE and ionic liquids would screen the interaction between betaine units to give a homogeneous solution. The combination of TFE and ionic liquid is expected to improve the controlled polymerization of various types of monomers bearing polar or charged functional groups and to produce well-defined polyelectrolyte brushes, which will contribute to more sophisticated analysis of soft interfaces.

Acknowledgment. The present work is supported by a Grant-in-Aid for the Global COE Program, "Science for Future

Molecular Systems", and partially supported by a Grant-in Aid for Young Scientist (B) (19750098) from the Ministry of Education, Culture, Science, Sports and Technology of Japan. Education, Culture, Science, Sports, and Technology of Japan. Y.T. acknowledges the financial support of a Grant-in-Aid for JSPS Fellows.

Supporting Information Available: Preparation of sulfobatine monomers. This material is available free of charge via the Internet at http://pubs.acs.org.

References and Notes

(1) Chen, M.; Briscoe, W. H.; Armes, S. P.; Klein, J. *Science* **2009**, *323*, 1698–1701.
(2) Kitano, H.; Suzuki, H.; Matsuura, K.; Ohno, K. *Langmuir* **2010**, *26*, 6767–6774.
(3) Kobayashi, M.; Terayama, Y.; Hosaka, N.; Kaido, M.; Suzuki, A.; Yamada, N.; Torikai, N.; Ishihara, K.; Takahara, A. *Soft Matter* **2007**, *3*, 740–746.
(4) Matsuda, Y.; Kobayashi, M.; Annaka, M.; Ishihara, K.; Takahara, A. *Langmuir* **2008**, *24*, 8772–8778.
(5) Kaewsaiha, P.; Matsumoto, K.; Matsuoka, H. *Langmuir* **2007**, *23*, 20–24.
(6) Kobayashi, M.; Terayama, Y.; Hino, M.; Ishihara, K.; Takahara, A. *J. Phys: Conf. Ser.* **2009**, *184*, 012010.
(7) Terayama, Y.; Kikuchi, M.; Kobayashi, M.; Hino, M.; Takahara, A. *J. Phys: Conf. Ser.* **2009**, *184*, 012011.
(8) Edmondson, S.; Nguyen, N. T.; Lewis, A. L.; Armes, S. P. *Langmuir* **2010**, *26*, 7216–7226.
(9) Hoffmann, M.; Jusufi, A.; Schneider, C.; Ballauff, M. *J. Colloid Interface Sci.* **2009**, *338*, 566–572.
(10) Kato, T.; Takahashi, A. *Ber. Bunsen-Ges. Phys. Chem.* **1996**, *100*, 784.
(11) Schulz, D. N.; Peiffer, D. G.; Agarwal, P. K.; Larabee, J.; Kaladas, J. J.; Soni, L.; Handwerker, B.; Garner, R. T. *Polymer* **1986**, *27*, 1734.
(12) Wang, H.; Hirano, T.; Seno, M.; Sato, T. *Eur. Polym. J.* **2003**, *39*, 2107–2114.
(13) Liaw, D.- J.; Lee, K.- R. *Polym. Int.* **1993**, *30*, 381–386.
(14) Lowe, A. B.; Billingham, N. C.; Armes, S. P. *Chem. Commum.* **1996**, *17*, 1555.
(15) Lowe, A. B.; McCormick, C. L. *Chem. Rev.* **2002**, *102*, 4177–4189.
(16) Donovan, M. S.; Sumerlin, B. S.; Lowe, A. B.; McCormick, C. L. *Macromolecules* **2002**, *35*, 8663–8666.
(17) Zhai, G.; Yu, W. H.; Kang, E. T.; Neoh, K. G.; Huang, C. C.; Liaw, D. J. *Ind. Eng. Chem. Res.* **2004**, *43*, 1673–1680.
(18) Yang, W.; Chen, S.; Cheng, G.; Vaisocherova, H.; Xue, H.; Li, W.; Zhang, J.; Jiang, S. *Langmuir* **2008**, *24*, 9211–9214.
(19) Cheng, N.; Brown, A. A.; Azzaroni, O.; Huck, W. T. S. *Macromolecules* **2008**, *41*, 6317–6321.
(20) Huglin, M. B.; Radwan, M. A. *Makromol. Chem.* **1991**, *192*, 2433–2445.
(21) Rankin, D. A.; P'Pool, S. J.; Schanz, H.-J.; Lowe, A. B. *J. Polym. Sci., Polym. Chem.* **2007**, *45*, 2113–2128.
(22) Rankin, D. A.; Lowe, A. B. *Macromolecules* **2008**, *41*, 614–622.
(23) Yu, B.; Lowe, A. B.; Ishihara, K. *Biomacromolecules* **2009**, *10*, 950–958.
(24) Kobayashi, M.; Terada, M.; Terayama, Y.; Kikuchi, M.; Takahara, A. *Macromolecules* **2010**, *43*, 8409−8415.
(25) Carmichael, A. J.; Haddleton, D. M.; Bona, S. A. F.; Seddonb, K. R. *Chem. Commun.* **2000**, *14*, 1237–1238.
(26) Sarbu, T.; Matyjaszewski, K. *Macromol. Chem. Phys.* **2001**, *202*, 3379–3391.
(27) Biedron, T.; Kubisa, P. *Macromol. Rapid Commun.* **2001**, *22*, 1237–1242.
(28) Biedron, T.; Kubisa, P. *J. Polym. Sci., Part A: Polym. Chem.* **2002**, *40*, 2799–2809.
(29) Zhang, H.; Zhang, Y.; Liu, W.; Wang, H. *J. Appl. Polym. Sci.* **2008**, *110*, 244–252.
(30) Ma, H.; Wan, X.; Chen, X.; Zhou, Q.-F. *Polymer* **2003**, *44*, 5311–5316.
(31) Hu, Z.; Shen, X.; Qiu, H.; Lai, G.; Wu, J.; Li, W. *Eur. Polym. J.* **2009**, *45*, 2313–2318.
(32) Ohno, K.; Morinaga, T.; Koh, K.; Tsujii, Y.; Fukuda, T. *Macromolecules* **2005**, *38*, 2137–2142.
(33) Kobayashi, M.; Takahara, A. *Chem. Lett.* **2005**, *34*, 1582–1583.
(34) Queffelec, J.; Gaynor, S. G.; Matyjaszewski, K. *Macromolecules* **2000**, *33*, 8629–8639.
(35) Koga, T.; Morita, M.; Ishida, H.; Yakabe, H.; Sasaki, S.; Sakata, O.; Otsuka, H.; Takahara, A. *Langmuir* **2005**, *21*, 905.
(36) Duanna, Y. −F.; Chena, Y. −C.; Shena, J. −T.; Lin, Y. −H. *Polymer* **2004**, *45*, 6839–6843.
(37) Gauther, M.; Carrozzella, T.; Penlidis, A. *J. Polym. Sci., Part A: Polym. Chem.* **2002**, *40*, 511–523.
(38) Starck, P.; Mosse, W. K. J.; Nicholas, N. J.; Spiniello, M.; Tyrrell, J.; Nelson, A.; Qiao, G. G.; Ducker, W. A. *Langmuir* **2007**, *23*, 7587–7593.
(39) Tsarevsky, N. V.; Pintauer, T.; Matyjaszewski, K. *Macromolecules* **2004**, *37*, 9768–9778.
(40) Li, Y.; Armes, S. P.; Jin, X.; Zhu, S. *Macromolecules* **2003**, *36*, 8268–8275.
(41) Husseman, M.; Malmstrom, E. E.; McNamura, M.; Mate, M.; Mecerreyes, D.; Benoit, D. G.; Hedrick, J. L.; Mansky, P.; Huang, E.; Russell, T. P.; Hawker, C. J. *Macromolecules* **1999**, *32*, 1424–1431.
(42) Tang, W.; Kwak, Y.; Braunecker, W.; Tsarevsky, N. V.; Coote, M. L.; Matyjaszewski, K. *J. Am. Chem. Soc.* **2008**, *130*, 10702–10713.
(43) Braunecker, W. A.; Tsarevsky, N. V.; Gennaro, A.; Matyjaszewski, K. *Macromolecules* **2009**, *42*, 6348–6360.
(44) Strehmel, V.; Laschewsky, A.; Wetzel, H. *e-Polym.* **2006**, *011*, 1–10.

112 *Macromolecules* **2011**, *44*, 112–121
DOI: 10.1021/ma101285m

Macromolecules
ARTICLE

Simulation of End-Coupling Reactions at a Polymer−Polymer Interface: The Mechanism of Interfacial Roughness Development

Anatoly V. Berezkin*

Max-Planck Institut für Eisenforschung GmbH, Max-Planck Strasse 1, 40237 Düsseldorf, Germany

Yaroslav V. Kudryavtsev*

A.V. Topchiev Institute of Petrochemical Synthesis, Russian Academy of Sciences, Leninsky prosp. 29, 119991 Moscow, Russia

Received June 9, 2010; Revised Manuscript Received November 22, 2010

ABSTRACT: End-coupling between immiscible melts of two monofunctionalized polymers of a same length was modeled by dissipative particle dynamics starting from a flat interface and up to the formation of a mature lamellar microstructure. Influence of the reaction rate, chain length, and incompatibility of components on the kinetics of copolymer formation and morphology development was investigated. Regimes of linear and logarithmic growth of the conversion with time were observed before the flat interface became unstable. The conditions and mechanism of interfacial roughness development were studied in detail. It was demonstrated that overcrowding the interface with the copolymer product causing its phase separation plays the main role in spontaneous interface distortion. The instability leads to autocatalytic interface growth with exponential kinetics, when each new portion of the product creates more area for further reactions. It was followed by a slower terminal regime including formation and ripening of the lamellar microstructure. The late stage kinetics of end-coupling was strongly influenced by depletion of reactants and formation of ordered product layers. At certain conditions, it became asymptotically diffusion controlled in agreement with published experimental data.

Introduction

Design of commercial polymer composites is based on combining different species to tailor material properties.[1] However, a straightforward melt blending is often ineffective due to the tendency to phase separation in most of polymer couples. Usually it results in a small area of polymer−polymer interface and hence weak adhesion between blend components. Adding copolymers that serve as surfactants and promote adhesion by increasing contact area, forming entanglements, and introducing chemical bonds between immiscible domains can solve the incompatibility problem.

Though premade graft, block, and random copolymers are widely used, the most promising strategy is related to the so-called reactive compatibilization,[1−5] which implies copolymer formation *in situ*. Its main advantage is that copolymers appear at the interface just where they are needed to improve thermodynamic and mechanical properties of a composite.[6]

Understanding the fundamentals of reactive polymer blending requires various contributions to be separated, which is possible only for relatively simple systems. One of the most popular models is a flat interface between melts of incompatible homopolymers A and B, end units of which are functionalized with complementary reactive groups. An end-coupling reaction produces a block copolymer AB, which modifies the interfacial tension, adhesion, etc. and in turn influences the reaction rate. Under quiescent conditions, diffusion and reaction are the only factors governing evolution of a bilayer system. Their interplay was investigated in theory,[7−11] by simulations,[12−16] and experimentally.[5,17−22]

*Corresponding authors. E-mail: (A.V.B.) berezkin.anatoly@rambler.ru; (Y.V.K.) yar@ips.ac.ru.

At the very beginning, the interfacial coverage n (the number of copolymer chains per unit interface area) grows linearly with time t. If the local reactivity Q of contacting end groups is much less than the inverse relaxation time for a monomer unit, which is realized in most of the experiments, then theories predict that a linear regime $n \sim t$ is followed by a diffusion controlled (DC) regime $n \sim t^{1/2}$. However, the characteristic time separating the regimes is very large being proportional to Q^{-2} so that the DC regime could be outside experimental time scales.[10] Indeed, the only evidence of a "depletion hole"[19] is related to the low-temperature reaction between PS−COCl and PMMA−NH_2 in supercritical CO_2, whereas melt studies with various functional groups suitable for chain coupling[23,24] demonstrate mean field kinetics without any DC regimes.

At the same time, diffusion controlled kinetics is well reproduced in molecular dynamics,[12] Monte Carlo[13−15] and hybrid model[16] simulations, while the linear regime is distorted or not observed at all. This can be explained by unrealistically high reaction rates used in all simulations of end-coupling performed so far. In fact, it was assumed[12−16] that each contact between reactive chain ends led to the formation of a covalent bond with probability one.

Another important factor influencing the reaction kinetics is saturation of the interface with the copolymer product. At a critical coverage $n_{cr} = 1/(3N^{1/2}b^2)$ (b is a segment size, N is a chain length assumed to be equal for both polymers) blocks start to feel one another and therefore begin to stretch. Copolymer chains gradually form a brush, which creates a potential barrier for unreacted homopolymers approaching the interface. Asymptotically, a new kinetic regime is established:[9]

$$n \sim n_{cr}\sqrt{\ln((N^{1/2}t)/(\tau_1 \ln N))} \sim (\ln t)^{1/2}$$

 Published on Web 12/10/2010 © 2010 American Chemical Society

where τ_1 is the terminal chain relaxation time. At weak reactivity and equal reactant concentrations, the copolymer begins retarding kinetics before the DC regime is set so that the linear regime is directly followed by the logarithmic one.

While theories are focused on the early stages of end-coupling, experiments demonstrate[18,20,25,26] that a slowdown in the kinetics caused by interface saturation can be spontaneously superseded by acceleration, which is accompanied by abrupt roughening and emulsification of the interface. Under simple shear flow, a fine microstructure can be easily formed in the reacting system at a shear rate that is not enough to increase interface area by itself.[27] The similar scenario is observed in melts where coupling reactions produce graft copolymers.[28,29]

It was shown that interface roughening does not occur and the kinetic curve levels off if reacting homopolymers are rather long ($\chi N = 10$) and therefore separated by a very narrow interface[18] or if their degree of functionalization is low (< 30 wt %).[26] However, those particular observations do not specify sufficient conditions for interfacial roughness development and its mechanism. An attempt to explain a steep increase in roughness in the reacting blend of dPS−NH_2 and P2VP−anhydride by the vanishing interfacial tension[20] was later challenged by the finding that coupling between those polymers is a reversible reaction, which influences a block copolymer amount at the interface.[21]

Previous computer simulations of end-coupling also captured the possibility of accelerating the reaction kinetics at late stages.[12,16] It was found that the flat interface became unstable after the interfacial tension had vanished, whereas subsequent growth of the interface width obeyed a diffusion law ($\sim t^{1/2}$) indicating about possible effect of thermal fluctuations. However, those studies were severely restricted in spatial and time scales by limitations in computational resources. The routine molecular dynamics simulation[12] only enabled detection of the interfacial instability. Investigating subsequent growth of fluctuations and transformation of the bilayer system into a lamellar structure[16] involved a number of simplifications: initial homopolymers were modeled by hard spherical particles while block copolymers by rigid dumbbells, the coupling rate was unrealistically high, the interfacial tension was approximated by the gradient energy density, hydrodynamic effects were neglected.

In this work, we use computer simulations to reexamine evolution of an incompatible polymer melt undergoing end-coupling reactions. The study is focused on understanding reasons and kinetics of interface roughening using more realistic probabilistic reaction kinetics. We model highly concentrated systems, where every chain carries a reactive end group. This promotes formation of an interfacial block copolymer layer in a mean field (reaction controlled) kinetic regime in agreement with most of the experiments. The dissipative particle dynamics method, which is used for simulations, provides high speed of relaxation and accounts for hydrodynamic effects. As a result, time scales are attained that are 2 orders of magnitude as large as the interface saturation time t_s. This enables us to study the development of interface roughening in detail. It is found that after the flat interface becomes unstable, the reaction is characterized by exponential kinetics. Subsequent formation and ripening of lamellas are considerably influenced by diffusion of reactants.

Simulation Technique and Model

We use a coarse-grained molecular dynamics method referred to as dissipative particle dynamics (DPD). This simulation technique was proposed by Hoogerbrugge and Koelman[30,31] and developed by Espanol, Groot, and Warren.[32,33] Its applicability to polymer systems was substantiated by mapping DPD onto the lattice Flory−Huggins theory.[33]

Consider an ensemble of interacting particles governed by Newton's equations of motion:

$$\frac{\mathrm{d}\mathbf{r}_i}{\mathrm{d}t} = \mathbf{v}_i, \quad m_i \frac{\mathrm{d}\mathbf{v}_i}{\mathrm{d}t} = \mathbf{f}_i + \mathbf{f}_i^{\mathrm{pol}} \tag{1}$$

Here $\mathbf{r}_i$, $\mathbf{v}_i$, m_i denote the radius vector, velocity, and mass of the ith particle, and $\mathbf{f}_i$ and $\mathbf{f}_i^{\mathrm{pol}}$ are nonpolymeric and polymeric forces acting on it. The former force, which describes interactions in the corresponding low-molecular liquid, may be written as a sum of pairwise additive contributions:

$$\mathbf{f}_i = \sum_{j \neq i} (\mathbf{F}_{ij}^{\mathrm{C}} + \mathbf{F}_{ij}^{\mathrm{D}} + \mathbf{F}_{ij}^{\mathrm{R}}) \tag{2}$$

where the summation is performed over all other particles within a certain cutoff radius r_c. We assume that all quantities in eq 1, 2 are dimensionless and for simplicity set all m_i and r_c to unity.

A conservative force $\mathbf{F}_{ij}^{\mathrm{C}}$ describes soft core repulsion between contacting particles

$$\mathbf{F}_{ij}^{\mathrm{C}} = \begin{cases} a_{ij}(1 - r_{ij})\bar{\mathbf{r}}_{ij}, & r_{ij} < 1 \\ 0 & r_{ij} \geq 1 \end{cases} \tag{3}$$

where $\mathbf{r}_{ij} = \mathbf{r}_j - \mathbf{r}_i$, $\mathbf{r}_{ij} = |\mathbf{r}_{ij}|$, $\bar{\mathbf{r}}_{ij} = \mathbf{r}_{ij}/\mathbf{r}_{ij}$, and a_{ij} is a maximum repulsion between particles i and j attained at $\mathbf{r}_i = \mathbf{r}_j$.

Other constituents of $\mathbf{f}_i$ are a dissipative force $\mathbf{F}_{ij}^{\mathrm{D}}$ (friction) and a random force $\mathbf{F}_{ij}^{\mathrm{R}}$:

$$\mathbf{F}_{ij}^{\mathrm{D}} = -\frac{\sigma^2}{2k_{\mathrm{B}}T}[\omega(r_{ij})]^2(\mathbf{v}_{ij} \cdot \bar{\mathbf{r}}_{ij})\bar{\mathbf{r}}_{ij},$$

$$\mathbf{F}_{ij}^{\mathrm{R}} = \sigma\omega(r_{ij})\frac{\zeta}{\sqrt{\delta t}}\bar{\mathbf{r}}_{ij}, \quad \omega(r) = \begin{cases} 1 - r, & r \leq 1 \\ 0, & r > 1 \end{cases} \tag{4}$$

where σ is a noise amplitude, k_{B} is the Boltzmann constant, T is temperature, $\mathbf{v}_{ij} = \mathbf{v}_i - \mathbf{v}_j$, ζ is a normally distributed random variable with zero mean and unit variance chosen independently for each pair of particles, and δt is a time step. We take that $k_{\mathrm{B}}T = 1$ and define a dimensionless time unit as

$$\tau = r_{\mathrm{c}}\sqrt{\frac{m}{k_{\mathrm{B}}T}} = 1 \tag{5}$$

Chain connectivity of particles is introduced using the standard bead−spring model so that $\mathbf{f}_i^{\mathrm{pol}}$ is a bond elasticity force

$$\mathbf{f}_i^{\mathrm{pol}} = \sum_j K_{ij}\mathbf{r}_{ij} \tag{6}$$

where K_{ij} is a spring constant (we take $K_{ij} = 4$ for bonded particles and zero for others).

Following Groot and Warren[33] we choose $\sigma = 3$, the reduced particle density $\rho_0 = 3$, and $a_{ii} = 25$. In that case, a_{ij} is related to the interaction parameter χ of the Flory−Huggins theory as

$$a_{ij} = \chi/0.306 + 25, \quad i \neq j \tag{7}$$

The Groot−Warren thermostat defined by eq 4, where the random and dissipative forces serve as a heat source and sink, respectively, preserves momentum for each pair of interacting particles and therefore enables one to account for hydrodynamic effects on microphase separation in block copolymers,[34,35] which are inaccessible by the Monte Carlo method and conventional molecular dynamics.

Simulations were performed with DPDChem freeware package.[36] The equations of motion 1 were solved using the so-called DPD-VV integration scheme,[37] which is a modified version of the velocity−Verlet algorithm (MD-VV), fast enough and more accurate than the latter. The time step $\delta t = 0.04$ was taken,

which allows to accurately model compatibilization during relatively long time intervals. Since some artifacts stemming from the choice of an integration scheme, time step, and relative intensity of dissipative and random forces in the DPD method were previously reported,[38] a part of our simulations was carried out at the smaller time step $\delta t = 0.02$ and almost the same kinetics was observed.

A *simulation box* initially contained two layers of incompatible macromonomers A and B of equal polymerization degree ($N_A = N_B = N$) taken in equal amounts and separated by a flat interface parallel to the *xy* plane. Periodic boundary conditions along all axes were imposed. Alternatively, impenetrable walls made of particles similar to the particles of an adjacent melt were used in the *z* direction. In both cases the same reaction kinetics was observed provided the difference in the interfacial area was taken into account.

Simulations were carried out in boxes of different shapes containing up to 10^5 particles at the average number density $\rho_0 = 3$. At short times ($t = 10^{-1} \div 10^3$) the best statistics were obtained for a slab of sizes $l_x \times l_y \times l_z = 50 \times 50 \times 20$ (in r_c units) with impenetrable walls perpendicular to the *z* axis. This can be explained by a maximum surface-to-volume ratio and number of elementary reactions per unit time attained in that box. In the range $t = 10^2 \div 10^4$ the most effective was a box of sizes $l_x \times l_y \times l_z = 25 \times 25 \times 50$ with periodic boundary conditions in all directions. At $t = 10^3 \div 10^5$, a rod-like box of sizes $l_x \times l_y \times l_z = 15 \times 15 \times 80$ and impenetrable walls in the *z* direction was chosen because it enabled studying the diffusion of reactants through a thick layer of the copolymer product. The last box contained 5.4×10^4 particles only and such reduction made it possible to expand the time interval for studying late stages of the process. Curves presented in the next Section were plotted using the data for a box providing the best statistics for a given time interval.

Simulations were performed for $N = 2$, 5, and 10 at the fixed repulsion parameter $a_{AB} = 50$ and for $a_{AB} = 25$, 30, 35, 40, 45, 50, 60, and 80 at the fixed macromonomer length $N = 5$. Four runs per each system were carried out starting from random initial configurations. Deviations in the kinetics for different runs never exceeded 7% at the initial stage (at a flat interface) and 3% at the late stage (after interface roughening).

It is easy to find that when *N* is varied, the product $\chi(N_A + N_B)$ takes the values of 30.6, 76.5, and 153.0, whereas increasing a_{AB} from 30 to 80 results in a wider range $\chi(N_A + N_B) = 15.3 \div 168.3$ ($a_{AB} = 25$ corresponds to an athermal and therefore compatible blend with $\chi = 0$). The lower boundary of that range corresponds to the outset of the strong segregation regime in a pure AB copolymer melt,[39] when block conformations are close to Gaussian, whereas the upper boundary lies within the superstrong segregation regime,[40] when blocks are highly stretched. In any case, blocks of the copolymer product are rather incompatible and therefore tending to form a brush at the A/B interface. According to the strong segregation theory,[39] the phase behavior of a polymer system is determined by the product χN and DPD correctly reproduces this scaling.[34] Therefore, properties of low N − high χ systems studied by simulations can be mapped onto those of high N−low χ blends usually investigated in laboratory experiments.

Chemical reactions were modeled using the probabilistic approach based on the following principles.

1. Two active centers can react (form a new bond) at a short distance only, which is called the reaction radius r_R.
2. Each pair of contacting active particles has to be considered for the possible reaction in a random order.
3. Reaction in every pair proceeds with a certain predefined probability p_R.
4. If the average number of pairs simultaneously formed by an active center equals η, then p_R value should obey the rule $\eta p_R < 1$ to prevent underestimating the reaction rate.

Similar approaches were implemented in MD,[41,42] DPD,[43] and Monte Carlo[44] simulations of polymerization.

In this work, the probability of end-coupling per unit time was chosen to be $p_R = 0.0025$, 0.025, or 0.25 for each pair of reactive particles situated within the distance $r_R = r_c = 1$. The reaction procedure was carried out every tenth integration step. First of all, pairs of reactive particles separated by distances $r \le 1$ were detected. Then, for each pair a random number λ ranging from 0 to 1 was generated and compared to p_R. At $\lambda < p_R$, the reaction took place and a new bond was irreversibly formed. If several complementary particles were closer than r_R from a given reactive particle, then the reaction was attempted with each of those particles in order of distances to them.

According to the generalized Flory principle, at a fixed reaction probability, the effective reaction rate should be the same for macromonomers of different lengths. However, our simulations demonstrated that it slowly decreases with *N*. It can be explained by displacement of reactive particles B from the surrounding of a given reactive particle A (and vice versa) by its unreactive macromonomer tail. The longer the tail is the lower is the local concentration of B particles. This effect can be quantified in terms of the parameter

$$\gamma = \frac{4\pi}{V_R}\int_0^{r_R} r^2 g(r)\, dr < 1 \qquad (8)$$

where $g(r)$ is the AB pair correlation function and integration is performed over the reaction radius r_R, $V_R = 4\pi r_R^3/3$. By definition, γ is a ratio of the concentration of reactive particles B within the reaction radius of particle A and their mean bulk concentration. Considering a homogeneous end-coupling of two miscible macromonomers, we found $\gamma = 0.9023$, 0.8778, and 0.8751 for $N = 2$, 5, and 10, respectively, i.e., the apparent reactivity slowly decreases with the tail size resulting in the 3% difference between the longest and shortest chains. A similar effect is expected for the reaction at a polymer/polymer interface. In the present simulation, it is neglected but should be taken into account when reactions in highly polydisperse or branched systems, such as radical polymerization or network formation, are modeled.

The relation between DPD time and real time can be roughly found as follows. Consider a homogeneous coupling between reactants A and B of densities ρ_A and ρ_B, which obeys the second-order kinetics:

$$\frac{\partial \rho_A}{\partial t} = -k\rho_A\rho_B \qquad (9)$$

The characteristic time of this reaction is $\tau_h = 1/(k\rho_B^0)$, where ρ_B^0 is the initial value of ρ_B. For our DPD model, $k = \gamma V_R p_R \approx 4\pi p_R/3$, $\rho_B^0 = \rho_0/N_B = 3/N$ so that $\tau_h \approx N/(4\pi p_R)$ is varied from 0.6 for $N = 2$ and $p_R = 0.25$ to 3×10^2 for $N = 10$ and $p_R = 0.0025$. The corresponding experimental value of τ_h can also range in wide limits for reacting groups of different chemical nature. For example, $k \approx 10^2$ kg/(mol·min) at 180 °C was reported[45] for aliphatic amine and anhydride attached to the ends of PMMA chains. The reaction rate was limited by the amine initial concentration of $\rho_B^0 = 3.5$ mmol/kg, which yields $\tau_h \approx 1.7 \times 10^2$ s. Therefore, the unit time for our slowest DPD simulation is equivalent to 0.57 s in the mentioned experiment.

The same reacting groups were used for studying an interfacial reaction between PS (18 kg/mol) and PMMA (23 kg/mol) layers at 175 °C.[26] After 10 min, which corresponds to ca. 10^3 units of

DPD time, a significant interface roughening was detected. In order to study late stages of the reaction, longer runs are needed so the simulations in this work were carried out up to 10^5 DPD time units.

As there are two dynamic processes in the modeled system, that is, chemical reaction and diffusion, it is instructive to compare their rates. Consider an initial bilayer melt of end-functionalized macromonomers A and B of densities $\rho_A^0 = \rho_B^0 = \rho_0/N$. The local reaction time for two contacting particles A and B is $\tau_R \approx 1/p_R$. Coupling takes place within an interfacial layer, the width h of which depends on the degree of macromonomer incompatibility. The interfacial area per reacting pair is $s = N/(2h\rho_0)$, where it is taken that the end-group concentration at the interface is twice as high as in the bulk.[46] The time necessary for a particle to explore this area by diffusion equals $s/(4D) = N/(8Dh\rho_0)$ and, since both types of reactive particles are mobile, the local diffusion time reads $\tau_d = N/(16Dh\rho_0)$, where D is the macromonomer diffusivity. The ratio $\tau_d/\tau_R = p_R N/(16Dh\rho_0)$ determines, whether the reaction is kinetically ($\tau_d/\tau_R \ll 1$) or diffusion ($\tau_d/\tau_R \gg 1$) controlled. Taking that $h \approx 1$, $\rho_0 = 3$, and $D = 0.16273$, 0.063909, and 0.03151 for $N = 2$, 5, and 10, respectively,[47] we estimate that for our model systems $6.4 \times 10^{-4} \le \tau_d/\tau_R \le 1.7$, i.e., a diffusion control is not expected. The lowest value of τ_d/τ_R ratio is consistent with the experimental data,[48] whereas in the previous simulations,[12−16] where particles reacted immediately after contact ($p_R = 1$), the role of diffusion was markedly overestimated.

It is known that the viscosity of DPD liquids is very low and this problem can be alleviated by using the Lowe−Anderson thermostat[49] as an alternative to eq 4. However, the above estimates allow concluding that it is hardly applicable in our case because higher viscosity would lead to decreasing the diffusion rate and hence emerging diffusion controlled regimes outlying most of the experimental observations.

Results and Discussion

Mean Field Linear Kinetics. The initial kinetics of end-coupling at a polymer/polymer interface approximately obeys the second-order mean field law[7,8]

$$\frac{dn}{dt} \approx k_0 \rho_A^0 \rho_B^0 \qquad (10)$$

where n is the copolymer coverage assuming a flat interface (the number of copolymer chains per unit area of the xy face of the simulation box), ρ_A^0 and ρ_B^0 are the initial bulk densities of reactive end groups, and k_0 is the reaction rate constant ($k_0 \sim p_R$). Since all macromonomers are of the same polymerization degree $N_A = N_B = N$ and functionalized with one reactive group, then $\rho_A^0 = \rho_B^0 = \rho_0/N$, where ρ_0 is the total particle density, which is assumed to be constant for a DPD liquid.

Neglecting the decay of reactants on a short time scale, we integrate eq 10 and get a linear dependence of n on time:

$$n = K \frac{p_R}{N^2} t, \quad K = \text{const} \qquad (11)$$

Corresponding renormalization of the time scale gives a universal $n(t)$ dependence for the earliest stage of the reaction (Figure 1). Coincidence of the kinetic curves for different values of N and p_R corroborates that the chosen range of end-coupling probabilities indeed corresponds to the mean field regime.

Formation of the Copolymer Layer. As is seen from Figure 1, the linear stage is over at $tp_R/N^2 \approx 0.03$. According to the theoretical analysis by O'Shaughnessy and Vavylonis,[10] the model parameters chosen for our simulation (low reactivity, complete functionalization of macromonomers, equal polymerization degree) make it possible to avoid DC kinetics

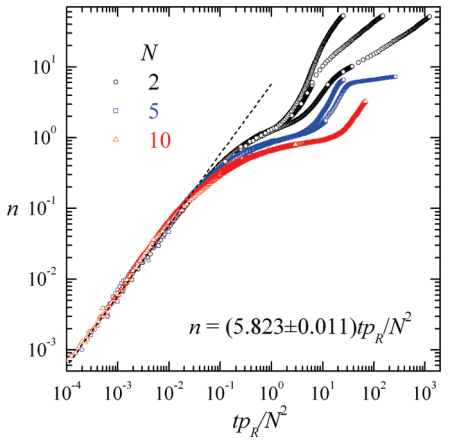

Figure 1. End-coupling kinetics: the dependence of the copolymer interfacial coverage n on scaled time. Curves are plotted for $N_A = N_B = N = 2, 5, 10$, $p_R = 0.25, 0.025, 0.0025$. The repulsion parameter $a_{AB} = 50$ in all the cases. The linear fit at the initial stage according to eq 11 is shown by the dashed line.

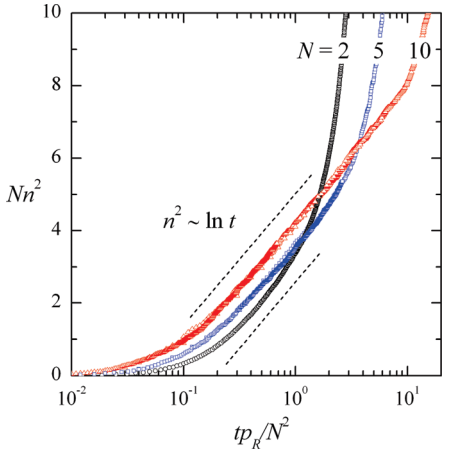

Figure 2. Saturation stage of end-coupling. Simulation curves and parameters are as in Figure 1. The slope of the logarithmic fit $n \sim (\ln t)^{1/2}$ is shown by dashed lines.

so that the linear regime is followed by the saturation regime when the reaction rate is slowed down due to adsorption of the copolymer product at the interface.

It is demonstrated in Figure 2 that there exists a range when the kinetic curves for $N = 5$ and 10 indeed obey the logarithmic dependence

$$n(t) \sim n_{cr} \sqrt{\ln((N^{1/2}t)/(\tau_1 \ln N))}$$

predicted by Fredrickson and Milner[9] using the brush model for an adsorbed copolymer. The duration of the saturation regime increases with the chain length because brushes of longer chains create higher thermodynamic barrier for the reactants. This effect is clearly seen in Figure 1, where nonlinearity of the curves is revealed earlier with increasing N. Termination of the regime is steeper also for longer chains. The logarithmic dependence is almost unobservable at $N = 2$ as a brush hardly can be formed by chains consisting of four units.

As in Figure 1, the curves for different reaction probabilities are coincide in Figure 2 indicating that the kinetics stays reaction controlled at least up to the end of the saturation regime.

Notwithstanding the adsorption layer suppresses end-coupling, the reaction continues and new portions of the product are

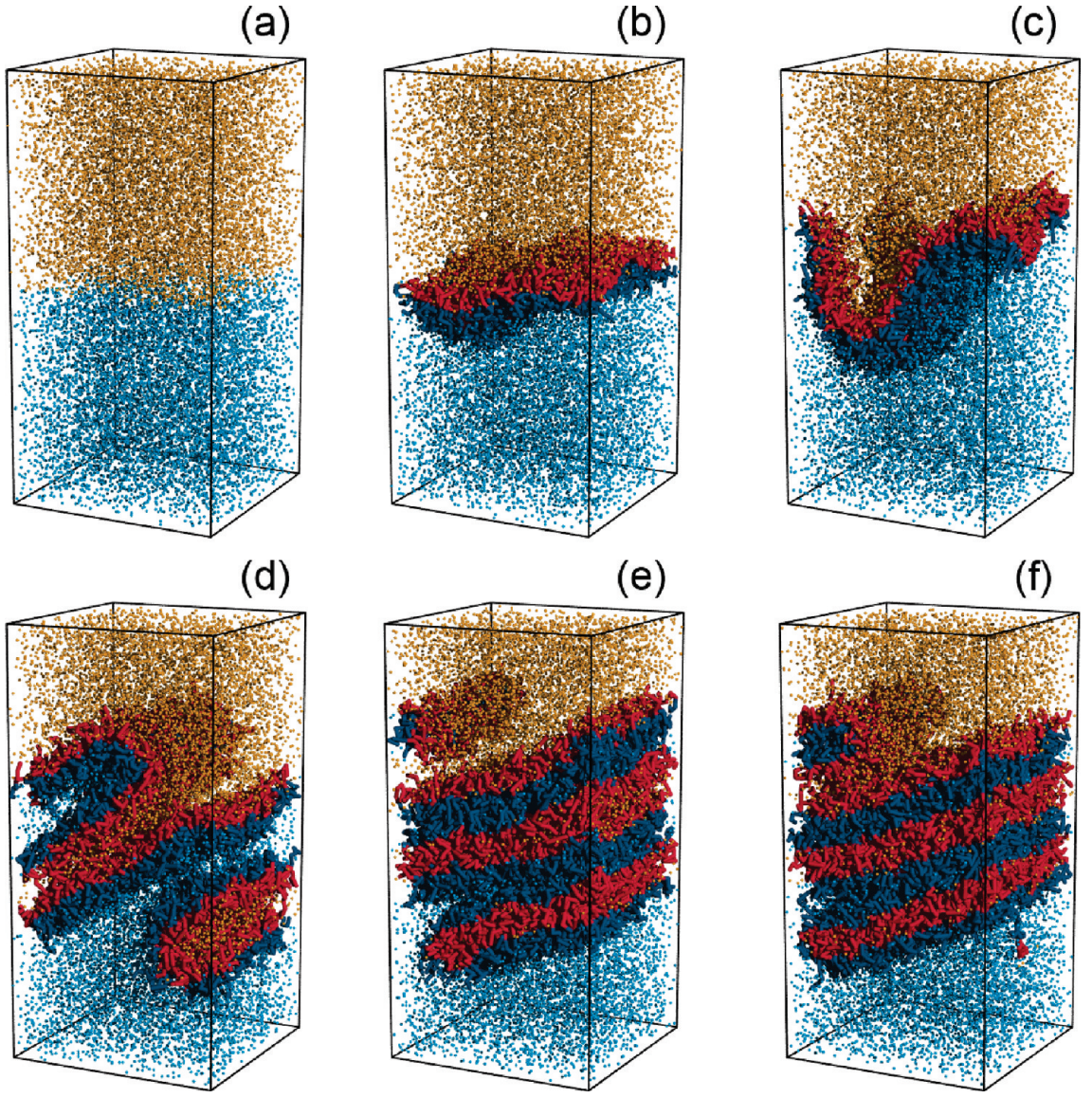

Figure 3. Snapshots of the reacting blend in the box of sizes 25 × 25 × 50 with impenetrable walls. Shown are active ends of the macromonomers (A groups in orange; B ones in light blue) and copolymer chains (A particles in red; B ones in dark blue): the initial system (a), saturated layer at $t = 400$ (b), and perturbed interface at $t = 1000$ (c), forming a lamellar microstructure at $t = 2000$ (d), 3000 (e), and 4000 (f). $p_R = 0.25$, $N = 5$, and $a_{AB} = 50$.

formed at the interface. According to experimental observations[18,20,25,26,28,29] and simulations[12,16] this can lead to an interfacial instability. Such behavior is reproduced in our simulations as well. Each kinetic curve in Figure 1 demonstrates an inflection point at a certain time t_s, which is called a saturation time marking the end of the corresponding regime.

The main questions are why and when does the instability arise, and what governs the reaction kinetics at later stages.

Interfacial Instability in the Reacting Blend. Figure 3 clearly demonstrates a buildup of lamellar microstructure after the flat interface becomes unstable.

The emerging microstructure, which is formed by diblock copolymer chains, strikingly resembles the result of a microphase separation. Based on these observations, we put forward a hypothesis that the interface roughening can be interpreted as a response of the growing diblock copolymer layer, when its density attains a maximum value corresponding to the equilibrium density of chains in lamellas formed by a pure copolymer melt, c_∞.

In order to calculate c_∞, we modeled by DPD the microphase separation in a melt of pure AB copolymer having the same characteristics as the copolymer formed by end-coupling (see Appendix A).

The interfacial copolymer coverage for a reacting bilayer system, n, which is calculated by dividing the number of copolymer molecules by the xy face area of the simulation box, S_{xy}, does not coincide with the interfacial density because even the initial interface between homopolymers is not perfectly flat. Its area S_0 found by applying the triangulation procedure[50] (see Appendix B) and dividing the resulting area by S_{xy} is given in Table 1 for the fixed block length $N = 5$ and repulsion parameter a_{AB} varying in the range 30÷80. It is seen that S_0 naturally decreases with growing incompatibility of the blend components. At $a_{AB} = 25$ the blend is compatible and no A/B interface exists.

Thus, the true copolymer density at the unperturbed interface is n/S_0 and it should be compared to the density of pure copolymer in lamellas c_∞ from Table A2. We calculated $n^* = c_\infty S_0$ and marked these values on the kinetic curves $n(t)$ in Figure 4.

It is seen that in all cases they are indeed close to the inflection points so that c_∞ well approximates the maximum

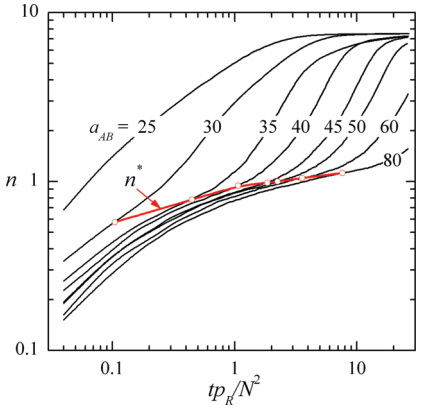

Figure 4. Copolymer interfacial coverage n vs scaled time for different values of the repulsion parameter a_{AB}, $p_R = 0.025$, $N = 5$. The red curve is drawn through the points that correspond to the interfacial coverage for a pure copolymer melt forming lamellas under the same conditions.

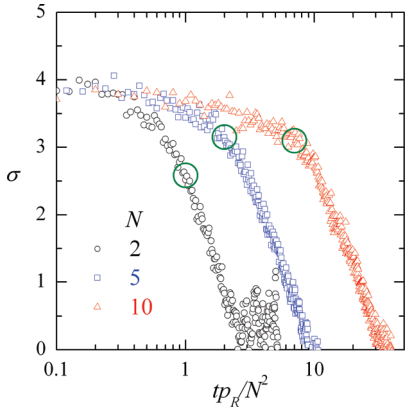

Figure 5. The dependence of the interfacial tension on scaled time for different block lengths at $a_{AB} = 50$. Large circle on each curve corresponds to the saturation time $t = t_s$, when $n = n^*$ is attained.

Table 1. Interfacial Area in the Melt of Incompatible Homopolymers A and B ($N_A = N_B = 5$)

a_{AB}	30	35	40	45	50	60	80
S_0	1.6169	1.2819	1.2495	1.2219	1.1814	1.1661	1.1331

copolymer interfacial density reached in the saturation regime. In other words, $n^* \approx n(t_s)$. Growth of n^* with a_{AB} can be explained by increasing the equilibrium domain width due to the stretching of copolymer chains, however, the dependence appears to be rather weak, in accordance with the strong segregation theory prediction $d \sim \chi^{1/6}$.[39] The characteristic saturation time t_s is much more sensitive to the blend incompatibility. As is seen from Figure 4, retardation of the kinetics is mostly pronounced at the end of the saturation regime so that forming a slightly denser layer (compare the curves for $a_{AB} = 30$ and 80) requires up to 2 orders of magnitude more time.

Thus, overcrowding the interface with the reaction product may be called the main reason for a spontaneous interfacial instability. Roughening and subsequent microstructure formation should be governed by the same driving forces as microphase separation in a pure copolymer, namely, the repulsion of dissimilar blocks, excluded volume interactions of blocks of one type and their conformational entropy.

It is interesting to compare the characteristic time of a microstructure formation in the diblock copolymer melt ($t_{1/2}$ from Table A1) and the interface saturation time t_s for the reacting blend. For $N = 10$ the saturated copolymer layer is formed at $t_s p_R/N^2 \cong 7$ that corresponds to a span $t_s = (2.8 \div 280) \cdot 10^3$ (depending on p_R), which is much larger than $t_{1/2} \approx 470$ (Table A1). At $N = 5$ we have $t_s p_R/N^2 \cong 2$, $t_s = 200 \div 20000$, $t_{1/2} \approx 380$ so that for the fastest reaction t_s and $t_{1/2}$ become comparable. For $N = 2$, $t_s p_R/N^2 \cong 1$ and $t_s = 16 \div 1600$, $t_{1/2} \approx 160$ and only at the highest reaction rate the rule $t_s \geq t_{1/2}$ is violated. Thus, for most of the modeled reacting systems, the saturated copolymer layer should be in a quasi-equilibrium state with respect to microphase separation. If the reaction were stopped, the instant spatial structure would not change. This statement was directly verified by simulations and appeared to be true.

In the previous studies,[12,16,20] the genesis of interfacial instability during reactive compatibilization was related to a drop in the interfacial tension. This macroscopic characteristic is introduced by integrating the difference of normal and tangential components of the pressure tensor across the interface:[51]

$$\sigma = \int_0^{l_z} (p_n(z) - p_t(z))\, dz \qquad (12)$$

Unfortunately, there is no unambiguous way to compute the normal (p_n) and tangential (p_t) components of the pressure tensor for a heterogeneous mixture. If, however, there is a flat interface in the modeled system, then the Kirkwood−Buff convention[52] may be used. The simulation box is divided into equal layers parallel to the xy plane and the local components of the pressure tensor are calculated:

$$p_n(z) = \rho_0(z) + \frac{1}{V}\left\langle \sum_{i \neq j}^{(k)} \frac{z_{ij}^2}{r_{ij}} F_{ij}^C \right\rangle,$$

$$p_t(z) = \rho_0(z) + \frac{1}{2V}\left\langle \sum_{i \neq j}^{(k)} \frac{x_{ij}^2 + y_{ij}^2}{r_{ij}} F_{ij}^C \right\rangle, \qquad (13)$$

$$F_{ij}^C = \begin{cases} a_{ij}(1 - r_{ij}) + K_{ij} r_{ij}, & r_{ij} < r_c \\ K_{ij} r_{ij}, & r_{ij} \geq r_c \end{cases}$$

Here ρ_0 is the average particle density in a slab with coordinate z, V is the layer volume, F_{ij}^C is the conservative repulsion force acting between i and j particles separated by the distance r_{ij}. The summation runs over all pairs of particles within a given slab.

The dependence of the interfacial tension σ on simulation time is shown in Figure 5. The tension is moderately decreased during the saturation regime but it remains clearly positive at $t = t_s$ when a critical amount of the copolymer product $n = n^*$ is attained and the interfacial instability begins to develop. Therefore, in our simulations the vanishing interfacial tension is not a prerequisite for the blend emulsification. Since the interfacial energy is far from zero, thermal fluctuations are not expected to considerably contribute to the development of interfacial instability, contrary to the conclusions of ref 16.

The subsequent steeper drop in σ observed in Figure 5 is related to deformations of the interface. However, a quantitative interpretation of data for the region where the interfacial tension is close to zero is hardly possible because multiple interfaces of a forming lamellar microstructure are not necessarily oriented perpendicular to the z axis, and therefore, eq 12 becomes inapplicable. Similar methodological difficulties were mentioned earlier in the literature.[13]

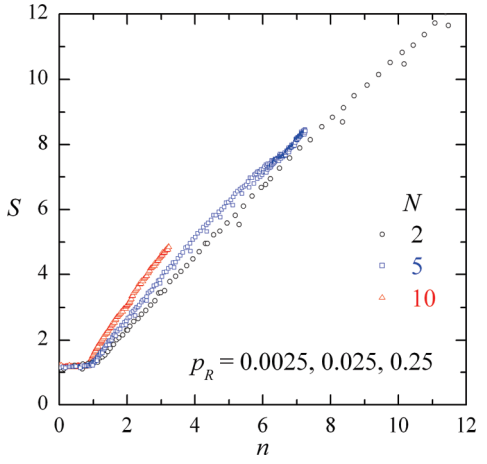

Figure 6. The total interfacial area vs the number of copolymer molecules formed by end-coupling (both divided by the *xy* face area of the simulation box) at $a_{AB} = 50$. The data for $p_R = 0.25$, 0.025, and 0.0025 almost coincide at a fixed N.

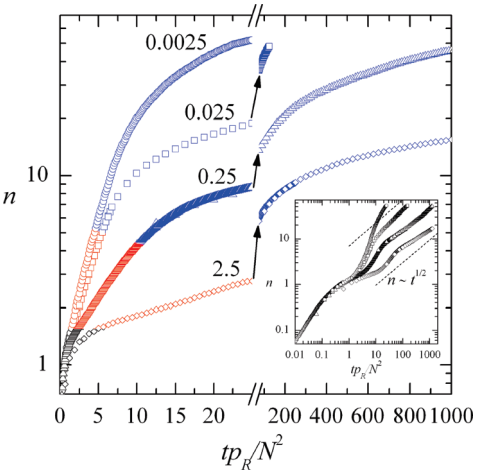

Figure 7. End-coupling kinetics at the late stage for $N_A = 2$, $a_{AB} = 50$ and different reaction probabilities p_R. Curve parts corresponding to the autocatalytic and terminal regimes are shown in red and blue, respectively. In the inset, the same curves are plotted in bilogarithmic coordinates to compare their terminal parts with the dashed lines corresponding to the pure DC kinetics ($n \sim t^{1/2}$).

Our findings correlate with the results of studies on compatibilizing polymer blends with premade copolymer additives. For a blend of PS and PMMA, it was argued[53,54] that the stability of a dispersed phase, especially under blending conditions, could be provided by a small (several wt %) amount of copolymer, which did not cause a significant reduction in the interfacial tension. Steric interactions of diblock copolymer shells covering droplet phase particles and hindering their coalescence were proposed as the main mechanism of stabilization.

Late Stage Kinetics. The interfacial density c_∞, which is attained just before the instability manifests itself, is kept nearly constant during its development. This is demonstrated in Figure 6, where the dependence of the total interfacial area on the amount of copolymer product is plotted up to the end of simulation. As long as the single flat A/B interface is retained (for $n \leq 1$), its area does not deviate much from the initial value S_0. However, later the interfacial area grows almost linearly with the copolymer amount so that the ratio n/S, which is nothing else but the interfacial copolymer density, remains approximately equal to $n^*/S_0 = c_\infty$. It is worth noting that c_∞, calculated as the thermodynamically equilibrium value for a pure copolymer melt, has the same meaning for the reacting system because it is almost independent of the reaction rate p_R at a fixed block length N.

Nearly linear dependencies $S(n)$ in Figure 6 correspond to an apparent rise of the kinetic curves in Figure 1 after the inflection point ($t = t_s$). If those curves are plotted in the semilogarithmic scale of Figure 7, their linear parts are clearly visible. It means that the kinetics is exponential and the reaction proceeds in an autocatalytic regime starting at $tp_R/N^2 \cong 1$ when the copolymer interfacial coverage $n \approx 1$ so that the initial flat interface is saturated with copolymer chains.

Close correspondence between Figures 6 and 7 indicates that during the autocatalytic regime end-coupling still obeys the second-order mean field law

$$\frac{dn}{dt} = k\rho_A\rho_B \tag{14}$$

Indeed, the effective rate constant k is proportional to the instant interfacial area S, which in turn linearly increases with the copolymer amount n as it follows from Figure 6:

$$\frac{k}{k_s} \approx \frac{S}{S_0} \approx \frac{n}{n^*} \tag{15}$$

Constants in the denominator of eq 15 correspond to the instability onset at $t = t_s$, when $n = n^*$, $S = S_0$, and $k = k_s$.

If we neglect a decrease in the initial reactants ($\rho_A = \rho_B \approx \rho_0/N$), then $dn/dt \sim n$. Integrating eq 14 we obtain that the total number of copolymer molecules per unit area of the box face grows exponentially in time:

$$n = n^* \exp(k_s\rho_0(t - t_s)/(N^2n^*)) \tag{16}$$

as is observed in Figure 7 for all modeled systems.

The duration of the autocatalytic stage decreases with increasing the reaction probability p_R (note that the abscissa coordinates in Figure 7 are proportional to the product tp_R rather than t itself). It correlates with our finding that the fastest reaction for $N = 2$ leaves microphase separation of the copolymer behind its formation ($t_s \leq t_{1/2}$). In other words, in the last case copolymer chains have not enough time to set up a quasi-equilibrium lamellar structure and this results in a lower interface area and higher copolymer density thus retarding end-coupling and deteriorating mean-field kinetics described by eq 16.

In order to emphasize this effect, we modeled the system behavior at even higher reaction rate $p_R = 2.5$, when macromonomers A and B react immediately at their first contact. In that case, the earliest linear stage is not visible at all, which agrees well with the previous simulations of end-coupling,[12,13] and only the final stage of the saturation regime is reproduced. As is seen from Figure 7 and especially from its inset, the corresponding curve has an inflection point at $tp_R/N^2 \cong 5$ and the subsequent autocatalytic regime is rather short.

For chains of 10 ($N = 5$) and especially of 4 beads ($N = 2$) it is superseded by a terminal regime with slower kinetics, just as the linear regime at the early stage is followed by the saturation one. It could happen that for longer chains of 20 beads ($N = 10$) the slowdown in kinetics is not attained due to computing restrictions.

In the terminal regime, the density of unreacted end groups decreases and the role of diffusion unavoidably grows. If the kinetic curves for $N = 2$ are plotted in the double logarithmic coordinates, they become linear (see inset in Figure 7) though the slope is not precisely equal to 1/2 and depends on the reaction rate. It means that a true diffusion

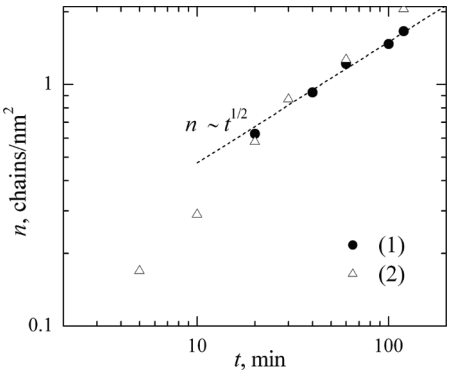

Figure 8. Coverage of an initially flat PS/PMMA interface by copolymer chains formed in situ according to the experimental data of ref 18 (1) and ref 26 (2). A dashed line shows the DC trend.

controlled regime is probably still not attained by simulations and some mixed type of kinetics is observed.

Yin et al.[18] applied SEC-UV for monitoring an end-coupling reaction in the PS/PMMA pair. Using anthracene-labeled PS chains as a probe, the authors directly measured the dependence of the copolymer interfacial coverage n on time. In the course of the reaction, the interfacial roughness sharply increased and n attained the value of ca. 1 chain per square nm of a flat interface, which is by an order larger than the equilibrium coverage n^* extracted from measurements of the lamellar spacing in a symmetric PS−*b*-PMMA copolymer of the same molecular weight (32 kg/mol). Note that the product $\chi(N_A + N_B)$ was equal to 12, which is quite close to our DPD parametrization. In a very similar research,[26] where the same macromonomers with the molecular weight of 18 kg/mol at $\chi(N_A + N_B) = 12.7$ were used, it was found by AFM that the interface roughness considerably increased after 5−10 min of annealing and afterward stayed approximately constant for 2 h. The kinetic curves obtained in refs 18 and 26 are plotted in Figure 8 in double logarithmic coordinates. It is seen that at the late stage ($t > 20$ min) the diffusion controlled kinetics ($n \sim t^{1/2}$) is asymptotically established, which is consistent with the terminal regime behavior in our simulations.

It is also worth mentioning a striking likeness of the whole kinetic curve $n(t)$ obtained in our work and the time dependence of the complex viscosity measured by Kim et al.[28] for a reacting blend of end-functional monocarboxylated PS and poly(methyl methacrylate-*ran*-glycidyl methacrylate). There is a second-order kinetics at the initial stage of the process, then retardation, and a first-order diffusion controlled regime in between (which is not observed in our case due to the high concentration of reactants). For some time, the viscosity stays constant, which corresponds to the slow reaction in a saturated copolymer layer. Later, a fast growth in conversion accompanied by a sharp increase in the interfacial roughness measured by AFM takes place,[28] similarly to our autocatalytic regime. Finally, the blend viscosity stops growing and tends to a constant value thus resembling the simulated behavior in the terminal regime.

The evolution of the interfacial morphology is visualized in Figure 9, which is similar to Figure 3 but reports on simulations with the shortest macromonomers carried out in a long narrow box, i.e., under conditions mostly suitable to follow late stages of the process. It is seen that the interface is disordered in the autocatalytic regime (at $2.5 < tp_R/N^2 < 7.5$), whereas a pronounced lamellar structure arises only in the terminal regime. Ordering starts in a "long-living" central region and gradually expands over the box volume.

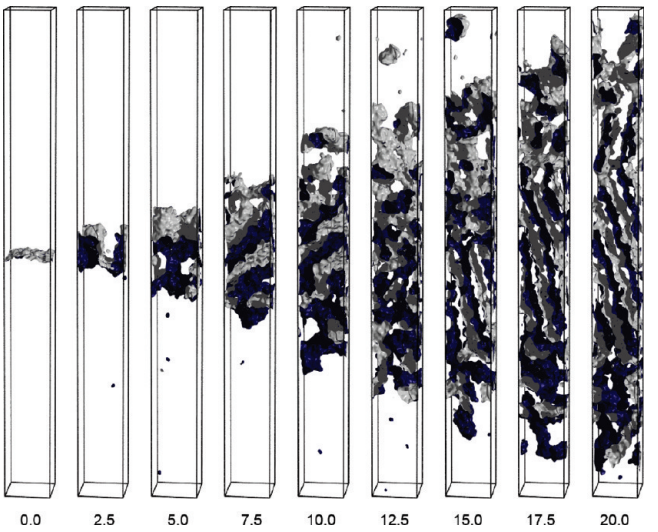

Figure 9. Interface in the reacting system ($N = 2, p_R = 0.0025, a_{AB} = 50$) at different moments of time. The values of tp_R/N^2 are shown below simulation boxes.

Very similar micrographs of partially ordered structures by TEM and AFM were obtained by Lyu et al.[25] who studied the reactive compatibilization in a bilayer system of PS end-capped with primary amine and PMMA end-capped with anhydride. It was demonstrated that the interfacial instability leads to a disordered morphology, which gradually transforms into local lamellar order.

Interestingly, in all our simulations lamellas are slanted like in Figure 9. Such orientation seems kinetically more stable when new copolymer chains are continuously formed. Initially, domains with all possible orientations of the interface appear but later some kind of a selection takes place. Lamellas that are parallel to the initial interface become unstable due to the lack of free space for their lateral growth. Quite the opposite, inclined lamellas can grow longer without realignment and therefore they survive in the course of the evolution in a reacting system. At the same time, a specific orientation of lamellar microdomains in our studies is related to the confined geometry of a simulation box rather than to real physical phenomena. Experiments[25] demonstrate that the orientation of domains is more or less arbitrary being governed by large-scale hydrodynamic fluctuations, which cannot be reproduced in a small model system.

Conclusions and Outlook

DPD modeling technique was applied for the first time to simulate *in situ* reactive compatibilization of immiscible polymer melts initially separated by a flat interface. Combining the molecular dynamics with probabilistic kinetics of an end-coupling reaction made it possible to reproduce the mean field (linear) and saturation (logarithmic) regimes at the early stage of the process, which is characterized by a low interface roughness. Such behavior is in the better agreement with experimental data than the results of preceding simulations, where too high reaction rates were used in order to observe diffusion controlled regimes, though very uncommon in laboratory experiments on macromolecular reactions.

The most attention in our work was paid to the practically interesting phenomenon of interfacial instability. Its mechanism was revealed through detailed analysis of the copolymer accumulation at different reaction rates, lengths of the initial polymers and repulsive interactions between their units. It was found that under realistic experimental conditions the interface roughening

just indicates microphase separation taking place when the interfacial copolymer density exceeds its equilibrium value. This important conclusion was supported by modeling the dynamic behavior of pure diblock copolymer melts with corresponding characteristics. It was demonstrated that the copolymer density at a newly formed interface in the reacting system is close to that in the microdomain structure of a pure copolymer melt. Thus, the interfacial instability development during reactive compatibilization is an irreversible, thermodynamically beneficial process, which however takes place only as long as the chemical reaction proceeds. As was shown, the interface roughening occurs before a substantial decrease in the interfacial tension takes place and therefore is not governed by thermal fluctuations.

It was found that after the interface distortion the reaction proceeds in an autocatalytic regime characterized by exponential kinetics, which is followed by a terminal, diffusion-controlled-like regime. It is during that experimentally observable stage the microdomain copolymer structure at first arises in the region where the initial interface was situated, then gradually expands in both directions and ripens until reactants are completely exhausted. Of course, under blending conditions the ordered regions could be also carried away by convective flows.

In this work, only lamellar microstructures were observed because of equal length and amount of modeled reactive polymers. It would be interesting to simulate reactive compatibilization in asymmetric systems, where microphase separation of the reaction product could result in different morphologies. Even more complex is the case of polydisperse melts, in which the preferential length and/or composition of a copolymer would be time dependent so that one may anticipate the formation of gradient microstructures with some characteristics depending on a distance from the initial polymer/polymer interface.

Acknowledgment. The work was supported by the Program of Fundamental Studies No. 3, Division of Chemistry and Materials Science, Russian Academy of Sciences. The authors thank Prof. P. G. Khalatur for useful discussions. They are also grateful for the opportunity to use computational cluster Chebyshev at the Moscow State University.

Appendix A. Microphase Separation in a Diblock Copolymer Melt

In this Appendix we consider the dynamics of microphase separation in a melt of pure AB diblock copolymer having the same characteristics as the copolymer formed by end-coupling. Our aim is to calculate equilibrium parameters of the microstructure and a characteristic time of its formation.

Simulations were performed in a box of sizes $30 \times 30 \times 30$ with periodic boundary conditions at the fixed repulsion parameter $a_{AB} = 50$ for $N_A = N_B = 2, 5, 10$ and at the fixed block length $N_A = N_B = 5$ for $a_{AB} = 30, 35, 40, 45, 50, 60$, and 80. In all the cases, an equilibrium lamellar microstructure was formed within 2×10^4 units of dimensionless time. Its structural characteristics were averaged over 100 configurations selected by the time step $\Delta t = 40$.

Let us introduce an order parameter

$$\theta_X = \langle \phi_{X,r_c} \rangle - \phi_X^0, \phi_X = \rho_X/\rho_0, \quad X = A, B \tag{A.1}$$

where ϕ_{X,r_c} is the volume fraction of X-particles within the cutoff distance r_c ($r_c = 1$ was taken) from a selected particle of type X, ϕ_X^0 is the mean fraction of X-particles in the system. Brackets denote averaging over the surrounding of all X-particles.

Evolution of the order parameter θ_A from a disordered initial state to the equilibrium is shown in Figure A1.

The behavior of different curves in Figure A1 cannot be described with a universal dependence. Therefore, we postulated

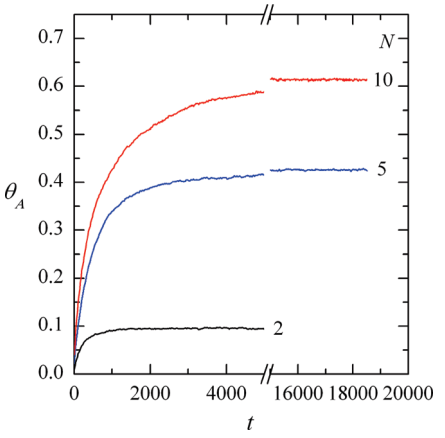

Figure A1. Time dependence of the order parameter θ_A for AB diblock copolymer melts at different block lengths N. The repulsion parameter $a_{AB} = 50$.

Table A1. Ordering in AB Diblock Copolymer Melts and Influence of the Block Length N

N	c_∞	d	$t_{1/2}$
2	1.188	1.5838 ± 0.0007	157.3
5	0.845	2.8158 ± 0.0044	380.3
10	0.630	4.1944 ± 0.0011	470.1

Table A2. Ordering in AB Diblock Copolymer Melts and Influence of the Repulsion Parameter a_{AB}

a_{AB}	χ_{AB}	c_∞	d
30	1.53	0.355 67	1.1856 ± 0.0007
35	3.06	0.608 04	2.0268 ± 0.0063
40	4.59	0.753 60	2.5120 ± 0.0081
45	6.12	0.804 31	2.6810 ± 0.0092
50	7.65	0.844 75	2.8158 ± 0.0044
60	10.71	0.897 41	2.9914 ± 0.0060
80	16.83	0.988 03	3.2934 ± 0.0101

that the characteristic time of a microstructure formation, $t_{1/2}$, satisfies the condition

$$\theta_A(t_{1/2}) = \frac{\theta_A(0) + \lim_{t \to \infty} \theta_A(t)}{2} \tag{A.2}$$

Since $\theta_A \approx 0$ in the initial state, $t_{1/2}$ is the time that is necessary to attain half of the order parameter value in the equilibrium state.

Simulation results for $t_{1/2}$, the equilibrium number density of copolymer molecules (per unit area of lamellar surface) c_∞, and the domain width d are summarized in Tables A1 and A2.

An accurate determination of c_∞ and d was possible with implementing the procedure for calculating the area of a polymer/polymer interface known as the "marching cubes" algorithm,[50] which is described in Appendix B.

Appendix B. Calculation of the Interfacial Area in a Polymer Blend

Here we briefly describe the procedure of calculating the area of a polymer/polymer interface. Let us introduce an auxiliary potential generated by particles, which may be an arbitrary function decreasing with distance and having different signs in A and B phases. In this work, the potential created at point $\mathbf{r}$ by i-th particle situated at point $\mathbf{r}_i$ is taken in a simple spring-like form:

$$\omega(\mathbf{r}, \mathbf{r}_i) = \begin{cases} \varepsilon(r_c - |\mathbf{r} - \mathbf{r}_i|)^2, & r < r_c \\ 0, & r \geq r_c \end{cases} \tag{B.1}$$

where ε_i equals 1 for particle A and -1 for particle B. It is easy to check that the net potential

$$\Omega(\mathbf{r}) = \sum_i \omega(\mathbf{r}, \mathbf{r}_i) \quad \text{(B.2)}$$

has different signs within the phases A and B.

The A/B interface is identified with a surface, where $\Omega(\mathbf{r})$ takes zero value. Its area can be calculated using the "marching cubes" cell-based triangulation scheme.[50] The simulation box is covered with a simple cubic lattice. Triangulation is performed separately for each lattice cell crossed by the interface. The values of $\Omega(\mathbf{r})$ are calculated at all lattice vertices and edges connecting the vertices with different sign of $\Omega(\mathbf{r})$ are detected. Assuming a linear dependence of the net potential along edges, one finds edge points, where $\Omega(\mathbf{r}) \approx 0$. These points belong to the interface and in each cell can be considered as vertices of a polygon. In this work, such polygons are determined "on the fly" in contrast to the original algorithm,[50] where a set of templates is used. If a polygon has more than three vertices, an extra point is added as the "center of masses" of those vertices and a perpendicular to the interface is dropped from it. The intersection point is used as a common vertex for dividing the polygon into triangles.

The "marching cubes" algorithm produces relatively small number of triangles and has high efficiency. Though the generated interface can have small topological defects,[55] its area converges with decreasing the grid size. Variations in the interface area were less than 1.0% at the grid size of $0.25r_c$, which was used in all calculations.

References and Notes

(1) *Polymer Blends*; Paul, D. R., Bucknall, C. B., Eds.; Wiley: New York, 2000; *2* Vols.; 1189 pp.
(2) Xanthos, M.; Dagli, S. S. *Polym. Eng. Sci.* **1991**, *31*, 929.
(3) Koning, C.; Van Duin, M.; Pagnoulle, C.; Jerome, R. *Prog. Polym. Sci.* **1998**, *23*, 707.
(4) Litmanovich, A. D.; Platé, N. A.; Kudryavtsev, Y. V. *Prog. Polym. Sci.* **2002**, *27*, 915.
(5) Macosko, C. W.; Jeon, H. K.; Hoye, T. R. *Prog. Polym. Sci.* **2005**, *30*, 939.
(6) Adedeji, A.; Lyu, S.; Macosko, C. W. *Macromolecules* **2001**, *34*, 8663.
(7) Fredrickson, G. H. *Phys. Rev. Lett.* **1996**, *76*, 3440.
(8) O'Shaughnessy, B.; Sawhney, U. *Phys. Rev. Lett.* **1996**, *76*, 3444.
(9) Fredrickson, G. H.; Milner, S. T. *Macromolecules* **1996**, *29*, 7386.
(10) O'Shaughnessy, B.; Vavylonis, D. *Europhys. Lett.* **1999**, *45*, 638.
(11) O'Shaughnessy, B.; Vavylonis, D. *Eur. Phys. J. E.* **2000**, *1*, 159.
(12) Yeung, Ch.; Herrmann, K. A. *Macromolecules* **2003**, *36*, 229.
(13) Müller, M. *Macromolecules* **1997**, *30*, 6353.
(14) Yang, Y.; Char, K. *Macromol. Theory Simul.* **2001**, *10*, 565.
(15) John, A.; Nagel, J.; Heinrich, G. *Macromol. Theory Simul.* **2007**, *16*, 430.
(16) Cheng, M. H.; Balazs, A. C.; Yeung, Ch.; Ginzburg, V. V. *J. Chem. Phys.* **2003**, *118*, 9044.
(17) Oyama, H. T.; Inoue, T. *Macromolecules* **2001**, *34*, 3331.
(18) Yin, Z.; Koulic, C.; Pagnoulle, C.; Jérôme, R. *Langmuir* **2003**, *19*, 453.
(19) Harton, S. E.; Stevie, F. A.; Spontak, R. J.; Koga, T.; Rafailovich, M. H.; Sokolov, J. C.; Ade, H. *Polymer* **2005**, *46*, 10173.
(20) Kim, B. J.; Kang, H.; Char, K.; Katsov, K.; Fredrickson, G. H.; Kramer, E. J. *Macromolecules* **2005**, *38*, 6106.
(21) Kim, B. J.; Fredrickson, G. H.; Kramer, E. J. *Macromolecules* **2007**, *40*, 3686.
(22) Chi, C.; Hu, Y. T.; Lips, A. *Macromolecules* **2007**, *40*, 6665.
(23) Orr, C. A.; Cernohous, J. J.; Guegan, P.; Hirao, A.; Jeon, H. K.; Macosko, C. W. *Polymer* **2001**, *42*, 8171.
(24) Oyama, H. T.; Ougizawa, T.; Inoue, T.; Weber, M.; Tamaru, K. *Macromolecules* **2001**, *34*, 7017.
(25) Lyu, S. P.; Cernohous, J. J.; Bates, F. S.; Macosko, C. W. *Macromolecules* **1999**, *32*, 106.
(26) Zhang, J.; Lodge, T. P.; Macosko, C. W. *Macromolecules* **2005**, *38*, 6586.
(27) Orr, C. A.; Adedeji, A.; Hirao, A.; Bates, F. S.; Macosko, C. W. *Macromolecules* **1997**, *30*, 1243.
(28) Kim, H. Y.; Jeong, U.; Kim, J. K. *Macromolecules* **2003**, *36*, 1594.
(29) Bhadane, P. A.; Tsou, A. H.; Cheng, J.; Favis, B. D. *Macromolecules* **2008**, *41*, 7549.
(30) Hoogerbrugge, P. J.; Koelman, J. M. V. A. *Europhys. Lett.* **1992**, *19*, 155.
(31) Koelman, J. M. V. A.; Hoogerbrugge, P. J. *Europhys. Lett.* **1993**, *21*, 363.
(32) Espanol, P.; Warren, P. B. *Europhys. Lett.* **1995**, *30*, 191.
(33) Groot, R. D.; Warren, P. B. *J. Chem. Phys.* **1997**, *107*, 4423.
(34) Groot, R. D.; Madden, T. J. *J. Chem. Phys.* **1998**, *108*, 8713.
(35) Roan, J. R.; Shakhnovich, E. *Phys. Rev. E* **1999**, *59*, 2109.
(36) Berezkin, A. V.; Khalatur, P. G.; et al., DPDChem version 1.0, http://polymer.physik.uni-ulm.de/~khalatur/exchange/DPD_Chem/index.htm.
(37) Besold, G.; Vattulainen, I.; Karttunen, M.; Polson, J. M. *Phys. Rev. E* **2000**, *62*, R7611.
(38) Karttunen, M.; Vattulainen, I.; Besold, G.; Polson, J. M. *J. Chem. Phys.* **2002**, *116*, 3968.
(39) Semenov, A. N. *Sov. Phys. JETP* **1985**, *61*, 733.
(40) Nyrkova, I. A.; Khokhlov, A. R.; Doi, M. *Macromolecules* **1993**, *26*, 3601.
(41) Akkermans, R. L. C.; Toxvaerd, S.; Briels, W. J. *J. Chem. Phys.* **1998**, *109*, 2929.
(42) Khokhlov, A. R.; Berezkin, A. V.; Khalatur, P. G. *J. Polym. Sci. A., Polym. Chem.* **2004**, *42*, 5339.
(43) Liu, H.; Qian, H. J.; Zhao, Y.; Lu, Z. Y. *J. Chem. Phys.* **2007**, *127*, 144903.
(44) Berezkin, A. V.; Solov'ev, M. A.; Khalatur, P. G.; Khokhlov, A. R. *J. Chem. Phys.* **2004**, *121*, 6011.
(45) Jeon, H. K.; Macosko, C. W.; Moon, B.; Hoye, T. R.; Yin, Z. *Macromolecules* **2004**, *37*, 2563.
(46) Zhao, W.; Zhao, X.; Rafailovich, M. H.; Sokolov, J.; Composto, R. J.; Smith, S. D.; Russell, T. P.; Dozier, W. D.; Mansfield, T.; Satkowski, M. *Macromolecules* **1993**, *26*, 561.
(47) Spenley, N. A. *Europhys. Lett.* **2000**, *49*, 534.
(48) Guégan, P.; Macosko, C. W.; Ishizone, T.; Hirao, A.; Nakahama, S. *Macromolecules* **1994**, *27*, 4993.
(49) Lowe, C. P. *Europhys. Lett.* **1999**, *47*, 145.
(50) Lorensen, W. E.; Cline, H. E. *Comput. Graphics* **1987**, *21*, 163.
(51) Walton, J. E. R. B.; Tildesley, D. J.; Rowlinson, J. S. *Mol. Phys.* **1983**, *48*, 1357.
(52) Nijmeijer, M. J. E.; Bakker, A. E.; Bruin, C.; Sikkenk, J. H. *J. Chem. Phys.* **1988**, *89*, 3789.
(53) Macosko, C. W.; Guegan, P.; Khandpur, A. K.; Nakayama, A.; Marechal, P.; Inoue, T. *Macromolecules* **1996**, *29*, 5590.
(54) Snodergaard, K.; Lyngaae-Jorgenson, J. *Polymer* **1996**, *37*, 509.
(55) Düurst, M. J. *Comput. Graphics* **1988**, *22*, 72.

122 *Macromolecules* **2011**, *44*, 122–133
DOI: 10.1021/ma101332s

Macromolecules
ARTICLE

Polymer-Grafted-Nanoparticles Nanocomposites: Dispersion, Grafted Chain Conformation, and Rheological Behavior

Chloé Chevigny,[†] Florent Dalmas,[‡] Emanuela Di Cola,[§] Didier Gigmes,[⊥] Denis Bertin,[⊥] François Boué,[†] and Jacques Jestin*[,†]

[†]*Laboratoire Léon Brillouin, CEA Saclay 91191 Gif-sur-Yvette Cedex, France,* [‡]*Institut de Chimie et des Matériaux Paris-Est, UMR 7182 CNRS/Université Paris-Est, 2-8 rue Henri Dunant 94320 Thiais, France,* [§]*ESRF 6 rue Jules Horowitz B.P. 220, 38043 Grenoble Cedex 9, France, and* [⊥]*Laboratoire Chimie Provence, UMR 6264, CNRS et Universités d'Aix-Marseille 1, 2 et 3, Site de St Jérôme, Av. Esc. Normandie-Niemen case 542, 13393 Marseille Cedex 20, France*

Received June 15, 2010; Revised Manuscript Received December 3, 2010

ABSTRACT: We investigate the dispersion mechanisms of nanocomposites made of well-defined polymer (polystyrene, PS) grafted-nanoparticles (silica) mixed with free chains of the same polymer using a combination of scattering (SAXS/USAXS) and imaging (TEM) techniques. We show that the relevant parameter of the dispersion, the grafted/free chains mass ratio R tuned with specific synthesis process, enables to manage the arrangement of the grafted nanoparticles inside the matrix either as large and compact aggregates ($R < 0.24$) or as individual nanoparticles dispersion ($R > 0.24$). From the analysis of the interparticles structure factor, we can extract the thickness of the spherical corona of grafted brushes and correlate it with the dispersion: aggregation of the particles is associated with a significant collapse of the grafted chains, in agreement with the theoretical models describing the free energy as a combination of a mixing entropy term between the free and the grafted chains and an elastic term of deformation of the grafted brushes. At fixed grafting density, the individual dispersion of particles below the theoretical limit of $R = 1$ can be observed, due to interdiffusion between the grafted and the free chains but also to processing kinetics effects, surface curvature and chains poly dispersity. Mechanical analysis of nanocomposites show the appearance of a longer relaxation time at low frequencies, more pronounced in the aggregated case even without direct connectivity between the aggregates. Correlation between the local structure and the rheological behavior suggests that the macroscopic elastic modulus of the nanocomposite could be described mainly by a short-range contribution, at the scale of the interactions between grafted particles, without significant effect of larger scale organizations.

I. Introduction

The properties of a polymer, an elastomeric matrix, can be amazingly enhanced by inclusion of hard inorganic particles. The resulting material, which makes use of both the softness of the polymer matrix and the specificities of the particles, constitutes an innovative way of designing new products for applications in mechanical, optical, fuel cells, or gas barrier engineering. Recently, more attention was focused on the size reduction of the particles down to the nanometer range, to increase the specific surface available and thus obtain improved macroscopic properties. At this scale, these properties are directly related to the local organization of the nanoparticles inside the matrix, which can present a large variety of structures: directly connected or not, from the well-dispersed case to the formation of large and compact aggregates, with intermediate structures like ramified or elongated objects. Different strategies were developed to tune and control the hierarchical structure of the particles distribution in order to tune and control the expected final properties: one can play on the initial shape using anisotropic fillers like carbon nanotubes[1] or fractal fillers,[2] or one can use an external trigger by simple control of the processing conditions,[3,4] such as for instance controlling the electrostatic repulsion[5] or a magnetic field.[6] An alternative route of tuning is to use an internal trigger: grafting chemistry to cover the particles with a corona of grafted polymer of the same nature as the matrix. Many recent studies[7] present various refined synthesis processes of well-defined grafted nanoparticles using radical-controlled polymerization (RCP), particles which can then be used as fillers by mixing with free chains of the same polymer. The resulting interactions between grafted chains and free chains from the matrix were described from a theoretical point of view for planar surfaces[8,9] as a function of two main parameters: the chain length ratio between the free and the grafted chains (expressed using the polymerization indexes N for the grafted chains and P for the free chains) and the chains grafting density. For $P \leq N$, the phase diagram exhibits a complete wetting region bound by two grafting density limits, a lower σ^* and an upper σ^{**} (defined as $P^{-1/2}$). These two limits coincide for $P = N$, namely when the free chains length is identical to that of the grafted ones, and incomplete wetting takes place. These theoretical concepts have been transferred to colloidal systems[10,11] for $P \leq N$: in this case, interparticles interactions and surface curvature have to be taken into account. For high grafting density, attractive interactions between grafted chains dominate and induce aggregation of particles.[12] For low grafting density, interparticles interactions dominate due to incomplete surface coverage and the particles can aggregate, or percolate into a continuous network. In the intermediate grafting density situation ($\sigma^* < \sigma < \sigma^{**}$), the dispersion is mainly dominated by the interactions between the grafted and the free chains, and thus by the grafted to free chain length ratio: the surface coverage is large enough to suppress the percolation but lower enough to reduce the attractions between grafted chains. The total free energy can be expressed as the sum

*Corresponding author. E-mail: jacques.jestin@cea.fr.

 Published on Web 12/14/2010 © 2010 American Chemical Society

Scheme 1

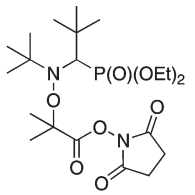

(a)

2-Methyl-2-[N-tert-butyl-N-(1-diethoxyphosphoryl-2,2-dimethylpropyl)aminoxy]-N-propionyloxysuccinimide. MAMA-NHS

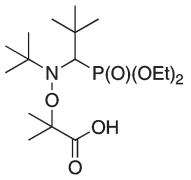

(b)

2-Methyl-2-[N-tert-butyl-N-(1-diethoxyphosphoryl-2,2-dimethylpropyl)aminoxy]-propionic acid. MAMA-SG1

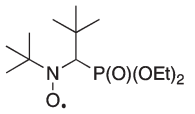

(c)

N-(2-methylpropyl)-N-(1-diethylphosphono-2,2-dimethylpropyl)-N-oxyl. SG1

of a mixing entropy term between the grafted and the free chains, and an elastic term of deformation (stretching or compression) of the grafted chains. The key parameter is then the ratio between the length of grafted chains (N) and of free chains (P), $R = N/P$. When an identical polymer is used for the free and for the grafted chains, which is our case all along this article, the ratio can then directly be expressed as $R = M_{n\ grafted}/M_{n\ matrix}$. When $R > 1$, the free chains, which are shorter, can penetrate into the grafted corona according to a favorable entropic potential and consequently swell it: the grafted chains are stretched and the brush is "wet". When $R < 1$, the mixing entropy is much lower, swelling elastic dominates, which expels free chains from the brush and changes its conformation: the grafted chains are compressed, and the brush becomes "dry". From an experimental point of view, these concepts have been studied mainly in the case of microgel systems[13−16] or for large particles[17] (micrometric scale) but less in the case of nanocomposites.[18]

The present paper first addresses the experimental validation of this theory, through the effect of R (expected to be the key parameter) on the dispersion of grafted nanoparticles inside a polymer matrix. We focus here on the specific case of $N < P$, i.e. $M_{n\ grafted} < M_{n\ matrix}$ or $R < 1$, while working at fixed intermediate grafting density. Our previous works[19,20] allowed us to develop a controlled synthesis process of well-defined polystyrene-grafted silica nanoparticles, with grafting densities around 0.2 molecules/nm^2 and varying grafted chains molecular masses between 5000 and 50 000 g/mol. We thus obtained the materials required to formulate nanocomposites filled with grafted nanoparticles, nanocomposites in which we are able to change the R parameter according to two different strategies: either by varying the mass of the free chains at constant mass of the grafted chains, or by varying the mass of the grafted chains at constant matrix mass. The second important purpose of this article is to link the dispersion of the particles with the conformation of the grafted brushes. We recently showed through a refined combination of X-rays and neutron scattering that we could directly observe the conformation of the grafted brushes inside the nanocomposite.[21] By comparison with the conformation of the grafted corona in solution, we showed a compression in the composite, a "wet" to "dry" conformational transition, which illustrates the competition between the mixing entropy of grafted and free chains and the elastic deformation of the grafted chains.

In this contribution, two main questions will then be addressed: first, the relation between the conformation of the grafted brush and the dispersion state, second the correlation between the dispersion and the macroscopic mechanical response of the material.

II. Material and Methods

1. Synthesis of the Grafted Nanoparticles. We developed our own versatile polymer-grafted nanoparticles synthesis method.[19] This method, based on nitroxide-mediated polymerization (NMP), consists of binding covalently the alkoxyamine (which acts as an initiator and controlling agent) to the silica nanoparticles surface in two steps, and then polymerize from the alkoxyamine-functionalized surface of the particles ("grafting from" method). For the grafting of the initiator, the first step is a reaction between aminopropylsilane and the silica particles in order to functionalize the particle surface with an amino group, and in a second step, the initiation-controlling alkoxyamine moiety is introduced via an overgrafting reaction between the amino group and the *N*-hydroxysuccinimide-based MAMA-SG1 activated ester (MAMA-NHS Scheme 1a). The initiator-grafted particles are then ready for the polymerization, which is performed at 120 °C, in the presence of free alkoxyamine MAMA-SG1 (Scheme 1b) (for a better control of the polymerization). To simplify both their chemical transformation and the polymerization step, the native silica particles, initially dispersed in water, are transferred to an organic solvent, dimethylacetamide (DMAc), which is also a good solvent of the polystyrene. The synthesis parameters were optimized to maximize grafting density, conversion rates, and enhance synthesis reproducibility, while keeping the colloidal stability and avoiding any aggregation of silica particles (which could be induced by the change in interparticles interaction during the synthesis). After synthesis, the final grafted objects are purified and the nongrafted polymer chains formed in the solvent washed out by ultrafiltration. The grafted particles were studied using small angle neutron scattering (SANS) coupled with a neutron contrast variation method from which we can extract a complete description of the grafted objects: number and mass of the grafted chains, number of particles. Using this first synthesis method, we synthesized two batches of particles grafted with deuterated PS chains: $M_{n\ grafted}$ = 24 000 g/mol, PDI = 1.3 and $M_{n\ grafted}$ = 24 400 g/mol, PDI = 1.27, similar chain length, polydispersity and grafting density (0.19 chains/nm^2). Alternatively to this first route, we also developed a new route[20] to obtain grafted nanoparticles with tunable grafted chain length, by replacing the free initiator in solution by the controller agent (SG1) (Scheme 1c) at the beginning of the polymerization process. This allowed us to obtain four batches of grafted nanoparticles with hydrogenated PS chains of $M_{n\ grafted}$ = 5300 g/mol, $M_{n\ grafted}$ = 19 000 g/mol, $M_{n\ grafted}$ = 32 000 g/mol, and $M_{n\ grafted}$ = 50 000 g/mol. Grafting densities are comprised between 0.15 and 0.20 chains/nm^2.

2. Preparation of Nanocomposites. The preparation of nanocomposites follows the process developed in the laboratory as described by Jouault et al.[3] The grafted nanoparticles, dispersed in the DMAc are mixed with a concentrated solution of atactic PS (10% v/v, also in DMAc), of M_n = 140 000 g/mol

(Aldrich, PDI = 2, used as received) or M_n = 98 000 g/mol (PDI = 1.7, synthesized by classical radical polymerization), at various fractions of particles ranging from 0 to 15% v/v. The mixtures are stirred (using a magnetic rod) for 2 h. They are then poured into Teflon molds (5 cm × 5 cm × 2.5 cm) and let cast in an oven at constant temperature T_{cast} = 130 °C during 1 week. This method of preparation enables us to obtain stable films whose local structure does not evolve with time. This yields dry not crystallized films of dimensions 5 cm × 5 cm × 0.1 cm (i.e., a volume of 2.5 cm^3). Disks are then cut out of the films (diameter 1 cm, thickness 1 mm) for the plate−plate oscillatory shear cell.

3. SAXS/USAXS Experiments. SAXS experiments were done at the ESRF at the high brilliance small-angle X-ray scattering beamline (ID2) using the pinhole configuration at single energy (12.46 keV) and two sample−detector distances 1.5 and 10 m covering a scattering vector Q range from 0.5 down to 0.001 $Å^{-1}$. Complementary ultrasmall X-ray (USAXS) measurements were done using the available Bonse-Hart camera allowing exploring a Q range from 0.0001 to 0.01 $Å^{-1}$.

4. Transmission Electronic Microscopy. In order to complete at larger scale the SAXS analysis of the nanocomposites structure, conventional TEM observations were also performed on the composite materials. The samples were cut at room temperature by ultramicrotomy using a Leica Ultracut UCT microtome with a diamond knife. The cutting speed was set to 0.2 mm·s^{-1}. The thin sections of about 40 nm thick were floated on deionized water and collected on a 400-mesh copper grid. Transmission electron microscopy was performed on a FEI Tecnai F20 ST microscope (field-emission gun operated at 3.8 kV extraction voltage) operating at 200 kV. Precise scans of various regions of the sample were systematically done first at small magnification, then at increasing magnification. The slabs observed were stable under the electron beam. The sample aspect was the same in every spot of every piece, and typically, 10 different slabs were observed. The pictures presented in the following are completely representative of the single aspect of the sample, which appears on average to be homogeneous.

5. Oscillatory Shear Small Deformation Tests. Shear tests, corresponding to low deformation levels (0.5%), were carried out in the dynamic mode in strain-controlled conditions with a plate−plate cell of an ARES rheometer (Rheometrics-TA) equipped with an air-pulsed oven. This thermal environment ensures a temperature control within 0.1 °C. The samples are placed between the two plates (diameter 10 mm) fixtures at high temperature (180 °C), far above the glass transition, put under slight normal stress (around 0.5 N), and temperature is decreased progressively, while gently reducing the gap to maintain a constant low normal stress under thermal retraction. The zero gap is set by contact, and the error on sample thicknesses is thus minimal and estimated to ±0.010 mm with respect to the indicated value. Slipping artifacts are noticeably reduced by this procedure, as checked by its reproducibility, and also by a sweeping in amplitude, at constant pulsation, which also makes it possible to determine the limit of the range of linear deformation. To stay below this limit, the shear amplitude is fixed to 0.5%. Samples are stabilized at the temperature for 30 min before starting measurements. The reproducibility was first tested on pure PS samples with an average of five repeated measurements, permitting an estimation of variations which is found to be of about 10%. In dynamic mode, the frequency range is from 0.5 to 100 rad/s for different temperatures (from 160 to 120 °C), and time−temperature superposition is applied. The obtained multiplicative factor can be adjusted to WLF law[22] as follows: $\log(a_T) = C_1(T_{ref} - T)/C_2 + (T - T_{ref})$, where a_T is the multiplicative factor, T_{ref} is the reference temperature of the master curve (in our case 143 °C), T is the temperature of the measurement, and C_1 and C_2 are the WLF parameters. We found C_1 = 6.19 and C_2 = 97.23 °C, which are commonly obtained values for PS.

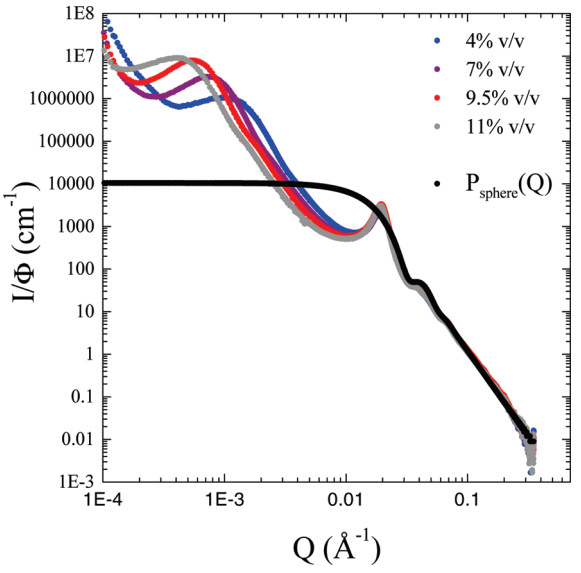

Figure 1. USAXS and SAXS scattering curves of PS nanocomposites ($M_{n\ matrix}$ = 140 000 g/mol) filled with PS grafted silica nanoparticles ($M_{n\ grafted}$ = 24 000 g/mol) corresponding to a grafted-free chain length ratio R = 0.17 as a function of the particles concentration (4, 7, 9.5 and 11% v/v). The pure matrix contribution has been subtracted and the curves have been normalized by the silica concentration. The full black line is the calculated form factor of a single particle (see text).

III. Results

1. Dispersion of the Grafted Nanoparticles in the Nanocomposite. *1.1. Varying the Mass of the Matrix Chains.* The first system we analyzed is a set of nanocomposites made of nanoparticles grafted with short chains ($M_{n\ grafted}$ = 24 000 g/mol) introduced in a matrix of longer chains ($M_{n\ matrix}$ = 140 000 g/mol), corresponding to a grafted/free chains length ratio R of 0.17. Four films containing silica volume fraction of Φ_{SiO_2} = 4, 7, 9.5, and 11% v/v were formed. The X-rays scattering, dominated by the strong contrast between the silica particles and the polymer, reveals the dispersion of the particles inside the melt without discrimination between the grafted and the free polymer chains. The corresponding scattered intensities are reported on the Figure 1a as a function of the wave vector Q. The scattering coming from the pure matrix was subtracted according to the following equation $I = I_{nanocomposite} - (1 - \Phi_{SiO_2}) \times I_{matrix}$. In the low Q region close to 10^{-4} $Å^{-1}$, we can observe a strong increase of the intensity (decreasing as a function of Q^{-3}) due to the formation of voids domains inside the composite during the film processing.[23] In the large Q region, all curves superimpose nicely indicating the good corrections by the sample thicknesses and the silica volume fractions. In this region, the intensity decreases as a function of Q^{-4}, which is a classical scattering behavior of flat surfaces in a continuous medium characteristic of silica particles. At glimpse, the scattering patterns present several features: at 4×10^{-2} $Å^{-1}$, we observe a first oscillation which is related to the form factor of the silica particles. This form factor, determined from the scattering of an aqueous dilute solution of particles,[19] can be easily modeled with the well-known sphere form factor convoluted with a log-normal dispersion of 0.14 (slight polydispersity of the silica particles) around a mean sphere radius of 134 Å (see the full black line in Figure 1a).

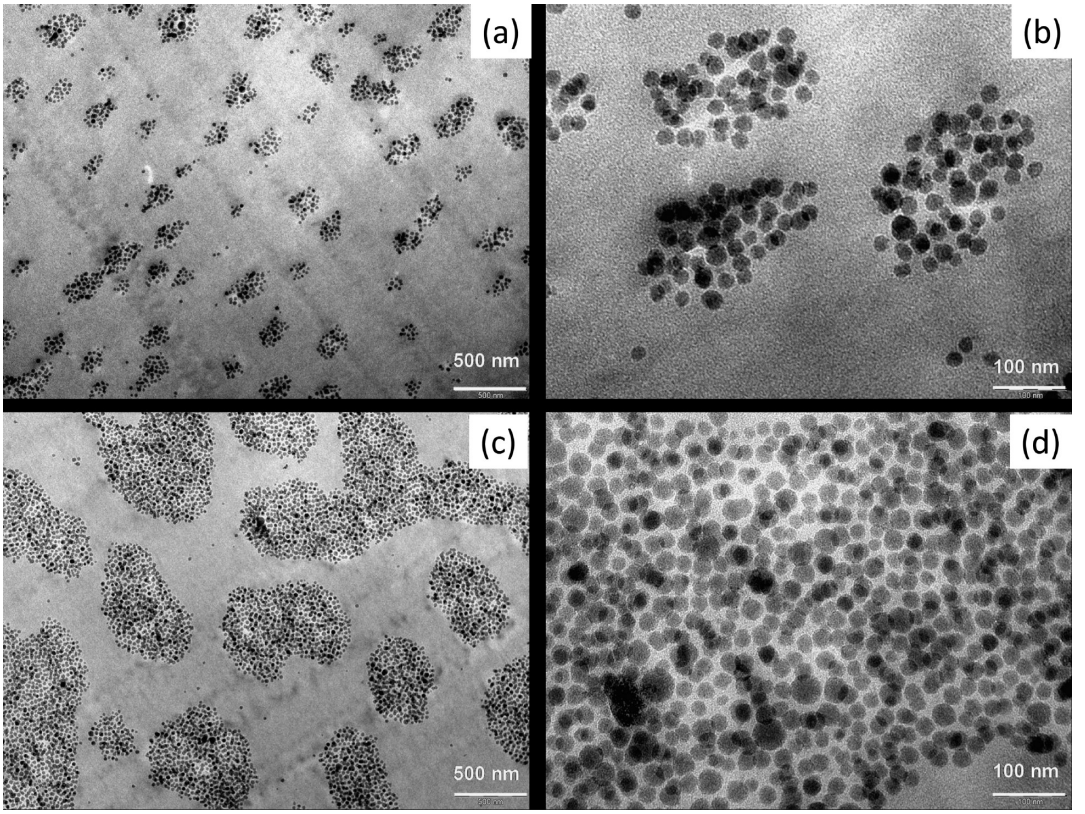

Figure 2. Transmission electronic microscopy on the nanocomposites ($M_{n\ matrix}$ = 140 000 g/mol) filled with 4% v/v of grafted silica particles ($M_{n\ grafted}$ = 24 000 g/mol) (the grafted-free chain length ratio R = 0.17) at low (a) and medium (b) magnification and filled with 11% v/v of grated particles at low (c) and medium (d) magnification.

At 2×10^{-2} Å^{-1}, we observe a strong peak whose position, noted Q^*, does not vary with the silica volume fraction. The presence of this peak and its behavior with the particle con centration is a first indication of particles aggregation inside the polymer matrix. Indeed, from the peak position, we can deduce the mean distance D between the center of masses of the particles in the real space using the relation $Q^* = 2\pi/D$. The resulting calculated distance D = 314 Å is close to the one for particles in close contact. Between $Q = 10^{-2}$ and 10^{-3} Å^{-1}, we observe a strong increase of the intensity, which indicates that we observe now objects bigger than the single particle: this confirms the aggregation of the grafted particles inside the film. Again in this range, the scattered intensity varies as Q^{-4}, meaning that at the corresponding scale, the aggregates behave as compact. Finally, between 10^{-3} and 2×10^{-4} Å^{-1}, we see a second maximum, noted here as Q^{**}, whose position and intensity change with the particles concentration: the position is shifting toward the small Q values and the intensity increases when the silica content increases. From the position of the peak, we can extract the mean distance between the center of masses of the aggregates, $D = 2\pi/Q^{**}$ equal respectively to 0.65, 0.85, 1.15, and 1.60 μm for Φ_{SiO_2} = 4, 7.5, 9, and 11% v/v. We can also estimate the number of silica particles per aggregates by assuming a cubic network: $N_{agg} = D^3\Phi_{SiO_2}/(^4/_3\pi {R_{particles}}^3)$, which gives 1000, 4200, 13100, and 40900 particles per aggregate for Φ_{SiO_2} = 4, 7.5, 9, and 11% v/v. To summarize, inside the matrix, the grafted particles of form factor $P_{particles}$ arrange in close contact according to an interparticle structure factor $S_{inter\text{-}particle}$, to form compact aggregates of form factor $P_{aggregates}$. The size of the aggregates and the distance between them, illustrated with a repulsive interaggregates structure factor $S_{inter\text{-}aggregate}$, increases with the particles content. This picture, extracted from the behavior in Q space, is nicely confirmed by direct observation in real space with the microscopy experiments (TEM) presented in Figure 2 for two particles concentrations: 4 and 11% v/v, at low (parts a and c) and high magnification (parts b and d). At low magnification and low particles content, we can observe the well-dispersed organization of small-sized aggregates of grafted particles, an organization which is preserved up to the micrometer scale. The typical sizes and interparticle distances deduced from SAXS and USAXS analysis are confirmed here and increase with Φ_{SiO_2}. The largest magnification picture confirms the evolution of the number of grafted particles per aggregates as a function of the particle content.

In a second step, we obtained and observed a different situation: we still used the same molecular mass of grafted chains ($M_{n\ grafted}$ = 24 400 g/mol), but reduced the mass of the free matrix chains ($M_{n\ matrix}$ = 98 000 g/mol), which gives a chain mass ratio R = 0.25. Four films at four particles content (Φ_{SiO_2} = 5, 9, 12 and 14% v/v), still using the same film processing conditions, are again characterized by X-rays scattering experiments (Figure 3). In the large Q domain, the intensities normalized by the particles content show the same behavior than for the previous films: the scattering is dominated by the signal of the single silica particles illustrated with the poly disperse sphere form factor calculation in full black line (R = 134 Å, $\sigma_{log\text{-}normal}$ = 0.14). On the reverse, the lower Q behavior is different: around 0.01 and 0.02 Å^{-1}, we see a correlation peak, whose intensity and position, Q^*, now varies with Φ_{SiO_2}: the intensity increases and the position is shifted toward higher Q values while increasing the particles content. However, the main difference with the previous set of data is the vanishing of the strong increase of the intensity in the low Q region (previously varying as Q^{-4}) and of the correlation peak Q^{**} between aggregates around 5×10^{-4} Å^{-1}. There is

only a slow increase of the intensity left in the low Q range, which comes from the scattering of crazes, the voids domains which form during the film processing. This is a strong indication that the particles are now individually dispersed inside the polymer matrix for this chain length ratio. This also matches

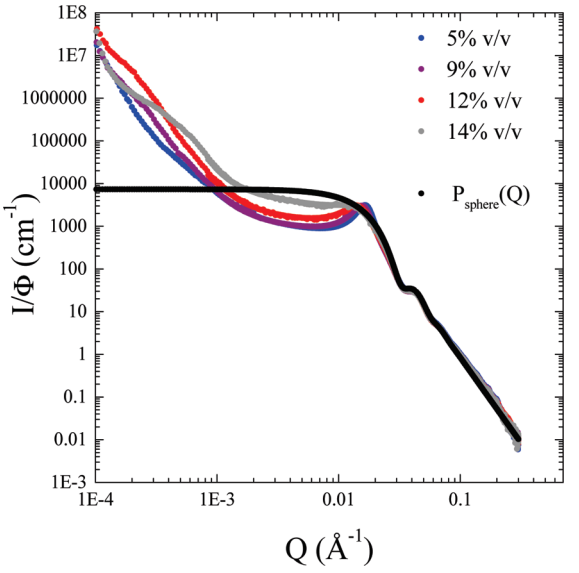

Figure 3. USAXS and SAXS scattering curves of PS nanocomposites ($M_{n\ matrix}$ = 98 000 g/mol) filled with PS grafted silica nanoparticles ($M_{n\ grafted}$ = 24 400 g/mol) corresponding to a grafted-free chain length ratio R = 0.25 as a function of the particles concentration (4, 9, 12, and 15% v/v). The pure matrix contribution has been subtracted and the curves have been normalized by the silica concentration. The full black line is the calculated form factor of a single particle (see text).

with the variation of Q^* around 0.01 and 0.02 Å^{-1} with Φ_{SiO_2}, which thus corresponds to particles coming closer when more concentrated. This Q space evidence of the grafted particles perfect dispersion inside the polymer matrix is one again nicely confirmed in the real space by TEM, in Figure 4 for two particles volume fractions, 5% and 14% v/v. From high magnification (Figure 4, parts b and d) up to lower magnification (Figure 4, parts a and c), one can see that the dispersion is homogeneous until the micrometer scale. The reduction of the interparticle distance with increase of concentration is also clearly highlighted.

1.2. Varying the Mass of the Grafted Chains. The dispersion of the grafted nanoparticles inside a polymer matrix can then be probed as a function of the grafted/free chain mass ratio with fixed free chains mass ($M_{n\ matrix}$ = 140 000 g/mol) and variable grafted chains mass. Four nanocomposite films were prepared and measured by SAXS as previously (Figure 5). The silica content is fixed at 5% v/v and the grafted/free chain length ratio is varied from R = 0.04, 0.14, 0.23, to 0.36 by the use of particles with grafted chains masses of respectively $M_{n\ grafted}$ = 5200, 19 000, 32 000, and 50 000 g/mol. In the large Q domain, all the normalized curves superimpose perfectly and the scattering is, as in both the previous cases, proportional to the form factor of single silica particles. In the intermediate Q range, we can observe a correlation peak of abscissa Q^* moving toward the small Q values while increasing the mass ratio R, indicating that the interparticles distance increases along with the grafted chains mass. Two different behaviors appear then, especially in the low Q domain: for the three lower values of R = 0.04, 0.14, and 0.23, we observe a strong increase of the scattered intensity, similar to the case of R = 0.17 in Figure 1 and characteristic of dense aggregates. Conversely, for the highest

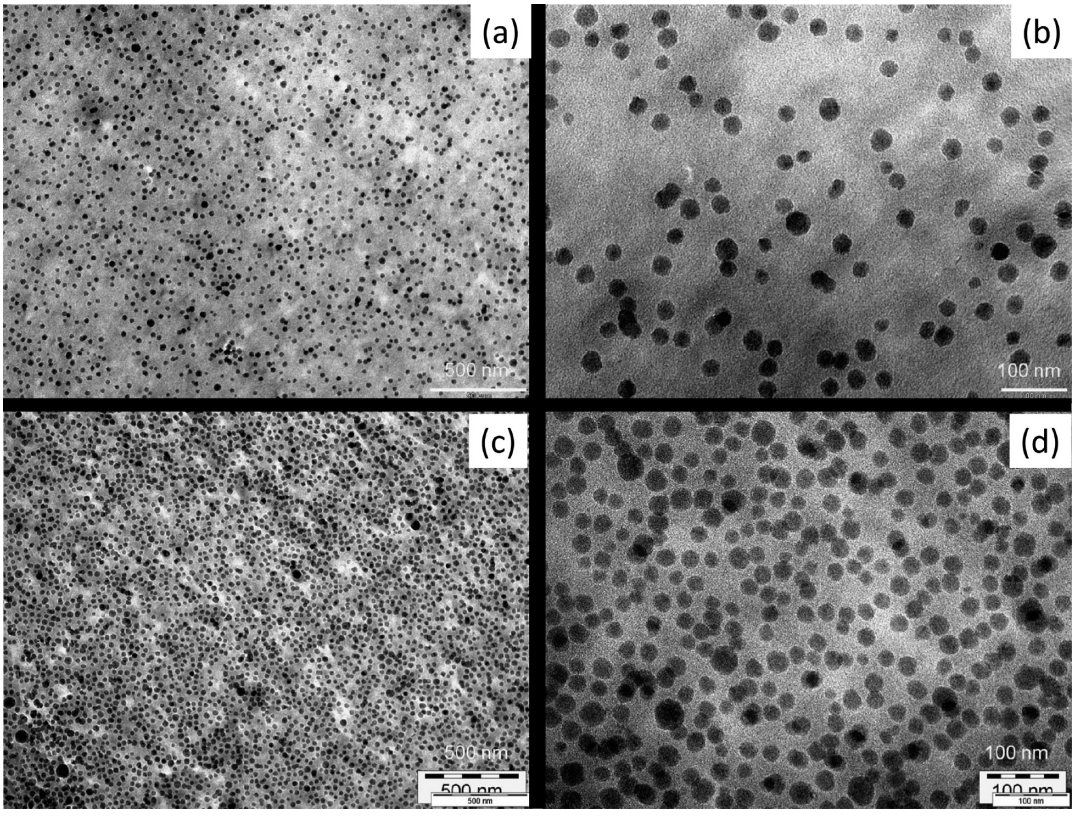

Figure 4. Transmission electronic microscopy on the nanocomposites ($M_{n\ matrix}$ = 98 000 g/mol) filled with 5% v/v of grafted silica particles ($M_{n\ grafted}$ = 24 400 g/mol) (the grafted-free chain length ratio R = 0.25) at low (a) and medium (b) magnification and filled with 14% v/v of grated particles at low (c) and medium (d) magnification.

value of $R = 0.36$, the intensity at small Q is close to a plateau, as for the case $R = 0.25$ in Figure 3, corresponding to a complete dispersion of the particles. So by varying the grafted chains mass, and thus varying the chains length ratio from $R = 0.04$ to $R = 0.36$, we are able to observe a transition:

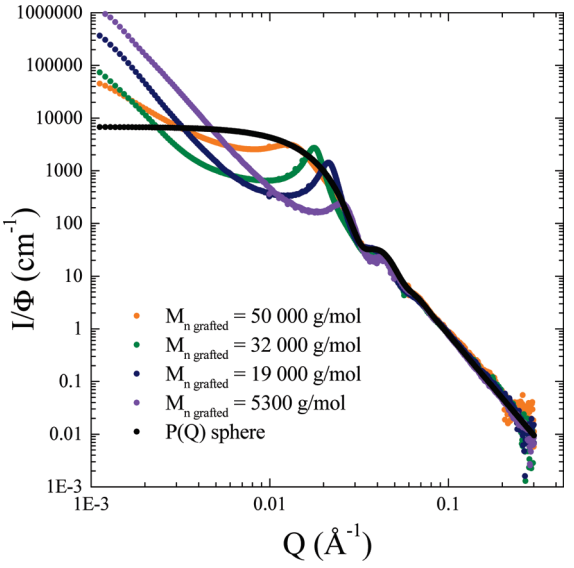

Figure 5. SAXS scattering curves of PS nanocomposites ($M_{n\ matrix}$ = 140 000 g/mol) filled with 5% v/v of PS grafted silica nanoparticles with variable grafted chain length $M_{n\ grafted}$ = 5300, 19 000, 32 000, and 50 000 g/mol corresponding to grafted-free chain length ratios $R = 0.04$, 0.14, 0.23, and 0.36. The pure matrix contribution has been subtracted and the curves have been normalized by the silica concentration. The full black line is the calculated form factor of a single particle (see text).

between the formation of dense aggregates of grafted nanoparticles for R < 0.24, and the complete dispersion of the grafted nanoparticles for $R > 0.24$. This transition is confirmed by TEM pictures shown in Figure 6, where we see directly the formation of aggregates for $R = 0.04$ (Figure 6a), $R = 0.14$ (Figure 6b), and $R = 0.23$ (Figure 6c) and a complete dispersion for $R = 0.36$ in Figure 6d. We also see distinctly that the interparticles distance increases along with the grafted chains mass.

2. Interparticles Structure Factor $S_{inter\text{-}particle}$. The combination of scattering and imaging methods showed that, whatever the way of varying the grafted over free chains mass ratio R (at constant grafted chain mass or at constant matrix mass), we observe a transition between the formation of compact aggregates of grafted nanoparticles, for $R < 0.24$, and a complete dispersion of the grafted nanoparticles inside the matrix for $R > 0.24$. We will now analyze more in details the interparticles structure factor, which can provide an indirect determination of the thickness of the polymer corona grafted around the nanoparticles. We first analyze the case described in Figure 3 and 4, i.e., $R = 0.25$, corresponding to a complete dispersion of the nanoparticles. Following the general behavior of the scattering intensity from particles:

$$I \sim \Delta\rho^2 \Phi \nu_{particle} P_{particles}(Q) S_{inter\text{-}particle}(Q) \quad (1)$$

(with $\Delta\rho^2$ as the contrast term), the interparticles structure factor can be extracted by dividing the total scattering intensity with the particle form factor:

$$S_{inter\text{-}particle}(Q) \sim I / P_{particles}(Q) \quad (2)$$

Since we measured the form factor of our silica particles, such operation can be easily done by dividing the total

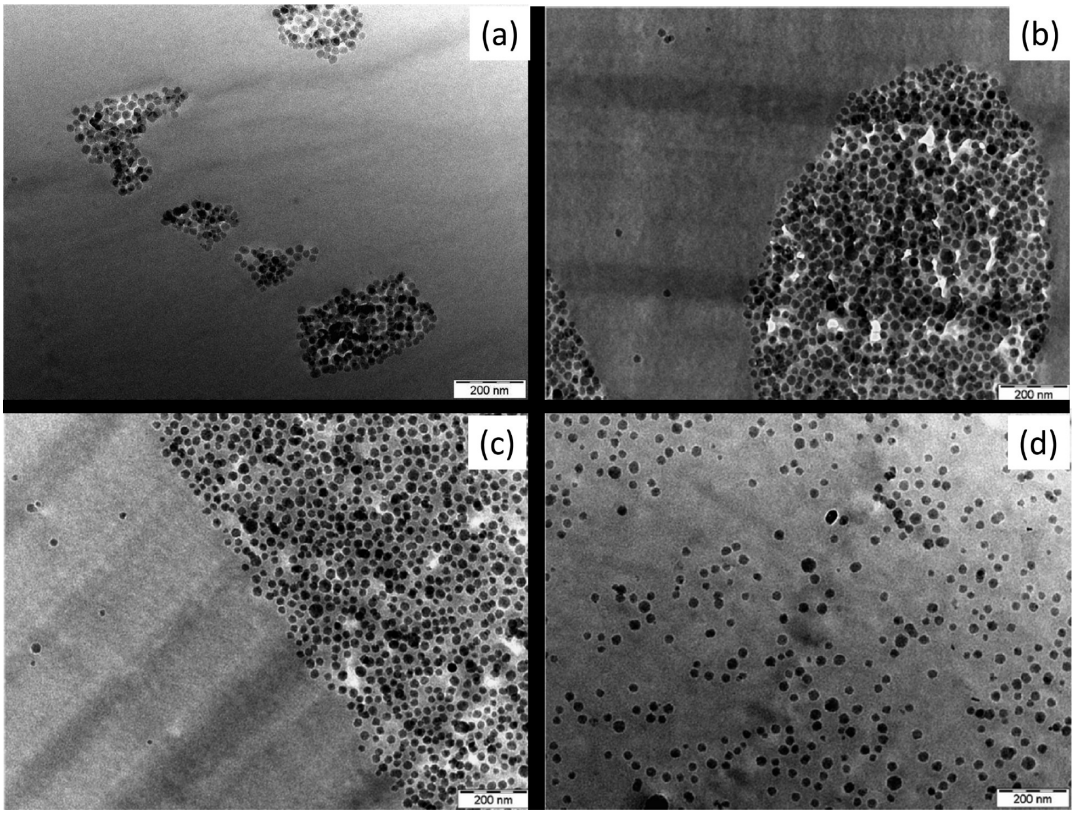

Figure 6. Transmission electronic microscopy on the nanocomposites ($M_{n\ matrix}$ = 140 000 g/mol) filled with 5% v/v of PS grafted silica nanoparticles with variable chain length $M_{n\ grafted}$ = 5300 g/mol, $R = 0.04$ (a), $M_{n\ grafted}$ = 19 000 g/mol, $R = 0.14$ (b), $M_{n\ grafted}$ = 32 000 g/mol, $R = 0.23$ (c), and $M_{n\ grafted}$ = 50 000 g/mol, $R = 0.36$ (d).

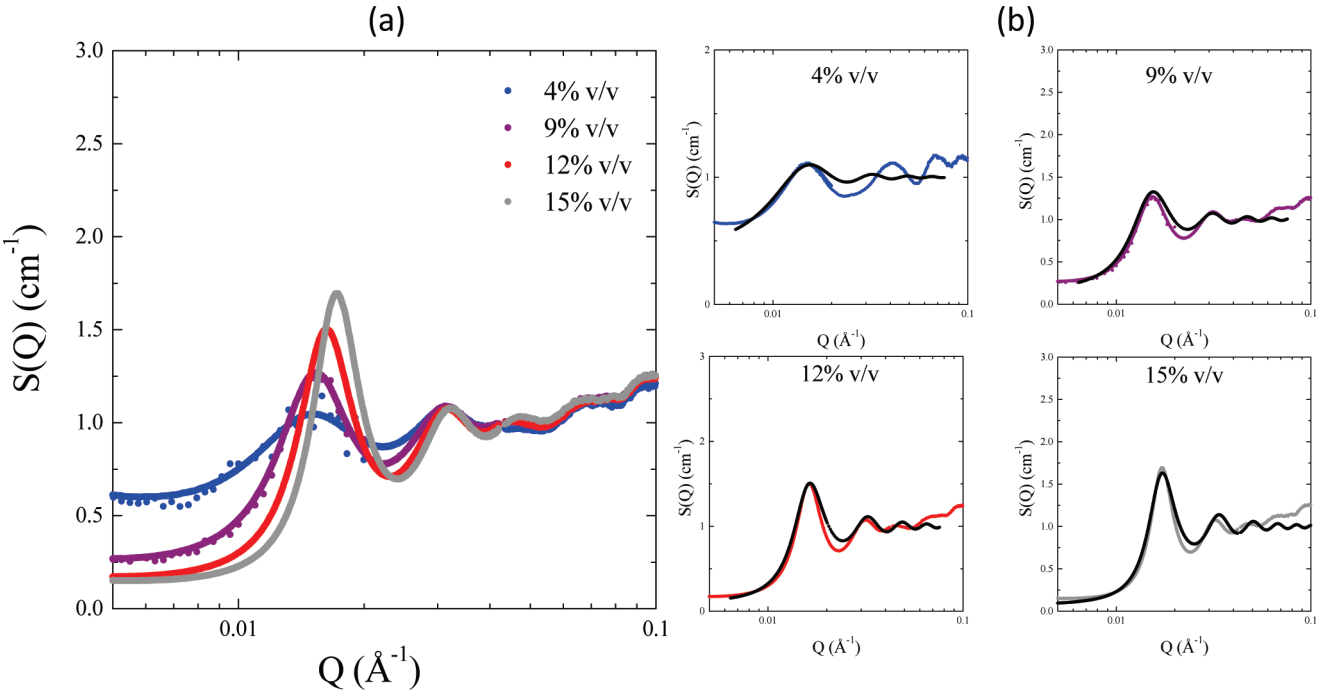

Figure 7. (a) Interparticle structure factor S(Q) deduced from the division of the total scattering intensity (Figure 3) by the silica form factor (full black line in Figure 3) for dispersed grafted nanoparticles ($M_{n\ grafted}$ = 24 400 g/mol) in a 98 000 g/mol matrix (R = 0.25) at the four particle contents. (b) Fits with the Percus−Yevick model (full black line) for each particle content.

intensity with the full black line from Figure 4 (representing the single silica particle form factor). The result is presented in Figure 7a (for silica content Φ_{SiO_2} = 4, 9, 12, and 14% v/v. While increasing Φ_{SiO_2} the peak position moves toward higher Q values and its intensity increases, indicating a decrease of the interparticles distance and (increase of the interparticles interactions). The interparticles structure factor can be modeled by the Percus−Yevick model,[24] for which an analytical solution was calculated by Wertheim, for a hard spheres system:[25] it models the interactions between noncharged hard spheres. This model mainly depends on two parameters: the volume fraction Φ_{eff} and the radius R_{eff} of the interacting particles. The best adjustments are presented in Figure 7b for all silica volume fractions. A rather good agreement is found between the experimental data and the model, even if the calculation does not take into account the polydispersity of the particles.

Knowing R_{SiO_2} from our previous solution measurements (R_{SiO_2} = 134 Å), we can extract the thickness of the grafted layer on particles, assuming the parameters of the Percus−Yevick to be related to the whole particles: polymer corona plus silica sphere. Then the R_{eff} represents the radius of a grafted particle $R_{grafted\ particle}$, and the thickness e of the corona is easily obtained by:

$$e = R_{eff} - R_{SiO_2} \tag{3}$$

The volume fraction of the grafted particles can be expressed as:

$$\Phi_{grafted\ particles} = N v_{grafted\ particles}/V \tag{4}$$

with N the number of particles and V the total volume. The silica volume fraction can be expressed as well:

$$\Phi_{SiO_2} = N v_{SiO_2}/V \tag{5}$$

Combining 4 and 5 allows expressing a *modeled* grafted particle volume fraction as a function of the silica volume fraction, the radius R_{SiO_2} of the silica particles, and the thickness e of the grafted polymer layer:

$$\Phi^{mod}{}_{grafted\ particles} = \Phi_{SiO_2}[1 + e/R_{SiO_2}]^3 \tag{6}$$

Besides, from thermo-gravimetric analysis (TGA) on the dry grafted particles, we know the mass ratio between silica and polymer and are then able to estimate an *experimental* volume fraction of grafted particles, $\Phi^{exp}{}_{grafted\ particles}$. If the approximation $R_{eff} = R_{grafted\ particles}$ is appropriate, both these $\Phi_{grafted\ particles}$ should be similar to Φ_{eff}. All the parameters useful for the fitting procedure (Φ_{SiO_2}, $\Phi^{exp}{}_{grafted\ particles}$) or deduced from it ($R_{eff}$, Φ_{eff}, e, $\Phi^{mod}{}_{grafted\ particles}$) are reported in Table 1. We find a good agreement between Φ_{eff} and $\Phi^{exp}{}_{grafted\ particles}$, which justifies the assimilation of the "interacting particles" from the Percus−Yevick model with the grafted particles. $\Phi^{mod}{}_{grafted\ particles}$ is also pretty close to both these parameters, which is one more justification of this assimilation. Besides, the effective radius of particles, and therefore the thickness of the polymer coronas as well, appear to be quite independent of the silica content

The interparticle structure factor was also derived for the chain length ratio R = 0.17 ($M_{n\ grafted}$ = 24 000 g/mol and $M_{n\ Matrix}$ = 140 000 g/mol). Here too, it is obtained by dividing the total intensities (Figure 1) by the form factor of the silica particle (full black line). The result is presented in Figure 8a for different silica contents (4, 7, 9.5, and 11% v/v). The modeling is shown in Figure 8b for each silica concentration and the fitting parameters reported in Table 2. Once more there is a good agreement between model and experiment. In this case where the grafted particles form compact aggregates inside the polymer matrix, the effective volume fraction of particle corresponds to a number of particles per aggregate and is thus very high, around 40% v/v. This value then cannot be directly expressed as a function of the number of grafted particles and compared with the volume fraction of grafted particles as for the previous well-dispersed case. However, the indirect evaluation of the thickness of the grafted corona e from the radius of particles deduced from the Percus−Yevick

Table 1. Fitting Parameters of the Inter-Particle Structure Factor by the Percus−Yevick Model for the Chain Length Ratio $R = 0.25$ as a Function of the Silica Volume Fraction (Particles Dispersed Inside the Polymer Matrix)

silica volume fraction Φ_{SiO_2} [a]	experimental grafted particles volume fraction $\Phi^{exp}_{\text{grafted particles}}$ [a]	effective volume fraction Φ_{eff} [b]	effective radius of particles R_{eff} [b]	thickness of the grafted corona e [d]	modeled grafted particles volume fraction $\Phi^{mod}_{\text{grafted particles}}$ [c]
5	14	11	189	55	14
9	26	24	198	64	29
12	36	31	195	61	37
14	42	34	187	53	38

[a] Experimental values. [b] Deduced from the fit with the Percus−Yevick model. [c] $e = R_{eff} - R_{SiO_2}$ with $R_{SiO_2} = 134$ Å. [d] Deduced from eq 6 (see text). Volume fractions are in % [v/v], lengths in Å.

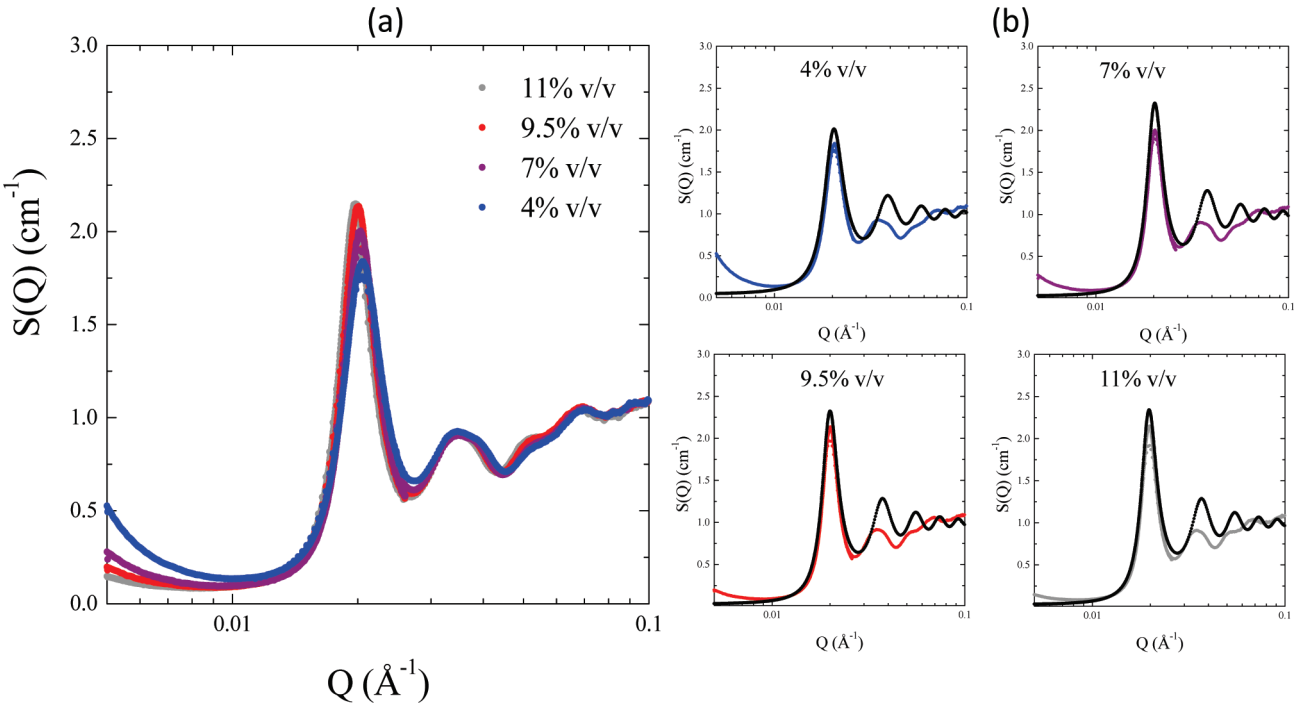

Figure 8. (a) Interparticle structure factor S(Q) deduced from the division of the total scattering intensity (Figure 1) by the silica form factor (full black line in Figure 1) for aggregated grafted nanoparticles ($M_{n\ \text{grafted}} = 24\,000$ g/mol) in a 140 000 g/mol matrix ($R = 0.17$) at the four particle contents. (b) Fits with the Percus−Yevick model (full black line) for each particle content.

fits is still valid inside an aggregate. We observe that the thickness e, still independent of the silica content, is smaller of about a factor two compared to the layer thicknesses corresponding to well-dispersed particles (Table 1): average value was then around 60 Å, and is now around 30 Å.

Finally, we analyzed the evolution of the interparticle structure factor when varying the grafted chains mass ratio R at constant matrix mass. It is again calculated by dividing the total intensities (Figure 5) with the form factor of the silica particles. The interparticles structure factors are presented in Figure 9a for $R = 0.04$, 0.14, 0.23, and 0.36. The Percus−Yevick modeling is shown in Figure 9(b) and the corresponding fitting parameters are reported in Table 3. The results correspond to the transition between the aggregation and the good dispersion of the particles previously observed when increasing the chain length ratio R. For the first three values ($R = 0.04$, 0.14, and 0.23), the high value (~40%) of the effective volume fraction of the particles deduced from the fit, reflects the particles aggregation: this Φ_{eff} is then about four times higher than the $\Phi^{exp}_{\text{grafted particles}}$ deduced from TGA. For the last value ($R = 0.36$), we find a good agreement between Φ_{eff} and $\Phi_{\text{grafted particles}}$ (both $\Phi^{exp}_{\text{grafted particles}}$ and $\Phi^{mod}_{\text{grafted particles}}$), illustrating the good dispersion of the particles. Yet independently of the dispersion state of the particles, we can still extract the thickness e of the grafted polymer layer from the radius of the particles deduced from the fit, except for the $R = 0.04$ (for which the effective radius is very close to the one of the naked silica meaning that the layer thickness is below the limit of detection of the method, which is estimated to be of the order of 10 Å).

Table 2. Fitting Parameters of the Inter-Particle Structure Factor by the Percus−Yevick Model for the Chain Length Ratio $R = 0.17$ as a Function of the Silica Volume Fraction (Particles Aggregated Inside the Polymer Matrix)

silica volume fraction Φ_{SiO_2} [a]	experimental grafted particles volume fraction $\Phi^{exp}_{\text{grafted particles}}$ [a]	effective volume fraction Φ_{eff} [b]	effective radius of particles R_{eff} [b]	thickness of the grafted corona e [c]
4	12	40.5	162	28
7.5	21	44	167	33
9	28	44	169	35
11	32	44.5	171	37

[a] Experimental values. [b] Deduced from the fit with the Percus−Yevick model. [c] $e = R_{eff} - R_{SiO_2}$ with $R_{SiO_2} = 134$ Å. Volume fractions are in % [v/v], lengths in Å.

3. Mechanical Behavior. We investigated the mechanical response of the composites for both the dispersion states described previously: complete dispersion, and large and compact aggregates. We used oscillatory shear measurements at small deformation (amplitude 0.5%) with a plate−plate rheometer ARES. The evolution of the elastic modulus G' and G'' was determined as a function of the filler content (% v/v) for the

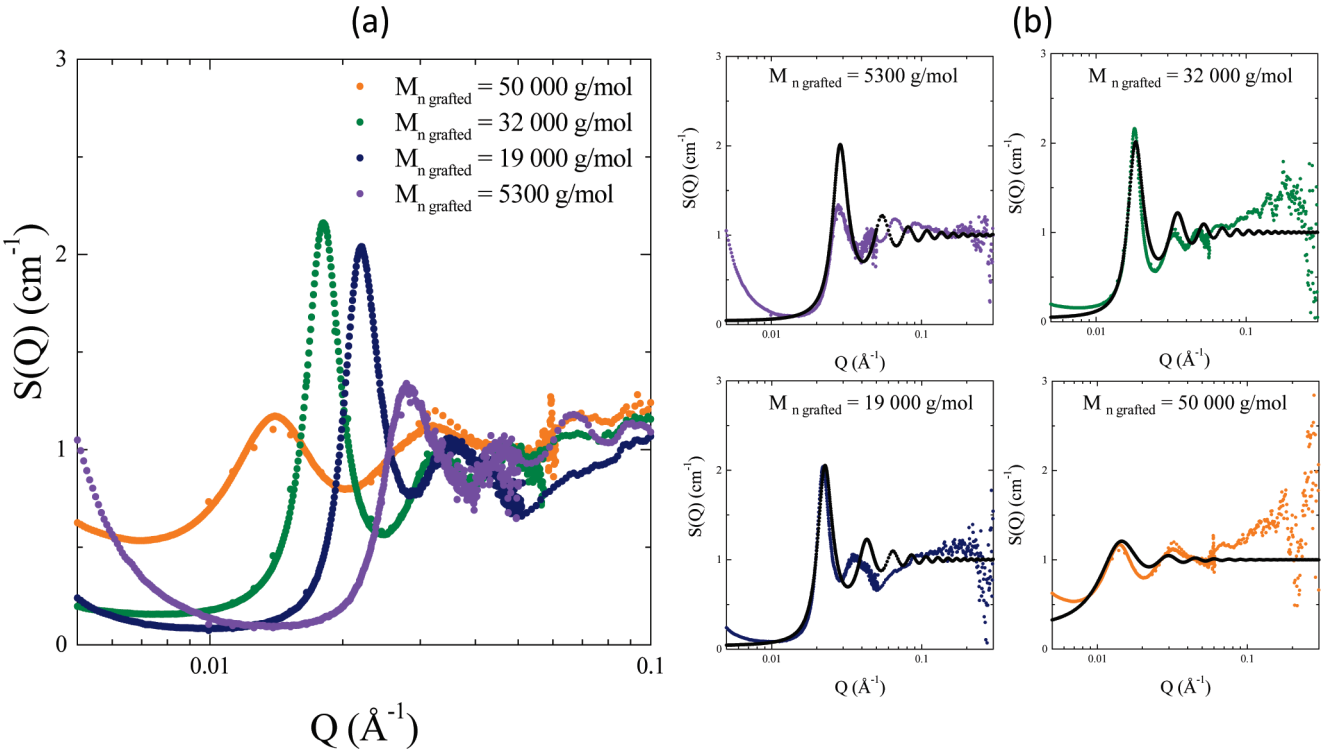

Figure 9. (a) Interparticle structure factor S(Q) deduced from the division of the total scattering intensity (Figure 5) by the silica form factor (full black line in Figure 5) as a function of the chain mass ratio R: matrix of mass $M_{n\ matrix}$ = 140 000 g/mol filled with 5% v/v of silica nanoparticles with grafted chain mass $M_{n\ grafted}$ = 5300, 19 000, 32 000 and 50 000 g/mol corresponding to R = 0.04, 0.14, 0.23 and 0.36. (b) Fits with the Percus−Yevick model (full black line) for each chain length ratio R.

Table 3. Fitting Parameters of the Inter-Particle Structure Factor by the Percus−Yevick Model at Fixed Silica Volume Fraction of 4.5% v/v for Various Chain Length Ratios R

chain length ratio R^a	experimental grafted particles volume fraction $\Phi^{exp}_{grafted\ particles}{}^a$	effective volume fraction $\Phi_{eff}{}^b$	effective radius of particles $R_{eff}{}^b$	thickness of the grafted corona e^c	modeled grafted particles volume fraction $\Phi^{mod}_{grafted\ particles}{}^d$
0.04	9	40	115		
0.14	9	41	146	12	
0.23	12	40	180	46	
0.36	17	18	207	73	17

[a] Experimental values. [b] Deduced from the fit with the Percus−Yevick model. [c] $e = R_{eff} - R_{SiO_2}$ with R_{SiO_2} = 134 Å. [d] Deduced from eq 6 (see text). Volume fractions are in % [v/v], lengths in Å.

complete dispersion, obtained with a grafted/free chain length ratio R = 0.25 ($M_{n\ grafted}$ = 24 400 g/mol, $M_{n\ matrix}$ = 98 000 g/mol) (Figure 10 (a), G' and 10 (b), G''), and for the case of dense aggregates of grafted particles, for R = 0.17 ($M_{n\ grafted}$ = 24 000 g/mol, $M_{n\ matrix}$ = 140 000 g/mol) (Figure 10 (c), G' and 10 (d), G''). The two matrices (98 000 and of 140 000 g/mol) used as references do not show significant differences as a function of the frequency, indicating that their contribution are similar for the two kinds of dispersion and will not influence the comparison of the nanocomposites. Whatever the silica content and the dispersion state, the curves (G' and G'') superimpose perfectly in the whole high frequencies range (above 0.1 rad·s^{-1}). This means that the short characteristic times (the Rouse modes) of the polymer matrix are not affected by the fillers. Conversely, in the lower frequencies domain (between 10^{-3} and 0.1 rad·s^{-1}), we observe, especially on the G', an increase of the modulus. This can be associated with the apparition of a longer time in the relaxation modes of the polymer chains, becoming longer with increasing filler content. In addition, the effect seems to be more pronounced for the aggregated case than for the dispersed one. Such a long-time effect at low frequencies can be seen as a process analogous to a liquid−solid transition inside the materials, whose origin can be interpreted in different ways. One of the main view postulates that the transition is associated with the formation of a connected network of the filler. This can be a direct connection[3,26] or a specific interaction between the particles[15,27,28] but also an indirect connection through the polymer chains. In addition, some interfacial effects can also contribute: mobility of the polymer chains at the interface with the fillers is modified because of confinement.[29,30]

IV. Discussion

We address the dispersion mechanisms of a model nanocomposite, formed by silica nanoparticles grafted with PS chains and spread inside a PS matrix, as a function of the key parameter R. Dispersion can be tuned either by coupling fixed grafted chains length ($M_{n\ grafted}$ = 24 000 g/mol) with variable free matrix chain length ($M_{n\ matrix}$ = 98 000 or $M_{n\ matrix}$ = 140 000 g/mol), or by coupling variable grafted chain length ($M_{n\ grafted}$ = 5300, 19 000, 32 000 and 50 000 g/mol) with fixed free chains length ($M_{n\ matrix}$ = 140 000 g/mol): we cover then a wide range of values from R = 0.04 up to 0.36. This specific approach allowed us to obtain a clear and unambiguous result:

When $R < 0.24$, the grafted nanoparticles organize inside the polymer matrix as dense and large aggregates, which size and distance between each other increase along with the silica content.

When $R > 0.24$, the grafted nanoparticles form a repulsive well-dispersed organization inside the polymer matrix: while

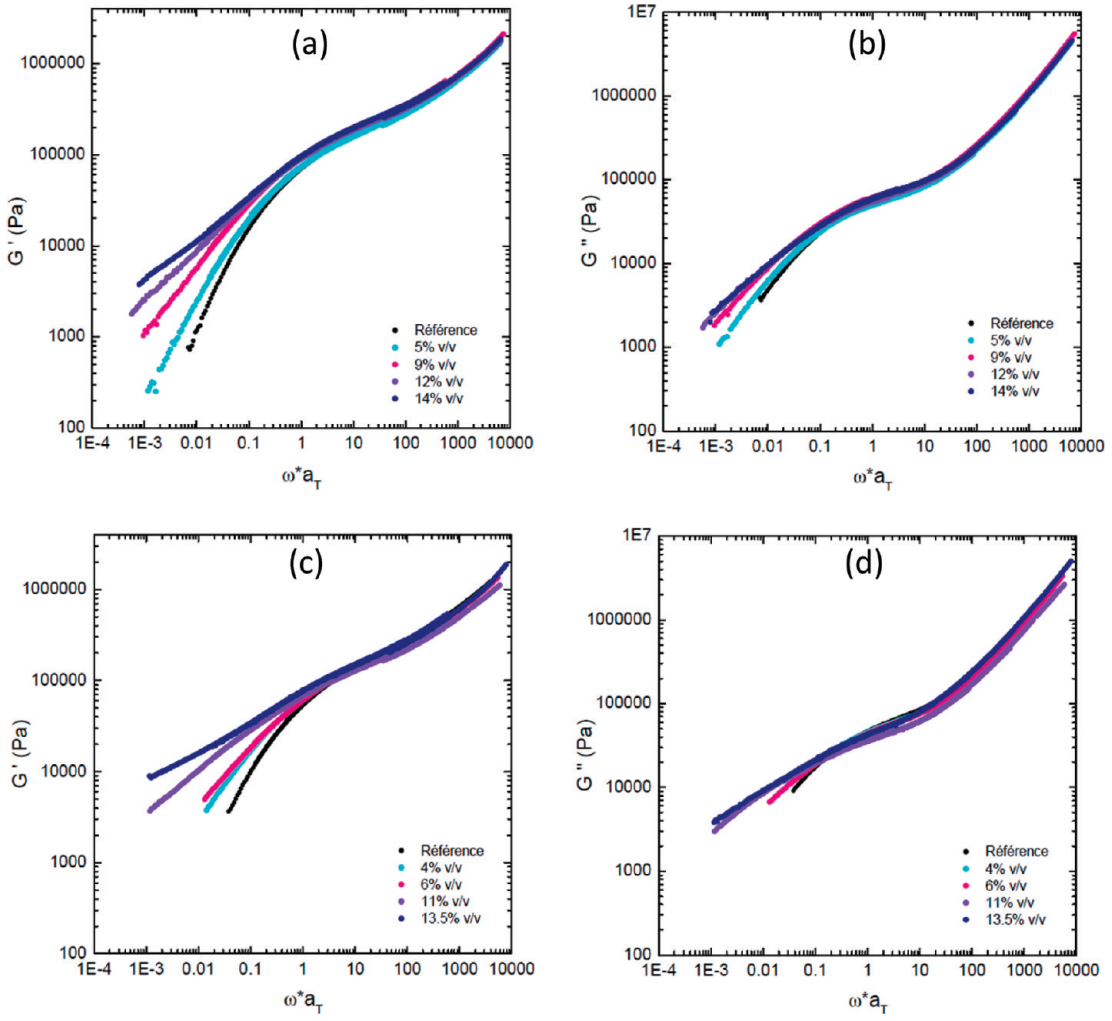

Figure 10. Elastic shear modulus as a function of pulsation ω, using time−temperature superposition (T_0 = 143 °C) coefficient a_T defined in the text, for different volume fractions (% v/v) of grafted particles in the composite for two dispersion state of the particles inside the polymer matrix: (a) G', (b) G'' complete dispersion of the particles inside the matrix corresponding to the grafted/free chain length ration R = 0.25 and (c) G', (d) G'', aggregation of grafted particles inside the matrix corresponding the grafted/free chain length ratio R = 0.17.

increasing the silica content, the mean interparticles distance decreases, according to a classical volume compression process. Using the Percus−Yevick hard-sphere model to fit our interparticles structure factor, we extracted the thickness e of the polymer layer grafted around the particles. In the case of complete dispersion, the values (53 Å < e < 64 Å for R = 0.25 and e = 73 Å for R = 0.36) obtained with this indirect method are to compare with the ones calculated in our previous work (e = 62 Å for R = 0.25, 0.43, and 0.71), in which the thickness was determined in a direct way using a specific neutron contrast technique.[21] As the thickness of the grafted layer depends intrinsically on the length of the grafted chains, we normalized the thicknesses e of the grafted layers by the radius of gyration R_g for Gaussian conformation ($R_g = 0.275M^{1/2}$ for polystyrene). The results deduced from both the ways of determination are reported as a function of R in Figure 11. We see an excellent agreement between the two methods. Besides, we observe that the transition between complete dispersion and formation of aggregates is accompanied by a significant reduction of the normalized thickness of the grafted polymer layer: by about a factor of 2. These results show that the dispersion can be tuned by a refined control of the grafted/free chains wetting properties.

These observations can be qualitatively described considering the total free energy as a combination of a mixing entropy term between the grafted and the free chain and an elastic term of compression or stretching of the grafted brushes. For R < 0.24, according to a depletion process, entropic expulsion of the free chains from the grafted corona is observed, and the corona eventually collapses. The resulting short-ranged interparticles potential induces therefore aggregation. For R > 0.24, the free chains can partly swell the grafted corona which is then more extended and creates a repulsive long-ranged interparticles potential, favoring the complete dispersion of the particles. If these observations are qualitatively in agreement with theoretical considerations,[8,10,11,31] open questions remain to be clarified, especially concerning the parameter fixing the R value separating dispersed from aggregated state. Indeed, we obtained a complete dispersion for value below R = 1, which is the theoretical limit below which no complete wetting is possible. Similar observations are reported in the literature[32−34] and are usually explained by kinetic effects, related to the processing conditions of the systems: the observed dispersed state is indeed a metastable state, in which particles should aggregate but cannot move anymore because of solvent evaporation. The depletion effects being stronger for larger differences in chain lengths, and stronger depletion then inducing quicker aggregation, it explains why we see aggregates for larger chains. Another explanation could be the presence of an interpenetration domain[35] between the grafted and the free chains, even when the free chains are longer than the grafted chains, which would then allow dispersion. This idea is supported by the fact that the

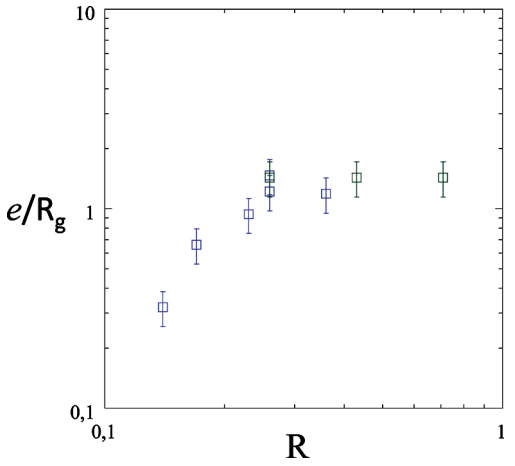

Figure 11. Evolution of the thickness e of the spherical grafted polymer layer normalized by the Gaussian radius of gyration R_g as a function of the grafted/free chain length ratio R determined indirectly with the analysis of the interparticle structure factor (open blue squares) and measured directly with SANS (open green squares) as reported by us in ref 21. The error bars are determined by taking into account for the cumulative experimental errors and the calculation approximations.

dispersed state corresponds to a collapse of the grafted chains which is only partial (e = 50−70 Å), in comparison with the complete collapse observed for the aggregated state (e = 30−40 Å) and the totally expanded conformation observed in solution (e = 120 Å), corresponding to wet brushes ($R \gg 1$). In addition, the surface curvature,[36] which can come in play for spherical particles, and the polydispersity of the grafted and of the matrix chains, constitute two other relevant contributions which could also have an influence on the transition between aggregated and individual particles. To progress in the understanding of the experimental limiting R parameter, varying the grafting density would certainly be an interesting method of investigation.

The direct correlation between the local structure and the macroscopic rheological response of a material is in many cases difficult to establish. At first order, the mechanical response of our nanocomposites as a function of the two dispersion states, aggregated particles or dispersed ones, shows in both cases the apparition of a much longer relaxation time in the low-frequencies range, which appears to be more pronounced in the case of aggregates. Because of grafting and as revealed by the entire dispersion study, the observed rise in time, which has some features of a liquid−solid transition, cannot be interpreted as a direct percolation[3,26] of the silica fillers or of the compact aggregates. However, it could be the signature of the formation of an indirect network by means of the grafted layer. For the individual dispersion, the particles come in brush-to-brush contact at Φ_{SiO_2} = 12% v/v, illustrating that the observed liquid−solid like transition could be related to the direct contact between grafted brushes. It was already observed in other well dispersed and diluted systems.[15,27,28] In the case of aggregated particles, the aggregates are not connected, but dispersed in a matrix which is liquid at the considered frequencies ($\omega^* a_T = 10^{-2}$ rad·s^{-1}). Moreover, the large distances between aggregates increase with silica content, while the modulus also increases: this is contradictory with a confinement effect between aggregates. Such behavior is indicative that at this given frequency, the elastic modulus of the filled nanocomposite should only be depending on short-ranged phenomena, governed by the interparticle interactions. No additional long-range contribution, as already shown in nanocomposites showing fractal dispersion,[3] seems to be observed. The short-range interparticles effects could be related to the interpenetration between the grafted brushes, which becomes then dominant compared to the interaction between grafted and free chains. Besides, confinement can also alter the dynamics of chains grafted to particles, especially by slowing-down effects. Finally, this new relaxation could also be related to the intrinsic relaxation of the polymer-silica aggregates, depending on the aggregates sizes. However, such interpretations remain to be experimentally validated, for instance by probing directly the dynamics of the chains with inelastic neutron scattering experiments.

V. Summary and Conclusion

Using a combination of refined synthesis of polymer-grafted nanoparticles with a controlled formation process of nanocomposites films, we investigated the complex problem of the dispersion of polymer grafted particles inside a matrix of the same polymer (PS). For a given intermediate density of grafted chains, the dispersion of the particles inside the films was analyzed with complementary scattering (SAXS/USAXS) and imaging (TEM) techniques as a function of the particle content. The relevant parameter in this case is the grafted/free chains length ratio R, which can be tuned either at fixed grafted chains length, by varying the molecular mass of the free chains, or at fixed molecular mass for the chains of the matrix, by varying the length of the grafted chains. In the probed range of the R parameter always below 1 in our case, between 0.04 and 0.36, we demonstrate the possibility of two dispersion states of the grafted particles inside the polymer matrix: for R below 0.24, the particles arrange in compact and large aggregates whose size and interaggregate distance increase when increasing the particle content. For R above 0.24, the particles form a complete well-defined repulsive organization inside the matrix, where interparticles distance decreases while increasing the silica content, without any aggregation. From the analysis of the interparticle structure factor, we indirectly extract the thickness of the spherical grafted brushes and correlate it with the dispersion state: aggregation of the particles is clearly associated with a significant collapse of the spherical grafted brushes. These results, showing the tuning of the dispersion by a refined control of the grafted/free chains wetting properties, are in qualitative agreement with the theoretical description of the dispersion mechanisms but also lead to questionings about the numerical value of R separating the two dispersion states. The mismatch with the expected theoretical frontier of R = 1 can be linked to the possible existence of an interdiffusion zone between the grafted and free chains, along with processing kinetics, surface curvature and chains polydispersity effects. Finally, mechanical analysis shows the appearance of a longer relaxation time at low frequencies more pronounced for the aggregates. The observed liquid−solid like transition can be attributed to the contact between the grafted brushes for the individual dispersion, while modulus increase for the aggregates seems to be also dominated by a short-ranged contribution, with no significant effect of larger scale organizations. This suggests a substantial influence of the interpenetration between grafted brushes or of grafted chains confinement, but this remains to establish with complementary techniques to clarify the contributions of the different effects described above. Such control on the design and the characterization of well-defined nanocomposites and the understanding of correlations between local dispersion, chain conformations and rheological behavior can have a significant impact on the progresses and design of new applicative materials.

Acknowledgment. We thank CEA for the PhD Grant of C. Chevigny and ESRF for beam-time allocation. The Laboratoire Léon Brillouin is a joined facility of CEA and CNRS.

References and Notes

(1) Dalmas, F.; Cavaillé, J.-Y.; Gauthier, C.; Chazeau, L.; Dendievel, R. *Compos. Sci. Technol.* **2007**, *67*, 829–839.

(2) Heinrich, G.; Klüppel, M.; Vilgis, T. A. *Curr. Opin. Solid State Mater. Sci.* **2002**, *6*, 195–203.
(3) Jouault, N.; Vallat, P.; Dalmas, F.; Said, S.; Jestin, J.; Boué, F. *Macromolecules* **2009**, *42*, 2031–2040.
(4) Sen, S.; Xie, Y.; Bansal, A.; Yang, H.; Cho, K.; Schadler, L. S.; Kumar, S. K. *Eur. Phys. J. Spec. Top* **2007**, *141*, 161–165.
(5) Oberdisse, J.; El Harrak, A.; Carrot, G.; Jestin, J.; Boué, F. *Polymer* **2005**, *46*, 6695–6705.
(6) Jestin, J.; Cousin, F.; Dubois, I.; Ménager, C.; Schweins, R.; Oberdisse, J.; Boué, F. *Adv. Mater.* **2008**, *20*, 2533–2540.
(7) Radhakrishnan, B.; Ranjan, R.; Brittain, W. J. *Soft Matter* **2006**, *2*, 386–396.
(8) de Gennes, P. G. *Macromolecules* **1980**, *13*, 1069–1075.
(9) Maas, J. H.; Fleer, G. J.; Leemakers, F. A. M.; Cohen Stuart, M. A. *Langmuir* **2002**, *18*, 8871–8880.
(10) Gast, A.; Leibler, L. *Macromolecules* **1986**, *19*, 686–691.
(11) Leibler, L.; Pincus, P. A. *Macromolecules* **1984**, *17*, 2922–2924.
(12) Hasegawa, R.; Aoki, Y.; Doi, M. *Macromolecules* **1996**, *29*, 6656–6662.
(13) Lindenblatt, G.; Schärtl, W.; Pakula, T.; Schmidt, M. *Macromolecules* **2001**, *34*, 1730–1736.
(14) Klos, J.; Pakula, T. *Macromolecules* **2004**, *37*, 8145–8151.
(15) Yezek, L.; Schärtl, W.; Chen, Y.; Gohr, K.; Schmidt, M. *Macromolecules* **2003**, *36*, 4226–4235.
(16) Lindenblatt, G.; Schärtl, W.; Pakula, T.; Schmidt, M. *Macromolecules* **2000**, *33*, 9340–9347.
(17) Green, D. L.; Mewis, J. *Langmuir* **2006**, *22*, 9546–9553.
(18) Akcora, P.; Liu, H.; Kumar, S. K.; Moll, J.; Li, Y.; Benicewicz, B. C.; Schadler, L. S.; Acehan, D.; Panagiotopoulos, A. Z.; Pryamitsyn, V.; Ganesan, V.; Ilavsky, J.; Thiyagarajan, P.; Colby, R. H.; Douglas, J. *Nat. Mater.* **2009**, *8*, 354–359.
(19) Chevigny, C.; Gigmes, D.; Bertin, D.; Jestin, J.; Boué, F. *Soft Matter* **2009**, *5* (19), 3741–3753.
(20) Chevigny, C.; Jestin, J.; Gigmes, D.; Bertin, D.; Boué, F., *Polym. Chem.* **2010**, DOI: 10.1039/C0PY00271B.
(21) Chevigny, C.; Jestin, J.; Gigmes, D.; Schweins, R.; Di Cola, E.; Dalmas, F.; Bertin, D.; Boué, F. *Macromolecules* **2010**, *43*, 4833–4837.
(22) Williams, M. L.; Landel, R. F.; Ferry, J. D. *J. Am. Chem. Soc.* **1955**, *77*, 3701.
(23) Rottler, J.; Robbins, M. O. *Phys. Rev. E* **2003**, *68*, 011801.
(24) Percus, J. K.; Yevick, G. J. *Phys. Rev. Second Ser.* **1958**, *110* (1), 1–13.
(25) Wertheim, M. S. *Phys. Rev. Lett.* **1963**, *10* (8), 321–323.
(26) Akcora, P.; Kumar, S. K.; Moll, J.; Lewis, S.; Schadler, L. S.; Li, Y.; Benicewicz, B. C.; Sandy, A.; Narayanan, S.; Ilavsky, J.; Thiyagarajan, P.; Colby, R. H.; Douglas, J. F. *Macromolecules* **2010**, *43*, 1003–1010.
(27) Inoubli, R.; Dagréou, S.; Lapp, A.; Billon, L.; Peyrelasse, J. *Langmuir* **2006**, *22*, 6683–6689.
(28) McEwan, M.; Green, D. *Soft Matter* **2009**, *5*, 1705–1716.
(29) Berriot, J.; Montes, H.; Lequeux, F.; Long, D.; Sotta, P. *Europhys. Lett.* **2003**, *64* (1), 50–56.
(30) Kropka, J. M.; Putz, K. W.; Pryamitsyn, V.; Ganesan, V.; Green, P. F. *Macromolecules* **2007**, *40*, 5424–5432.
(31) Gohr, K.; Schärtl, W. *Macromolecules* **2000**, *33*, 2129–2135.
(32) Corbierre, M. K.; Cameron, N. S.; Sutton, M.; Laaziri, K.; Lennox, R. B. *Langmuir* **2005**, *21*, 6063–6072.
(33) Xu, C.; Ohno, K.; Ladmiral, V.; Composto, R. J. *Polymer* **2008**, *49*, 3568–3577.
(34) Lan, Q.; Francis, L. F.; Bates, F. S. *J. Polym. Sci., Part B: Polym. Phys.* **2007**, *45* (16), 2284–2299.
(35) Geoghegan, M.; Boue, F.; Bacri, G.; Menelle, A.; Bucknall, D. G. *Eur. Phys. J. B* **1998**, *3* (1), 83–96.
(36) Xu, J. J.; Qiu, F.; Zhang, H. D.; Yang, Y. L. *J. Polym. Sci., Part B: Polym. Phys.* **2006**, *44*, 2811–2820.

134 *Macromolecules* **2011**, *44*, 134–139
DOI: 10.1021/ma1020227

Macromolecules
ARTICLE

Hole Nucleation and Growth in Free-Standing Polystyrene Ultrathin Films

Jeremy M. Rathfon,[†,‡] Robert W. Cohn,[‡] Alfred J. Crosby,[†] and Gregory N. Tew*[,†]

[†]*Department of Polymer Science and Engineering, University of Massachusetts Amherst, 120 Governors Drive, Amherst, Massachusetts 01003, United States, and* [‡]*ElectroOptics Research Institute and Nanotechnology Center, University of Louisville, Louisville, Kentucky 40292, United States*

Received August 31, 2010; Revised Manuscript Received October 20, 2010

ABSTRACT: Nucleation and growth of holes in free-standing ultrathin (< 100 nm) polymer films are examined via optical microscopy in order to gain a better understanding of these phenomena. Hole nucleation is quantified with a free energy barrier based on a simple capillary model. Additionally, holes are found to grow exponentially in accordance with previous studies in the literature. Ultrathin films of polystyrene (between 50 and 100 nm) cast via flow coating are suspended atop lithographically patterned arrays of pillars. The films are then annealed above the glass transition temperature to study the nucleation and growth of holes via optical microscopy. Image analysis is performed to measure the density of nucleated holes as well as hole radius as a function of time. Holes are found to grow exponentially with time in a nonlinear viscoelastic, shear thinning regime under high shear strain. The energy barrier model is applied to the nucleation of holes in free-standing thin films and is found to describe the phenomenon well. This analysis of hole nucleation and growth extends the understanding of ongoing research into suspended fiber formation from the melting of free-standing polymer thin films.

Introduction

The study of the dynamics of thin film stability, such as rupture and dewetting phenomena, has been a major research area in polymer science due to its applications in adhesives, coatings, and lithographic techniques for device fabrication. In ultrathin films, films less than 100 nm in thickness, the natural length scale of a polymer chain, represented by the radius of gyration, R_g, is comparable to or greater than the film thickness. In this confined regime, polymer conformational changes can result in large deviations in dynamics and phase behavior from the bulk.[1−12] Because systems of very small dimensions are easily fabricated and manufactured, these problems can now be probed with new interesting geometries. These confined geometries allow for the study of polymer molecules as they relate to polymer−surface interactions and the effect of confinement on the motion of the chains. Many studies have shown how confinement of polymer chains within thin films effects the mobility and dynamics of chains and thus the glass transition temperature, T_g, of the polymer. High-molecular-weight (M_w > 350 kDa) polystyrene (PS) thin films exhibit a linear dependence on molecular weight, below a critical thickness,[1,3,4,7] while low-M_w films show a nonlinear, M_w-independent T_g reduction described by the empirical Keddie, Jones, and Cory functional form.[10−12] These T_g confinement effects have been summarized by Roth et al.[7]

Previous studies on polymer dynamics in thin films have focused on the dewetting of polymers from a surface, examining the growth rate of holes formed as well as the developing shape of rims surrounding the holes.[5,13−28] Many of these studies have relied on assumptions of a "frictionless surface" or neglect the effects of the surface upon which the polymer dewets. Comparatively, much less work has been performed analyzing the growth of holes in free-standing, polymeric thin films.[2,6,9,29−31] Dependent upon the temperature regime, holes have been found to grow linearly close to the T_g of the polymer or exponentially with time when well above the T_g. Debregeas et al. probed the viscous bursting of thick, 5−50 μm suspended polydimethylsiloxane films and characterized the exponential growth of nucleated holes showing uniform thickening of the film and an absence of a rim formed at the hole edge.[32,33] Dutcher and co-workers studied the growth of holes in free-standing polystyrene (PS) thin films as a function of molecular weight, film thickness, and temperature, showing exponential hole growth above the T_g.[2,6,29,30] Xavier et al. show the growth of holes in exponential and linear growth modes, with linear hole growth occurring as film thickness is decreased or the temperature is decreased close to the T_g of the bulk polymer (T_g^{bulk}).[9] Roth et al. show that this observed linear response, and the largest deviations from exponential growth at early hole growth times, occur at higher M_w and at temperatures very close to T_g^{bulk}, resulting from an exponential decay of the initial long-lived transient response and suggest this is due to the decay of elastic chain entanglements during the onset of shear thinning.[6] This linear regime was observed to transition to exponential growth at longer times where large shear strain rates disentangle the chains rapidly, giving rise to the shear thinning regime and a reduced viscosity.

Although the study of hole growth has been investigated, to date there exists a lack of studies in the literature on the spontaneous nucleation of holes in free-standing, polymer thin films. Reports investigating hole growth in free-standing films attribute two mechanisms to hole formation in the melt state: spontaneously through a process analogous to spinodal decomposition or by nucleation from defects such as dust (< 0.2 μm) or density inhomogeneities.[2,13] In most examples where hole growth is studied, holes are nucleated with a heated scanning tunneling microscope tip, laser, or needle. Hole formation in thin films has been addressed while on a substrate such as in the case of dewetting.[5,14,19,21,24,26,27,34] Reiter and co-workers reported

*Corresponding author. E-mail: tew@mail.pse.umass.edu.

 Published on Web 12/14/2010 © 2010 American Chemical Society

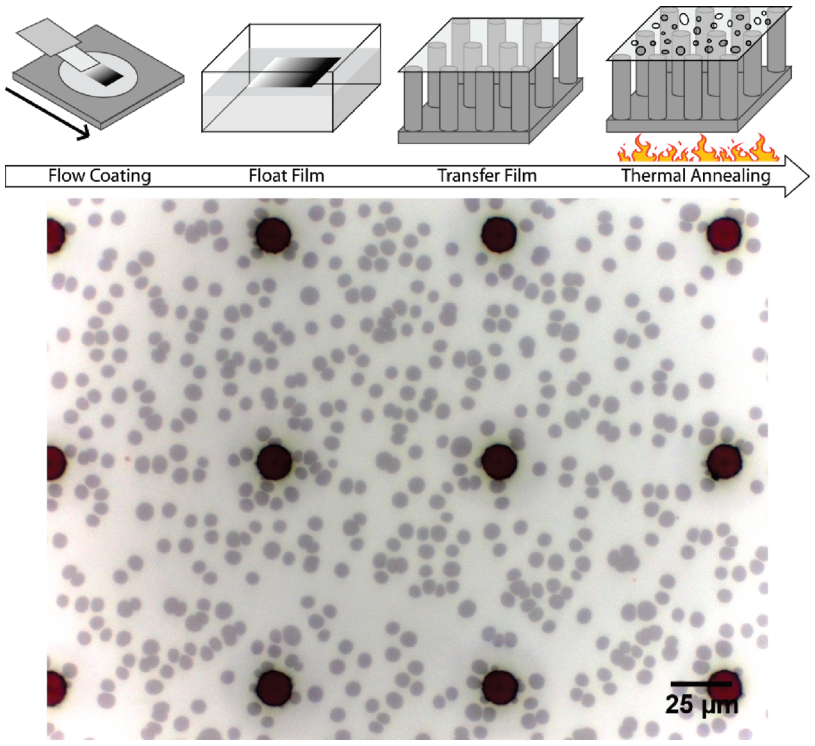

Figure 1. Experimental approach toward hole formation via flow coating and thin film melting with a representative image of the nucleation of holes (h = 65 nm, 400 kDa PS). The very dark red uniform circles in the image are the supporting pillars, 15 μm in diameter with 75 μm spacing.

on instabilities and the development of holes in PS thin films on coated substrates and determined the number of holes formed, N_h, had a power law dependence on film thickness, h, stated as $N_h \propto h^p$, where $p \sim -4$.[21,26,34] The formation of instabilities is attributed to van der Waals forces giving rise to a disjoining pressure which attempts to adjust and minimize the free energy while the surface tension competes to maintain the flat film. Although assumptions are made that this hole nucleation theory can be extended to free-standing thin films, given that the models are based on frictionless surfaces or are independent of the substrate, no direct study has been performed.

In this study, the nucleation and growth of holes in free-standing, ultrathin polymer films are probed atop lithographically patterned arrays of microscale pillars. This study is extended from work on the formation of oriented, suspended fibers from the melting of free-standing polystyrene thin films, derived from the nucleation of holes in the same films.[35] The growth of holes is shown to be an exponential expansion of the holes in a shear thinning, high shear strain regime, unencumbered by the pillar array substrate. Hole nucleation in free-standing, ultrathin polymer films is modeled using an energy barrier approach,[36] and estimates for this energy barrier are made.

Results and Discussion

Thin Film Preparation. Gradient thickness ultrathin polymer films in the submicrometer to nanoscale regime were fabricated via a technique called "flow coating", in which a bead of polymer solution is sandwiched between a blade and is drawn across a substrate.[28,37] A schematic of thin film sample preparation is given in Figure 1. For this study, gradient thickness polystyrene films, from approximately 50 to 100 nm in thickness, were cast from 0.75−1.5 wt % solutions in toluene using an acceleration of 6 mm/s^2. Monodisperse polystyrene standard samples of various molecular weights were used (PS, M_n = 123, 400, 2000, 6000 kDa; M_w/M_n = 1.08, 1.06, 1.20, 1.22, respectively, Alfa Aesar). After flow coating, film thickness was measured across the film profile via a UV−vis interferometer (Model F20, Filmetrics, Inc.). Films were then floated off the silicon substrate onto clean water (Milli-Q) and subsequently transferred atop a lithographically patterned array of pillars. The pillars have dimensions of 15 μm in diameter and 75 μm spacing (65 nm thickness, 400 kDa PS samples were also tested on 15, 25, and 35 μm pillar spacings). Films were dried and annealed just below the T_g of the polymer under vacuum for 24 h to remove water and residual solvents.

Table 1. Molecular Weight, M_n, Polydispersity Index, M_w/M_n, Film Thickness, h, and Annealing Temperature, T, for the Hole Expansion Study

M_n (kDa)	M_w/M_n	h	T (°C)
123	1.08	65[b]	116
400	1.06	53,[a] 65,[c] 80,[a] 100[a]	130
2000	1.20	65[b]	161
6000	1.22	65[b]	196

[a] Tested on arrays with 75 μm pillar spacings. [b] Tested on arrays with 25 and 75 μm pillar spacings. [c] Tested on arrays with 15, 25, 35, and 75 μm pillar spacings.

Hole Expansion. Ultrathin PS film samples of various thicknesses and molecular weights (Table 1) were annealed using an enclosed Linkham LTS350 microscopy thermal stage and a Zeiss Axio Imager M2m optical microscope at 50× magnification for imaging. A specific area of a film with a corresponding thickness was selected for imaging in each experiment. The variation of thickness over the resultant images was approximately ±0.16 nm for a film with a 50 nm gradient thickness over a 45 mm width. Samples were taken from room temperature and heated quickly (30 °C/min) to the annealing temperature, 130 °C, for M_n = 400 kDa samples and held at this temperature while hole formation and expansion occurred. Samples of other molecular weights were annealed at temperatures (116, 161, and 196 °C for 123,

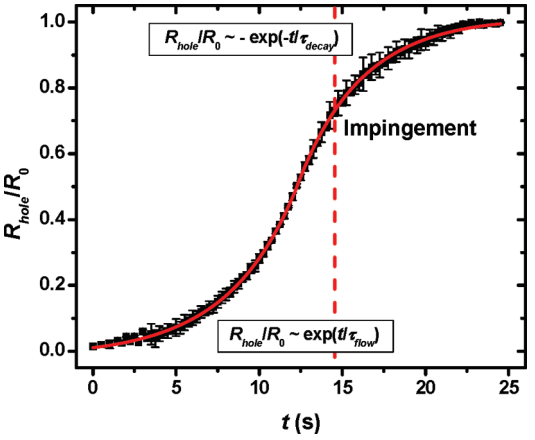

Figure 2. Normalized hole radius as a function of time showing both exponential growth of holes, followed by exponential decay in growth at the midpoint transition ($R_{hole}/R_0 = 0.5$), after impingement with other holes as well as pillars (h = 65 nm, 400 kDa PS, T = 130 °C). The dashed line is given to indicate where holes visually impinge upon the pillars as seen by optical microscopy.

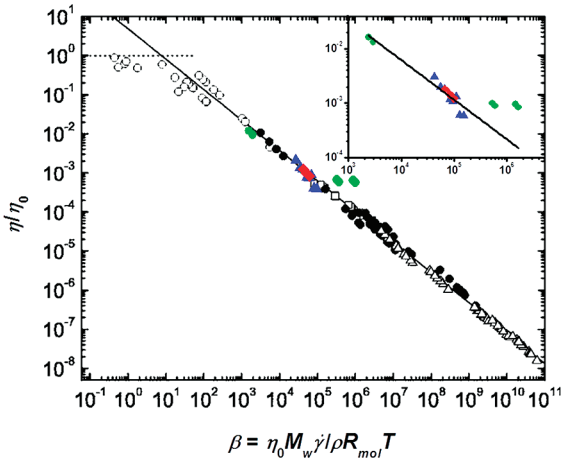

Figure 3. Reduced viscosity, η/η_0, versus reduced shear strain rate, β, for samples with varying molecular weight (●), thickness (▲), and pillar spacing (◆). Figure adapted from ref 29 with a best fit line of slope -0.78 ± 0.01. The inset shows data from the present study fitted by least-squares regression to give a slope of -0.73 ± 0.05.

2000, and 6000 kDa, respectively) to match the zero shear rate viscosity, η_0, of this experiment (1.73×10^9 Pa·s), calculated using the empirical VFT equation

$$\eta_0(T) = A \exp\left(\frac{T_A}{T - T_0}\right) \tag{1}$$

where $T_A = 2022$ K and $T_0 = 311$ K and determined from the value $\eta_0 = 1.2 \times 10^{11}$ Pa·s at $T = 119.4$ °C for 600 kDa PS and scaled using $\eta_0 \sim M_w^{3.4}$.[38,39] Optical microscopy was used to take images of hole formation over time, typically at a rate of 2 fps for 30 min, over the annealing experiment. A novel image analysis technique developed for the acquisition of suspended fiber properties, such as diameter, orientation and branching, was applied to images of growing holes to identify, track, and measure individual hole radii.[35] Hole radius was measured as a function of time as soon as holes could be optically resolved, typically ~0.5 μm in diameter, and then normalized against their initial respective radii.

Figure 2 shows a representative example of hole radius as a function of time, $R_{hole}(t)$, for a hole expansion experiment with a parent film of 400 kDa PS, having a thickness of 65 nm. Initial exponential growth is seen, followed by a decay in growth, corresponding to holes impinging upon each other and the pillar array. This impingement is illustrated by the dashed line in Figure 2, where the leading holes edges can be visually observed to contact each other and supporting pillars in optical microscopy images. The onset of this decay in growth and the point at which holes begin to compete for space to grow occurs just before this impingement point, at the midpoint transition ($R_{hole}/R_0 = 0.5$). The curve in Figure 2 is from an average of hole data from at minimum five representative holes and is fitted with both exponential growth and decay curves, before and after the midpoint transition, respectively. The fits for both exponential curves are given. Similar exponential growth curves (see Supporting Information) were attained for all samples in this study (Table 1), yielding viscosity values at the hole edge, as discussed in detail next.

Hole expansion is driven by an energy balance between a surface tension stress pulling the hole open and viscous dissipation within the film resisting flow. An exponential growth law for the radius of a hole, $R_{hole}(t)$, with respect to time t, has been developed and confirmed experimentally[2,6,9,29,33]

$$R_{hole}(t) = R_0 \exp(t/\tau_{flow}) \tag{2}$$

$$\tau_{flow} = \eta h/\varepsilon \tag{3}$$

where R_0 is the initial hole radius, τ_{flow} is the characteristic growth time, η is the viscosity at the hole edge, h is the film thickness, and ε is the surface tension of the polymer−air interface, with ε for PS at different temperatures calculated using the equation[40]

$$\varepsilon = -0.072(T - 20) + 40.7 \tag{4}$$

with ε in mN/m for T in °C. This surface tension gives a shear stress $\sigma = 2\varepsilon/h$ and produces a shear strain rate at the hole edge of $\dot{\gamma} = 2/\tau$. At higher viscosities, lower temperatures, and higher molecular weights, the importance of nonlinear viscoelastic effects such as shear thinning becomes greater.[41,42] Shear thinning is described as a power law of the viscosity normalized by the zero shear rate viscosity versus the reduced shear strain rate, β

$$\log(\eta/\eta_0) = -d \log \beta \tag{5}$$

where the power law exponent, d, in the bulk is typically ~0.8 in the shear thinning regime,[42] experimentally found to be between ~0.65 and 0.78 by Dutcher and co-workers.[2,6,29,30] The reduced shear strain rate is defined as

$$\beta = \eta_0 M_w \frac{\dot{\gamma}}{\rho R_{mol} T} \tag{6}$$

where R_{mol} is the molar gas constant and ρ is the density of the polymer, with ρ for PS at different temperatures calculated using the equation[43,44]

$$\rho = 1.0865 - 6.19 \times 10^{-4} T + 0.136 \times 10^{-6} T^2 \tag{7}$$

with ρ in g/cm^3 for T in °C. Figure 3 shows the reduced viscosity at the hole edge, as calculated from the hole growth experiments, for all samples in Table 1, as a function of the reduced shear strain rate. The horizontal dashed line indicates the linear viscoelastic regime of hole growth where $\eta = \eta_0$. The solid line with slope of -0.78 ± 0.01 indicates the power law fitting of the nonlinear viscoelastic regime where shear thinning effects dominate the flow. Exponential

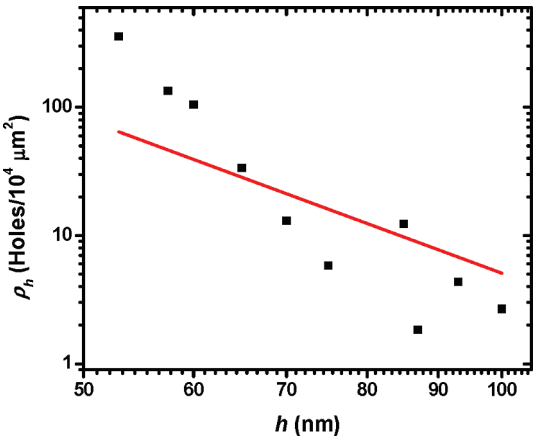

Figure 4. Hole density, ρ_h, as a function of film thickness, h, for 400 kDa PS samples, T = 130 °C, with a −4 power law ($\rho_h \sim h^{-4}$) determined by least-squares regression applied.

growth time scale data from the current study is overlaid on data from ref 29. Figure 3 clearly indicates that the hole growth regime of this study lies within the shear thinning, nonlinear viscoelastic regime, with all samples of varying M_w, thickness, and pillar spacing reducing to fit well upon the trend line, $\eta(\beta)/\eta_0 \sim |\beta|^{-0.78}$. Furthermore, no noticeable effect of the pillars upon the film can be detected as the viscosity data clearly falls in line with literature reported trends for hole expansion. The inset in Figure 3 is data from the present study, fitted with a power law determined by least-squares regression to give a slope of −0.73 ± 0.05, which is slightly smaller than the bulk value of −0.8 but fits well within the previous given range of literature values (d = 0.65−0.78). The deviation of data from the trend at large M_w (2 and 6 MDa) is thought to be contributions of additional driving forces, such as from weak residual strain in the film due to suspension or from residual stresses remnant from the flow coating process. Although films were annealed just below T_g, this would likely not allow gross chain reorientation due to lack of mobility. Annealing films for long times over T_g could be applied in future studies to better ensure equilibration of residual stresses and molecular conformations within the films. However, strain due to suspension is unavoidable for the purpose of thin film melting for the eventual fabrication of suspended fibers in this architecture. These additional stresses could add to the effective surface tension ($\eta \sim \tau_{flow}\varepsilon/h$) and would be expected to play a more significant role at higher values of M_w.

Hole Nucleation. As discussed earlier, Reiter and co-workers have developed a scaling for the hole nucleation and rupture of unstable, thin polymer films.[21,26,34] For a liquid film on a substrate, a competition between van der Waals forces, giving rise to a disjoining pressure, and viscous loss, due to a Poiseuille flow of the fluid, results in fluctuations of the surface with a specific wavelength. These undulating surface modulations have a characteristic dimensionality of h^2, and thus a hole density per area, N_h, which scales with thickness to the −4 power ($N_h \propto h^p$, where $p \sim -4$), yielding a scaling for the nucleation of holes. In order to probe hole nucleation in free-standing, ultrathin films, numerous annealing experiments on 400 kDa PS films were carried out at various thicknesses between 50 and 100 nm. The density of nucleated holes was calculated by counting the number of holes initiated in the annealed samples in a given area. All holes in a given sample typically initiated instantaneously, within the limitations of this experiment. Figure 4 shows the hole nucleation data plotted as a log−log graph and fitted

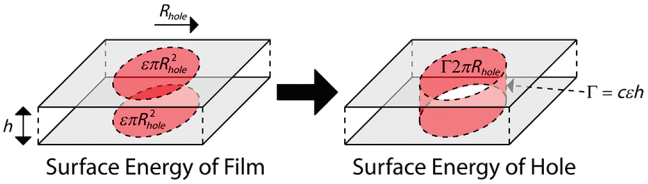

Figure 5. Schematic of the free energy of a free-standing film before and after hole nucleation.

with a power law ($N_h \propto h^{-4}$) using least-squares regression. As clearly shown, a −4 power law does not represent the data very accurately and provides evidence that the observed hole nucleation mechanism is obeying a stronger scaling, which would correspond to a fit with a higher power and thus a steeper "slope" (see Supporting Information). This stronger scaling is attributed to the two surfaces of the free-standing film influencing hole nucleation. In contrast to Poiseuille flow, a free-standing film would be expected to undergo plug flow, and therefore the power law scaling of Reiter is not in fact a clear expectation. Thus, this data suggests that the nucleation of holes in thin free-standing polymer films in the melt state should not be considered in the same manner as unstable, rupturing films on a solid surface. These models only consider surface modulations of the supported films, i.e., independent of substrate surface energy or morphology, and they do not adequately describe hole nucleation in free-standing films.

The nucleation of holes in a free-standing polymer film can be considered as a balance of free energy. A suspended polymer film in the melt/fluid state is metastable; however, there is an energy barrier resisting breakup of the film. A schematic representation of the free energy balance of hole nucleation is depicted in Figure 5. The free energy, F, of a hole formed in a free-standing film can be written as

$$F = -2\varepsilon\pi R_{hole}^2 + \Gamma 2\pi R_{hole} \quad (8)$$

where $-2\varepsilon\pi R_{hole}^2$ represents the loss of surface energy from the two circular areas of the film where the hole is generated and Γ is an edge tension of the hole.[36] A hole created through the thickness of a film should have an energy cost of the newly formed hole edge; thus $\Gamma = c\varepsilon h$, with c being a geometric factor of 1, and the newly formed hole edge has an energy of $\Gamma 2\pi R_{hole}$. From this free energy expression, Croll et al. have developed a scaling for the nucleation of holes that considers hole nucleation as a classic energy barrier problem, in which the number of nucleated holes, N_h, thus the density of holes, ρ_h, can be expressed as a Boltzmann distribution

$$\rho_h = a \exp\left(-\frac{F^*}{kT}\right) \quad (9)$$

where a is the attempt frequency, F^* is the energy barrier for creating a hole, and k is the Boltzmann constant.[36] Given the geometry of a hole, the energy barrier can be written as

$$F^* = \pi\Gamma^2/2\varepsilon = \pi\varepsilon c^2 h^2/2 \quad (10)$$

utilizing the simple assumption of the edge tension ($\Gamma = c\varepsilon h$). Therefore, with a film thickness of 50 nm and surface tension of 32.8 mN/m at 130 °C,[40] the energy barrier, F^*, is expected to be about 10^{-16} J.

In order to examine the free energy model for hole nucleation, the hole nucleation density data from Figure 4 is plotted in Figure 6 as $\log(\rho_h)$ as a function of the square of thickness, h^2. The capillary model and energy barrier scaling

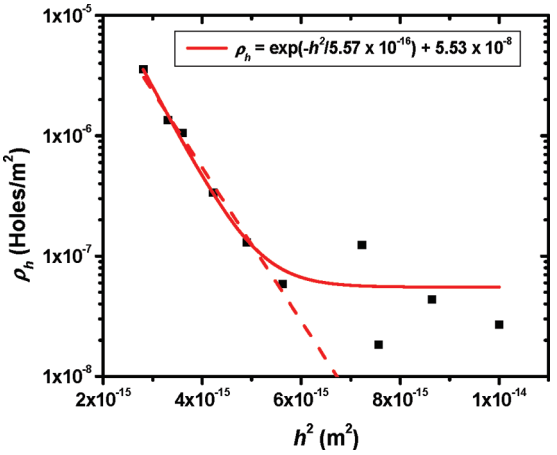

Figure 6. Hole density, ρ_h, as a function of the square of film thickness, h^2, for 400 kDa PS samples of varying thickness, T = 130 °C. The data are fit using eq 9, both with and without an asymptotic limit.

shown in eq 9 was applied to the data in Figure 6. The data in this report encompasses a range up to a greater thickness (53−100 nm) than that investigated by the study of Croll et al. (∼20−70 nm). While the energy barrier model agrees remarkably well with the hole nucleation data in this lower range, hole nucleation data above ∼80 nm begins to deviate from the pure exponential scaling, approaching an asymptotic limit of hole density. With the addition of an offset hole density value (5.5×10^{-8} holes/m^2), the exponential function maintains the same "slope" and agreement in thinner films and captures this limit seen in films above ∼80 nm. This minimum hole density suggests that other mechanisms for hole nucleation must be considered above a certain film thickness. In this thicker regime, the energy barrier becomes large; thus, nucleation from additional effects may dominate, such as nucleation from inhomogeneities in the film, like those of residual density fluctuations from the casting of films. Both the pure exponential scaling characterizing the thinner regime as well as the offset exponential fit are given for reference in Figure 6, both calculated using least-squares regression. As shown, the fits vary only slightly and do not significantly affect the energy barrier calculation discussed below.

The data are well fit by the energy barrier model of eq 9 giving a value of $F^*/kT = 4.4$, corresponding to a nucleation event that occurs readily and frequently. Calculating F^* from the exponential curve fit of this data gives a value for F^* of 2.50×10^{-20} J for a 50 nm thick film. Though the data qualitatively agree with the fit curve from eq 9, the calculated value for F^* is lower than the predicted energy barrier of 10^{-16} J, indicating that another driving force is influencing hole nucleation. Croll et al. discuss this hole nucleation model and make a comparison between PS films and PS/poly(methyl methacrylate) block copolymer (PS-*b*-PMMA) films with disordered, cylindrical, and lamellar morphologies.[36] Their hole nucleation data gives a free energy barrier of $\sim 1.5 \times 10^{-20}$ J for a 40 nm thick film, which is remarkably close to the calculated value from the data in the present study ($F^* = 1.57 \times 10^{-20}$ J for h = 40 nm) and deviates from the simple prediction of 10^{-16} J in the same manner. This difference from the theoretical value of the energy barrier shows that the free energy of the capillary model (eq 8) captures just the general scaling. These markedly reproducible deviations can be attributed to the attempt frequency, a, having some dependence upon thickness. This difference in calculated energy barriers may also result from an effective surface energy which is dependent on thickness due to this change in thickness modifying the disjoining pressure. Additionally, nucleation from defects could work to lower the energy barrier of nucleation. In the thinner film thickness regime, where the data are well described by the energy barrier scaling, nucleation from defects are unlikely to be an influence of the lowered energy barrier due to the replication of the same free energy barrier over numerous experiments conducted between this present study and Croll et al., where samples were created with different polymers and with different experimental conditions. However, as stated earlier, the asymptotic limit of hole density observed in thicker films is likely to be influenced by nucleation from inhomogeneities as the energy barrier becomes large. Although the attempt frequency prefactor is not quantitative, hole nucleation in this study scales well with the simple capillary model. A more detailed molecular model that captures the attempt frequency variations is needed to quantitatively understand the nucleation mechanism in free-standing thin films.

Conclusions

The growth of holes in free-standing polymer thin films was determined to be exponential in a shear thinning dominated, nonlinear viscoelastic, high shear strain regime. Additionally, hole growth was unencumbered by the supporting pillar array substrate. A simple capillary model was applied to the analysis of hole nucleation. The scaling predicts the relationship between hole nucleation and thickness well; however, quantitative measurements of the energy barrier for hole nucleation did not match the theoretical values. Hole nucleation data yield an energy barrier of 2.45×10^{-20} J, which deviates from the predicted value of 10^{-16} J for a 50 nm film. This deviation is lower than expected, indicating the influence of an additional driving force and could be attributed to the variation of surface tension and attempt frequency with thickness. The collected hole nucleation density data did not fit with the standard hole nucleation theory ($N_h \propto h^{-4}$) in the literature from the study of thin film rupture and dewetting where surface modulations from van der Waals forces are considered, indicating nucleation in free-standing thin films must be approached with different considerations.

Acknowledgment. The authors thank the National Science Foundation's Nanoscale Interdisciplinary Research Team (ECCS 0506941) for their generous support of this work. This work utilized facilities supported in part by the National Science Foundation Materials Research Science and Engineering Center (DMR 0820506) and Center for Hierarchical Manufacturing (CMMI 0531171). The authors thank Prof. Andrew B. Croll from North Dakota State University and Prof. Jonathan P. Rothstein from the University of Massachusetts, Amherst, for their extensive and insightful discussions.

Supporting Information Available: Exponential growth curves for all samples and a representative hole nucleation and expansion movie. This material is available free of charge via the Internet at http://pubs.acs.org.

References and Notes

(1) Dalnoki-Veress, K.; Forrest, J. A.; Murray, C.; Gigault, C.; Dutcher, J. R. *Phys. Rev. E* **2001**, *63*, 031801.
(2) Dalnoki-Veress, K.; Nickel, B. G.; Roth, C.; Dutcher, J. R. *Phys. Rev. E* **1999**, *59*, 2153.
(3) de Gennes, P. G. *Eur. Phys. J. E* **2000**, *2*, 201.
(4) Herminghaus, S.; Jacobs, K.; Seemann, R. *Eur. Phys. J. E* **2003**, *12*, 101.
(5) Reiter, G.; Al Akhrass, S.; Hamieh, M.; Damman, P.; Gabriele, S.; Vilmin, T.; Raphael, E. *Eur. Phys. J.: Spec. Top.* **2009**, *166*, 165.

(6) Roth, C. B.; Deh, B.; Nickel, B. G.; Dutcher, J. R. *Phys. Rev. E* **2005**, *72*, 021802.
(7) Roth, C. B.; Dutcher, J. R. *J. Electroanal. Chem.* **2005**, *584*, 13.
(8) Si, L.; Massa, M. V.; Dalnoki-Veress, K.; Brown, H. R.; Jones, R. A. L. *Phys. Rev. Lett.* **2005**, *94*, 127801.
(9) Xavier, J. H.; Pu, Y.; Li, C.; Rafailovich, M. H.; Sokolov, J. *Macromolecules* **2004**, *37*, 1470.
(10) Forrest, J. A.; Dalnoki-Veress, K. *Adv. Colloid Interface Sci.* **2001**, *94*, 167.
(11) Keddie, J. L.; Jones, R. A. L.; Cory, R. A. *Europhys. Lett.* **1994**, *27*, 59.
(12) Mattsson, J.; Forrest, J. A.; Borjesson, L. *Phys. Rev. E* **2000**, *62*, 5187.
(13) Brochard-Wyart, F.; Daillant, J. *Can. J. Phys.* **1990**, *68*, 1084.
(14) Brochard-Wyart, F.; Debregeas, G.; Fondecave, R.; Martin, P. *Macromolecules* **1997**, *30*, 1211.
(15) Jacobs, K.; Herminghaus, S.; Mecke, K. R. *Langmuir* **1998**, *14*, 965.
(16) Jacobs, K.; Seemann, R.; Schatz, G.; Herminghaus, S. *Langmuir* **1998**, *14*, 4961.
(17) Lambooy, P.; Phelan, K. C.; Haugg, O.; Krausch, G. *Phys. Rev. Lett.* **1996**, *76*, 1110.
(18) Martin, P.; Buguin, A.; Brochardwyart, F. *Europhys. Lett.* **1994**, *28*, 421.
(19) Masson, J. L.; Green, P. F. *Phys. Rev. Lett.* **2002**, *88*, 205504.
(20) Redon, C.; Brochard-Wyart, F.; Rondelez, F. *Phys. Rev. Lett.* **1991**, *66*, 715.
(21) Reiter, G. *Phys. Rev. Lett.* **1992**, *68*, 75.
(22) Reiter, G. *Phys. Rev. Lett.* **2001**, *87*, 186101.
(23) Reiter, G.; Sharma, A.; Casoli, A.; David, M. O.; Khanna, R.; Auroy, P. *Langmuir* **1999**, *15*, 2551.
(24) Seemann, R.; Herminghaus, S.; Jacobs, K. *Phys. Rev. Lett.* **2001**, *86*, 5534.
(25) Seemann, R.; Herminghaus, S.; Jacobs, K. *Phys. Rev. Lett.* **2001**, *87*, 196101.
(26) Sharma, A.; Reiter, G. *J. Colloid Interface Sci.* **1996**, *178*, 383.
(27) Vilmin, T.; Raphael, E. *Eur. Phys. J. E* **2006**, *21*, 161.
(28) Meredith, J. C.; Smith, A. P.; Karim, A.; Amis, E. J. *Macromolecules* **2000**, *33*, 9747.
(29) Roth, C. B.; Dutcher, J. R. *Phys. Rev. E* **2005**, *72*, 021803.
(30) Roth, C. B.; Dutcher, J. R. *J. Polym. Sci., Part B: Polym. Phys.* **2006**, *44*, 3011.
(31) Roth, C. B.; Nickel, B. G.; Dutcher, J. R.; Dalnoki-Veress, K. *Rev. Sci. Instrum.* **2003**, *74*, 2796.
(32) Debregeas, G.; de Gennes, P. G.; Brochard-Wyart, F. *Science* **1704**, *279*, 1998.
(33) Debregeas, G.; Martin, P.; Brochardwyart, F. *Phys. Rev. Lett.* **1995**, *75*, 3886.
(34) Reiter, G. *Langmuir* **1993**, *9*, 1344.
(35) Rathfon, J. M.; Grolman, J. M.; Crosby, A. J.; Tew, G. N. *Macromolecules* **2009**, *42*, 6716.
(36) Croll, A. B.; Dalnoki-Veress, K. *Soft Matter*, in press.
(37) Stafford, C. M.; Roskov, K. E.; Epps, T. H.; Fasolka, M. J. *Rev. Sci. Instrum.* **2006**, *77*, 023908.
(38) Ngai, K. L.; Plazek, D. J. In *Physical Properties of Polymers Handbook*; Mark, J. E., Ed.; AIP: Woodbury, NY, 1996.
(39) Plazek, D. J.; Orourke, V. M. *J. Polym. Sci., Part A-2: Polym. Phys.* **1971**, *9*, 209.
(40) Brandrup, J.; Immergut, E. H.; Grulke, E. A. *Polymer Handbook*; John Wiley & Sons, Inc.: Hoboken, NJ, 1999.
(41) Bird, R. B.; Curtiss, C.; Armstrong, R.; Hassager, O. *Dynamics of Polymeric Liquids*; Wiley: New York, 1987.
(42) Graessley, W. W. *Adv. Polym. Sci.* **1974**, *16*, 1.
(43) Hocker, H.; Blake, G. J.; Flory, P. J. *Trans. Faraday Soc.* **1971**, *67*, 2251.
(44) Orwoll, R. A. In *Physical Properties of Polymers Handbook*; Mark, J. E., Ed.; AIP: Woodbury, NY, 1996.

140 *Macromolecules* **2011**, *44*, 140–146
DOI: 10.1021/ma102154u

Macromolecules
ARTICLE

Universality in Nonlinear Elasticity of Biological and Polymeric Networks and Gels

Andrey V. Dobrynin* and Jan-Michael Y. Carrillo

Polymer Program, Institute of Materials Science and Department of Physics, University of Connecticut, Storrs, Connecticut 06269, United States

Received September 16, 2010; Revised Manuscript Received November 18, 2010

ABSTRACT: Networks and gels are part of our everyday experience starting from automotive tires and rubber bands to biological tissues and cells. Biological and polymeric networks show remarkably high deformability at relatively small stresses and can sustain reversible deformations up to 10 times their initial size. A distinctive feature of these materials is highly nonlinear stress−strain curves leading to material hardening with increasing deformation. This differentiates networks and gels from conventional materials, such as metals and glasses, showing linear stress−strain relationship in the reversible deformation regime. Using theoretical analysis and molecular dynamics simulations, we propose and test a theory that describes nonlinear mechanical properties of a broad variety of biological and polymeric networks and gels by relating their macroscopic strain-hardening behavior with molecular parameters of the network strands. This theory provides a universal relationship between the strain-dependent network modulus and the network deformation and explains strain-hardening of natural rubber, synthetic polymeric networks, and biopolymer networks of actin, collagen, fibrin, vimentin, and neurofilaments.

The characteristic feature of biological and polymeric networks and gels is the predominantly entropic nature of their elasticity.[1] The elastic response of these materials is due to extension of the individual chains or filaments reducing the number of available molecular conformations and hence the configurational entropy of the system. The entropic nature of the network elasticity allows large reversible deformations. In Figure 1, we combined stress−strain curves for natural rubber,[1,2] synthetic polymeric networks,[2,3] and biopolymer networks[4] of actin, collagen, fibrin, vimentin, and neurofilaments. The natural rubber[1,2] and synthetic networks[2,3] are dense polymeric systems consisting of highly coiled polymeric chains. The typical stress necessary for network deformations is on the order of 10^4-10^7 Pa. These networks can recover their initial form after up to a 10-fold increase in their original size, $\varepsilon \propto 10$. The biological networks are sparse and filled with water such that the filaments making up the network are only slightly coiled.[4] The deformation of these networks requires significantly low stresses ($10^{-1}-10^2$ Pa) and they can reversibly deform under the shear strain, $\gamma \leq 10$.[4] The striking similarity between two different classes of the network materials is the stress-induced network hardening which is manifested in the highly nonlinear stress−strain deformation curves (see Figure 1).

Modern theories of elasticity of networks and gels are based on the elastic response of the individual network strands making up the network.[1,5] These theories treat polymeric and biological networks as two different classes of systems. The deformation of strands of polymeric networks is usually described by the freely jointed chain model.[1,5] The deformation of biological networks made of stiff biological macromolecules or filaments[4,6−10] is modeled by the worm-like chain model.[6,11−14] In the small deformation limit both models give linear relationship between the magnitude of the local tension and the strand deformation.[5] But for the large strand deformations that correspond to the nonlinear network deformation regime, two models demonstrate qualitatively different divergence of the local tension f as a size of the deformed network strand R approaches its maximum value R_{max}. For the freely jointed chain model the local tension diverges as, $f \propto (R_{max} - R)^{-1}$, while for the worm-like chain model the tension f exhibits a faster divergence $f \propto (R_{max} - R)^{-2}$.[5] This results in a qualitatively different strain-hardening behavior of polymeric and biological networks and gels.

However, it was shown recently that polymer chains behave as a worm-like chain under tension in the interval of the applied forces f smaller than the crossover force f_c and as a freely jointed chain for $f > f_c$.[15−18] Magnitude of the crossover force $f_c \propto Kk_BT/b$ depends on the effective chain bending constant K (or chain persistence length l_p) and bond length b (k_B is the Boltzmann constant and T is the absolute temperature). For biological macromolecules like DNA the crossover force is estimated to be on the order of 4 nN while for flexible chains such as polystyrene, single stranded DNA, and PDMS it is on the order of 20−300 pN.[15,18] Universality in single chain deformation behavior indicates that one should expect universality in elastic properties of polymeric and biological networks and gels in the range of strains for which the forces acting on the network strands are smaller than a crossover force. Below we will show that this universality exists. To prove this we use a nonlinear deformation model of a worm-like chain[19] and derive expressions for the network stress under uniaxial and shear deformations. The derivation details are worked out in the Appendix A.

In the case of the uniaxial deformation at a constant volume the network extends in one direction say along the x-axis $\lambda_x = \lambda$ while it contracts in two others

$$\lambda_y = \lambda_z = 1/\sqrt{\lambda}$$

(see Figure 2).[1,5] The true stress generated in the uniaxially deformed network is equal to

$$\sigma_{xx}(\lambda) = \frac{G}{3}(\lambda^2 - \lambda^{-1})\left(1 + 2\left(1 - \frac{\beta I_1(\lambda)}{3}\right)^{-2}\right) \qquad (1)$$

*Corresponding author.

 Published on Web 12/09/2010 © 2010 American Chemical Society

where the first strain invariant for the uniaxial deformation is $I_1(\lambda) = (\lambda^2 + 2/\lambda)$. Thus, the magnitude of the network stress depends on two parameters: the network shear modulus G and the chain elongation ratio β. The network shear modulus $G \approx k_B T\rho\langle R_{in}^2\rangle/\langle R_0^2\rangle N_s$ depends on the monomer density ρ, the average number of bonds N_s between cross-links, and the intrinsic chain extension $\langle R_{in}^2\rangle/\langle R_0^2\rangle$—the ratio of the mean-square average end-to-end distance of the strand in the undeformed network $\langle R_{in}^2\rangle$ to its ideal value $\langle R_0^2\rangle$. Note that in the case of the natural rubber $\langle R_{in}^2\rangle = \langle R_0^2\rangle$. The second molecular parameter describing network properties is $\beta = \langle R_{in}^2\rangle/R_{\max}^2$ which is the ratio of $\langle R_{in}^2\rangle$ and the square of the end-to-end distance of the fully extended strand $R_{\max}^2$.

For a shear deformation a shear strain γ is equal to $\gamma = \tan\phi$ (see Figure 2).[1] The shear stress can be written as follows

$$\sigma_{xy}(\gamma) = \frac{G\gamma}{3}\left(1+2\left(1-\frac{\beta I_1(\gamma)}{3}\right)^{-2}\right) \qquad (2)$$

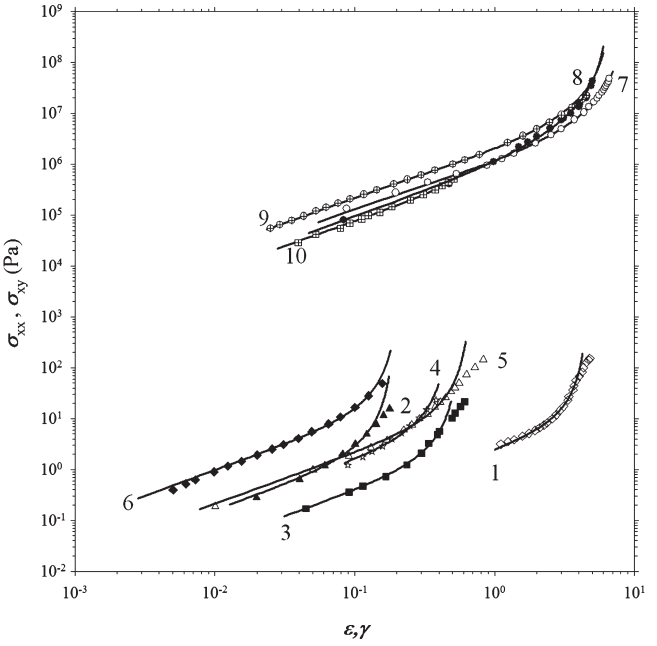

Figure 1. Stress−strain deformation curves of neurofilament network (1), collagen network (2), vimentin network (3), fibrin network (4, 5), actin network (6), natural rubber (7−9), and PPG BisAcAc−EA−HMDI−EA network (10). For natural rubber (7−9) and polymeric network (10) we have converted the original data sets for the engineering stress to the true stress $\sigma_{xx} = (1+\varepsilon)\sigma_{xx}^{eng}$. The lines represent a best fit to the theoretical expression for stress−strain deformation curve (see text for details).

where the first strain invariant for the shear deformation is given by $I_1(\gamma) = \gamma^2 + 3$.

The diverging term appearing in eqs 1 and 2 reflects finite extensibility of the strands between cross-links. It has the same quadratic divergence as the singular term in the expression for tension in a stretched worm-like chain (see Appendix A).

We have applied eqs 1 and 2 to fit the stress−strain curves for networks shown in Figure 1. For uniaxial deformation the elongation strain $\varepsilon = \lambda - 1$. The lines in Figure 1 correspond to the best fits to eqs 1 and 2. Note that for the weakly cross-linked networks at small deformations the part of the stress is supported by entanglements. To account for the entanglement contributions we have added a Mooney−Rivlin term[1,5] to the chain's free energy and to the network stress (see Appendix B). From fitting experimental data sets to eqs 1 and 2, we have obtained values of the network shear modulus G and the chain elongation ratio β. These parameters are summarized in Table 1. The data presented in Table 1 show that polymeric networks have a shear modulus G on the order of MPa and chain elongation ratios $\beta \propto 10^{-2}$−0.4. The small values of the chain elongation ratio support the idea that in polymeric networks the network strands are coiled. On the contrary, the chain elongation ratios for biological networks are close to unity indicating that filaments forming these networks are almost fully extended due to high values of the filament bending modulus and persistence length. Furthermore, the typical values of the shear modulus for biological networks are on the order of $G \propto 10^{-2}$−1 Pa with the largest value of the shear modulus corresponding to a network of the neurofilaments and the smallest value obtained for a collagen network. The network shear modulus decreases with increasing the filament rigidity, $G \propto k_B T\rho b/l_p$, which immediately follows from dependence of the network shear modules G on the system parameters $\langle R_{in}^2\rangle \approx R_{\max}^2 \approx b^2 N_s^2$ (for $\beta \approx 1$), and $\langle R_0^2\rangle \approx 2 l_p R_{\max}$.

To test predictions of our theory, we have performed molecular dynamics simulations[21] of the coarse-grained model of randomly cross-linked networks. The simulations details are described in Appendix C. We have performed simulations of the networks undergoing uniaxial and shear deformations. Figure 3 presents simulation results for uniaxial deformation of networks consisting of polymeric strands with different values of the chain bending constant. The lines correspond to the best fit to eq 1 considering shear modulus G and elongation ratio β as adjustable parameters. The values of the fitting parameters are given in Table 1. Note that the values of the chain elongation ratios obtained from the fitting procedure are close to the one directly calculated from the structures of the undeformed networks (see Appendix C). As one can see from this plot the agreement between simulation results and theoretical expression for uniaxial network deformation eq 1 is excellent. It is interesting to point out that the simulations also show a decrease in network shear modulus with increasing strand stiffness (persistence length) (see Appendix C).

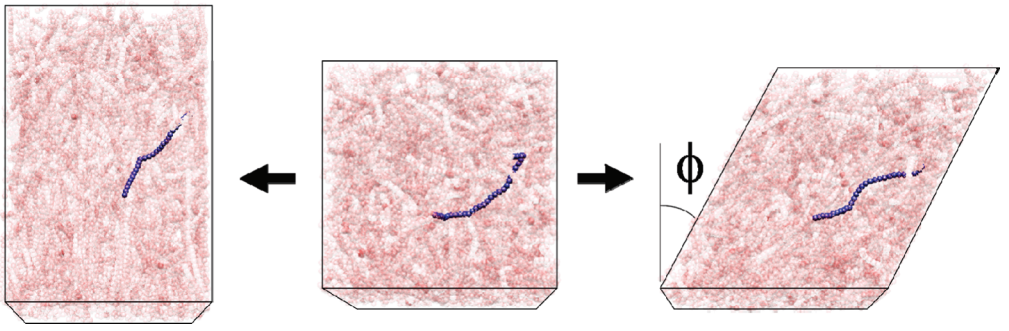

Figure 2. Snapshots of the simulation box of the network deformation at a constant volume. Uniaxial deformation (left) and shear (right).

Table 1. Network Parameters: Shear Modulus G, Chain Elongation Ratio β and Ratio of the Shear Modulus Due to Entanglements G_e to the Shear Modulus G, G_e/G

		experiments		
	system	G	β	G_e/G
1	neurofilaments[4]	1.9283 Pa	0.1182	--
2	collagen[4]	0.0039 Pa	0.9873	--
3	vimentin[4]	0.0582 Pa	0.8988	--
4	fibrin (steady state)[4]	0.1275 Pa	0.9246	--
5	fibrin (oscillatory)[4]	0.5982 Pa	0.8619	--
6	actin[4]	0.0319 Pa	0.9852	--
7	natural rubber[1]	0.198 MPa	0.0294	1.25
8	natural rubber[20]	0.294 MPa	0.0477	--
9	natural rubber[2]	0.356 MPa	0.0438	1.06
10	PPG BisAcAc−EA−HMDI−EA network[3]	0.1084 MPa	0.4056	--
11	PPG BisAcAc−NPGDA network[3]	0.0399 MPa	0.042	0.71
12	SBR[2]	0.187 MPa	0.0255	2.41

		Simulations		
	system	$G \times 10^3[k_BT/\sigma^3]$	β	G_e/G
13	$K = 2$, $N_s = 17.88 \pm 7.4$, uniaxial deformation	7.40	0.198	--
14	$K = 5$, $N_s = 18.03 \pm 6.7$, uniaxial deformation	4.73	0.45	--
15	$K = 10$, $N_s = 17.90 \pm 6.7$, uniaxial deformation	3.04	0.633	--
16	$K = 10$, $N_s = 17.90 \pm 6.7$, shear deformation	3.04	0.654	--
17	$K = 20$, $N_s = 17.98 \pm 6.7$, uniaxial deformation	2.27	0.752	--
18	$K = 20$, $N_s = 17.98 \pm 6.7$, shear deformation	2.27	0.742	--
19	$K = 30$, $N_s = 17.83 \pm 6.6$, uniaxial deformation	2.15	0.791	--
20	$K = 40$, $N_s = 17.99 \pm 6.7$, uniaxial deformation	1.30	0.806	--
21	$K = 40$, $N_s = 17.99 \pm 6.7$, shear deformation	1.30	0.808	--

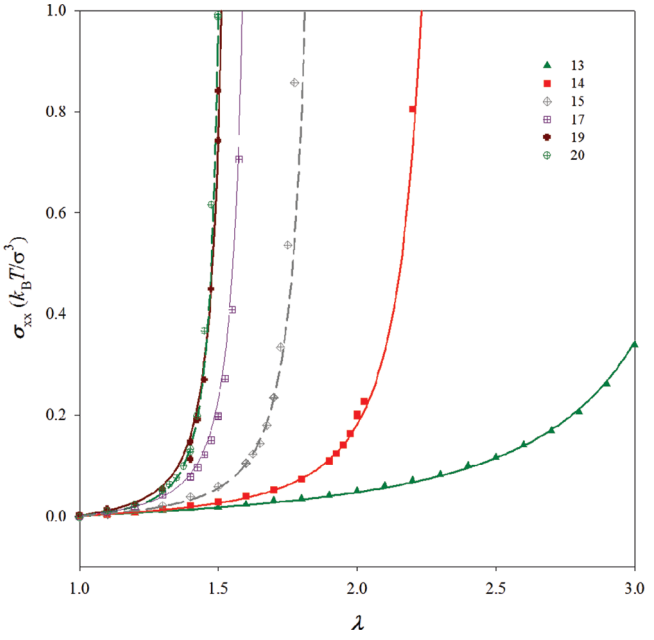

Figure 3. Dependence of the true stress σ_{xx} on the deformation ratio λ for uniaxially deformed networks. Numbers correspond to the networks described in Table 1.

Using eqs 1 and 2 we can introduce a deformation dependent network shear modulus in the case of the uniaxial and shear deformations as

$$G(I_1) \equiv \frac{\sigma_{xx}(\lambda)}{\lambda^2 - \lambda^{-1}} = \frac{G}{3}\left(1 + 2\left(1 - \frac{\beta I_1(\lambda)}{3}\right)^{-2}\right) \qquad (3a)$$

and

$$G(I_1) \equiv \sigma_{xy}(\gamma)/\gamma \qquad (3b)$$

Equations 3a and 3b are the main results of the paper. They are different from the previous theoretical results on nonlinear network elasticity.[1,4,6−10] For the first time, we have been able to derive the invariant expression for the strain-dependent network shear modulus. This modulus is a universal function of the strain invariant I_1 characterizing network deformation and parameter β determining the stretching ability of the strands between cross-links. Thus, biological and polymeric networks and gels should demonstrate similar nonlinear behavior, because molecular specificity of strands forming networks or gels enters the problem through the shear modulus G and chain elongation ratio β.

To illustrate universality in nonlinear network elasticity we plotted reduced network shear modulus $G(I_1)/G$ as a function of the parameter $\beta I_1/3$ for the natural rubber, synthetic and biological networks (Figure 4). We have also included data obtained from computer simulations of the coarse-grained network model with different values of the persistence length. Remarkably, all data sets collapse into one universal line. (Note that for weakly cross-linked networks to obtain the value of the deformation dependent shear modulus we have subtracted entanglement contribution from the network stress, $\sigma_{xx}(\lambda) - \sigma^e_{xx}(\lambda)$ (see Appendix B).) The natural rubber, neurofilament networks and networks modeled in computer simulations can experience large deformations for which the extension ratio λ could be much larger than unity. These networks are made of strands with $\beta \approx \langle R_{in}^2\rangle/R_{max}^2 \ll 1$ such that there are many Kuhn segments per network strand. Note that for these networks the value of the network shear modulus is on the order of k_BT per network strand, $G(3) \equiv G \approx k_BT\rho/N_s$. The data sets for these systems occupy the region on the plot corresponding to the interval $G(I_1)/G \leq 10$ (see Table 1). The data sets covering the interval $G(I_1)/G \geq 10$ correspond to biological networks made of rigid strands (filaments) (see Table 1). For such networks, the strands between cross-links are almost fully stretched $\langle R_{in}^2\rangle \approx R_{max}^2$ ($\beta \approx 1$). The simulation data cover almost the entire interval of the strain-dependent shear modulus and support this observation.

It is important to point out that the deviation from the universal behavior takes place when the shortest strands of the network begin to support majority of the stress. Our simulations show that at such high deformations the bonds belonging to these strands begin to deform. This changes the nature of the network elasticity from

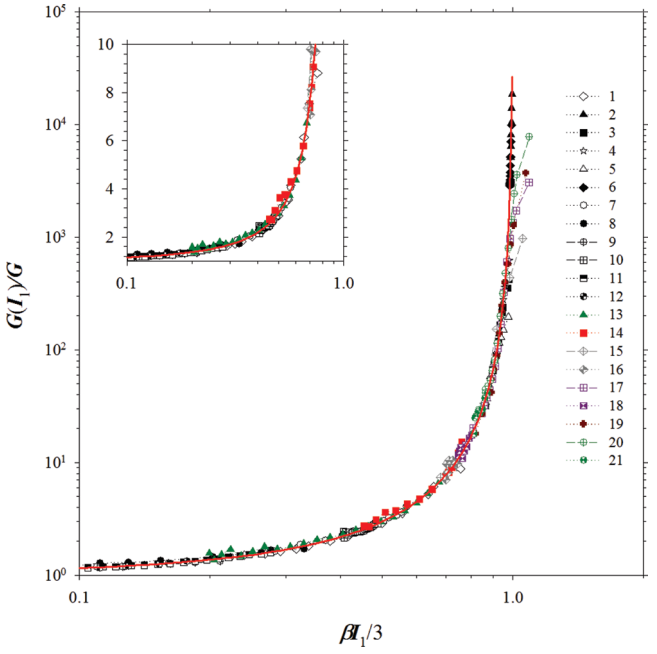

Figure 4. Dependence of the reduced strain dependent shear modulus $G(I_1)/G$ on the parameter $\beta I_1/3$. Numbers correspond to networks described in Table 1 and the solid line corresponds to eq 3.

entropic to enthalpic. Single chain stretching experiments show that a crossover to the bond stretching regime occurs when the pulling forces exceed 40−100 pN.[13,14] This onset of the local forces acting on the network strands should be considered as a crossover between the entropic and enthalpic origin of the network elasticity. Note that in the case of biological networks the crossover from entropic to enthalpic regimes in network elasticity could occur due to overstretching of the protein cross-links connecting network filaments.[22]

The uniqueness of our model of the nonlinear network elasticity is that it relates molecular parameters of the network strands with network nonlinear mechanical response. This is vital for understanding mechanical properties of rubber-like materials,[1] muscles, biological tissues,[4,23,24] cells,[25,26] and blood clots.[27] Furthermore, understanding the mechanism of the nonlinear elasticity of network and gels opens possibility for design of new materials with programmed nonlinear elastic properties. This can have a significant impact on development of synthetic substitutes for biological tissues such as skin, arterial walls, and muscles whose functions require nonlinear elastic response in a particular range of external loads.

To the end we want to comment on the crossover to the nonlinear freely jointed chain deformation regime and range of applicability of our eqs 1−3. For flexible chains this crossover occurs when external forces acting on the polymer chains are on the order of 20−300 pN. In this interval of forces the chain's end-to-end distance is about 70−90% of its fully extended length, $R/R_{\max} \approx 0.7-0.9$. Taking this into account we can estimate a value of the network elongation ratio from the following relationship, $\beta\lambda^2/3 \approx (R/R_{\max})^2 \approx 0.5-0.8$. Thus, for natural rubber samples used in the Treloar's experiments[1] the network extension ratio at the crossover to the nonlinear freely jointed chain deformation regime is on the order of $\lambda \approx 7-9$. These values are close to the largest network deformations studied by Treloar.[1] The majority of the experimental data on deformation of the polymeric networks have covered the range of the network extension ratios, $\lambda < 6$.[1] For such network deformations the deformation dependent network shear modulus can be approximated by the eqs 3a and 3b. Note that one can derive a more general expression for the network deformation by starting from expression for the chain deformation which includes the crossover to the nonlinear freely jointed chain deformation regime (see ref 18). We will consider this approach in our future publications.

Acknowledgment. This research was supported by the National Science Foundation under the grant DMR# 1004576.

Appendix A

Here we use our result for the nonlinear force-deformation relation[19] between applied force f and the average distance between chain ends $\langle R\rangle$ along the direction of the applied force for a worm-like chain with the number of bonds N

$$\frac{f}{k_B T} \approx \frac{\langle R\rangle}{\langle R_0^2\rangle} + \frac{2}{\langle R_0^2\rangle}\frac{\langle R\rangle}{(1-\langle R\rangle^2/R_{\max}^2)^2} \qquad (A.1)$$

where $R_{\max} = bN$ is a length of the fully extended chain with bond length b, $\langle R_0^2\rangle \approx 2l_p R_{\max}$ is the mean-square average end-to-end distance of an ideal chain with the persistence length equal to l_p. We assume that the chain's end-to-end distance R is equal to its average value $\langle R\rangle$ and neglect effect of fluctuations. Note that this approximation improves with increasing the chain deformation when the chain's end-to-end distance becomes on the order of its average value, $R \approx \langle R\rangle$, and the ratio of fluctuations of a chain's end-to-end distance δR to its average value is smaller than unity, $\delta R/\langle R\rangle \ll 1$. In the case of small chain deformations, $R \approx \langle R_0^2\rangle^{1/2}$ and $R/R_{max} \ll 1$, the fluctuations δR can be on the order of $\langle R_0^2\rangle^{1/2}$. In this chain deformation regime, our approximation of the eq A.1 results in an expression for the chain deformation similar to the one obtained from the Flory-like chain's elastic free energy.[5] The dependence of the chain's free energy on the chain end-to-end distance R can be obtained by using the principle of virtual work by considering eq A.1 as an equation describing force-deformation relationship of the nonlinear spring with the spring length R. The chain's free energy is calculated as a work done by stretching a chain (nonlinear spring) by a constant force f pointing along the end-to-end vector $\vec{R}$ by a distance $d\vec{R}$

$$dF = (\vec{f}\cdot d\vec{R}) \approx f(R)\, dR \qquad (A.2)$$

Performing integration over R one obtains

$$\frac{F(R)}{k_B T} \approx \frac{R^2}{2\langle R_0^2\rangle} + \frac{R_{\max}}{2l_p(1-R^2/R_{\max}^2)} \qquad (A.3)$$

Note that in the limit of the small chain deformations, $R/R_{\max} \ll 1$, eq A.3 reproduces the elastic free energy of an ideal chain.[5] Thus, our expression for the chain's free energy eq A.3 can be considered as a generalization of the Flory-like elastic free energy[5] of an ideal chain to the case of large chain deformations.

We will assume that a network is isotropic and cross-links connecting polymeric strands have in average N_s bonds each. In the framework of the affine network model[1,5] each strand deforms affinely ($R_s^x = \lambda_x R_{in}^x$, $R_s^y = \lambda_y R_{in}^y$, $R_s^z = \lambda_y R_{in}^z$) and the free energy of a network is equal to the sum of contributions from strands between cross-links.

$$F_{net}(\{\lambda_i\}) = \sum_s F(R_s) \approx GV\left(\frac{I_1(\{\lambda_i\})}{6} + \beta^{-1}\left(1-\frac{\beta I_1(\{\lambda_i\})}{3}\right)^{-1}\right) \qquad (A.4)$$

where V is the system volume, $I_1(\{\lambda_i\}) = \lambda_x^2 + \lambda_y^2 + \lambda_z^2$ is the first strain invariant of the deformation matrix, $\langle R_{in}^2\rangle$ is the mean-square average end-to-end distance of a strand between cross-links in the undeformed network, $G \approx k_B T\rho\langle R_{in}^2\rangle/\langle R_0^2\rangle N_s$ is the shear modulus of the network with monomer density ρ. $\beta = \langle R_{in}^2\rangle/R_{\max}^2$ is the ratio of the mean-square average distance

between cross-links in the undeformed network and the square of the end-to-end distance of the fully extended strand. This parameter determines how much the polymeric strands between cross-links can be stretched. In deriving expression eq A.4 we have assumed an affine deformation of the network such that $\langle R_s^2\rangle = I_1(\{\lambda_i\})\langle R_{in}^2\rangle/3$ and used a preaveraging approximation substituting $\langle(1/[1-x^2])\rangle$ by $1/(1-\langle x^2\rangle)$. Note that the accuracy of the preaveraging approximation improves when the value of the parameter $x \approx 1$ and $x \ll 1$. In the case $x \approx 1$, the fluctuations δx around the average value are small, $\delta x/\langle x\rangle \ll 1$, such that $\langle x^2\rangle \approx \langle x\rangle^2 \approx x^2$. In the opposite limit, when $x \ll 1$, we can use the following approximation $\langle 1/(1-x^2)\rangle \approx 1 + \langle x^2\rangle \approx 1/(1-\langle x^2\rangle)$. Equation A.4 is the main result of the paper. It allows us to describe elasticity of a network using two parameters: the network shear modulus G and the chain elongation ratio β.

We apply this equation to describe nonlinear stress−strain relation in a network undergoing uniaxial and shear deformations. For the uniaxial deformation at a constant volume, the product of the deformation (elongation) ratios is a constant $\lambda_x\lambda_y\lambda_z = 1$, such that the network extends in one direction while contracts in two others (see Figure 2) resulting in $\lambda_x = \lambda$; $\lambda_y = \lambda_z = 1/\sqrt{\lambda}$.[1,5] The true stress generated in the uniaxially deformed network is equal to

$$\sigma_{xx}(\lambda) = \frac{\lambda}{V}\frac{\partial F_{net}(\lambda)}{\partial\lambda} = \frac{G}{3}(\lambda^2-\lambda^{-1})\left(1+2\left(1-\frac{\beta I_1(\lambda)}{3}\right)^{-2}\right) \quad (A.5)$$

where the first strain invariant for the uniaxially deformed network is $I_1(\lambda) = (\lambda^2+2/\lambda)$. Note that for uniaxial network deformation the magnitude of the true stress is related to the engineering stress as $\sigma_{xx}^{eng} = \sigma_{xx}/\lambda$.[1,5]

For a shear the three principle extension ratios are $\lambda_1 = \lambda$; $\lambda_2 = 1/\lambda$; $\lambda_3 = 1$. It is important to point out that the direction of the principle axes of strain are not related to the direction of shear in any simple way and dependent on the magnitude of the strain. The shear strain γ is equal to $\gamma = \tan\phi = \lambda - \lambda^{-1}$[1] (see Figure 2) and the shear stress generated in the deformed network is equal to

$$\sigma_{xy}(\gamma) = \frac{1}{V}\frac{\partial F_{net}(\gamma)}{\partial\gamma} = \frac{G\gamma}{3}\left(1+2\left(1-\frac{\beta I_1(\gamma)}{3}\right)^{-2}\right) \quad (A.6)$$

where the first strain invariant for the shear deformation is given by $I_1(\gamma) = \gamma^2 + 3$.

Appendix B

The analysis of experimental data presented in Figure B1 shows that we have to modify the expression for the network free energy eq A.4 to include effect of entanglements in the range of small deformation ratios $\lambda < 2$. To account for the entanglements we added the Mooney-Rivlin term[1]

$$F_e \approx \frac{G_e V}{2}(\lambda_1^2\lambda_2^2 + \lambda_1^2\lambda_3^2 + \lambda_2^2\lambda_3^2) \quad (B.1)$$

where G_e is the contribution to the network shear modulus due to entanglements. Note that the Mooney−Rivlin term[1] is one of the possible forms of the correction term to account for the entanglement contribution. The detailed discussion of this subject can be found in refs 5 and 28 and is beyond the scope of this paper. Thus, adding this term to the network free energy eq A.4 we have for the uniaxial network deformation

$$F_{net}(\lambda) \approx GV\left(\frac{I_1(\lambda)}{6} + \beta^{-1}\left(1-\frac{\beta I_1(\lambda)}{3}\right)^{-1}\right) + \frac{G_e V}{2}\left(2\lambda + \frac{1}{\lambda^2}\right) \quad (B.2)$$

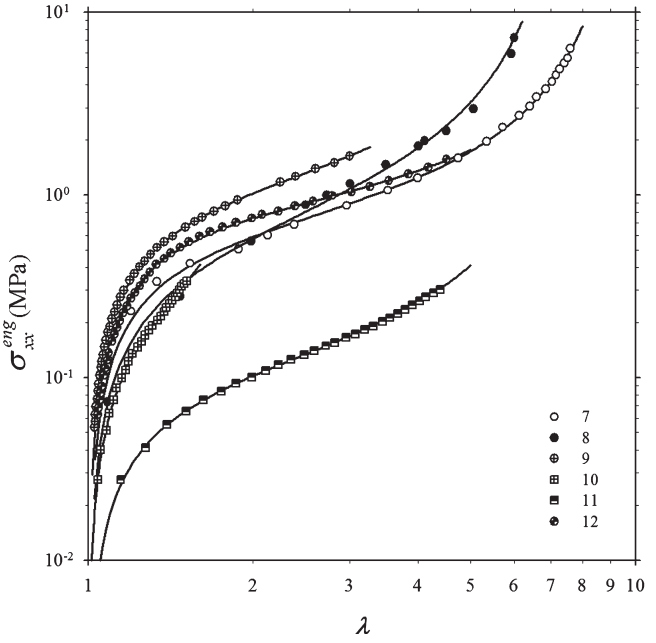

Figure B1. Dependence of the engineering stress σ_{xx}^{eng} on deformation ratio λ for polymeric networks. Numbers correspond to the networks described in Table 1, and the lines are the best fit to eq B.3.

The last expression can be considered as a generalization of the Mooney−Rivlin expression for the network free energy as a function of the first and second strain invariants. The experimental data of the uniaxial network deformation are usually report the value of the engineering stress. The engineering stress is defined as a ratio of the elongation force applied to a sample and the original cross section area of the sample. This leads to

$$\sigma_{xx}^{eng}(\lambda) = \frac{\sigma_{xx}(\lambda)}{\lambda} = \frac{G}{3}\left(\lambda-\frac{1}{\lambda^2}\right)\left(1+\frac{3G_e}{G\lambda}+2\left(1-\frac{\beta}{3}\left(\lambda^2+\frac{2}{\lambda}\right)\right)^{-2}\right) \quad (B.3)$$

We used eq B.3 to fit experimental data for uniaxial network deformation shown in Figure B1. As one can see, the agreement between the experimental data and the expression for the engineering stress is a very good. To extract from the experimental data contribution of the cross-links to the strain-dependent shear modulus $G(I_1)$ presented in Figure 4 we have subtracted from the total stress contribution from entanglements

$$G(I_1) \equiv \frac{\sigma_{xx}^{eng}(I_1)}{(\lambda-\lambda^{-2})} - \frac{G_e}{\lambda} \quad (B.4)$$

Appendix C

We have performed molecular dynamics simulations[21] of deformation of networks of semiflexible chains. Chains forming a network were modeled by bead−spring chains consisting of monomers with diameter σ. The connectivity of beads in polymer chains and the cross-link bonds were maintained by the finite extension nonlinear elastic (FENE) potential[29]

$$U_{FENE}(r) = -0.5k_sR_m^2\ln\left(1-\frac{r^2}{R_m^2}\right) \quad (C.1)$$

where k_s is the spring constant set to $k_s = 500k_BT/\sigma^2$, the maximum bond length is $R_m = 1.5\sigma$, k_B is the Boltzmann constant and T is the absolute temperature. (The large value of the spring constants was selected to minimize the effect of the

bond stretching at large network deformations). The repulsive part of the bond potential was modeled by the shifted Lennard-Jones potential with the values of the Lennard-Jones interaction parameter $\varepsilon_{LJ} = 1.5k_BT$. The chain bending rigidity was introduced into the model through a bending potential controlling the mutual orientations between two neighboring along the polymer backbone unit bond vectors $\vec{n}$ and $\vec{n}_{i+1}$

$$U_{i,i+1}^{bend} = k_B TK(1-(\vec{n}_i \cdot \vec{n}_{i+1})) \quad \text{(C.2)}$$

In our simulations the value of the bending constant K was equal to 2, 5, 10, 20, 30, and 40. For this chain model a chain persistence length l_p is related to the chain's bending constant as $l_p = b(1 + \coth(K) - K^{-1})/2(1 - \coth(K) + K^{-1})$, where $b = 0.8375 \pm 0.010\,\sigma$ is the bond length. (The system parameters are listed in Table C1). We did not have any additional interactions between monomers. This was done to maintain isotropic structure of the network and to avoid a nematic ordering of semiflexible chains.

Simulations were carried out in a constant number of particles, and temperature ensemble. The constant temperature was maintained by coupling the system to a Langevin thermostat implemented in LAMMPS.[29] In this case, the equation of motion of i^{th} bead is

$$m\frac{d\vec{v}_i(t)}{dt} = \vec{F}_i(t) - \xi\vec{v}_i(t) + \vec{F}_i^R(t) \quad \text{(C.3)}$$

where $\vec{v}_i(t)$ is the ith bead velocity, and $\vec{F}_i(t)$ is the net deterministic force acting on ith bead with mass m. $\vec{F}_i^R(t)$ is the stochastic force with zero average value $\langle \vec{F}_i^R(t)\rangle = 0$ and δ-functional correlations $\langle \vec{F}_i^R(t)\vec{F}_i^R(t')\rangle = 6\xi k_B T\delta(t-t')$. The friction coefficient ξ was set to $\xi = m/\tau_{LJ}$, where τ_{LJ} is the standard LJ-time

$$\tau_{LJ} = \sigma\sqrt{m/\varepsilon_{LJ}}$$

The velocity−Verlet algorithm with a time step $\Delta t = 0.005\tau_{LJ}$ was used for integration of the equations of motion (eq C.3). All simulations were performed using LAMMPS.[29]

The networks were prepared by starting with simulations of the 3-D periodic solutions of 96 chains with the degree of polymerizations $N = 200$ at polymer concentration $c = 0.5\sigma^{-3}$. (The initial simulation box size in all simulations was $L_0 = 33.74\sigma$). The systems were equilibrated for 10^7 integration steps. The second step involved cross-linking of polymer solutions. During this procedure neighboring monomers were randomly cross-linked by FENE bonds if they fall within 1.5σ cutoff distance from each other. One cross-link bond was allowed per monomer, thus creating a randomly cross-linked network. To minimize the polydispersity of the strands between cross-links we set the minimum number of bonds between cross-links to be $N_s = 9$. For all networks the cross-linking density was equal to $0.0125\sigma^{-3}$. After completion of the cross-linking process we have eliminated the bending potential between adjacent to the cross-link chain's bonds. Networks were relaxed by performing NVT molecular dynamics simulation runs lasting 10^7 integration steps. This was followed by a production run lasted 10^7 integration steps. During this simulation run we have obtained value of the parameter β by averaging $R_s^2/(N_s b)^2$ for each network strand between cross-links.

In order to obtain stress−strain relation for networks of semiflexible chains we have performed sets of simulations of uniaxial network deformations.[30] The networks were deformed by changing the initial box size L_0 along x direction to λL_0 and to $L_0/\sqrt{\lambda}$ in the y and z directions. Under such deformation the system volume remained the same. This deformation was achieved by a series of small affine deformations

$$\{x_i, y_i, z_i\} \rightarrow \{\Delta\lambda x_i, y_i/\sqrt{\Delta\lambda}, z_i/\sqrt{\Delta\lambda}\}$$

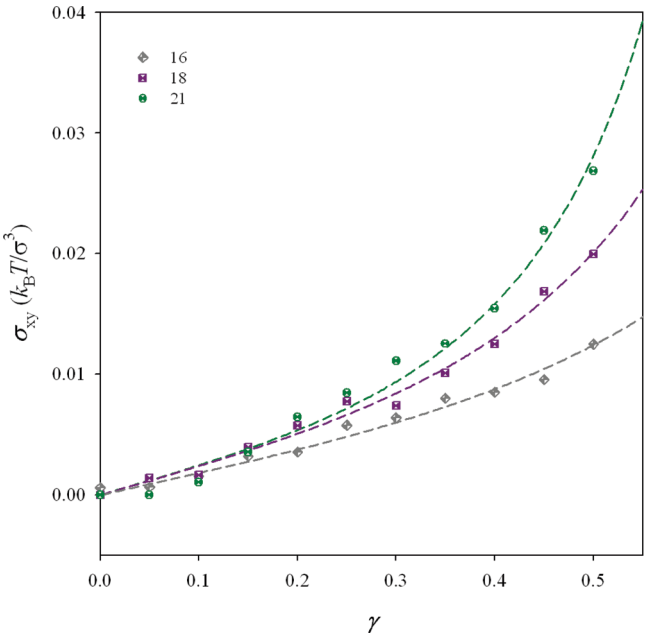

Figure C1. Dependence of the shear stress σ_{xy} on shear strain γ. Numbers correspond to networks described in Table 1.

until the desired strain was obtained. The molecular dynamics simulation proceeded during the constant-volume deformation process such that the network was allowed to adjust its conformations for 10^7 integration steps. The final 5×10^6 integration steps we used for the data averaging. The stress σ_{xx} in the direction of the strain was evaluated from the simulations through the pressure tensor P_{ij} as follows

$$\sigma_{xx} = \frac{3}{2}P_{xx} - \frac{1}{2}\sum_i P_{ii} \quad \text{(C.4)}$$

Figure 3 presents our simulation results for uniaxial network deformation.

In addition to uniaxial network deformation we have also performed simulations of networks undergoing shear deformation. The stress−strain curves for this type of the network deformation are shown in Figure C1. The lines correspond to the best fits to the following equation

$$\sigma_{xy}(\gamma) = \frac{G\gamma}{3}\left(1 + 2\left(1 - \frac{\beta}{3}(\gamma^2+3)\right)^{-2}\right) \quad \text{(C.5)}$$

Note that we only fitted the values of the chain size ratio β while the values of the shear modulus G were set to the values obtained from fitting data sets of corresponding uniaxially deformed networks.

We can use computer simulation results to test a scaling dependence of the network shear modulus on the system parameters (see Appendix A).

$$G \approx k_B T\rho\frac{\langle R_{in}^2\rangle}{\langle R_0^2\rangle N_s} \approx k_B T\rho\beta\frac{b}{b_K} \quad \text{(C.6)}$$

In simplifying the last equation we take into account that $\langle R_{in}^2\rangle \approx \beta R_{max}^2 \approx \beta b^2 N_s^2$, and $\langle R_0^2\rangle \approx b_k R_{max}$, where b_K is the Kuhn length, $b_K = 2l_p$. It follows from eq C.6 that the reduced network shear modulus $G/(k_BT\rho\beta)$ is proportional to the ratio of the bond length to the Kuhn length, b/b_K. Before proceeding further we have to point out that not all network strands support stress.[1,5] The dangling ends, connected to the network by only one end, should be excluded. The effect of the dangling ends is particularly important for networks prepared by cross-linking short polymer

Table C1. System Parameters

l_p [σ]	K [k_BT]	N_s	β_{sim}	$\beta_{fit\text{-}U}$ ($\beta_{fit\text{-}S}$)
1.391	2	17.88 ± 7.4	0.177 ± 0.130	0.198
3.771	5	18.03 ± 6.7	0.368 ± 0.181	0.450
7.956	10	17.90 ± 6.7	0.545 ± 0.175	0.633 (0.654)
16.331	20	17.98 ± 6.7	0.681 ± 0.150	0.752 (0.742)
24.706	30	17.83 ± 6.6	0.735 ± 0.141	0.791
33.081	40	17.99 ± 6.7	0.761 ± 0.144	0.806 (0.808)

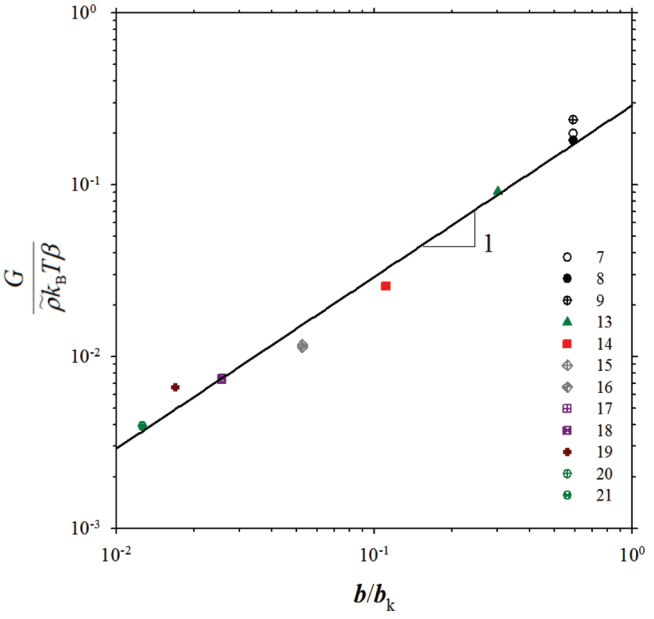

Figure C2. Dependence of the reduced shear modulus on the ratio of the bond length b to the Kuhn length b_K. Numbers correspond to networks described in Table 1.

chains. In our simulations we have prepared networks by cross-linking chains with the number of monomers $N = 200$. After cross-linking each chain has in average N/N_s network strands and two of those strands are dangling ends. Thus, the actual monomer density of the network strands that support stress is equal to

$$\tilde{\rho} \approx N_s \frac{\rho}{N}\left(\frac{N}{N_s} - 2\right) \approx \rho\left(1 - \frac{2N_s}{N}\right) \qquad (C.7)$$

The effect of the dangling ends diminishes with decreasing the ratio N_s/N.

In Figure C2, we plot the reduced network shear modulus $G/(k_BT\beta\tilde{\rho})$ as a function of b/b_K. Our simulations show that the network shear modulus decreases with increasing the chain rigidity or chain Kuhn length, $G/(k_BT\beta\tilde{\rho}) \propto b/b_K$. In addition to simulation data, we have also added to this plot data points corresponding to natural rubber. For these data, we used for the bond length $b = 0.484$ nm (this value corresponds to the total length of all four bonds of the monomeric unit of the 1,4-poly-isoprene along the chain axis in the ground state), for the Kuhn length $b_K = 0.82$ nm,[5] and for the density of the natural rubber 0.93 g/cm^3. For these networks we did not correct for the effect of the dangling ends, $\rho = \tilde{\rho}$. The simulation data are in a good agreement with experimental results for natural rubber.

References and Notes

(1) Treloar, L. R. G., *The Physics of Rubber Elasticity*; Clarendon Press: Oxford, U.K., 2005.

(2) Becker, G. W.; Kruger, O. On the nonlinear biaxial stress-strain behavior of rubberlike polymers. In *Deformation and Fracture of High Polymers*; Kausch, H. H., Hessell, J. A., Jaffee, R. I., Eds. Plenum Press: New York, 1972.

(3) Williams, S. R.; Mather, B. D.; Miller, K. M.; Long, T. E. Novel michael addition networks containing urethane hydrogen bonding. *J. Polym. Sci. A* **2007**, *45* (17), 4118–4128.

(4) Storm, C.; Pastore, J. J.; MacKintosh, F. C.; Lubensky, T. C.; Janmey, P. A. Nonlinear elasticity in biological gels. *Nature* **2005**, *435* (7039), 191–194.

(5) Rubinstein, M.; Colby, R. H. *Polymer Physics*; Oxford University Press: New York, 2003.

(6) MacKintosh, F. C. Elasticity and dynamics of cytoskeletal filaments and their networks. In *Soft condensed matter physics in molecular and cell biology*; Poon, W. C. K., Andelman, D., Eds.; Taylor & Francis: New York, 2006; pp 139−155.

(7) Kroy, K. Elasticity, dynamics and relaxation in biopolymer networks. *Curr. Opin. Colloid Interface Sci.* **2006**, *11* (1), 56–64.

(8) Heussinger, C.; Schaefer, B.; Frey, E. Nonaffine rubber elasticity for stiff polymer networks. *Phys. Rev. E* **2007**, *76* (3), 031906.

(9) Conti, E.; MacKintosh, F. C. Cross-Linked Networks of Stiff Filaments Exhibit Negative Normal Stress. *Phys. Rev. Lett.* **2009**, *102* (8), 088102.

(10) Onck, P. R.; Koeman, T.; van Dillen, T.; van der Giessen, E. Alternative explanation of stiffening in cross-linked semiflexible networks. *Phys. Rev. Lett.* **2005**, *95* (17), 178102.

(11) Marko, J. F.; Siggia, E. D. Stretching DNA. *Macromolecules* **1995**, *28* (26), 8759–8770.

(12) Smit, S. B.; Cui, Y. J.; Bustamante, C. Overstretching B-DNA: The elastic response of individual double-stranded and single-stranded DNA molecules. *Science* **1996**, *271*, 795–799.

(13) Bustamante, C.; Smith, S. B.; Liphardt, J.; Smith, D. Single-molecule studies of DNA mechanics. *Curr. Opin. Struct. Biol.* **2000**, *10* (3), 279–285.

(14) Williams, M. C.; Rouzina, I. Force spectroscopy of single DNA and RNA molecules. *Curr. Opin. Struct. Biol.* **2002**, *12* (3), 330–336.

(15) Toan, N. M.; Thirumalai, D. Theory of biopolymer stretching at high force. *Macromolecules* **2010**, *43*, 4394–4400.

(16) Rosa, A.; Hoang, T. X.; Marenduzzo, D.; Maritan, A. Elasticity of semiflexible polymers with and without self-interactions. *Macromolecules* **2003**, *36*, 10095–10102.

(17) Livadaru, L.; Netz, R. R.; Kreuzer, H. J. Stretching response of discrete semiflexible polymers. *Macromolecules* **2003**, *36*, 3732–3744.

(18) Dobrynin, A. V.; Carrillo, J.-M. Y.; Rubinstein, M. Chains are more flexible under tension. *Macromolecules* **2010**, *43*, 9181–9190.

(19) Carrillo, J.-M. Y.; Dobrynin, A. V. Effect of the electrostatic interactions on stretching of semiflexible and biological polyelectrolytes. *Macromolecules* **2010**, *43*, 2589–2604.

(20) Pechhold, W. Deformation of polymers as explained by the meander model. In *Deformation and Fracture of High Polymers*; Kausch, H. H., Hessell, J. A., Jaffee, R. I., Eds.; Plenum: New York, 1972; pp 301−315.

(21) Frenkel, D.; Smit, B., *Understanding Molecular Simulations*; Academic Press: New York, 2002.

(22) Kasza, K. E.; Koenderink, G. H.; Lin, Y. C.; Broedersz, C. P.; Messner, W.; Nakamura, F.; Stossel, T. P.; MacKintosh, F. C.; Weitz, D. A. Nonlinear elasticity of stiff biopolymers connected by flexible linkers. *Phys. Rev. E* **2009**, *79*, 041928.

(23) Janmey, P. A.; McCormick, M. E.; Rammensee, S.; Leight, J. L.; Georges, P. C.; Mackintosh, F. C. Negative normal stress in semiflexible biopolymer gels. *Nat. Mater.* **2007**, *6* (1), 48–51.

(24) Kang, H.; Wen, Q.; Janmey, P. A.; Tang, J. X.; Conti, E.; MacKintosh, F. C. Nonlinear Elasticity of Stiff Filament Networks: Strain Stiffening, Negative Normal Stress, and Filament Alignment in Fibrin Gels *J. Phys. Chem. B* **2009**, *113* (12), 3799–3805.

(25) Gardel, M. L.; Kasza, K. E.; Brangwynne, C. P.; Liu, J. Y.; Weitz, D. A. Mechanical Response of Cytoskeletal Networks. In *Biophysical Tools for Biologists, Vol. 2: In Vivo Techniques*; 2008; Vol. *89*, p 487.

(26) Kasza, K. E.; Rowat, A. C.; Liu, J. Y.; Angelini, T. E.; Brangwynne, C. P.; Koenderink, G. H.; Weitz, D. A. The cell as a material *Curr. Opin. Cell Biol.* **2007**, *19* (1), 101–107.

(27) Weisel, J. W. Biophysics - Enigmas of blood clot elasticity. *Science* **2008**, *320* (5875), 456–457.

(28) Rubinstein, M.; Panyukov, S. Elasticity of polymer networks. *Macromolecules* **2002**, *35*, 6670–6686.

(29) Plimpton, S. J. Fast parallel algorithms for short-range molecular dynamics. *J. Comput. Phys.* **1995**, *117*, 1–19; lammps.sandia.gov .

(30) Grest, G. S.; Putz, M.; Everaers, R.; Kremer, K. Stress-strain relation of entangled polymer networks. *J. Non-Cryst. Solids* **2000**, *274* (1−3), 139–146.

Macromolecules
ARTICLE

Macromolecules **2011**, *44*, 147–158 **147**
DOI: 10.1021/ma102312y

Molecular Theory of Weak Polyelectrolyte Gels: The Role of pH and Salt Concentration

Gabriel S. Longo,[†,‡,§] Monica Olvera de la Cruz,*[,†,∥,‡,§] and I. Szleifer*[,⊥,‡,∥,§]

[†]*Department of Materials Science and Engineering,* [‡]*Department of Chemistry,* [§]*Chemistry of Life Processes Institute,* [∥]*Department of Chemical and Biological Engineering, and* [⊥]*Department of Biomedical Engineering, Northwestern University, Evanston, Illinois 60208, United States*

Received October 9, 2010; Revised Manuscript Received November 24, 2010

ABSTRACT: We develop a detailed molecular theory that describes the response of weak polyelectrolyte gels to changes in both the pH and salt concentration, c, of the solution. This approach includes specific molecular details and conformational degrees of freedom of the polymeric gel, acid−base equilibrium, and solution entropy as well as electrostatic, van der Waals, and excluded-volume interactions. Here, we study polyacid gels in good solvent. The physical properties of the gel are found to depend on the coupling between charge regulation and the molecular interactions. In particular, the gel's degree of dissociation is not only determined by the bath pH and ionic strength but also by the polymer's ability in regulating charge to modify the local environment and in swelling or shrinking that depends on the externally controlled variables. The gel pH can be several units smaller than the bath pH depending on the salt ion concentration. The gel pH does not respond linearly to changes in neither bath pH nor c, and its behavior results from the complex interplay between the conformational degrees of freedom and all of the interactions mentioned above. The gel system swells if pH > pK_a and collapses if pH < pK_a. The continuous transition between collapsed and swollen regimes occurs in a very narrow range of bath pH around pK_a whose width depends on the salt concentration. In this intermediate region the volume fraction of the polyacid can be controlled by both c and pH.

1. Introduction

Charged gels undergo large volume changes induced by external stimuli that include changes of temperature and/or osmotic pressure variations[1−3] and electric field.[4] Because of their large deformations and fast responses to external stimuli, hydrogels of charged chains have generated great interest for potential applications such as microactuators,[5] muscle-like actuators,[6−8] and filtration/separation[9] and microfluidic[10] devices. Moreover, it has been argued that hydrogels have structures and properties that resemble biological tissues[11,12] and biological networks.[13,14] Indeed, nucleoids of bacteria such as *E. coli*[15] and mitotic chromosomes have been described to show many of the physical[16] and mechanical[17] properties of hydrogels: these biological networks undergo large salt-induced volume changes.[18] In addition, mammalian cytoplasm responds to extracellular pH resembling the physical behavior of hydrogels, having the ability to absorb large quantities of water and modify its volume manyfold.[19]

There are two types of polyelectrolytes: strong and weak polyelectrolytes. The acid (basic) groups of strong polyelectrolytes are deprotonated (protonated) in the typical range of pH values. Therefore, they have charge densities that are nearly insensitive to pH changes; their volume and thermodynamics are controlled by the salt concentration and the valency of the salt in a rather universal way.[20−23] This group includes nucleic acids and polystyrenesulfonate. In the presence of gelling molecules, such as proteins capable of hydrogen bonding to their backbone, they can also form gels.[24−27] The physical properties of strong polyelectrolyte gels, including swelling, have been previously analyzed mainly using linear-response theory.[28−30] In addition, simulations have been used to analyze gels of charged chains in different solvent conditions[31,32] that includes the case of multivalent ions presence.[33]

On the other hand, the state of charge of polyacids or polybases depends more strongly on the acid−base equilibrium. These polymers are often referred to as weak polyelectrolytes. In weak polyelectrolyte chains, not only the salt concentration but also the pH controls the effective charge of the chains,[34] i.e., the fraction of chain monomers whose acid (basic) groups are dissociated or degree of dissociation, f_d. Salt-free solutions of weak polyelectrolytes[35] and grafted layers of polyacids[36−38] have been theoretically studied before. In many applications, gels of weak polyelectrolyte chains are preferred. These gels are ubiquotous in nature and can be formed, for example, using triblock copolymers with associating end groups.[1] If the chain ends undergo thermoreversible reactions with the ends of other chains, charged gels that are highly regular are formed.[39] In this work, we analyze permanently cross-linked chains that form regular gels as a function of their degree of ionization; we assume the backbone is in good-solvent conditions.

There are various competing physicochemical interactions that determine the size of weak polyelectrolyte gels. The acid−base equilibrium must be established inside the gel under the constraint of fixed chemical potential of the protons given by the bath solution in contact with the gel. Charge dissociation is favored by an entropy increase in production of charged groups. However, the charge present on the chain backbone swells the gel and consequently decreases the entropy of the chains. Moreover, ions are required to cancel the charge of the chains, which generate a strong penalty to charge dissociation. These competitions determine the charge and size of the swollen gel: charge dissociation of the chains favors homogeneous mixing of hydrated counterions and of swollen charged chains. The macroscopic shrinking of the gel occurs when the charge of the chains is screened by salt and/or

*To whom correspondence should be addressed. E-mail: m-olvera@northwestern.edu (M.O.d.l.C.); igal@northwestern.edu (I.S.).

© 2010 American Chemical Society

Published on Web 12/13/2010

pH changes, such that the degree of dissociation is negligible. In present paper, we develop a theory to determine how the equilibrium conformation of weak polyelectrolyte hydrogels changes in response to external stimuli. The contributions to the free energy of the acid−base equilibrium, the solution mixing entropy, the steric repulsions, the van der Waals attractions, and the conformational degrees of freedom of the gel molecule are all explicitly included. In addition, starting from the electrostatic energy, we derive a generalized nonlinear Poisson−Boltzmann equation whose solution provides the electrostatic potential. In this theoretical approach, the thermodynamic equilibrium is determined by the coupling between all of these contributions. We ask the question of how the thermodynamic equilibrium of the hydrogel changes as a consequence of externally fixing the pH and ionic salt concentration of the outer bath solution in equilibrium with the gel.

This work is organized as follows: In section 2, the general molecular-level theory is introduced, while the molecular model used to evaluate the approach is presented in section 3. Then, in section 4, the behavior of the polyacid gel, whose total number of cross-links is independent of its density, in good solvent is described using results obtained with our general theoretical method. Finally, concluding remarks and directions for future work are presented in the last section.

2. Theoretical Approach

Consider a weak polyelectrolyte gel (G) with n_G monomer units in a solution containing water (w), protons (H^+), hydroxyl ions (OH^-), and completely dissociated salt, resulting in the presence of anions (−) and cations (+). Each monomer has one acid group that can be either protonated (AH) or deprotonated (A^-). Namely, we are considering a polyacid such as poly(acrylic acid). This system is in equilibrium with a homogeneous solution that provides a bath for all of the free species whose chemical potentials are determined by the bath pH and salt concentration, c. Our approach to this problem consists of defining a detailed molecular-level theory,[37,38] which is described in the following.

First, we write the free energy of the system, which explicitly includes the conformational entropy of the flexible gel molecule, the mixing entropy of the different free species in the solution, the repulsive excluded volume interactions as well as the attractive van der Waals interactions, the chemical equilibrium resulting from the acid−base reaction, and the electrostatic interactions due to both charged free species and dissociated acid groups in the gel monomers. This free energy is expressed as a functional of the probability of the different molecular conformations of the gel, the local density distribution of the mobile species in the solution, the gel degree of dissociation, and the electrostatic field. Then, this free energy is optimized with respect to those functions subject to two constraints: the incompressibility constraint, which accounts for the intermolecular repulsions, and the global electroneutrality constraint, which requires the total charge of the system be zero. Finally, any thermodynamic quantity of interest can be computed after all these functions are determined by taking the proper derivative of the minimized thermodynamic potential.

In this framework, the total Helmholtz free energy of the system can be expressed as

$$F = -TS_{conf} - TS_{mix} + U_{vdw} + F_{chm} + U_{elec} \qquad (1)$$

where T is the temperature and S_{conf}, S_{mix}, U_{vdw}, F_{chm}, and U_{elec} denote the configurational entropy of the gel, mixing entropy of the free species, van der Waals interaction energy, chemical free energy associated with the acid−base equilibrium, and electrostatic interaction energy arising from charged species, respectively. The conformational entropy of the gel is given by

$$-\frac{S_{conf}}{k_B} = \sum_{\alpha} P(\alpha)\ln(P(\alpha))$$

where $P(\alpha)$ is the probability of finding the gel in conformation α. A conformation denotes a given spatial distribution of all the monomers of the gel.

The mixing (translational) entropy of the free species within the hydrogel is

$$-\frac{S_{mix}}{k_B} = \sum_{\gamma}\int d^3r\,\rho_\gamma(\mathbf{r})[\ln(\rho_\gamma(\mathbf{r})v_w) - 1]$$
$$(\gamma = w, +, -, H^+, OH^-)$$

where v_w is the volume of a solvent molecule and $\rho_w(\mathbf{r})$, $\rho_+(\mathbf{r})$, $\rho_-(\mathbf{r})$, $\rho_{H^+}(\mathbf{r})$, and $\rho_{OH^-}(\mathbf{r})$ are the local number density of the different mobile species in the solution.

The total van der Waals attractive energy between gel monomers can be written as

$$\beta U_{vdw} = \sum_{\alpha} P(\alpha)\beta U_{vdw}(\alpha) = \frac{1}{2}\sum_{\alpha} P(\alpha)\sum_{i,j}\beta u_{mm}(r_{ij}^{\alpha})$$

where $\beta = 1/k_BT$ and $u_{mm}(r_{ij}^{\alpha})$ is the pairwise attractive interaction between monomers i and j: in configuration α, these two monomers are a distance r_{ij}^{α} apart, and $U_{vdw}(\alpha) = {}^1/_2\sum_{i,j}u_{mm}(r_{ij}^{\alpha})$ is the total van der Waals energy of the gel in that conformation. Note that this expression considers the exact van der Walls attractive energy of the gel.

On the other hand, the repulsive interactions are separated into intramolecular and intermolecular. The intramolecular repulsions are exactly taken into account through the gel conformations which are self-avoiding while the intermolecular ones are included in an approximate fashion through the use of local packing (incompressibility) constraints.

The free energy term describing the chemical reactions takes into account the acid−base equilibrium ($AH \rightleftharpoons A^- + H^+$) as follows:

$$\beta F_{chm} = \int d^3r\frac{\langle\phi_G(\mathbf{r})\rangle}{v_G}f_d(\mathbf{r})(\ln f_d(\mathbf{r}) + \beta\mu^0_{A^-})$$
$$+ \int d^3r\frac{\langle\phi_G(\mathbf{r})\rangle}{v_G}(1-f_d(\mathbf{r}))[\ln(1-f_d(\mathbf{r})) + \beta\mu^0_{AH}]$$
$$+ \int d^3r(\rho_{OH^-}(\mathbf{r})\beta\mu^0_{OH^-} + \rho_{H^+}(\mathbf{r})\beta\mu^0_{H^+})$$

where $\phi_G(\alpha,\mathbf{r})$ is the local volume fraction of gel in conformation α at $\mathbf{r}$, and $\langle\phi_G(\mathbf{r})\rangle = \sum_\alpha P(\alpha)\phi_G(\alpha,\mathbf{r})$. The quantity $\langle\,\rangle$ represents the ensemble average over the set of configurations $\{\alpha\}$. The volume of a gel segment is v_G, and $\langle\phi_G(\mathbf{r})\rangle/v_G$ is the average local polymer number density. The quantity $f_d(\mathbf{r})$ is the local degree of dissociation, which gives the fraction of monomers that are charged in the element of volume between $\mathbf{r}$ and $\mathbf{r} + d\mathbf{r}$. The quantities ${\mu_{A^-}}^0$ and μ^0_{AH} are the standard chemical potentials of charged and uncharged monomers, respectively. In addition, ${\mu_{H^+}}^0$ and ${\mu_{OH^-}}^0$ are respectively the standard chemical potentials of protons and hydroxyl ions which are needed since we explicitly consider the self-ionization of water ($H_2O \rightleftharpoons OH^- + H^+$).

The electrostatic energy term in eq 1 is given by

$$\beta U_{elec} = \int d^3r\left[\langle\rho_q(\mathbf{r})\rangle\beta\Psi(\mathbf{r}) - \frac{1}{2}\beta\varepsilon(\mathbf{r})(\nabla\Psi(\mathbf{r}))^2\right]$$

where $\Psi(\mathbf{r})$ is the electrostatic potential, $\varepsilon(\mathbf{r})$ denotes the dielectric permittivity of the medium at $\mathbf{r}$, and $\langle\rho_q(\mathbf{r})\rangle$ is the ensemble average total charge at $\mathbf{r}$ which is given by

$$\langle\rho_q(\mathbf{r})\rangle = f_d(\mathbf{r})\frac{\langle\phi_G(\mathbf{r})\rangle}{v_G}q_G + \sum_\gamma \rho_\gamma(\mathbf{r})q_\gamma \quad (\gamma = +, -, H^+, OH^-)$$

The quantity q_G in the total charge density represents the electric charge of the deprotonated gel monomer, while q_+, q_-, q_{H^+}, and q_{OH^-} denote the electric charge of the various charged free species.

To the above total free energy of the gel system, we now impose two physical constraints: the incompressibility constraint that accounts for the intermolecular repulsions (excluded volume) in the system. Namely, at each position $\mathbf{r}$ the total volume must be completely filled by some of the molecular species, i.e.

$$1 = \langle\phi_G(\mathbf{r})\rangle + \sum_\gamma \rho_\gamma(\mathbf{r})v_\gamma \quad (\gamma = w, +, -, H^+, OH^-) \quad (2)$$

where v_+, v_-, v_{H^+}, and v_{OH^-} are the volume of the corresponding molecules. In addition, we require the system to be globally electroneutral, i.e.

$$\int d^3r\langle\rho_q(\mathbf{r})\rangle = 0 \quad (3)$$

In total, the unknowns in eq 1 consist of the probability density function, $P(\alpha)$, the free species local densities, $\rho_\gamma(\mathbf{r})$ (γ = w, −, +, H^+, OH^-), the local degree of dissociation, $f_d(\mathbf{r})$, and the electrostatic potential, $\Psi(\mathbf{r})$. To obtain these quantities, a functional minimization of the free energy with respect to each of these variables is performed, subject to the two aforementioned constraints. Once these functions are obtained, any thermodynamic quantity can be derived in a straightforward manner.

The explicit function to minimize is

$$\begin{aligned}\beta F = {} & \sum_\alpha P(\alpha)[\ln(P(\alpha)) + \beta U_{vdw}(\alpha)] \\ & + \sum_{\gamma = w, +, -, H^+, OH^-} \int d^3r\rho_\gamma(\mathbf{r})[\ln(\rho_\gamma(\mathbf{r})v_w) - 1] \\ & + \int d^3r\frac{\langle\phi_G(\mathbf{r})\rangle}{v_G}f_d(\mathbf{r})(\ln f_d(\mathbf{r}) + \beta\mu^0_{A^-}) \\ & + \int d^3r\frac{\langle\phi_G(\mathbf{r})\rangle}{v_G}(1 - f_d(\mathbf{r}))[\ln(1 - f_d(\mathbf{r})) + \beta\mu^0_{AH}] \\ & + \int d^3r(\rho_{OH^-}(\mathbf{r})\beta\mu^0_{OH^-} + \rho_{H^+}(\mathbf{r})\beta\mu^0_{H^+}) \\ & + \int d^3r\left[\langle\rho_q(\mathbf{r})\rangle\beta\Psi(\mathbf{r}) - \frac{1}{2}\beta\varepsilon(\mathbf{r})(\nabla\Psi(\mathbf{r}))^2\right] \end{aligned} \quad (4)$$

Minimization subject to the constraints leads to

$$\begin{aligned}\rho_w(\mathbf{r}) &= \frac{1}{v_w}\exp(-\beta\pi(\mathbf{r})v_w) \\ \rho_\gamma(\mathbf{r}) &= \frac{\rho_\gamma{}^{hm}}{(v_w\rho_w{}^{hm})^{v_\gamma/v_w}}\exp(-\beta\pi(\mathbf{r})v_\gamma - \beta\Psi(\mathbf{r})q_\gamma) \\ & \quad (\gamma = H^+, OH^-, +, -)\end{aligned} \quad (5)$$

for the mobile species where $\pi(\mathbf{r})$ are the local Lagrange multipliers conjugated with the packing constraint, eq 2, at each point in space. ρ_γ^{hm} (γ = w,+, −, H^+, OH^-) is the density of free species γ in the homogeneous bath solution. These quantities are input constants that depend only on bath pH and c and appear since we require the free species to have a constant chemical potential which must be that of the bath solution. Moreover, the probability of a gel conformation α is given by

$$\begin{aligned}P(\alpha) = {} & \frac{1}{Q}\exp(-\beta U_{vdw}(\alpha) \\ & - \int d^3r\phi_G(\mathbf{r},\alpha)\beta\pi(\mathbf{r}))\exp\left[-\int d^3r\frac{\phi_G(\mathbf{r},\alpha)}{v_G}(\beta\Psi(\mathbf{r})q_G + \ln f_d(\mathbf{r}))\right]\end{aligned} \quad (6)$$

where the factor Q imposes $\sum_\alpha P(\alpha) = 1$. The functional form of the probability density function shows the very strong coupling expected between the physical interactions in the system, the gel conformation, and the local degree of dissociation. The manifestation of this coupling will be discussed in the next section together with the presentation of the results. The local degree of dissociation, $f_d(\mathbf{r})$, that minimizes the free energy functional, after algebraic manipulation, is given by

$$\frac{f_d(\mathbf{r})}{1 - f_d(\mathbf{r})} = \frac{K_a^0}{v_w\rho_{H^+}^{hm}}(v_w\rho_w^{hm})^{v_{H^+}/v_w}\exp(-\beta\Psi(\mathbf{r})q_G) \quad (7)$$

where K_a^0 is the dimensionless standard equilibrium constant, which is proportional to the standard equilibrium constant of the acid−base reaction, K_a, expressed in molar units, and defined by

$$K_a = \frac{[A^-][H^+]}{[AH]} \quad (8)$$

The standard chemical potentials of the protons and the hydroxyl ions can be expressed in terms of the densities of the free species in the homogeneous bath (see section A of the Appendix), and the standard chemical potential of the ionized acid groups is obtained using $K_a^0 = \exp(\beta\mu^0_{AH} - \beta\mu_{H^+}{}^0 - \beta\mu_{A^-}{}^0)$.

Furthermore, the variation of the free energy with respect to the electrostatic potential results in the Poisson equation:

$$\varepsilon\nabla^2\Psi(\mathbf{r}) = -\langle\rho_q(\mathbf{r})\rangle \quad (9)$$

where it is clear the strong coupling that exists between the electrostatic potential and all the other degrees of freedom and the chemical equilibrium through the average of the local charge density.

The unknowns left after minimization of the free energy are the Lagrange multipliers, $\pi(\mathbf{r})$, and the electrostatic potential, $\Psi(\mathbf{r})$, which are obtained by solving, at each position, the packing constraint, eq 2, and the Poisson equation, eq 9, respectively. The pH and salt concentration are input variables of the molecular theory and determine bath densities of the free species. Moreover, a molecular model of the polyelectrolyte gel must be defined to obtain the set of gel conformations needed to calculate results using this theory. We introduce the molecular model used in this work in the next section. Further details on the molecular theory of the polyelectrolyte gel are presented in section A of the Appendix.

3. Molecular Model

As an initial approach to the problem, a simple model of polyelectrolyte (PE) gel molecule is considered (see Figure 1). The gel is modeled as monodisperse chains connected at nodal monomers. Each chain has 25 segments excluding the nodes. In the calculations, a cubic box of volume V is considered, and periodic boundary conditions are imposed. There are 64 nodes in

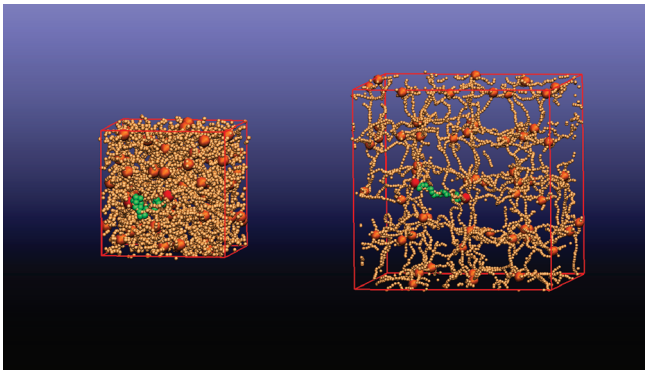

Figure 1. Molecular model of the polyelectrolyte gel at two different volume fractions, $\phi_G = 0.095$ (left) and $\phi_G = 0.013$ (right). Nodes are represented by larger spheres, and one chain is shown in a different color (for illustration purposes only).

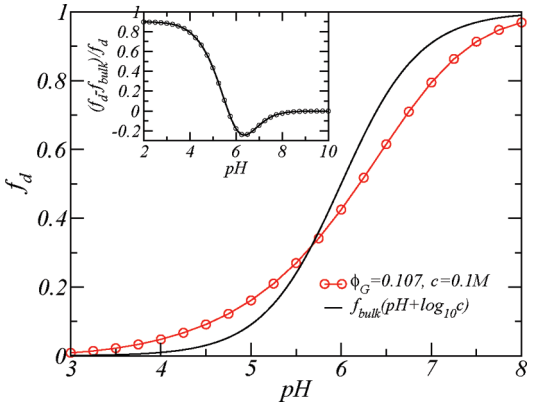

Figure 2. Our results (open red circles) are compared to the bulk degree of dissociation, f_{bulk}, including the correction for Donnan effect (black curve). The relative difference between the curves, $(f_d - f_{bulk})/f_d$, is shown in the inset as a function of pH.

the calculation box, each connected to six chains. Thus, the total number of monomers in the box is $n = 64 + 64 \times 6/2 \times 25 = 4864$. All monomers, including the nodes, are set to have the same volume, v_G. As such, the global gel volume fraction is given by $\phi_G = (1/V)\int d^3r\langle\phi_G(\mathbf{r})\rangle = n(v_G/V)$. Different box sizes with box length between 9.84 and 25.87 nm (ϕ_G between 0.334 and 0.0184) were considered. The system size is chosen as large as possible to reduce box size effects but still allow the computation of our results. For each volume fraction, a large set ($\sim 10^4$) conformations are generated using molecular dynamics simulations whose technical details are presented in section C of the Appendix.

The PE gel is taken under good solvent conditions, which is modeled by selecting $u_{mm} \equiv 0$. The monomer segment length is taken as $l_G = 0.5$ nm, its volume $v_G = (\pi/6){l_G}^3 = 0.0655$ nm^3, and its charge either zero or $q_G = -e$, with e being the absolute value of the electron charge. The acid−base equilibrium constant is taken $pK_a = 5$.

The water dissociation equilibrium constant is $pK_w = 14$. The aqueous medium is assumed to have a homogeneous dielectric constant, $\varepsilon(\mathbf{r}) \equiv \varepsilon_w\varepsilon_0$, with $\varepsilon_w = 80$ and ε_0 denoting the vacuum permittivity.

The monovalent salt is taken as sodium chloride, which is assumed to be completely dissociated in solution. Salt ions are described by $v_+ = v_- = 0.0335$ nm^3 and $q_+ = -q_- = e$. For the rest of the mobile species in the solution, the values used are $v_{H^+} = v_{OH^-} = v_w = 0.03$ nm^3 and $q_{H^+} = -q_{OH^-} = e$.

4. Results

Consider the acid−base reaction, described by eq 8, taking place in a bulk system, where all of the reacting species are mobile in the solution. Under the assumption of ideal solution, the degree of dissociation, which is the fraction of unprotonated acid groups, is given by

$$f_{bulk} = \frac{[A^-]}{[AH]+[A^-]} = \frac{1}{1+\dfrac{[H^+]}{K_a}} \tag{10}$$

where $[H^+]$ is the bulk concentration of protons. Then, given the pK_a of the acid, f_{bulk} depends only on the pH of the solution.

In the gel, the acid groups are part of the interconnected polyelectrolyte chains, which imposes a constraint that modifies the equilibrium conditions as compared to the bulk reaction. f_{bulk} is, however, often used to estimate the gel degree of dissociation. We shall show that this is a poor approximation and that the gel degree of dissociation can deviate substantially from f_{bulk}, and it does so in a nontrivial way.

Following eq 7, the local degree of dissociation, $f_d(\mathbf{r})$, can be expressed as

$$f_d(\mathbf{r}) = \frac{1}{1+\dfrac{[H^+]}{K_a}C_1\exp(\beta\Psi(\mathbf{r})q_G)} \tag{11}$$

where C_1 is a constant close to unity, whose dependence on the salt concentration of the solution is very weak. The quantity $[H^+]$ is the concentration of protons in the bath solution. Comparison between eqs 11 and 10 seems to suggest that the only difference between the bulk and the local gel expression is given by the local electrostatic potential. However, one should recall that the electrostatic potential is the result of the interplay between the packing of the different species, gel-chain statistics, distribution of free species, and chemical equilibrium, which is clear by looking at the Poisson equation (eq 9) where this coupling enters through the total charge density. Therefore, as we will show, the acid−base equilibrium behaves in a nontrivial way as compared to the bulk solution. Furthermore, the local dissociation is only defined in the regions of space where there is polymer, something that cannot be deduced from eq 11. To quantify the comparison between the dissociation in the bulk and within the gel, we define the gel degree of dissociation, f_d, as the spatial average of the local degree of dissociation weighted by the polymer volume fraction, i.e., $f_d = (\int d^3r f_d(\mathbf{r})\langle\phi_G(\mathbf{r})\rangle)/(\int d^3r\langle\phi_G(\mathbf{r})\rangle)$.

Figure 2 compares the dependence on bath pH of the gel and bulk degrees of dissociation. In the presence of salt ions, it is more natural to consider the bulk degree of dissociation as a function of pH + log c due to the Donnan effect.[40] This is, simply, a translation by log c along the abscissa of the f_{bulk}(pH) curve given by eq 10. When pH is increased, the gel degree of dissociation varies with a slope that changes more smoothly as compared to the bulk situation. The bulk system goes from uncharged to completely dissociated in a narrow range of pH values. The PE gel responds less abruptly to changes in bath pH, and there is a wider range of pH values for which the protonated and unprotonated monomers are mixed. The more broad transition between charged and uncharged segements can be explained by noticing that in the gel the chemical equilibrium between protonated and unprotonated species does not only depend on the local concentration of both species but also on the local electrostatic potential, which in turn results from the solution of a Poisson equation in which all of the interactions in the system are coupled. The gel degree of charge results from the complex balance between electrostatic interactions, chemical equilibrium osmotic pressure, counterion release, and the conformational degrees of freedom of the gel. We will

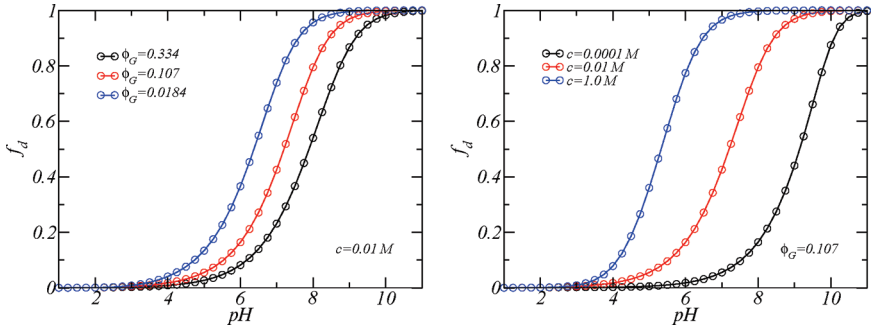

Figure 3. Degree of dissociation, f_d, as a function of pH. Left: different volume fraction curves are shown. Right: f_d vs pH at various salt concentrations.

show how this interplay works by describing a variety of conditions below.

Deviations of the gel degree of dissociation from the bulk are large in most of the pH range studied. The difference between the bulk and gel degrees of dissociation relative to the gel value, $(f_d - f_{bulk})/f_d$, is shown in the inset of Figure 2. Note that using f_{bulk} as an approximation to f_d leads to an understimation of the gel charge of as much as 90% at low pH and close 30% near pH = pK_a = 5. For larger pH values, the gel degree of ionization can be overestimated by as much as 20% using such an approximation, which is only justified at very large pH. In absolute terms, the difference between bulk and gel degrees of dissociation ($|f_d - f_{bulk}|$) can be as much as 0.1 at low pH or 0.15 at high pH, in the case shown in Figure 2. We conclude that the gel degree of ionization cannot be approximated by using the bulk value because such huge deviations of f_d from f_{bulk} can have important physical consequences. For example, we will show later that the difference between the degree of ionization in the collapsed and swollen regimes of the gel is less than that observed between our results and the bulk curve.

The dependence of f_d on pH for different volume fractions and different salt conditions is shown in Figure 3. The results are presented for fixed values of the volume fraction of the gel, $\phi_G = (1/V)\int d^3r\langle\phi(\mathbf{r})\rangle$. Compressing the gel (by increasing ϕ_G) results in a much less charged system at fixed pH, except in the regions where the system is either uncharged or minimally charged ($f_d \approx 0$, pH $\ll$ pK_a) and in the region where the gel is fully charged ($f_d \approx 1$, large pH). This is expected since, for intermediate values of pH, compressing the gel implies higher electrostatic repulsions between the monomers, and the system responds by decreasing the number of charged monomers in order to mitigate the increasing repulsions. Namely, the system sacrifices chemical free energy in order to relax some of the electrostatic repulsions and gain in counterion realease at the same time. The effect of salt concentration can be also interpreted in terms of the balance between electrostatic repulsions and chemical free energy. Increasing the salt concentration at fixed pH and ϕ_G results in a larger screening of the repulsions between monomers, and therefore the hydrogel increases its degree of dissociation. However, a description of the gel behavior based only on the electrostatic interaction is too simplistic and may lead to wrong conclusions: the degree of dissociation as a function of pH, c, and ϕ_G is the result of the coupling between the acid−base equilibrium, the gel conformational degrees of freedom, mobile species entropy, and excluded volume as well as electrostatic interactions.

Let us now define pK_{app} as the pH at which the degree of dissociation is one-half, i.e., f_d(pH = pK_{app}) = $^1/_2$. This quantity is experimentally known as the apparent pK_a. The dependence of pK_{app} on salt concentration and polymer volume fraction is displayed in Figure 4. The apparent pK_a increases monotonically with increasing gel volume fraction or decreasing salt concentration. This quantity can be thought as an intrinsic property of the

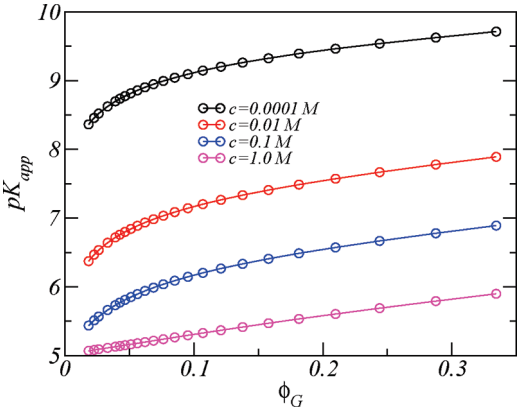

Figure 4. Apparent pK_a, pK_{app}, vs gel volume fraction at different salt concentration conditions. The apparent pK_a is defined by the equation f_d(pH = pK_{app}) = $^1/_2$.

PE gel that measures when (in terms of varying pH) the gel becomes charged: if pH > pK_{app}, most of the acid groups in the gel will be deprotonated (charged). In the case of the bulk reaction of the isolated acid group, pK_{app} = pK_a. The lower the salt concentration, the largest the minimum pH needed to charge the system. In fact, for the lowest salt concentration shown in the figure the gel is uncharged in almost all the range of pH values studied. Namely, all this can be interpreted as a local Le Chatellier principle, where the equilibrium is shifted as a response to changes in the environment. The interesting and important finding is that in gels this is a local effect since the gel is locally inhomogeneous. For more compressed systems (ϕ_G > 0.15, for example) the different c curves are roughly parallel, and the difference in pK_{app} can be mainly attributed to salt concentration differences. In the limit of infinite dilution, $\phi_G \to 0$, and high c, pK_{app} seems to converge to pK_a as expected. Note, however, that as the salt concentration decreases, the variation from pK_{app} to pK_a, at very low gel volume fractions, has a very steep gradient.

The hydrogels we consider are in equilibrium with a bath solution whose pH and c are the variables controlled experimentally; i.e., their bath values determine the constant chemical potential of charged mobile species in the gel. In other words, the chemical potentials of the charged free species are identical in the gel and the bath solution. The concentration of protons in the gel is found to be different from that of the bath solution. To quantify the difference between the proton concentration in the bath solution and inside the gel, we define the gel pH as $\overline{\text{pH}} = 1/V\int d^3r\ \text{pH}(\mathbf{r})$, where the local gel pH is pH($\mathbf{r}$) = −log([H$^+$] ($\mathbf{r}$)) = −log($\rho_{H^+}/(\mathbf{r})N_A$) with N_A denoting Avogadro's number, and show in Figure 5 how this quantity varies as a function of the bath pH. The two different panels in the figure illustrate the dependence of $\overline{\text{pH}}$ on both volume fraction and salt concentration. The dashed line represents the case in which the pH inside the gel and that of the bath are identical.

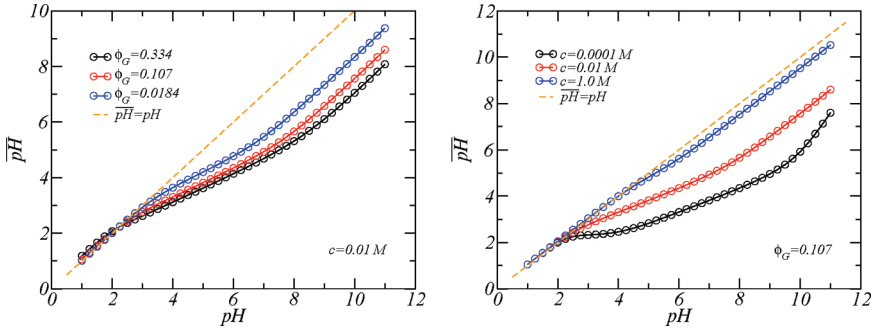

Figure 5. Gel pH, $\overline{\text{pH}}$, vs the pH of the bath solution.

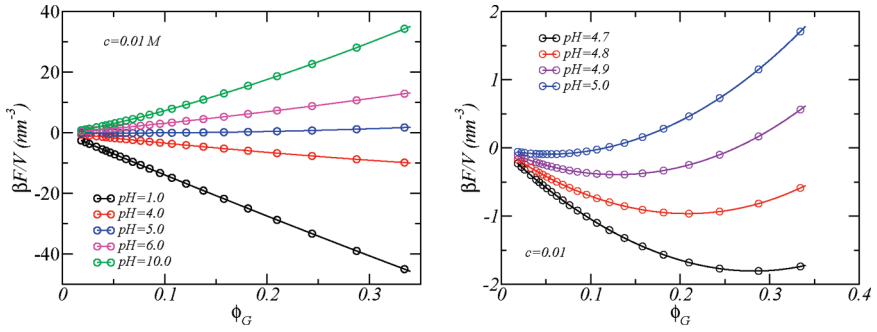

Figure 6. Free energy density vs gel volume fraction for different values of pH. Left: all pH range is represented. Right: a close-up of the cases pH $\sim$ pK_a = 5.

For very low pH, the concentration of protons is roughly the same in the bath solution as in the gel, but there is a particular pH value at which $\overline{\text{pH}}$(pH) starts to deviate from the bath value ($\overline{\text{pH}}$(pH) = pH). This value depends strongly on the salt concentration and more weakly on the gel's volume fraction. In most of the range pH values, $\overline{\text{pH}}$ is lower than the bath pH, which means that the concentration of protons is higher in the hydrogel than in the bath. Moreover, depending on the ionic strength of the solution, the proton concentration can be several orders of magnitude larger in the gel. There is a contribution to this phenomenon resulting from the Donnan potential, established because the deprotonated monomers cannot cross to the bath solution. However, this contribution alone is not enough to describe the behavior of the system; otherwise, different c curves should be parallel, and there should be no dependence on ϕ_G; see also Figure 2 which demostrates that the Donnan potential is not enough to even quantitatively explain the predictions of the molecular theory. The gel pH is the consequence of the complex balance between acid−base equilibrium, the gel molecular organization, and the resulting electrostatic interactions. These contributions are coupled in our approach, resulting in the observed nonlinear behavior of the PE gel which means that the response of the system to external stimuli cannot be analyzed in terms of just one of such contributions, except in very limiting cases. The reason for the pH inside the gel to be higher than in the bath solution under all conditions can be explained on the basis of a local Le Chatellier principle or more formally due to the proton activity. Namely, inside the gel there is always a tendency to have a larger proton concentration in order to shift the chemical equilibrium toward the protonated (uncharged) state. This is due to the increased chemical potential that arises from the electrostatic interactions. To decrease the chemical potentials, the gel becomes uncharged. This effect is stronger when the ionic strength is lower and the gel volume fraction increases, since both effects increase the strength of the electrostatic repulsions. Therefore, we see the tendencies shown in Figure 5 where the chemical equilibrium strongly couples to the steric and electrostatic interactions by reducing the gel's pH.

In all the preceding discussion, we have assumed that the volume fraction of polyelectrolyte gel was an externally controlled variable. Let us now consider the case in which the polyacid gel can find its optimal volume fraction once the external variables, pH and c, have been set. Figure 6 shows the free energy as a function of polymer volume fraction at different bath solution pH values. Three different regimes are observed here: if pH < pK_a = 5, the gel shrinks to a highly dense state. The optimal volume fraction ϕ_0, such that $(\partial(\beta F/V(\phi_G))/\partial\phi_G)_{\phi_0} = 0$, is actually larger than the volume fractions considered in this study. However, even though the exact value is not obtained, it is clear by looking at the trend of the free energy that ϕ_0 corresponds to a highly collapsed hydrogel (ϕ_0 very large). On the other side, if pH > pK_a, the optimal volume fraction corresponds to a swollen state ($\phi_0 \sim 0$). Interestingly, if pH $\sim$ pK_a, the free energy displays a minimum that does not correspond to either a collapsed or a swollen state of the gel. It is also worth noticing that varying the pH by a small amount leads to big changes in the optimal volume fraction.

Figure 7 shows the free energy of the gel as a function of the volume fraction in the three distinctive regimes. In this case, we try to analyze the role of salt concentration in determining the gel equilibrium conformation in the different regimes. In the collapsed regime (pH < pK_a), the free energy as a function of the volume fraction is almost independent of c. The electrostatic interactions do not play a significant role since effectively the gel is uncharged, and the system finds equilibrium by optimizing the packing of the gel segments. On the contrary, the free energy depends strongly on the salt concentration for the swollen state (pH > pK_a) because in this case the degree of dissociation is significantly higher than in the collapsed regime. Near the optimal volume fraction, however, all curves seem to converge since it is expected that all of them have a very small ϕ_0. As such, the differences between the optimal volume fraction at different c will be even smaller. Here, the deprotonated (charged) PE gel minimizes the free energy by expanding and thereby reducing electrostatic repulsions. Thus, changing the salt concentration cannot cause further structural changes in the already swollen gel, and this explains the system behavior near the optimal volume

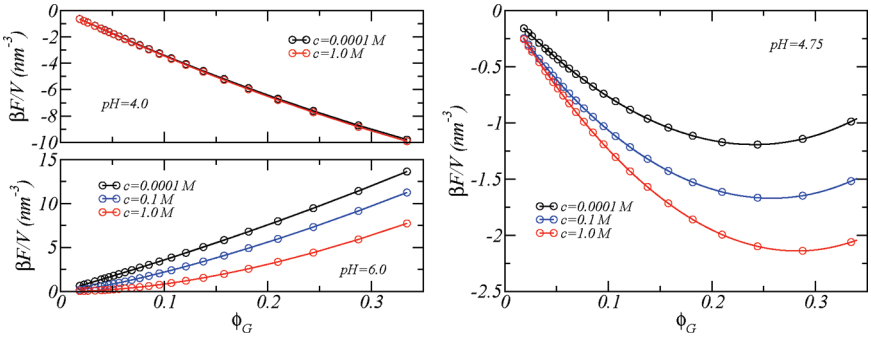

Figure 7. Dependence of the free energy density, $F(\phi_G)/V$, on the ionic strength of the solution for the collapsed (left upper panel), swollen (left lower panel), and intermediate (right panel) gel volume fraction regimes.

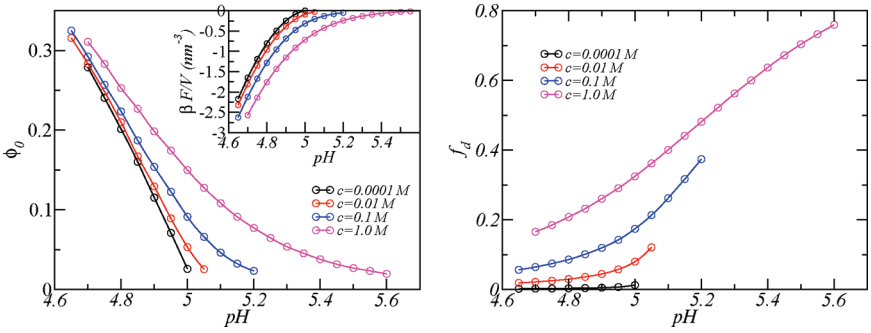

Figure 8. Left: the optimal gel volume fraction, ϕ_0 as a function of pH. The free energy density at the optimal gel volume fraction is shown in the inset. Right: the degree of dissociation at the optimal gel volume fraction. In both panels different salt conditions are included.

fraction. In the intermediate cases (right panel, pH ~ pK_a), both the free energy and the exact location of the minima depend on the concentration of salt ions and higher ionic salt concentrations shift the minimum to higher volume fractions: as the screening increases, the polymers are more charged and thus the volume fraction of the equilibrium state is larger. Namely, the degree of gel swelling is the optimal interplay between the dual action of adding salt to the system, which decreases the range of the interactions and at the same time increases the electric charge of the gel. This interplay is ubiquitous in the charge regulation of confined weak polyelectrolytes; similar behavior is found, for example, in grafted layers of polyacids.[36,38]

The left panel of Figure 8 shows the dependence of the optimal volume fraction on pH at different c conditions. The ϕ_0(pH) curves are very steep and go from high (collapsed) to low (swollen) values of ϕ_0 within a very narrow range of pH. The transition from one regime to the other, however, seems to be continuous. Decreasing c leads to a more sudden transition with respect to the pH. In transitioning from the collapsed to the swollen regime, the gel increases its charge. At low salt concentrations, increasing the degree of dissociation will lead to a sharp swelling due to the large Debye length, and therefore one expects this transition from uncharged to charged states to be sharp. Higher concentrations of salt allow the hydrogel more flexibility in terms of modifying the local environment via charge regulation with less degree of swelling. At lower salt concentrations, on the other hand, the increase in monomer ionization has to be accompanied by a higher degree of swelling. This behavior can also be observed by looking at the degree of dissociation for the unconstrained gel, which is displayed in the right panel of Figure 8. The gel is always uncharged for low salt concentrations, while for high ionic concentrations, the system transitions from a poorly charged state (at low ϕ_0) to a highly charged state at (high ϕ_0) in the intermediate range of pH. Note that in the collapsed regime a poorly charged gel is always the case independently of the salt concentration. In contrast, the gel in the swollen regime can have different degrees of charge depending on c, though a highly charged PE gel is expected, if the pH is high enough (see for example Figure 3). These effects are also a manifestation of the dual role of the solution ionic strength to screen the electrostatic interactions while increasing the charge on the polymers.

5. Concluding Remarks

In this work, we describe a theory designed to analyze the response of weak polyelectrolyte gels to changes in pH and salt concentration. This theoretical approach incorporates specific molecular details pertaining to the gel molecule, including its conformational degrees of freedom, coupled to the acid−base equilibrium, as well as to the underlying electrostatic, attractive van der Waals, and repulsive excluded-volume interactions and solution entropy. Specifically, we have applied the theoretical approach developed here to study a polyacid gel under good solvent conditions.

The hydrogel's local degree of charge is a function of the externally imposed pH and of the local electrostatic potential. This electrostatic potential results from a generalized Poisson equation in which the contributions from the various interactions described in the previous paragraph are coupled with the acid−base chemical equilibrium. As a result, the average degree of dissociation differs from the bulk value which is normally considered for these systems. Depending on the ionic strength of the solution, these differences in polymer charge can be higher than those observed between swollen and collapsed regimes. Therefore, we conclude that the common use of the bulk formula to estimate the gel degree of dissociation is incorrect, and the interplay between acid−base equilibrium and local interactions needs to be appropriately treated.

The polyacid gel can regulate charge and modify its local environment. We found that the pH within the gel's surrounding can drop significantly when compared to that of the bath solution. This nonlinear dependence of the gel pH with respect to the bath medium's pH has an enormous importance in, for example, the design of hydrogel applications such as pH-controlled drug delivery systems.[41,42]

In a good solvent, the weak PE gel responds to external changes of pH in a dramatic way. If pH is near pK_a, the volume faction of gel can be controlled, depending on the exact value of pH and on the ionic strength of the solution. However, slightly increasing the pH rapidly leads to a swollen state, while a small reduction of pH results in a collapsed gel. Therefore, fluctuations in bath pH could potentially lead to large fluctuations in the gel volume fraction. The collapsed state corresponds always to a poorly charged system, where excluded-volume interactions are dominant. In the swollen state, on the other hand, electrostatic forces are dominant, and therefore the degree of charge depends more critically on the salt concentration. These interactions, however, are coupled in our approach and their net contribution to determining the gel's thermodynamic equilibrium cannot be clearly separated. The transition between those two regimes is continuous and drastic, occurring within a very narrow range of pH whose width depends upon the bath salt concentration.

The presence of salt ions in the system has two opposing roles. On the one hand, increasing salt concentration decreases the range and strength of the electrostatic interactions. On the other hand, an increase in salt concentration results in a more charged system which augments the importance of the electrostatic interactions in determining the behavior of the system, particularly its swelling. This coupling between charge regulation, electrostatic interactions, and gel swelling shows the importance of optimizing all the degrees of freedom together within a single theoretical framework, and it explains why considering the charge state of weak polyelectrolytes to be homogeneous and given by the bath value provides with the incorrect qualitative behavior.

The theoretical approach presented here can be applied using any molecular model of the weak polyelectrolyte gel. As our initial approach to the problem, we have chosen a relatively simple and regular model in which the connectivity of all monomer nodes is the same and in which all the chains are monodisperse. However, the degree of cross-linking and the molecular weight of gel chains modify the quantitative swelling behavior in response to external stimuli.[43] Therefore, this molecular model will need to be refined in future applications of such molecular theory. In addition, further research using this approach should include the study of weak PE gels under bad solvent conditions, which requires a non-negligible definition of monomer−monomer van der Waals attractive interactions as opposed to the case studied here.

In poor solvent conditions charged gels undergo large volume changes induced by external changes.[2] These changes have been associated with the formation of nanophase or microphase segregation transitions.[44] Polyelectrolyte gels with attractive interactions, such as those induced by hydrophobic backbones, can form locally segregated patterns in aqueous solutions[14] that consist of regions where the gel is locally collapsed, interdispersed in regions where the gel is expanded. In the case of gels with acid groups and poor solvent backbones, one expects self-regulated local composition, charge, and pH heterogeneities, which can be controlled by temperature, ionic concentrations, pH values, and electric fields as it has been found to be the case in grafted hydrophobic weak polyelectrolyte layers.[38]

Acknowledgment. This work is supported by the MRSEC program of the NSF (DMR-0520513) at Northwestern University.

Appendix

A. Molecular Theory. In this work, the theoretical approach developed previously in refs 37 and 38 is now extended to investigate the behavior of a weak PE gel under different pH and salt concentration conditions. The previous studies described extensively the application of the theory in examining weak polyacid-grafted layers. In this section, we only describe the most important aspects of the theoretical framework as well as introduce the necessary modifications.

The hydrogel system is in equilibrium with a homogeneous solution that provides a bath for all of the mobile species. In this context, homogeneity means that the densities of the different species in this bath solution are independent of position. Namely, in this region of the solution, the quantity $\rho_\gamma(\mathbf{r}) \equiv \rho_\gamma^{hm}$ (γ = w, +, −, H^+, OH^-) is a constant that depends only on pH and c.

The thermodynamic equilibrium is, therefore, given by the Lagrange transform of the free energy that is a function of the chemical potentials for the mobile species, which consist of the water molecules, the protons, the hydroxyl ions, and the salt anions and cations. The existence of two constraints reduces the total number of independent thermodynamic variables by two.[37] Thus, we can introduce exchange chemical in such a way that those of water, protons, and hydroxyl ions do not represent relevant thermodynamic variables. Then, the semi-grand canonical potential, $W = F - \mu_+ N_+ - \mu_- N_-$, with μ_+ and μ_- being the exchange chemical potentials conjugated to the number of salt cations (N_+) and anions (N_-), respectively, is indeed the thermodynamic potential whose minimum yields the equilibrium state. In our formalism, W is expressed as

$$W = F - \mu_+ \int d^3r \rho_+(\mathbf{r}) - \mu_- \int d^3r \rho_-(\mathbf{r})$$

Furthermore, the solution to our problem must satisfy both incompressibility and electroneutrality constraints (eqs 2 and 3). To impose each of these constraints, the Lagrange multipliers $\pi(\mathbf{r})$ and λ need to be introduced, respectively. In its complete form, the functional that we need to extremize becomes

$$\Phi = \beta W + \int d^3r \beta\pi(\mathbf{r})[\langle\phi_G(\mathbf{r})\rangle + \sum_\gamma \rho_\gamma(\mathbf{r}) v_\gamma - 1] + \lambda \int d^3r \langle\rho_q(\mathbf{r})\rangle$$

Minimization of Φ yields the following results for the densities of the free species:

$$\rho_w(\mathbf{r}) = \frac{1}{v_w} \exp(-\beta\pi(\mathbf{r}) v_w)$$

$$\rho_\gamma(\mathbf{r}) = \frac{\rho_\gamma^{hm}}{(v_w \rho_w^{hm})^{v_\gamma/v_w}} \exp(-\beta\pi(\mathbf{r}) v_\gamma - \beta\Psi(\mathbf{r}) q_\gamma) \quad (\gamma = H^+, OH^-, +, -)$$

Moreover, assuming that the dialectic constant of the medium is homogeneous ($\varepsilon(\mathbf{r}) \equiv \varepsilon$), the probability density function of gel conformations is given by

$$P(\alpha) = \frac{1}{Q} \exp(-\beta U_{vdw}(\alpha) - \int d^3r \phi_G(\mathbf{r}, \alpha) \beta\pi(\mathbf{r})) \exp\left[- \int d^3r \frac{\phi_G(\mathbf{r}, \alpha)}{v_G} (\beta\Psi(\mathbf{r}) q_G + \ln f_d(\mathbf{r})) \right]$$

where the factor Q ensures the satisfaction of $\sum_\alpha P(\alpha) = 1$.

For the local degree of dissociation, we obtain

$$\frac{f_d(\mathbf{r})}{1 - f_d(\mathbf{r})} = \frac{K_a^0}{v_w \rho_{H^+}^{hm}} (v_w \rho_w^{hm})^{v_{H^+}/v_w} \exp(-\beta\Psi(\mathbf{r}) q_G)$$

where K_a^0 is the dimensionless thermodynamic equilibrium constant for the acid−base reaction, related to the standard

chemical potentials of the protons, the unprotonated and protonated species via $K_a^0 = \exp(\beta\mu_{AH}^0 - \beta\mu_{H^+}{}^0 - \beta\mu_{A^-}{}^0)$. Note that the more commonly mentioned experimental equilibrium constant K_a, given in molar units, is defined by

$$K_a = \frac{[A^-][H^+]}{[AH]}$$

so that K_a and K_a^0 are proportional. The standard chemical potentials of the protons and the hydroxyl ions are respectively given by

$$\exp(-\beta\mu_\gamma^0) = \frac{v_w\rho_\gamma^{hm}}{(v_w\rho_w^{hm})^{v_\gamma/v_w}} \quad (\gamma = H^+, OH^-)$$

while the chemical potential of the salt ions are expressed as

$$\exp(\beta\mu_\gamma) = \frac{v_w\rho_\gamma^{hm}}{(v_w\rho_w^{hm})^{v_\gamma/v_w}} \quad (\gamma = +, -)$$

In addition, the variation of Φ with respect to the electrostatic potential readily yields the Poisson equation

$$\varepsilon\nabla^2\Psi(\mathbf{r}) = -\langle\rho_q(\mathbf{r})\rangle$$

Because we are modeling a volumetric hydrogel, periodic boundary conditions are imposed to the electrostatic potential; this periodicity of $\Psi(\mathbf{r})$ guarantees electroneutrality.

At this point, the free energy have been expressed in terms of the position-dependent osmotic pressure, $\pi(\mathbf{r})$, the electrostatic potential, $\Psi(\mathbf{r})$, the densities of the different mobile species in the bath homogeneous solution, ρ_γ^{hm} (γ = w, H^+, OH^-, +, −) as well as inputs provided by the molecular model that include the polymer pK_a (p$K_a = -\log K_a$), the gel volume fraction distribution, $\phi_G(\mathbf{r},\alpha)$, etc. Once the independent variables of a calculation, pH, c, and ϕ_G are set, all of the homogeneous bath densities ρ_w^{hm}, $\rho_{H^+}{}^{hm}$, $\rho_{OH^-}{}^{hm}$, ρ_+^{hm}, and ρ_-^{hm} can be obtained via imposing the incompressibility and electroneutrality constraints in the bath solution. Another relationship to be used at this point is the self-ionization of water described by $K_W = [OH^-][H^+] \propto \exp(-\beta\mu_{OH^-}{}^0 - \beta\mu_{OH^+}{}^0)$. Lastly, the quantities $\pi(\mathbf{r})$ and $\Psi(\mathbf{r})$ are determined by substituting the expressions for the local densities of free species and ensemble average local gel volume fraction into the incompressibility constraint (eq 2) and the Poisson equation (eq 9). The solution can then be obtained numerically (see section A.1 of the Appendix).

Finally, it is important to mention that the theory requires the input of the complete set of gel conformations for each volume fraction. The free energy term, $-k_B\sum_\alpha P(\alpha)\ln P(\alpha)$, represents the exact conformational entropy of the gel if all possible molecular configurations are included in the sum. It is, however, only possible to include a finite number of conformations in practice. To calculate the conformational entropy, we define $-k_B\sum_\alpha P(\alpha)\ln P(\alpha) = -k_B\sum_{\tilde{\alpha}} P(\tilde{\alpha})\ln P(\tilde{\alpha}) + \Delta_\alpha F$, where $\{\tilde{\alpha}\}$ is a finite set of conformations, large enough to describe the gel's conformational degree of freedom properly, and $\Delta_\alpha F$ is the correction needed as a result of this truncation of the gel's conformational space. It is important to mention that the main contribution to the conformational entropy comes from the term $-k_B\sum_{\tilde{\alpha}} P(\tilde{\alpha})\ln P(\tilde{\alpha})$ and not from the correction (see Figure 11 in Appendix B). The gel conformations included in $\{\tilde{\alpha}\}$ are generated using molecular dynamics simulations as described in section 3 and Appendix C. At fixed volume fraction, $\Delta_\alpha F$ represents only an additive constant to the free energy in which case it can be ignored. However, this correction needs to be considered when comparing thermodynamic states having different volume fractions because of the different dimensions of the conformational space. In section B of the Appendix, we derive an exact expression for $\Delta_\alpha F$ and then use an approximation to estimate its value.

A.1. Numerical Solution. To obtain results from the microscopic-level theory that incorporates molecular details as presented here, we must numerically solve the nonlinear integro-differential equations described in the previous section. To this end, the volume of the system is discretized in cubic cells of length $\delta = 0.5$ nm. The number of equations to be solved after discretization ranges from 2×10^4 for the largest gel volume fraction to 2.5×10^5 for the smallest gel volume fraction, with each equation containing roughly 10^4 terms (the number of gel conformations included). Note that because the volume fraction is inversely proportional to the system volume (the total number of gel segments is contant), the number of equations increases with decreasing gel volume fraction. These equations are solved using Jacobian−free Newton method. Figure 9, for example, shows the free energy as a function of the pH of the bath solution, at different gel volume fractions and salt conditions. Each point in these curves represent a single calculation.

B. Free Energy Correction. For each volume fraction, the complete set of gel conformations should be included when calculating the free energy of the system using the approach presented in this work. Unfortunately, this is impossible from a practical standpoint, and we consequently include a large but finite set of gel conformations that is adequate enough to describe the behavior of the system.

At fixed volume fraction, if the set of configurations included is large enough, this truncation of the conformational space results merely in a translation of the free energy, which is of no importance. The problem arises, however, from comparing calculations at different volume fractions, since the relative dimension of the conformational space contributes to the entropy difference between the states under consideration.

In this section, we estimate the corrections to the system entropy that must be included due to the truncation of the gel conformational space.

B.1. Conformational Entropy of a Finite Set. Let $\{\alpha\}$ be the complete set of gel configurations. The conformational entropy is given by

$$S = \sum_{\alpha\in\{\alpha\}} P(\alpha)\ln(P(\alpha))$$

Suppose that $\{\alpha\}$ contains many configurations that are equivalent (in a sense that will be clear later). Let now $\{\alpha'\}$ be the minimal (degenerate) set of independent configurations. A conformation α' in $\{\alpha'\}$ is an arbitrary choice within the many configurations α_k in $\{\alpha\}$, for $k = 1, \ldots, n(\alpha')$ that satisfies $P(\alpha') = P(\alpha_k)$. The quantity $n(\alpha')$ is the degeneracy of α', and the system entropy can then be written as

$$S = \sum_{\alpha'\in\{\alpha'\}} n(\alpha')P(\alpha')\ln(P(\alpha'))$$

In general, the average value of a quantity O is defined as

$$\langle O\rangle_\alpha = \sum_\alpha P(\alpha)O(\alpha) = \sum_{\alpha'} n(\alpha')P(\alpha')O(\alpha')$$

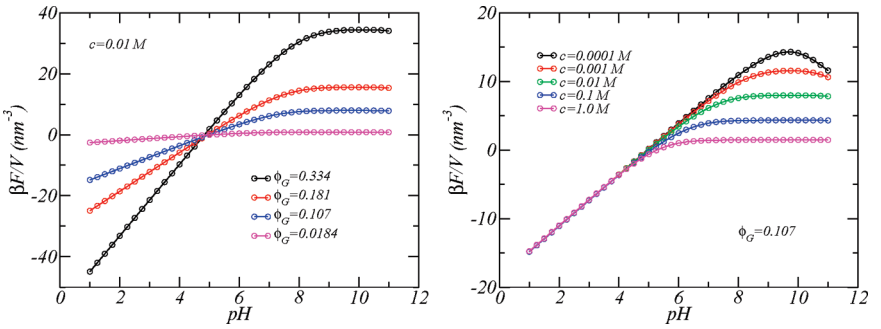

Figure 9. Free energy density $\beta(F/V)$ vs pH for different volume fractions, ϕ_G, and salt concentrations, c.

with $\sum_\alpha P(\alpha) = \sum_{\alpha'} n(\alpha')P(\alpha') = 1$. Now, we generate a set of configurations $\{\tilde{\alpha}\}$ that is a subset of $\{\alpha\}$. The subset $\{\tilde{\alpha}\}$ is such that the ensemble average value of a quantity O over the subset, $\langle O\rangle_{\tilde{\alpha}}$, is equal to that over the complete set, i.e., $\langle O\rangle_{\tilde{\alpha}} = \sum_{\tilde{\alpha}\in\{\tilde{\alpha}\}} R(\tilde{\alpha})O(\tilde{\alpha}) = \sum_\alpha P(\alpha)O(\alpha) = \langle O\rangle_\alpha$. Here, the quantity $R(\tilde{\alpha})$ is the probability of a configuration $\tilde{\alpha}$.

Configurations in $\{\tilde{\alpha}\}$ are randomly generated from $\{\alpha\}$. Therefore, the probability of generating a configuration α' of $\{\alpha'\}$ within the subset $\{\tilde{\alpha}\}$ is $(n(\alpha'))/(\Omega)$, where $\Omega = \dim\{\alpha\}$ is the total number of configurations in $\{\alpha\}$. If the $\tilde{\Omega}$ configurations are generated in $\{\tilde{\alpha}\}$, the degeneracy of a configuration α' is given by $\tilde{\Omega}[n(\alpha')/\Omega]$, where $\tilde{\Omega}$ is large enough so that $\langle O\rangle_\alpha = \langle O\rangle_{\tilde{\alpha}}$. Therefore, we must have the following relation

$$\langle O\rangle_{\tilde{\alpha}} = \sum_{\tilde{\alpha}} R(\tilde{\alpha})O(\tilde{\alpha}) = \sum_{\alpha'} \tilde{\Omega}\frac{n(\alpha')}{\Omega}O(\alpha')R(\alpha')$$

However, since by definition

$$\langle O\rangle_{\tilde{\alpha}} = \langle O\rangle_{\alpha'} = \sum_{\alpha'} P(\alpha')n(\alpha')O(\alpha')$$

which implies that we must have the following relation:

$$R(\alpha')\frac{\tilde{\Omega}}{\Omega} = P(\alpha')$$

Substituting this last expression into S, we then obtain the following:

$$S = \sum_\alpha P(\alpha)\ln(P(\alpha)) = \sum_{\alpha'} P(\alpha')n(\alpha')\ln(P(\alpha'))$$

$$= \sum_{\alpha'} n(\alpha')P(\alpha')\ln\left(R(\alpha')\frac{\tilde{\Omega}}{\Omega}\right)$$

$$= \sum_{\alpha'} n(\alpha')P(\alpha')\ln(R(\alpha')) + \sum_{\alpha'} n(\alpha')P(\alpha')\ln\left(\frac{\tilde{\Omega}}{\Omega}\right)$$

$$= \langle\ln(R)\rangle_\alpha + \ln\left(\frac{\tilde{\Omega}}{\Omega}\right)\sum_{\alpha'} n(\alpha')P(\alpha') = \langle\ln(R)\rangle_\alpha + \ln\left(\frac{\tilde{\Omega}}{\Omega}\right)$$

Since $\langle\ln(R)\rangle_\alpha = \langle\ln(R)\rangle_{\tilde{\alpha}} = \sum_{\tilde{\alpha}} R(\tilde{\alpha})\ln(R(\tilde{\alpha}))$, the conformational entropy can be now expressed in terms of $\{\tilde{\alpha}\}$ in the following form:

$$S = \sum_{\tilde{\alpha}} R(\tilde{\alpha})\ln(R(\tilde{\alpha})) + \ln\left(\frac{\tilde{\Omega}}{\Omega}\right) \qquad (12)$$

B.2. Volume-Fraction Dependence of the Correction. From eq 12, we see that the correction to the entropy at constant volume (fraction) is given by

$$\Delta_\alpha S = \ln\left(\frac{\Omega(\phi_G)}{\Omega_t(\phi_G)}\right)$$

where $\Omega(\phi_G)$ is the number of gel configurations included $[\Omega(\phi_G) = \dim\{\alpha(\phi_G)\}]$ and $\Omega_t(\phi_G)$ denotes the total number of configurations $[\Omega_t(\phi_G) = \dim\{\alpha(\phi_G)\} + \dim\{\alpha(\phi_G)\}^c]$.

Consider a reference state ϕ_G^0. At volume fraction ϕ_G, the free energy needs to be corrected by a factor of

$$\Delta_\alpha F(\phi_G) = \ln\left(\frac{\Omega(\phi_G)}{\Omega_t(\phi_G)}\right) - \ln\left(\frac{\Omega(\phi_G^0)}{\Omega_t(\phi_G^0)}\right)$$

$$= \ln\left(\frac{\Omega(\phi_G)}{\Omega(\phi_G^0)}\frac{\Omega_t(\phi_G^0)}{\Omega_t(\phi_G)}\right)$$

Note that up to this point, we have not made any approximation, and the previous expression is general. In our calculations, we include the same number of gel configurations for all volume fractions, which means that $\Omega(\phi_G)/\Omega(\phi_G^0) = 1$ and that

$$\Delta_\alpha F(\phi_G) = \ln\left(\frac{\Omega_t(\phi_G^0)}{\Omega_t(\phi_G)}\right) \qquad (13)$$

B.3. Estimation of the Correction. Let us first assume that the chains connecting the nodes are independent. Then, it follows that

$$\Omega_t(\phi_G) = \Omega_1(\phi_G)^{n_{chains}}$$

where $\Omega_1(\phi_G)$ denotes the number of configurations of a chain in the gel and n_{chains} represents the total number of chains.

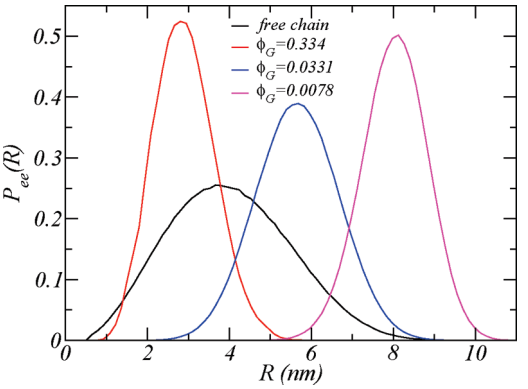

Figure 10. End-to-end distance distribution for different gel volume fractions.

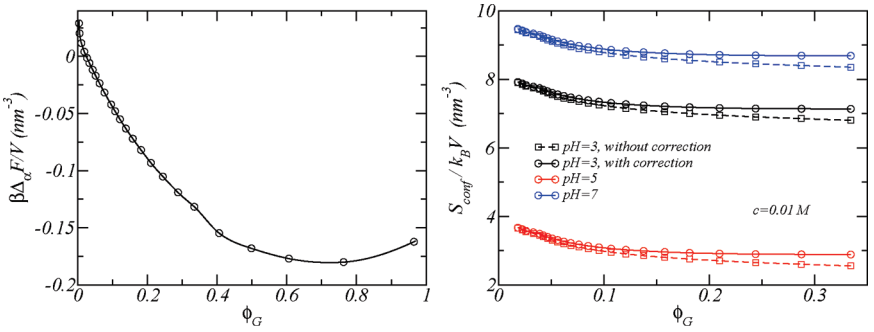

Figure 11. Left: free energy correction $\Delta_\alpha F$ vs gel volume fraction. Right: configurational entropy density vs volume fraction, for three typical cases, with (open circles-solid lines) and without (open squares-dashed lines) including the correction.

If the chain is free and not connected to the network, we must have

$$\Omega_{1,\,\mathrm{free}}(\phi_G) \equiv \Omega_{1,\,\mathrm{free}} = \int \omega_{1,\,\mathrm{free}}(R)\,\mathrm{d}^3R$$

where $\omega_{1,\mathrm{free}}(R)$ is the number of configurations of the free chain with end-to-end distance between R and $R + \mathrm{d}R$.

In the gel, however, end-to-end distances are constrained by the network:

$$\Omega_1(\phi_G) = \int \omega_{1,\,\mathrm{free}}(R) P_{\mathrm{node}}(R,\phi_G)\,\mathrm{d}^3R$$

where $P_{\mathrm{node}}(R,\phi_G)$ denotes the probability that the nodes connecting the chain are separated by a distance R given that the volume fraction of the gel is ϕ_G. Let us now define the quantity $P_{1,\mathrm{free}}(R) = (\omega_{1,\mathrm{free}}(R))/\Omega_{1,\mathrm{free}}$, which represents the probability that the free chain has end-to-end distance R. We thus have

$$\Omega_1(\phi_G) = \Omega_{1,\,\mathrm{free}} \int P_{1,\,\mathrm{free}}(R) P_{\mathrm{node}}(R,\phi_G)\,\mathrm{d}^3R$$

and

$$\Omega_t(\phi_G) = (\Omega_{1,\,\mathrm{free}} \int P_{1,\,\mathrm{free}}(R) P_{\mathrm{node}}(R,\phi_G)\,\mathrm{d}^3R)^{n_{\mathrm{chains}}}$$

Using eq 13, the correction to the free energy is therefore given by

$$\Delta_\alpha F(\phi_G) = n_{\mathrm{chains}} \ln\left(\frac{\int P_{1,\,\mathrm{free}}(R) P_{\mathrm{node}}(R,\phi_G^0)\,\mathrm{d}^3R}{\int P_{1,\,\mathrm{free}}(R) P_{\mathrm{node}}(R,\phi_G)\,\mathrm{d}^3R}\right) \quad (14)$$

Figure 10 shows the end-to-end distance probability distribution, $P_{ee}(R)$, for the different gel volume fractions ($P_{\mathrm{node}}(R,\phi_G)$) and for the free chain ($P_{1,\mathrm{free}}(R)$). In the case of the gel, the distributions correspond to the set of conformations used in this work and averaged over the different chains. The quantity R is the distance between two nodes that are connected by a chain. The free-chain distribution is obtained by performing a MD simulation under the same conditions as described for each volume fraction of gel (see section C). Each chain includes two additional segments representing the nodes, which allows for the proper comparison with gel chains. In both cases, once a large number of configurations have been generated, the criterion to stop further generation of gel configurations hinges on the condition that adding more conformations would not modify the quantity $P_{ee}(R)$ any further.

Finally, Figure 11 shows the magnitude of the free energy correction as a function of the gel volume fraction. Note that only changes in $\Delta_\alpha F$ are important, since the free energy itself can be defined with respect to an arbitrary constant. The right panel also shows that the main contribution to configurational entropy comes from the Gibbs entropy, $-k_B\sum_{\tilde{\alpha}} P(\tilde{\alpha}) \ln (P(\tilde{\alpha}))$, over the truncated set of gel configurations, $\{\tilde{\alpha}\}$, generated as described in section 3.

C. Molecular Dynamics. The specification of conformations of the gel molecule, which is needed for the evaluation of our theory, is obtained by molecular dynamics simulations using GROMACS 3.3.2.[45,46] For each volume fraction, the system is equilibrated for 500 ps, and then the simulation is continued for another 10 ns. During the production time, one configuration is recorded during every 1 ps, which results in a total of 10^4 configurations.

The force field used in the MD simulations has been described previously.[47] All monomers interact via a repulsive (shifted) Lennard-Jones potential of the following form:

$$U^{\mathrm{LJ}}(r_{ij}) = \begin{cases} 4\varepsilon\left[\left(\dfrac{\sigma}{r_{ij}}\right)^{12} - \left(\dfrac{\sigma}{r_{ij}}\right)^{6} + \dfrac{1}{4}\right] & \text{if } r_{ij} \le 2^{1/6}\sigma \\ 0 & \text{if } r_{ij} > 2^{1/6}\sigma \end{cases}$$

where r_{ij} is the distance between monomers i and j. Neighboring monomers along the chain interact additionally via a FENE potential:

$$U^{\mathrm{FENE}}(r_{ij}) = \begin{cases} -\dfrac{kR_0^2}{2}\ln\left[1 - \left(\dfrac{r_{ij}}{R_0}\right)^2\right] & \text{if } r_{ij} \le R_0 \\ \infty & \text{if } r_{ij} > R_0 \end{cases}$$

Here we set $\sigma = 1$ and $\varepsilon = 1$, since all energetic and spatial dimensions can be rescaled later by the values assigned to these parameters. We set $R_0 = 1.5\sigma$ and $k = 30(\varepsilon/\sigma^2)$ in order to avoid any bond crossing.[47] The distance between bonded monomers was found to be larger than 0.87σ for all simulations across different volume-fraction values. As such, we set this value as the segment length l_G.

References and Notes

(1) Guvendiren, M.; Shull, K. R. *Soft Matter* **2007**, *3*, 619–626.
(2) De, S.; Aluru, N.; Johnson, B.; Crone, W.; Beebe, D.; Moore, J. *J. Microelectromech. Syst.* **2002**, *11*, 544–555.

(3) Kang, Y.; Walish, J. J.; Gorishnyy, T.; Thomas, E. L. *Nature Mater*. **2007**, *6*, 957–960.
(4) Kaneko, D.; Gong, J. P.; Osada, Y. *J. Mater. Chem*. **2002**, *12*, 2169–2177.
(5) Kim, P.; Zarzar, L. D.; Zhao, X.; Sidorenko, A.; Aizenberg, J. *Soft Matter* **2010**, *6*, 750–755.
(6) Shahinpoor, M. *J. Intell. Mater. Syst. Struct*. **1995**, *6*, 307–314.
(7) Brock, D.; Lee, W.; Segalman, D.; Witkowski, W. *J. Intell. Mater. Syst. Struct*. **1994**, *5*, 764–771.
(8) Sidorenko, A.; Krupenkin, T.; Taylor, A.; Fratzl, P.; Aizenberg, J. *Science* **2007**, *315*, 487–490.
(9) Helfferich, F. *Ion Exchange*; McGraw-Hill: New York, 1962.
(10) Beebe, D. J.; Moore, J. S.; Bauer, J. M.; Yu, Q.; Liu, R. H.; Devadoss, C.; Jo, B.-H. *Nature* **2000**, *404*, 588–590.
(11) Eisenberg, S. R.; Grodzinsky, A. J. *J. Biomech. Eng*. **1987**, *109*, 79–89.
(12) Myers, E. R.; Lai, W. M.; Mow, V. C. *J. Biomech. Eng*. **1984**, *106*, 151–158.
(13) Matsuo, E. S.; Tanaka, T. *Nature* **1992**, *358*, 482–485.
(14) Ikkai, F.; Suzuki, T.; Karino, T.; Shibayama, M. *Macromolecules* **2007**, *40*, 1140–1146.
(15) Zimmerman, S. B. *J. Struct. Biol*. **2006**, *156*, 255–261.
(16) Pope, L. H.; Xiong, C.; Marko, J. F. *Mol. Biol. Cell* **2006**, *17*, 104–113.
(17) Poirier, M.; Eroglu, S.; Chatenay, D.; Marko, J. F. *Mol. Biol. Cell* **2000**, *11*, 269–276.
(18) Poirier, M. G.; Monhait, T.; Marko, J. F. *J. Cell. Biochem*. **2002**, *85*, 422–434.
(19) Fels, J.; Orlov, S. N.; Grygorczyk, R. *Biophys. J*. **2009**, *96*, 4276–4285.
(20) Widom, J.; Baldwin, R. L. *J. Mol. Biol*. **1980**, *144*, 431–453.
(21) Bloomfield, V. A.; Crothers, D. M.; Tinoco, I., Jr. *Nucleic Acids: Structures, Properties and Functions*, University Science Press: Mill Valley CA, 2000.
(22) Raspaud, E.; Olvera de la Cruz, M.; Sikorav, J.-L.; Livolant, F. *Biophys. J*. **1998**, *74*, 381–393.
(23) de la Cruz, M. O.; Belloni, L.; Delsanti, M.; Dalbiez, J. P.; Spalla, O.; Drifford, M. *J. Chem. Phys*. **1995**, *103*, 5781–5791.
(24) Kudlay, A.; de la Cruz, M. O. *J. Chem. Phys*. **2004**, *120*, 404–412.
(25) Kudlay, A.; Ermoshkin, A. V.; Olvera de la Cruz, M. *Macromolecules* **2004**, *37*, 9231–9241.
(26) Ermoshkin, A. V.; Olvera de la Cruz, M. *J. Polym. Sci., Part B: Polym. Phys*. **2004**, *42*, 766–776.
(27) Ermoshkin, A. V.; Kudlay, A. N.; de la Cruz, M. O. *J. Chem. Phys*. **2004**, *120*, 11930–11940.
(28) Zeldovich, K. B.; Dormidontova, E. E.; Khokhlov, A. R.; Vilgis, T. A. *J. Phys. II* **1997**, *7*, 627–635.
(29) Rabin, Y.; Panyukov, S. *Macromolecules* **1997**, *30*, 301–312.
(30) Boudaoud, A.; Chaieb, S. *Phys. Rev. E* **2003**, *68*, 021801.
(31) Schneider, S.; Linse, P. *Macromolecules* **2004**, *37*, 3850–3856.
(32) Yin, D.-W.; Yan, Q.; de Pablo, J. J. *J. Chem. Phys*. **2005**, *123*, 174909.
(33) Yin, D.-W.; de la Cruz, M. O.; de Pablo, J. J. *J. Chem. Phys*. **2009**, *131*, 194907.
(34) Sabbagh, I.; Delsanti, M. *Eur. Phys. J. E* **2000**, *1*, 75–86.
(35) Muthukumar, M.; Hua, J.; Kundagrami, A. *J. Chem. Phys*. **2010**, *132*, 084901.
(36) Gong, P.; Wu, T.; Genzer, J.; Szleifer, I. *Macromolecules* **2007**, *40*, 8765–8773.
(37) Nap, R.; Gong, P.; Szleifer, I. *J. Polym. Sci., Part B: Polym. Phys*. **2006**, *44*, 2638–2662.
(38) Tagliazucchi, M.; de la Cruz, M. O.; Szleifer, I. *Proc. Natl. Acad. Sci. U.S.A*. **2010**, *107*, 5300–5305.
(39) Olvera de la Cruz, M.; Ermoshkin, A. V.; Carignano, M. A.; Szleifer, I. *Soft Matter* **2009**, *5*, 629–636.
(40) Overbeek, J. *Prog. Biophys. Biophys. Chem*. **1956**, *6*, 58–84.
(41) Kohman, R. E.; Cha, C.; Zimmerman, S. C.; Kong, H. *Soft Matter* **2010**, *6*, 2150–2152.
(42) Murthy, N.; Thng, Y. X.; Schuck, S.; Xu, M. C.; Frechet, J. M. J. *J. Am. Chem. Soc*. **2002**, *124*, 12398–12399.
(43) Schmidt, J. J.; Cha, C.; Kong, H. *Soft Matter* **2010**, *6*, 3930–3938.
(44) Ikkai, F.; Shibayama, M. *Polymer* **2007**, *48*, 2387–2394.
(45) Berendsen, H. J. C.; van der Spoel, D.; van Drunen, R. *Comput. Phys. Commun*. **1995**, *91*, 43–56.
(46) Lindahl, E.; Hess, B.; van der Spoel, D. *J. Mol. Model*. **2001**, 306–317.
(47) Kremer, K.; Grest, G. S. *J. Chem. Phys*. **1990**, *92*, 5057–5086.

Macromolecules
ARTICLE

Macromolecules **2011**, *44*, 159–165 **159**
DOI: 10.1021/ma1016264

Novel Photolabile Diblock Copolymers Bearing Truxillic Acid Derivative Junctions

Hong Yang,*,† Lin Jia,‡ Zhifei Wang,†,‡ Aurélie Di-Cicco,‡,§ Daniel Lévy,‡,§ and Patrick Keller*,‡,⊥

†*School of Chemistry and Chemical Engineering, Southeast University, Nanjing 211189, China,* ‡*Institut Curie, Centre De Recherche, CNRS UMR 168, Université Pierre et Marie Curie, 26 rue d'Ulm 75248 Paris Cedex 05, France,* §*Pict-IbiSA, Institut Curie, Paris, France, and* ⊥*Department of Chemistry and Biochemistry, University of Colorado, Boulder, Colorado 80309-0215, United States*

Received July 20, 2010; Revised Manuscript Received November 22, 2010

ABSTRACT: Amphiphilic diblock copolymers, poly(ethylene glycol)-*block*-poly(acrylate), bearing truxillic acid derivatives at the junction point between the two blocks are described. The truxillic acid junction can be selectively cut by UV light, leading to a disassembly of the nano-objects made by self-assembly of the amphiphilic copolymers in water.

Introduction

Amphiphilic block copolymers have the ability to self-assemble in water to form various nano- or microsized objects,[1] which have potential applications in many domains such as drug delivery,[2] biotechnology,[3] catalysis,[4] and materials chemistry.[5] Recently, polymer micelles and vesicles prepared from amphiphilic block copolymers have received increasing interest because several of their morphological parameters can be modified by the action of external stimuli,[6] either chemical stimuli (pH change,[7] redox reaction,[8] hydrolysis,[9] enzymatic reaction[10]) or physical stimuli (thermal,[11] magnetic,[12] electrical,[13] mechanical (i.e., ultrasound sonication),[14] or photochemical[15]). In particular, stimuli-triggered disassembly could be used to promote reactions locally, such as controlling chemical reactions in microfluidics[16] or in drug delivery.[17]

Light, as a remote stimulus, is an attractive nano-object disassembling driving force, which has been intensively investigated for two obvious advantages: (1) light can be accurately targeted and highly selective; (2) in contrast to chemical stimuli, no acids, bases, or other reagents have to be brought into the system from outside, which in many cases could be technically challenging.

Light-responsive polymer micelles/vesicles can be divided into two main categories, depending on the kind of transformation brought by the photochemical event: (1) The reversible structural changes of the chromophores exposed to light modify the hydrophilic−hydrophobic balances and therefore transform the nanostructures of micelles/vesicles. Typical photochemically induced transition examples use as chromophores azobenzenes (*trans*-to-*cis* isomerization, change of dipole moment, size, and shape),[18] spyrobenzopyran (formation of zwitterionic species),[19] triphenylmethane leucohydroxide (generation of charges),[20] and cinnamoyl (photodimerization).[21] (2) The chromophores actually behave as photolabile covalent junctions between the polymer main body and the sacrificial parts. In this case, the photoirradiation-induced chemical reaction is an irreversible, permanent photocleavage process. For this approach, basically there are two general strategies. One strategy is using the monomer units as the sacrificial parts. For example, *o*-nitrobenzyl acrylates were polymerized to form hydrophobic polymer blocks, which could be photocleaved to become hydrophilic poly(acrylic acid).[22] Another one is to use polymer blocks as the sacrificial parts. The latter is very promising and more efficient potentially, since only one chromophore linker is required, which will need less light power consumption to be cleaved. Up to now, there are only a few examples of such photolabile block copolymers in the literature, based on *o*-nitrobenzyl,[23] 2-nitrophenylalanine,[24] and anthracene[25] photosensitive derivatives (Scheme 1). Herein, we present novel photolabile diblock copolymers bearing α-truxillic acid derivatives as photocleavable junctions (Scheme 2B).

Our design was inspired by a well-studied photochemical system: the cinnamic acid−truxillic acid reversible photochemical [2 + 2] cycloaddition reaction (Scheme 2A).[26] Cinnamic acid forms, under illumination with ultraviolet light source with wavelengths above 260 nm, a dimer, truxillic acid,[27] which is stable at elevated temperature and under a wide range of wavelengths of UV light. The cyclobutane ring of truxillic acid is however photolabile under deep-UV light, below 260 nm, giving back the original cinnamic acid. This [2 + 2] photodimerization of the cinnamic acid is in fact very similar to the [4 + 4] photodimerization of the anthracene developed by Goldbach et al.[25]

Our strategy, starting from α-truxillic acid, was to first synthesize an ATRP (atom transfer radical polymerization)[28] macroinitiator by functionalizing an α-truxillic acid−ATRP small molecule initiator with the hydrophilic poly(ethylene glycol) block via ester or amid bonds, and then to prepare the hydrophobic block via ATRP reaction, to create novel photolabile diblock copolymers (Scheme 3).

Experimental Section

Materials and Instrumentation. MeO-PEG_{2000}-OH was purchased from Aldrich Inc. MeO-PEG_{2000}-NH_2 was purchased from Polysciences Inc. The catalyst $Cu^{I}Br$ (98%, Aldrich) was purified as described previously.[29] Monomer *n*-butyl acrylate

*Corresponding authors: Tel 86 25 52090619, Fax 86 25 52090616, e-mail pkuyh9@gmail.com (H.Y.); Tel 33 1 56246762, Fax 33 1 40510636, e-mail patrick.keller@curie.fr (P.K.).

© 2010 American Chemical Society

Published on Web 12/09/2010

Scheme 1. Representative Photocleavable Covalent Junctions of Reported Diblock Copolymers[23−25]

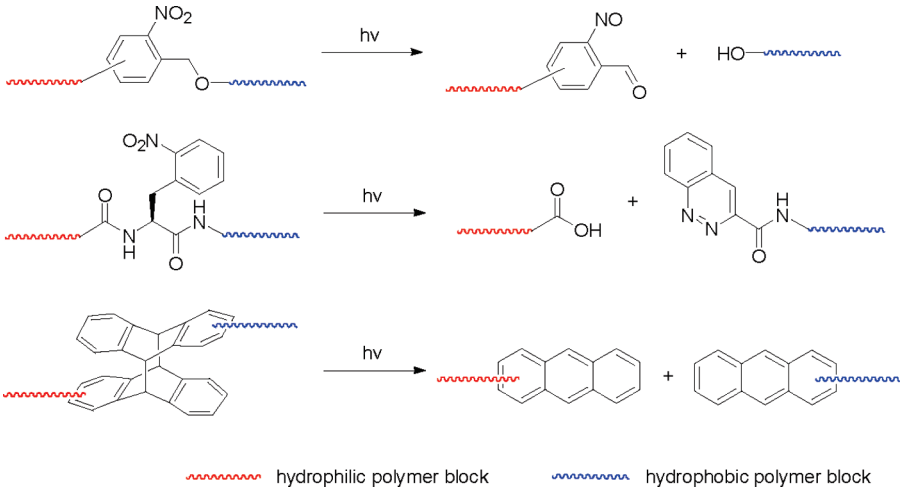

Scheme 2. Principle and Design of Applying α-Truxillic Acid Derivatives as Photocleavable Junctions

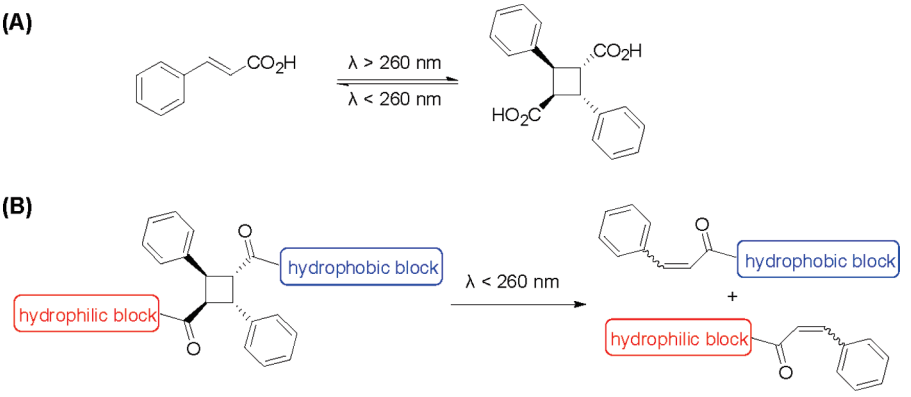

Scheme 3. Synthesis of Diblock Copolymers[a]

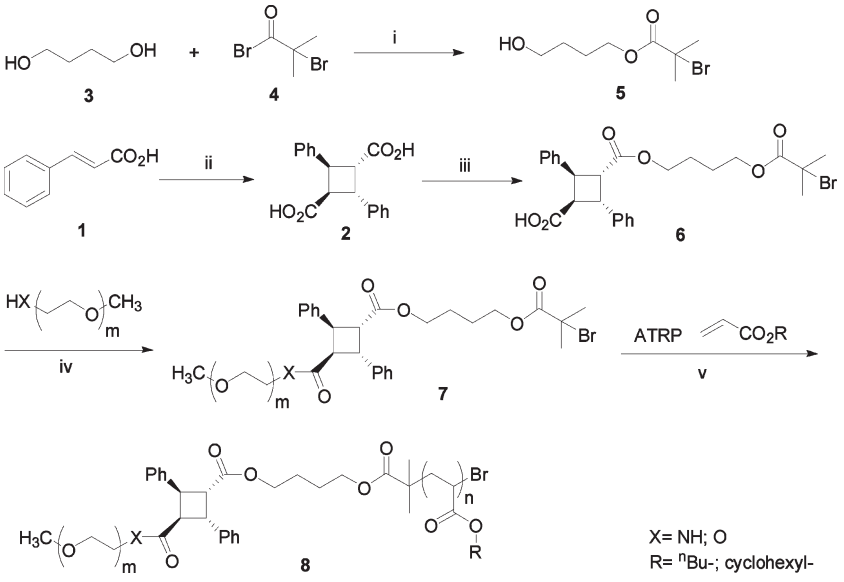

[a] Reagents and conditions: (i) NEt_3, DCM; (ii) UV, solid state; (iii) 1: $(COCl)_2$, DCM; 2: NEt_3, **5**, DCM; (iv) 1: $(COCl)_2$, DCM; 2: NEt_3, PEG-XH, DCM; (v) CuBr, PMDETA, 1,4-dioxane, 70 °C.

(*n*-BA) and cyclohexyl acrylate (99%, Aldrich) were filtered through a short column of neutral Al_2O_3 before use. Dichloromethane, 1, 4-dioxane, and *N*,*N*′,*N*′,*N*″,*N*″-pentamethyldiethylenetriamine were distilled from CaH_2 under argon. THF was distilled from sodium benzophenone ketyl under argon. Other chemical reagents were used without further purification. All nonaqueous reactions were

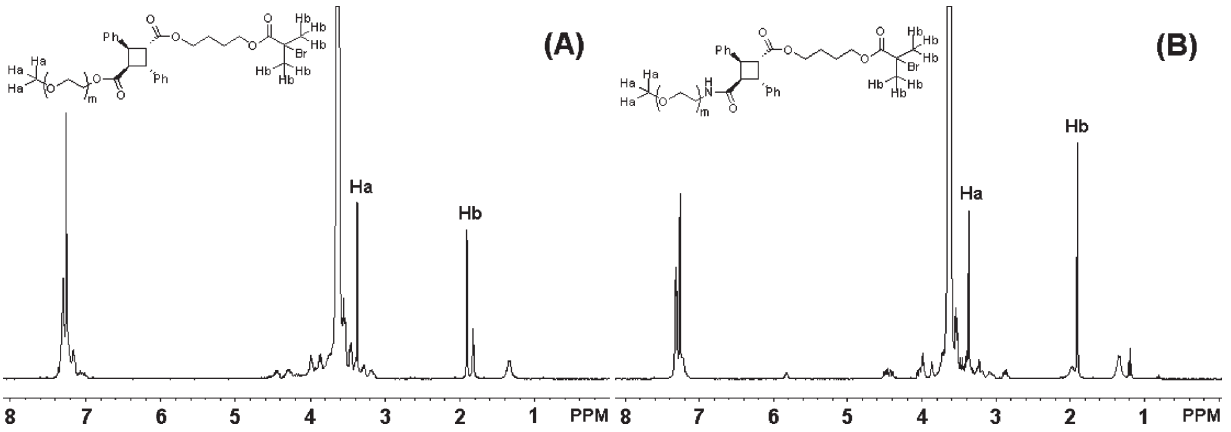

Figure 1. (A) ^{1}H NMR spectra of PEG-*O*-macroinitiator. (B) ^{1}H NMR spectra of PEG-*NH*-macroinitiator.

conducted in oven-dried glassware under a dry argon atmosphere. All flash chromatography was performed using a Macherey-Nagel MN Kieselgel 60 (0.063−1.2 mm).

All ^{1}H NMR spectra were obtained using a Bruker HW300 MHz spectrometer and recorded in $CDCl_3$ (internal reference 7.26 ppm). The molecular weights and the molecular weight distributions of all the polymers were measured by size exclusion chromatography (SEC) using two Waters Styragel HR 5E columns, a Waters 4110 differential refractometer (λ = 930 nm), and a Waters 486 UV detector, in line with a Wyatt miniDAWN light scattering instrument (Ar laser, λ = 690 nm). THF was used as the eluent at 1 mL/min.

The morphological analysis of self-assembled aggregates was performed by transmission electron microscopy (TEM) on samples stained by uranyl acetate or by cryogenic transmission electron microscopy (cryo-TEM) on samples fast frozen in liquid ethane. TEM images were recorded using a Philips CM120 electron microscope equipped with a Gatan SSC 1K_1K CCD camera, and the cryo-TEM images were recorded using a Philips CM 120 kV Lab6. Image acquisition and image analysis were performed at the PICT IBISA Imaging Facility.

A UV lamp (180 mW cm^{-2}, λ = 365 nm; ELC-4001light curing unit; Electro-Lite Corp.) and a low-pressure mercury vapor pencil-style lamp (3.5 mW cm^{-2}, λ = 253.7 nm; inert gas double bore lamp, Jelight Corp.) were used to irradiate the samples to perform the photochemical reactions respectively at different wavelengths. A quartz cell (3.0 cm high, 1.0 cm wide, and 0.1 cm thick) was used to contain sample solutions for irradiation experiments at 254 nm wavelength.

Synthesis of Intermediates 2, 5, and 6 and Macroinitiator 7. The detailed experimental procedures and ^{1}H NMR spectra of compounds **2**, **5**, **6**, and **7** are listed in the Supporting Information. Typical procedure to prepare the macroinitiators **7**: Oxalyl chloride (760 μL, 8.71 mmol) was added into a solution of compound **6** (450 mg, 0.87 mmol) in 20 mL of dry THF. One drop of DMF was added into this reaction mixture, which was then allowed to stir for 1 h at room temperature. The reaction mixture was concentrated by rotary evaporation first and then submitted to a high-vacuum oil pump to completely remove the volatiles. The residue was redissolved in 10 mL of dry $CHCl_3$. Triethylamine (73 μL, 0.52 mmol), DMAP (11 mg, 0.09 mmol), and MeO-PEG_{2000}-OH (830 mg, 0.42 mmol) were added into this resulting solution. The reaction mixture was allowed to stir for 48 h at 60 °C and then poured into a saturated ammonium chloride solution. The resulting solution was extracted by CH_2Cl_2 (100 mL, twice). The combined organic layers were washed by H_2O (40 mL, twice), sodium bicarbonate aqueous solution (40 mL, twice), brine (40 mL, once), dried over sodium sulfate, and then concentrated by rotary evaporation to a 2 mL solution, which was precipitated from 100 mL of diethyl ether to give the desired compound, MeO-PEG_{2000}-O-macroinitiator (810 mg), as a white solid.

Table 1. Characterization of Amphiphilic Diblock Copolymers

entry	copolymers[a]	M_n[b] (g/mol)	M_w[b] (g/mol)	M_w/M_n	R[c]
1	PEG_{45}-^{O}*b*-PBA_{28}	5130	5900	1.15	33/67
2	PEG_{45}-^{O}*b*-PBA_{63}	6050	6660	1.10	19/81
3	PEG_{45}-^{O}*b*-$PCHA_{192}$	11670	13890	1.19	6/94
4	PEG_{45}-^{N}*b*-PBA_{108}	11400	13680	1.20	12/88
5	PEG_{45}-^{N}*b*-PBA_{135}	13890	15720	1.13	10/90
6	PEG_{45}-^{N}*b*-$PCHA_{48}$	7160	8680	1.21	20/80
7	PEG_{45}-^{N}*b*-$PCHA_{36}$	5550	6240	1.13	25/75

[a] DP (degree of polymerization) of acrylates was determined by ^{1}H NMR. [b] Molecular weight measurements were analyzed by SEC based on calibration using polystyrene standards. [c] R represents the ratio of hydrophilic block weight/hydrophobic block weight.

Based on ^{1}H NMR spectra, MeO-PEG_{2000}-O-macroinitiator contained some unreacted PEG_{2000}-OH while PEG_{2000}-NH-macroinitiator had no PEG_{2000}-NH_2 left over.

Synthesis of PEO-*b*-PBA/PCHA Copolymers. Typical procedure: MeO-PEG_{2000}-macroinitiator (100 mg, 0.04 mmol), CuBr (11.5 mg, 0.08 mmol), *n*-butyl acrylate (220 mg, 1.72 mmol), 1, 4-dioxane (0.35 mL), and PMDETA (16.7 μL, 0.08 mmol) were added into a Schlenk-type flask. The flask was degassed and exchanged with argon via three freeze−thaw cycles and then sealed in a pressure tube which was heated at 70 °C for 18 h. The reaction mixture was diluted with THF and passed through a short basic aluminum oxide column to remove Cu salts. The resulting solution was concentrated by rotary evaporation and a high-vacuum oil pump to remove all the solvent and the unreacted *n*-butyl acrylate, finally providing the corresponding polymer as colorless oil (215 mg).

For MeO-PEG_{2000}-O-macroinitiator, in order to remove unreacted PEG-OH, the copolymer was further dialyzed against THF-H_2O (1:3 volume ratios) solution to remove MeO-PEG_{2000}-OH, using a Spectra/Por regenerated cellulose membrane with a molar mass cutoff of 3500 Da, and then lyophilized to give a pure compound. Alternatively, the crude copolymer could also be purified by silica column chromatography (eluting solvents: CH_2Cl_2/MeOH, 95/5). However, the trace acids present in regular silica gel decomposed the copolymer into two homopolymers by cutting off the linker. For MeO-PEG_{2000}-NH-macroinitiator, the above dialysis−lyophilization step was unnecessary.

Self-Assembly of the Amphiphilic Block Copolymers in Water. The block copolymers were first dissolved in 1,4-dioxane or THF at a concentration of 1.0 mg/mL. Deionized water was then added very slowly (5 μL portions) into 1.0 mL of the copolymer solution with gentle shaking. After each addition of water droplet, the solution was left to equilibrate for 5 min. The cycles of water addition and equilibration were stopped after a total amount of 1.5 mL of water has been added. The turbid solution was then dialyzed against deionized water (water

changed every 6 h) for 3 days to remove all the organic solvents, using a Spectra/Por regenerated cellulose membrane with a molar mass cutoff of 3500 Da.

Results and Discussion

Synthesis and Characterization of Amphiphilic Block Copolymers. The amphiphilic diblock copolymers synthesis protocol is shown in Scheme 3. Recrystallized *trans*-cinnamic acid **1** was irradiated in solid state in open air with a UV lamp (180 mW cm^{-2}, λ = 365 nm; ELC-4001 light curing unit; Electro-Lite Corp.) for 24 h. The corresponding dimer, α-truxillic acid (**2**), was first monofunctionalized with

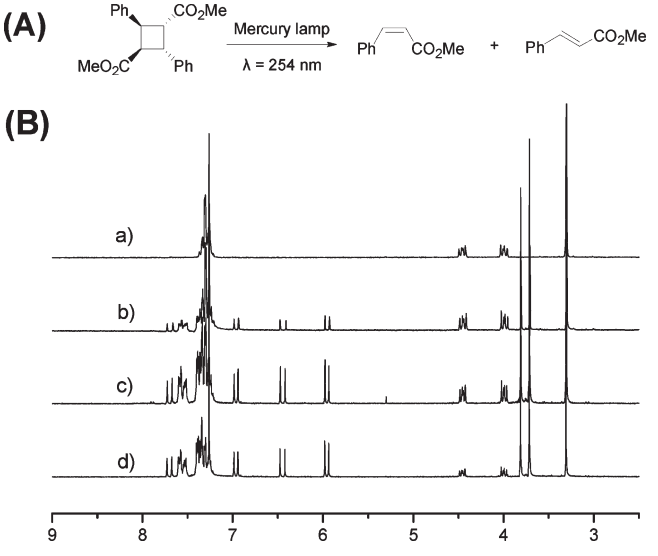

Figure 2. (A) Deep-UV illumination of α-truxillic acid dimethyl ester. (B) ^{1}H NMR spectra of α-truxillic acid dimethyl ester: (a) without illumination, (b) 1 h illumination, (c) 2 h illumination, (d) 4 h illumination.

(4-hydroxybutyl)-2-bromo-2-methylpropanoate (**5**), which was prepared by a simple esterification reaction between 1, 4-butanediol (**3**) and 2-bromo-2-methylpropionyl bromide (**4**) and then reacted with monomethoxypoly(ethylene glycol), PEG-OH, or PEG-NH_2 to provide the macroinitiators **7**. The macroinitiators were then used in the atom-transfer radical polymerization (ATRP) of different acrylate monomers to give the desired amphiphilic diblock copolymers **8**.

In the above synthetic protocol (Scheme 3), steps i and iii generated difunctional byproducts in addition to the desired monofunctional compounds, which could be easily separated by flash column chromatography since they were all small molecules. However, the synthesis and purification of macroinitiator **7** in step iv was very tedious but was also the key step in the whole work. Our first try was to use the standard DCC/DMAP coupling reaction[30] to form an ester bond linking PEG-OH and compound **6**, which resulted in a very low yield. Then, we used oxalyl chloride to activate the carbonyl acid group to form a carbonyl chloride, which was reacted with PEG-OH or PEG-NH_2 (0.5 mol equiv of compound **6**). Despite several optimization tests, PEG-*O*-macroinitiator still had some unreacted PEG-OH inside (Figure 1A; for detailed integration values, see the Supporting Information), which could not be purified in this step. PEG-NH_2, as a much stronger nucleophile, provided pure PEG-*NH*-macroinitiator (Figure 1B). Fortunately, the contaminated PEG-OH could be removed in the final stage through a simple dialysis−lyophilization process.

Seven different amphiphilic diblock copolymers were synthesized and characterized (Table 1). The hydrophilic block was always monomethoxylpoly(ethylene glycol) (PEG_{45}-OH or PEG_{45}-NH_2, MW 2000, DP 45); the hydrophobic block was either poly(butyl acrylate) or poly(cyclohexyl acrylate). The degrees of polymerization of the poly(acrylate) blocks were determined by ^{1}H NMR using the integration value of the methylene protons (−O−CH_2CH_2−O−) of PEG as the

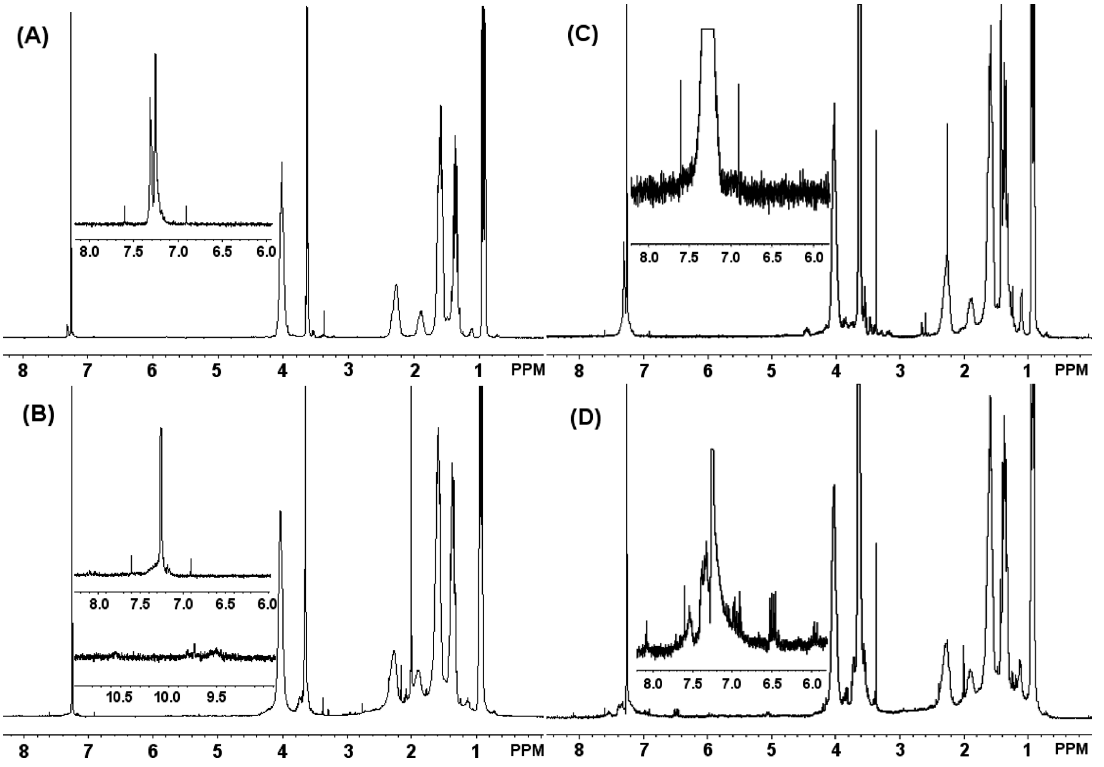

Figure 3. ^{1}H NMR spectra of PEG_{45}-^{N}*b*-PBA_{135} before illumination (A) and after 8 h illumination (B). ^{1}H NMR spectra of PEG_{45}-^{O}*b*-PBA_{28} before illumination (C) and after 8 h illumination (D).

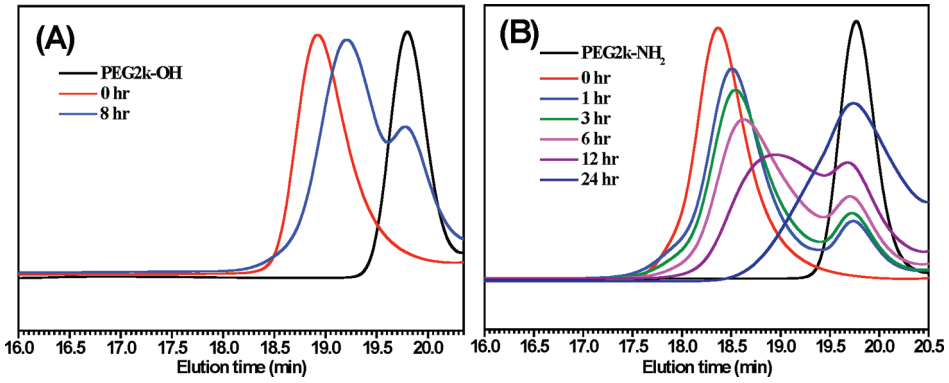

Figure 4. (A) SEC chromatograms of PEG_{45}-^{O}b-PBA_{28} with increasing UV exposure times. (B) SEC chromatograms of PEG_{45}-^{N}b-PBA_{108} with increasing UV exposure times.

reference (see the Supporting Information). Herein, -^{O}b- represents an ester bond linker between PEG and truxillic acid, while -^{N}b- represents an amide bond linker between PEG and truxillic acid.

Model Molecule Illumination Test. Before studying the photocleavage of amphiphilic diblock copolymers, a simple model molecule illumination test was performed on a small molecule, α-truxillic acid dimethyl ester, which is supposed to be capable of being photocleaved into two cinnamic acid methyl ester molecules. Assuming the cyclobutane ring of α-truxillic acid dimethyl ester might have two random cutoff directions, we should recover both *trans*-cinnamic acid methyl ester and *cis*-cinnamic acid methyl ester (Figure 2A).

The initial concentration of α-truxillic acid dimethyl ester was 5.0 mg/mL in THF. According to Spectral Database for Organic Compounds SDBS,[31] δ 3.81, 6.45, and 7.69 belong to *trans*-cinnamic acid methyl ester, while δ 3.71, 5.96, and 6.97 belong to *cis*-cinnamic acid methyl ester. After 1, 2, and 4 h of irradiation (3.5 mW cm^{-2}, λ = 253.7 nm; inert gas double bore lamp, Jelight Corp.), based on the ^{1}H NMR integration value ratio of three methyl protons (α-truxillic acid dimethyl ester at δ 3.30, *trans*-cinnamic acid methyl ester at δ 3.81, *cis*-cinnamic acid methyl ester at δ 3.71), we could calculate the molar ratios of the three compounds (Figure 2B and Supporting Information). Interestingly, the molar ratio of *cis*-cinnamic acid methyl ester and *trans*-cinnamic acid methyl ester remains constant at 1.3 during the whole illumination.

Photoirradiation of Diblock Copolymers. We applied proton NMR and size exclusion chromatography (SEC) techniques to study the photocleavage of four amphiphilic diblock copolymers: PEG_{45}-^{O}b-PBA_{28} (poly(ethylene glycol)-*block*-poly(butyl acrylate)), PEG_{45}-^{N}b-$PCHA_{48}$ (poly(ethylene glycol)-*block*-poly(cyclohexyl acrylate)), PEG_{45}-^{N}b-PBA_{135}, and PEG_{45}-^{N}b-PBA_{108}. The initial concentrations of these amphiphilic diblock copolymers were all of 5.0 mg/mL in THF. Since our available mercury lamp had a very low power intensity of 3.5 mW cm^{-2}, we have had to illuminate our copolymer solutions for several hours.

At first, a series of PEG_{45}-^{N}b-PBA_{135} samples were irradiated for 6, 8, 12, and 16 h. We expected to observe the olefin protons of cinnamic group appearing at δ 7−6 on ^{1}H NMR spectra. However, as shown in Figure 3A,B, neither olefin protons nor even the aromatic protons were visualized. Then, we realized that our mercury lamp would generate ozone which could destroy all the olefins and even aromatic rings. Meanwhile, since the initial concentrations of PEG_{45}-^{N}b-PBA_{135} was only 5.0 mg/mL, a relatively long hydrophobic block (135 BA units) in the copolymer made the concentration of the α-truxillic acid linker much lower, which was more susceptible to the trace amount of ozone generated in THF solvent. Thus, a shorter copolymer, PEG_{45}-^{O}b-PBA_{28} dissolved in degassed THF was illuminated for 8 h in inert gas environment. As shown in Figure 3D, olefin protons around δ 6.5 on ^{1}H NMR spectra were clearly visualized, peaks that were absent from the original before-illumination sample (Figure 3C).

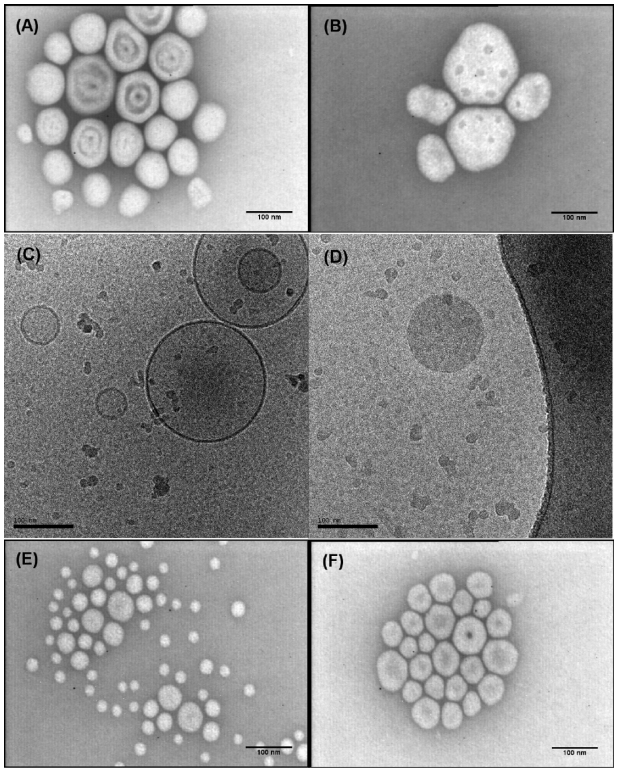

Figure 5. TEM images of block copolymer self-assemblies. In the 1,4-dioxane−H_2O system: PEG_{45}-^{N}b-$PCHA_{48}$ (A) and PEG_{45}-^{N}b-$PCHA_{36}$ (E). In the THF−H_2O system: PEG_{45}-^{N}b-$PCHA_{48}$ (B) and PEG_{45}-^{N}b-$PCHA_{36}$ (F). (C) and (D) show cryo-TEM images of PEG_{45}-^{N}b-$PCHA_{48}$ block copolymer self-assemblies in the 1,4-dioxane−H_2O system. Scale bar = 100 nm for all the figures.

The photocleavage was also confirmed by SEC. As shown in Figure 4A, when PEG_{45}-^{O}b-PBA_{28} was illuminated for 8 h, it showed a new peak appearing close to the peak of pure PEG_{45}-OH. A further cleavage-by-irradiation overtime experiment was performed on PEG_{45}-^{N}b-PBA_{108} (Figure 4B). With increasing times of irradiation, the original peak intensity decreased while the new peak close to the peak of pure PEG_{45}-NH_2 increased. Finally, 24 h illumination seemed to completely break all the cyclobutane ring junctions.

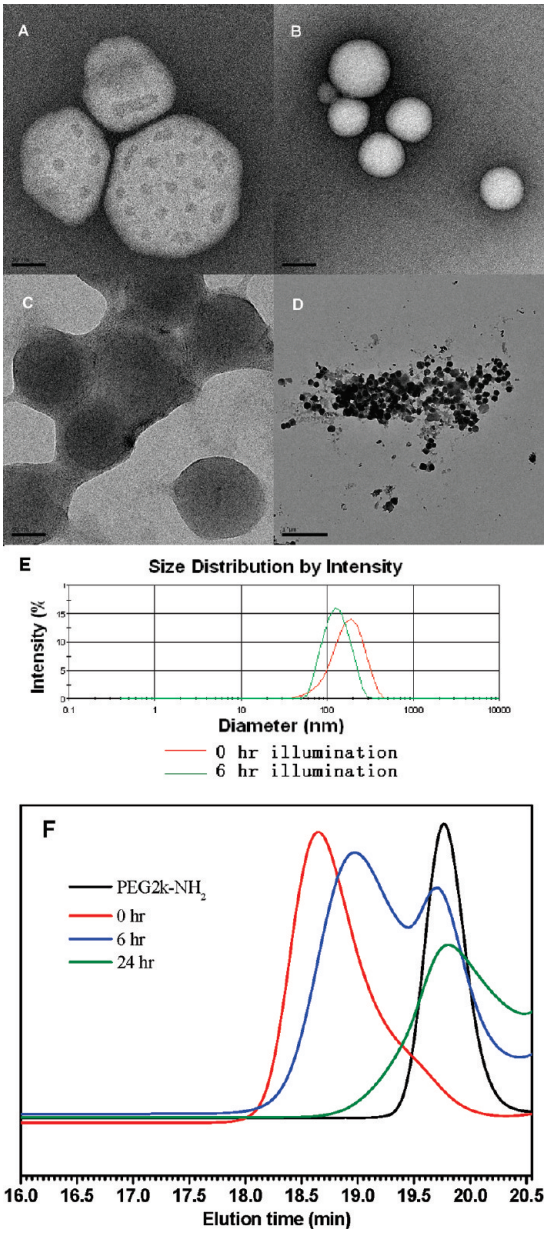

Figure 6. (A) TEM images of PEG_{45}-^{N}b-$PCHA_{48}$ self-assembly in water before illumination (scale bar = 50 nm). (B) TEM images of PEG_{45}-^{N}b-$PCHA_{48}$ self-assembly in water after 6 h illumination (scale bar = 50 nm). (C, D) TEM images of PEG_{45}-^{N}b-$PCHA_{48}$ self-assembly in water after 24 h illumination (scale bar = 50 nm for C, 1 μm for D). (E) DLS size distribution by intensity graph of the formed nano-objects before illumination and after 6 h illumination. (F) SEC chromatograms of PEG_{45}-^{N}b-$PCHA_{48}$ with increasing UV exposure times.

Photoirradiation of Self-Assembled Nano-objects. Our ultimate goal was to observe a UV-light-induced disassembly of the nano-objects made by self-assembly of the amphiphilic block copolymers in water. The ideal scenario was to have an original self-assembled vesicle broken after photoirradiation. In order to get vesicles, we chose to use a much stiffer PCHA (poly(cyclohexyl acrylate)) hydrophobic block instead of PBA (poly(butyl acrylate)) since the cyclohexyl ring system is much more rigid which would help build the hydrophobic shells of vesicles.

On the basis of our previous experiences,[32] when the hydrophilic block/hydrophobic block weight ratio, R, is between 20/80 and 40/60, the block copolymer has better chance to form vesicles in aqueous solution. Thus, PEG_{45}-^{N}b-$PCHA_{48}$ (R = 20/80) and PEG_{45}-^{N}b-$PCHA_{36}$ (R = 25/75) were chosen for the self-assembly experiments in aqueous solution at a low concentration of 1 mg/mL in deionized water with the aid of 1, 4-dioxane or THF as cosolvent. The morphologies of all the observed nano-objects are shown in Figure 5.

Analysis by TEM with negative staining revealed that PEG_{45}-^{N}b-$PCHA_{48}$ formed a mixture of spherical micelles and spherical vesicles in the 1,4-dioxane$-H_2O$ system (Figure 5A). Cryo-TEM showed vesicles as being the minority nano-objects (Figure 5C) while micelles were unfortunately the majority ones (Figure 5D). In the THF$-H_2O$ system, PEG_{45}-^{N}b-$PCHA_{48}$ self-assembled into irregular micelles (Figure 5B). Another copolymer, PEG_{45}-^{N}b-$PCHA_{36}$, appeared as giving almost pure micelles in 1,4-dioxane$-H_2O$ and THF$-H_2O$ systems (Figure 5E,F).

Although we did not find monodisperse vesicle morphology in these photolabile amphiphilic block copolymer systems, disassembly of micelles under photoirradiation should still be attractive. When the irregular micelles of PEG_{45}-^{N}b-$PCHA_{48}$ sample self-assembled in THF$-H_2O$ (Figure 6A) was illuminated by a deep UV source, the nano-objects were transformed into much smaller polydisperse condensed nanospheres (Figure 6B) after 6 h exposure and became micrometer-sized precipitates (Figure 6C,D) after 24 h exposure. Dynamic light scattering (DLS) and SEC experiments (Figure 6E,F) confirmed these observations. As shown in Figure 6F, 6 h of irradiation did not break all the block copolymers but changed the hydrophilic$-$hydrophobic balance of the whole system, thus changing the morphology of the nano-objects.[1] However, when all the copolymers were photocleaved after 24 h of irradiation, the pure hydrophobic polymer chains were not stable in aqueous solution, resulting in their precipitation as solid.

Conclusion

In conclusion, we developed and studied novel photolabile diblock copolymers bearing α-truxillic acid derivative junctions. Although the photocleavage of these copolymers requires a strong UV source (λ < 260 nm) and long irradiation time which is harmful to cells and tissues, these "proof-of-idea" block copolymers could still be attractive candidates for applications in nanoreactors and templates for micro- or nanostructured materials. Furthermore, since α-truxillic acid derivatives can survive UV irradiation of λ > 260 nm, wavelengths that are not supported by *o*-nitrobenzyl groups, multiblock copolymers bearing these two photolabile junctions could be selectively cut off in specific blocks using different wavelengths of light. This will be the subject of a future publication.

Acknowledgment. This research was supported in part by National Natural Science Foundation of China (Grant No. 21002012) and Agence Nationale de la Recherche (Award No. ANR-07-MAPR-0020-02), and by NSF MRSEC (Grant No. DMR-0820579). We thank Dr. J. Plastino for her critical reading of the manuscript.

Supporting Information Available: Details of the synthesis and characterization; ^{1}H NMR spectra. This material is available free of charge via the Internet at http://pubs.acs.org.

References and Notes

(1) (a) Discher, D. E.; Eisenberg, A. *Science* **2002**, *297*, 967–973. (b) Kita-Tokarczyk, K.; Grumelard, J.; Haefele, T.; Meier, W. *Polymer* **2005**, *46*, 3540–3563. (c) Kukula, H.; Schlaad, H.; Antonietti, M.; Forster, S. *J. Am. Chem. Soc.* **2002**, *124*, 1658–1663. (d) Riess, G. *Prog. Polym. Sci.* **2003**, 1107–1170.

(2) (a) Joralemon, M. J.; McRae, S.; Emrick, T. *Chem. Commun.* **2010**, *46*, 1377–1393. (b) York, A. W.; Kirkland, S. E.; McCormick, C. L.

Adv. Drug Delivery Rev. **2008**, 1018–1036. (c) Ganta, S.; Devalapally, H.; Shahiwala, A.; Amiji, M. *J. Controlled Release* **2008**, *126*, 187–204. (d) Discher, D. E.; Ortiz, V.; Srinivas, G.; Klein, M. L.; Kim, Y.; Christian, D.; Cai, S.; Photos, P.; Ahmed, F. *Prog. Polym. Sci.* **2007**, *32*, 838–857. (e) Mahmud, A.; Xiong, X. B.; Aliabadi, H. M.; Lavasanifar, A. *J. Drug Targeting* **2007**, *15*, 553–583. (f) Nishiyama, N.; Kataoka, K. *Pharm. Ther.* **2006**, *112*, 630–648.

(3) (a) Alemdaroglu, F. E.; Herrmann, A. *Org. Biomol. Chem.* **2007**, *5*, 1311–1320. (b) Taubert, A.; Napoli, A.; Meier, W. *Curr. Opin. Chem. Biol.* **2004**, *8*, 598–603.

(4) (a) Vriezema, D. M.; Aragonès, M. C.; Elemans, J. A. A. W.; Cornelissen, J. J. L. M.; Rowan, A. E.; Nolte, R. J. M. *Chem. Rev.* **2005**, *105*, 1445–1490. (b) Rodionov, V.; Gao, H.; Scroggins, S.; Unruh, D. A.; Avestro, A.-J.; Frechet, J. M. J. *J. Am. Chem. Soc.* **2010**, *132*, 2570–2572.

(5) (a) Ahn, S. K.; Kasi, R. M.; Kim, S. C.; Sharma, N.; Zhou, Y. X. *Soft Matter* **2008**, *4*, 1151–1157. (b) Discher, B. M.; Hammer, D. A.; Bates, F. S.; Discher, D. E. *Curr. Opin. Colloid Interface Sci.* **2000**, *5*, 125–131.

(6) (a) Smith, A. E.; Xu, X. W.; McCormick, C. L. *Prog. Polym. Sci.* **2010**, *35*, 45–93. (b) Wang, Y.; Xu, H.; Zhang, X. *Adv. Mater.* **2009**, *21*, 2849–2864. (c) Meng, F. H.; Zhong, Z. Y.; Jan, F. *Biomacromolecules* **2009**, *10*, 197–209. (d) Li, M. -H.; Keller, P. *Soft Matter* **2009**, *5*, 927–937. (e) Rapoport, N. *Prog. Polym. Sci.* **2007**, *32*, 962–990. (f) Rijcken, C. J. F.; Soga, O.; Hennink, W. E.; van Nostrum, C. F. *J. Controlled Release* **2007**, *120*, 131–148.

(7) (a) Du, J.; Wang, Y.; Lewis, A. L.; Armes, S. P. *J. Am. Chem. Soc.* **2005**, *127*, 17982–17983. (b) Borchert, U.; Lipprandt, U.; Bilang, M.; Kimpfler, A.; Rank, A.; Peschka-Süss, R.; Schubert, R.; Lindner, P.; Förster, S. *Langmuir* **2006**, *22*, 5843–5847. (c) Chiu, H.-C.; Lin, Y.-W.; Huang, Y.-F.; Chuang, C.-K.; Chern, C.-S. *Angew. Chem., Int. Ed.* **2008**, *47*, 1875–1878. (d) Bellomo, E. G.; Wyrsta, M. D.; Pakstis, L.; Pochan, D. J.; Deming, T. J. *Nature Mater.* **2004**, *3*, 244–248. (e) Rodriguez-Hernandez, J.; Lecommandoux, S. *J. Am. Chem. Soc.* **2005**, *127*, 2026–2027. (f) Klaikherd, A.; Nagamani, C.; Thayumanavan, S. *J. Am. Chem. Soc.* **2009**, *131*, 4830–4838. (g) Liu, C.; Hillmyer, M. A.; Lodge, T. P. *Langmuir* **2009**, *25*, 13718–13725.

(8) (a) Power-Billard, K. N.; Spontak, R. J.; Manners, I. *Angew. Chem., Int. Ed.* **2004**, *43*, 1260–1264. (b) Ma, N.; Li, Y.; Xu, H.; Wang, Z.; Zhang, X. *J. Am. Chem. Soc.* **2010**, *132*, 442–443. (c) Napoli, A.; Valentini, M.; Tirelli, N.; Müller, M.; Hubbell, J. A. *Nature Mater.* **2004**, *3*, 183–189. (d) Wang, X.; Wang, H.; Coombs, N.; Winnik, M. A.; Manners, I. *J. Am. Chem. Soc.* **2005**, *127*, 8924–8925. (e) Cerritelli, S.; Velluto, D.; Hubbell, J. A. *Biomacromolecules* **2007**, *8*, 1966–1972. (f) Dong, W.-F.; Kishimura, A.; Anraku, Y.; Chuanoi, S.; Kataoka, K. *J. Am. Chem. Soc.* **2009**, *131*, 3804–3805.

(9) (a) Ahmed, F.; Pakunlu, R. I.; Brannan, A.; Bates, F.; Minko, T.; Discher, D. E. *J. Controlled Release* **2006**, *116*, 150–158. (b) Sanson, C.; Schatz, C.; Le Meins, J. F.; Brulet, A.; Soum, A.; Lecommandoux, S. *Langmuir* **2010**, *26*, 2751–2760.

(10) (a) Azagarsamy, M. A.; Sokkalingam, P.; Thayumanavan, S. *J. Am. Chem. Soc.* **2009**, *131*, 14184–14185. (b) Amir, R. J.; Zhong, S.; Pochan, D. J.; Hawker, C. J. *J. Am. Chem. Soc.* **2009**, *131*, 13949–13951.

(11) (a) Dimitrov, I.; Trzebicka, B.; Muller, A. H. E.; Dworak, A.; Tsvetanov, C. B. *Prog. Polym. Sci.* **2007**, *32*, 1275–1343. (b) Morishama, Y. *Angew. Chem., Int. Ed.* **2007**, *46*, 1370–1372. (c) Li, Y.; Lotiz, B.; McCormick, C. L. *Angew. Chem., Int. Ed.* **2006**, *45*, 5792–5795.

(12) Liu, T. Y.; Hu, S. H.; Liu, D. M.; Chen, S. Y.; Chen, I. W. *Nano Today* **2009**, *4*, 52–65.

(13) Yan, Q.; Yuan, J.; Cai, Z.; Xin, Y.; Kang, Y.; Yin, Y. *J. Am. Chem. Soc.* **2010**, *132*, 9268–9270.

(14) (a) Caruso, M. M.; Davis, D. A.; Shen, Q.; Odom, S. A.; Sottos, N. R.; White, S. R.; Moore, J. S. *Chem. Rev.* **2009**, *109*, 5755. (b) Kryger, M. J.; Ong, M. T.; Odom, S. A.; Sottos, N. R.; White, S. R.; Martinez, T. J.; Moore, J. S. *J. Am. Chem. Soc.* **2010**, *132*, 4558–4559. (c) Gao, Z. G.; Fain, H. D.; Rapoport, N. *J. Controlled Release* **2005**, *102*, 203–222. (d) Nelson, J. L.; Roeder, B. L.; Carmen, J. C.; Roloff, F.; Pitt, W. G. *Cancer Res.* **2002**, *62*, 7280–7283.

(15) (a) Goodwin, A. P.; Mynar, J. L.; Ma, Y.; Fleming, G. R.; Frechet, J. M. J. *J. Am. Chem. Soc.* **2005**, *127*, 9952–9953. (b) Alvarez-Lorenzo, C.; Bromberg, L.; Concheriro, A. *Photochem. Photobiol. Sci.* **2009**, *85*, 848–860.

(16) (a) DeMello, A. J. *Nature* **2006**, *442*, 394–402. (b) Song, H.; Chen, D. L.; Ismagilov, R. F. *Angew. Chem., Int. Ed.* **2006**, *45*, 7336–7356.

(17) Fomina, N.; McFearin, C.; Sermsakdi, M.; Edigin, O.; Almutairi, A. *J. Am. Chem. Soc.* **2010**, *132*, 9540–9542.

(18) (a) Mabrouk, E.; Cuvelier, D.; Brochard-Wyart, F.; Nassoy, P.; Li, M.-H. *Proc. Natl. Acad. Sci. U.S.A.* **2009**, *106*, 7294–7298. (b) Wang, G.; Tong, X.; Zhao, Y. *Macromolecules* **2004**, *37*, 8911–8917. (c) Liu, X.; Jiang, M. *Angew. Chem., Int. Ed.* **2006**, *45*, 3846–3850. (d) Desponds, A.; Freitag, R. *Langmuir* **2003**, *19*, 6261–6270.

(19) (a) Li, C.; Zhang, Y.; Hu, J.; Cheng, J.; Liu, S. *Angew. Chem., Int. Ed.* **2010**, *49*, 5120–5124. (b) Konak, C.; Rathi, R. C.; Kopeckova, P.; Kopecek, J. *Macromolecules* **1997**, *30*, 5553–5556.

(20) Kono, K.; Nishihara, Y.; Takagishi, T. *J. Appl. Polym. Sci.* **1995**, *56*, 707–713.

(21) Yuan, X.; Fischer, K.; Schärtl, W. *Langmuir* **2005**, *21*, 9374–9380.

(22) (a) Jiang, X.; Lavender, C. A.; Woodcock, J. W.; Jeremiah, W.; Zhao, B. *Macromolecules* **2008**, *41*, 2632–2643. (b) Ionov, L.; Diez, S. *J. Am. Chem. Soc.* **2009**, *131*, 13315–13319.

(23) (a) Kang, M.; Moon, B. *Macromolecules* **2009**, *42*, 455–458. (b) Schumers, J. M.; Gohy, J. F.; Fustin, C. A. *Polym. Chem.* **2010**, *1*, 161–163. (c) Katz, J. S.; Zhong, S.; Ricart, B. G.; Pochan, D. J.; Hammer, D. A.; Burdick, J. A. *J. Am. Chem. Soc.* **2010**, *132*, 3654–3655. (d) Sundararjan, S.; Sengupta, S.; Ibele, M. E.; Sen, A. *Small* **2010**, *6*, 1479–1482.

(24) Peters, F. B.; Brock, A.; Wang, J.; Schultz, P. G. *Chem. Biol.* **2009**, *16*, 148–152.

(25) Goldbach, J. T.; Russell, T. P.; Penelle, J. *Macromolecules* **2002**, *35*, 4271–4276.

(26) (a) Lendlein, A.; Jiang, H.; Junger, O.; Langer, R. *Nature* **2005**, *434*, 879–882. (b) Akabori, S.; Habata, Y.; Nakazawa, M.; Yamada, Y.; Shindo, Y.; Sugimura, T.; Sato, S. *Bull. Chem. Soc. Jpn.* **1987**, *60*, 3453–3455. (c) Caccamese, S.; Maravigna, P.; Montaudo, G.; Recca, A.; Scamporrino, E. *J. Polym. Sci., Polym. Chem. Ed.* **1978**, *16*, 3123–3130. (d) Caccamese, S.; Maravigna, P.; Montaudo, G.; Recca, A.; Scamporrino, E. *J. Polym. Sci., Polym. Chem. Ed.* **1979**, *17*, 1463–1471.

(27) (a) Bernstein, H. I.; Quimby, W. C. *J. Am. Chem. Soc.* **1943**, *65*, 1845–1846. (b) Chi, Y.-M.; Nakamura, M.; Yoshizawa, T.; Zhao, X.-Y.; Yan, W.-M.; Hashimoto, F.; Kinjo, J.; Nohara, T.; Sakurada, S. *Biol. Pharm. Bull.* **2005**, *28*, 1776–1778.

(28) Wang, J.; Matyjaszewski, K. *J. Am. Chem. Soc.* **1995**, *117*, 5614–5615.

(29) Li, M. H.; Keller, P.; Grelet, E.; Auroy, P. *Macromol. Chem. Phys.* **2002**, *203*, 619–626.

(30) Neises, B.; Steglich, W. *Angew. Chem.* **1978**, *90*, 556–557.

(31) http://riodb01.ibase.aist.go.jp/sdbs/cgi-bin/direct_frame_top.cgi.

(32) (a) Yang, J.; Levy, D.; Deng, W.; Keller, P.; Li, M.-H. *Chem. Commun.* **2005**, 4345–4347. (b) Yang, J.; Pinol, R.; Gubellini, F.; Levy, D.; Albouy, P.-A.; Keller, P.; Li, M.-H. *Langmuir* **2006**, *22*, 7907–7911. (c) Pinol, R.; Jia, L.; Gubellini, F.; Levy, D.; Albouy, P.-A.; Keller, P.; Cao, A.; Li, M.-H. *Macromolecules* **2007**, *40*, 5625–5627. (d) Boisse, S.; Rieger, J.; Di-Cicco, A.; Albouy, P.-A.; Bui, C.; Li, M.-H.; Charleux, B. *Macromolecules* **2009**, *42*, 8688–8696. (e) Xu, B.; Pinol, R.; Nono-Djamen, M.; Pensec, S.; Keller, P.; Albouy, P.-A.; Levy, D.; Li, M.-H. *Faraday Discuss.* **2009**, *143*, 235–250. (f) Jia, L.; Cao, A.; Levy, D.; Xu, B.; Albouy, P.-A.; Xing, X.; Bowick, M. J.; Li, M.-H. *Soft Matter* **2009**, *5*, 3446–3451.

166 *Macromolecules* **2011**, *44*, 166–174
DOI: 10.1021/ma101893u

Macromolecules
ARTICLE

Photoinduced Conjugation of Dithioester- and Trithiocarbonate-Functional RAFT Polymers with Alkenes

Till Gruendling,‡ Michael Kaupp, James P. Blinco,‡ and Christopher Barner-Kowollik*

Preparative Macromolecular Chemistry, Institut für Technische Chemie und Polymerchemie, Karlsruhe Institute of Technology (KIT), Engesserstrasse 18, 76128 Karlsruhe, Germany. ‡First author and third author contributed equally to the publication

Received August 18, 2010; Revised Manuscript Received September 24, 2010

ABSTRACT: We report the photoinduced conjugation of polymers synthesized via reversible addition−fragmentation chain transfer (RAFT) polymerization with a number of low molecular weight (functional) olefins. Upon irradiation of a solution of an aliphatic alkene and the benzyl dithioacetic acid ester (CPDA) or dodecyl trithiocarbonate (DoPAT) functional poly(alkyl acrylate) at the absorption wavelength of the thiocarbonyl group (315 nm), incorporation of the alkene at the polymer chain-end occurred. The most efficient systems identified with regard to the rate of reaction and yield were poly(butyl acrylate)/CPDA/ethyl vinyl ether (78% monoinsertion product after 1 h) and poly(butyl acrylate)/CPDA/1-pentene (73% insertion product after 7 h) at ambient temperature. An in-depth analysis of the reaction mechanism by ^{1}H NMR and online size-exclusion chromatography-electrospray ionization tandem mass spectrometry (SEC/ESI−MS^n) revealed that a possible [2 + 2] photoaddition mechanism of conjugation does not take place. Instead, fast β-cleavage of the photoexcited RAFT-end group with subsequent radical addition of an alkene was observed for all employed systems. The presented reaction thus provides a means of spatial and temporal control for the conjugation of alkenes to thiocarbonyl thio-capped macromolecules via the use of UV radiation.

Introduction

Chemistries which enable the efficient and mild conjugation of two or more polymer building blocks have greatly enhanced the toolbox which macromolecular chemists can draw from to generate diverse polymeric architectures. The incorporation of functional groups within the polymer backbone or chain-end, which exhibit orthogonal reactivity to the polymerization chemistries employed, allows conjugation of macromolecular building blocks synthesized by a number of otherwise incompatible living/controlled radical and nonradical polymerization protocols. The numerous applications of orthogonal conjugation chemistries in polymer and materials science have been reviewed by Hawker and co-workers,[1,2] Sumerlin and Vogt,[3] Schubert and co-workers,[4] and by our group.[5,6] Examples include the copper-catalyzed azide−alkyne cycloaddition,[7] thiol−ene[8] and thiol−yne chemistries,[9] oxime formation,[10] and Diels−Alder.[11] The rising interest and developments in ultrarapid and biocompatible conjugation approaches, including copper-free azide−alkyne cycloadditions,[12] and inverse electron demand Diels−Alder,[13] have recently been documented.[6]

The dithioester, trithiocarbonate and xanthate functional group created at the polymer chain end during reversible addition−fragmentation chain transfer (RAFT) polymerization may act as an excellent precursor in macromolecular conjugations. Two approaches have been developed. First, after aminolysis of the RAFT-end group, the produced thiol functionality is able to undergo a number of reactions including thiol−ene, thiol−isocyanate, and thiol−bromide, of which many adhere to the "*click*" chemistry concept. These approaches have been used multifold, e.g., for efficient end group attachment,[14] the generation of hyperbranched polymers[15] and three-arm star polymers.[16] Another powerful concept pioneered within our group uses the ability of the RAFT end group to act as a highly reactive dienophile in hetero Diels−Alder reactions (RAFT−HDA). By means of this approach, star-block copolymers have ben constructed[17] and surface modification of microspheres has been performed in a highly atom-economical manner.[18,19] Recently, we have shown that the introduction of the extremely reactive cyclopentadiene end group enabled quantitative block copolymer formation within a few minutes reaction time.[20,21]

The conjugation approaches so far described are highly efficient and their ongoing evolution with regard to the rate of reaction, orthogonality and compatibility is astounding. However, as these reactions are thermally induced they lack means of efficiently controlling the spatial resolution of the conjugation reaction. Surface modification reactions with polymer brushes are of great importance in controlling the surface wettability characteristics, chemical reactivity and the adhesion of biomolecules and cells in applications such as lab-on-a-chip and cell cultures.[22] Locally constrained modification with functional polymer brushes today is often achieved by UV-induced radical and nonradical grafting-from approaches with masked irradiation.[23] As is the case in solution, the use of efficient conjugation reactions in a grafting-onto approach can significantly enhance the diversity of polymerization protocols applicable to achieve optimal surface characteristics, while UV-induction of the grafting-onto approach allows spatial and temporal control. From the available "*click*"-concepts thiol−ene and thiol−yne using radical photoinitiators are the only systems that can be regarded as photocontrolled.

Analogous to the RAFT−HDA approach, a coupling reaction that utilizes the remaining thiocarbonyl-thio end group that is present after polymerization would be favorable. The ability to

*Corresponding author. E-mail: christopher.barner-kowollik@kit.edu. Fax: (+49) 721 608 5740.

 Published on Web 11/08/2010 © 2010 American Chemical Society

Scheme 1. Possible Reaction Pathways of Photo-Excited Dithioester- and Trithiocarbonate-Functional Compounds Leading to an Effective Conjugation of the Polymer with Alkenes

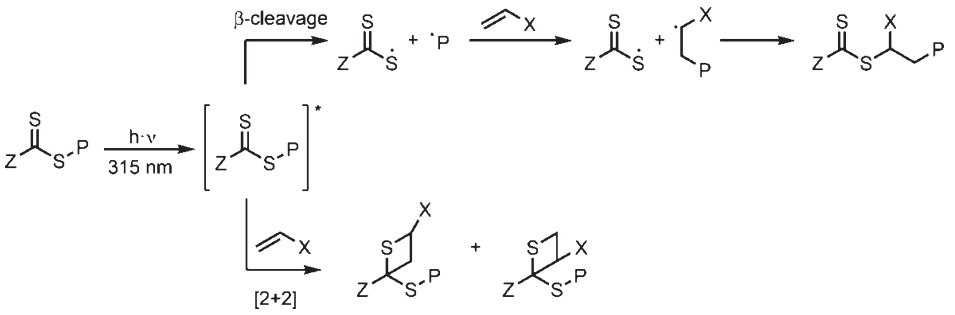

perform photoinduced reactions on such a system will provide the synthetic chemist with a means of photoconjugation that does not require any prior end-group modification steps, thereby significantly increasing the net reaction efficiency. Upon investigation of the current literature, photoinduced [2 + 2] cycloadditions employing the dithioate functional group appear as potential candidates to achieve this task.

The current contribution details the results of a systematic study of the dithioester and trithiocarbonate groups from RAFT polymerization as potential precursors for these photoinduced conjugations. A number of electronically diverse, small molecular weight olefins as well as different RAFT-functional groups were investigated in their ability to undergo such reactions. As it became clear in these studies that the targeted cycloaddition reaction did not take place, an alternative mechanism was identified that operated under the employed conditions. While this reaction clearly does not adhere to the principles defining "*click*"-reactions,[24] it has the potential to serve as a useful means of controlled end group functionalization. An account is given of the possible photochemical pathways of this interesting photoinduced conjugation reaction (Scheme 1) based on SEC/ESI−MS^n measurements of the formed reaction products and on low molecular weight model studies.

Experimental Part

Materials. Isobornyl acrylate (iBoAc, technical grade, Alfa-Aesar) and butyl acrylate (BA, 99+%, Acros) were passed through a column of basic alumina (VWR) to remove inhibitor and stored at −19 °C. 2,2′-Azobis(2-methylpropionitrile) (AIBN, Sigma-Aldrich) was recrystallized twice from methanol (VWR) and stored at −19 °C. 2-Phenylpropan-2-yl 2-phenylethanedithioate (CPDA) was synthesized according to the literature.[25] 2-([(Dodecylsulfanyl)carbonothioyl]sulfanyl) propanoic acid (DoPAT, Orica), 1-pentene (Fluka), benzene (*puriss.*, Sigma-Aldrich), ethyl vinyl ether (EVE, Fluka), maleic anhydride (MAn, Acros), and 1-dodecene (Acros), 1,4-dioxene (TCI Europe) were used as received.

Synthesis of Poly(isobornyl acrylate). A mixture of isobornyl acrylate, AIBN and RAFT agent was deoxygenated by purging with nitrogen for 30 min. After this time the flask was sealed and heated to 60 °C. At a predetermined time, *t*, the reaction was stopped by cooling in an ice bath and the reaction mixture was exposed to oxygen. The polymers were isolated by 3-fold precipitation in cold methanol. Conditions of DoPAT-mediated polymerization: $[M]_0/[DoPAT]_0/[AIBN]_0$ = 92:1:0.06, t = 20 min, M_n = 3750 g·mol^{-1}, PDI = 1.11, conversion = 4%. Conditions of CPDA-mediated polymerization: $[M]_0/[CPDA]_0/[AIBN]_0$ = 92:1:0.06, t = 120 min, M_n = 2850 g·mol^{-1}, PDI = 1.20, convn = 5%.

Synthesis of Poly(butyl acrylate). A solution of AIBN and RAFT agent in butyl acrylate was deoxygenated by purging with nitrogen for 30 min. After this time the flask was sealed and heated to 60 °C. At a predetermined time, *t*, the reaction was stopped by cooling in liquid nitrogen and the reaction mixture was exposed to oxygen. Residue monomer was removed *in vacuo*. Conditions of DoPAT-mediated polymerization: $[M]_0/[DoPAT]_0/[AIBN]_0$ = 110:1:0.06, t = 30 min, M_n = 3250 g·mol^{-1}, PDI = 1.11, conversion = 23%. Conditions of CPDA-mediated polymerization: $[M]_0/[CPDA]_0/[AIBN]_0$ = 205:1:0.20, t = 70 min, M_n = 3000 g·mol^{-1}, PDI = 1.14, convn = 13%.

Photoreactions. *For Single Reactions*. A 40 mg sample of the polymer was dissolved in 1 mL of the olefin or, in the case of solid olefins, 1 mL of benzene and transferred to a Schlenk flask (Pyrex, diameter 15−20 mm). The solution was deoxygenated by three consecutive freeze−pump−thaw cycles. The flasks were backfilled with an inert atmosphere and irradiated by rotating around a compact low-pressure fluorescent lamp (Philips, Medical Therapy UV−B Narrow Band/01, 36W) emitting at 315 nm (±10 nm) at a distance of 40−50 mm in a custom built photo reactor (see Supporting Information for details). After the reaction, the solvent and remaining alkene were evaporated *in vacuo* and the isolated product was redissolved in THF and analyzed via SEC/ESI−MS^n.

For Time Series Reactions. A 160 mg sample of polymer was dissolved in 12−14 mL of an olefin solution in benzene (refer to Table 1 for molar equivalents). In case of maleic anhydride, 30 mL of benzene were used. The solution was deoxygenated by three consecutive freeze−pump−thaw cycles. In an argon glovebox, equal volumes of the solution were aliquoted into headspace vials (Pyrex, diameter 20 mm) which were crimped airtight with styrene/butadiene rubber seals. The vials were subsequently irradiated under the conditions described above. The irradiated solutions were analyzed with no prior purification via SEC/ESI−MS^n.

Small Molecule Model Reaction. DoPAT (1016 mg, 2.85 mmol, 1 equiv) and 1-pentene (2 mL, 9.14 mmol, 3.2 equiv) were dissolved in 20 mL of benzene. The solution was deoxygenated by three consecutive freeze−pump−thaw cycles. The mixture was irradiated through a quartz filter with an 8 W TLC-lamp (CAMAC) at 366 nm at the least possible distance for 23 h. After the reaction solvents were evaporated *in vacuo*. The product was isolated via column chromatography using a gradient of solvents from ethylacetate/hexane 1:2 to pure ethyl acetate. The single insertion product 4-(dodecylthiocarbonothioylthio)-2-methylhexanoic acid was afforded as a yellowish wax (330 mg, 28%, ^{1}H NMR ($CDCl_3$), 250 MHz, δ (ppm): 0.81 (t, −S−CH_2−CH_2−C_9H_{18}−C**H$_3$**, 3H, J = 7.0 Hz), 0.85 (t, −S−CH−(R)−$(CH_2)_2$C**H$_3$**, 3H, ^3J = 7.2 Hz), 1.19 (s_{br}, −S−CH_2−CH_2−C_9**H$_{18}$**−CH_3, −S−CH−(R)−(C**H$_2$**)$_2$-CH_3, S−CH−(R)−CH_2−CH−(C**H$_3$**)−COOH, 26H), 1.62 (m, −S−CH_2−C**H$_2$**−C_9H_{18}−CH_3, S−CH−(R)−C**H$_2$**−CH−(CH_3)−COOH, 5H), 2.69 (m, S−CH−(R)−CH_2−C**H**−(CH_3)−COOH, 1H), 3.27 (dt, −S−C**H$_2$**−CH_2−C_9H_{18}−CH_3, 2H, ^3J = 7.5 Hz, ^3J = 8.2 Hz), 4.25 (m, −S−C**H**−(R)−$(CH_2)_2CH_3$, 1H)).

SEC/ESI−MS^n. Spectra were recorded on an LXQ mass spectrometer (ThermoFisher Scientific, San Jose, CA) equipped with an atmospheric pressure ionization source operating in the nebulizer assisted electrospray mode. The instrument was calibrated in the m/z range 195−1822 using a standard containing caffeine, Met-Arg-Phe-Ala acetate (MRFA) and a mixture of

Table 1. Comparison of the Influence of the RAFT Agent, Monomer, and Olefin Chemical Composition on the Relative Abundances of the Main Product Species and Side Products Observed in the Electrospray Ionization Mass Spectrum[a]

RAFT agent/ monomer	olefin	t_r /h	eq_{ene}	$\int P_RZ+$ En/%	$\int P_RZ$/%	$\int P_RZ+$ 2En/%	$\int S_R+En+$ $\int V_R+En$/%	$\int V_R+$ $\int S_R$/%	$\int P_RZ+$ 3En/%	$\int P_RZ-$ CS/%	$\int P_RZ-$ CS_2/%	$\int$unknown[e]/ %
DoPAT/BA	1-pentene	22	1000	**61.7**	**11.6**	6.7	5.0[d]	3.2	5.0[c]	*c*	*d*	7.0
		47	100	**33.2**	**32.6**	4.8	9.4[d]	9.1	3.1[c]	*c*	*d*	7.8
	MAn[h]	47	1000[f]	**36.7**	**31.8**	4.8	2.2	2.2	1.4	1.4	*c*	19.3[c]
	EVE[h]	2.5	1000	**62.8**	**6.7**	11.0	2.1[d]	1.4	5.6[c]	*c*	*d*	10.3
	1,4-dioxene	4	200	**46.8**[c]	**30.4**[d]	4.5	2.9	10.8	*d*	*c*	4.5	
DoPAT/iBoAc	1-pentene[b]	16.5	2100	**49.0**	**15.8**[d]	9.1	*c*	7.5	*c*	4.5	5.4	8.8
	MAn[h]	47	1000[f]	**23.1**	**59.9**	3.1	2.2	2.5[c]	0.9	4.2	*c*	14.3
	1-dodecene	4	320	**20.3**	**52.3**	4.5	2.5	9.7[c]	0.2	1.6	*c*	9.9
	EVE[h]	5	1000	**53.5**	**18.4**[c]	4.1	*c*	1.2[d]	1.2	3.3	*d*	18.6[g]
CPDA/BA	1-pentene	7	1000	**73.0**	**7.7**	6.3	3.8	6.9[c]	*c*	*c*	2.1	
	MAn[h]	47	1000[f]	**61.1**[c]	**12.1**	14.0	2.9	4.0[c]	4.7	*d*	1.2	*c*
	EVE[h]	1	1000	**78.1**	**5.0**	9.8	1.6	4.2[c]	*c*	*c*	1.3	

[a] The last column lists species of significant mass spectral abundance yet unknown identity. The relative ratios in the table are based on a rationing of all peaks with a significant intensity above 1% of the main signal. [b] With CAMAC 8W TLC-lamp at 366 nm. [c] Species pair with mass spectral overlap, minor species was not included in the integration. [d] Species pair with mass spectral overlap, minor species was not included in the integration. [e] This species exhibits different *m*/*z* for different system (DoPAT/BA/MA, 1774.2 Th; DoPAT/BA/EVE, 1685.6 Th; DoPAt/iBoAc, 1774.2 Th; CPDA/BA, 1692.2 Th). [f] Saturated maleic anhydride solution. [g] Includes two peaks that may be assigned to $\mathbf{P_RZ+En+O}$ and $\mathbf{P_RZ+2En+O}$ from oxidation of the RAFT-end group. [h] EVE: Ethyl vinyl ether, MAn: Maleic anhydride.

fluorinated phosphazenes (Ultramark 1621) (all from Aldrich). A constant spray voltage of 4.5 kV was used and nitrogen at a dimensionless sweep gas flow-rate of 2 (approximately 3 $L \cdot min^{-1}$) and a dimensionless sheath gas flow-rate of 12 (approximately 1 $L \cdot min^{-1}$) were applied. The capillary voltage, the tube lens offset voltage and the capillary temperature were set to 60 V, 110 V and 275 °C respectively. The LXQ was coupled to a Series 1200 HPLC-system (Agilent, Santa Clara, CA, USA) consisting of a solvent degasser (G1322A), a binary pump (G1312A), a high-performance autosampler (G1367B), followed by a thermostated column compartment (G1316A). Separation was performed on two mixed bed size exclusion chromatography columns (Polymer Laboratories, Mesopore 250 × 4.6 mm, particle diameter 3 μm) with precolumn (Mesopore 50 × 4.6 mm) operating at 30 °C. THF at a flow rate of 0.30 $mL \cdot min^{-1}$ was used as eluent. The mass spectrometer was coupled to the column in parallel to an RI-detector (G1362A with SS420x A/D) in a setup described earlier.[26] 0.27 $mL \cdot min^{-1}$ of the eluent were directed through the RI-detector and 30 $\mu L \cdot min^{-1}$ infused into the electrospray source after postcolumn addition of a 100 μM solution of sodium iodide in methanol at 20 $\mu L \cdot min^{-1}$ by a microflow HPLC syringe pump (Teledyne ISCO, Model 100DM). Flow-rates, instrument settings and salt concentrations were optimized to yield maximum ionization efficiency while keeping salt cluster formation to a minimum.[27] A 20 μL aliquot of a polymer solution with a concentration of 3 mg mL^{-1} was injected onto the HPLC system. Data treatment was performed, using the procedure outlined in a recent publication.[28]

Molecular Weight Analysis by SEC. For the determination of molecular weight distributions (MWD), a SEC system (Polymer Laboratories PL-GPC 50 Plus), comprising an auto injector, a guard column (PLgel Mixed C, 50 × 7.5 mm) followed by three linear columns (PLgel Mixed C, 300 × 7.5 mm, 5 μm bead-size) and a differential refractive index detector was employed. THF was used as the eluent at 40 °C, with a flow rate of 1 $mL \cdot min^{-1}$. The SEC system was calibrated using narrow poly(methyl methacrylate) standards ranging from 600 to 5105 $g \cdot mol^{-1}$ and polystyrene standards (Polymer Standards Service, Mainz, Germany) ranging from 200 to 6106 $g \cdot mol^{-1}$. The resulting molecular weight distributions were determined by universal calibration using Mark−Houwink parameters for PiBoAc ($K = 5.00 \times 10^{-5}$ dL g^{-1}, $\alpha = 0.745$),[29] pBA ($K = 12.2 \times 10^{-5}$ dL g^{-1}, $\alpha = 0.70$),[30] and for polystyrene ($K = 14.0 \times 10^{-5}$ dL g^{-1} and $\alpha = 0.70$).[31]

Results and Discussion

As a member of the class of thiocarbonyls, RAFT-functional polymers show a weak absorption band (400−600 nm) for the dipole forbidden n → π^* ($S_0 \rightarrow S_1$) transition.[32−34] Another strong absorption band is observed at 240−320 nm, which is attributed to the $\pi \rightarrow \pi^*$ ($S_0 \rightarrow S_2$) transition. Experimentally determined extinction coefficients of the RAFT agents employed in the current study were 15 800 $L \cdot mol^{-1}$ ($\lambda_{max} = 309$ nm) for the trithiocarbonate DoPAT and 11 400 $L \cdot mol^{-1}$ ($\lambda_{max} = 311$ nm) for the dithioester CPDA. Electronically excited thiocarbonyls are able to undergo a number of reactions from both the S_2 as well as the lower T_1 excited states, as $S_1 \rightarrow T_1$ intersystem crossing occurs rapidly, at least for the larger aromatic thioketones.[35] The photochemistry of thiocarbonyls, which is somewhat distinct from their carbonyl analogues, includes pathways toward cycloaddition, cleavage, dimerization, reduction, and oxidation of which the first two are of interest with regards to conjugation reactions. The reader is advised of several exhaustive reviews on the topic.[36−38] Cycloaddition toward electron-rich as well as electron deficient double bonds is observed upon S_1 ($n\pi^*$) or S_2 ($\pi\pi^*$) band irradiation of aliphatic thioketones. Aromatic thioketones show cycloaddition preferably with electron rich alkyl and alkoxy substituted olefins with formation of dithianes and thietanes. Quenching studies as well as the lack of stereoselectivity in these reactions suggest that the reactive species is the T_1 triplet and that diradical intermediates are involved in the reaction pathway. A wavelength dependency of the reactivity has been observed for both aliphatic[39] and aromatic thioketones.[40,41] Relatively little interest has been paid to the photochemistry of thioesters and trithiocarbonates. Thiolactones,[42,43] dithiolactones,[43] *O*-alkyl thiobenzoates,[41,44,45] thiocarbonates[46] and 1,3-thiazole-5-thione[47] have been found to undergo intra- and intermolecular photocycloadditions to olefins upon irradiation. It was argued that effective reaction occurs from the $n\pi^*$ excited state for thioesters.[45] An investigation of the current literature examples reveals, however, an important prerequisite for [2 + 2]-photocycloadditions of these compounds to occur: The β-substituents should be tethered intramolecularly and/or they should exhibit poor radical leaving-group character. Irradiation of an *O*-alkyl thiobenzoate leads to the formation of an *S*-alkyl thiobenzoate via 1,3-shift by a formal β-cleavage process.[36] Norrish type II photoelimination is observed if a hydrogen is available in γ−position.[48,49] The stabilizing nature of the phenyl group and the resonance stabilization of the formed thiocarboxyl radical by the oxygen/sulfur lone pair seem to dramatically enhance the ability of thiocarboxylates to undergo β-cleavage reactions over cycloaddition.[37] β-cleavage has also been observed for the structurally similar phenacyl sulphides.[49] In the context of

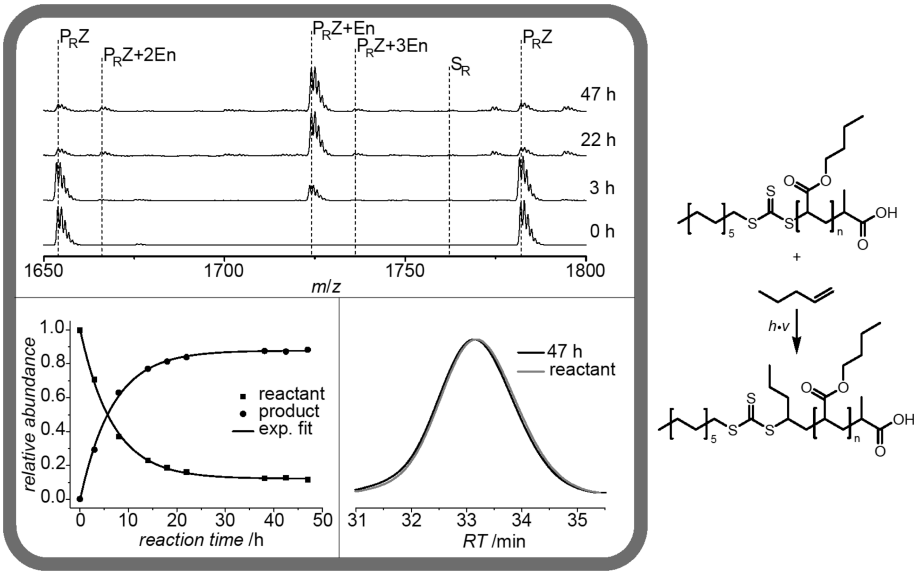

Figure 1. SEC/ESI−MS investigation of the species formed during the conjugation reaction between 1-pentene and poly(butyl acrylate) carrying a trithiocarbonate end group from DoPAT-mediated polymerization at 315 nm. The development of the relative abundances of the major components during the reaction and the SEC traces before and after the conjugation are shown in the lower left and lower right graphs of each inset, respectively. Please refer to Scheme 2 for structural formulas corresponding to the shorthand assignments in the spectra.

living/controlled radical polymerization this behavior is also well-known for the group of dithiocarbamate photoiniferters.[50−53] Upon irradiation these compounds undergo reversible β-cleavage at the carbon sulfur bond and thus yield some control over the radical polymerization process.[54] Some studies have focused on UV-induced RAFT-polymerization and the effect of UV−vis radiation on the living/controlled nature of the polymerization process.[55−59]

Both reaction pathways may potentially be operating concomitantly during the current photochemical coupling reaction of dithioester and trithiocarbonate RAFT-agents with alkenes as is shown in Scheme 1. The photoexcited RAFT-end group may either react by the [2 + 2] Paterno−Büchi analogous mechanism, or it may undergo radical β-cleavage and insertion of the alkene molecule. In addition, other reaction pathways, such as Norrish type II cleavage, CS- and CS_2-extrusion, radical propagation, and bimolecular termination may also be operating in the investigated system. These will be discussed in the following section.

Electrospray ionization mass spectrometry (ESI−MS) as a sensitive and gentle mass spectrometric technique has successfully been employed to elucidate the mechanism of controlled/living and conventional free radical polymerization as well as polymer end group transformations.[28,60,61] Because of the softness of the ionization process, the method allows access to a greater number of possibly labile product species than, for example, matrix-assisted laser desorption/ionization (MALDI).[62] ESI−MS was therefore employed to monitor the progress of the coupling reaction and for a structural analysis of the formed reaction products. Figure 1, 4, and 5 show the results of the mass spectrometric analysis of the reaction of poly(butyl acrylate) carrying CPDA or DoPAT end groups with an excess of 1-pentene or ethyl vinyl ether. In the top inset of each figure, a cut-out of the ESI mass spectrum is given, corresponding to one repeat unit of the polymer. The progress of the reaction can be monitored—assuming negligible influence of end groups on the ionization efficiency—by following the development of the main mass spectral components at different reaction times. The reaction of poly(butyl acrylate) carrying the DoPAT end group with 1-pentene is shown in Figure 1. At t = 0 h, only the DoPAT-functional polymer, $\mathbf{P_RZ}$ (see Scheme 2 for structural formulas) is observed in the spectrum. Conjugation with the olefin proceeds smoothly toward a species corresponding in mass to the desired conjugation product, $\mathbf{P_RZ}$+**En**. The SEC-traces recorded of the reactant polymer and after 47 h of reaction are given in the lower right inset of Figure 1. A precise overlap of the reactant and product elution curves indicates that neither chain-propagation nor bimolecular combination have taken place during the reaction.

An integration of the mass spectral abundances is possible and it allows the derivation of quantitative data on the concentrations and concentration ratios of species formed during the end group conversion.[28,63] This procedure was also employed in the current study to graphically follow the relative abundance of the product peak ($\mathbf{P_RZ}$+**En**) to the reactant peak ($\mathbf{P_RZ}$) (lower left inset in Figure 1). As can be seen, apparent conversion only taking into account the relative ratio of reactant and product peak reaches 90% after about 25 h for this system. With increasing reaction time some minor additional species are identified in the spectrum, which correspond in mass to saturated polymer, carrying only the leaving R group ($\mathbf{S_R}$) and possibly some vinyl terminated polymer ($\mathbf{V_R}$), shifted by −2 Th relative to $\mathbf{S_R}$. These species may have been formed by Norrish type II fragmentation or alternatively may be the result of radical termination by disproportionation. Other minor products are those corresponding to an addition of two ($\mathbf{P_RZ}$+**2En**) or three 1-pentene units ($\mathbf{P_RZ}$+**3En**) respectively. Formation of these species would only be expected in case of a radical reaction pathway, initiated by radical β-cleavage, as the thietane ring formed by a putative [2 + 2] is expected to be inert against any further photoinduced cleavage or alkene insertion.

In a subsequent in-depth quantitative analysis of the mass spectrum, the relative abundances of all peaks with a peak area of more than 1% of the total mass spectral integral was determined.[28,63] The results are collated in Table 1. For the system BA/DoPAT/1-pentene, the table reveals that under optimum reaction conditions and at 88.4% conversion (11.6% $\mathbf{P_RZ}$), 61.7% of the mass spectral area correspond to the desired conjugation product ($\mathbf{P_RZ}$+**En**), whereas double and triple insertion products amount to 6.7% and 5.0% respectively. Termination products of the polymer radical formed by β-cleavage ($\mathbf{V_R}$ and $\mathbf{S_R}$) amount to 3.2% and peaks indicative of insertion of

Scheme 2. Structural Formulas of Major Species Observed during the Conjugation of Dithioester- and Trithiocarbonate-Functional Poly(alkyl acrylates) with Low Molecular Weight Olefins[a]

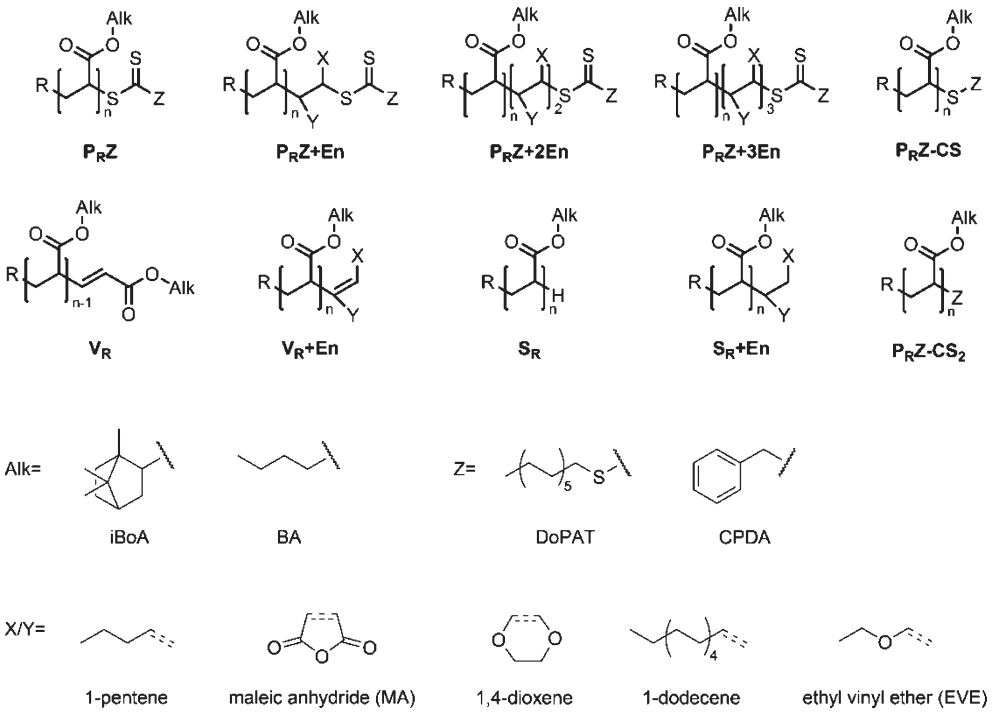

[a] The Z-groups of the employed RAFT-agents as well as the structures of the olefins are given in the lower part of the scheme.

olefin followed by radical termination ($\mathbf{V_R}$+**En** and $\mathbf{S_R}$+**En**) make up 5.0% of the spectral area. Minor peaks are possibly present in the spectrum, which can be assigned to photoinduced expulsion of CS ($\mathbf{P_RZ-CS}$) or CS_2 ($\mathbf{P_RZ-CS_2}$). Because of spectral peak overlap with other more abundant species, an integration of these peaks is not possible. The abundance of the peaks that have not been integrated due to spectral overlap never exceed that of the more abundant species. Additional unassigned species of significant abundance ("unknown" in Table 1) are present in the spectrum, which together amount to 7.0% of the total spectral area. It is likely that the true abundances of the formed products may vary slightly, as the impact of noise on the mass spectral area is difficult to account for since it may be affected by background suppression effects and adduct peaks of solvents and salt molecules. Because of a low quantum yield of the radical dissociation step and possible slow addition of the formed poly(butyl acryloyl) radical to the alkene double bond, about 1000 eq of alkene were needed to enable reaction within a reasonable time frame. When reducing the excess of olefin to 100 eq, the reaction proceeded significantly slower. After 47 h of irradiation, and 67.4% conversion (32.6% $\mathbf{P_RZ}$), only 33.2% of the mass spectral species corresponded to the desired insertion product $\mathbf{P_RZ}$+**En**. The amount of termination products $\mathbf{S_R}$/$\mathbf{V_R}$ and $\mathbf{S_R}$+**En**/$\mathbf{V_R}$+**En** increased to 9.1% and 9.4% respectively, which is explained—in accordance with a presumed radical addition mechanism—by a reduced rate of addition over bimolecular termination, due to the decreased olefin concentration. Interestingly, a comparison of the mass spectral abundances recorded for the different olefins reveals that species devoid of RAFT-functionality ($\mathbf{S_R}$/$\mathbf{V_R}$ and $\mathbf{S_R}$+**En**/$\mathbf{V_R}$+**En**) seem to be enhanced in cases where alkenes with abstractable hydrogen atoms in α-position relative to the double bond are employed. Such an observation can be explained by a hydrogen-abstraction mechanism of the polymer radical to the olefin, which operates as a competitive pathway.

From the fact that double and triple insertion play a minor part in the photoreaction in the aforementioned system, the radical mechanism depicted in Scheme 1 is certainly to be preferred over the [2 + 2] Paterno-Büchi-analogous insertion mechanism. However, it is important to note that the species $\mathbf{P_RZ}$+**En** resulting from either reaction pathway are isomers of each other. As such, their structures cannot possibly be distinguished by mass measurement alone. Further structural proof was therefore required to finally exclude the [2 + 2] pathway as a competitive side reaction. Collision induced dissociation (CID) ESI−MS/MS was performed of the species corresponding in mass-to-charge ratio (m/z) to the alkene adduct of the RAFT-functional polymer $\mathbf{P_RZ}$+**En** (Figure 2). As can be taken from the figure, collisional excitation of the molecule with m/z = 1595.9 Th leads to the loss of a neutral molecule with m/z = 278.0 Th and formation of polymer corresponding to $\mathbf{V_R}$+**En**. The fragment is proposed to be trithiocarbonic acid dodecyl ester (278.1 Da). The loss of the trithiocarbonic acid ester is also the dominant fragmentation pathway of the intact DoPAT-capped poly(alkyl acrylate). For $\mathbf{P_RZ}$+**En** the expulsion of this moiety would not be expected if a thietane-ring had been formed by a [2 + 2] process. After formation of a thietane ring, it is expected that bond breakage still occurs at the relatively weak C−S σ-bonds. If this took place at the polymer side of the thietane-ring, formation of a thiol-terminated ($\mathbf{P_RZ}$+**SH**) or vinyl functional polymer ($\mathbf{V_R}$) would have been expected. Retro-[2 + 2] would lead to expulsion of thioformaldehyde ($\mathbf{P_RZ}$+**En**−$\mathbf{CH_2S}$) or butanethial ($\mathbf{P_RZ}$+**En**−$\mathbf{C_4H_8S}$), depending on the regioisomers formed during the cycloaddition reaction. The fact that neither species is observed, even at high collision energies (where the parent ion fully fragments) supports the assumption that no thietane is present. Scission of the (CS)−S bond was observed ($\mathbf{P_R}$+**En**+**SH**), yielding a species which is another indicator of the radical insertion mechanism. Analogous fragmentation was observed in the case of conjugation of CPDA-functional poly(butyl acrylate) with pentene (see Supporting Information for a spectrum). As further proof of the radical insertion mechanism, photoreactions were carried out on a small molecule trithiocarbonate so that NMR could be utilized for structural elucidation. In this

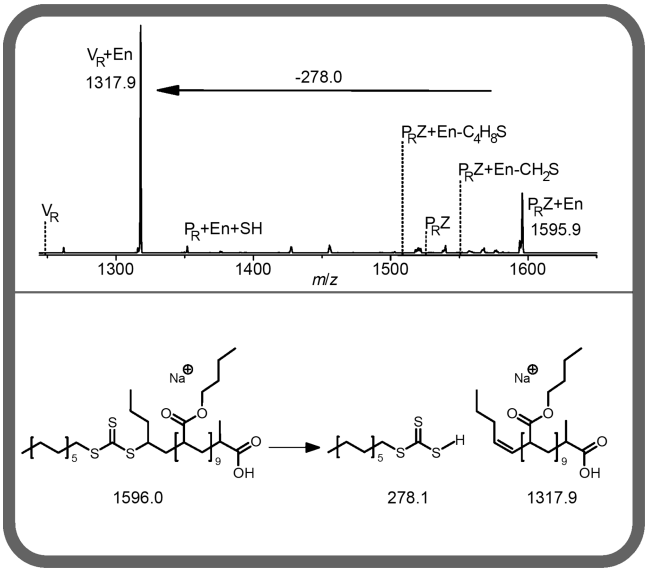

Figure 2. Tandem electrospray ionization mass spectrometric analysis of the main functional polymer species (**P_RZ+En**, m/z = 1595.9 Th) formed by the photoreaction between 1-pentene and poly(butyl acrylate) carrying a trithiocarbonate end group from DoPAT-mediated polymerization. Loss of a species with mass-to-charge ratio of 278.0 Th indicates that the trithiocarbonic acid mono dodecyl ester is lost during CID. Other species indicative of a [2 + 2] insertion mechanism (**P_RZ**, **P_RZ+En−C_4H_8S**, **P_RZ+En−CH_2S**) cannot be identified in the spectrum.

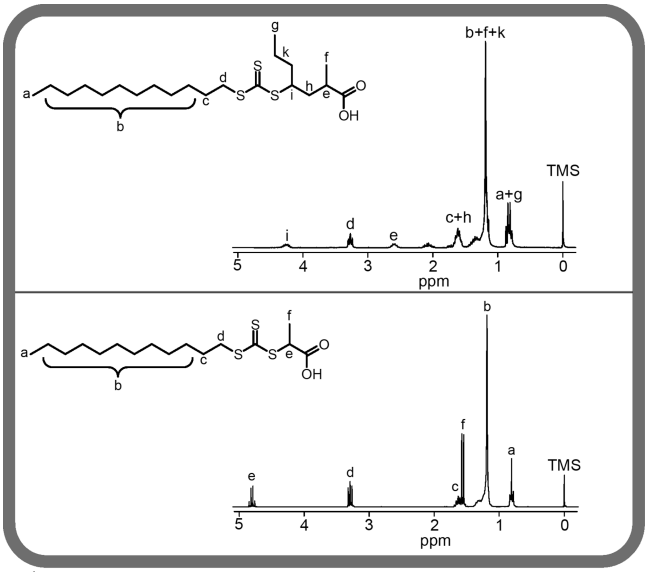

Figure 3. ^{1}H NMR analysis of the pure DoPAT RAFT reagent (bottom) and of the product formed by the model-photoreaction between 1-pentene and the DoPAT RAFT-reagent together with the most conclusive structural assignment (top).

case DoPAT was irradiated in the presence of 1-pentene and subsequently the major photoadduct separated from unreacted starting materials via column chromatography. A ^{1}H NMR comparison between pure DoPAT and its photoadduct is shown in Figure 3. Had a [2 + 2] cycloaddition occurred, it would be expected that the protons of the thietane ring were well resolved and could be observed between 3 and 4 ppm. The other signals were not expected to shift significantly. As is seen in the figure, no new protons are observed in this area. The major differences in the spectra is the shift of protons e and f, the appearance of a second triplet at 0.85 ppm and of a multiplet at 4.5 ppm indicative of the insertion reaction. The dormant RAFT-functional polymer may also undergo chain transfer thus effectively leading to an enhancement of the quantum yield of the current reaction, since an initially formed polymeric radical may cause multiple olefin insertion processes to occur after chain transfer. A similar effect has been shown to be operative before by Chen et al.[64] As the products arising from degenerative chain transfer cannot be distinguished analytically, such a mechanism must also be considered in the current case.

A more detailed analysis of the reaction products from the model reaction, using, e.g., HPLC/MS seems an interesting additional study. However, the gained data allow the conclusion that the operating mechanism of conjugation is radical insertion of the double bond. As mentioned before, side products, resulting from multiple insertion of alkene and the formation of saturated and vinyl-terminated polymer also observed in the spectrum are in good agreement with the radical mechanism. As a general rule of thumb for an efficient radical photoconjugation, alkenes can be employed that exhibit a high affinity for addition to the poly(butyl acryloyl) radical in copolymerization reactions (low r_1) and a low homopropagation rate (low k_p and/or r_2). This is the case for 1-hexene ($r_1 = -0.13 \pm 0.6$, $r_2 = -0.67 \pm 0.03$ (95% CI) for methyl acrylate[65]) and arguably for all other medium chain aliphatic alkenes including the 1-pentene employed here. Photoreactions with alkenes such as vinyl acetate (r_1 = 3.318, r_2 = 0.018 for BA[66]) and styrene (r_1 = 0.25, r_2 = 0.79 for BA[67]) exhibiting homopolymerization ability lead to chain-extension of the RAFT-functional acrylates as witnessed by an SEC analysis of the reaction products (see Supporting Information for details).

As is shown in Figure 4, the insertion reaction with 1-pentene is significantly accelerated when changing from the trithiocarbonate (DoPAT) to a dithioester (CPDA) capped poly(butyl acrylate). Because of a possibly higher quantum yield of the photoinduced radical β-cleavage reaction, conjugation proceeds within 7 h reaction time. The main product of this reaction at 92.3% conversion (7.7% **P_RZ**) is the expected conjugation product **P_RZ+En** (73.0%) with very little multiple insertion product and few other side products. The SEC traces before and after the conjugation reaction agree well with each other, underpinning the notion that coupling reactions of the transient radicals were minimal or nonexistent.

The system can be even further optimized by using a more electron-rich olefin (ethyl vinyl ether, EVE) which still shows low tendency for homopropagation (r_1 = 3.0, r_2 = 0 for methyl acrylate[68]). In Figure 5 the result of the mass spectrometric analysis of the system BA/DoPAT/ethyl vinyl ether is given. The rapid reaction proceeds to 95.0% conversion (5.0% **P_RZ**) after 1 h irradiation time where 78.1% of **P_RZ+En** are formed. Because of an apparently increased oligomerization ability of this monomer, 9.8% double insertion product (**P_RZ+2En**) are also formed at this reaction time. As is observed in the figure, the system can be described by a sequential A → B → C reaction mechanism with a ratio of the apparent rate coefficients for the first and second insertion k_2/k_1 = 0.021 (fitted curves in Figure 5, bottom left). Interestingly, some reaction product could already be observed at the beginning of the reaction. This may be an indication that the reaction also proceeds under visible light irradiation, in this case by the ambient laboratory light during preparation.

Other olefins which have been tested and for which the product abundances are shown in Table 1 are 1,4-dioxene, which gives generally a very good reaction rate, 1-dodecene and maleic anhydride ($r_1 = 2.788 \pm 0.051$, $r_2 = 0.012 \pm 0.013$ (95% CI) for methyl acrylate[69]). Although the transformation does proceed in an excess of maleic anhydride, the reaction is rather sluggish. 47 h

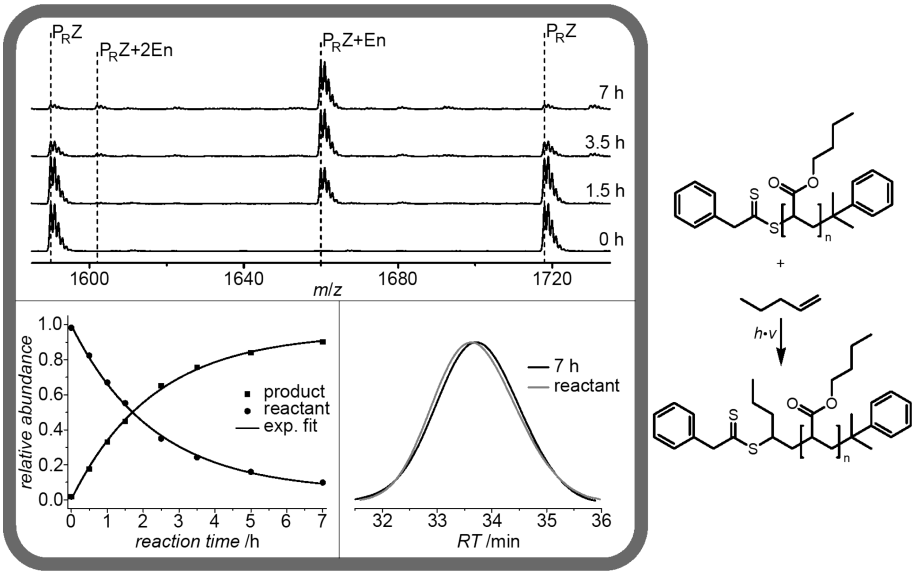

Figure 4. SEC/ESI−MS investigation of the species formed during the conjugation reaction between 1-pentene and poly(butyl acrylate) carrying a dithioester end group from CPDA-mediated polymerization at 315 nm. The development of the relative abundances of the major components during the reaction and the SEC traces before and after the conjugation are shown in the lower left and lower right graphs of each inset, respectively. Please refer to Scheme 2 for structural formulas corresponding to the shorthand assignments in the spectra.

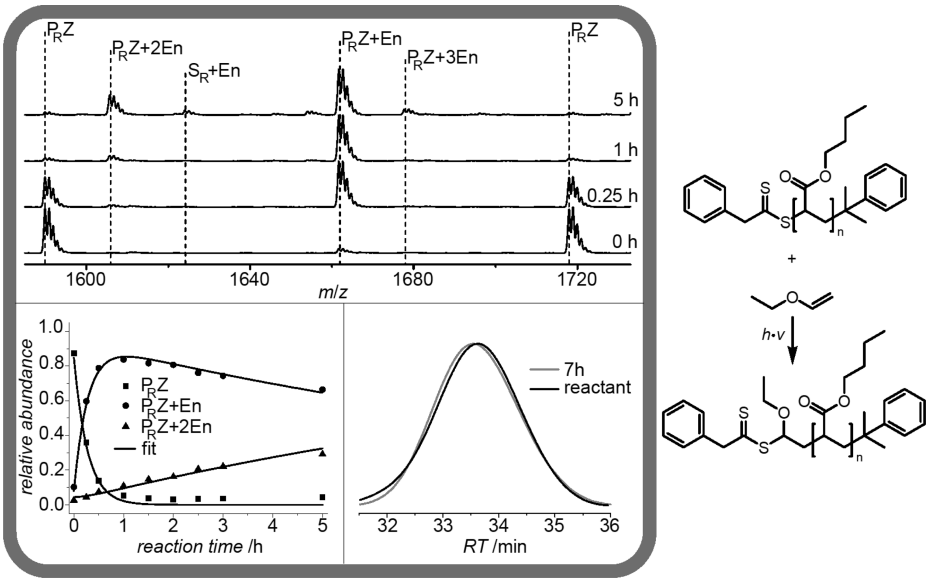

Figure 5. SEC/ESI−MS investigation of the species formed during the conjugation reaction between ethyl vinyl ether and poly(butyl acrylate) carrying a dithioester end group from CPDA-mediated polymerization at 315 nm. The development of the relative abundances of the major components during the reaction and the SEC traces before and after the conjugation are shown in the lower left and lower right graphs of each inset, respectively. Please refer to Scheme 2 for structural formulas corresponding to the shorthand assignments in the spectra.

are needed to achieve 87.9% (12.1% $\mathbf{P_RZ}$) conversion, after which time the insertion product is formed in 61.1% relative abundance (see Supporting Information for mass spectra and conversion vs time plots).

Conclusions

The photoinduced reaction of benzyl dithioacetate (CPDA) and dodecyl trithiocarbonate (DoPAT) functional poly(alkyl acrylates) with a number of electronically diverse low molecular weight alkenes was studied. It was shown that irradiation at the wavelength of the $\pi \rightarrow \pi^*$ transition induced the insertion of a single alkene at the polymer chain-end. An in-depth mechanistic study of the reaction revealed that conjugation proceeded by UV-induced radical β-cleavage of the dithioester/trithiocarbonate-end group followed by an addition of the alkene and subsequent recapping by the RAFT-end group. The most efficient systems identified with regard to rate of reaction and yield were poly(butyl acrylate)/CPDA/ethyl vinyl ether (1 h reaction time at ambient temperature) and poly(butyl acrylate)/CPDA/1-pentene (7 h reaction time at ambient temperature). Although high equivalents of alkene are required, the resulting end group modified polymer can be readily isolated by precipitation. In the case of liquid olefins, the product polymer can simply be isolated by vacuum drying and unreacted olefin can be recycled. The presented photoinduced end group modification reactions may thus provide a convenient means not only for thiocarbonylthio capped polymer modification in solution, but open the possibility

of the temporally and spatially resolved introduction of functionality to RAFT polymers anchored on variable solid substrates.

Acknowledgment. C.B.-K. acknowledges financial support from the Karlsruhe Institute of Technology (KIT) in the context of the Excellence Initiative for leading German universities as well as the German Research Council (DFG) and the Ministry of Science and Arts of the state of Baden-Württemberg. J.B. thanks the Alexander von Humboldt Foundation for financial support via a Humboldt Research Fellowship for Postdoctoral Researchers. We thank Prof. Axel G. Griesbeck from the University of Cologne for helpful discussions regarding mechanistic details of the investigated photoreaction and Orica for the kind donation of the DoPAT RAFT agent.

Supporting Information Available: A table of maximum absorption wavelength, molar extinction coefficients and figure showing an irradiance spectrum of the compact fluorescent lamp used, a schematic drawing of the employed custom-built photoreactor, results of the SEC/ESI−MS analysis of the conjugation reactions with maleic anhydride, ethyl vinyl ether and 1-pentene employing CPDA- and DoPAT-functional poly(butyl acrylate) as well as DoPAT-functional poly(isobornyl acrylate), additional CID/MS^2 studies of the addition product between CPDA-functional poly(butyl acrylate) and pentene, and SEC traces of the chain-extension with vinyl acetate and styrene. This material is available free of charge via the Internet at http://pubs.acs.org.

References and Notes

(1) Hawker, C. J.; Wooley, K. L. *Science* **2005**, *309* (5738), 1200–1205.
(2) Iha, R. K.; Wooley, K. L.; Nyström, A. M.; Burke, D. J.; Kade, M. J.; Hawker, C. J. *Chem. Rev.* **2009**, *109* (11), 5620–5686.
(3) Sumerlin, B. S.; Vogt, A. P. *Macromolecules* **2009**, *43* (1), 1–13.
(4) Becer, C. R.; Hoogenboom, R.; Schubert, U. S. *Angew. Chem., Int. Ed.* **2009**, *48* (27), 4900–4908.
(5) Barner-Kowollik, C.; Inglis, A. J. *Macromol. Chem. Phys.* **2009**, *210* (12), 987–992.
(6) Inglis, A. J.; Barner-Kowollik, C. *Macromol. Rapid Commun.* **2010**, *31* (14), 1247–1266.
(7) Narumi, A.; Fuchise, K.; Kakuchi, R.; Toda, A.; Satoh, T.; Kawaguchi, S.; Sugiyama, K.; Hirao, A.; Kakuchi, T. *Macromol. Rapid Commun.* **2008**, *29* (12−13), 1126–1133.
(8) Shin, J.; Nazarenko, S.; Hoyle, C. E. *Macromolecules* **2009**, *42* (17), 6549–6557.
(9) Chan, J. W.; Shin, J.; Hoyle, C. E.; Bowman, C. N.; Lowe, A. B. *Macromolecules* **2010**, *43*, 4937–4942.
(10) Wu, Z.; Liang, H.; Lu, J. *Macromolecules* **2010**, *43* (13), 5699–5705.
(11) Dag, A.; Durmaz, H.; Demir, E.; Hizal, G.; Tunca, U. *J. Polym. Sci. A Polym. Chem.* **2008**, *46* (20), 6969–6977.
(12) Lutz, J.-F. *Angew. Chem., Int. Ed.* **2008**, *47* (12), 2182–2184.
(13) Blackman, M. L.; Royzen, M.; Fox, J. M. *J. Am. Chem. Soc.* **2008**, *130* (41), 13518–13519.
(14) Li, H.; Yu, B.; Matsushima, H.; Hoyle, C. E.; Lowe, A. B. *Macromolecules* **2009**, *42* (17), 6537–6542.
(15) Xu, J.; Tao, L.; Boyer, C.; Lowe, A. B.; Davis, T. P. *Macromolecules* **2009**, *43* (1), 20–24.
(16) Chan, J. W.; Yu, B.; Hoyle, C. E.; Lowe, A. B. *Chem. Commun.* **2008**, *40*, 4959–4961.
(17) Sinnwell, S.; Inglis, A. J.; Stenzel, M. H.; Barner-Kowollik, C. *Macromol. Rapid Commun.* **2008**, *29* (12−13), 1090–1096.
(18) Nebhani, L.; Sinnwell, S.; Inglis, A. J.; Stenzel, M. H.; Barner-Kowollik, C.; Barner, L. *Macromol. Rapid Commun.* **2008**, *29* (17), 1431–1437.
(19) Nebhani, L.; Schmiedl, D.; Barner, L.; Barner-Kowollik, C. *Adv. Funct. Mat.* **2010**, *20* (12), 2010–2020.
(20) Inglis, A. J.; Sinnwell, S.; Stenzel, M. H.; Barner-Kowollik, C. *Angew. Chem., Int. Ed.* **2009**, *48* (13), 2411–2414.
(21) Inglis, A. J.; Stenzel, M. H.; Barner-Kowollik, C. *Macromol. Rapid Commun.* **2009**, *30* (21), 1792–1798.
(22) Ayres, N. *Polym. Chem.* **2010**, *1* (6), 769–777.
(23) Deng, J.; Wang, L.; Liu, L.; Yang, W. *Prog. Polym. Sci.* **2009**, *34* (2), 156–193.
(24) Kolb, H. C.; Finn, M. G.; Sharpless, K. B. *Angew. Chem.* **2001**, *113* (11), 2056–2075.
(25) Barner-Kowollik, C.; Quinn, J. F.; Nguyen, U. L.; Heuts, J. P. A.; Davis, T. P. *Macromolecules* **2001**, *34* (22), 7849–7857.
(26) Gruendling, T.; Guilhaus, M.; Barner-Kowollik, C. *Anal. Chem.* **2008**, *80* (18), 6915–6927.
(27) Gruendling, T.; Guilhaus, M.; Barner-Kowollik, C. *Macromol. Rapid Commun.* **2009**, *30*, 589–597.
(28) Junkers, T.; Koo, S. P. S.; Davis, T. P.; Stenzel, M. H.; Barner-Kowollik, C. *Macromolecules* **2007**, *40* (25), 8906–8912.
(29) Dervaux, B.; Junkers, T.; Schneider-Baumann, M.; Du Prez, F. E.; Barner-Kowollik, C. *J. Polym. Sci. A Polym. Chem.* **2009**, *47* (23), 6641–6654.
(30) Beuermann, S.; Paquet, D. A.; McMinn, J. H. *Macromolecules* **1996**, *29* (12), 4206–4215.
(31) Strazielle, C.; Benoit, H.; Vogl., O. *Eur. Polym. J.* **1978**, *14*, 331–334.
(32) Rao, V. P. *Sulfur Chemistry* **1992**, *12* (2), 359–399.
(33) Barrett, J.; Deghaidy, F. S. *Spectrochim. Acta A: Mol. Spectrosc.* *31* (5−6), 707−713.
(34) Mahaney, M.; Huber, J. R. *J. Mol. Spectrosc.* **1981**, *87* (2), 438–448.
(35) Molenkamp, L. W.; Weitekamp, D. P.; Wiersma, D. A. *Chem. Phys. Lett.* **1983**, *99* (5−6), 382–387.
(36) Rao, V. P. *Sulfur Chem.* **1992**, *12* (2), 359–399.
(37) Coyle, J. D. *Chem. Rev.* **1978**, *78* (2), 97–123.
(38) Coyle, J. D. *Tetrahedron* **1985**, *41* (23), 5393–5425.
(39) Lawrence, A. H.; Liao, C. C.; Mayo, P. D.; Ramamurthy, V. *J. Am. Chem. Soc.* **1976**, *98* (12), 3572–3579.
(40) Gotthardt, H.; Nieberl, S. *Tetrahedron Lett.* **1976**, *17* (44), 3999–4002.
(41) Ohno, A.; Ohnishi, Y.; Tsuchihashi, G. *J. Am. Chem. Soc.* **1969**, *91* (18), 5038–5045.
(42) Devanathan, S.; Ramamurthy, V. *J. Org. Chem.* **1988**, *53* (4), 741–744.
(43) Nishio, T. *J. Chem. Soc., Perkin Trans. 1* **1995**, No. 5, 561–568.
(44) Ooms, P.; Hartmann, W. *Tetrahedron Lett.* **1987**, *28* (24), 2701–2704.
(45) Ohno, A.; Koizumi, T.; Akazaki, Y. *Tetrahedron Lett.* **1972**, *13* (49), 4993–4996.
(46) Gotthardt, H.; Listl, M. *Chem. Ber.* **1974**, *107* (8), 2552–2557.
(47) Wipf, P.; Heimgartner, H. *Helv. Chim. Acta* **1987**, *70* (4), 992–994.
(48) Barton, D. H. R.; Bolton, M.; Magnus, P. D.; Marathe, K. G.; Poulton, G. A.; West, P. J. *J. Chem. Soc., Perkin Trans. 1* **1973**, 1574–1579.
(49) Wagner, P. J.; Lindstrom, M. J. *J. Am. Chem. Soc.* **1987**, *109* (10), 3062–3067.
(50) Turner, S. R.; Blevins, R. W. *Macromolecules* **1990**, *23* (6), 1856–1859.
(51) Otsu, T.; Matsunaga, T.; Doi, T.; Matsumoto, A. *Eur. Polym. J.* **1995**, *31* (1), 67–78.
(52) Kwak, Y.; Matyjaszewski, K. *Macromolecules* **2010**, *43* (12), 5180–5183.
(53) Otsu, T. *J. Polym. Sci. A Polym. Chem.* **2000**, *38* (12), 2121–2136.
(54) Doi, T.; Matsumoto, A.; Otsu, T. *J. Polym. Sci. A Polym. Chem.* **1994**, *32* (12), 2241–2249.
(55) Ran, R.; Wan, T.; Gao, T.; Gao, J.; Chen, Z. *Polym. Int.* **2008**, *57*, 28–34.
(56) You, Y.-Z.; Hong, C.-Y.; Bai, R.-K.; Pan, C.-Y.; Wang, J. *Macromol. Chem. Phys.* **2002**, *203*, 477–483.
(57) Quinn, J. F.; Barner, L.; Barner-Kowollik, C.; Rizzardo, E.; Davis, T. P. *Macromolecules* **2002**, *35* (20), 7620–7627.
(58) Lu, L.; Zhang, H.; Yang, N.; Cai, Y. *Macromolecules* **2006**, *39*, 3770–3776.
(59) Shi, Y.; Guhuan, L.; Gao, H.; Lu, L.; Cai, Y. *Macromolecules* **2009**, *42*, 3917–3926.
(60) Gruendling, T.; Pickford, R.; Guilhaus, M.; Barner-Kowollik, C. *J. Polym. Sci. A Polym. Chem.* **2008**, *46* (22), 7447–7461.
(61) Buback, M.; Frauendorf, H.; Günzler, F.; Huff, F.; Vana, P. *Macromol. Chem. Phys.* **2009**, *210* (19), 1591–1599.
(62) Hart-Smith, G.; Lammens, M.; Du Prez, F. E.; Guilhaus, M.; Barner-Kowollik, C. *Polymer* **2009**, *50* (9), 1986–2000.
(63) Gruendling, T.; Guilhaus, M.; Barner-Kowollik, C. *Macromolecules* **2009**, *42* (17), 6366–6374.
(64) Chen, M.; Ghiggino, K. P.; Mau, A. W. H.; Rizzardo, E.; Sasse, W. H. F.; Thang, S. H.; Wilson, G. J. *Macromolecules* **2004**, *37* (15), 5479–5481.

(65) Doak, K. W. *J. Am. Chem. Soc.* **1950**, *72* (10), 4681–4686.
(66) Nikolaev, A. F.; Vishnevetskaya, L. P.; Gromova, O. A.; Grigor'eva, M. M.; Kleshcheva, M. S. *Vysokomol. Soedin. A* **1969**, *11*, 2418.
(67) Kostanski, L. K.; Hamielec, A. E. *Polymer* **1992**, *33*, 3706.
(68) Mayo, F. R.; Lewis, F. M.; Walling, C. *J. Am. Chem. Soc.* **1948**, *70* (4), 1529–1533.
(69) DeWilde, M. C.; Smets, G. *J. Polym. Sci.* **1950**, *50* (153), 127–132.

Macromolecules
ARTICLE

Macromolecules **2011**, *44*, 175–180 **175**
DOI: 10.1021/ma102279y

Significant Impact of Thermo-Mechanical Conditions on Polymer Triple-Shape Memory Effect

Junjun Li and Tao Xie*

Chemical Sciences & Materials Systems Laboratory General Motors Research & Development Center, Mail Code: 480-106-710, 30500 Mound Road, Warren, Michigan 48090-9055, United States

Received October 4, 2010

ABSTRACT: A polymer triple-shape memory effect represents one of the most recent discoveries in the rapidly expanding field of shape memory polymers. It refers to the capability of a polymer to memorize two temporary shapes and subsequently recover them, all in one shape memory cycle. Although several examples of triple-shape polymers had been reported in the literature, they were notably evaluated under very different thermo-mechanical conditions. In this study, the effect of various thermo-mechanical conditions on the polymer triple-shape properties was investigated using Nafion as a model material. The choice of the programming and recovery heating methods in constructing triple-shape cycles was found to have a profound impact on the triple-shape properties. As such, the results of this study provided useful reference for future development of triple-shape polymers.

Introduction

A conventional shape memory polymer can fix one temporary shape and recover to its permanent shape when exposed to an appropriate external stimulus.[1−10] With a total of two shapes involved in each shape memory cycle, this effect can be called the dual-shape memory effect. Such a concept of polymer dual-shape memory effect has been known for at least half a century and is the basis for most SMP applications known today.[11−20] Within the past decade or so, the field of shape memory polymers has grown in an accelerated pace. Among the most recent and exciting discoveries are the multishape memory effects, which refer to the capability of a polymer to memorize multiple temporary shapes and subsequently recover them, all in one shape memory cycle.[21−29]

At the molecular scale, the dual-shape memory effect requires the combination of a reversible thermal transition and a mechanism for setting the permanent shape. The former is referred to as a shape memory transition and is commonly a melting or glass transition, while the latter can be physical or chemical cross-linking.[1−10] As such, the expansion from dual- to triple-shape memory effect follows the logic that an additional distinctive shape memory transition allows a second temporary shape to be fixed in the shape memory cycle.[22−29] For this type of triple-shape polymers, the two temporary shapes are introduced and later recovered above and in between the two shape memory transition temperatures (T_{trans}'s), respectively.[22−29] Accordingly, tuning the triple-shape memory effect can be accomplished by changing the T_{trans}'s and/or the ratio between the two shape memory transition phases.

Representing significant deviation from the above strategy is our recent report of the tunable multishape memory effect.[21] It refers to the phenomenon that a polymer with a single yet sufficiently broad thermo-mechanical transition can exhibit multishape memory effects at arbitrarily chosen deformation and recovery temperatures (within the broad transition).[21] In other words, the multishape memory effect can be tuned without changing the material composition, which is in sharp contrast to the triple-shape polymers with two distinct thermal transitions. Putting aside the tunability and different strategies to achieve multishape memory effects, only triple- and quadruple-memory effects have been experimentally demonstrated thus far, although the potential beyond quadruple- is feasible.[21] For simplification, however, we hereby focus on the triple-shape memory effect, noting in particular that the issues discussed hereafter are also applicable to multishape memory effects beyond triple-.

In general, all shape memory effects can be quantitatively evaluated in appropriate thermo-mechanical shape memory cycles.[1−10,21−26] For the dual-shape memory effect, this task is relatively straightforward. It is usually sufficient to determine the extent of shape fixing (shape fixity, R_f) and the degree of recovery (shape recovery, R_r), both of which can be extracted conveniently from a dual-shape memory cycle.[1−10] In such a cycle, deformation (or programming) can be conducted by applying a constant force (i.e., a stress controlled mode) or a target strain (i.e., a strain controlled mode). The stress free shape recovery, on the other hand, can be carried out by either continuously heating or holding the polymer at a constant temperature above its shape memory transition (i.e., isothermal) until the strain reaches an equilibrium value. Although the impact of various thermo-mechanical conditions on dual-shape memory properties have been investigated,[30−34] the specific distinction between different deformation and recovery modes is typically overlooked. Presumably, this is due to the fact that these two factors are not expected to noticeably impact the evaluation of R_f and R_r.

For triple-shape polymers, a careful examination of the literature reveals significant differences in thermo-mechanical conditions under which triple-shape memory cycles were constructed.[21−29] The most notable ones lie in the deformation modes (stress versus strain controlled) and shape recovery conditions (continuous versus staged heating). Since triple-shape memory cycles are intrinsically more complicated than dual-shape memory cycles, it is not clear how much these differences may impact the evaluation of the polymer triple-shape memory effect. In this work, the triple-shape memory effect of Nafion is investigated under carefully designed experimental conditions. We show that, unlike the dual-shape memory effect, the thermo-mechanical conditions greatly impact the triple-shape effect. In the context of the broader

*Corresponding author. E-mail: tao.xie@gm.com.

© 2010 American Chemical Society

Published on Web 12/13/2010

literature on triple-shape polymers, we demonstrate that the protocols employed to construct triple-shape cycles could even challenge the very definition of triple-shape polymers. Although only a few triple-shape memory polymer systems have been reported thus far, we fully anticipate that many more will be developed in the near future. This study thus provides valuable guidelines which will benefit this emerging area of triple-shape polymers.

Experimental Section

Materials. Nafion (acid form, equivalent weight of 1000, and thickness of 0.08 mm) was obtained from DuPont. It was annealed at 140 °C for 25 min prior to investigation.

Shape Memory Characterization. All the thermo-mechanical analysis (TMA) experiments were conducted in a tensile mode using a DMA Q800 (TA Instruments).

Stress controlled deformation was performed by applying a deformation force at a target deformation temperature (T_d) and the force was maintained constant during the subsequent cooling stage. By contrast, strain controlled deformation was conducted by ramping the strain at T_d at 10%/min to a target strain, which was maintained constant during subsequent cooling. All strain recovery experiments were carried out under stress free condition (note: a minimum static force of 0.001 N was used). The strain recovery upon staged heating was conducted by holding the polymer at the target temperatures (recovery temperatures, T_r's) equal to the corresponding deformation temperatures (T_d's) for 25 min. For strain recovery under continuous heating conditions, the experiments were performed by linearly ramping the temperature to 140 °C. Unless otherwise noted, a temperature ramping rate of 5 °C/min was used for both heating and cooling in all experiments.

Results and Discussion

In our previous work, we demonstrated in a broad sense that Nafion possesses tunable multishape memory and temperature memory effects.[21] Of relevance to the current study is that Nafion shows the triple-shape memory effect at any two sufficiently separated deformation temperatures (T_{d1} and T_{d2}) across its broad thermo-mechanical transition (from 55 to 130 °C).[21] This allows its triple-shape memory effect to be tuned based on the selection of T_d's, instead of changing the material composition. Since the focus of the current investigation is not on tunability of the shape memory effect, we concentrate primarily on two deformation temperatures (T_{d1} = 100 °C and T_{d2} = 60 °C) in this investigation.

A triple-shape memory cycle constructed under strain controlled programming and staged heating recovery conditions is shown in Figure 1. In the first deformation (or programming) step, the polymer is deformed at T_{d1} to a target strain ($\varepsilon_{1,load}$) by linear strain ramping. The strain is maintained constant during subsequent cooling (i.e., a strain controlled mode). At this step, stress relaxation is observed. Once the temperature reaches T_{d2} and is equilibrated, the stress is removed. The stress removal leads to an instantaneous strain recovery (i.e., spring back). Isothermal and stress free holding at T_{d2} leads to an equilibrium strain (ε_1). This completes the first programming step and ε_1 is regarded as the first fixed temporary shape. The second programming step proceeds in a similar fashion except that the deformation temperature is T_{d2} and the isothermal and stress free holding temperature is 25 °C. $\varepsilon_{2,load}$ and ε_2 are similarly obtained. The first and second shape fixities (R_{f1} and R_{f2}) are 63.8%, and 98.1%, as calculated using

$$R_{f1} = 100\% \times (\varepsilon_1/\varepsilon_{1,load}) \quad (1)$$

and

$$R_{f2} = 100\% \times (\varepsilon_2 - \varepsilon_1)/(\varepsilon_{2,load} - \varepsilon_1) \quad (2)$$

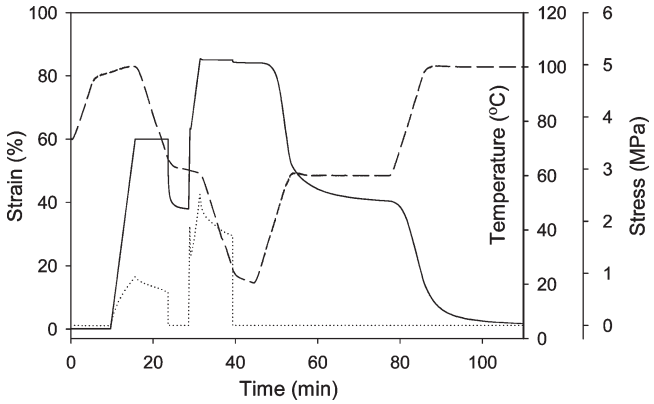

Figure 1. Triple-shape memory cycle obtained under strain controlled programming and staged heating recovery conditions. $T_{d1} = T_{r2} = 100$ °C, $T_{d2} = T_{r1} = 60$ °C. Key: solid line, strain; dotted line, stress; dashed line, temperature.

After programming, the polymer is heated under a stress free condition to induce the strain recovery. In the first recovery step, the temperature is ramped to T_{d2} and held constant until the strain reaches an equilibrium value, which is taken as $\varepsilon_{1,rec}$. Further heating to T_{d1} followed by isothermal holding leads to a second equilibrium strain of $\varepsilon_{0,rec}$. The two shape recoveries (R_{r2} and R_{r1}) are 95.1%, and 106.0%, based on

$$R_{r2} = 100\% \times (\varepsilon_2 - \varepsilon_{1,rec})/(\varepsilon_2 - \varepsilon_1) \quad (3)$$

and

$$R_{r1} = 100\% \times (\varepsilon_{1,rec} - \varepsilon_{0,rec})/(\varepsilon_1 - \varepsilon_0) \quad (4)$$

Here, R_{r1} above 100% is due to the incomplete recovery of the previous recovery event (R_{r2} = 95.1%). The portion that was not recovered in the first recovery event was recovered at the second recovery event, thus leading to a R_{r1} value above 100%.

Close examination of the strain evolution curve in Figure 1 revealed that, in the second strain ramping step from ε_1 to $\varepsilon_{2,load}$, the slop of the strain curve undergoes a sudden change. This is rather surprising as a single strain ramping rate was designated in the corresponding TMA method. In addition, this change appears to occur when the strain reaches a value close to the previous $\varepsilon_{1,load}$. To investigate whether such a correlation is a coincident or not, two experiments were conducted in which only the target value of $\varepsilon_{1,load}$ was varied from 60% to 40% and 80%, respectively. The results (shown in Figure 2a and 2b) confirm that, regardless of the $\varepsilon_{1,load}$, this abrupt slope change in the strain curve always occurs at a strain in the vicinity of the corresponding $\varepsilon_{1,load}$. An experiment was further carried out under conditions identical to Figure 1 except that T_{d1} was changed to 120 °C. The strain evolution curve (Figure 2c) shows again the same slope change at the $\varepsilon_{1,load}$. The above results imply that the instantaneously recovered strain (or nonfixed strain, $\varepsilon_{1,load} - \varepsilon_1$), while erased, shows a quantitative impact at a later stage. We refer to it a strain *history* memory effect. Such an effect is in sharp contrast to the traditional understanding of shape memory polymers, for which the recovered strain cannot be traced. Here, the entropy corresponding to the strain ($\varepsilon_{1,load} - \varepsilon_1$) was lost instantaneously upon load removal, but the contributing molecular segmental movement remained at an "activated" state mechanically. Surprisingly, this "activated" state appears to be thermally stable as the observed phenomenon did not diminish even when the isothermal holding time between ε_1 to $\varepsilon_{2,load}$ was increased from 5 min (Figure 2a) to 1 h (Figure 2d). Together with the tunable multishape memory and temperature memory effects recently reported,[21,35] this strain history memory effect suggests that that a polymer memory effect can be more broadly understood as a

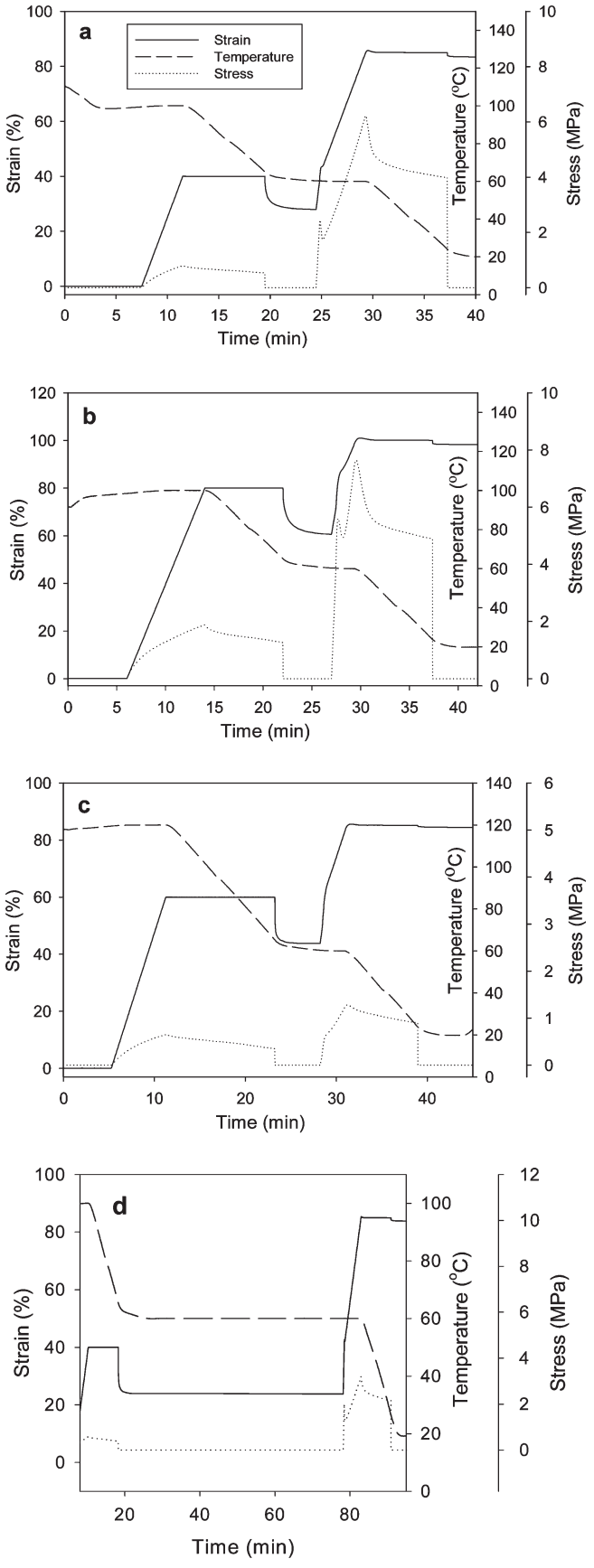

Figure 2. Thermo-mechanical curves for strain controlled programming (T_{d2} = 60 °C in all cases): (a) T_{d1} = 100 °C, $\varepsilon_{1,load}$ = 40%, $\varepsilon_{2,load}$ = 85%; (b) T_{d1} = 100 °C, $\varepsilon_{1,load}$ = 80%, $\varepsilon_{2,load}$ = 100%; (c) T_{d1} = 120 °C, $\varepsilon_{1,load}$ = 60%, $\varepsilon_{2,load}$ = 85%; (d) condition same as part a except the isothermal holding time (1 h).

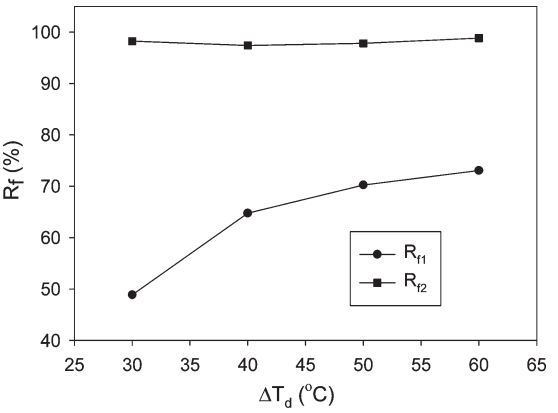

Figure 3. Effect of ΔT_d on R_fs. In all cases, T_{d2} = 60 °C and $\varepsilon_{1,load}$ = 60%.

thermo-mechanical memory effect rather than just strain (or shape) memory. On a broader basis, the strain history effect uncovered above implies that the thermo-mechanical history of a polymer could have a *hidden* effect on its thermo-mechanical properties.

Under various experimental conditions studied, R_{r1} and R_{r2} for Nafion were generally close to 100%, but the difference between the two T_d's (ΔT_d) had a strong impact on R_{f1}.[21] Under the stress controlled programming conditions previously used in our previous work,[21] it was difficult to reach the same $\varepsilon_{1,load}$ for different experiments, we thus did not attempt to quantify the impact of ΔT_d on R_{f1} due to this uncertainty. The strain controlled programming method currently employed allows quantification of such an impact at the same $\varepsilon_{1,load}$ value. The results (Figure 3) show that, whereas R_{f2} is independent of ΔT_d and generally above 95%, R_{f1} has a strong dependence on ΔT_d. Specifically, R_{f1} is around 50% for ΔT_d of 30 °C and increased gradually to 70% for ΔT_d of 60 °C (Figure 3). This trend can be explained by an analogy we used to explain the tunable multishape memory effect. On the basis of such an analogy, Nafion's broad thermal transition can be viewed as the collective contribution of an infinite number of transitions, which can be further considered as individual memory elements corresponding to infinitely sharp transition temperatures continuously distributed across the broad transition. Using this analogy, if the ΔT_d is higher, a higher population of memory elements is "frozen" upon cooling, yet the number of "non-frozen" memory elements remains the same since T_{d2} is identical. The frozen memory elements act against the nonfrozen memory elements to fix the strain. Consequently, a higher ΔT_d leads to a higher R_{f1} value. Here, we note that the dependence of R_{f1} on ΔT_d may also be attributed to T_{d1}, the change of which led to different ΔT_d values in the series of the experiments summarized in Figure 3.

For comparison purposes, two triple-shape memory cycles were obtained under a stress controlled condition (Figure 4). Here, T_{d1}'s for Figures 4a and 4b are 100 and 140 °C, respectively, whereas T_{d2}'s are kept identical at 60 °C. In these stress controlled experiments, the deformation stress was applied at the target deformation temperature (T_{d1}). While the stress was held constant during cooling, strain continued to increase during cooling (i.e., creep). In other words, the strain was actually introduced across a temperature range instead of at a single temperature in a strain controlled programming. The creep upon cooling led to strain development at temperatures lower than the designated T_d, which would be recovered at lower temperatures during the corresponding recovery step(s). Here, noticeable levels of creep are observed in the first deformation steps in both Figures 4a and 4b, but not in their second deformation steps. Relatively speaking, the creep in Figure 4b is much more pronounced than Figure 4a.

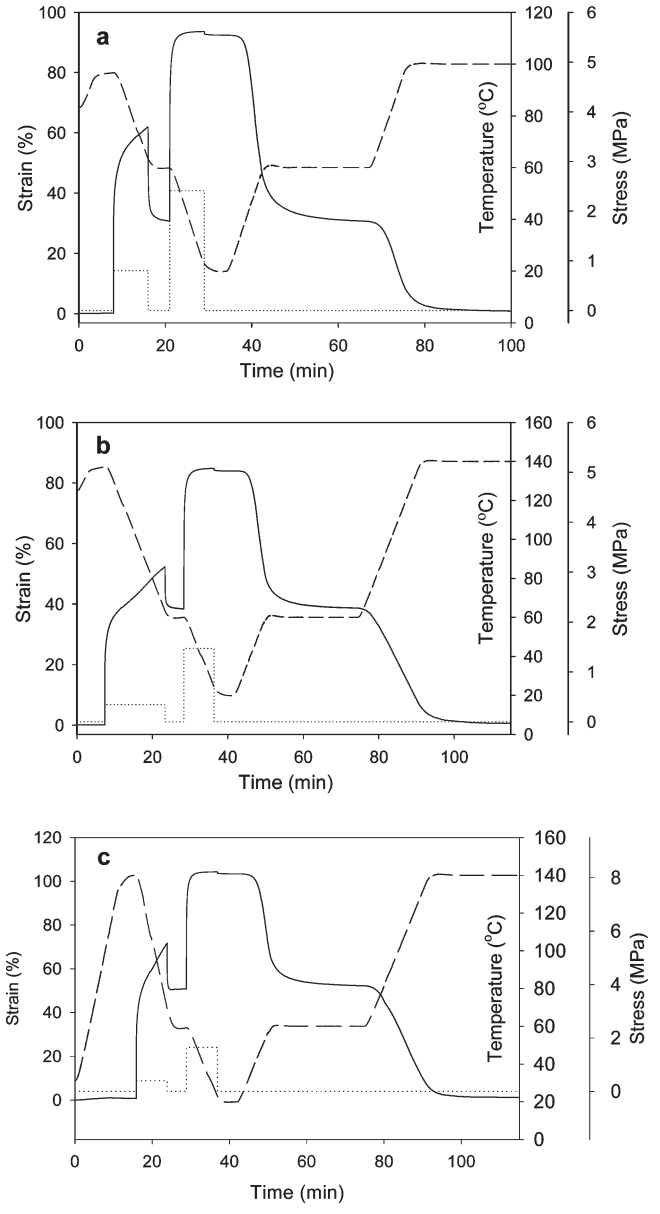

Figure 4. Triple-shape memory cycle obtained under stress controlled programming and staged heating recovery conditions. (a) $T_{d1} = T_{r2} = 100\,°C$, $T_{d2} = T_{r1} = 60\,°C$; (b) $T_{d1} = T_{r2} = 140\,°C$, $T_{d2} = T_{r1} = 60\,°C$. (c) Conditions similar to part b except that a faster cooling rate of 10 °C/min was used in the first fixing step. Key: solid lines, strain; dotted lines, stress; dashed lines, temperature.

The creep upon cooling leads to the much broader second shape recovery event in Figure 4b, when compared to the first recovery in the same figure or the second shape recovery in Figure 4a. The extent of creep upon cooling was reduced to 34% of the total $\varepsilon_{1,load}$ when a faster cooling rate of 10 °C/min was employed (Figure 4c), compared to 40% for a cooling rate of 5 °C/min (Figure 4b).

The above stress controlled programming was widely utilized by different groups.[21−25,29] For our own amorphous epoxy based triple-shape memory systems reported earlier, however, the creep upon cooling under the constant load is rather minimal, if any.[23] This is due to the very tightly cross-linked nature of the epoxy network that resists the creep. Consequently, the selection of the programming method is unimportant for such a system. The triple-shape systems by Lendlein et al are lightly cross-linked networks comprising of at least one crystalline phase.[22,24,25] Under a constant stress, a crystalline phase is known to undergo rearrangement upon temperature changes, leading to significant strain change. In fact, such is the basis for the two way shape memory effect for semicrystalline polymers.[26,36] As for the triple-shape memory effect discussed here, significant strain changes upon cooling were indeed observed in the semicrystalline based triple-shape systems.[22,25] Consequently, we anticipate that the choice of the programming method would affect the recovery behavior for such systems, although the exact impact has yet to be reported. Nevertheless, the comparison between Nafion and our previously reported epoxy system is sufficient to conclude that the selection of the programming method may significantly affect the multi-recovery behavior, depending on the specific molecular structures.

Here, we should note that the isothermal and stress free holding between the two programming steps (Figures 1 and 4) is sometimes omitted in the literature. Regardless of the programming methods, this step is necessary to determine ε_1, which is a critical parameter in the complete quantification of the triple-shape performance (eqs 1−4).

In the context of different programming methods for the triple-shape memory effect, the so-called one-step programming process should also be mentioned. It refers specifically to the phenomenon that only one programming step is needed for a multishape capable polymer to exhibit multiple shape recovery events upon heating.[21,24] Fundamentally, the multiple recovery events arise from the fact that a single strain introduced at a high temperature in a one-step programming process is in fact differentiated as multiple strains occurring to different memory elements in Nafion[21] or two distinct phases in other polymers.[24,25] Notably, the examples of one-step programming multishape effect were all realized through stress control.[21,24,25] Under such a programming condition, if creep occurs, the memory elements corresponding to transition temperatures lower than the designated T_d (or the lower temperature phase) could sustain a larger share of the total strain. This could favor more strain recovery at lower temperatures, relative to a situation in which a strain controlled one-step programming is used.

As for the shape recovery, Figures 1 and 4 were both obtained by staged heating, which is a condition used for our triple-shape epoxy polymers[23] and the triple-shape poly(ester urethane) by Pretsch.[27] This staged heating method is analogous to the isothermal recovery condition for dual-shape memory polymers except that the two isothermal recovery events are needed for triple-shape memory polymers. Other triple-shape systems reported in the literature adopted a continuous heating method to evaluate triple-shape properties.[21,25,28,29] Whereas the distinction between the two heating methods for dual-shape memory polymers is typically overlooked, the difference in the recovery heating method for triple-shape polymers should be carefully considered. Here, two critical questions arise: is it possible that a polymer displays two separate recovery events under a staged heating condition, but not under a continuous heating condition? If the answer is yes, then the next question would be: could both heating methods be accepted in qualifying a triple-shape polymer? The answers to these questions may impact the very definition of a triple-shape polymer.

We believe that both the staged heating and continuous heating methods are valid methods for triple-shape evaluation. In fact, even for triple-shape polymer systems quantitatively evaluated under continuous heating recovery conditions, it appears that the actual visual demonstration of the triple-shape memory effect was carried out by "subsequent heating".[22,25] Presumably, this is due to the fact that, in a practical setting, it is easier to achieve staged heating than finely controlled continuous heating.

Fundamentally, however, the question on whether or not Nafion can display multiple recovery events by continuous heating remains interesting, given the fact that its triple-shape behavior rely on one broad thermal transition rather than two

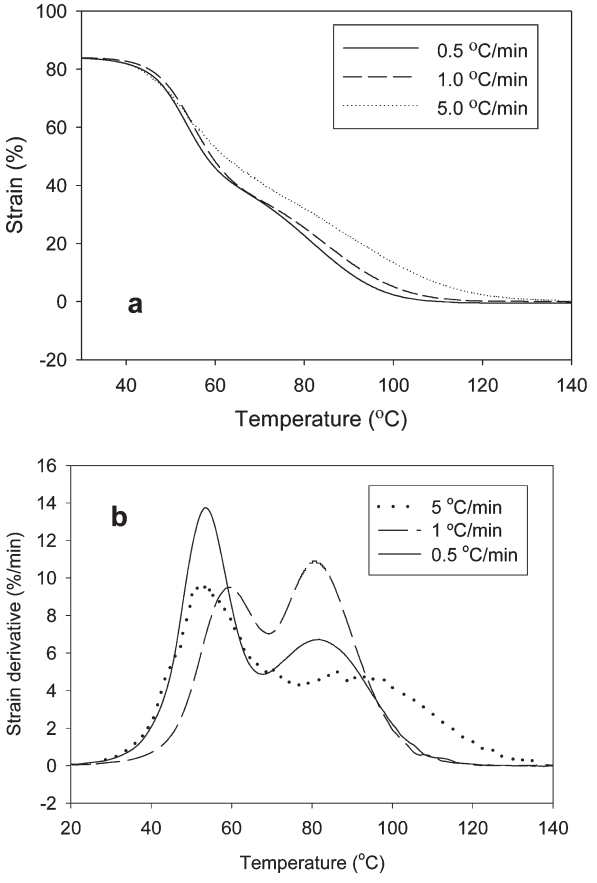

Figure 5. Strain recovery behavior under continuous heating conditions: (a) strain evolution; (b) strain derivative curve.

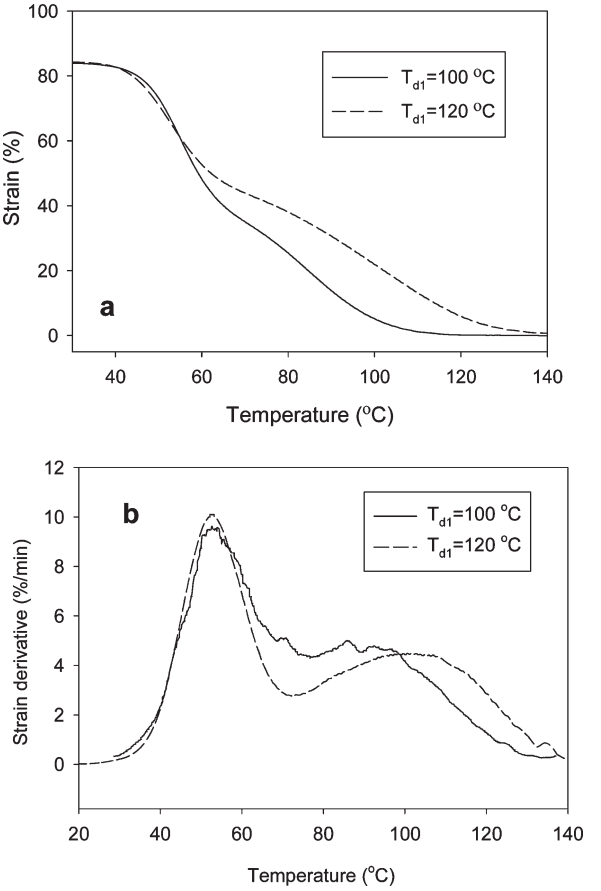

Figure 6. Comparison of shape recovery curves under continuous heating conditions for two deformation temperatures T_{d1}'s (all the other themomechanical conditions are identical to Figure 1). Key: (a) strain evolution; (b) strain derivative curve.

distinctive ones. A series of experiments were thus conducted in which the two programming steps were identical to Figure 1, but the subsequent recovery was performed by continuous heating at different heating rates. The corresponding recovery curves are shown in Figure 5a. At a heating rate of 5 °C/min, only vaguely separated two recovery events can be identified. Such a separation becomes much more evident when the heating rate is reduced to 1 °C/min. Further reduction of the heating rate to 0.5 °C/min yields only slight difference. Unlike Figures 1 and 4, no strain plateau is observed between the two recovery events in Figure 5a. We note that this is an issue that is applicable to all other known triple-shape memory polymer systems under continuous heating conditions. The existence of two recovery events is more clearly illustrated by plotting the strain derivatives (i.e., instantaneous recovery rate) against the temperature (Figure 5b). Two maxima are clearly visible regardless of the heating rate, although the relative peak height and positions do vary.

We believe that this dependence between the recovery behavior and the heating rate is linked to the recovery kinetics. At a high heating rate, the first recovery event does not have sufficient time to complete before the temperature raises high enough to trigger the next recovery event (i.e., recovery overlap). The relative separation between the recovery events is dependent on the overlap, which is reduced at a lower heating rate. Here, it is noteworthy that a heating rate of 1 °C/min was used for the shape recovery in the literature despite the fact that a faster temperature ramping rate of 5 °C/min was employed in all other stages in the same triple-shape cycles.[22,24,25] This seems to indicate a similar need for a low heating rate for those material systems.

Comparing the recovery curve in Figure 1 to those in Figure 5a, it is also evident that it is easier to obtain the plateau strain values using staged heating. This method is thus suitable for evaluating the maximum recovery capability. Recovery by continuous heating, on the other hand, is affected by both the maximum recovery capability and the recovery kinetics, the latter of which suggests heating rate dependence. In principle, the recovery overlap under a continuous heating condition may be reduced if the recovery events can be further distinguished. For a triple-shape polymer enabled by two distinct thermal transitions, one approach is to widen the difference between the two transition temperatures through material compositional tuning. For Nafion, owing to its tunable nature, this can be conveniently achieved by selecting two T_d's that are further apart (i.e., a larger ΔT_d). To verify this hypothesis, two triple-shape cycles were constructed under identical thermo-mechanical conditions except the T_{d1}. The corresponding recovery behaviors (Figures 6a and 6b) clearly show that the two recovery events obtained for the higher T_{d1} (thus greater ΔT_d) are indeed better separated.

As a separate but important note, we should point out that, despite its versatile shape memory properties, a significant limitation for Nafion lies in its poor processability. As a result, Nafion typically exists in thin film form, which prohibits its use as a bulk shape memory material. Nevertheless, the fact that Nafion's multishape memory properties arise from a single thermal transition suggests an alternative platform on which future more processable multishape memory polymers can be based.

Conclusion

We show in this study that the impact of various thermomechanical conditions on the polymer triple-shape memory effect is much more complex than for the more conventional dual-shape

memory effect. While material chemistry (two distinct thermal transitions versus a single broad transition) is critical, the thermo-mechanical treatment is just as important in determining polymer triple-shape functions. Here, the material chemistry provides the basis, whereas significant variations in memory functions can be expected by selecting the appropriate thermo-mechanical treatment. In particular, the choices of the programming method (stress versus strain controlled) and recovery heating method (staged versus continuous heating) were found to greatly affect the evaluation of triple-shape polymers. The results further support that staged and continuous heating are both valid methods for triple-shape evaluation. The staged heating method allows better evaluation of the equilibrium recovery behavior. Recovery behavior under a continuous heating condition may strongly depend on the recovery kinetics and a low heating rate is thus preferred to realize the multiple recovery events. Overall, this study suggests that, relative to the conventional dual-shape memory properties, greater care should be taken to achieve and/or evaluate triple-shape performance.

Acknowledgment. The authors thank Prof. Patrick Mather at Syracuse University for his comments on the relevance of the different recovery heating methods for triple-shape polymers.

References and Notes

(1) Mather, P. T.; Luo, X.; Rousseau, I. A. *Annu. Rev. Mater. Res.* **2009**, *39*, 445.
(2) Lendlein, A.; Kelch, S. *Angew. Chem., Int. Ed.* **2002**, *41*, 2034.
(3) Liu, C.; Qin, H.; Mather, P. T. *J. Mater. Chem.* **2007**, *17*, 1543.
(4) Xie, T.; Rousseau, I. A. *Polymer* **2009**, *50*, 1852.
(5) Ratna, D.; Karger-Kocsis, J. *J. Mater. Sci.* **2008**, *43*, 254.
(6) Koerner, H.; Price, G.; Pearce, N.; Alexander, M.; Vaia, R. *Nat. Mater.* **2004**, *3*, 115.
(7) Lendlein, A.; Jiang, H.; Junger, O.; Langer, R. *Nature* **2005**, *434*, 879.
(8) Rousseau, I. A. *Polym. Eng. Sci.* **2008**, *48*, 2075.
(9) Weiss, R.; Izzo, E.; Mandelbaum, S. *Macromolecules* **2008**, *41*, 2978.
(10) Li, J.; Viveros., J. A.; Wrue, M. H.; Anthamatten, M. *Adv. Mater.* **2007**, *19*, 2851.
(11) Lendlein, A.; Langer, R. *Science* **2002**, *296*, 1673.
(12) Xie, T.; Xiao, X. *Chem. Mater.* **2008**, *20*, 2866.
(13) Xiao, X.; Xie, T.; Cheng, Y. T. *J. Mater. Chem.* **2010**, *20*, 3508.
(14) Gall, K.; Kreiner, P.; Turner, D.; Hulse, M. *J. MEMS.* **2004**, *13*, 472.
(15) Wang, R.; Xie, T. *Langmuir* **2010**, *26*, 2999.
(16) Wang, R.; Xie, T. *Chem. Commun.* **2010**, *46*, 1341.
(17) Wang, R.; Xiao, X.; Xie, T. *Macromol. Rapid Commun.* **2010**, *31*, 295.
(18) Kunzelman, J.; Chung, T.; Mather, P. T.; Weder, C. *J. Mater. Chem.* **2008**, *18*, 1082.
(19) Kim, S.; Sitti, M.; Xie, T.; Xiao, X. *Soft Matter* **2009**, *5*, 3689.
(20) Hu, J. *Shape memory polymers and textiles*; CRC Press, Woodhead Publishing Limited: Boca Raton FL, Boston, MA, New York, and Washington, DC, 2007.
(21) Xie, T. *Nature* **2010**, *464*, 267.
(22) Bellin, I.; Kelch, S.; Langer, R.; Lendlein, A. *Proc. Natl. Acad. Sci. U.S.A.* **2006**, *103*, 18043.
(23) Xie, T.; Xiao, X.; Cheng, Y. T. *Macromol. Rapid Commun.* **2009**, *30*, 1823.
(24) Behl, M.; Bellin, I.; Kelch, S.; Wagermaier, W.; Lendlein, A. *Adv. Func. Mater.* **2009**, *19*, 102.
(25) Behl, M.; Lendlein, A. *J. Mater. Chem.* **2010**, *20*, 3335.
(26) Zotzmann, J.; Behl, M.; Hofmann, D.; Lendlein, A. *Adv. Mater.* **2010**, *22*, 3424.
(27) Pretsch, T. *Smart Mater. Struct.* **2010**, *19*, 015006.
(28) Kolesov, I. S.; Radusch, H. J. *eXPRESS Polymer Lett.* **2008**, *2*, 461.
(29) Luo, X.; Mather, P. T. *Adv. Funct. Mater.* **2010**, *20*, 2649.
(30) Rousseau, I. A.; Xie, T. *J. Mater. Chem.* **2010**, *20*, 3431.
(31) Yakacki, C. M.; Willis, S.; Luders, C.; Gall, K. *Adv. Eng. Mater.* **2008**, *10*, 112.
(32) Gall, K.; et al. *J. Biomed. Mater. Res. A* **2005**, *73A*, 339.
(33) Yakacki, C. M.; et al. *Biomaterials* **2007**, *28*, 2255.
(34) Wong, Y. S.; Venkatraman, S. S. *Acta Mater.* **2010**, *58*, 49.
(35) Miaudet, P.; et al. *Science* **2007**, *318*, 1294.
(36) Chung, T.; Rorno-Uribe, A.; Mather, P. T. *Macromolecules* **2008**, *41*, 184.